

IN SITU U–PB GEOCHRONOLOGY OF HYDROTHERMAL XENOTIME AND MONAZITE TO DATE GOLD MINERALIZATION IN THE NORTHERN CAPRICORN OROGEN, WESTERN AUSTRALIA

by
IOH Fielding





Government of **Western Australia**
Department of **Mines, Industry Regulation and Safety**

REPORT 194

IN SITU U–PB GEOCHRONOLOGY OF HYDROTHERMAL XENOTIME AND MONAZITE TO DATE GOLD MINERALIZATION IN THE NORTHERN CAPRICORN OROGEN, WESTERN AUSTRALIA

by
IOH Fielding

PERTH 2019



**Geological Survey of
Western Australia**

MINISTER FOR MINES AND PETROLEUM
Hon Bill Johnston MLA

DIRECTOR GENERAL, DEPARTMENT OF MINES, INDUSTRY REGULATION AND SAFETY
David Smith

EXECUTIVE DIRECTOR, GEOLOGICAL SURVEY AND RESOURCE STRATEGY
Jeff Haworth

REFERENCE

The recommended reference for this publication is:

Fielding, IOH 2019, In situ U–Pb geochronology of hydrothermal xenotime and monazite to date gold mineralization in the northern Capricorn Orogen, Western Australia: Geological Survey of Western Australia, Report 194, 304p.

ISBN 978-1-74168-841-2

ISSN 1834-2280



A catalogue record for this book is available from the National Library of Australia

Grid references in this publication refer to the Geocentric Datum of Australia 1994 (GDA94). Locations mentioned in the text are referenced using Map Grid Australia (MGA) coordinates, Zone 50. All locations are quoted to at least the nearest 100 m.



Curtin University



LP130100922

Australian Government

Australian Research Council

About this publication

This Report is a PhD thesis researched, written and compiled as part of an ongoing collaborative project between the Geological Survey of Western Australia (GSWA) and Curtin University. Although GSWA has provided field support for this project, the scientific content of the Report, and the drafting of figures, was the responsibility of the author. No editing has been undertaken by GSWA.

Disclaimer

This product was produced using information from various sources. The Department of Mines, Industry Regulation and Safety (DMIRS) and the State cannot guarantee the accuracy, currency or completeness of the information. Neither the department nor the State of Western Australia nor any employee or agent of the department shall be responsible or liable for any loss, damage or injury arising from the use of or reliance on any information, data or advice (including incomplete, out of date, incorrect, inaccurate or misleading information, data or advice) expressed or implied in, or coming from, this publication or incorporated into it by reference, by any person whatsoever.

Published 2019 by the Geological Survey of Western Australia

This Report is published in digital format (PDF) and is available online at <www.dmp.wa.gov.au/GSWApublications>.



© State of Western Australia (Department of Mines, Industry Regulation and Safety) 2019

With the exception of the Western Australian Coat of Arms and other logos, and where otherwise noted, these data are provided under a Creative Commons Attribution 4.0 International Licence. (<http://creativecommons.org/licenses/by/4.0/legalcode>)

Further details of geological publications and maps are available from:

Information Centre
Department of Mines, Industry Regulation and Safety
100 Plain Street
EAST PERTH WESTERN AUSTRALIA 6004
Telephone: +61 8 9222 3459 Facsimile: +61 8 9222 3444
www.dmp.wa.gov.au/GSWApublications

Cover photograph: Ashburton Basin looking to the southeast towards Mount De Courcy

**Faculty of Science and Engineering
Department of Applied Geology**

**In Situ U–Pb Geochronology of Hydrothermal Xenotime and
Monazite to Date Gold Mineralization in the Northern Capricorn
Orogen, Western Australia**

Imogen Olivia Heather Fielding

**This thesis is presented for the Degree of
Doctor of Philosophy
of
Curtin University**

May 2018

DECLARATION

To the best of my knowledge and belief this thesis contains no material previously published by any other person except where due acknowledgment had been made. This thesis contains no material that has been accepted for the award of any other degree or diploma in any university.

The author acknowledges that copyright of published works contained within this thesis resides with the copyright holder(s) of those works. I warrant that I have obtained, where necessary, permission from the copyright owners to use any third-party copyright material reproduced in the thesis (e.g. questionnaires, artwork, unpublished letters), or to use any of my own published work (e.g. journal articles) in which the copyright is held by another party (e.g. publisher, co-author).



Date: 30/04/2018

Imogen Olivia Heather Fielding

ABSTRACT

In situ geochronology of the phosphate minerals, monazite and xenotime, has proven to be a robust method for dating gold mineralization and low-temperature hydrothermal fluid flow events. Their resistance to isotopic resetting makes them ideal chronometers for assessing the low-temperature history of Proterozoic orogens with a complex geological evolution consisting of multiple overprinting tectonic events. The timing of gold mineralization in such settings is often poorly constrained, however, it is imperative to understand the link between the timing of gold mineralization and crustal architecture in order to recognise regional-scale factors that affect successful exploration targeting.

The Proterozoic Capricorn Orogen of Western Australia has a long-lived and complex geological history comprising at least eight tectonic events spanning 1.6 billion years. The northern margin of the orogen is host to numerous gold deposits, including the Mount Olympus and Paulsens deposits with gold endowments of >1 Moz. A spatial relationship between gold occurrences and crustal-scale faults, and their ancillary structures, is evident from seismic imaging and geological mapping. Prior to this study the timing of gold formation and fault reactivation were poorly constrained, hampering production of effective models for exploration targeting. In situ phosphate geochronology of monazite and xenotime intergrown with ore stage alteration and sulfide minerals provides an age of mineralization and hydrothermal activity at five locations including the Paulsens, Belvedere, Mount Olympus and Star of the West gold deposits and the Amazon Shear Zone. At least three discrete episodes of gold mineralization at c. 2400, 1770 and 1680 Ma and two additional episodes of hydrothermal activity at c. 2260 and 1730 Ma have been identified.

Hydrothermal and mineralizing fluids migrated along pre-existing crustal-scale faults during episodes of fault reactivation. At c. 2400 Ma orogenic gold mineralization at Paulsens and hydrothermal xenotime growth near Belvedere is linked to uplift and erosion and widespread hydrothermal activity affecting the southern Pilbara margin. It is possible that this event redefines the onset of the 2215–2145 Ma Ophthalmia Orogeny. Hydrothermal xenotime near the Belvedere deposit is dated at c. 2260 Ma, and is probably associated with the Ophthalmia Orogeny during which the Pilbara Craton collided with the Glenburgh Terrane. Carlin-like gold mineralization at Mount

Olympus formed at c. 1770 Ma during the final stages of the 1820–1770 Ma intracratonic Capricorn Orogeny when a change from compressional stresses to dextral reactivation of the Nanjilgardy Fault occurred. At c. 1730 Ma monazite replaced florencite porphyroblasts in areas of high strain along the Hardey Fault at the Paulsens deposit, and hydrothermal xenotime growth along the Zoe Fault at the Mount Olympus deposit took place. These events are not related to gold mineralization or any known orogenic events; however, they are interpreted to represent a period of hydrothermal fluid flow along the Nanjilgardy Fault and its second order structures at this time. Finally, at c.1680 Ma gold mineralization at the Belvedere, Star of the West and Paulsens gold deposits and hydrothermal activity at Mount Olympus and the Amazon Shear Zone is linked to reactivation of the Nanjilgardy and Baring Downs Faults. This took place during the early stages of the intracratonic 1680–1620 Ma Mangaroon Orogeny, which, farther to the south, is characterised by high-temperature metamorphism in the Gascoyne Province. In the northern Capricorn Orogen and Pilbara Craton, this event is characterised by the reactivation of crustal-scale faults and widespread hydrothermal activity.

Results presented in this study demonstrate that in situ phosphate geochronology can reveal the low-temperature and mineralization history which may otherwise have remained unknown. The mineralization history of the northern Capricorn Orogen is much more complex than previously recognised with multiple over printing mineralization events related to hydrothermal fluid flow along crustal-scale faults and associated structures during discrete orogenic events.

ACKNOWLEDGMENTS

There are so many people who have been involved in my project that I would like to thank. Firstly, Grant Noble, if it was not for your support and all the sacrifices that you have made I could not have completed this PhD. Thank you for taking a job up north so that I could quit mine.

I would like to thank my supervisors, Birger Rasmussen, Simon Johnson, Jianwei Zi and Steve Sheppard, for their ongoing encouragement, support, advice and assistance over the past 3 years. Thank you for teaching me new techniques and always being available to answer my questions. Simon I am so glad that you told me about this PhD project. I have learnt so much from you both on field trips and back in the office. Birger allowing me to be a part of your research team has been such an amazing experience. Jianwei your help with phosphate geochronology, showing me how to use the SEM and make SHRIMP mounts has been fundamental in this project. Steve your help with developing ideas for paper and editing when it came time to write has been invaluable.

Other people who have played a vital role include Michael Wingate for assisting with the zircon geochronology. Daniel Dunkley and Janet Muhling, although you only been involved at the start of my project your help with my candidacy and the Paulsens manuscript was greatly appreciated. Sebastien Meffre and Ross Large for assistance with LA-ICP-MS images of pyrite.

Fieldwork would not have been possible without the logistical support of the Geological Survey of Western Australia, in particular Scott Jones for organising field crews, vehicles and scheduled calls. David Martin, Alan Thorne, and Simon Johnson for geological insight on the field trip and sharing some of your unlimited knowledge on the Capricorn Orogen. Umar Azad, Joshua Guillianse, Ray MacFarlane and John Oxnam for helping out on field trips and getting me from point A to B safely.

This thesis would not have been possible without funding and financial support provided by the Australian Research Council (LP130100922), the Exploration Incentive Scheme and Northern Star Resources Ltd. Acknowledgement goes to the Geological Survey of Western Australia and Northern Star Resources Ltd for permission to publish all documents pertaining to this thesis.

LIST OF PUBLICATIONS INCLUDED AS PART OF THE THESIS

This thesis comprises a series of research papers that were either published, accepted for publication or under review at the time of writing this document. The objectives and relationships amongst the different papers are described in the introductory chapter. All papers have statement of co-authorship, along with reprints of published papers in the Appendix 1.

The research papers included as a part of this thesis are listed below:

Fielding, I. O. H., Johnson, S. P., Zi, J.-W., Rasmussen, B., Muhling, J. R., Dunkley, D. J., Sheppard, S., Wingate, M. T. D., and Rogers, J. R., 2017, Using In Situ SHRIMP U-Pb Monazite and Xenotime Geochronology to Determine the Age of Orogenic Gold Mineralization: An Example from the Paulsens Mine, Southern Pilbara Craton: *Economic Geology*, v. 112, no. 5, p. 1205-1230. DOI <https://doi.org/10.5382/econgeo.2017.4507>

Fielding, I. O. H., Johnson, S. P., Zi, J. W., Sheppard, S., and Rasmussen, B., 2018, Neighbouring orogenic gold deposits may be the products of unrelated mineralizing events: *Ore Geology Reviews*, v. 95, p. 593-603. DOI <https://doi.org/10.1016/j.oregeorev.2018.03.011>

Fielding, I. O. H., Johnson, S. P., Meffre, S., Zi, J. W., Sheppard, S., Large, R. R., and Rasmussen, B., 2019, Linking gold mineralization to regional-scale drivers of mineral systems using in situ U-Pb geochronology and pyrite LA-ICP-MS element mapping: *Geoscience Frontiers*, v. 10, p. 89–105. DOI <https://doi.org/10.1016/j.gsf.2018.06.005>

Fielding, I. O. H., Johnson, S. P., Zi, J. W., and Rasmussen, B., U-Pb dating of fault reactivation and gold mineralization in the northern Capricorn Orogen, Western Australia: Under review in *Australian Journal of Earth Sciences* since 12th April, 2018.

Fielding, I. O. H., Johnson, S. P., Rasmussen, B., Sheppard, S., and Zi, J. W., Gold metallogeny of a Proterozoic orogen; the relationship between crustal architecture, fault reactivation and hydrothermal fluid flow: Under review in *Ore Geology Reviews* since 17th April, 2018.

Due to the nature of this thesis as a composite of peer-reviewed manuscripts, there is a degree of repetition throughout. Reference style in each chapter varies due to requirements of individual journals.

LIST OF ADDITIONAL PUBLICATIONS RELEVANT TO THE THESIS

- Fielding, I. O. H., Johnson, S. P., Rasmussen, B., Muhling, J. R., Dunkley, D. J., Zi, J.-W., Wingate, M. T. D., and Sheppard, S., 2016, Dating orogenic gold mineralization at the Paulsens deposit, Western Australia: Australian Earth Science Convention 2016: Adelaide, South Australia, p. 221.
- Fielding, I. O. H., Johnson, S. P., Rasmussen, B., Muhling, J. R., Dunkley, D. J., Zi, J.-W., Wingate, M. T. D., and Sheppard, S., 2016, Application of in situ SHRIMP U–Pb geochronology to orogenic gold exploration: 35th International Geological Congress: Cape Town, South Africa, Abstract 4339.
- Fielding, I. O. H., Johnson, S. P., Zi, J.-W., Rasmussen, B., Muhling, J. R., Dunkley, D. J., Sheppard, S., and Wingate, M. T. D., 2016, In situ SHRIMP geochronology of monazite and xenotime to date orogenic gold mineralization: *in* Thermochronology and Noble Gas Geochemistry and Geochronology Organization Workshop 2016, eds. Danišík, M., Jourdan, F., Talavera, C., and McInnes, B. I. A: TANG³O 2016: Perth, Western Australia, p. 7.
- Fielding, I. O. H., Johnson, S. P., Rogers, J. R., and Elliot, L. K., 2017, Paulsens gold deposit, *in* Australian Ore Deposits, The Australasian Institute of Mining and Metallurgy, Melbourne, pp. 405–410.
- Fielding, I. O. H., Johnson, S. P., Sheppard, S., Zi, J.-W., and Rasmussen, B., 2017, Gold metallogeny of the northern Capricorn Orogen: 2017 TIGeR Conference, Timescales of Geological Processes: Perth, Western Australia, p. 47.
- Fielding, I. O. H., Johnson, S. P., Zi, J.-W., Rasmussen, B., Muhling, J. R., Dunkley, D. J., Sheppard, S., and Wingate, M. T. D., 2017, In situ phosphate dating of orogenic gold mineralization at Paulsens mine, southern Pilbara, *in* GSWA 2017 extended abstracts: Geological Survey of Western Australia, Record 2017/2, 47p.
- Fielding, I. O. H., Zi, J.-W., Johnson, S. P., Sheppard, S., and Rasmussen, B., 2017, Linking multiple gold mineralizing events to reactivation of crustal-scale faults: *in* Geological Society of America Abstracts with Programs. Vol. 49, No. 6: GSA 2017 Annual Meeting: Seattle, Washington, USA, Abstract 304719.
- Fielding, I. O. H., Zi, J.-W., Johnson, S. P., Sheppard, S., and Rasmussen, B., 2017, Linking gold mineralization to tectonothermal events using in situ xenotime U–Pb geochronology: *in* Geological Society of America Abstracts with Programs. Vol. 49, No. 6: GSA 2017 Annual Meeting: Seattle, Washington, USA, Abstract 304845.
- Johnson, S. P., Fielding, I. O. H., Rasmussen, B., Zi, J.-W., Muhling, J. R., Wingate, M. T. D., and Sheppard, S., 2017, Metallogeny of the Capricorn Orogen, Western Australia: *in* Future Understanding of Tectonics, Ores, resources, Environment and Sustainability Abstract Volume, eds. Huizenga, J. M., Chang, Z., Spandler, C., Camuti, K., Corkeron, M., Roberts, E., Ford, A., Placek, C.,

and Parker. A: FUTORES II Conference 2017, Townsville, Queensland, Australia, p. 62.

Johnson, S. P., Tyler, I. M., Dentith, M. C., Kennett, B., Yuan, H., Fielding, I. O. H., Korhonen, F. J., Piña-Varas, P., Gessner, K., Korsch, R. J., Murdie, R. E., Blewett, R. S., Heinson, G., Rasmussen, B., and Hough, R. M., 2017, Linking deep crustal architecture to mineral systems, *in* Geological Society of America Abstracts with Programs. Vol. 49, No. 6: GSA 2017 Annual Meeting: Seattle, Washington, USA, Abstract 304800.

TABLE OF CONTENTS

Declaration	i
Abstract	ii
Acknowledgments	iv
List of Publications included as part of the thesis	v
List of additional publications relevant to the thesis	vi
Table of Contents	viii
List of Figures	xvi
List of Tables	xxvi
Chapter 1: INTRODUCTION	1
1.1 Background	1
1.2 Geological Setting	4
1.3 In Situ Phosphate Geochronology	6
1.3.1 Phosphate Geochronology	7
1.3.2 In Situ Geochronology	7
1.4 Project Aims	9
1.5 Methods and Approaches	9
1.5.1 Fieldwork and Sample Selection	10
1.5.2 Petrography	11
1.5.3 SHRIMP Geochronology	11
1.5.3.1 <i>Monazite</i>	12
1.5.3.2 <i>Xenotime</i>	13
1.5.4 LA-ICP-MS	14

1.6 Thesis Structure.....	14
1.7 References	16
Chapter 2: USING IN SITU SHRIMP U–PB MONAZITE AND XENOTIME GEOCHRONOLOGY TO DETERMINE THE AGE OF OROGENIC GOLD MINERALIZATION: AN EXAMPLE FROM THE PAULSENS MINE, SOUTHERN PILBARA CRATON.....	24
2.1 Abstract.....	25
2.2 Introduction.....	25
2.3 Geological Setting.....	28
2.4 Local Geology.....	30
2.5 Mineralization and Alteration.....	31
2.6 Styles of Gold Mineralization	35
2.7 Samples and Analytical Methods	35
2.8 Geochronology Results and Interpretation.....	37
2.8.1 Detrital Zircon.....	37
2.8.1.1 GSWA 209903 – Quartz sandstone, Hardey Formation.....	37
2.8.1.2 GSWA 209911 – Quartz sandstone, Hardey Formation.....	38
2.8.2 Baddeleyite.....	38
2.8.2.1 GSWA 209905 – Altered dolerite, Paulsens gabbro.....	38
2.8.3 Xenotime.....	39
2.8.3.1 GSWA 209907 – Auriferous quartz–sulfide vein	39
2.8.3.2 GSWA 209909B – Ankerite–quartz vein.....	41
2.8.4 Monazite.....	41

2.8.4.1	<i>GSWA 2099025 – Carbonaceous phyllites, Hardey Formation</i>	41
2.8.4.2	<i>GSWA 209909A – Altered dolerite, Paulsens gabbro</i>	43
2.8.4.3	<i>GSWA 209912 – Carbonaceous phyllites, Hardey Formation</i>	44
2.8.4.4	<i>GSWA 219512, 219513 and 219517 – Micaceous phyllites, Hardey Formation</i>	44
2.9	Discussion	46
2.9.1	Age of the Host Rocks	46
2.9.2	Timing of Hydrothermal Activity and Gold Mineralization	47
2.9.3	Relationship to Regional Orogenic Events	48
2.10	Conclusions	50
2.11	Acknowledgments	52
2.12	References	52
2.13	Supplementary Data	57
2.13.1	Analytical Methods	57
2.13.1.1	<i>U–Pb zircon geochronology</i>	57
2.13.1.2	<i>In situ U–Pb baddeleyite, monazite and xenotime geochronology</i>	58
2.13.1.3	<i>References</i>	59
2.13.2	Data Tables	61
Chapter 3: NEIGHBOURING OROGENIC GOLD DEPOSITS MAY BE THE PRODUCTS OF UNRELATED MINERALIZING EVENTS		78
3.1	Abstract	79

3.2 Introduction.....	79
3.3 Geological Setting.....	81
3.4 Local Geology	82
3.5 Deposit Description	84
3.6 Geochronology Methods	86
3.7 Sample Details and Results	87
3.7.1 Baddeleyite.....	87
3.7.1.1 GSWA 219544: <i>Belvedere dolerite</i>	87
3.7.2 Xenotime.....	88
3.7.2.1 GSWA 219549: <i>Auriferous quartz–carbonate–arsenopyrite vein</i>	88
3.7.2.2 GSWA 219551: <i>Auriferous quartz–carbonate–arsenopyrite vein</i>	89
3.7.2.3 GSWA 219539: <i>Crenulated muscovite schist</i>	90
3.8 Discussion	90
3.8.1 Host Rocks to Auriferous Quartz–Carbonate–Arsenopyrite Veins.....	90
3.8.2 Timing of Hydrothermal Activity and Gold Mineralization..	91
3.8.3 Comparison With the Paulsens Gold Deposit.....	91
3.8.4 Relationship of Mineralization to Regional Orogenic Events..	93
3.8.5 Implications for Exploration Targeting.....	94
3.9 Conclusions	95
3.10 Acknowledgments.....	95
3.11 References	96

3.12	Supplementary Data	101
3.12.1	Analytical Methods	101
3.12.2	References	102
3.12.3	Data Tables	103
Chapter 4:	LINKING GOLD MINERALIZATION TO REGIONAL-SCALE DRIVERS OF MINERAL SYSTEMS USING IN SITU U–PB GEOCHRONOLOGY AND PYRITE LA-ICP-MS	107
4.1	Abstract	108
4.2	Introduction	108
4.3	Geological Background	110
4.4	Deposit Description	111
4.5	Methods	112
4.5.1	LA-ICP-MS	112
4.5.2	Geochronology	113
4.6	Results	114
4.6.1	LA-ICP-MS	114
4.6.1.1	<i>Zoe Fault</i>	<i>114</i>
4.6.1.2	<i>Strata-bound mineralization</i>	<i>116</i>
4.6.2	Geochronology	119
4.6.2.1	<i>GSWA 219594: Zoe Fault mineralization</i>	<i>119</i>
4.6.2.2	<i>GSWA 209985: Strata-bound mineralization</i>	<i>120</i>
4.6.2.3	<i>GSWA 219959: Strata-bound mineralization</i>	<i>121</i>
4.6.2.4	<i>Pooled age data</i>	<i>122</i>
4.7	Discussion	123

4.7.1	Deposit Classification.....	123
4.7.2	Timing of Gold Mineralization.....	126
4.7.3	Setting of Mineralization.....	126
4.7.4	Regional-Scale Drivers to Mineral Systems.....	127
4.8	Conclusions.....	127
4.9	Acknowledgments.....	128
4.10	References.....	128
4.11	Supplementary Data.....	133
4.11.1	Data Tables.....	133
 Chapter 5: U–PB DATING OF FAULT REACTIVATION AND GOLD MINERALIZATION IN THE NORTHERN CAPRICORN OROGEN, WESTERN AUSTRALIA.....		138
5.1	Abstract.....	139
5.2	Introduction.....	139
5.3	Geological Setting.....	141
5.4	Regional Geology.....	141
5.5	Amazon Shear Zone.....	142
5.6	Start of the West Gold Deposit.....	144
5.6.1	Local Geology.....	144
5.6.2	Deposit Description.....	145
5.7	Geochronology Methods.....	147
5.8	Sample Details and Results.....	148
5.8.1	GSWA 219504: Calcite Vein.....	148
5.8.2	GSWA 219560: Gold-Mineralized Siltstone.....	148

5.9 Discussion	150
5.10 Conclusions	152
5.11 Acknowledgments	152
5.12 References	153
5.13 Supplementary Data	157
5.13.1 Data Tables	157
 Chapter 6: GOLD METALLOGENY OF A PROTEROZOIC OROGEN: THE RELATIONSHIP BETWEEN CRUSTAL ARCHITECTURE, FAULT REACTIVATION AND HYDROTHERMAL FLUID FLOW	 160
6.1 Abstract	161
6.2 Introduction	161
6.3 Geological Setting	164
6.3.1 Gascoyne Province	164
6.3.2 Northern Capricorn Orogen	166
6.3.3 Eastern Capricorn Basins	166
6.3.4 Edmund and Collier Basins	168
6.4 Crustal Architecture	168
6.5 Gold Mineralization in the Northern Capricorn Orogen	169
6.5.1 Paulsens	170
6.5.2 Mount Olympus	172
6.5.3 Belvedere	173
6.5.4 Star of the West	174
6.6 Discussion	175
6.6.1 Priming the Crust for Gold Mineralization	175

6.6.2 Implication for Mineral Systems.....	177
6.6.3 Exploration Targeting.....	180
6.7 Conclusions.....	181
6.8 Acknowledgments.....	181
6.9 References.....	181
Chapter 7: THESIS CONCLUSIONS.....	190
7.1 Future Research.....	192
7.2 References.....	193
Chapter 8: BIBLIOGRAPHY.....	194
APPENDIX 1.....	210
Appendix 1A.....	210
Appendix 1B.....	240
Appendix 1C.....	253
Appendix 1D.....	273
Appendix 1E.....	275

LIST OF FIGURES

Figure 1-1: Number of deposits found, metres drilled and exploration expenditures between 1985 to 2014 (Jennings and Schodde, 2016).....	1
Figure 1-2: A: Simplified geological map of the Capricorn Orogen in Western Australia, showing location of the seismic transect (red line) and the orogen boundaries (thick grey line). Abbreviations: GC = Gawler Craton, KC = Kimberley Craton, MI = Marymia Inlier, NAC = North Australian Craton, PC = Pilbara Craton, SAC = South Australian Craton, WAC = West Australian Craton, YC = Yilgarn Craton, YGC = Yarlalweelor Gneiss Complex. B: distribution of gold occurrences within the orogen with >1 Moz deposits shown as large symbols and dashed lines representing suture zones. C: pie chart and table showing the relative and estimated total mineral endowment (contained gold) for different parts of the orogen (after Johnson et al., 2017a).....	3
Figure 1-3: Cross section across the Capricorn Orogen showing seismic lines 10GA-CP1, 10GA-CP2 and 10GA-CP3, showing how mineralization is spatially associated with crustal-scale faults (Johnson et al., 2013).....	3
Figure 1-4: Time–space plot for the Capricorn Orogen. Abbreviations: AB, Ashburton Basin; BBZ, Boora Boora Zone; ESZ, Errabiddy Shear Zone; HFTB, Hamersley, Fortescue and Turee Creek basins; LZ, Limejuice Zone; ManZ, Mangaroon Zone; MooZ, Mooloo Zone; MutZ, Mutherbukin Zone; NT, Narryer Terrane; PC, Pilbara Craton; PCS, Petter Calc-silicate; PWd, Paradise Well diatexite PZ, Paradise Zone; QP, Quartpot Pelite; YC, Yilgarn Craton; YGC, Yarlalweelor Gneiss Complex (from Johnson et al., 2013).....	5
Figure 1-5: Summary of the in situ technique. Textural relationships are retained by drilling the mineral to be dated (and surrounding minerals) out of a polished thin section. By using in situ geochronology we can directly date phosphates and, hence, provide ages for hydrothermal activity and gold mineralization and link this back to what is observed at the outcrop.....	8
Figure 1-6: A) small (~10 µm) xenotime crystal intergrown with pyrite which contains visible gold (Vielreicher et al., 2015). B) Monazite aligned along a deformation fabric (Sheppard et al., 2007).....	9

Figure 1-7: Location of gold prospects studied as a part of this PhD project.....	10
Figure 2-1: Regional geological setting of the northern Capricorn Orogen, showing the location of the Paulsens gold mine. Abbreviations: GC, Gawler Craton; KC, Kimberley Craton; MI, Marymia Inlier; NAC, North Australian Craton; PC, Pilbara Craton; SAC, South Australian Craton; WAC, West Australian Craton; YC, Yilgarn Craton; YGC, Yarlalweelor Gneiss Complex (after Johnson et al., 2013).....	27
Figure 2-2: Geological map of the northwest corner of the Wyloo Inlier, showing the location of the Paulsens, Gabbro Offset and Paulsens East deposits. Coordinates are in metres (MGA94 zone 50).....	27
Figure 2-3: A: Lithostratigraphic column and chronology of events for units in the northern Capricorn Orogen. B: Lithostratigraphic column, ages, and depositional environments for the Fortescue Group (adapted from Thorne et al., 2011).....	29
Figure 2-4: Schematic vertical cross-section of the Paulsens deposit (adapted from Fielding and Stokes, 2014). Viewed southeast with no vertical exaggeration.....	32
Figure 2-5: A: Photograph of Paulsens Upper Zone mineralization, showing massive pyrite at the margin of the auriferous quartz–sulfide vein. B: Paulsens Lower Zone mineralization, showing laminated quartz–sulfide veins with abundant wall rock inclusions and stylolites parallel to the vein margin.....	32
Figure 2-6: A: Reflected light photomicrograph showing rounded blebs of native gold and chalcopyrite contained within pyrite (GSWA 209907). B: Reflected light photomicrograph showing brecciated pyrite with native gold, chalcopyrite and pyrrhotite along the fractures (GSWA 209907). C: Reflected light photomicrograph showing local remobilization of gold along a fracture in pyrite, the arrows highlight local remobilization of gold from the primary rounded blebs of gold (GSWA 209907). D: Scanning Electron Microscope backscattered electron image (SEM-BSE) showing a large monazite crystal with inclusions of muscovite from the alteration halo surrounding an auriferous quartz–sulfide vein at the Paulsens East deposit (GSWA 219517). Mineral abbreviations, Au, gold; cpy, chalcopyrite; mon, monazite; mu, muscovite; po, pyrrhotite; py, pyrite; qtz, quartz.....	34

Figure 2-7: Cathodoluminescence (CL) images of representative detrital zircon grains in Hardey Formation sandstone samples. A: Sample GSWA 209903, B: Sample GSWA 209911.....36

Figure 2-8: Probability density diagrams and histograms of zircon ages for A: sample GSWA 209903 (63 analyses of 63 zircons), B: sample GSWA 209911 (42 analyses of 42 zircons). Black curves include only data <5% discordant. C and D: Tera-Wasserburg concordia diagrams of U–Pb data for detrital zircons from samples GSWA 209903 and GSWA 209911. Dark grey ellipses indicate analyses comprising the youngest detrital age component; light grey ellipses are the remaining data <5% discordant, and dashed ellipses indicate data >5% discordant.....38

Figure 2-9: A: SEM-BSE image of euhedral baddeleyite crystals with altered rim of very fine-grained zircon (GSWA 209905). B: SEM-BSE image of florencite–monazite porphyroblast (GSWA 219512). C: Reflected light image of euhedral xenotime grains enclosed entirely within pyrite grains with analytical sites marked by dots showing c. 2400 Ma dates (GSWA 209907). D: SEM-BSE image of xenotime intergrown with pyrite (oval pits on the grain are SHRIMP analysis sites) revealing a c. 2400 Ma core surrounded by a c. 1680 Ma rim. Mineral abbreviation: bd, baddeleyite; fl, florencite; mon, monazite, mu, muscovite; py, pyrite; xt, xenotime; zr, zircon.....39

Figure 2-10: Tera-Wasserburg concordia diagrams of U–Pb data for baddeleyite, xenotime and monazite. A: Baddeleyite in gabbroic host rock to gold mineralization at the Gabbro Offset deposit (GSWA 209905). B: Xenotime in auriferous quartz-sulfide veins at the Gabbro Offset deposit (GSWA 209907). C: Xenotime in ankerite–quartz vein within the strongly altered Paulsens Gabbro at the Gabbro Offset deposit (GSWA 209909b). D: Monazite porphyroblasts in carbonaceous phyllites at Gabbro Offset deposit (GSWA 209902). E: Monazite in pervasively altered portion of the Paulsens gabbro at the Gabbro Offset deposit (GSWA 209909a). F: Monazite porphyroblasts in carbonaceous phyllites at the Gabbro Offset deposit (GSWA 209912). G: Monazite in micaceous phyllites surrounding gold mineralization at the Paulsens East deposit (GSWA 219513 and 219517). H: Monazite porphyroblasts in micaceous phyllites at the Paulsens East deposit (GSWA 219512 and 219513). Key: coloured ellipses (yellow, c. 2700 Ma dates; red, c. 2400 Ma dates; green, c. 1730 Ma dates; dark blue, c. 1680 Ma dates) show data used in the age calculations, unshaded

ellipses are for inferior data (pale blue, mixed ages; dashed ellipses, discordance >5%; red ellipses, outliers; black ellipses, high common Pb).....42

Figure 2-11: Summary diagram for all samples dated in this study. Known orogenic events are highlighted; showing that mineralization at Paulsens is not associated with either the Ophthalmia Orogeny or Capricorn Orogeny. A proposed cryptic orogenic event at c. 2400 Ma is highlighted in pink. Depositional age ranges for sedimentary basins are indicated by grey boxes, mafic intrusions as green and felsic volcanic rocks as orange. The number of analyses in each sample is marked next to the 95% error bars.....47

Figure 3-1: Location of the Capricorn Orogen in Western Australia, showing location of the Wyloo Inlier (dashed red ellipse) and inset location for Figure 3-2. Abbreviations: GC = Gawler Craton, KC = Kimberley Craton, MI = Marymia Inlier, NAC = North Australian Craton, PC = Pilbara Craton, SAC = South Australian Craton, WAC = West Australian Craton, YC = Yilgarn Craton, YGC = Yarlalweelor Gneiss Complex (after Johnson et al., 2013).....81

Figure 3-2: Geology map of the northern part of the Wyloo Inlier (courtesy of Northern Star Resources Ltd. Pty) showing the location of the Belvedere and Paulsens Deposits. Coordinates are in meters (MGA94 zone 50). Red box shows the location of Figure 3-3.....83

Figure 3-3: Local geology map of the Belvedere deposit showing location of the samples, Belvedere dolerite, mineralized quartz–carbonate–arsenopyrite veins and Belvedere and Hardey Faults. Coordinates are in meters (MGA94 zone 50).....83

Figure 3-4: Backscattered electron microscope (BSEM) images of accessory minerals from the Belvedere deposit. A) Native gold inclusions in arsenopyrite crystals (GSWA 219551). B) Euhedral baddeleyite crystal from the Belvedere dolerite surrounded by thin zircon fringes (GSWA 219544). C) Former crystals of baddeleyite from the Belvedere dolerite, which have been replaced by zircon with abundant very fine-grained inclusions (GSWA 219544). D) Anhedral xenotime crystal containing laths of ore-stage muscovite from quartz–carbonate–arsenopyrite veins (GSWA 219549). E) Anhedral xenotime crystal contained within auriferous arsenopyrite from quartz–carbonate–arsenopyrite veins (GSWA 219551). F) Elongate clusters of xenotime at

the margins of a quartz clast from crenulated schist that is locally cross cut by the Belvedere dolerite (GSWA 219539). Abbreviations: asp = arsenopyrite, Au = gold, bd = baddeleyite, chl = chlorite, ga = galena, mu = muscovite, qtz = quartz, xt = xenotime, and zr = zircon.....85

Figure 3-5: Tera-Wasserburg concordia diagrams of U–Pb data for baddeleyite and xenotime. A) Baddeleyite from the Belvedere dolerite (GSWA 219544). B) Xenotime containing laths of ore-stage muscovite within auriferous quartz-carbonate-sulfide vein (GSWA 219549), data with high common lead is not plotted; refer to Supplementary Table 3-2 for analysis details. C) Xenotime intergrown with ore-stage muscovite and auriferous arsenopyrite within auriferous quartz-carbonate-sulfide vein (GSWA 219551). D) Xenotime within a crenulated muscovite schist that is locally cross cut by the Belvedere dolerite (GSWA 219539). Key: Dark-coloured ellipses (green = c. 2080 Ma, red = c. 1680 Ma, blue = c. 2360 Ma, yellow = c. 2260 Ma) show data used in the age calculations; other ellipses are for inferior data (solid grey = young outliers, dashed ellipses = high common Pb, open black ellipses = discordant data). 88

Figure 3-6: Massive fine-grained dolerite dyke (~1 m wide) in the drive wall at the Paulsens gold deposit. The dolerite is part of the same north-trending suite of dykes as the Belvedere dolerite, dated here at c. 2080 Ma. These dykes cross cut and offset auriferous, laminated quartz veins from the Lower mineralized zone at the Paulsens deposit. Level 1095E, face 36 viewed to the southeast.....93

Figure 4-1: Regional geology of the northern Capricorn Orogen showing the location of Mount Olympus and Paulsens gold mines. White box indicates the inset map shown in Figure 4-2a. Abbreviations: GC = Gawler Craton, KC = Kimberley Craton, MI = Marymia Inlier, NAC = North Australian Craton, PC = Pilbara Craton, SAC = South Australian Craton, WAC = West Australian Craton, YC = Yilgarn Craton, YGC = Yarlalweelor Gneiss Complex (after Johnson et al., 2013).....110

Figure 4-2: A) Prospect scale geological map of the Mount Olympus pit showing geochronology sample locations. B) Schematic cross section of the Mount Olympus ore body with geochronology sample locations.....111

Figure 4-3: Textures of pyrite types at the Mount Olympus deposit. A) NMOD002 377.7 m depth showing py1 surrounding py2 and tetrahedrite. B) NMOD002 377.7 m

depth showing a narrow band of py1, py2 and carbonaceous material separating py2 from py3. C) NMOD002 376.2 m depth growth zoning in py3. D) NMOD002 376.2 m depth py1, py2 and large euhedral py4. E) Summary image showing the py1, py2 and tetrahedrite separated from py3 by a carbonaceous rich band. F) MOD13 130.6 m depth, showing large pyrite and arsenopyrite crystals from the strata-bound mineralization. Abbreviations py = pyrite, t = tetrahedrite, sbs – silicified black shale, q = quartz, c = carbonaceous material, apy = arsenopyrite.....115

Figure 4-4: LA-ICP-MS images of trace elements in pyrite from NMOD002 377.7 m depth showing py2 and tetrahedrite surrounded by a py1 (see Figure 4-3a). Py1 which is associated with elevated Au, As, Tl and Pb, py2 is slightly enriched in Au and As and tetrahedrite is enriched in Cu, Hg, Sb, Ag and Zn.....117

Figure 4-5: LA-ICP-MS images of trace elements in pyrite from NMOD002 376.2 m depth showing py4 with no trace element associations; py1 is enriched in Au, As, Tl, Pb, and py2 and tellurium are intergrown and enriched in Au, As, Cu, Hg, Sb, Ag and Zn (see Figure 4-3d).....117

Figure 4-6: LA-ICP-MS image of trace element from pyrite in NMOD002 377.7 m depth showing a narrow band of py1, py2 and carbonaceous material separating py2 from py3 (see Figure 4-3b). The carbonaceous band is enriched in Au, U, V, Mo and Al.....118

Figure 4-7: LA-ICP-MS image of trace elements from pyrite in NMOD002 376.2 m depth showing zoning in py3 with a core enriched in As, Hg, Sb and Pb, an internal band enriched in Au, As, Cu, Hg, Tl, Sb and Pb, and a rim zone associated with elevated Co and Ni.....118

Figure 4-8: LA-ICP-MS images of trace elements from pyrite in MOD13 130.6 m depth showing elevated As with a diffusive rim zone enriched in Au.....119

Figure 4-9: Scanning electron microscope-backscattered electron (SEM-BSE) images of dated xenotime crystals. White ellipses show analysis pits. Analysis pits with no ages represent discordant data. A) Xenotime overgrowth on zircon (GSWA 219594). B) Xenotime intergrown with muscovite and quartz from strata-bound mineralization (GSWA 909985). C) Xenotime encased in auriferous pyrite (GSWA 209985). D)

Xenotime with inclusions of rutile (GSWA 219595). Mineral abbreviations: gr-graphite, mu-muscovite, py-pyrite, qtz-quartz, rt-rutile, xt-xenotime and zr-zircon. 120

Figure 4-10: Tera-Wasserburg Concordia diagrams of U–Pb data for xenotime and probability density diagrams and histograms of xenotime ages for mineralized samples A and B: GSWA 219594 C and D: GSWA 209985 and E and F: GSWA 219595. Key for Concordia diagrams: colored ellipses (blue = ca. 1770 Ma, green = ca. 1730 Ma, red = ca. 1680 Ma) show data used in age calculations; other ellipses are for inferior data (unshaded black ellipses = >10% discordant data, dashed ellipses = poor spot placement). Probability density diagrams, red curve includes only data <10% discordant, colours used correspond to the Concordia diagrams. 121

Figure 4-11: Probability plots and histograms with 10 Ma bin width for hydrothermal xenotime. Upper panel contains data from the strata-bound ore zone (GSWA 209985 and 219595) and from the Zoe Fault (GSWA 209594). The lower panel contains data from Şener et al. (2005). Grey text indicates inferior data (poor spot placement or younger outliers). Weighted mean $^{207}\text{Pb}^*/^{206}\text{Pb}^*$ dates are reported with 95% confidence levels including data <10% discordant that contain $\leq 1\%$ common Pb. 122

Figure 4-12: Binary plots showing comparisons of trace element concentrations in pyrite between Carlin (Large et al., 2009) and Mount Olympus mineralization. A) Au-As; B) Au-Ni and C) Au-V. 125

Figure 5-1: Location of the Capricorn Orogen in Western Australia. The white ellipse shows the location of the Wyloo Inlier; white box is the inset location for Figure 5-2; yellow star represents the Star of the West gold deposit location; red line is the 10GA-CP1 seismic line. Abbreviations: GC = Gawler Craton, KC = Kimberley Craton, MI = Marymia Inlier, NAC = North Australian Craton, PC = Pilbara Craton, SAC = South Australian Craton, WAC = West Australian Craton, YC = Yilgarn Craton, YGC = Yarlalweelor Gneiss Complex (after Johnson et al., 2013). 140

Figure 5-2: Local geology map of the Amazon Shear Zone with sample location for GSWA 219504 and the location of the Belvedere and Paulsens Gold deposits which are associated with the Hardey Fault, a second order structure to the Nanjilgardy Fault. 140

Figure 5-3: Seismic line 10GA–CP1 showing major faults in the northern Capricorn Orogen (after Johnson et al., 2013). The yellow star represents the location of the Star of the West gold deposit.....142

Figure 5-4: Quartz veins in the Amazon Shear Zone. A) Pre-deformation quartz vein formed as boudins along the foliation. B) Syn-deformation calcite vein aligned in the foliation with weakly developed foliation in the vein. C) Post-deformation quartz-calcite vein slightly oblique to the foliation. D) Post-deformation quartz veins that are weakly boudinaged.....143

Figure 5-5: Star of the West local geology map, the mine symbol shows the location of the historical workings and sample site for GSWA 219560 (after Rolfe, 2012)....145

Figure 5-6: A) Alteration zone surrounding barren quartz vein at Star of the West gold deposit. Host rock comprises siltstone and sandstone with hydrothermal muscovite and oxidised, pyrite crystals. B) Back-scattered electron (BSE) image of xenotime containing laths of muscovite from the Star of the West ore zone. C) BSE image of oxidised pyrite from the Star of the West ore zone showing inclusions of monazite and gold surrounded by ore-stage muscovite alteration. D) Syn-deformational calcite vein formed along the Amazon Shear Zone that is sampled for geochronology (GSWA 219504). E) Cross-polarized light (XPL) image of curved twin planes in calcite from GSWA 219504. F) XPL image of euhedral xenotime interlocking with calcite crystals from sample GSWA 219504. G) BSE image of detrital xenotime sampled for geochronology from GSWA 219560. H) BSE image of detrital monazite sampled for geochronology (GSWA 219560). Abbreviations: Au = gold, mon = monazite, mu = muscovite, ox py = oxidised pyrite, zr = zircon.....146

Figure 5-7: Tera-Wasserburg concordia diagrams of U–Pb data for xenotime and monazite. A) Xenotime from a syn-deformational calcite vein in the Amazon Shear Zone (GSWA 219504). B) Xenotime containing laths of ore-stage muscovite within altered siltstone at the Star of the West gold deposit (GSWA 219560). C) Monazite in altered siltstone at the Star of the West gold deposit (GSWA 219560), data high in common lead are not plotted, refer to Supplementary Table 5 3 for analysis details. Key: coloured ellipses show data used in the age calculations (yellow = hydrothermal activity at c. 1670 Ma, red = c. 1670 Ma hydrothermal gold mineralization, blue = c.

1830 Ma detrital grains). All other ellipses are for inferior data (unshaded red = >10% discordant, black dashed = >1% common Pb).....149

Figure 6-1: A: Simplified geological map of the Capricorn Orogen in Western Australia, showing location of the seismic transect (red line) and the orogen boundaries (thick grey line). Abbreviations: GC = Gawler Craton, KC = Kimberley Craton, MI = Marymia Inlier, NAC = North Australian Craton, PC = Pilbara Craton, SAC = South Australian Craton, WAC = West Australian Craton, YC = Yilgarn Craton, YGC = Yarlalweelor Gneiss Complex. B: distribution of gold occurrences within the orogen with >1 Moz deposits shown as large symbols and dashed lines representing suture zones. C: pie chart and table showing the relative and estimated total mineral endowment (contained gold) for different parts of the orogen (after Johnson et al., 2017b).....163

Figure 6-2: Time-space plot of the Capricorn Orogen showing the timing of hydrothermal activity and gold mineralization and how it relates to the host rocks...165

Figure 6-3: Geological map of the northern Capricorn Orogen showing the location of the seismic line (10GA-CP1) and gold deposits.....168

Figure 6-4: Seismic transect showing major faults, stratigraphic interpretations, and gold deposits as yellow stars (Johnson et al., 2013).....169

Figure 6-5: Geological map of the northern part of the Wyloo Inlier showing the location of the Paulsens and Belvedere gold deposits (yellow stars), the Hardey and Nanjilgardy faults. Coordinates are in meters (MGA94 zone 50).....170

Figure 6-6: Schematic cross sections of the Paulsens ore deposit. View to the south with no vertical exaggeration.....171

Figure 6-7: A: Prospect scale geological map of the Mount Olympus deposit. B: Schematic cross section showing strata-bound and fault hosted gold mineralization in orange. Coordinates are in meters (MGA94 zone 50).....173

Figure 6-8: Local geology map of the Belvedere deposit showing the location of the Hardey and Belvedere faults and the Belvedere dolerite. Coordinates are in meters (MGA94 zone 50).....174

Figure 6-9: Local geology map of the Star of the West gold deposit. Coordinates are in meters (MGA94 zone 50).175

Figure 6-10: Summary histograms showing age peaks of gold mineralization at the Paulsens, Mount Olympus, Belvedere and Star of the West gold mines defined by xenotime. Known orogenic events are defined by blue shading = cryptic orogenic event at c. 2400, pink = collisional orogenies, grey = intracratonic orogenies.178

LIST OF TABLES

Table 2-1: List of sample locations and descriptions.....	36
Table 2-2: Summary of geochronology results.....	46
Table 3-1: SHRIMP operating parameters for all analytical sessions.....	87
Table 4-1: LA-ICP-MS sample location, descriptions and gold grades.....	112
Table 4-2: Summary of paragenetic sequence from py1 to py4.....	116
Table 4-3: Comparison between Orogenic, Carlin-type and Mount Olympus ores...	124
Table 5-1: SHRIMP operating parameters for all analytical sessions.....	147

CHAPTER 1. INTRODUCTION AND OVERVIEW

1.1. BACKGROUND

Gold is a significant economic driver of many developed and developing countries but despite continued high levels of funding for gold exploration, the rate of discovery has drastically fallen over the past decade (Figure 1-1; Groves and Santosh, 2015; Hronsky and Groves, 2008; Jennings and Schodde, 2016; McCuaig and Hronsky, 2014; McKeith et al., 2010). Elevated exploration costs can be partially explained by economic factors related to the recent mining boom including, increases in wages, operational cost and the cost of equipment hire (Jennings and Schodde, 2016). However, exploration practices have also played a critical role in the high discovery cost. Over the past decade a trend towards brownfields exploration with drilling focused around known deposits has led to lower grade, smaller sized discoveries with an overall high cost of discovery (McKeith et al., 2010). While these methods have their merits, the odds for exploration success can be vastly improved by understanding the large-scale controlling factors that affect the distribution and occurrences of gold within a region (Hronsky et al., 2012; McCuaig et al., 2010; Huston et al., 2010, 2016).

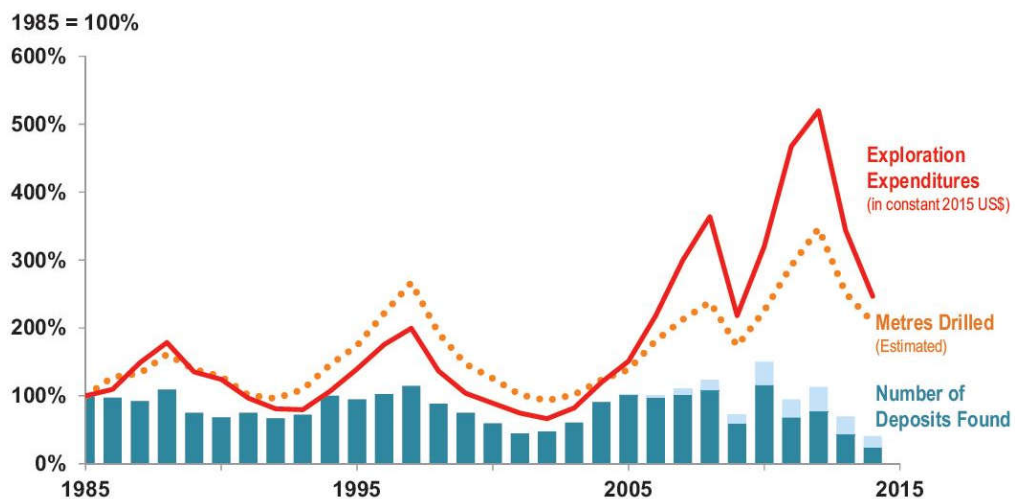


Figure 1-1: Number of deposits found, metres drilled and exploration expenditures between 1985 to 2014 (Jennings and Schodde, 2016)

Determining how gold mineralization relates to the regional-scale tectonothermal evolution of a given region is fundamental for effective exploration targeting (e.g. Rasmussen et al., 2006). This is particularly important in Proterozoic orogens as they

commonly have complex geological histories derived from multiple overprinting tectonic events (Johnson et al., 2017a; Raimondo et al., 2010). Such areas commonly lack a detailed chronology for the timing of gold mineralization. Dating hydrothermal gold mineralization in these settings can be challenging as many common chronometers (e.g. zircon, Re-Os dating of molybdenite) are reset during hydrothermal activity postdating the ore formation events (Chesley, 1999; Vielreicher et al., 2003).

The Proterozoic Capricorn Orogen in Western Australia is a major zone of deformation, metamorphism and magmatism between the Yilgarn and Pilbara cratons (Figure 1-2; Cawood and Tyler, 2004; Tyler and Thorne, 1990). It is the product of at least eight tectonic events spanning over 1.6 billion years, including intracratonic reworking and basin formation (Johnson et al., 2011a, 2013; Martin and Morris, 2010; Sheppard et al., 2010). The northern part of the Capricorn Orogen hosts numerous gold deposits, including the Mount Olympus and Paulsens deposits (Figure 1-2b) both with gold endowments of >1 million ounces (Northern Star Resources Limited, 2013, July, 2015, January, 2016). However, despite the area's economic significance, there has been limited research relating to the timing and setting of the gold occurrences, which has hampered models for mineralization and exploration targeting. A deep-crustal seismic reflection survey across the orogen has provided new insights into the crustal architecture (Figure 1-3; Johnson et al., 2013), and provided the impetus for renewed geological investigations. The seismic imaging demonstrated a spatial link between crustal-scale faults and gold distribution across the northern Capricorn Orogen (Johnson et al., 2013).

Since many of the known gold occurrences in the northern Capricorn Orogen cluster around major crustal-scale faults (Figure 1-3; Johnson et al., 2013), it is imperative to understand the timing, tectonic and structural setting for mineralization, as well as to identify the location, style and reactivation history of any trans-lithospheric structures that may have served as the principal fluid conduits. In this PhD study, I address the absolute timing of gold mineralization at several of the key gold prospects throughout the northern Capricorn Orogen. This project is the first field-based, multi-mineral geochronological study to address the low-temperature tectonothermal history of the northern Capricorn Orogen in relation to gold mineralization. In situ analysis of xenotime, monazite and baddeleyite, and traditional techniques involving zircon separates were carried out using the sensitive high-resolution ion micro-probe

(SHRIMP) housed at Curtin University. This information has been used to establish the regional-scale controls and distribution of the gold mineralization across the northern part of the Capricorn Orogen throughout both space and time.

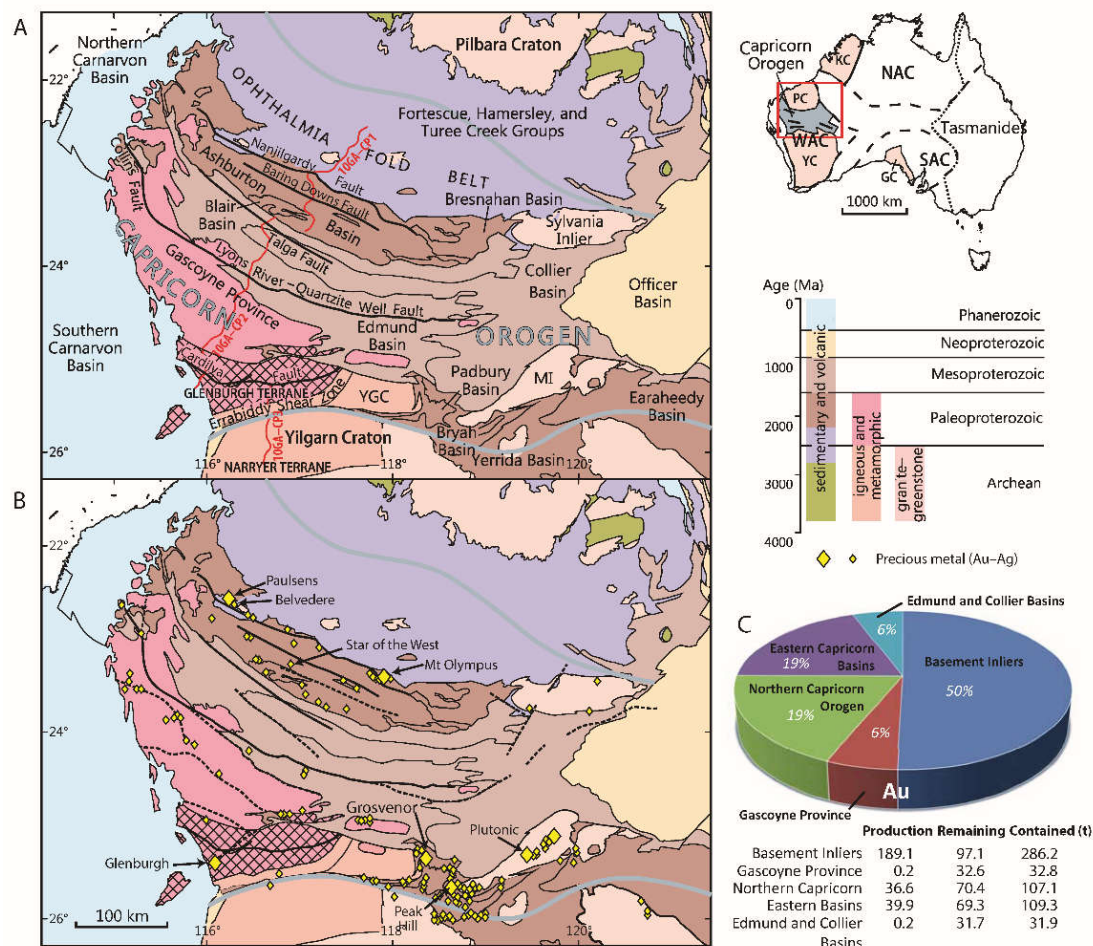


Figure 1-2: A: Simplified geological map of the Capricorn Orogen in Western Australia, showing location of the seismic transect (red line) and the orogen boundaries (thick grey line). Abbreviations: GC = Gawler Craton, KC = Kimberley Craton, MI = Marymia Inlier, NAC = North Australian Craton, PC = Pilbara Craton, SAC = South Australian Craton, WAC = West Australian Craton, YC = Yilgarn Craton, YGC = Yarlalweelor Gneiss Complex. B: distribution of gold occurrences within the orogen with >1 Moz deposits shown as large symbols and dashed lines representing suture zones. C: pie chart and table showing the relative and estimated total mineral endowment (contained gold) for different parts of the orogen (after Johnson et al., 2017b).

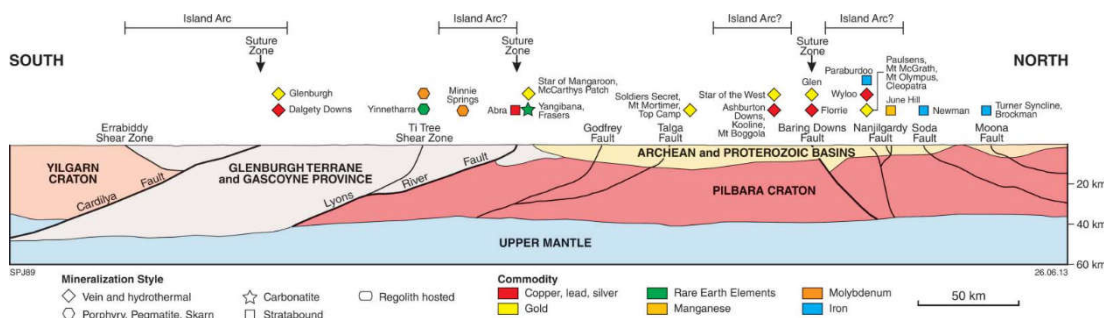


Figure 1-3: Cross section across the Capricorn Orogen showing seismic lines 10GA-CP1, 10GA-CP2 and 10GA-CP3, showing how mineralization is spatially associated with crustal-scale faults (Johnson et al., 2013).

1.2. GEOLOGICAL SETTING

This thesis is prepared as a series of peer-reviewed journal articles including 3 published and 2 under review at the time of writing this document. A brief summary of the geological setting is provided in order to give background information pertinent to the project design.

Research over the past ~20 years has resulted in a well-established tectonothermal evolution for the central and southern parts of the Capricorn Orogen, in particular for the high-grade core of the orogen, the Gascoyne Province (Cawood and Tyler, 2004; Johnson et al., 2011a, 2013, 2017a; Korhonen and Johnson, 2015; Korhonen et al., 2017; Martin and Thorne, 2004; Martin et al., 2008; Occhipinti et al., 1998, 2004; Occhipinti and Reddy, 2009; Sheppard et al., 2003, 2004, 2005, 2007, 2016). The high-temperature evolution has been defined by SHRIMP U–Pb zircon geochronology (Johnson et al., 2011a; Kinny et al., 2004; Occhipinti et al., 1998; Sheppard et al., 2004, 2005) and detailed P–T–t work (Johnson et al., 2010; Korhonen and Johnson, 2015; Korhonen et al., 2017; Sheppard et al., 2007). The low-temperature and hydrothermal evolution is defined mostly by in situ SHRIMP U–Pb dating of the phosphate minerals monazite and xenotime (Rasmussen et al., 2005, 2007a, 2007b; Sheppard et al., 2010; Zi et al., 2015) including the timing of base metal mineralization in the central and eastern part of the orogen (Zi et al., 2015).

The Proterozoic Capricorn Orogen has a complex and long-lived tectonic history involving two stages of continental collision followed by six episodes of intracratonic reworking and reactivation (Johnson et al., 2011a, 2013; Sheppard et al., 2010). Collisional events include the 2215–2145 Ma Ophthalmia Orogeny (Johnson et al., 2011a; Rasmussen et al., 2005), during which the Pilbara Craton and Glenburgh Terrane collided (Johnson et al., 2011a, 2017a; Occhipinti et al., 2004), followed by the 2005–1950 Ma Glenburgh Orogeny where the combined Pilbara Craton — Glenburgh Terrane collided with the Yilgarn Craton marking the assembly of the West Australian Craton (Johnson et al., 2011a; Occhipinti et al., 2004; Sheppard et al., 2004). Following the assembly of the West Australian Craton, the orogen was subject to over a billion years of intracratonic reworking and reactivation (Figure 1-4) during the 1820–1770 Ma Capricorn Orogeny (Johnson et al., 2017a; Sheppard et al., 2010), the 1680–1620 Ma Mangaroon Orogeny (Johnson et al., 2017a; Sheppard et al., 2005),

the 1321–1171 Ma Mutherbukin Tectonic Event (Korhonen et al., 2017), the 1030–955 Ma Edmundian Orogeny (Sheppard et al., 2007), the 931–749 Ma Kuparr Tectonic Event (Cutten and Johnson, 2018; Occhipinti and Reddy., 2009; Piechocka et al., 2018) and the c. 570 Ma Mulka Tectonic Event (Cawood and Tyler, 2004; Johnson et al., 2011b; Korhonen et al., 2017; Sheppard et al., 2005, 2007, 2010).

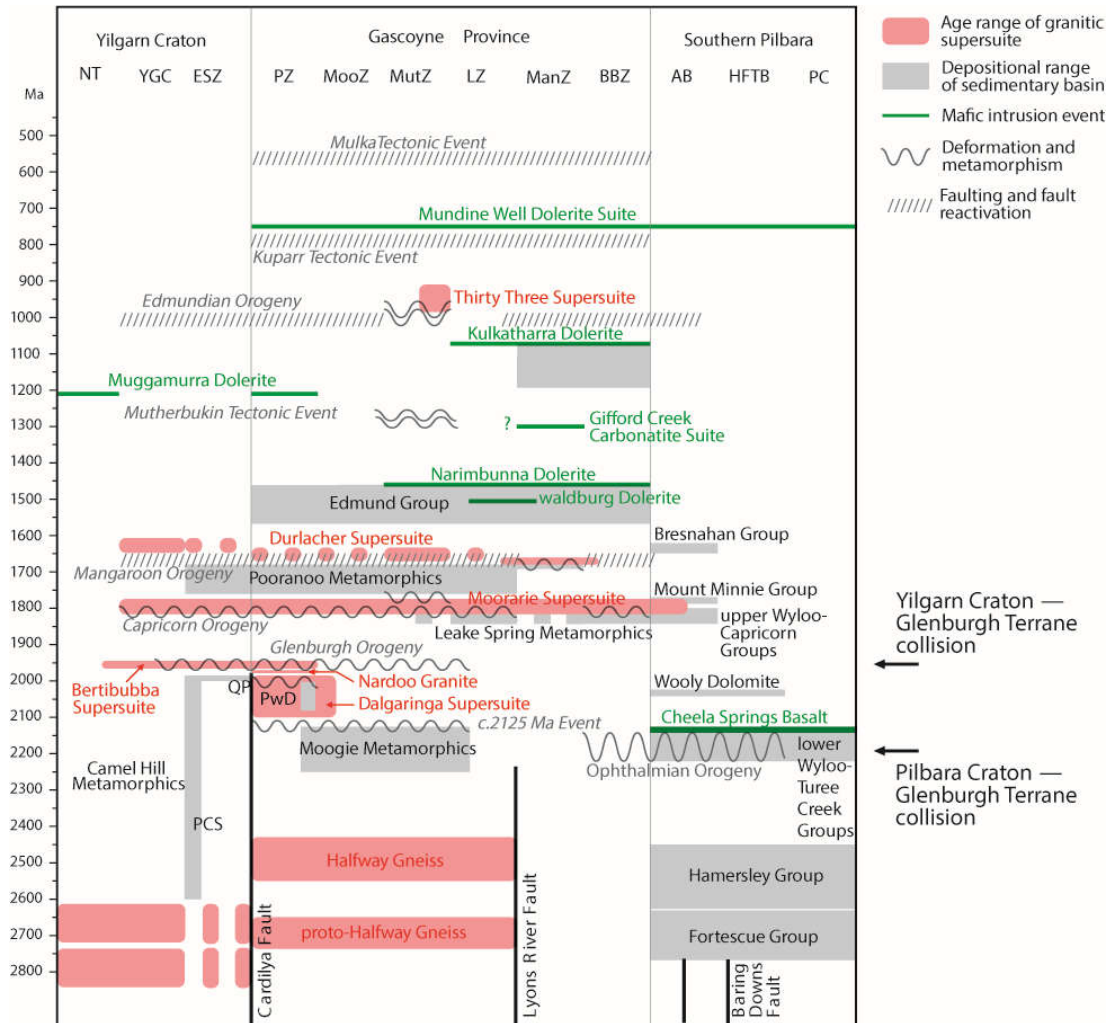


Figure 1-4: Time-space plot for the Capricorn Orogen. Abbreviations: AB, Ashburton Basin; BBZ, Boora Boora Zone; ESZ, Errabiddy Shear Zone; HFTB, Hamersley, Fortescue and Turee Creek basins; LZ, Limejuice Zone; ManZ, Mangaroo Zone; MooZ, Mooloo Zone; MutZ, Mutherbukin Zone; NT, Narryer Terrane; PC, Pilbara Craton; PCS, Petter Calc-silicate; PwD, Paradise Well diatexite PZ, Paradise Zone; QP, Quatpot Pelite; YC, Yilgarn Craton; YGC, Yarlalweelor Gneiss Complex (from Johnson et al., 2013).

Early interpretations of the Capricorn Orogen favoured a single stage, oblique convergence between the Yilgarn and Pilbara cratons during an extended c. 2200 to 1600 Ma Capricorn Orogeny (Evans et al., 2003; Tyler and Thorne, 1990). As a result, exploration companies focused their efforts on locating Proterozoic orogenic gold deposits (Cawood and Tyler, 2004; Pirajno, 2004). While many of the gold deposits in the orogen are associated with quartz veins (Thorne and Seymour, 1991), a common

trait of orogenic gold deposits (Goldfarb et al., 2001; Groves et al., 1998), other types of gold mineralization are also evident. For example, the Mount Olympus gold deposit in the northern part of the orogen is reported as having characteristics of both orogenic and Carlin-type deposits (Young et al., 2003).

Many of the known gold deposits cluster around the Archaean Pilbara and Yilgarn craton margins (Figure 1-2). This PhD focuses on the northern part of the Capricorn Orogen as the timing of the gold mineralization is poorly constrained, with only two ages for mineralization available. Lead isotope data for the Belvedere deposit suggested mineralization was Paleoproterozoic in age, although the results were ambiguous due to data sitting away from the model growth curve (Richards et al., 1981). The second age for mineralization was obtained from xenotime intergrown with quartz–sericite alteration at the Mount Olympus deposit dated at c. 1740 Ma and interpreted to represent the timing of gold mineralization (Şener et al., 2005; Young et al., 2003). At the time of these studies these ages were linked to collisional tectonics related to the Capricorn Orogeny, however, there are no orogenic events of this age in the Capricorn Orogen (Figure 1-4). A better understanding of the tectonic history of the Capricorn Orogen shows it to be much more complex than first thought. Equally, the types of gold deposits suggest that the gold mineralization history is equally complex. In situ phosphate geochronology allows dating of accessory minerals associated with gold mineralization and hydrothermal activity. This information can be integrated into the tectonothermal evolution of the Capricorn Orogen to improve the understanding of how gold mineralization relates to the tectonothermal history of the region.

1.3. IN SITU PHOSPHATE GEOCHRONOLOGY

The ages of hydrothermal alteration, gold mineralization and their host rocks at various gold deposits throughout the northern part of the Capricorn Orogen were determined by in situ geochronology. The phosphate minerals, monazite and xenotime, were the principle chronometers used for dating the mineralization and hydrothermal activity and form a major part of this PhD. In situ dating of baddeleyite was used to constrain the age of mafic intrusive host rocks to gold mineralization and detrital zircon mineral separates were used to determine the maximum depositional ages of the sedimentary

rocks. These techniques are discussed in detail in section 1.5.3 SHRIMP Geochronology.

1.3.1. PHOSPHATE GEOCHRONOLOGY

Dating hydrothermal activity and associated gold mineralization is inherently difficult as many chronometers are either scarce (e.g. zircon, Re-Os dating of molybdenite), or susceptible to isotopic resetting during subsequent tectonothermal events (e.g. Ar/Ar of mica; Chesley, 1999; Kerrich and Cassidy, 1994). However, the rare earth element (REE) rich phosphate minerals monazite ((Ce, La, Th)PO₄) and xenotime (YPO₄) are ideal chronometers for dating hydrothermal activity and gold mineralization (Rasmussen et al., 2001, 2006; Vielreicher et al., 2003) because:

- they are common accessory minerals in hydrothermal ores,
- both minerals generally have high U contents and low common Pb, and yield precise, concordant ages (Harrison et al., 2002; Rasmussen et al., 2001, 2005; Stern and Berman, 2001; Vielreicher et al., 2003; Zi et al., 2015),
- they both form over a wide range of geological conditions and are resistant to diffusive Pb-loss at temperatures up to 750°C for xenotime (Cherniak, 2010; Harrison et al., 2002) and >900°C for monazite (Cherniak et al., 2004),
- at lower temperatures (<400 °C), monazite and xenotime undergo dissolution and reprecipitation reactions leading to crystals with multiple phases of phosphate growth resulting in discrete age domains (Rasmussen and Muhling, 2007; Townsend et al., 2000). This allows for the precise dating of multiple hydrothermal/mineralizing events within a single rock.

1.3.2. IN SITU GEOCHRONOLOGY

Traditional methods of extracting minerals for geochronology involve crushing a sample of rock and extracting the minerals to be dated via heavy liquid separation and hand picking individual crystals (Wingate and Lu, 2016). While this process has its advantages, for example, large data sets can be acquired from one SHRIMP mount, it may not always be obvious what the acquired dates relate to, especially if more than one age is obtained. In situ geochronology differs from this approach because the

petrographic relationship between the minerals being dated and the surrounding minerals is retained.

Samples for in situ geochronology are collected during field mapping. Polished thin sections are prepared and minerals suitable for geochronology are identified by scanning electron microscope (SEM) and/or TESCAN Integrated Mineral Analyzer (TIMA). Areas containing these minerals are then drilled out of the thin section using a 2–3 mm hollow core drill bit before being cast into 25 mm epoxy SHRIMP mounts. The SHRIMP mounts are imaged by reflected light and SEM to allow for individual crystals to be located during the SHRIMP analytical session. Once data has been collected and interpreted the results can be linked to features observed at a macroscopic scale. Figure 1-5 summaries the in situ methodology.

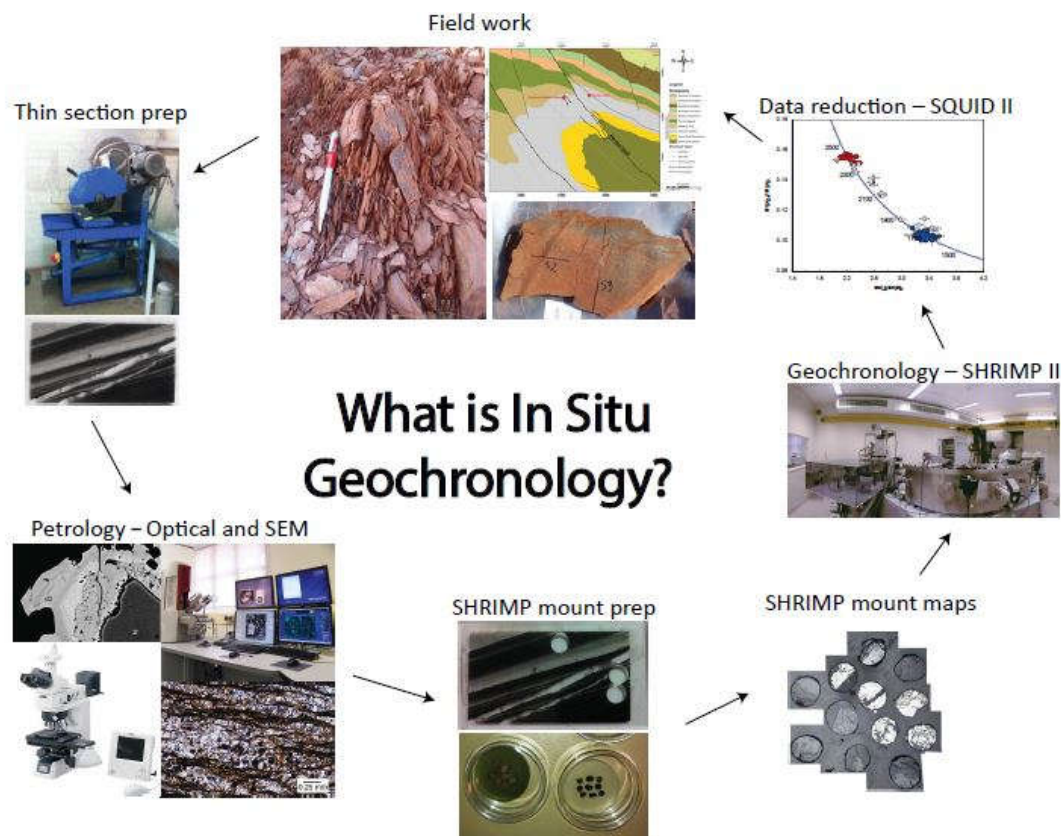


Figure 1-5: Summary of the in situ technique. Textural relationships are retained by drilling the mineral to be dated (and surrounding minerals) out of a polished thin section. By using in situ geochronology we can directly date phosphates and, hence, provide ages for hydrothermal activity and gold mineralization and link this back to what is observed at the outcrop.

This method has several advantages in that:

- it allows for analysis of very small crystals ($>10\ \mu\text{m}$; Figure 1-6a) which would not survive the traditional crushing and separating process,

- it preserves the textural relationships between dated minerals and surrounding minerals. This allows the obtained dates to be linked directly to geological features observed on an outcrop scale and includes gold mineralization where phosphate crystals are intergrown with ore-stage alteration or sulfide minerals (Figure 1-6a) and deformation events when phosphate minerals are growing within deformation fabrics (Figure 1-6b).

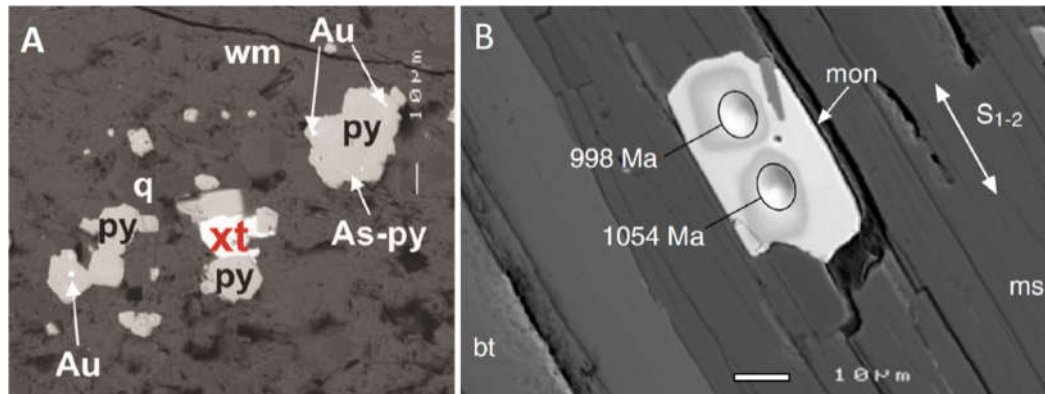


Figure 1-6: A) small (~10 µm) xenotime crystal intergrown with pyrite which contains visible gold (Vielreicher et al., 2015). B) Monazite aligned along a deformation fabric (Sheppard et al., 2007).

1.4. PROJECT AIMS

This thesis aims to combine in situ U–Th–Pb geochronology with targeted field mapping to develop an integrated tectonic — mineralization framework for the northern Capricorn Orogen. In detail, the project aims to:

- date gold mineralization, and the host rocks, within the northern Capricorn Orogen,
- link the timing of gold mineralization to the tectonothermal evolution and crustal architecture of the northern Capricorn Orogen,
- identify the structural events associated with gold mineralization,
- use the results to develop improved exploration models for target generation.

1.5. METHODS AND APPROACHES

This study involved a multi-disciplinary approach to meet the project outcomes and includes fieldwork, petrography, SHRIMP geochronology and Laser-ablation

inductively coupled plasma mass spectrometry (LA-ICP-MS) trace element geochemical mapping of pyrite crystals. Limited published literature is available on the individual gold prospects in the northern Capricorn Orogen and as a result this thesis draws on information published in open access company reports, brief mentions in Geological Survey of Western Australia reports, conference abstracts and Australian Securities Exchange (ASX) reports.

1.5.1. FIELDWORK AND SAMPLE SELECTION

Targeted field mapping was carried out around the Paulsens, Paulsens East, Gabbro Offset, Belvedere, Mount Olympus, Waugh, Peake, Star of the West, Big Sarah, Lewis, Monster Lode and Mount Clement gold prospects (Figure 1-7) so that samples could be collected with an understanding of the relationship between gold mineralization, hydrothermal alteration and the host rocks, and to allow for the gold mineralization to be placed in a regional context.

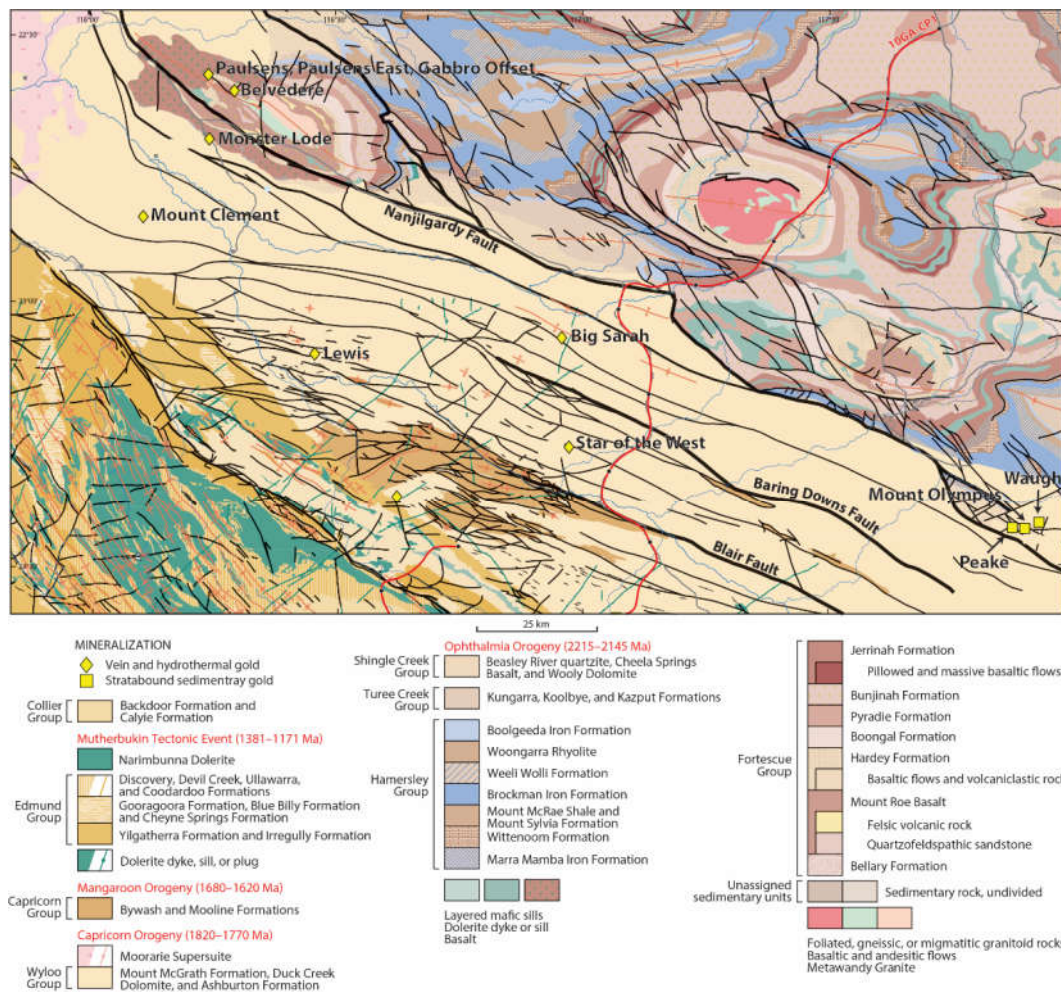


Figure 1-7: Location of gold prospects studied as a part of this PhD project.

Samples of gold mineralization, ore-stage hydrothermal alteration, deformation fabrics, and host rocks to gold mineralization were collected from surface outcrops, diamond drill core, underground drives and historical mine shafts with permission of Northern Star Resources. Detailed geological descriptions including coordinates (MGA 94 Zone 50), rock types, structural measurements, photography and mineralogy were recorded for each sample and entered into WAROX database (GSWA's field observation and rock database). These data will be made publically available on the WAROX USB (Geological Survey of Western Australia, 2018) completion of this thesis in the next compilation of WAROX data available via the Department of Mines, Industry Regulation and Safety.

1.5.2. PETROGRAPHY

A large number of polished thin sections were prepared by Spectrum Petrographics in Vancouver, Washington in order to investigate the mineral assemblages, textures and microstructures. A combination of transmitted and reflected light microscopy, SEM and TIMA identified minerals suitable for geochronology.

Many of the thin sections either did not contain any suitable chronometers, or contained datable minerals that were not amenable to analysis due to their small size ($<10\text{ }\mu\text{m}$), the presence of abundant inclusions, or did not show textures that could be linked directly to mineralization or alteration events. Additionally, many grains had low U contents or high ^{204}Pb values producing results that were inaccurate or imprecise, or both, and thus considered geologically meaningless. As a result, only six out of the 12 gold prospects studied contained phosphate minerals suitable for dating.

1.5.3. SHRIMP GEOCHRONOLOGY

Xenotime, monazite, zircon and baddeleyite analyses were carried out on the Sensitive high-resolution ion microprobe (SHRIMP) housed at the John de Laeter Centre at Curtin University. SHRIMP is used in preference to other instruments because of the machine's high mass resolution (>5000), small spot size ($\sim 10\text{ }\mu\text{m}$), shallow penetration depth ($1\text{--}2\text{ }\mu\text{m}$) and high precision (up to $\pm 1\text{--}2\%$ at 2σ). The SHRIMP instrumentation is described in detail in de Laeter and Kennedy (1998), Ireland and Williams (2003), Ireland et al (2008), Stern (1997) and Williams (1998).

Analytical procedure for monazite and xenotime are based on those of Fletcher et al (2004 and 2010) and a summary is provided here with detailed descriptions of operating parameters used during each analytical session provided in Chapters 2–5.

For monazite and xenotime analysis a primary beam of O_2^- ions was focused through a 30–50 μm Kohler aperture to produce a $\sim 10 \mu m$ spot on the sample surface with a current of 0.2 to 0.8 nA. The secondary ion system was focused through a 100 μm collector slit on to an electron multiplier to produce mass peaks with flat tops and a mass resolution (1 % peak height) of >5200 in all sessions. Background counts from scattered ions were reduced using a retardation lens, which is known to cause slight session-dependent instrumental mass fractionation (IMF) of Pb isotopes.

1.5.3.1. MONAZITE

Data were collected in sets of eight scans, with monazite standards analysed every three to six sample analyses using a 13-peak run-table: $^{202}[LaPO_2]$ (2 s), $^{203}[CePO_2]$ (2 s), ^{204}Pb (10 s), background ($^{204}Pb+0.045$, 10 s), $^{205.8}[NdPO_2]$ (2 s), ^{206}Pb (10 s), ^{207}Pb (30 s), ^{208}Pb (10 s), ^{232}Th (4 s), $^{245}[YCeO]$ (3 s), $^{254}[UO]$ (3 s), $^{264}[ThO]$ (3 s), and $^{270}[UO_2]$ (3 s). Corrections were made for matrix effects in Pb/U and Pb/Th ratios, fractionation of the $^{207}Pb/^{206}Pb$ ratio caused by use of the retardation lens (Rasmussen et al 2008) and an unresolvable isobaric interference on $^{204}Pb^+$ (Williams et al, 1996; Ireland et al., 1999).

Matrix effects in Pb/U and Pb/Th SHRIMP data are caused by variations in U, Th, Pb, REE and Y which can significantly bias $^{238}U/^{206}Pb$ and $^{208}Pb/^{232}Th$ dates. These effects can be corrected using a one dimensional calibration where ratios of $^{206}Pb^{+}/^{270}[UO_2]^+$ and $^{208}Pb^{+}/^{264}[ThO_2]^+$ are calibrated against known ratios for the monazite standard French using the following equations:

$$^{206}Pb/^{238}U_{unk} = (^{206}Pb^{+}/^{270}[UO_2]^+)_{unk}/av. (^{206}Pb^{+}/^{270}[UO_2]^+)_{std} * (^{206}Pb/^{238}U)_{std}$$

$$^{208}Pb/^{232}Th_{(unk)} = (^{208}Pb^{+}/^{248}[ThO]^+)_{unk}/av. (^{208}Pb^{+}/^{248}[ThO]^+)_{std} * (^{208}Pb/^{232}Th)_{std}$$

Since the REE and Y have significant impacts on the matrix effects, these elements are monitored using the monazite standards Z2908 and Z2234. REE compositions of monazites can be determined with SHRIMP data alone, without the need for prior electron microprobe analysis. The composition of REE within monazite is approximated by the La using the $LaPO_2^+/CePO_2^+$ ratio as a proxy, however, Nd can

dominate the REE composition in some monazite. As a result La, Ce and Nd are all monitored. Y is monitored by assessing $^{245}[\text{YCeO}]^+ / ^{203}[\text{CePO}_2]^+$ and Nd is monitored by $^{206}[\text{NdPO}_2]^+ / ^{203}[\text{CePO}_2]^+$ against monazite standards Z2908 and Z2234.

Fractionation of the $^{207}\text{Pb}/^{206}\text{Pb}$ ratio can be caused by use of the retardation lens. This is monitored using Z2908 and corrections are made if necessary. Monazite has an unresolved isobaric interference on $^{204}\text{Pb}^+$ which correlates with ThO_2^+ . A correction factor can be applied to the sample data by calculating the common ^{206}Pb (f_{206}) using the known $^{207}\text{Pb}/^{206}\text{Pb}$ content of Z2908 and the initial common Pb defined by Stacey and Kramers (1975). The amount of common Pb is known and excess counts at mass-204 can be determined for the measured component of $^{204}\text{Pb}^+ / ^{206}\text{Pb}^+$ from the f_{206} . Once the excess mass-204 counts are known the correction factor can be applied using $[\text{excess counts}] / \text{ThO}_2^+$.

1.5.3.2. *XENOTIME*

Xenotime data were collected in sets of 8 scans, with xenotime standards analysed every four to six sample analyses using a 9-peak run-table: $^{194}[\text{Y}_2\text{O}]$ (2 s), ^{204}Pb (10 s), background ($^{204}\text{Pb}+0.045$, 10 s), ^{206}Pb (10 s), ^{207}Pb (30 s), ^{208}Pb (10 s), ^{238}U (5 s), $^{248}[\text{ThO}]$ (5 s) and $^{254}[\text{UO}]$ (3 s). Matrix effects in the Pb/U and Pb/Th ratios are affected by variations in U, Th and REE abundances which bias $^{238}\text{U}/^{206}\text{Pb}$ and $^{208}\text{Pb}/^{232}\text{Th}$ dates. However these matrix effects can be corrected using a range of standards.

Pb/U calibrations and matrix corrections for U and Th contents were based on concurrent measurements of the monazite standards MG-1 and Xenol. Pb/Th was determined indirectly, using a fixed Th/U calibration using the following calibration schemes:

$$\ln[^{206}\text{Pb}/^{254}\text{UO}^+]:\ln[^{238}\text{U}^+/^{254}\text{UO}^+] \text{ for Pb/U}$$

$$\ln[^{208}\text{Pb}^+/\text{ThO}^+]:\ln[^{264}\text{ThO}_2^+/^{248}\text{ThO}^+] \text{ for Pb/Th}$$

Ideally, it is necessary to collect REE data by electron microprobe prior to SHRIMP analysis. However, matrix corrections for $\sum\text{REE}$ assumed the samples have $\sum\text{REE}$ abundances similar to Xenol. This assumption is valid considering that i) Xenol has moderate total REE contents typical among known xenotime samples, ii) the weighting of REE in the matrix correction is insignificant compared with that of U and Th, and

iii) even though this approach may introduce extra uncertainties in Pb/U and Pb/Th, it is less problematic for older samples (>1 Ga) in which $^{207}\text{Pb}/^{206}\text{Pb}$ ages are used, and the accuracy of $^{207}\text{Pb}/^{206}\text{Pb}$ data is monitored (and corrected for IMF where needed) using xenotime standard Xenotime2.

1.5.4. LA-ICP-MS

Mapping of trace element distributions within pyrite by LA-ICP-MS was conducted at CODES, ARC Centre of Excellence in Ore Deposits, University of Tasmania. This technique is useful to discriminate different classes of ore deposits (e.g. Large et al., 2009; Belousov et al., 2016). Pyrite from the Mount Olympus deposit was assessed to assist with the classification of the deposit, which is described as having characteristics of both Carlin-type and orogenic mineralization (Young et al., 2003; Şener et al., 2005). A detailed description of the methods used is provided in Chapter 4.

1.6. THESIS STRUCTURE

Chapter 1 is the introductory chapter of this thesis and provides relevant background information, aims and objectives of this PhD. The main body of the thesis (Chapters 2–6) comprises five manuscripts including 3 published papers and 2 currently under review. Copies of the published manuscripts, as well co-authors approvals are included in Appendix 1. All published papers are open access so publisher copyright is not required.

Chapter 2 *Using In Situ SHRIMP U-Pb Monazite and Xenotime Geochronology to Determine the Age of Orogenic Gold Mineralization: An Example from the Paulsens Mine, Southern Pilbara Craton*. This chapter discusses the importance of understanding how orogenic gold deposits form through space and time for developing effective models for exploration targeting. Monazite, xenotime, zircon and baddeleyite geochronology determined the age of host rocks, and the timing of hydrothermal activity and associated gold mineralization at the Paulsens deposit. Results indicate that gold mineralization occurred much earlier than previously thought and does not correspond to any known deformation events in the area indicating a significantly different, and more complicated low-temperature tectonothermal evolution for the southern Pilbara region.

Chapter 3 *Neighbouring orogenic gold deposits may be the products of unrelated mineralizing events.* This chapter discusses how gold deposits within a geological terrane that exhibit similar characteristics are commonly thought to have formed during the same hydrothermal event. As a result, models for exploration targeting are often developed by assessing the known gold deposits in a region, and targeting similar geological features such as geochemical anomalies, favourable host rocks or structural settings with the assumption that they represented the footprint of the same mineralizing event. However, these models often overlook the age of the gold mineralization and host rocks. In this chapter, new geochronological information for the Belvedere gold deposit is documented and compared to data from the Paulsens deposits presented in Chapter 2. Results indicate that similar deposits in an area may undergo different geological histories, and that rock overprinted by multiple mineralizing events can be prospective for larger and more economically significant gold deposits.

Chapter 4: *Linking gold mineralization to regional-scale drivers of mineral systems using in situ U–Pb geochronology and pyrite LA-ICP-MS element mapping.* This chapter demonstrates that in situ U–Pb SHRIMP geochronology of hydrothermal xenotime can not only precisely determine the timing of gold mineralization, but when integrated into a well-established tectonic evolution, can provide critical information that will lead to better understanding of the fundamental controls on gold mineralization at a regional-scale. Results presented challenge previous interpretations of the timing and style of gold mineralization at the Mount Olympus deposit. In doing so they demonstrate that the drivers for contrasting styles of hydrothermal gold ores (orogenic, epithermal and Carlin) are fundamentally different, and that substantial Carlin-like gold deposits can form in an intracratonic setting during regional-scale crustal reworking.

Chapter 5: *U–Pb dating of fault reactivation and gold mineralization in the northern Capricorn Orogen, Western Australia.* In this chapter, fault movement and gold mineralization is dated by in situ U–Pb SHRIMP geochronology of xenotime. Gold deposits in the northern Capricorn Orogen show a spatial relationship to crustal-scale faults and their ancillary structures. The assumption is that gold mineralization formed when hydrothermal fluids moved along these faults during periods of episodic reactivation associated with known orogenic events. However, due to limited surface

exposures and complex geological histories this link is largely interpretive. Xenotime intergrown with calcite from a syn-tectonic vein within the Amazon Shear Zone demonstrates that hydrothermal activity accompanied fault movement at 1674 ± 54 Ma. This age is coeval with the timing of 1672 ± 18 Ma gold mineralization at the Star of the West Deposit, as well as widespread hydrothermal activity and gold mineralization throughout the northern Capricorn Orogen and Pilbara Craton. Together these data indicate that both fault movement and gold mineralization are synchronous and are related to the early stages of the 1680–1620 Ma intracratonic Mangaroon Orogeny.

Chapter 6: *Gold metallogeny of a Proterozoic orogen: the relationship between crustal architecture, fault reactivations and hydrothermal fluid flow*. This chapter provides a summary of all work completed as a part of this PhD. Geochronological results presented in chapters 2–5 are drawn on, placing them in a broader geological context with regards to crustal architecture and the timing of gold mineralization. Results demonstrate that gold deposits occur at the margin of the Pilbara Craton and are related to the pre-existing, crustal-scale Nanjilgardy and Baring Downs faults. Deep crustal seismic imaging and geochronological data show that both faults have long reactivation histories associated with episodes of intracratonic reworking. Although intracratonic settings are not considered prospective for gold mineralization due to a lack of input of juvenile material, the geochronological data presented here demonstrate that episodic fault activity and accompanying hydrothermal fluid flow may be required to upgrade ore deposits from small gold occurrences into an economically viable deposit within an intracratonic setting.

Chapter 7: *Thesis conclusions* gives a summary of the project outcomes and potential future work.

Chapter 8: *Bibliography* a list of all references within this thesis.

1.7. REFERENCES

Belousov, I., Large, R. R., Meffre, S., Danyushevsky, L. V., Steadman, J., and Beardsmore, T., 2016, Pyrite compositions from VHMS and orogenic Au deposits in the Yilgarn Craton, Western Australia: Implications for gold and copper exploration: *Ore Geology Reviews*, v. 79, p. 474-499.

- Cawood, P. A., and Tyler, I. M., 2004, Assembling and reactivating the Proterozoic Capricorn Orogen: lithotectonic elements, orogenies, and significance: *Precambrian Research*, v. 128, no. 3-4, p. 201-218.
- Cherniak, D. J., Watson, E. B., Grove, M., and Harrison, T. M., 2004, Pb diffusion in monazite: a combined RBS/SIMS: *Geochimica et Cosmochimica Acta*, v. 68, no. 4, p. 829-840.
- Cherniak, D. J., 2010, Diffusion in accessory minerals: zircon, titanite, apatite, monazite and xenotime: *Reviews in Mineralogy and Geochemistry*, v. 72, no. 1, p. 827-869.
- Chesley, J. T., 1999, Integrative geochronology of ore deposits: new insights into the duration and timing of hydrothermal circulation, *in* Lambert, D. D., and Brown, P. E., eds., *Reviews in economic geology*, Volume 12, p. 115-142.
- Cutten, H. N. C., and Johnson, S. P., 2018, Kuparr Tectonic Event (KU): Geological Survey of Western Australia, WA Geology Online, Explanatory Notes extract, viewed 12 December 2018, <www.dmp.wa.gov.au/ens>
- De Laeter, J. R., and Kennedy, A. K., 1998, A double focusing mass spectrometer for geochronology: *International Journal of Mass Spectrometry*, v. 178, no. 1, p. 43-50.
- Evans, D. A. D., Sircombe, K. N., Wingate, M. T. D., Doyle, M., McCarthy, M., Pidgeon, R. T., and Van Niekerk, H. S., 2003, Revised geochronology of magmatism in the western Capricorn Orogen at 1805-1785 Ma: diachroneity of the Pilbara-Yilgarn collision: *Australian Journal of Earth Sciences*, v. 50, no. 6, p. 853-864.
- Fletcher, I. R., McNaughton, N. J., Aleinikoff, J. A., Rasmussen, B., and Kamo, S. L., 2004, Improved calibration procedures and new standards for U–Pb and Th–Pb dating of Phanerozoic xenotime by ion microprobe: *Chemical Geology*, v. 209, p. 295–314.
- Fletcher, I. R., McNaughton, N. J., Davis, W. J., and Rasmussen, B., 2010, Matrix effects and calibration limitations in ion probe U–Pb and Th–Pb dating of monazite: *Chemical Geology*, v. 270, p. 31–44.
- Geological Survey of Western Australia, 2018, Compilation of WAROX data, 2018: Geological Survey of Western Australia, digital data package.
- Goldfarb, R. J., Groves, D. I., and Gardoll, S., 2001, Orogenic gold and geologic time: a global synthesis: *Ore Geology Reviews*, v. 18, no. 1–2, p. 1-75.
- Groves, D. I., Goldfarb, R. J., Gebre-Mariam, M., Hagemann, S. G., and Robert, F., 1998, Orogenic gold deposits: A proposed classification in the context of their crustal distribution and relationship to other gold deposit types: *Ore Geology Reviews*, v. 13, no. 1–5, p. 7-27.

- Groves, D. I., and Santosh, M., 2015, Province-scale commonalities of some world-class gold deposits: Implications for mineral exploration: *Geoscience Frontiers*, v. 6, no. 3, p. 389-399.
- Harrison, T. M., Catlos, E. J., and Montel, J. M., 2002, U-Th-Pb Dating of Phosphate Minerals: *Reviews in Mineralogy and Geochemistry*, v. 48, no. 1, p. 524-558.
- Hronsky, J. M., Groves, D. I., Loucks, R. R., and Begg, G. C., 2012, A unified model for gold mineralisation in accretionary orogens and implications for regional-scale exploration targeting methods: *Mineralium Deposita*, v. 47, no. 4, p. 339-358.
- Hronsky, J. M. A., and Groves, D. I., 2008, Science of targeting: definition, strategies, targeting and performance measurement: *Australian Journal of Earth Sciences*, v. 55, no. 1, p. 3-12.
- Huston, D. L., Mernagh, T. P., Hagemann, S. G., Doublier, M. P., Fiorentini, M., Champion, D. C., Lynton Jaques, A., Czarnota, K., Cayley, R., Skirrow, R., and Bastrakov, E., 2016, Tectono-metallogenic systems — The place of mineral systems within tectonic evolution, with an emphasis on Australian examples: *Ore Geology Reviews*, v. 76, p. 168-210.
- Huston, D. L., Pehrsson, S., Eglington, B. M., and Zaw, K., 2010, The geology and metallogeny of volcanic-hosted massive sulfide deposits: Variations through geologic time and with tectonic setting; *Economic Geology*, v. 105, p. 571-591.
- Ireland, T., Clement, S., Compston, W., Foster, J., Holden, P., Jenkins, B., Lanc, P., Schram, N., and Williams, I., 2008, Development of SHRIMP: *Australian Journal of Earth Sciences*, v. 55, no. 6, p. 937-954.
- Ireland, T., and Williams, I. S., 2003, Considerations in zircon geochronology by SIMS: *Reviews in Mineralogy and Geochemistry*, v. 53, p. 215-241.
- Ireland, T.R., Wooden, J.L., Persing, H., Ito, B., 1999, Geological applications and analytical development of the SHRIMP-RG. *Eos Trans., American Geophysics Union* 80, F1117.
- Jennings, K., and Schodde, R., 2016, From mineral discovery to project delivery: *SEG Newsletter*, v. 105, p. 20-25.
- Johnson, S. P., Korhonen, F. J., Kirkland, C. L., Cliff, J. B., Belousova, E. A., and Sheppard, S., 2017a, An isotopic perspective on growth and differentiation of Proterozoic orogenic crust: From subduction magmatism to cratonization: *Lithos*, v. 268-271, p. 76-86.
- Johnson, S. P., Cutten, H. N., Korhonen, F. J., and Wyche, N. L., 2017b, Geology and metallogeny of the Capricorn Orogen, *in* Phillips, G. N., ed., *Australian Ore Deposits*, The Australian Institute of Mining and Metallurgy: Melbourne, p. 289-392.

- Johnson, S. P., Sheppard, S., Rasmussen, B., Wingate, M. T. D., Kirkland, C. L., Muhling, J. R., Fletcher, I. R., and Belousova, E. A., 2011a, Two collisions, two sutures: Punctuated pre-1950Ma assembly of the West Australian Craton during the Ophthalmian and Glenburgh Orogenies: *Precambrian Research*, v. 189, no. 3-4, p. 239-262.
- Johnson, S. P., Sheppard, S., Rasmussen, B., Wingate, M. T. D., Kirkland, C. L., Muhling, J. R., Fletcher, I. R., and Belousova, E. A., 2010, The Glenburgh Orogeny as a record of Paleoproterozoic continent-continent collision, Geological Survey of Western Australia, Record 2010/5, 60 p.
- Johnson, S. P., Thorne, A. M., and Tyler, I. M., 2011b, Capricorn Orogen seismic and magnetotelluric (MT) workshop 2011: Extended abstracts: Geological Survey of Western Australia, Record 2011/25, 132 p.
- Johnson, S. P., Thorne, A. M., Tyler, I. M., Korsch, R. J., Kennett, B. L. N., Cutten, H. N., Goodwin, J., Blay, O., Blewett, R. S., Joly, A., Dentith, M. C., Aitken, A. R. A., Holzschuh, J., Salmon, M., Reading, A., Heinson, G., Boren, G., Ross, J., Costelloe, R. D., and Fomin, T., 2013, Crustal architecture of the Capricorn Orogen, Western Australia and associated metallogeny: *Australian Journal of Earth Sciences*, v. 60, no. 6-7, p. 681-705.
- Kerrich, R., and Cassidy, K. F., 1994, Temporal relationships of lode gold mineralization to accretion, magmatism, metamorphism and deformation — Archean to present: A review: *Ore Geology Reviews*, v. 9, no. 4, p. 263-310.
- Kinny, P. D., Nutman, A. P., and Occhipinti, S. A., 2004, Reconnaissance dating of events recorded in the southern part of the Capricorn Orogen: *Precambrian Research*, v. 128, no. 3, p. 279-294.
- Korhonen, F. J., and Johnson, S. P., 2015, The role of radiogenic heat in prolonged intraplate reworking: The Capricorn Orogen explained?: *Earth and Planetary Science Letters*, v. 428, p. 22-32.
- Korhonen, F. J., Johnson, S. P., Wingate, M. T. D., Kirkland, C. L., Fletcher, I. R., Dunkley, D. J., Roberts, M. P., Sheppard, S., Muhling, J. R., and Rasmussen, B., 2017, Radiogenic heating and craton-margin plate stresses as drivers for intraplate orogeny: *Journal of Metamorphic Geology*, v. 35, no. 6, p. 631-661.
- Large, R. R., Danyushevsky, L., Hollit, C., Maslennikov, V., Meffre, S., Gilbert, S., Bull, S., Scott, R., Emsbo, P., Thomas, H., Singh, B., and Foster, J., 2009, Gold and trace element zonation in pyrite using a laser imaging technique: implications for the timing of gold in orogenic and Carlin-style sediment-hosted deposits: *Economic Geology*, v. 104, no. 5, p. 635-668.
- Martin, D. M., and Morris, P. A., 2010, Tectonic setting and regional implications of ca2.2 Ga mafic magmatism in the southern Hamersley Province, Western Australia: *Australian Journal of Earth Sciences*, v. 57, no. 7, p. 911-931.
- Martin, D. M., Sircombe, K. N., Thorne, A. M., Cawood, P. A., and Nemchin, A. A., 2008, Provenance history of the Bangemall Supergroup and implications for

- the Mesoproterozoic paleogeography of the West Australian Craton: *Precambrian Research*, v. 166, no. 1, p. 93-110.
- Martin, D. M., and Thorne, A., 2004, Tectonic setting and basin evolution of the Bangemall Supergroup in the northwestern Capricorn Orogen: *Precambrian Research*, v. 128, no. 3, p. 385-409.
- McCuaig, T. C., Beresford, S., and Hronsky, J., 2010, Translating the mineral systems approach into an effective exploration targeting system: *Ore Geology Reviews*, v. 38, no. 3, p. 128-138.
- McCuaig, T. C., and Hronsky, J. M. A., 2014, The mineral systems concept: The key to exploration targeting *in* Kelly, K. D., and Golden, H. C., eds., *Building Exploration Capability for the 21st Century*, Volume Special Publication 18: Society of Economic Geologists, p. 153-175.
- McKeith, T. D., Schodde, R. C., and Baltus, E. J., 2010, Gold Discovery Trends: *SEG Newsletter*, v. 81, p. 1, 18-24.
- Northern Star Resources Limited, 2013, Ashburton Resource Soars 66% to 1.7MOz, <http://www.nsr ltd.com/wp-content/uploads/2013/02/AshburtonResourceIncreases66to1point7Moz.pdf>.
- Northern Star Resources Limited, January, 2016, Resources and Reserves, (<http://www.nsr ltd.com/our-assets/resources-and-reserves/>).
- Northern Star Resources Limited, July, 2015, Northern Star Paulsens operations fact sheet, (<http://www.nsr ltd.com/wp-content/uploads/2015/08/NSR-Paulsens-Operations-Fact-Sheet-July-2015-FINAL.pdf>).
- Occhipinti, S., and Reddy, S., 2009, Neoproterozoic reworking of the Palaeoproterozoic Capricorn Orogen of Western Australia and implications for the amalgamation of Rodinia. Geological Society of London, Special Publication, v. 327, p. 445–456
- Occhipinti, S. A., Sheppard, S., Nelson, D. R., Myers, J. S., and Tyler, I. M., 1998, Syntectonic granite in the southern margin of the Palaeoproterozoic Capricorn Orogen, Western Australia: *Australian Journal of Earth Sciences*, v. 45, no. 4, p. 509-512.
- Occhipinti, S. A., Sheppard, S., Passchier, C., Tyler, I. M., and Nelson, D. R., 2004, Palaeoproterozoic crustal accretion and collision in the southern Capricorn Orogen: the Glenburgh Orogeny: *Precambrian Research*, v. 128, no. 3–4, p. 237-255.
- Piechocka, A. M., Sheppard, S., Fitzsimons, I. C. W., Johnson, S. P., Rasmussen, B., and Jordan, F., 2018, Neoproterozoic $^{40}\text{Ar}/^{39}\text{Ar}$ mica ages mark the termination of a billion years of intraplate reworking in the Capricorn Orogen, Western Australia: *Precambrian Research*, v. 310, p. 391–406.

- Pirajno, F., 2004, Metallogeny in the Capricorn Orogen, Western Australia, the result of multiple ore-forming processes: *Precambrian Research*, v. 128, no. 3–4, p. 411–439.
- Raimondo, T., Collins, A. S., Hand, M., Walker-Hallam, A., Smithies, R. H., Evins, P. M., and Howard, H. M., 2010, The anatomy of a deep intracontinental orogen: *Tectonics*, v. 29, no. 4, 31 p.
- Rasmussen, B., Fletcher, I. R., and McNaughton, N. J., 2001, Dating low-grade metamorphic events by SHRIMP U-Pb analysis of monazite in shales: *Geology*, v. 29, no. 10, p. 963–966.
- Rasmussen, B., Fletcher, I. R., and Muhling, J. R., 2007a, In situ U–Pb dating and element mapping of three generations of monazite: Unravelling cryptic tectonothermal events in low-grade terranes: *Geochimica et Cosmochimica Acta*, v. 71, no. 3, p. 670–690.
- Rasmussen, B., Fletcher, I.R., Muhling, J.R., 2008. Pb/Pb geochronology, petrography and chemistry of Zr-rich accessory minerals (zirconolite, tranquillityite and baddeleyite) in mare basalt 10047. *Geochimica et Cosmochimica Acta*, v. 72, p. 5799–5818.
- Rasmussen, B., Fletcher, I. R., Muhling, J. R., Thorne, W. S., and Broadbent, G. C., 2007b, Prolonged history of episodic fluid flow in giant hematite ore bodies: Evidence from in situ U–Pb geochronology of hydrothermal xenotime: *Earth and Planetary Science Letters*, v. 258, no. 1–2, p. 249–259.
- Rasmussen, B., Fletcher, I. R., and Sheppard, S., 2005, Isotopic dating of the migration of a low-grade metamorphic front during orogenesis: *Geology*, v. 33, no. 10, p. 773–776.
- Rasmussen, B., and Muhling, J. R., 2007, Monazite begets monazite: evidence for dissolution of detrital monazite and reprecipitation of syntectonic monazite during low-grade regional metamorphism: *Contributions to Mineralogy and Petrology*, v. 154, no. 6, p. 675–689.
- Rasmussen, B., Sheppard, S., and Fletcher, I. R., 2006, Testing ore deposit models using in situ U-Pb geochronology of hydrothermal monazite: Paleoproterozoic gold mineralization in northern Australia: *Geology*, v. 34, no. 2, p. 77–80.
- Richards, J. R., Fletcher, I. R., and Blockley, J. G., 1981, Pilbara galenas: Precise isotopic assay of the oldest Australian leads model ages and growth-curve implications: *Mineralium deposita*, v. 16, no. 1, p. 7–30.
- Şener, A. K., Young, C., Groves, D. I., Krapez, B., and Fletcher, I. R., 2005, Major orogenic gold episode associated with Cordilleran-style tectonics related to the assembly of Paleoproterozoic Australia?: *Geology*, v. 33, no. 3, p. 225–228.
- Sheppard, S., Bodorkos, S., Johnson, S. P., Wingate, M. T. D., and Kirkland, C. L., 2010, The Paleoproterozoic Capricorn Orogeny: intracontinental reworking not continent–continent collision, Volume 108: Geological Survey of Western Australia, Report 108, 33 p.

- Sheppard, S., Fletcher, I. R., Rasmussen, B., Zi, J.-W., Muhling, J. R., Occhipinti, S. A., Wingate, M. T. D., and Johnson, S. P., 2016, A new Paleoproterozoic tectonic history of the eastern Capricorn Orogen, Western Australia, revealed by U–Pb zircon dating of micro-tuffs: *Precambrian Research*, v. 286, p. 1-19.
- Sheppard, S., Occhipinti, S. A., and Nelson, D. R., 2005, Intracontinental reworking in the Capricorn Orogen, Western Australia: the 1680–1620 Ma Mangaroon Orogeny*: *Australian Journal of Earth Sciences*, v. 52, no. 3, p. 443-460.
- Sheppard, S., Occhipinti, S. A., and Tyler, I. M., 2003, The relationship between tectonism and composition of granitoid magmas, Yarlalweelor Gneiss Complex, Western Australia: *Lithos*, v. 66, no. 1, p. 133-154.
- Sheppard, S., Occhipinti, S. A., and Tyler, I. M., 2004, A 2005–1970 Ma Andean-type batholith in the southern Gascoyne Complex, Western Australia: *Precambrian Research*, v. 128, no. 3–4, p. 257-277.
- Sheppard, S., Rasmussen, B., Muhling, J. R., Farrell, T. R., and Fletcher, I. R., 2007, Grenvillian-aged orogenesis in the Palaeoproterozoic Gascoyne Complex, Western Australia: 1030–950Ma reworking of the Proterozoic Capricorn Orogen: *Journal of Metamorphic Geology*, v. 25, no. 4, p. 477-494.
- Stern, R. A., 1997, The GSC Sensitive High Resolution Ion Microprobe (SHRIMP): analytical techniques of zircon U-Th-Pb age determinations and performance evaluation, in *Radiogenic age and isotope studies: Report 10; Geological Survey of Canada, Current Research 1997-F*, p. 1-31.
- Stern, R. A., and Berman, R. G., 2001, Monazite U–Pb and Th–Pb geochronology by ion microprobe, with an application to in situ dating of an Archean metasedimentary rock: *Chemical Geology*, v. 172, no. 1, p. 113-130.
- Thorne, A. M., and Seymour, D. B., 1991, Geology of the Ashburton Basin Western Australia, Geological Survey of Western Australia, Bulletin 139, 162 p.
- Townsend, K. J., Miller, C. F., D'Andrea, J. L., Ayers, J. C., Harrison, T. M., and Coath, C. D., 2000, Low temperature replacement of monazite in the Ireteba granite, Southern Nevada: geochronological implications: *Chemical Geology*, v. 172, no. 1, p. 95-112.
- Tyler, I. M., and Thorne, A. M., 1990, The northern margin of the Capricorn Orogen, Western Australia—an example of an Early Proterozoic collision zone: *Journal of Structural Geology*, v. 12, no. 5–6, p. 685-701.
- Vielreicher, N., Groves, D., Fletcher, I., McNaughton, N., and Rasmussen, B., 2003, Hydrothermal monazite and xenotime geochronology: a new direction for precise dating of orogenic gold mineralization: *Society of Economic Geologists Newsletter*, v. 53, no. 1, p. 10-16.
- Vielreicher, N., Groves, D., McNaughton, N., and Fletcher, I., 2015, The timing of gold mineralization across the eastern Yilgarn craton using U–Pb geochronology of hydrothermal phosphate minerals: *Mineralium Deposita*, v. 50, no. 4, p. 391-428.

- Williams, I. S., 1998, U-Th-Pb geochronology by ion microprobe. *in* Application of Microanalytical Techniques to Understanding Mineralizing Processes. Eds., McKibben, M. A., Shanks W., C and Ridley, W. I., Reviews of Economic Geology, v. 7, p. 1-35.
- Williams, I.S., Buick, I.S., Cartwright, I., 1996, An extended episode of early Mesoproterozoic metamorphic fluid flow in the Reynolds Range, central Australia. *Journal of Metamorphic Geology*, v. 14, p. 29–47.
- Wingate, M. T. D., and Lu, Y., 2016, Introduction to geochronology information released in 2014: Geological Survey of Western Australia, 5 p.
- Young, C. J., Groves, D. I., and Morant, P., 2003, Sediment-hosted disseminated gold mineralisation in the Palaeoproterozoic Ashburton Province, Western Australia: a new epizonal orogenic gold province related to Capricorn Orogeny?, *in* Eliopoulos et al., eds., Mineral exploration and sustainable development: proceedings of the 7th Biennial SGA Meeting: Athens, Greece, Millpress, p. 835-838.
- Zi, J.-W., Rasmussen, B., Muhling, J. R., Fletcher, I. R., Thorne, A. M., Johnson, S. P., Cutten, H. N., Dunkley, D. J., and Korhonen, F. J., 2015, In situ U–Pb geochronology of xenotime and monazite from the Abra polymetallic deposit in the Capricorn Orogen, Australia: Dating hydrothermal mineralization and fluid flow in a long-lived crustal structure: *Precambrian Research*, v. 260, p. 91-112.

CHAPTER 2. USING IN SITU SHRIMP U–PB
MONAZITE AND XENOTIME GEOCHRONOLOGY TO
DETERMINE THE AGE OF OROGENIC GOLD
MINERALIZATION: AN EXAMPLE FROM THE
PAULSENS MINE, SOUTHERN PILBARA CRATON

The following chapter has been published in ECONOMIC GEOLOGY. The original format has been modified for the purposes of this thesis, but all content remains the same. The original, formatted and published version can be found in Appendix 1A.

I.O.H. Fielding¹, S.P. Johnson², J.-W. Zi¹, B. Rasmussen¹, J.R. Muhling^{1, 3}, D.J. Dunkley¹, S. Sheppard¹, M.T.D. Wingate^{2, 3} and J.R. Rogers⁴., 2017, Using In Situ SHRIMP U-Pb Monazite and Xenotime Geochronology to Determine the Age of Orogenic Gold Mineralization: An Example from the Paulsens Mine, Southern Pilbara Craton: Economic Geology, v. 112, no. 5, p. 1205-1230, doi: <https://doi.org/10.5382/econgeo.2017.4507>

¹ Department of Applied Geology, Curtin University, Kent Street, Bentley, WA 6102, Australia.

² Geological Survey of Western Australia, 100 Plain Street, East Perth, WA 6004, Australia.

³ School of Earth and Environment, The University of Western Australia, 35 Stirling Highway, Crawley, WA 6009, Australia.

⁴ Northern Star Resources Ltd, Level 1, 388 Hay Street, Subiaco, WA 6008, Australia.

2.1. ABSTRACT

Paulsens is a mesothermal orogenic gold deposit located in the Wyloo Inlier on the southern margin of the Pilbara Craton of Western Australia. Gold occurs in quartz–sulfide veins hosted within a folded and faulted gabbro dike, from which baddeleyite yields a SHRIMP U–Pb crystallization age of 2701 ± 11 Ma. Monazite and xenotime in the veins and from hydrothermally altered country rocks yield three distinct U–Pb dates of c. 2400, 1730 and 1680 Ma. Textural relationships between euhedral xenotime and pyrite with rounded native gold inclusions from within the quartz–sulfide veins show that the primary gold mineralization was synchronous with xenotime crystallization at 2403 ± 5 Ma, and coeval with pervasive alteration of the host rocks, which yield monazite ages of 2398 ± 37 Ma and 2403 ± 38 Ma. Regional-scale hydrothermal events at c. 1730 and 1680 Ma are linked to the growth of monazite within phyllitic rocks at 1730 ± 28 Ma and 1721 ± 32 Ma, carbonate veining at 1655 ± 37 Ma, and gold remobilization or introduction of new gold at 1680 ± 9 Ma. The c. 2400 Ma age for mineralization and hydrothermal alteration does not correspond to any known deformation event in the region, indicating a significantly different, and more complicated, low-temperature tectonothermal evolution for the southern Pilbara region than previously recognized. The in situ SIMS dating of monazite and xenotime employed here will lead to better targeting of orogenic gold deposits in the northern Capricorn Orogen, and these techniques can be utilized for orogenic gold exploration worldwide.

2.2. INTRODUCTION

Exploration targeting of gold deposits can be significantly improved by understanding metallogenic events in both space and time (Hronsky et al., 2012). By knowing the ages of hydrothermal mineralization, host rocks, and regional tectonothermal events, the search space can be minimized, and the financial risk to explorers greatly reduced (Rasmussen et al., 2006; Hronsky and Groves, 2008). However, many chronometers are either scarce in orogenic gold deposits, or they are susceptible to isotopic resetting during subsequent metamorphism and deformation (Kerrick and Cassidy, 1994; Chesley, 1999) so that the ages of many gold deposits worldwide are poorly constrained (Chesley, 1999). Nevertheless, many orogenic gold deposits contain trace

amounts of the rare earth element (REE) bearing phosphate minerals monazite ((Ce,La,Nd,Th)PO₄) or xenotime (YPO₄) intergrown with ore minerals (Vielreicher et al., 2003; Carpenter et al., 2005; Zhang et al., 2014). These phosphate minerals are robust chronometers that are resistant to diffusive Pb-loss at temperatures up to 750 °C (Harrison et al., 2002; Cherniak, 2010). Instead, monazite and xenotime undergo dissolution and reprecipitation reactions at temperatures <400 °C (Townsend et al., 2001; Rasmussen and Muhling, 2007) leading to crystals that have multiple, but discrete, age domains from which precise dates can be obtained.

The Paulsens gold deposit is located in the northern part of the Capricorn Orogen, on the southern margin of the Pilbara Craton in Western Australia, and is hosted in low-grade metasedimentary and metavolcanic rocks of the 2775–2629 Ma Fortescue Group in the Wyloo Inlier (Figure 2-1; Thorne and Trendall, 2001; Thorne et al., 2011). Paulsens has an endowment of 1,114,000 ounces of gold, comprising 854,000 ounces mined between 2005 and 2016 (Northern Star Resources Limited, 2015, Northern Star Resources Limited, January, 2016), and a remaining resource of 943,000 t at 8.58 g/t of gold for a total of 260,000 ounces contained gold as of the 30th June 2016 (Northern Star Resources Limited, January, 2016). Historically, Paulsens was known as the Melrose mine, which was active in the 1930s with reports of 916 ounces of gold recovered from 2,955 t of ore (Forman, 1938; Blight, 1985; Northern Star Resources Limited, July, 2015). The geological evolution of the area around Paulsens is not well known, and information is restricted to exploration company reports and short summaries in reports of the Geological Survey of Western Australia. Gold mineralization is contained within auriferous quartz–sulfide veins hosted in a folded and faulted gabbro dike (Fielding and Stokes, 2014; Northern Star Resources Limited, July, 2015).

In this study, a combination of field mapping, petrography, and multi-mineral U–Th–Pb Sensitive High-Resolution Ion Microprobe (SHRIMP) geochronology has been used to address the absolute timing of mineralization at Paulsens, and its relationship to known tectonothermal events in the region. Samples were taken from the Paulsens East and Gabbro Offset prospects that are located adjacent to the main Paulsens deposit (Figure 2-2). These prospects share many similarities with Paulsens, but have not been subject to the same degree of deformation, thereby making it easier to establish relationships between deformation and ore formation. Results from this study provide

U–Pb ages for: i) the emplacement of the gabbroic host-rocks and maximum depositional ages for the Hardey Formation, and ii) the timing of punctuated hydrothermal alteration and gold mineralization.

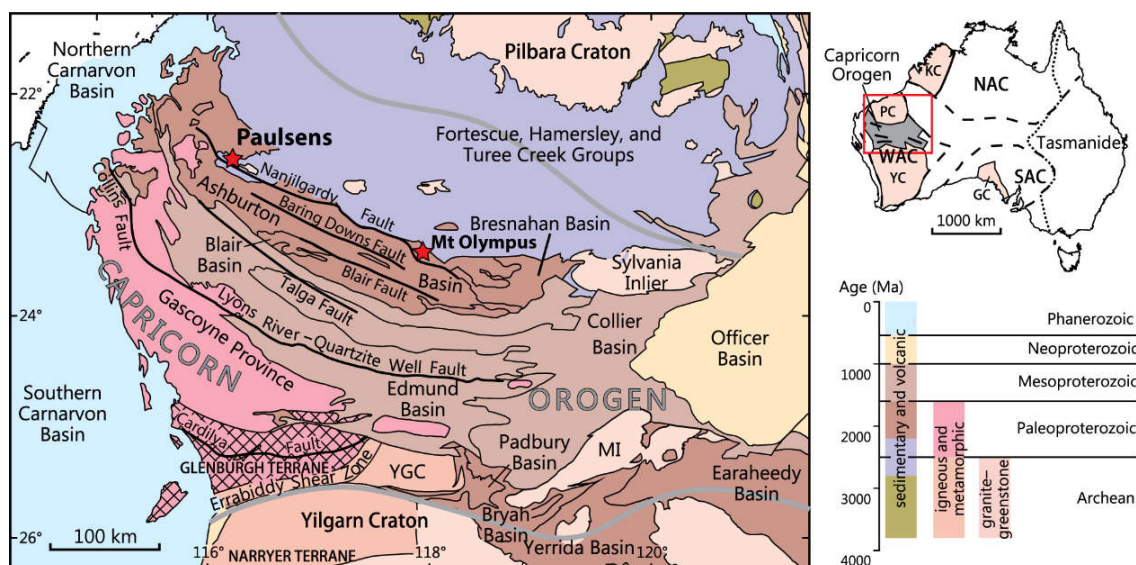


Figure 2-1: Regional geological setting of the northern Capricorn Orogen, showing the location of the Paulsens gold mine. Abbreviations: GC, Gawler Craton; KC, Kimberley Craton; MI, Marymia Inlier; NAC, North Australian Craton; PC, Pilbara Craton; SAC, South Australian Craton; WAC, West Australian Craton; YC, Yilgarn Craton; YGC, Yarlalweelor Gneiss Complex (after Johnson et al., 2013).

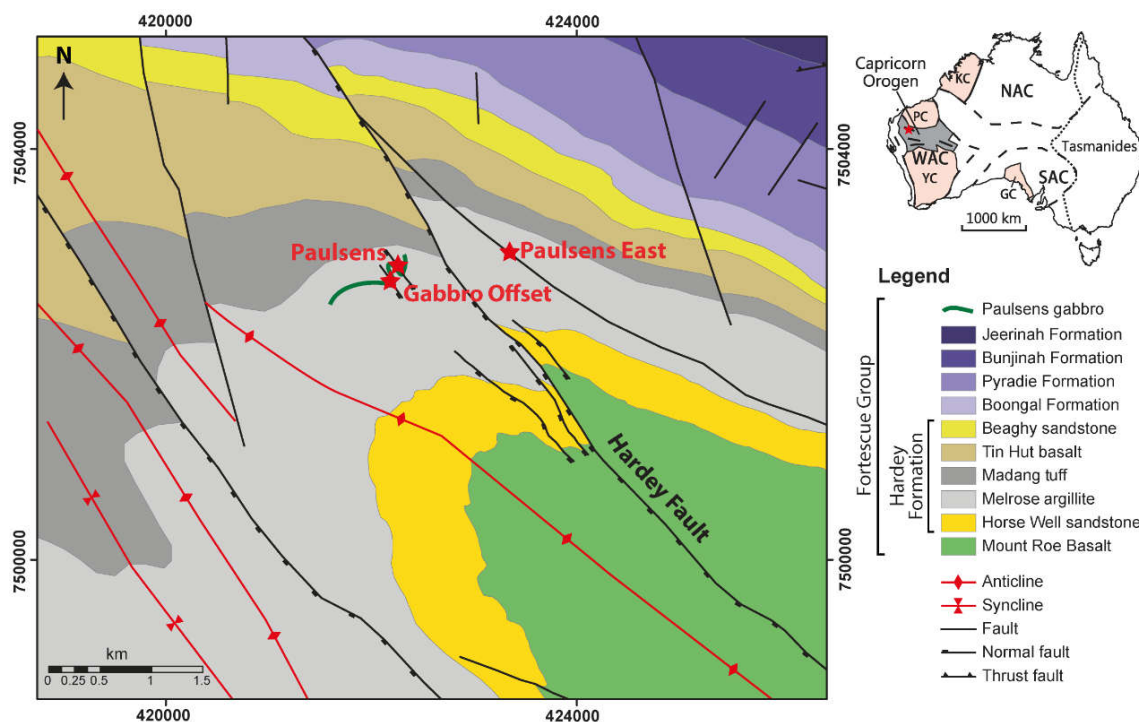


Figure 2-2: Local geological map of the northwest corner of the Wyloo Inlier, showing the location of the Paulsens, Gabbro Offset and Paulsens East deposits. Coordinates are in metres (MGA94 zone 50).

2.3. GEOLOGICAL SETTING

The Proterozoic Capricorn Orogen in Western Australia is a major zone of deformation, metamorphism, and magmatism located between the Yilgarn and Pilbara Cratons (Tyler and Thorne, 1990; Cawood and Tyler, 2004; Sheppard et al., 2010; Thorne et al., 2011). It is the product of at least seven tectonic events, with intracratonic reworking and basin formation spanning more than 1.6 billion years (Martin and Morris, 2010; Sheppard et al., 2010; Johnson et al., 2011; Johnson et al., 2013). Tectonothermal events include the 2215–2145 Ma Ophthalmia Orogeny, which is thought to reflect collision of the Pilbara Craton with the Glenburgh Terrane (Occhipinti et al., 2004; Johnson et al., 2011), and the 2005–1950 Ma Glenburgh Orogeny, which records collision of the Yilgarn Craton with the combined Pilbara Craton – Glenburgh Terrane and marks the assembly of the West Australian Craton (Johnson et al., 2011). This was followed by intracontinental reworking during the 1820–1770 Ma Capricorn Orogeny (Cawood and Tyler, 2004; Sheppard et al., 2010), the 1680–1620 Ma Mangaroon Orogeny (Sheppard et al., 2005), the 1320–1170 Ma Mutherbukin Tectonic Event (Korhonen et al., 2017), the 1030–955 Ma Edmundian Orogeny (Martin and Thorne, 2004; Sheppard et al., 2007), and the c. 570 Ma Mulka Tectonic Event (Johnson et al., 2013). The northern part of the Capricorn Orogen includes Archean rocks of the Pilbara Craton, which are overlain by Archean to Paleoproterozoic rocks of, in ascending order, the Fortescue Group, Hamersley Group, Turee Creek Group, Shingle Creek Group (formerly the lower Wyloo Group), Wyloo Group (formerly the upper Wyloo Group), and Capricorn Group (Figure 2-3a; Thorne and Trendall, 2001).

The Fortescue Group was deposited during protracted rifting of the Pilbara Craton between c. 2775 and 2629 Ma. In the South Pilbara Sub-basin, deposition was controlled by east- to southeast-trending extensional faults (Blake, 1993; Thorne and Trendall, 2001; Trendall et al., 2004; Thorne et al., 2011). Here the group comprises a 6.5 km-thick succession of metasedimentary and metavolcanic rocks deposited unconformably on granite–greenstone rocks of the Pilbara Craton, and comprises, in ascending order, the Bellary Formation, Mt Roe Basalt, Hardey Formation, Boongal Formation, Pyradie Formation, Bunjinah Formation and Jeerinah Formation (Figure 2-3b; Thorne and Trendall, 2001; Thorne et al., 2011).

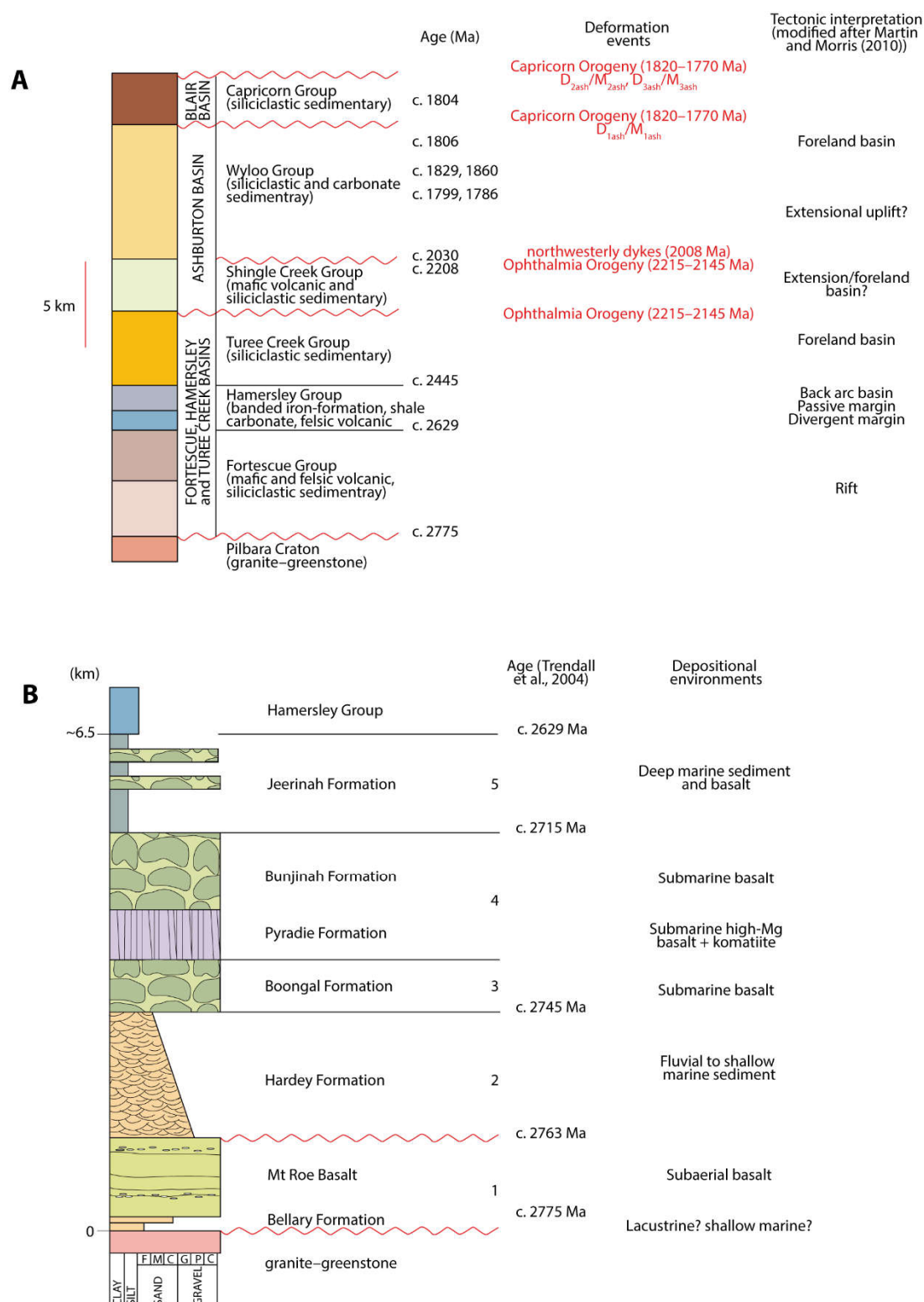


Figure 2-3: A: Lithostratigraphic column and chronology of events for units in the northern Capricorn Orogen. B: Lithostratigraphic column, ages, and depositional environments for the Fortescue Group (adapted from Thorne et al., 2011).

Thorne and Trendall (2001) divided the stratigraphy into five major tectono-stratigraphic sequences with different depositional settings. Sequences 1 and 2 were deposited in fault-bounded sub-basins in a coastal to shallow-marine environment, and

comprise, respectively, sedimentary rocks, basaltic lavas, and volcanoclastic rocks of the Bellary Formation and Mt Roe Basalt, and mixed sedimentary and volcanic rocks of the Hardey Formation. Merging of the sub-basins, subsidence, and regional tilting resulted in deposition of Sequences 3 and 4, which consists of subaqueous basaltic to komatiitic lavas of the Boongal Formation, and the Bunjinah and Pyradie Formations, respectively, that were deposited in a deep shelf setting. Further subsidence resulted in a major marine transgression and the deposition of Sequence 5, consisting of interbedded deep-marine sedimentary and volcanoclastic rocks, and basaltic lavas of the Jeerinah Formation.

A deep-crustal seismic reflection survey across the Capricorn Orogen imaged the crustal architecture of the orogen and the cratonic margins, identifying at least five major mantle-tapping structures (Johnson et al., 2013). In the northern Capricorn Orogen, the Nanjilgardy, Baring Downs and Blair Faults are of particular interest because they are spatially associated with gold and base metal occurrences, including the Paulsens and Mount Olympus deposits (Figure 2-1; Johnson et al., 2013). Deformation, metamorphism and hydrothermal activity in the Wyloo Inlier have been interpreted to be related to either the 2215–2145 Ma Ophthalmia Orogeny (Rasmussen et al., 2005; Martin and Morris, 2010) or the 1820–1770 Ma Capricorn Orogeny (Thorne and Trendall, 2001), or both, although no geochronological data are available from around Paulsens to verify these suggestions.

2.4. LOCAL GEOLOGY

The Paulsens gold mine is situated at the northwestern end of the Wyloo Inlier, within metasedimentary and metavolcanic rocks of the Hardey Formation, near the base of the Fortescue Group (Owen, 2000; Thorne and Trendall, 2001). The mine geologists at Paulsens divided the Hardey Formation into five informal members, from oldest to youngest, the Horsewell sandstone, Melrose argillite, Madang tuff, Tin Hut basalt, and Beaghy sandstone (Figure 2-2; Owen, 2000). These strata are cut at a low angle by a ~ 50 m thick, folded and faulted, medium- to coarse-grained mafic dike, known as the Paulsens gabbro which, over short distances, follows the contact between fine-grained sandstone and laminated carbonaceous shale of the Melrose argillite (Fielding and

Stokes, 2014). Regional scale epidote–actinolite greenschist facies metamorphism has affected the rocks throughout the Wyloo Inlier (White et al., 2014a).

Structural observations across the Wyloo Inlier, as well as from underground drives and diamond drill core, show that the rocks were subjected to at least three low-grade deformation events (Owen, 2000). The first two events were responsible for the production of two dominant regional-scale cleavages. The S_1 cleavage is axially planar to regional-scale, tight to upright folds that define the long axis of the Wyloo Inlier. The S_1 fabric is a penetrative, spaced cleavage with an average orientation of 140/85SW, and is tentatively correlated with the D_{3oph} event of the Ophthalmia Orogeny (Tyler and Thorne 1990; Tyler 1991). The D_2 event is also marked by a spaced cleavage (S_2), that is subparallel to the regional S_1 fabric, with an average orientation of 125/85SW. D_2 caused the tightening of F_1 folds and attenuation of the northern limbs to form narrow, intense shear zones up to 50 m wide. The D_2 event may be equivalent to the D_{2ash} event of the Capricorn Orogeny, during which pre-existing structures were either reactivated or tightened (Thorne and Seymour 1991). Due to the near-coaxial nature of the two cleavages, distinguishing between S_1 and S_2 in the field can be difficult. The third event (D_3) is characterized by strike-slip faulting, possibly through the reactivation of pre-existing faults such as the Hardey Fault to the northeast of the Paulsens mine (Figure 2-2). The Hardey Fault is a splay of the crustal-scale Nanjilgardy Fault which may have been a conduit for both hydrothermal and mineralized fluids during reactivation over multiple deformation events (Johnson et al., 2013).

2.5. MINERALIZATION AND ALTERATION

The Paulsens orebody is hosted by a 40 m-thick auriferous quartz–sulfide vein within the Paulsens gabbro, where the gabbro crosscuts fine-grained carbonaceous sandstone and siltstone of the Melrose argillite. Rheological contrasts between the gabbro and surrounding sedimentary rocks resulted in brittle fracturing of the gabbro during regional-scale F_1 folding, allowing for deposition of the auriferous quartz–sulfide vein (Figure 2-4; Fielding and Stokes, 2014). Mineralization is located at the margins of the vein and is referred to as Paulsens Upper Zone and Paulsens Lower Zone

mineralization (Northern Star Resources Limited, July, 2015). Upper Zone mineralization is defined by brecciated massive pyrite (Figure 2-5a; Owen, 2000).

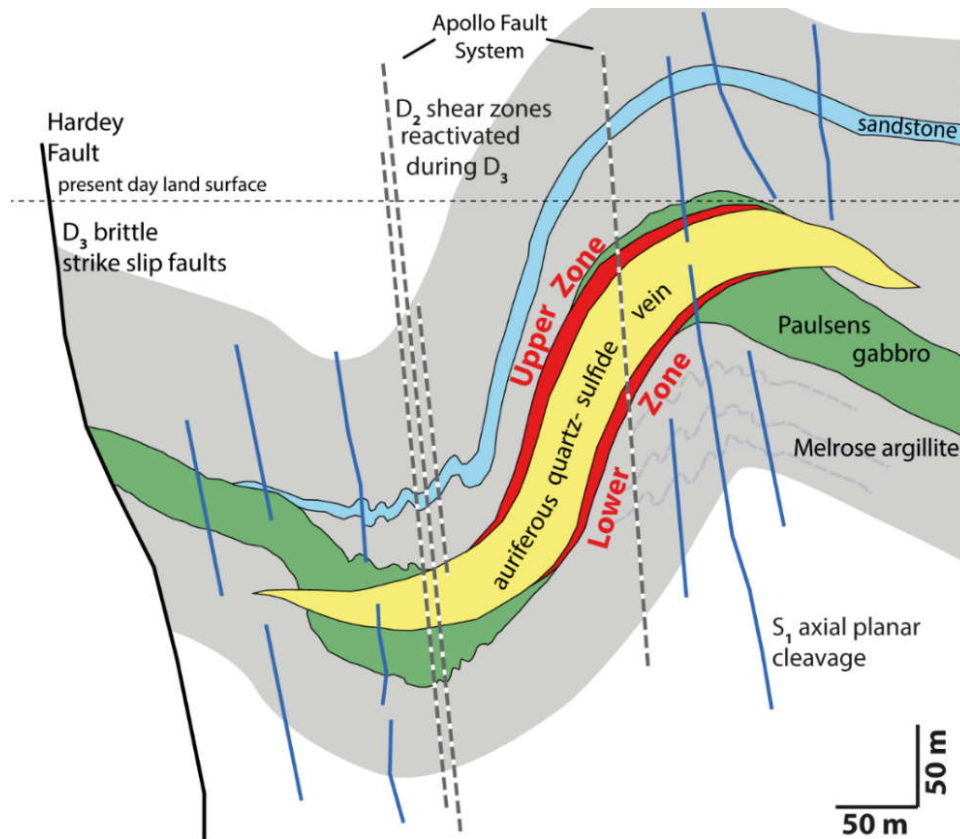


Figure 2-4: Schematic vertical cross-section of the Paulsens deposit (adapted from Fielding and Stokes, 2014). Viewed southeast with no vertical exaggeration.

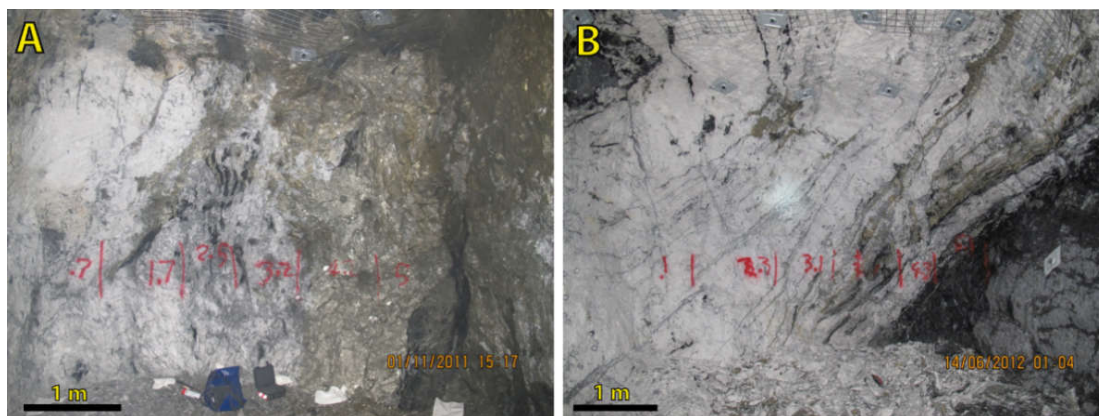


Figure 2-5: A: Photograph of Paulsens Upper Zone mineralization, showing massive pyrite at the margin of the auriferous quartz-sulfide vein. B: Paulsens Lower Zone mineralization, showing laminated quartz-sulfide veins with abundant wall rock inclusions and stylolites parallel to the vein margin.

Gold is rarely observed in hand specimen in the Upper Zone but petrographic studies show that early gold forms rounded inclusions within pyrite crystals and displays simple monocrystalline twinned microstructures with silver contents of 8.0 – 8.5 wt%. A second phase of gold formed along fractures and at grain boundaries where the pyrite

is brecciated. This style of gold is typically associated with chalcopyrite and pyrrhotite, and has a lower silver content, ranging from 6.6 – 7.2 wt%, with simple monocrystalline microstructure and some twin planes (Hancock and Thorne, 2016). Lower Zone mineralization is hosted within the finely laminated basal part of the quartz–sulfide vein, which contains abundant carbonaceous stylolites and highly altered wall rock inclusions of argillite that are pervasively altered to muscovite–ankerite \pm chlorite (Figure 2-5b). The stylolites and wall rock inclusions are associated with abundant free gold (Fielding and Stokes, 2014), with silver contents between 6.8 and 7.6 wt% and simple polycrystalline microstructure with polysynthetic and incoherent twins similar to the second style of gold in the Upper Zone mineralization (Hancock and Thorne, 2016).

Proximal to the Paulsens mineralization, regional-scale greenschist facies metamorphic assemblages are overprinted by a hydrothermal alteration assemblage that is associated with gold mineralization. Primary mineral assemblages within the Paulsens gabbro are almost entirely replaced, with plagioclase altered to muscovite, and pyroxene replaced mainly by ankerite but with patches of muscovite–quartz–ankerite. Iron oxide minerals, possibly originally ilmenite and titanomagnetite, have been totally altered to leucoxene. Sedimentary rocks of the Melrose argillite member are now composed almost entirely of muscovite with minor quartz–ankerite \pm chlorite. Alteration distal to the ore body is difficult to differentiate from the regional metamorphic background; however, a change from ankerite to calcite along with an increase in chlorite and decrease in muscovite content occurs progressively away from the ore body.

Gabbro Offset and Paulsens East are two smaller prospects adjacent to the main Paulsens ore body (Figure 2-2). They share many characteristics of Paulsens, but have not been subject to the same degree of deformation, which allows more straightforward determination of timing relationships between ore formation and the regional geological history.

Gabbro Offset is located 350 meters southwest of the main Paulsens orebody and consists of a series of parallel quartz–carbonate–sulfide veins within the Paulsens gabbro. Mineralized veins are typically narrow, usually between 0.1 and 10 m wide, with visible gold along their margins or within massive pyrite similar to Paulsens

Upper Zone mineralization. Petrographic examination of pyrite from samples (GSWA 209907) from Gabbro Offset reveals two styles of native gold inclusions within the pyrite. Pyrite crystals show subtle zoning with an inclusion-rich core surrounded by a thin rim (<1mm) of solid pyrite. Rounded blebs of native gold and chalcopyrite within the cores are interpreted to be primary inclusions (Figure 2-6a). These inclusions are up to 200 μm in diameter and form the majority of visible gold in the samples. The pyrite is locally brecciated, and chalcopyrite, pyrrhotite, and gold occur along fractures and pyrite grain boundaries (Figure 2-6b). Although there is some evidence for gold remobilization (from the rounded gold inclusions in the cores of pyrites) at a local scale (Figure 2-6c), it is possible that this secondary gold represents the introduction of new gold from an additional hydrothermal event.

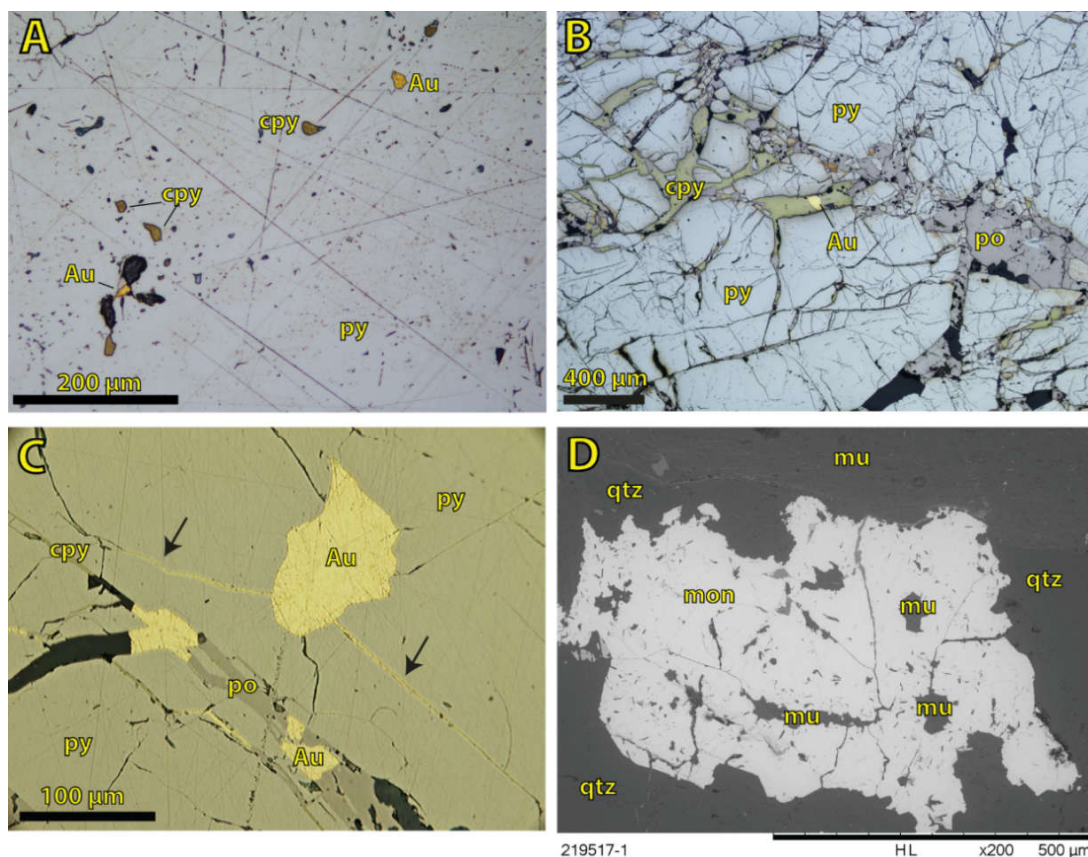


Figure 2-6: A: Reflected light photomicrograph showing rounded blebs of native gold and chalcopyrite contained within pyrite (GSWA 209907). B: Reflected light photomicrograph showing brecciated pyrite with native gold, chalcopyrite and pyrrhotite along the fractures (GSWA 209907). C: Reflected light photomicrograph showing local remobilization of gold along a fracture in pyrite, the arrows highlight local remobilization of gold from the primary rounded blebs of gold (GSWA 209907). D: Scanning Electron Microscope backscattered electron image (SEM-BSE) showing a large monazite crystal with inclusions of muscovite from the alteration halo surrounding an auriferous quartz-sulfide vein at the Paulsens East deposit (GSWA 219517). Mineral abbreviations, Au, gold; cpy, chalcopyrite; mon, monazite; mu, muscovite; po, pyrrhotite; py, pyrite; qtz, quartz.

Paulsens East mineralization is located approximately one kilometre east of the main Paulsens orebody (Figure 2-2) and, historically, gold was extracted from a series of

shallow workings. Mineralization is hosted within parallel, steeply northeast-dipping, 1–5 m-wide veins comprising quartz, carbonate, and oxidized sulfides that are hosted within the Melrose argillite on the northern side of the Hardey Fault. Sedimentary rocks in contact with the mineralized veins at Paulsens East have been deformed and pervasively altered to an assemblage containing muscovite–quartz \pm ankerite \pm chlorite \pm monazite (Figure 2-6d), similar to that of the main Paulsens orebody.

2.6. STYLE OF GOLD MINERALIZATION

The Paulsens deposit exhibits many of the characteristics of a typical orogenic gold deposit. Orogenic gold deposits form in the upper to middle crust in compressional tectonic settings related to accretionary or collisional orogenesis, and tend to have a close spatial relationship to trans-crustal structures which mark the boundaries between continental blocks (Groves et al., 1998; Goldfarb et al., 2001; Hronsky et al., 2012). Host rocks are varied, with Archean deposits commonly formed in volcanic-dominated sequences and Paleoproterozoic and Phanerozoic deposits formed in siliciclastic sequences (Goldfarb and Groves, 2015). Most deposits are hosted by rocks that have been metamorphosed to greenschist facies and commonly have alteration assemblages of carbonate–iron sulfide \pm white mica \pm chlorite (Goldfarb et al., 2001). Gold mineralization is characteristically high grade (5–30 g/t Au) and associated with quartz \pm carbonate veins with \leq 3–5 % sulfides (Groves et al., 1998). Unlike other styles of mineralization (e.g. epithermal and intrusion related), orogenic gold deposits cannot be related to individual intrusions and do not display zoned alteration halos (Goldfarb and Groves, 2015, Sillitoe, 1997). Paulsens has many of these traits: a spatial relationship to the mantle-tapping Nanjilgardy Fault, siliciclastic sedimentary host rocks that have been metamorphosed to greenschist facies, the high-grade nature of gold mineralization (average 8.59 g/t Au), gold hosted in quartz-carbonate-sulfide veins surrounded by muscovite-ankerite \pm chlorite alteration, and an absence of coeval igneous intrusions.

2.7. SAMPLES AND ANALYTICAL METHODS

Samples from Gabbro Offset were collected from three drill cores supplied by Northern Star Resources (PDU2153, PLDD015W1 and PDU2217); samples from

Paulsens East were collected from outcrops where relationships between mineralization and deformation could be ascertained. A list of dated samples is provided in **Error! Reference source not found..**

GSWA Sample ID	Deposit	Target mineral	MGA94 Zone 50		Drillcore number	Depth (m)	Sample description
			East	North			
209902	Gabbro Offset	monazite	421626	7503994	PDU2153	164.2-164.3	Carbonaceous phyllite – Hardey Formation
209903	Gabbro Offset	zircon	421626	7503994	PDU2153	109.3-109.7	Quartz sandstone – Hardey Formation
209905	Gabbro Offset	baddeleyite	421626	7503994	PDU2153	346.0-346.2	Dolerite sill – Paulsens gabbro
209907	Gabbro Offset	xenotime	421626	7503994	PDU2153	394.4-395.5	Massive Au-bearing sulfide vein
209909a	Gabbro Offset	monazite	421626	7503994	PDU2153	345.1-345.3	Altered part of Paulsens gabbro (209905)
209909b	Gabbro Offset	xenotime	421626	7503994	PDU2153	345.1-345.3	Ankerite–quartz vein in dolerite sill (209905)
209911	Gabbro Offset	zircon	421995	7503917	PLDD015W1	473.6-473.9	Quartz sandstone – Hardey Formation
209912	Gabbro Offset	monazite	421617	7503972	PDU2217	103.8-104.0	Carbonaceous phyllite – Hardey Formation
219512	Paulsens East	monazite	423092	7503087	Outcrop	Surface	Micaceous phyllite – Hardey Formation
219513	Paulsens East	monazite	423092	7503087	Outcrop	Surface	Micaceous phyllite – Hardey Formation
219517	Paulsens East	monazite	423068	7503073	Outcrop	Surface	Micaceous phyllite – Hardey Formation

Table 2-1: List of sample locations and descriptions.

Monazite, xenotime, zircon and baddeleyite were analysed for U, Th and Pb isotopes using the SHRIMP II instrument at the John de Laeter Centre at Curtin University in Perth, Western Australia. Details of the methodology are described in 2.13. Supplementary Data.

Detrital zircons were separated from sedimentary host rocks using standard magnetic and density techniques. Zircons, together with zircon reference materials (BR266 and OGC), were cast in 25 mm epoxy mounts and polished to expose the interiors of the crystals. Each mount was gold coated and characterized using transmitted light, reflected light, and cathodoluminescence (CL) images (Figure 2-7).

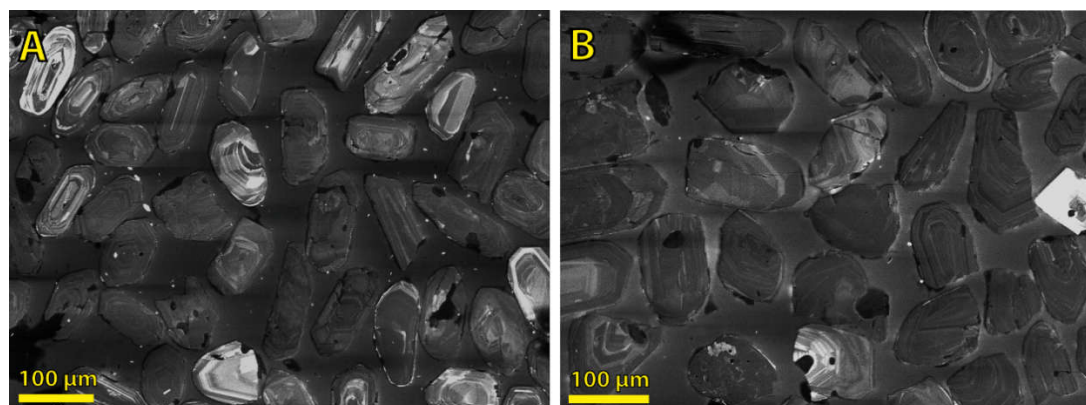


Figure 2-7: Cathodoluminescence (CL) images of representative detrital zircon grains in Hardey Formation sandstone samples. A: Sample GSWA 209903, B: Sample GSWA 209911.

U–Th–Pb analysis of monazite, xenotime and baddeleyite was conducted in situ in order to preserve textural context. Grains for analysis were identified using a scanning electron microscope (SEM) in polished thin sections, and 2 or 3 mm-diameter plugs were extracted from the polished thin sections with a hollow-core rotary drill and mounted in 25 mm-diameter epoxy discs. The mounts were cleaned and gold coated before each analytical session. Reference materials were set into separate mounts and gold coated simultaneously with sample mounts. Standard and sample mounts were loaded together into the SHRIMP for concurrent analysis during each analytical session.

2.8. GEOCHRONOLOGY RESULTS AND INTERPRETATION

For all samples, age estimates are derived from 204-corrected $^{207}\text{Pb}^*/^{206}\text{Pb}^*$ ratios. Results for individual analyses are quoted with 1-sigma (1σ) uncertainties; weighted mean $^{207}\text{Pb}^*/^{206}\text{Pb}^*$ dates are quoted with 95% confidence intervals. All data table can be found in the supplementary data in section 2.13.2 Data Tables.

2.8.1. DETRITAL ZIRCON

Detrital zircons from two Hardey Formation sandstone samples (**Error! Reference source not found.**) were dated to provide a maximum depositional age for the supracrustal rocks into which the Paulsens gabbro was emplaced.

2.8.1.1. GSWA 209903 – QUARTZ SANDSTONE, HARDEY FORMATION

Medium-grained, strongly cleaved, quartz sandstone of the Melrose argillite member of the Hardey Formation was collected from 109.3–109.7 m depth in drill core PDU2153 in the hanging wall of the Gabbro Offset deposit.

Zircons are generally colorless, up to 150 μm in length, and euhedral, although rounded terminations and pitting are indicative of detrital transport (Figure 2-7a). Sixty-five analyses were made of 64 zircons, of which two analyses >5% discordant were excluded from the age analysis. The zircons range in age from c. 3456 to 2923 Ma ($n=63$). The youngest detrital zircon age component consists of 15 analyses that yield a weighted mean $^{207}\text{Pb}^*/^{206}\text{Pb}^*$ date of 2941 ± 5 Ma (MSWD = 1.4; Supplementary Table 2-1, Figure 2-8a and c), providing a maximum age for deposition of the quartz sandstone.

2.8.1.2. GSWA 209911 – QUARTZ SANDSTONE, HARDEY FORMATION

Medium- and fine-grained quartz sandstone, with very fine-grained matrix, from the Melrose argillite member was collected from the hanging wall to the Gabbro Offset deposit from drill core PLDD015W1 between 473.6 and 473.9 m depth.

Zircons are euhedral, up to 150 μm long, mainly colorless, and have rounded terminations and pitting characteristic of detrital transport (Figure 2-7b). Sixty-two analyses were made on 62 grains, of which 20 analyses >5% discordant were excluded from the age analysis. The zircons range in age from c. 3450 to 2700 Ma. The youngest detrital zircon age component, consisting of 9 analyses, yields a weighted mean $^{207}\text{Pb}^*/^{206}\text{Pb}^*$ date of 2750 ± 10 Ma (MSWD = 1.5; Supplementary Table 2-2, Figure 2-8b and d), providing a maximum age for deposition of the sandstone.

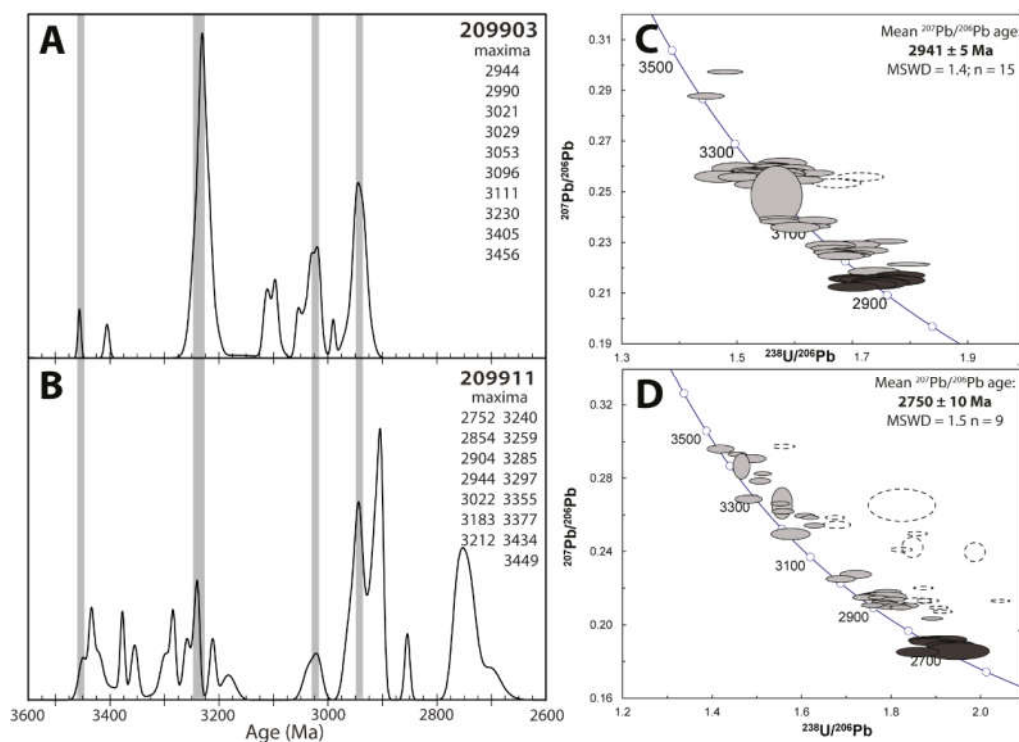


Figure 2-8: Probability density diagrams and histograms of zircon ages for A: sample GSWA 209903 (63 analyses of 63 zircons), B: sample GSWA 209911 (42 analyses of 42 zircons). Black curves include only data <5% discordant. C and D: Tera-Wasserburg concordia diagrams of U–Pb data for detrital zircons from samples GSWA 209903 and GSWA 209911. Dark grey ellipses indicate analyses comprising the youngest detrital age component; light grey ellipses are the remaining data <5% discordant, and dashed ellipses indicate data >5% discordant.

2.8.2. BADDELEYITE

2.8.2.1. GSWA 209905 – ALTERED DOLERITE, PAULSENS GABBRO:

A fine-grained, dark-colored portion of the Paulsens gabbro that is host to the Gabbro Offset deposit was collected from 346.0–346.2 m depth in drill core PDU2153 (Table

2-1). At this locality the gabbro is highly altered and primary plagioclase and pyroxene are replaced by muscovite and ankerite \pm muscovite \pm chlorite, respectively, and iron oxide minerals have been altered to leucoxene. However, euhedral baddeleyite crystals up to 100 μm long are preserved throughout the sample. The outer surfaces of baddeleyite grains are commonly altered to very fine-grained aggregates of zircon (Figure 2-9a).

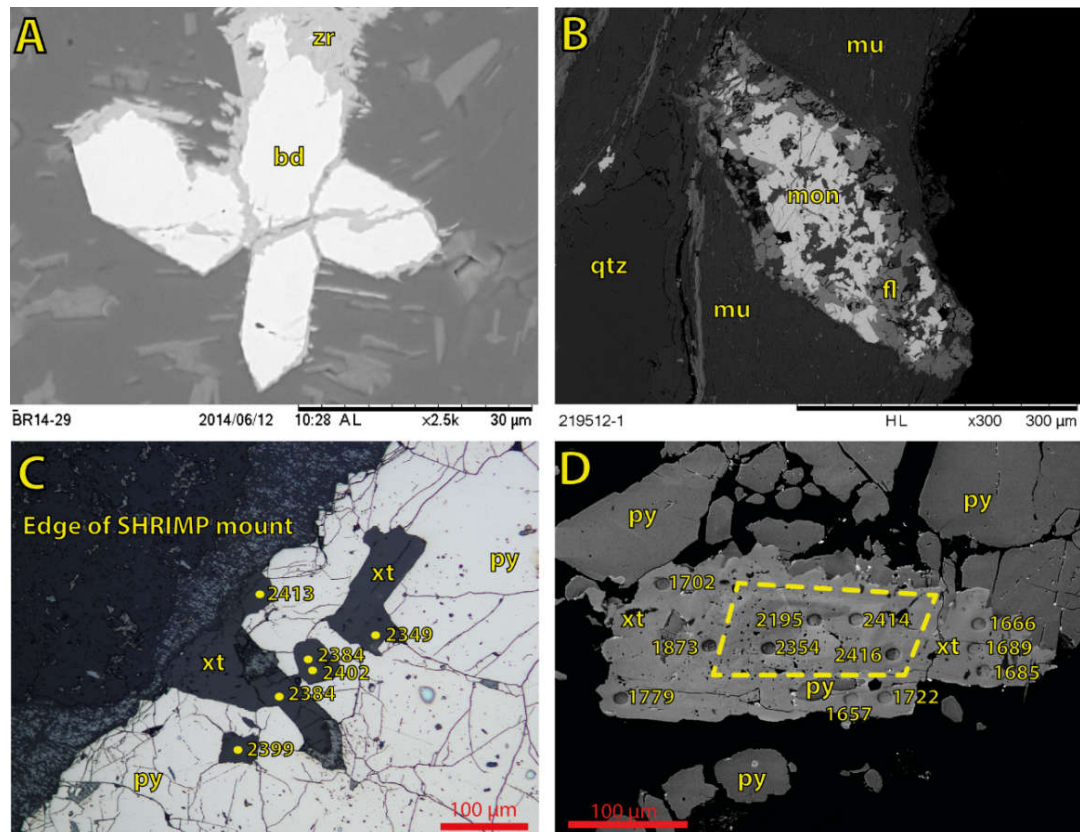


Figure 2-9: A: SEM-BSE image of euhedral baddeleyite crystals with altered rim of very fine-grained zircon (GSWA 209905). B: SEM-BSE image of florencite–monazite porphyroblast (GSWA 219512). C: Reflected light image of euhedral xenotime grains enclosed entirely within pyrite grains with analytical sites marked by dots showing c. 2400 Ma dates (GSWA 209907). D: SEM-BSE image of xenotime intergrown with pyrite (oval pits on the grain are SHRIMP analysis sites) revealing a c. 2400 Ma core surrounded by a c. 1680 Ma rim. Mineral abbreviation: bd, baddeleyite; fl, florencite; mon, monazite; mu, muscovite; py, pyrite; xt, xenotime; zr, zircon.

Seventeen analyses were made of 11 baddeleyite grains. Two analyses with elevated common Pb and two analyses $>5\%$ discordant were excluded from the age analysis. A single analysis yielded a concordant $^{207}\text{Pb}^*/^{206}\text{Pb}^*$ date significantly younger than the main cluster, and is interpreted to reflect ancient Pb-loss during alteration. The remaining 12 analyses yield a weighted mean $^{207}\text{Pb}^*/^{206}\text{Pb}^*$ date of 2701 ± 11 Ma (MSWD = 1.4; Supplementary Table 2-3, Figure 2-10a), interpreted as the time of igneous crystallization of the Paulsens gabbro, the host-rock to gold mineralization.

2.8.3. XENOTIME

2.8.3.1. GSWA 209907 – AURIFEROUS QUARTZ–SULFIDE VEIN

In the lower part of drill core PDU2153 between 394.4 and 395.5 m, a series of 1 cm to 1–2 m-wide massive sulfide and quartz–sulfide veins are abundant. These veins are part of the Gabbro Offset deposit and share similarities to Paulsens Upper Zone mineralization. A massive sulfide vein was sampled for geochronology (Table 2-1), the lower 10 cm of which contained xenotime. The sample is associated with gold grades of 21 ppm, with gold formed as rounded inclusions within pyrite crystals (Figure 2-6a) and along grain boundaries and fractures in areas where the pyrite is brecciated (Figure 2-6b). The sample comprises an interlocking assemblage of quartz and pyrite, and contains xenotime in a number of textural settings: as euhedral grains enclosed entirely within pyrite (Figure 2-9c), as subhedral grains within the quartz–pyrite matrix commonly intergrown along the margins of brecciated pyrite (Figure 2-9d), and as euhedral to subhedral grains within the quartz matrix. Commonly the matrix xenotime grains are chemically zoned showing core and rim growth structures (Figure 2-9d).

Eighty analyses were made on 37 grains, with multiple analyses performed within or across single grains. Irrespective of age or site of analysis, uranium and thorium contents range from 104 to 928 ppm and 2 to 695 ppm, respectively. Six analyses >5% discordant, and 12 analyses that represent mixed ages, or parts of grains that have undergone Pb loss, are not considered geologically significant and are excluded from the age analysis. Twenty-six analyses of euhedral xenotime grains entirely enclosed within pyrite grains or as core zones of matrix xenotime present along brecciated pyrite grain boundaries (Figure 2-9d), yield a weighted mean $^{207}\text{Pb}^*/^{206}\text{Pb}^*$ date of 2403 ± 5 Ma (MSWD = 1.1; Supplementary Table 2-4, Figure 2-10b). Thirty-six analyses of xenotime rims and discrete grains within the quartz matrix yield a weighted mean $^{207}\text{Pb}^*/^{206}\text{Pb}^*$ date of 1680 ± 9 Ma (MSWD = 1.4). We interpret these two dates to represent times of xenotime growth and subsequent dissolution-reprecipitation during two discrete periods of hydrothermal activity. The first event at c. 2403 Ma is interpreted to date the formation of the quartz–sulfide vein, because grains of this age are contained entirely within the pyrite crystals. The second date at c. 1680 Ma is interpreted to represent a subsequent period of hydrothermal activity, responsible for

the brecciation and fracturing of pyrite grains and the dissolution-reprecipitation of pre-existing c. 2403 Ma xenotime.

2.8.3.2. *GSWA 209909B – ANKERITE–QUARTZ VEIN*

Minor, 5–10 cm-wide carbonate veins within the fine-grained portion of the Paulsens gabbro (GSWA 209905) at the Gabbro Offset deposit were sampled from drill core PDU2153 between 345.1 and 345.3 m depth (Table 2-1). Assays from depths between 345 and 346 m returned up to 48 ppm Au. Xenotime occurs in the carbonate vein as irregular grains up to 50 µm across, interstitial to, and included within, other minerals.

Seven analyses were made on seven xenotime grains. Uranium and thorium contents vary from 200 to 550 ppm and 250 to 1350 ppm, respectively. Two analyses >5% discordant were not used in the age analysis. One grain is significantly older than the others, with a date of 2415 ± 11 Ma (1σ). There are no textural or chemical differences between this grain and the others analysed. The remaining four analyses of four grains yield a weighted mean $^{207}\text{Pb}^*/^{206}\text{Pb}^*$ date of 1655 ± 37 Ma (MSWD = 1.3; Supplementary Table 2-5, Figure 2-10c). The older xenotime date corresponds with the age of monazite in the altered host gabbro (GSWA 209909a) and is interpreted to be inherited from the hydrothermally altered host rocks. The younger age of xenotime growth at c. 1655 Ma, obtained from multiple grains, is attributed to a second, discrete hydrothermal event, probably dating emplacement of the ankerite–quartz veins, and is within uncertainty of xenotime rims in the auriferous quartz–sulfide vein (GSWA 209907).

2.8.4. MONAZITE

2.8.4.1. *GSWA 209902 – CARBONACEOUS PHYLLITE, HARDEY FORMATION*

Very fine-grained, black, carbonaceous, quartz–muscovite–chlorite phyllite of the Melrose argillite member was sampled from drill core PDU2153 between 164.2 and 164.3 m depth in the hanging wall to the Gabbro Offset deposit (Table 2-1). The phyllite has a very strong foliation that has disrupted and deformed 3–20 mm-thick quartz ± pyrite veins. The sample contains randomly distributed, 1 mm-long elongate porphyroblasts consisting of intergrown monazite and apatite, in equal amounts, with

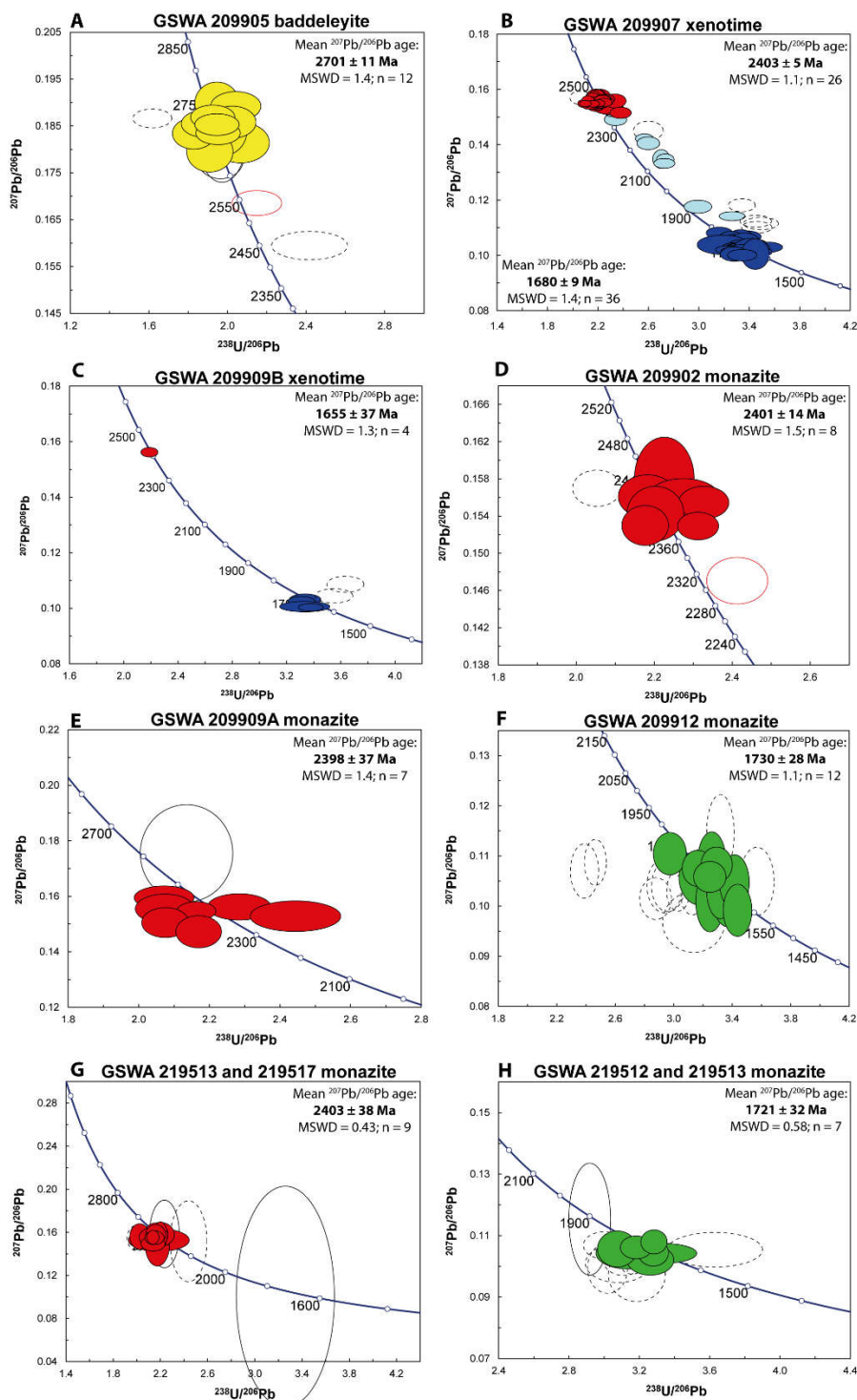


Figure 2-10: Tera-Wasserburg concordia diagrams of U-Pb data for baddeleyite, xenotime and monazite. A: Baddeleyite in gabbroic host rock to gold mineralization at the Gabbro Offset deposit (GSWA 209905). B: Xenotime in auriferous quartz-sulfide veins at the Gabbro Offset deposit (GSWA 209907). C: Xenotime in ankerite-quartz vein within the strongly altered Paulsens Gabbro at the Gabbro Offset deposit (GSWA 209909b). D: Monazite porphyroblasts in carbonaceous phyllites at Gabbro Offset deposit (GSWA 209902). E: Monazite in pervasively altered portion of the Paulsens gabbro at the Gabbro Offset deposit (GSWA 209909a). F: Monazite porphyroblasts in carbonaceous phyllites at the Gabbro Offset deposit (GSWA 209912). G: Monazite in micaceous phyllites surrounding gold mineralization at the Paulsens East deposit (GSWA 219513 and 219517). H: Monazite porphyroblasts in micaceous phyllites at the Paulsens East deposit (GSWA 219512 and 219513). Key: coloured ellipses (yellow, c. 2700 Ma dates; red, c. 2400 Ma dates; green, c. 1730 Ma dates; dark blue, c. 1680 Ma dates) show data used in the age calculations, unshaded ellipses are for inferior data (pale blue, mixed ages; dashed ellipses, discordance >5%; red ellipses, outliers; black ellipses, high common Pb).

lesser chlorite and quartz. It is possible that the apatite has replaced monazite, a common reaction during greenschist to amphibolite facies metamorphism and hydrothermal alteration (Finger et al., 1998; Rasmussen and Muhling, 2009; White et al., 2014b). However, it is not clear whether the monazites are primary metamorphic or hydrothermal porphyroblasts or whether they replaced former regional-scale peak-metamorphic porphyroblasts such as ?andalusite that grew at the same time as the foliation.

Monazite within two porphyroblasts was analysed, with five spots on each. Uranium and Th contents are 200–300 ppm and 2000–10000 ppm, respectively. Of the 10 analyses, one analysis is >5% discordant, and one is significantly younger than other analyses from the same grain, and probably reflects partial Pb-loss. These two analyses are not considered to be geologically significant and were not included in the age analysis. The remaining eight analyses define a weighted mean $^{207}\text{Pb}^*/^{206}\text{Pb}^*$ date of 2401 ± 14 Ma (MSWD = 1.5; Supplementary Table 2-6, Figure 2-10d), interpreted as the age of monazite growth during hydrothermal alteration of the carbonaceous phyllite. This date is indistinguishable from that obtained on xenotime interpreted to date the timing of emplacement of the auriferous quartz–sulfide vein (GSWA 209907).

2.8.4.2. GSWA 209909A – ALTERED DOLERITE, PAULSENS GABBRO

A fine-grained, highly-altered portion of the Paulsens gabbro (that is host to the Gabbro Offset deposit) containing a thin ankerite–quartz vein (GSWA 209909b), was collected from drill core PDU2153 between 345.1 and 345.3 m (Table 2-1). This sample is located one meter above gabbro sample GSWA 209905, which yielded a baddeleyite crystallization age of c. 2701 Ma. Locally, the sampled dolerite is pervasively altered by muscovite–ankerite–leucoxene \pm chlorite, cross-cut by ankerite–quartz veins, and contains up to 48 ppm Au. Monazite in the sample occurs as irregular grains up to 100 μm across, intergrown with and containing inclusions of, leucoxene after iron oxide minerals.

Eight analyses were made of five monazite grains. Uranium and thorium contents are 30–140 ppm and 15000–55000 ppm, respectively. Among the eight analyses, one indicates high common Pb and is excluded. The remaining seven analyses yield consistent $^{207}\text{Pb}^*/^{206}\text{Pb}^*$ dates, but $^{238}\text{U}/^{206}\text{Pb}^*$ dates that vary broadly with Th content, which is probably a residual effect from the Th-correlated interference correction on

^{204}Pb or from the matrix correction. Therefore a less rigorous (10%) discordance cut-off was applied to these analyses. The seven analyses yield a weighted mean $^{207}\text{Pb}^*/^{206}\text{Pb}^*$ date of 2398 ± 37 Ma (MSWD = 1.4; Supplementary Table 2-7, Figure 2-10e), interpreted as the age of monazite growth during hydrothermal alteration of the dolerite. This age is indistinguishable from that obtained from hydrothermal monazite in sample GSWA 209902 and the age of xenotime cores in the auriferous quartz–sulfide (GSWA 209907).

2.8.4.3. GSWA 209912 – CARBONACEOUS PHYLLITE, HARDEY FORMATION

A fine-grained, strongly foliated, black carbonaceous muscovite phyllite of the Melrose argillite member was sampled from drill core PDU2217 between 103.8 and 104.0 m in the footwall to the Gabbro Offset deposit (Table 2-1). The sample is located in a D₂/D₃ high-strain zone and contains lenses and stringers of quartz veins and coarse-grained pyrite. The sample also contains elongate porphyroblasts up to 3 mm long comprising intergrowths of monazite and florencite in sub-equal amounts with lesser quartz and chlorite. In this sample it appears that the monazite is partially replaced by florencite, which is common during greenschist facies metamorphism (Rasmussen and Muhling, 2009). However, it is unclear if the growth of monazite is related to low-grade metamorphism and deformation associated with fault reactivation or if it has locally replaced former regional-scale peak metamorphic porphyroblasts (such as ?andalusite) during hydrothermal alteration.

Twenty-two analyses were made on three monazite grains within the porphyroblasts. Uranium and thorium contents vary from 50 to 120 ppm and 3400 to 14000 ppm, respectively. The largest grain yielded 12 analyses < 5% discordant; the remaining data vary in their $^{238}\text{U}/^{206}\text{Pb}^*$ ages, partly due to the low precision of low-U analyses. The 12 concordant analyses define a weighted mean $^{207}\text{Pb}^*/^{206}\text{Pb}^*$ date of 1730 ± 28 Ma (MSWD = 1.1; Supplementary Table 2-8, Figure 2-10f). This date is interpreted as the age of monazite growth during hydrothermal alteration of the carbonaceous phyllite, possibly during fault reactivation.

2.8.4.4. GSWA 219512, 219513 AND 219517 – MICACEOUS PHYLLITES, HARDEY FORMATION

Fine-grained and slightly weathered phyllites were collected from shallow adits at Paulsens East (Table 2-1) in a 0.5–1.0 m-wide hydrothermal alteration halo

surrounding 1–2 m-wide mineralized quartz–sulfide veins. Samples 219513 and 219517 contain large monazite grains up to 3 mm long intergrown with minerals that define the main hydrothermal alteration assemblage (muscovite, quartz and pyrite) (Figure 2-6d). The quartz–sulfide veins yielded rock-chip assays up to 6.65 ppm Au (Owen, 2000).

Sixteen analyses were made on seven monazite grains. Uranium and thorium contents of the samples varied from 30 to 135 ppm and 590 to 5280 ppm, respectively. Four analyses >5% discordant and three with elevated common Pb were excluded from the age analysis. The remaining nine analyses provide concordant data that define a weighted mean $^{207}\text{Pb}^*/^{206}\text{Pb}^*$ date of 2403 ± 38 Ma (MSWD = 0.43; Supplementary Table 2-9, Figure 2-10g). This date is interpreted to represent the timing of hydrothermal alteration associated with the emplacement of the auriferous quartz–sulfide veins at Paulsens East and is within uncertainty of ages of hydrothermal monazite from altered samples at the Gabbro Offset deposit (GSWA 209902 and 209909a) as well as ages of xenotime cores from the auriferous quartz–sulfide vein at Gabbro Offset (GSWA 209907).

Samples GSWA 219512 and 219513 also contain abundant 1–3 mm-long, elongate porphyroblasts of interlocking monazite–florencite (Figure 2-9b), together with minor chlorite and quartz, similar to the monazite–florencite porphyroblasts in sample GSWA 209912. Fifteen analyses were made on three monazite porphyroblasts. Uranium and thorium contents vary from 170 and 1210 ppm and 380 to 8945 ppm, respectively. Seven analyses >5% discordant and one analysis with elevated common Pb were excluded from the age analysis. The remaining 7 concordant analyses define a weighted mean $^{207}\text{Pb}^*/^{206}\text{Pb}^*$ date of 1721 ± 32 Ma (MSWD = 0.58; Supplementary Table 2-10, Figure 2-10h). Because sample GSWA 219513 also contains abundant, coarse-grained c. 2403 Ma monazite intergrown with the main hydrothermal alteration assemblage (i.e. not detrital), the date of c. 1721 Ma for the monazite porphyroblasts must represent the age of a secondary hydrothermal event that affected the phyllites. This age is within uncertainty of that of monazite porphyroblasts (GSWA 209912) in a D₂/D₃ shear zone at the Gabbro Offset deposit.

2.9. DISCUSSION

SHRIMP U–Th–Pb geochronology has been used to define the age of the host rocks to gold mineralization at the Gabbro Offset deposit, as well as the timing of regional-scale hydrothermal activity associated with the emplacement of the auriferous quartz–sulfide veins and subsequent regional-scale hydrothermal events (Figure 2-11 and Table 2-2).

GSWA Sample ID	Deposit	Target mineral	Grain textures	$^{207}\text{Pb}^*/^{206}\text{Pb}^*$ date (Ma)	No. of analyses	MSWD	Interpretation
209903	Gabbro Offset	zircon	Detrital	2941 ± 5	15	1.4	youngest detrital component
209911	Gabbro Offset	zircon	Detrital	2750 ± 10	9	1.5	youngest detrital component
209905	Gabbro Offset	baddeleyite	Magmatic	2701 ± 11	12	1.4	gabbro crystallization
209907	Gabbro Offset	xenotime	Euhedral/cores	2403 ± 5	26	1.1	growth during hydrothermal alteration assoc. with vein emplacement
209907	Gabbro Offset	xenotime	Matrix/rims	1680 ± 9	36	1.4	dissolution and reprecipitation of xenotime during hydrothermal activity
209909b	Gabbro Offset	xenotime	Matrix	1655 ± 37	4	1.3	carbonate vein emplacement
209902	Gabbro Offset	monazite	Matrix	2401 ± 14	8	1.5	growth during hydrothermal alteration
209909a	Gabbro Offset	monazite	Matrix	2398 ± 37	7	1.4	growth during hydrothermal alteration
209912	Gabbro Offset	monazite	Porphyroblasts	1730 ± 28	12	1.1	growth during hydrothermal alteration
219512/13	Paulsens East	monazite	Porphyroblasts	1721 ± 32	7	0.6	growth during hydrothermal alteration
219513/17	Paulsens East	monazite	Matrix	2403 ± 38	9	0.4	alteration assoc. with vein emplacement

Table 2-2: Summary of geochronology results.

2.9.1. AGE OF THE HOST ROCKS

Sedimentary rocks of the Hardey Formation were deposited between c. 2763 and 2745 Ma (Trendall et al., 2004). The detrital zircon data presented here from two quartz sandstone samples from near the middle of the Hardey Formation (Melrose argillite) have relatively similar detrital age modes (Figure 2-8), although sample GSWA 209911 contains a significant proportion of detritus older than c. 3400 Ma and younger than c. 2900 Ma compared to sample GSWA 209903. Despite these differences, the similarity in age modes at c. 3450, 3240–3230, 3020 and 2944 Ma indicate that they both shared a common source region. The age of 2750 ± 10 Ma for the youngest detrital zircon age component in sandstone sample GSWA 209911 (Figure 2-8) therefore provides a maximum depositional age for the Hardey Formation in the South Pilbara Sub-basin. A minimum age constraint is provided by the baddeleyite crystallization age of 2701 ± 11 Ma for the Paulsens gabbro (GSWA 209905; Figure 2-10a), which intrudes these sedimentary rocks. The crystallization age of the Paulsens gabbro

suggests it may have been a feeder to mafic volcanic horizons in the 2715–2629 Ma Jeerinah Formation (Trendall et al., 2004).

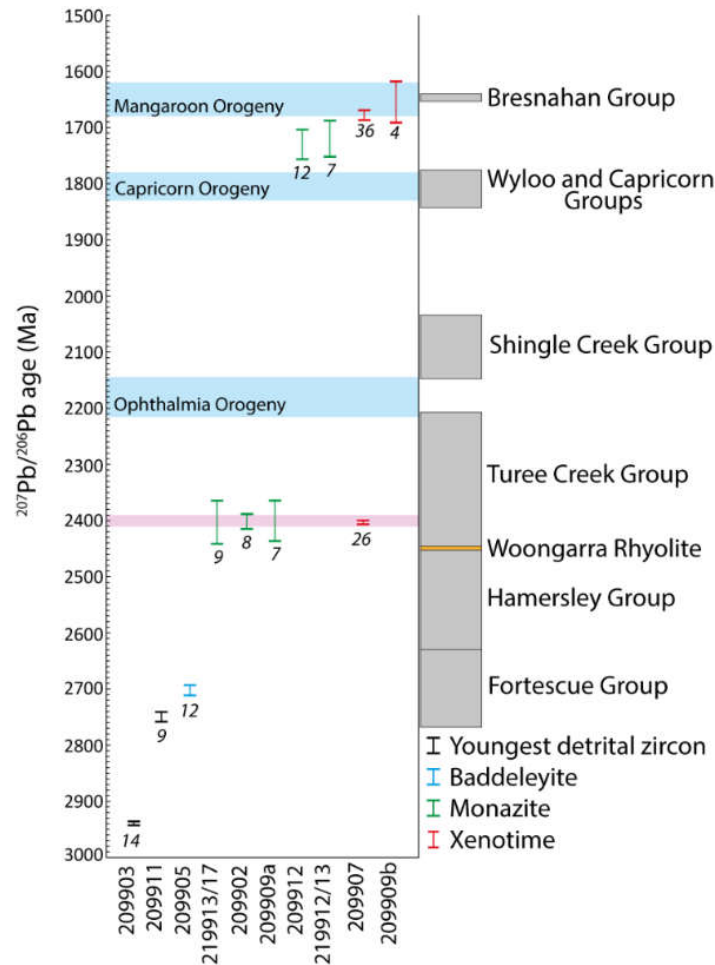


Figure 2-11: Summary diagram for all samples dated in this study. Known orogenic events are highlighted, showing that mineralization at Paulsens is not associated with either the Ophthalmia Orogeny or Capricorn Orogeny. A proposed cryptic orogenic event at c. 2400 Ma is highlighted in pink. Depositional age ranges for sedimentary basins are indicated by grey boxes, mafic intrusions as green and felsic volcanic rocks as orange. The number of analyses in each sample is marked next to the 95% error bars.

2.9.2. TIMING OF HYDROTHERMAL ACTIVITY AND GOLD MINERALIZATION

Euhedral xenotime within, and interlocking with, pyrite grains is dated at 2403 ± 5 Ma (GSWA 209907, Figure 2-9c), providing a direct crystallization age for the auriferous quartz–sulfide veins at the Gabbro Offset deposit, which are peripheral to the main Paulsens lode. Additionally, hydrothermal monazite within a pervasively altered part of the Paulsens gabbro (2398 ± 37 Ma; GSWA 209909a), and in the altered wall-rock margins to quartz–sulfide veins at Paulsens East (2403 ± 38 Ma; GSWA 219513 and 219517) also record a period of regional- to local-scale hydrothermal activity associated with the emplacement of auriferous quartz–sulfide veins at c. 2400 Ma.

Within the main quartz–sulfide vein at Gabbro Offset, xenotime crystals were also dated at 1680 ± 9 Ma. These grains only occur within the quartz matrix, or at the margins of brecciated sulfide grains, suggesting that this date represents a second period of hydrothermal alteration during which c. 2400 Ma xenotime grains underwent dissolution and reprecipitation.

Gold mineralization at Gabbro Offset is present in two distinct forms: i) as rounded inclusions within euhedral pyrite grains (Figure 2-6a), and ii) as free gold located along cracks and fractures of brecciated pyrite grains (Figure 2-6b). Because the euhedral pyrite is intergrown with, and contains euhedral grains of xenotime dated at c. 2400 Ma, the rounded, primary gold inclusions in this pyrite are also interpreted to have formed at this time. However, where the pyrite is locally fractured or brecciated, containing flakes of free gold (Figure 2-6b), chalcopyrite, and pyrrhotite, xenotime in the matrix and along pyrite grain boundaries has undergone dissolution and reprecipitation reactions at c. 1680 Ma. This suggests that these rocks were subjected to a secondary hydrothermal event responsible for the brittle deformation of pyrite grains, xenotime dissolution and reprecipitation, and either the local remobilization (Figure 2-6c) or introduction of new gold, or both, at c. 1680 Ma. Additionally, xenotime from ankerite–quartz veins emplaced within the Paulsens gabbro, which are associated with up to 48 ppm Au, have been dated at 1655 ± 37 Ma (GSWA 209909b). This indicates that this second hydrothermal event was also responsible for the emplacement of gold-bearing ankerite–quartz veins. A study on the mineralogy and chemistry of gold at the main Paulsens lode indicates that the youngest phase of gold mineralization is also associated with free gold with elevated Hg- and Ag- which formed in pyrite fractures and along stylolites (Hancock and Thorne, 2016), indicating a commonality between the youngest gold mineralizing event at the main Paulsens lode and the secondary event at the Gabbro Offset deposit.

2.9.3. RELATIONSHIPS TO REGIONAL OROGENIC EVENTS

Our in situ dating of monazite and xenotime at the Paulsens deposit has identified three discrete hydrothermal events at c. 2400, 1730, and 1680 Ma. The first hydrothermal event at c. 2400 Ma is marked by the emplacement of auriferous quartz–sulfide veins at Gabbro Offset and Paulsens East, resulting in pervasive alteration of gabbroic and phyllitic host-rocks as well as the growth of monazite within carbonaceous phyllites,

either as primary porphyroblasts or as pseudomorphs of former metamorphic porphyroblasts. The timing of the mineralizing hydrothermal event (c. 2400 Ma) does not correlate with any known hydrothermal or deformational event in the northern Capricorn Orogen. However, cryptic events, including the growth of monazite in phyllitic rocks across the Pilbara Region from Whim Creek in the north to Mt Tom Price in the south (Rasmussen et al., 2005), and resetting of high-U zircons in tuffaceous mudstones of the Hamersley Group (Pickard, 2002), are recorded between c. 2430 and 2399 Ma. The age of monazite growth decreases progressively southward (Rasmussen et al., 2005) and the data presented here are within uncertainty of monazite growth at 2399 ± 6 Ma at Mt Tom Price, located 150 km to the east of the Paulsens deposit (Rasmussen et al., 2005).

In the Pilbara region, the cause of this cryptic event is currently unknown, but indirect evidence for a tectonic event at c. 2400 Ma is present in the stratigraphic record of Proterozoic sedimentary rocks along the southern Pilbara margin. A study of detrital zircons from the matrix of the Meteorite Bore Member of the Kungarra Formation in the 2445–2208 Ma Turee Creek Group indicates that they were sourced, together with abundant rhyolite clasts, from the 2449–2445 Ma Woongarra Rhyolite (Blake and Barley, 1992; Takahara et al., 2010; Simonson et al., 2014). In the Hardey Syncline, from where the samples were taken, the Woongarra Rhyolite is situated 1500 m stratigraphically below the Meteorite Bore Member, implying at least 500 to 1000 m of uplift and erosion of sedimentary rocks along the southern Pilbara margin between c. 2445 and 2208 Ma (Takahara et al., 2010). Our data show that this event was associated with the emplacement of quartz–sulfide veins during extensive hydrothermal activity and gold mineralization at Paulsens (Figure 2-11).

The second hydrothermal event is marked by the growth of monazite within carbonaceous phyllites of the Hardey Formation at 1730 ± 27 Ma and 1721 ± 32 Ma. It is unclear if the monazite in these samples grew during low-grade metamorphism and deformation associated with fault reactivation (GSWA 209912 is located in a D₂/D₃ shear zone at the Gabbro Offset deposit), or if it has locally pseudomorphed former regional-scale peak metamorphic porphyroblasts during subsequent hydrothermal activity. However, we note that this event is within uncertainty of dextral strike-slip faulting and hydrothermal gold mineralization at the Mt Olympus deposit,

dated at 1738 ± 5 Ma (Young et al., 2003; Şener et al., 2005), about 150 km to the southeast of Paulsens.

The youngest hydrothermal event is recorded at the Gabbro Offset deposit by the dissolution and reprecipitation of xenotime rims, dated at 1680 ± 9 Ma, on older c. 2400 Ma xenotime cores within the quartz matrix of the auriferous quartz–sulfide vein, and by xenotime grains, dated at 1655 ± 37 Ma, within discrete ankerite–quartz veins. This hydrothermal event appears to have been responsible for the local brecciation and fracturing of pyrite grains in the quartz–sulfide vein, and for the local remobilization of gold (Figure 2-6c). However, it is possible that this event was also responsible for the introduction of new gold precipitated as free gold in pyrite fractures and within stylolites at the main Paulsens lode (Hancock and Thorne, 2016). This event is coincident with medium- to high-grade metamorphism, deformation and magmatism during the 1680–1620 Ma Mangaroon Orogeny (Sheppard et al., 2005), which affected rocks of the Gascoyne Province farther south. Rasmussen et al. (2007a) also noted hydrothermal monazite growth at c. 1650 Ma in the Soansville Group in the Pilbara Craton and attributed it to reactivation along pre-existing north- to northeast-trending, craton-scale structures that acted as conduits for hydrothermal fluid flow during the Mangaroon Orogeny. Rasmussen et al. (2007b) also documented the presence of c. 1670 Ma hydrothermal xenotime at the Mt Tom Price iron ore mine. The structural effect of this event at Paulsens is not known, but may have resulted in the reactivation of pre-existing faults such as the Nanjilgardy and Hardey Faults.

Importantly, we find no evidence for hydrothermal activity related to either the 2215–2145 Ma Ophthalmia Orogeny or the 1820–1770 Ma Capricorn Orogeny. This is surprising, because elsewhere in the southern Pilbara Craton and northern Capricorn Orogen these events played a significant role in the tectonic evolution of the region (Young et al., 2003; Rasmussen et al., 2005; Şener et al., 2005; Rasmussen et al., 2006; Thorne et al., 2011).

2.10. CONCLUSIONS

Our results reveal a significantly different, and more complicated, low-temperature tectonothermal evolution for the southern Pilbara region than had been thought. Previous studies (e.g. Thorne and Seymour, 1991) suggested that gold mineralization

in the Wyloo Inlier is associated with post-Wyloo Group quartz veins, linking the timing of orogenic gold mineralization to the 1820–1770 Ma Capricorn Orogeny. Results from this study show that two gold mineralizing events occurred at Paulsens. Primary gold mineralization at Paulsens was much older, occurring at c. 2400 Ma, and does not correlate with a known orogenic event in the northern Capricorn Orogen. However, uplift, erosion, and hydrothermal activity throughout the Pilbara Craton may reflect a previously unrecognized orogenic event at c. 2400 Ma. The second gold event, at c. 1680 Ma, may be linked to reactivation of the Hardey Fault which forms a splay off the lithospheric-scale Nanjilgardy Fault (Figure 2-1).

Recognition of a new orogenic event has important implications for exploration targeting of orogenic gold deposits in the northern Capricorn Orogen. Previously, rocks affected by the Capricorn Orogeny, up to and including the Ashburton Formation, were considered the most prospective for orogenic gold mineralization similar to that at Paulsens. However, we have demonstrated that the primary mineralization at Paulsens, which shares many of the characteristics of orogenic gold deposits, occurred at c. 2400 Ma, about 570 million years prior to deposition of Wyloo Group sedimentary rocks. Therefore, older rocks of the Fortescue and Hamersley Groups are more likely candidates to host significant gold mineralization similar to Paulsens. The second gold event occurring at c. 1680 Ma is possibly related to the reactivation of major lithospheric fault structures and their splays. This event, at least locally, caused the remobilization of pre-existing gold, but may also have been responsible for the introduction of new gold along these mantle-tapping structures. Nevertheless, the age constraints for mineralization at Paulsens differ to those proposed by Young et al. (2003) and Şener et al. (2005) for the timing of gold mineralization at Mount Olympus (1738 ± 5 Ma) in the Wyloo Group, suggesting the potential for several different gold mineralizing events across the northern Capricorn Orogen associated with major structures such as the Nanjilgardy Fault.

For exploration of orogenic gold, it is critical to have an understanding of the distribution of mineralization through both space and time. In situ geochronology of monazite and xenotime has important implications for exploration targeting by providing absolute ages for orogenic gold mineralization, and allowing mineralization to be linked to specific orogenic events. In turn, this allows explorers to minimize their

exploration search area by targeting the most prospective tectonothermal events and host stratigraphy.

2.11. ACKNOWLEDGEMENTS

The research presented here forms a part of a PhD project by I. Fielding and is funded through an ARC Linkage grant (LP130100922) and industry scholarship by Northern Star Resources. All geochronology was carried out using a SHRIMP II ion microprobe at the John de Laeter Centre at Curtin University. SPJ and MTDW publish with the permission of the director of the Geological Survey of Western Australia. Thanks go to Northern Star Resources, in particular Philip Tornatora and Paul Howard for supplying samples and for permission to publish.

2.12. REFERENCES

- Blake, T. S., 1993, Archaean and early Proterozoic geology of the Pilbara region, Western Australia Late Archaean crustal extension, sedimentary basin formation, flood basalt volcanism and continental rifting: the Nullagine and Mount Jope Supersequences, Western Australia: *Precambrian Research*, v. 60, p. 185–241.
- Blake, T. S., and Barley, M. E., 1992, Tectonic evolution of the Late Archaean to Early Proterozoic Mount Bruce Megasequence Set, Western Australia: *Tectonics*, v. 11, p. 1415–1425.
- Blight, D. F., 1985, Economic potential of the lower Fortescue Group and adjacent units in the southern Hamersley Basin; A study of depositional environments: Geological Survey of Western Australia, Report 13, 32 p.
- Carpenter, R. L., Duke, N. A., Sandeman, H. A., and Stern, R., 2005, Relative and absolute timing of gold mineralization along the Meliadine trend, Nunavut, Canada: Evidence for Paleoproterozoic gold hosted in an Archean greenstone belt: *Economic Geology*, v. 100, p. 567–576.
- Cawood, P. A., and Tyler, I. M., 2004, Assembling and reactivating the Proterozoic Capricorn Orogen: lithotectonic elements, orogenies, and significance: *Precambrian Research*, v. 128, p. 201–218.
- Cherniak, D. J., 2010, Diffusion in accessory minerals: zircon, titanite, apatite, monazite and xenotime: *Reviews in Mineralogy and Geochemistry*, v. 72, p. 827–869.

- Chesley, J. T., 1999, Integrative geochronology of ore deposits: new insights into the duration and timing of hydrothermal circulation, *in* Lambert, D. D., and Brown, P. E., eds., *Reviews in economic geology*, 12, p. 115-142.
- Fielding, I., and Stokes, L., 2014, Gabbro Offset drilling, Ashburton Basin, Pilbara - Western Australia, M08/196, Exploration Incentive Scheme Final Report: Geological Survey of Western Australia Open-file Report, Northern Star Resources, 13 p.
- Finger, F., Broska, I., Roberts, M. P., and Schermaier, A., 1998, Replacement of primary monazite by apatite-allanite-epidote coronas in an amphibolite facies granite gneiss from the Eastern Alps: *The American mineralogist*, v. 83, p. 248–258.
- Forman, F. G., 1938, The Melrose and Belvedere gold mines and vicinity, Mt Stewart Station, Ashburton Goldfields, Geological Survey of Western Australia, Annual Report 1937, p. 62–63.
- Goldfarb, R. J., and Groves, D. I., 2015, Orogenic gold: Common or evolving fluid and metal sources through time: *Lithos*, v. 233, p. 2–26.
- Goldfarb, R. J., Groves, D. I., and Gardoll, S., 2001, Orogenic gold and geologic time: a global synthesis: *Ore Geology Reviews*, v. 18, p. 1–75.
- Groves, D. I., Goldfarb, R. J., Gebre-Mariam, M., Hagemann, S. G., and Robert, F., 1998, Orogenic gold deposits: A proposed classification in the context of their crustal distribution and relationship to other gold deposit types: *Ore Geology Reviews*, v. 13, p. 7–27.
- Hancock, E. A., and Thorne, A. M., 2016, Mineralogy of gold from the Paulsens and Mount Olympus deposits, northern Capricorn Orogen: Geological Survey of Western Australia, Record 2016/14, 16 p.
- Harrison, T. M., Catlos, E. J., and Montel, J. M., 2002, U-Th-Pb dating of phosphate minerals: *Reviews in Mineralogy and Geochemistry*, v. 48, p. 524–558.
- Hronsky, J. M. A., and Groves, D. I., 2008, Science of targeting: definition, strategies, targeting and performance measurement: *Australian Journal of Earth Sciences*, v. 55, p. 3–12.
- Hronsky, J. M., Groves, D. I., Loucks, R. R., and Begg, G. C., 2012, A unified model for gold mineralisation in accretionary orogens and implications for regional-scale exploration targeting methods: *Mineralium Deposita*, v. 47, p. 339–358.
- Johnson, S. P., Sheppard, S., Rasmussen, B., Wingate, M. T. D., Kirkland, C. L., Muhling, J. R., Fletcher, I. R., and Belousova, E. A., 2011, Two collisions, two sutures: Punctuated pre-1950Ma assembly of the West Australian Craton during the Ophthalmian and Glenburgh Orogenies: *Precambrian Research*, v. 189, p. 239–262.
- Johnson, S. P., Thorne, A. M., Tyler, I. M., Korsch, R. J., Kennett, B. L. N., Cutten, H. N., Goodwin, J., Blay, O., Blewett, R. S., Joly, A., Dentith, M. C., Aitken, A. R. A., Holzschuh, J., Salmon, M., Reading, A., Heinson, G., Boren, G., Ross, J., Costelloe, R. D., and Fomin, T., 2013, Crustal architecture of the

- Capricorn Orogen, Western Australia and associated metallogeny: *Australian Journal of Earth Sciences*, v. 60, p. 681–705.
- Kerrick, R., and Cassidy, K. F., 1994, Temporal relationships of lode gold mineralization to accretion, magmatism, metamorphism and deformation — Archean to present: A review: *Ore Geology Reviews*, v. 9, p. 263–310.
- Korhonen, F. J., Johnson, S. P., Rasmussen, B., Sheppard, S., Muhling, J. R., Dunkley, D. J., Wingate, M. T. D., Fletcher, I. R., and Roberts, M. P., 2017, Circum-Yilgarn orogenesis: P–T–t constraints and implications from the Capricorn Orogen, Western Australia: *Journal of Metamorphic Geology*, accepted.
- Krapez, B., and McNaughton, N. J., 1999, SHRIMP zircon U–Pb age and tectonic significance of the Palaeoproterozoic Boolaloo Granodiorite in the Ashburton Province, Western Australia: *Australian Journal of Earth Sciences*, v. 46, p. 283–287.
- Martin, D. M., and Thorne, A. M., 2004, Tectonic setting and basin evolution of the Bangemall Supergroup in the northwestern Capricorn Orogen: *Precambrian Research*, v. 128, p. 385–409.
- Martin, D. M., and Morris, P. A., 2010, Tectonic setting and regional implications of ca.2.2 Ga mafic magmatism in the southern Hamersley Province, Western Australia: *Australian Journal of Earth Sciences*, v. 57, p. 911–931.
- Martin, D. M., Powell, C. M., and George, A. D., 2000, Stratigraphic architecture and evolution of the early Paleoproterozoic McGrath Trough, Western Australia: *Precambrian Research*, v. 99, p. 33–64.
- Martin, D. M., Sheppard, S., and Thorne, A. M., 2005, Geology of the Maroonah, Ullawarra, Capricorn, Mangaroon, Edmund and Elliott Creek 1:100 000 sheets: Geological Survey of Western Australia, 1:100 000 Geological Series Explanatory Notes, 81 p.
- Müller, S. G., 2005, The tectonic evolution and volcanism of the Lower Wyloo Group, Ashburton Province, with timing implications for giant iron-ore deposits of the Hamersley Province, Western Australia: Unpublished Ph.D thesis, Perth, Western Australia, University of Western Australia, 192 p.
- Northern Star Resources Limited, 2015, Northern Star Resources Limited 2015 annual report, (<http://www.nsrld.com/wp-content/uploads/2015/08/NST-Annual-Report-2015-26-8-2015-new-cover1.pdf>).
- Northern Star Resources Limited, January, 2016, Resources and Reserves, (<http://www.nsrld.com/our-assets/resources-and-reserves/>).
- Northern Star Resources Limited, July, 2015, Northern Star Paulsens operations fact sheet, (<http://www.nsrld.com/wp-content/uploads/2015/08/NSR-Paulsens-Operations-Fact-Sheet-July-2015-FINAL.pdf>).

- Occhipinti, S. A., Sheppard, S., Passchier, C., Tyler, I. M., and Nelson, D. R., 2004, Paleoproterozoic crustal accretion and collision in the southern Capricorn Orogen: the Glenburgh Orogeny: *Precambrian Research*, v. 128, p. 237–255.
- Owen, S., 2000, Ashburton Project, Paulsens E08/665, E08/906, M08/99 and M08/196, Annual report to the Department of Minerals and Energy for the Period 15 November 1999 to 14 November 2000, Taipan Resources N.L; Geological Survey of Western Australia Open-file report, 39 p.
- Pickard, A. L., 2002, SHRIMP U–Pb zircon ages of tuffaceous mudrocks in the Brockman Iron Formation of the Hamersley Range, Western Australia: *Australian Journal of Earth Sciences*, v. 49, p. 491–507.
- Powell, C. M., and Horwitz, R. C., 1994, Late Archaean and Early Proterozoic tectonics and basin formation of the Hamersley Ranges, Geological Society of Australia (WA Division) Excursion Guidebook, 4, 57 p.
- Rasmussen, B., and Muhling, J. R., 2007, Monazite begets monazite: evidence for dissolution of detrital monazite and reprecipitation of syntectonic monazite during low-grade regional metamorphism: *Contributions to Mineralogy and Petrology*, v. 154, p. 675–689.
- Rasmussen, B., and Muhling, J. R., 2009, Reactions destroying detrital monazite in greenschist-facies sandstones from the Witwatersrand basin, South Africa: *Chemical Geology*, v. 264, p. 311–327.
- Rasmussen, B., Fletcher, I. R., and Sheppard, S., 2005, Isotopic dating of the migration of a low-grade metamorphic front during orogenesis: *Geology*, v. 33, p. 773–776.
- Rasmussen, B., Sheppard, S., and Fletcher, I. R., 2006, Testing ore deposit models using in situ U–Pb geochronology of hydrothermal monazite: Paleoproterozoic gold mineralization in northern Australia: *Geology*, v. 34, p. 77–80.
- Rasmussen, B., Fletcher, I. R., and Muhling, J. R., 2007a, In situ U–Pb dating and element mapping of three generations of monazite: Unravelling cryptic tectonothermal events in low-grade terranes: *Geochimica et Cosmochimica Acta*, v. 71, p. 670–690.
- Rasmussen, B., Fletcher, I. R., Muhling, J. R., Thorne, W. S., and Broadbent, G. C., 2007b, Prolonged history of episodic fluid flow in giant hematite ore bodies: Evidence from in situ U–Pb geochronology of hydrothermal xenotime: *Earth and Planetary Science Letters*, v. 258, p. 249–259.
- Şener, A. K., Young, C., Groves, D. I., Krapez, B., and Fletcher, I. R., 2005, Major orogenic gold episode associated with Cordilleran-style tectonics related to the assembly of Paleoproterozoic Australia?: *Geology*, v. 33, p. 225–228.
- Sheppard, S., Occhipinti, S. A., and Nelson, D. R., 2005, Intracontinental reworking in the Capricorn Orogen, Western Australia: the 1680–1620 Ma Mangaroon Orogeny*: *Australian Journal of Earth Sciences*, v. 52, p. 443–460.

- Sheppard, S., Rasmussen, B., Muhling, J. R., Farrell, T. R., and Fletcher, I. R., 2007, Grenvillian-aged orogenesis in the Paleoproterozoic Gascoyne Complex, Western Australia: 1030–950 Ma reworking of the Proterozoic Capricorn Orogen: *Journal of Metamorphic Geology*, v. 25, p. 477–494.
- Sheppard, S., Bodorkos, S., Johnson, S. P., Wingate, M. T. D., and Kirkland, C. L., 2010, The Paleoproterozoic Capricorn Orogeny: intracontinental reworking not continent–continent collision: Geological Survey of Western Australia, Report 108, 33 p.
- Sillitoe, R. H., 1997, Characteristics and controls of the largest porphyry copper-gold and epithermal gold deposits in the circum-Pacific region: *Australian Journal of Earth Sciences*, v. 44, p. 373–388.
- Simonson, B. M., O'Brien, M., Buchwaldt, R., Bowring, S. A., Hassler, S. W., and Beukes, N. J., 2014, New geochronological data from the Boolgeeda BIF and Woongarra Rhyolite, Hamersley Group (Western Australia), 2014 GSA Annual Meeting: Vancouver, British Columbia.
- Takahara, M., Komure, M., Kiyokawa, S., Horie, K., and Yokoyama, K., 2010, Detrital zircon SHRIMP U-Pb age of the 2.3 Ga diamictites of the Meteorite Bore Member in the south Pilbara, Western Australia, Fifth International Archean Symposium: Perth, Western Australia, 2 p.
- Thorne, A. M., and Seymour, D. B., 1991, Geology of the Ashburton Basin Western Australia: Geological Survey of Western Australia, Bulletin 139, 162 p.
- Thorne, A. M., and Trendall, A. F., 2001, Geology of the Fortescue Group, Pilbara Craton, Western Australia: Geological Survey of Western Australia, Bulletin 144, 266 p.
- Thorne, A. M., Johnson, S. P., Tyler, I. M., Cutten, H. N., and Blay, O., 2011, Geology of the northern Capricorn Orogen, in Johnson, S. P., Thorne, A. M., and Tyler, I. M., eds., Capricorn Orogen seismic and magnetotelluric (MT) workshop 2011, Geological Survey of Western Australia, 12 p.
- Townsend, K. J., Miller, C. F., D'Andrea, J. L., Ayers, J. C., Harrison, T. M., and Coath, C. D., 2000, Low temperature replacement of monazite in the Ireteba granite, Southern Nevada: geochronological implications: *Chemical Geology*, v. 172, p. 95–112.
- Trendall, A. F., Compston, W., Nelson, D. R., De Laeter, J. R., and Bennett, V. C., 2004, SHRIMP zircon ages constraining the depositional chronology of the Hamersley Group, Western Australia: *Australian Journal of Earth Sciences*, v. 51, p. 621–644.
- Tyler, I. M., 1991, The Geology of the Sylvania Inlier and the Southeast Hamersley Basin: Geological Survey of Western Australia, Bulletin 138, 124 p.
- Tyler, I. M., and Thorne, A. M., 1990, The northern margin of the Capricorn Orogen, Western Australia—an example of an early Proterozoic collision zone: *Journal of Structural Geology*, v. 12, p. 685–701.

- Vielreicher, N., Groves, D., Fletcher, I., McNaughton, N., and Rasmussen, B., 2003, Hydrothermal monazite and xenotime geochronology: a new direction for precise dating of orogenic gold mineralization: Society of Economic Geologists Newsletter, v. 53, p. 10–16.
- White, A. J. R., Smith, R. E., Nadoll, P., and Legras, M., 2014a, Regional-scale metasomatism in the Fortescue Group Volcanics, Hamersley Basin, Western Australia: implications for hydrothermal ore systems: Journal of Petrology, v. 55, p. 977–1009.
- White, A., Burgess, R., Charnley, N., Selby, D., Whitehouse, M., Robb, L., and Waters, D., 2014b, Constraints on the timing of late-Eburnean metamorphism, gold mineralisation and regional exhumation at Damang mine, Ghana: Precambrian research., v. 243, p. 18–38.
- Young, C. J., Groves, D. I., and Morant, P., 2003, Sediment-hosted disseminated gold mineralisation in the Paleoproterozoic Ashburton Province, Western Australia: a new epizonal orogenic gold province related to Capricorn Orogeny?, in Eliopoulos et al., eds., Mineral exploration and sustainable development: proceedings of the 7th Biennial SGA Meeting: Athens, Greece, Millpress, p. 835–838.
- Zhang, J., Linnen, R., Lin, S., Davis, D., and Martin, R., 2014, Paleoproterozoic hydrothermal reactivation in a Neoarchean orogenic lode-gold deposit of the southern Abitibi subprovince: U-Pb monazite geochronological evidence from the Young-Davidson mine, Ontario: Precambrian Research, v. 249, p. 263–272.

2.13. SUPPLEMENTARY DATA

2.13.1. ANALYTICAL METHODS

2.13.1.1. U–Pb ZIRCON GEOCHRONOLOGY

Analytical methods for U–Pb zircon geochronology are described in detail by Wingate and Lu (2016), and only a summary is provided here. During all analytical sessions, an O_2^- primary beam with a spot size of 20–30 μm was used with beam intensity of 1.5–3.5 nA. The secondary ion beam was focused through a 100 μm collector slit onto an electron multiplier to produce mass peaks with flat tops and a mass resolution (1% peak height) of 5100–5460.

Data were collected in sets of 6 scans, with reference standards analysed after every five sample analyses. Count times per scan for Pb isotopes 204, background positions 204.1, 206, 207 and 208 were 10 s, 10 s, 10 s, 30 s and 10 s respectively. U–Th–Pb

ratios and absolute abundances were determined relative to the BR266 standard zircon (559 Ma, 903 ppm U; Stern (2001)) analyses of which were interspersed with those of unknown zircons. Instrumental mass fractionation (IMF) in $^{207}\text{Pb}/^{206}\text{Pb}$ ratios was monitored during each session by repeated analysis of the 3465 Ma OGC zircon standard (OG1 of Stern et al. (2009)). No IMF correction was required since the measured values of OGC were in agreement with the reference value within 2σ uncertainties. Raw zircon data were processed using the SQUID 2 add-in (v. 2.50.12.03.08) for Excel 2003 (Ludwig, 2009), and plotted using the ISOPLOT add-in (v. 3.76.12.02.24) (Ludwig, 2003). Measured compositions were corrected for common Pb using non-radiogenic ^{204}Pb and contemporaneous Pb composition according to the terrestrial Pb evolution model of Stacey and Kramers (1975). Mean ages are quoted with 95% confidence levels.

2.13.1.2. *IN SITU U–Pb BADDELEYITE, MONAZITE AND XENOTIME GEOCHRONOLOGY*

For in situ baddeleyite, monazite and xenotime analysis, a primary beam of O_2^- ions was focused through a 50 μm Kohler aperture to produce an oval 10 μm wide spot on the sample surface with a current of 0.2–0.4 nA. The secondary ion system was focused through a 100 μm collector slit onto an electron multiplier to produce mass peaks with flat tops and a mass resolution (1% peak height) of >5200 in all sessions. Background counts from scattered ions were reduced using a flight retardation lens, which is known to cause slight session-dependent IMF of Pb isotopes. IMF corrections were applied to all analyses using the monazite standard Z2908 as an IMF monitor (see below).

Data were collected in sets of 8 scans, with monazite, xenotime or baddeleyite reference material analysed every 4–6 sample analyses. Count times per scan for Pb isotopes 204, background position 204.045, 206, 207, and 208 were 10 s, 10 s, 10 s, 30 s and 10 s, respectively.

Baddeleyite was analysed using the conventional zircon 9-peak run table, calibrated against baddeleyite reference material Phalaborwa (Heaman and LeCheminant, 1993). Monazite was analysed with a 13-peak run table as defined in Fletcher et al., (2010), which includes mass stations for the estimation of La, Ce and Nd (REEPO_2^+), and Y (YCeO^+). Measurements of monazite standards FRENCH, Z2234, and Z2908 (see

Fletcher et al. (2010) for details) were done concurrently for Pb/U and Pb/Th calibration (FRENCH), IMF corrections (Z2908), and matrix corrections required for variable U, Th, Y and Nd contents (Z2234 and Z2908).

Xenotime was analysed with a 9-peak run table following analytical protocols in Fletcher et al. (2004) and Fletcher et al. (2010). Pb/U calibrations and matrix corrections for U and Th contents were based on concurrent measurements of the standards MG-1 (Fletcher et al., 2004) and Z6413 (“Xenol”; (Stern and Rayner, 2003)). Pb/Th was determined indirectly, using a fixed Th/U calibration (Fletcher et al., 2004). Matrix corrections for REE assumed the samples have REE abundances similar to Xenol.

Raw data from analyses on baddeleyite, monazite and xenotime were processed using the SQUID 2 add-in (v. 2.50.12.03.08) for Excel 2003 (Ludwig, 2009), and plotted using the ISOPLOT add-in (v. 3.76.12.02.24) (Ludwig, 2003). Common-Pb corrections were based on measured $^{204}\text{Pb}/^{206}\text{Pb}$ ratios and contemporaneous Pb composition according to the terrestrial Pb evolution model of Stacey and Kramers (1975). Matrix effect corrections were made for all monazite and xenotime data using procedures described by Fletcher et al (2010) and Fletcher et al (2004), respectively. Pooled ages are quoted with 95% confidence levels, whereas individual analyses are presented with 1σ errors.

2.13.1.3. REFERENCES

- Fletcher, I. R., McNaughton, N. J., Aleinikoff, J. A., Rasmussen, B., and Kamo, S. L., 2004, Improved calibration procedures and new standards for U–Pb and Th–Pb dating of Phanerozoic xenotime by ion microprobe: *Chemical Geology*, v. 209, p. 295–314.
- Fletcher, I. R., McNaughton, N. J., Davis, W. J., and Rasmussen, B., 2010, Matrix effects and calibration limitations in ion probe U–Pb and Th–Pb dating of monazite: *Chemical Geology*, v. 270, p. 31–44.
- Heaman, L. M., and LeCheminant, A. N., 1993, Geochemistry of Accessory Minerals Paragenesis and U–Pb systematics of baddeleyite (ZrO₂): *Chemical Geology*, v. 110, p. 95–126.
- Ludwig, K. R., 2003, Isoplot/Ex version 3.00, A geochronological toolkit for Microsoft Excel: Berkeley Geochronology Centre Special Publication No. 4, 73 p.

- Ludwig, K. R., 2009, Squid 2.50, a user's manual: Berkeley Geochronology Centre, Berkeley, California, USA, 95 p.
- Stacey, J. S., and Kramers, J. D., 1975, Approximation of terrestrial lead isotope evolution by a two-stage model: *Earth and Planetary Science Letters*, v. 26, p. 207–221.
- Stern, R. A., 2001, New isotopic and trace-element standard for the ion microprobe: preliminary thermal ionization mass spectrometry (TIMS) U–Pb and electron microprobe data; *Radiogenic Age and Isotopic Studies: Report 14*, Geological Survey of Canada, Current Research 2001-F1, p. 7.
- Stern, R. A., Bodorkos, S., Kamo, S. L., Hickman, A. H., and Corfu, F., 2009, Measurement of SIMS Instrumental Mass Fractionation of Pb Isotopes During Zircon Dating: *Geostandards and Geoanalytical Research*, v. 33, p. 145–168.
- Stern, R. A., and Rayner, N., 2003, Ages of several xenotime megacrysts by ID-TIMS: potential reference materials for ion microprobe U–Pb geochronology: *Radiogenic Age and Isotopic Studies: Report 16*, Geological Survey of Canada: Current Research 2003-F1, p. 7.
- Wingate, M. T. D., and Lu, Y., 2016, Introduction to geochronology information released in 2014: Geological Survey of Western Australia, 5 p.

2.13.2. DATA TABLES

Supplementary Table 2-1: GSWA 209903 quartz sandstone (Hardey Formation)

<i>Mount no.</i>	<i>Grain spot</i>	<i>²³⁸U (ppm)</i>	<i>²³²Th (ppm)</i>	<i>²³²Th ²³⁸U</i>	<i>f206 (%)</i>	<i>²³⁸U/²⁰⁶Pb ± 1σ</i>	<i>²⁰⁷Pb/²⁰⁶Pb ± 1σ</i>	<i>²³⁸U/²⁰⁶Pb* ± 1σ</i>	<i>²⁰⁷Pb*/²⁰⁶Pb* ± 1σ</i>	<i>²³⁸U/²⁰⁶Pb* date (Ma) ±1σ</i>	<i>Disc. (%)</i>	<i>²⁰⁷Pb*/²⁰⁶Pb* date (Ma) ±1σ</i>						
Older detrital zircons																		
G14-15	903-2.1	701	205	0.302	0.045	1.478	0.020	0.2976	0.0005	1.479	0.020	0.2972	0.0006	3330	36	3.6	3456	3
G14-15	903-45.1	251	258	1.062	0.025	1.445	0.021	0.2879	0.0008	1.446	0.021	0.2877	0.0008	3389	39	0.5	3405	4
G14-15	903-49.1	73	87	1.220	0.260	1.575	0.027	0.2635	0.0012	1.579	0.027	0.2612	0.0013	3163	44	2.8	3254	8
G14-15	903-59.1	143	121	0.877	0.083	1.558	0.024	0.2608	0.0009	1.559	0.024	0.2601	0.0010	3195	40	1.6	3247	6
G14-15	903-35.1	104	96	0.955	0.040	1.547	0.026	0.2600	0.0012	1.548	0.026	0.2597	0.0012	3213	43	1.0	3245	7
G14-15	903-43.1	67	36	0.561	0.292	1.494	0.028	0.2616	0.0015	1.499	0.028	0.2590	0.0016	3295	50	-1.7	3241	10
G14-15	903-27.1	74	48	0.673	0.100	1.564	0.029	0.2598	0.0014	1.566	0.029	0.2589	0.0014	3183	47	1.8	3240	9
G14-15	903-64.2	84	47	0.585	0.212	1.589	0.027	0.2605	0.0012	1.593	0.027	0.2587	0.0013	3141	43	3.0	3239	8
G14-15	903-61.1	180	92	0.531	0.056	1.524	0.023	0.2589	0.0008	1.525	0.023	0.2584	0.0008	3250	39	-0.4	3237	5
G14-15	903-3.1	163	61	0.387	0.066	1.559	0.026	0.2588	0.0011	1.560	0.026	0.2582	0.0011	3193	42	1.3	3236	7
G14-15	903-37.1	241	190	0.815	0.039	1.585	0.023	0.2584	0.0008	1.585	0.023	0.2581	0.0008	3153	37	2.5	3235	5
G14-15	903-22.1	86	31	0.378	0.227	1.547	0.027	0.2596	0.0013	1.551	0.027	0.2577	0.0013	3208	45	0.7	3232	8
G14-15	903-24.1	334	9	0.027	0.036	1.519	0.022	0.2577	0.0006	1.519	0.022	0.2574	0.0006	3260	37	-0.9	3231	4
G14-15	903-20.1	271	54	0.205	0.042	1.507	0.022	0.2577	0.0007	1.508	0.022	0.2573	0.0007	3280	38	-1.5	3230	4
G14-15	903-38.1	263	262	1.028	0.102	1.631	0.023	0.2582	0.0007	1.633	0.023	0.2573	0.0007	3080	35	4.7	3230	5
G14-15	903-5.1	217	221	1.052	0.148	1.581	0.024	0.2584	0.0008	1.583	0.024	0.2571	0.0009	3156	38	2.2	3229	5
G14-15	903-46.1	61	44	0.746	0.169	1.569	0.030	0.2585	0.0015	1.571	0.030	0.2570	0.0016	3175	49	1.7	3228	10
G14-15	903-64.1	55	38	0.716	0.263	1.531	0.029	0.2589	0.0015	1.535	0.029	0.2566	0.0016	3234	49	-0.2	3226	10
G14-15	903-63.1	49	34	0.712	0.252	1.525	0.030	0.2588	0.0015	1.529	0.030	0.2566	0.0017	3244	51	-0.6	3226	10
G14-15	903-4.1	65	37	0.597	0.034	1.536	0.030	0.2568	0.0015	1.537	0.030	0.2565	0.0015	3231	50	-0.2	3225	9
G14-15	903-57.1	139	85	0.629	0.082	1.515	0.024	0.2567	0.0009	1.516	0.024	0.2560	0.0010	3266	41	-1.4	3222	6
G14-15	903-18.1	70	45	0.658	0.143	1.466	0.028	0.2572	0.0015	1.468	0.028	0.2560	0.0015	3350	50	-4.0	3222	10

G14-15	903-39.1	110	56	0.527	0.174	1.518	0.025	0.2574	0.0011	1.520	0.025	0.2559	0.0012	3259	43	-1.1	3222	7
G14-15	903-44.1	109	114	1.083	0.135	1.523	0.025	0.2570	0.0011	1.525	0.025	0.2559	0.0011	3251	43	-0.9	3221	7
G14-15	903-30.1	112	110	1.007	0.072	1.504	0.025	0.2564	0.0011	1.505	0.025	0.2558	0.0011	3285	43	-2.0	3221	7
G14-15	903-14.1	80	61	0.787	0.216	1.572	0.028	0.2576	0.0013	1.576	0.028	0.2557	0.0014	3168	46	1.6	3221	8
G14-15	903-32.1	151	148	1.015	0.095	1.609	0.025	0.2554	0.0009	1.611	0.025	0.2546	0.0010	3113	39	3.1	3214	6
G14-15	903-7.1	119	84	0.723	0.111	1.532	0.025	0.2538	0.0011	1.534	0.025	0.2529	0.0011	3236	43	-1.0	3203	7
G14-15	903-25.1	66	24	0.368	0.165	1.566	0.029	0.2500	0.0077	1.568	0.029	0.2485	0.0077	3180	47	-0.1	3175	49
G14-15	903-23.1	250	206	0.851	0.038	1.572	0.023	0.2397	0.0007	1.572	0.023	0.2393	0.0007	3173	37	-1.9	3115	5
G14-15	903-33.1	138	152	1.141	0.185	1.630	0.026	0.2401	0.0009	1.633	0.026	0.2385	0.0010	3079	39	1.0	3110	7
G14-15	903-13.1	257	196	0.786	0.030	1.573	0.023	0.2386	0.0007	1.574	0.023	0.2383	0.0007	3171	37	-2.0	3109	5
G14-15	903-36.1	269	154	0.591	0.075	1.616	0.023	0.2372	0.0007	1.617	0.023	0.2365	0.0007	3103	36	-0.2	3097	5
G14-15	903-15.1	250	179	0.739	0.047	1.625	0.024	0.2369	0.0007	1.626	0.024	0.2364	0.0007	3090	36	0.2	3096	5
G14-15	903-31.1	86	45	0.540	0.234	1.597	0.028	0.2380	0.0012	1.601	0.028	0.2359	0.0013	3128	44	-1.2	3093	9
G14-15	903-62.1	311	100	0.332	0.071	1.756	0.025	0.2311	0.0006	1.757	0.025	0.2305	0.0006	2905	33	4.9	3055	4
G14-15	903-40.1	120	58	0.499	0.058	1.704	0.028	0.2297	0.0010	1.705	0.028	0.2292	0.0011	2975	40	2.3	3046	7
G14-15	903-51.1	81	60	0.767	0.060	1.660	0.029	0.2294	0.0011	1.661	0.029	0.2288	0.0012	3038	42	0.2	3044	8
G14-15	903-54.1	153	149	1.005	0.049	1.666	0.026	0.2281	0.0009	1.667	0.026	0.2276	0.0009	3030	38	0.2	3036	6
G14-15	903-6.1	393	313	0.822	0.037	1.696	0.024	0.2274	0.0006	1.697	0.024	0.2270	0.0006	2987	34	1.5	3031	4
G14-15	903-8.1	196	285	1.501	0.091	1.720	0.026	0.2276	0.0008	1.722	0.026	0.2268	0.0009	2952	36	2.6	3030	6
G14-15	903-48.1	167	112	0.696	0.249	1.666	0.025	0.2283	0.0007	1.670	0.025	0.2261	0.0008	3025	36	0.0	3024	6
G14-15	903-21.1	259	249	0.994	0.141	1.698	0.025	0.2270	0.0007	1.700	0.025	0.2258	0.0007	2982	35	1.3	3022	5
G14-15	903-53.1	201	171	0.878	0.193	1.687	0.025	0.2269	0.0007	1.690	0.025	0.2252	0.0008	2997	36	0.7	3018	6
G14-15	903-11.1	439	212	0.498	0.099	1.694	0.024	0.2258	0.0005	1.696	0.024	0.2249	0.0006	2988	34	0.9	3016	4
G14-15	903-41.1	138	156	1.168	0.283	1.675	0.027	0.2272	0.0009	1.679	0.027	0.2247	0.0010	3011	39	0.1	3015	7
G14-15	903-16.1	555	1109	2.062	0.074	1.795	0.025	0.2220	0.0005	1.797	0.025	0.2213	0.0005	2853	32	4.6	2990	4
G14-15	903-10.1	97	50	0.533	0.098	1.736	0.030	0.2193	0.0011	1.738	0.030	0.2184	0.0012	2930	41	1.3	2969	8

Youngest detrital zircon age component (2941 ± 5 Ma)

G14-15	903-60.1	108	51	0.492	0.060	1.781	0.029	0.2174	0.0010	1.782	0.029	0.2169	0.0010	2871	38	2.9	2958	8
G14-15	903-17.1	111	59	0.553	0.070	1.755	0.029	0.2164	0.0011	1.756	0.030	0.2158	0.0011	2906	40	1.5	2950	8

G14-15	903-29.1	110	65	0.606	0.109	1.699	0.028	0.2166	0.0010	1.701	0.028	0.2156	0.0010	2980	40	-1.1	2948	8
G14-15	903-55.1	236	151	0.658	0.068	1.723	0.025	0.2161	0.0007	1.724	0.025	0.2155	0.0007	2949	35	-0.1	2947	5
G14-15	903-28.1	132	74	0.574	0.027	1.706	0.027	0.2157	0.0009	1.706	0.027	0.2154	0.0010	2974	39	-0.9	2947	7
G14-15	903-34.1	137	65	0.494	0.131	1.717	0.028	0.2165	0.0009	1.719	0.028	0.2153	0.0010	2955	39	-0.3	2946	7
G14-15	903-47.1	91	48	0.545	0.063	1.746	0.029	0.2158	0.0010	1.747	0.029	0.2153	0.0010	2917	39	1.0	2946	8
G14-15	903-50.1	63	28	0.458	0.112	1.775	0.032	0.2158	0.0012	1.777	0.032	0.2148	0.0013	2879	43	2.2	2942	10
G14-15	903-9.1	130	72	0.570	0.030	1.741	0.028	0.2149	0.0010	1.741	0.028	0.2146	0.0010	2925	39	0.5	2941	8
G14-15	903-1.1	161	86	0.550	0.125	1.754	0.029	0.2151	0.0010	1.756	0.029	0.2140	0.0010	2906	39	1.0	2936	8
G14-15	903-58.1	187	94	0.517	0.006	1.736	0.026	0.2140	0.0007	1.736	0.026	0.2140	0.0008	2933	36	0.1	2936	6
G14-15	903-26.1	92	53	0.591	0.172	1.745	0.030	0.2152	0.0014	1.748	0.030	0.2137	0.0015	2916	41	0.6	2933	11
G14-15	903-56.1	221	29	0.136	0.046	1.727	0.025	0.2139	0.0007	1.728	0.025	0.2135	0.0007	2944	35	-0.4	2932	5
G14-15	903-12.1	147	78	0.547	0.072	1.736	0.027	0.2138	0.0011	1.737	0.027	0.2132	0.0011	2931	37	0.0	2930	9
G14-15	903-42.1	103	61	0.608	0.214	1.697	0.029	0.2142	0.0010	1.701	0.029	0.2123	0.0011	2981	41	-2.0	2923	9

Discordance >5%

G14-15	903-52.1	91	47	0.529	0.060	1.672	0.028	0.2539	0.0011	1.673	0.028	0.2534	0.0012	3021	41	5.8	3206	7
G14-15	903-19.1	185	19	0.108	0.023	1.713	0.027	0.2561	0.0010	1.714	0.027	0.2559	0.0010	2963	37	8.0	3221	6

Pb* indicates radiogenic Pb.

f_{206} is the proportion of common Pb in ^{206}Pb , determined using the measured $^{204}\text{Pb}/^{206}\text{Pb}$ and a common Pb composition from the Stacey and Kramers (1975) model at the approximate age of the sample.

Disc. Is apparent discordance, as $100([^{207}\text{Pb}^*/^{206}\text{Pb}^*] - [^{238}\text{U}/^{206}\text{Pb}^*])/[^{207}\text{Pb}^*/^{206}\text{Pb}^*]$.

Same footnote applies to Supplementary Tables 2-1 to 2- 10.

Supplementary Table 2-2: GSWA 209911 quartz sandstone (Hardey Formation)

Mount no.	Grain spot	²³⁸ U (ppm)	²³² Th (ppm)	²³² Th ²³⁸ U	f206 (%)	²³⁸ U/ ²⁰⁶ Pb ± 1 σ	²⁰⁷ Pb/ ²⁰⁶ Pb ± 1 σ	²³⁸ U/ ²⁰⁶ Pb* ± 1 σ	²⁰⁷ Pb*/ ²⁰⁶ Pb* ± 1 σ	²³⁸ U/ ²⁰⁶ Pb* date (Ma) ±1σ	Disc. (%)	²⁰⁷ Pb*/ ²⁰⁶ Pb* date (Ma) ±1σ						
Older detrital zircons																		
G14-13	911-42.1	86	45	0.538	0.038	1.418	0.020	0.2964	0.0015	1.419	0.020	0.2960	0.0015	3439	37	0.3	3450	8
G14-13	911-40.1	244	135	0.570	0.004	1.456	0.014	0.2931	0.0009	1.456	0.014	0.2931	0.0009	3370	25	1.9	3434	5
G14-13	911-31.1	79	47	0.618	0.029	1.487	0.021	0.2910	0.0015	1.488	0.021	0.2908	0.0015	3314	38	3.1	3422	8
G14-13	911-38.1	375	338	0.933	0.017	1.466	0.012	0.2868	0.0046	1.466	0.012	0.2866	0.0046	3353	22	1.4	3399	25
G14-13	911-11.1	494	293	0.614	0.006	1.513	0.013	0.2826	0.0007	1.513	0.013	0.2826	0.0007	3271	21	3.2	3377	4
G14-13	911-21.1	300	184	0.633	0.000	1.507	0.016	0.2785	0.0011	1.507	0.016	0.2785	0.0011	3281	27	2.2	3355	6
G14-13	911-13.1	103	171	1.706	-0.043	1.482	0.020	0.2683	0.0014	1.482	0.020	0.2687	0.0014	3325	36	-0.8	3298	8
G14-13	911-5.1	256	32	0.128	-0.019	1.556	0.015	0.2663	0.0056	1.556	0.015	0.2664	0.0056	3199	25	2.6	3285	33
G14-13	911-43.1	319	218	0.705	0.008	1.552	0.014	0.2663	0.0007	1.552	0.014	0.2662	0.0007	3206	22	2.4	3284	4
G14-13	911-25.1	181	104	0.592	0.028	1.558	0.016	0.2623	0.0010	1.558	0.016	0.2620	0.0010	3196	27	1.9	3259	6
G14-13	911-27.1	236	252	1.102	0.030	1.606	0.015	0.2598	0.0008	1.607	0.015	0.2596	0.0008	3119	24	3.8	3244	5
G14-13	911-19.1	567	386	0.703	0.003	1.619	0.013	0.2587	0.0007	1.619	0.013	0.2586	0.0007	3101	20	4.2	3238	4
G14-13	911-14.1	318	161	0.522	0.017	1.628	0.015	0.2544	0.0009	1.628	0.015	0.2543	0.0009	3087	23	3.9	3212	5
G14-13	911-1.1	67	54	0.825	-0.149	1.577	0.029	0.2483	0.0019	1.575	0.029	0.2496	0.0020	3169	47	0.4	3182	13
G14-13	911-8.1	143	129	0.932	-0.071	1.722	0.023	0.2270	0.0014	1.720	0.023	0.2277	0.0014	2954	32	2.7	3036	10
G14-13	911-62.1	109	81	0.766	0.075	1.686	0.021	0.2259	0.0011	1.687	0.021	0.2252	0.0012	3001	31	0.6	3018	8
G14-13	911-39.1	138	131	0.977	0.053	1.790	0.020	0.2184	0.0010	1.791	0.020	0.2180	0.0010	2860	27	3.6	2966	8
G14-13	911-53.1	157	97	0.642	0.040	1.765	0.020	0.2167	0.0010	1.766	0.020	0.2163	0.0010	2893	26	2.1	2954	8
G14-13	911-7.1	130	61	0.490	0.066	1.757	0.024	0.2161	0.0013	1.758	0.024	0.2155	0.0013	2903	32	1.5	2947	10
G14-13	911-41.1	49	50	1.044	0.000	1.787	0.031	0.2155	0.0017	1.787	0.031	0.2155	0.0017	2865	41	2.8	2947	12
G14-13	911-2.1	201	170	0.873	0.086	1.743	0.020	0.2159	0.0010	1.745	0.020	0.2151	0.0011	2920	28	0.8	2944	8
G14-13	911-28.1	280	141	0.522	0.056	1.771	0.016	0.2155	0.0007	1.772	0.016	0.2150	0.0007	2884	21	2.0	2944	5
G14-13	911-23.1	376	80	0.218	0.024	1.805	0.017	0.2143	0.0008	1.805	0.017	0.2141	0.0008	2841	22	3.2	2937	6
G14-13	911-36.1	387	295	0.787	0.009	1.781	0.016	0.2127	0.0008	1.782	0.016	0.2126	0.0008	2872	21	1.8	2926	6
G14-13	911-60.1	207	171	0.850	-0.014	1.789	0.018	0.2115	0.0008	1.789	0.018	0.2116	0.0008	2863	23	1.9	2918	6

G14-13	911-24.1	241	258	1.106	0.056	1.758	0.017	0.2113	0.0008	1.759	0.017	0.2108	0.0008	2902	23	0.4	2912	6
G14-13	911-17.1	242	170	0.724	0.009	1.833	0.018	0.2107	0.0009	1.833	0.018	0.2107	0.0009	2807	23	3.6	2911	7
G14-13	911-56.1	200	191	0.986	0.038	1.808	0.018	0.2108	0.0008	1.809	0.018	0.2105	0.0009	2837	23	2.5	2909	7
G14-13	911-32.1	442	306	0.715	0.010	1.795	0.014	0.2097	0.0006	1.795	0.014	0.2096	0.0006	2854	19	1.7	2903	4
G14-13	911-33.1	354	352	1.026	0.022	1.795	0.015	0.2098	0.0006	1.796	0.015	0.2096	0.0007	2854	20	1.7	2902	5
G14-13	911-15.1	378	239	0.655	0.039	1.820	0.016	0.2099	0.0007	1.821	0.016	0.2095	0.0007	2822	20	2.8	2902	6
G14-13	911-29.1	368	322	0.903	0.035	1.891	0.016	0.2038	0.0006	1.891	0.016	0.2035	0.0006	2736	19	4.1	2854	5
G14-13	911-37.1	136	50	0.383	-0.013	1.906	0.022	0.1926	0.0010	1.906	0.022	0.1927	0.0010	2719	26	1.7	2765	9
Youngest detrital zircon age component (2750 ± 10 Ma)																		
G14-13	911-4.1	108	42	0.397	0.000	1.926	0.029	0.1922	0.0014	1.926	0.029	0.1922	0.0014	2696	33	2.3	2761	12
G14-13	911-10.1	114	65	0.587	-0.084	1.879	0.026	0.1910	0.0013	1.878	0.026	0.1917	0.0013	2752	31	0.2	2757	11
G14-13	911-12.1	112	77	0.707	-0.074	1.892	0.025	0.1909	0.0012	1.890	0.025	0.1915	0.0013	2737	30	0.7	2755	11
G14-13	911-45.1	99	75	0.787	-0.071	1.880	0.025	0.1903	0.0012	1.878	0.025	0.1909	0.0012	2752	30	-0.1	2750	11
G14-13	911-35.1	85	42	0.512	0.059	1.936	0.027	0.1903	0.0012	1.937	0.027	0.1898	0.0013	2683	31	2.1	2741	11
G14-13	911-61.1	92	57	0.633	0.054	1.944	0.026	0.1900	0.0012	1.945	0.026	0.1895	0.0012	2674	30	2.3	2738	11
G14-13	911-51.1	83	57	0.702	0.061	1.916	0.027	0.1895	0.0013	1.918	0.027	0.1889	0.0013	2705	32	1.0	2733	11
G14-13	911-46.1	25	13	0.540	0.577	1.934	0.048	0.1909	0.0024	1.945	0.048	0.1858	0.0030	2674	55	1.2	2705	27
G14-13	911-9.1	68	39	0.597	0.231	1.854	0.031	0.1873	0.0016	1.859	0.031	0.1852	0.0018	2775	39	-2.8	2700	16
Discordance >5%																		
G14-13	911-22.1	522	415	0.822	0.020	1.560	0.017	0.2975	0.0008	1.560	0.017	0.2974	0.0008	3193	27	7.6	3456	4
G14-13	911-16.1	665	471	0.731	0.014	1.824	0.050	0.2654	0.0058	1.824	0.050	0.2653	0.0058	2818	63	14.1	3278	34
G14-13	911-47.1	376	191	0.524	0.004	1.675	0.014	0.2586	0.0007	1.675	0.014	0.2585	0.0007	3018	20	6.8	3238	4
G14-13	911-49.1	117	4	0.036	0.120	1.677	0.020	0.2557	0.0012	1.679	0.020	0.2546	0.0012	3012	29	6.3	3214	8
G14-13	911-57.1	390	320	0.847	0.012	1.857	0.016	0.2499	0.0007	1.857	0.016	0.2497	0.0007	2777	19	12.8	3183	5
G14-13	911-58.1	391	255	0.674	0.012	1.847	0.015	0.2424	0.0037	1.848	0.015	0.2423	0.0037	2789	19	11.1	3135	24
G14-13	911-3.1	421	144	0.354	0.005	1.822	0.017	0.2410	0.0008	1.822	0.017	0.2410	0.0008	2820	21	9.8	3127	5
G14-13	911-52.1	576	501	0.899	0.037	1.987	0.015	0.2400	0.0034	1.987	0.015	0.2397	0.0034	2627	16	15.7	3118	23
G14-13	911-18.1	317	124	0.405	0.013	2.202	0.020	0.2272	0.0008	2.202	0.020	0.2271	0.0008	2413	18	20.4	3032	6

G14-13	911-44.1	545	180	0.342	0.037	1.872	0.014	0.2204	0.0005	1.872	0.014	0.2201	0.0006	2759	17	7.5	2982	4
G14-13	911-59.1	255	42	0.172	0.031	1.880	0.017	0.2134	0.0008	1.880	0.017	0.2132	0.0008	2749	21	6.2	2930	6
G14-13	911-26.1	133	67	0.521	0.044	1.856	0.021	0.2135	0.0010	1.857	0.021	0.2131	0.0010	2777	26	5.2	2929	8
G14-13	911-30.1	688	291	0.437	0.026	2.043	0.015	0.2133	0.0005	2.043	0.015	0.2131	0.0005	2568	16	12.3	2929	4
G14-13	911-48.1	497	418	0.868	0.034	1.905	0.015	0.2097	0.0005	1.905	0.015	0.2094	0.0005	2720	17	6.2	2901	4
G14-13	911-54.1	462	301	0.674	0.007	1.914	0.015	0.2072	0.0006	1.914	0.015	0.2072	0.0006	2710	18	6.0	2883	4
G14-13	911-20.1	691	89	0.133	0.026	2.402	0.019	0.2038	0.0007	2.403	0.019	0.2035	0.0007	2243	15	21.4	2855	6
G14-13	911-34.1	650	781	1.242	0.007	2.105	0.016	0.1969	0.0005	2.105	0.016	0.1969	0.0005	2506	15	10.5	2800	4
G14-13	911-6.1	901	565	0.649	0.022	2.405	0.018	0.1922	0.0006	2.406	0.018	0.1920	0.0006	2241	14	18.8	2760	5
G14-13	911-55.1	598	129	0.223	0.033	2.698	0.020	0.1852	0.0005	2.699	0.020	0.1849	0.0005	2032	13	24.7	2698	5
G14-13	911-50.1	803	859	1.105	0.048	2.554	0.019	0.1802	0.0055	2.555	0.019	0.1798	0.0055	2129	13	19.7	2651	50

Supplementary Table 2-3: GSWA 209905 Paulsens gabbro: baddeleyite

<i>Mount no.</i>	<i>Grain spot</i>	²³⁸ U (ppm)	²³² Th (ppm)	²³² Th ²³⁸ U	<i>f</i> 206 (%)	²³⁸ U/ ²⁰⁶ Pb* ± 1 σ	²⁰⁷ Pb*/ ²⁰⁶ Pb* ± 1 σ	²³⁸ U/ ²⁰⁶ Pb* <i>date (Ma)</i> ±1 σ	<i>Disc.</i> (%)	²⁰⁷ Pb*/ ²⁰⁶ Pb* <i>date (Ma)</i> ±1 σ				
Crystallization (2701 ± 11 Ma)														
1429	I.1-1	510	107	0.217	0.027	1.9080	0.0781	0.1796	0.0029	2717	91	-3.1	2649	26
1429	H.1-2	241	29	0.126	0.257	2.0650	0.0961	0.1814	0.0028	2546	98	5.4	2666	26
1429	A.2-2	263	52	0.203	0.171	1.8272	0.0718	0.1834	0.0022	2814	90	-6.0	2684	20
1429	B.2-1	456	33	0.074	0.318	1.9508	0.0750	0.1835	0.0016	2668	84	0.8	2685	15
1429	C.1-2	181	15	0.088	-0.256	1.9727	0.0818	0.1839	0.0034	2644	90	2.0	2689	31
1429	H.1-1	477	50	0.108	0.080	1.9889	0.0933	0.1852	0.0018	2626	101	3.3	2700	16
1429	D.1-1	492	15	0.031	0.244	1.9436	0.0746	0.1853	0.0015	2676	84	1.1	2701	14
1429	J.1-1	278	32	0.120	-0.045	1.8749	0.0740	0.1855	0.0019	2756	88	-2.4	2703	17
1429	G.1-1	314	31	0.101	0.063	2.0217	0.0796	0.1858	0.0023	2591	84	5.1	2705	20
1429	F.1-1	534	67	0.129	0.000	1.9219	0.0744	0.1869	0.0017	2701	85	0.7	2715	15
1429	C.1-1	475	25	0.054	0.142	2.0402	0.0840	0.1892	0.0021	2571	87	7.3	2736	18
1429	D.1-2	590	30	0.053	-0.067	1.9445	0.0743	0.1899	0.0030	2675	84	3.0	2741	26
Young outlier														
1429	E.1-1	281	111	0.407	0.125	2.1479	0.0840	0.1686	0.0018	2464	80	3.8	2544	17
Discordance >5% or high common lead														
1429	I.1-2	366	144	0.406	0.412	2.4155	0.1279	0.1596	0.0020	2233	100	10.5	2451	21
1429	F.1-3	337	13	0.041	0.637	1.9625	0.0768	0.1779	0.0027	2655	85	-1.0	2633	25
1429	F.1-2	215	16	0.076	1.540	1.9693	0.0796	0.1818	0.0058	2647	88	1.0	2670	53
1429	B.1-1	1206	33	0.029	0.021	1.6160	0.0656	0.1866	0.0013	3105	100	-18.3	2713	12

Supplementary Table 2-4: GSWA 209907 auriferous quartz–sulfide vein: xenotime

<i>Mount no.</i>	<i>Grain spot</i>	²³⁸ U (ppm)	²³² Th (ppm)	²³² Th ²³⁸ U	<i>f</i> 206 (%)	²³⁸ U/ ²⁰⁶ Pb* ± 1σ	²⁰⁷ Pb*/ ²⁰⁶ Pb* ± 1σ	²⁰⁸ Pb*/ ²³² Th ± 1σ	²³⁸ U/ ²⁰⁶ Pb* date (Ma) ± 1σ	<i>Disc.</i> %	²⁰⁷ Pb*/ ²⁰⁶ Pb* date (Ma) ±1σ					
Euhedral xenotime and matrix xenotime cores (2403 ± 5 Ma)																
1421	D.7-1	278	36	0.128	0.293	2.197	0.041	0.1569	0.0020	0.1481	0.0100	2418	37	0.2	2422	22
1421	C.5-1	884	10	0.011	-0.011	2.171	0.033	0.1568	0.0018	0.1266	0.0101	2443	31	-0.9	2421	19
1421	D.2-2	473	12	0.025	0.083	2.156	0.039	0.1566	0.0014	0.1068	0.0102	2457	36	-1.6	2419	16
1421	D.5-3	338	25	0.074	0.086	2.242	0.042	0.1565	0.0010	0.1090	0.0098	2378	37	1.7	2419	11
1421	D.3-1	212	71	0.338	0.044	2.259	0.047	0.1565	0.0012	0.1299	0.0098	2362	41	2.3	2418	13
1421	D.1-1	131	35	0.264	0.000	2.188	0.059	0.1565	0.0025	0.1226	0.0100	2427	54	-0.4	2418	27
1421	D.4-2	404	27	0.067	-0.013	2.235	0.041	0.1563	0.0009	0.1282	0.0099	2384	36	1.4	2416	10
1421	C.6-1	125	17	0.133	0.106	2.221	0.058	0.1562	0.0025	0.1262	0.0099	2397	52	0.8	2415	27
1421	C.2-2	876	7	0.008	-0.024	2.121	0.032	0.1560	0.0010	0.1726	0.0103	2490	31	-3.2	2413	11
1421	F.1-1	163	11	0.068	0.111	2.334	0.060	0.1559	0.0016	0.0969	0.0095	2298	49	4.7	2411	17
1421	F.1-4	309	2	0.005	0.036	2.252	0.046	0.1557	0.0011	0.0462	0.0098	2369	41	1.7	2409	12
1421	C2.1-1	325	3	0.009	0.030	2.171	0.042	0.1557	0.0010	0.0902	0.0101	2442	39	-1.4	2409	11
1421	D.3-2	139	37	0.268	0.000	2.178	0.054	0.1553	0.0014	0.1300	0.0101	2435	50	-1.3	2405	15
1421	D.4-1	410	15	0.037	0.038	2.252	0.041	0.1552	0.0009	0.1072	0.0099	2369	36	1.5	2404	10
1421	D.6-1	443	24	0.054	0.025	2.203	0.036	0.1550	0.0008	0.1301	0.0100	2413	33	-0.5	2402	9
1421	D.8-1	126	27	0.213	0.098	2.191	0.054	0.1550	0.0015	0.1214	0.0101	2424	49	-0.9	2402	16
1421	C.1-1	319	52	0.164	0.040	2.181	0.053	0.1550	0.0018	0.1260	0.0101	2433	50	-1.3	2402	20
1421	D.5-4	398	51	0.128	0.025	2.224	0.041	0.1550	0.0009	0.1241	0.0100	2393	37	0.3	2402	10
1421	C2.1-2	274	85	0.310	0.034	2.219	0.044	0.1549	0.0011	0.1326	0.0100	2398	40	0.1	2401	12
1421	F.7-2	928	18	0.020	0.006	2.099	0.032	0.1549	0.0007	0.1294	0.0105	2511	32	-4.6	2401	8
1421	D.5-2	423	21	0.051	0.045	2.095	0.037	0.1549	0.0009	0.1246	0.0105	2516	37	-4.8	2401	10
1421	D.2-1	749	68	0.091	0.007	2.159	0.035	0.1549	0.0008	0.1282	0.0102	2453	33	-2.2	2400	8
1421	C.3-1	195	75	0.384	0.000	2.130	0.044	0.1547	0.0012	0.1358	0.0103	2481	43	-3.5	2399	13
1421	D.1-2	129	4	0.033	0.167	2.253	0.063	0.1539	0.0017	0.0883	0.0099	2368	55	1.0	2390	19

1421	C2.2-1	520	20	0.038	0.043	2.309	0.072	0.1523	0.0009	0.1136	0.0098	2319	60	2.2	2372	10
1421	F.8-1	173	31	0.180	-0.029	2.379	0.055	0.1516	0.0013	0.1157	0.0096	2262	44	4.3	2364	15

Matrix xenotime discrete grains and rims (1680 ± 9 Ma)

1421	F.1-8	246	103	0.420	0.208	3.165	0.069	0.1085	0.0013	0.0850	0.0100	1770	34	0.2	1774	22
1421	G.1-5	150	147	0.982	-0.102	3.375	0.080	0.1070	0.0014	0.0872	0.0096	1673	35	4.4	1749	24
1421	G.1-4	265	371	1.403	0.266	3.335	0.065	0.1068	0.0019	0.0883	0.0097	1691	29	3.1	1745	32
1421	F.11-2	239	352	1.471	0.950	3.257	0.070	0.1059	0.0020	0.0919	0.0100	1726	33	0.2	1730	35
1421	F.1-9	253	149	0.588	0.106	3.306	0.071	0.1056	0.0012	0.0870	0.0099	1704	32	1.2	1724	21
1421	F.1-2	104	57	0.543	0.084	3.309	0.097	0.1052	0.0018	0.0872	0.0099	1702	44	0.9	1717	31
1421	F.2-2	179	169	0.944	-0.055	3.364	0.082	0.1050	0.0023	0.0850	0.0098	1678	36	2.2	1715	40
1421	D.5-6	352	189	0.538	0.000	3.439	0.063	0.1047	0.0009	0.0865	0.0096	1645	27	3.8	1710	15
1421	F.9-1	151	134	0.883	0.214	3.254	0.082	0.1044	0.0016	0.0889	0.0101	1728	38	-1.4	1703	28
1421	G.1-10	341	140	0.412	0.072	3.190	0.135	0.1042	0.0023	0.0895	0.0103	1758	65	-3.4	1699	40
1421	G.1-9	352	159	0.452	0.072	3.438	0.061	0.1039	0.0010	0.0867	0.0097	1646	26	2.9	1695	17
1421	E.1-2	290	248	0.857	-0.071	3.329	0.063	0.1037	0.0015	0.0878	0.0100	1693	28	-0.1	1691	26
1421	E.1-5	337	192	0.570	0.000	3.354	0.061	0.1036	0.0008	0.0871	0.0100	1682	27	0.4	1689	15
1421	F.2-3	248	435	1.753	0.150	3.453	0.074	0.1035	0.0013	0.0836	0.0097	1640	31	2.9	1688	23
1421	F.12-1	364	173	0.476	-0.046	3.285	0.062	0.1035	0.0009	0.0866	0.0102	1713	28	-1.5	1687	16
1421	F.1-12	232	264	1.141	0.000	3.549	0.077	0.1033	0.0012	0.0807	0.0095	1600	31	5.0	1684	21
1421	F.11-1	272	492	1.808	-0.063	3.321	0.068	0.1032	0.0011	0.0889	0.0101	1697	30	-0.8	1683	19
1421	F.1-11	196	140	0.715	0.055	3.428	0.086	0.1032	0.0014	0.0846	0.0098	1650	36	1.9	1682	25
1421	G.1-7	347	297	0.857	0.023	3.426	0.062	0.1031	0.0009	0.0860	0.0098	1651	26	1.8	1681	16
1421	F.1-10	258	209	0.808	0.111	3.337	0.073	0.1031	0.0012	0.0871	0.0101	1690	32	-0.5	1680	22
1421	G.1-1	294	160	0.546	0.000	3.407	0.064	0.1029	0.0013	0.0865	0.0099	1659	27	1.1	1677	24
1421	F.2-5	135	209	1.553	0.068	3.412	0.092	0.1028	0.0016	0.0849	0.0099	1657	39	1.1	1676	28
1421	F.5-2	306	165	0.539	0.000	3.332	0.067	0.1027	0.0010	0.0884	0.0101	1692	30	-1.1	1673	17
1421	G.1-3	209	86	0.414	0.035	3.323	0.106	0.1025	0.0011	0.0891	0.0102	1696	48	-1.6	1670	20
1421	F.7-1	274	130	0.474	0.070	3.374	0.071	0.1025	0.0011	0.0864	0.0100	1673	31	-0.3	1669	20
1421	E.1-3	318	239	0.751	0.043	3.222	0.059	0.1024	0.0009	0.0887	0.0104	1742	28	-4.5	1668	16

1421	F.1-3	116	97	0.842	0.227	3.417	0.098	0.1021	0.0029	0.0791	0.0100	1655	42	0.5	1663	53
1421	G.1-2	284	163	0.574	0.245	3.341	0.062	0.1020	0.0015	0.0868	0.0102	1688	27	-1.7	1661	28
1421	F.10-1	281	113	0.402	0.029	3.277	0.067	0.1018	0.0010	0.0888	0.0104	1717	31	-3.6	1657	18
1421	F.2-1	316	695	2.200	0.090	3.476	0.070	0.1016	0.0011	0.0841	0.0099	1630	29	1.4	1653	19
1421	F.4-1	297	202	0.679	0.087	3.445	0.069	0.1012	0.0010	0.0823	0.0100	1643	29	0.2	1646	19
1421	E.1-1	303	188	0.621	0.070	3.348	0.062	0.1012	0.0009	0.0852	0.0102	1685	27	-2.4	1645	17
1421	F.6-1	227	84	0.372	0.116	3.325	0.073	0.1009	0.0012	0.0829	0.0103	1695	33	-3.3	1641	23
1421	F.3-1	274	130	0.475	0.807	3.450	0.072	0.1008	0.0036	0.0817	0.0100	1641	30	-0.1	1639	66
1421	E.1-4	167	165	0.987	0.503	3.284	0.073	0.1008	0.0017	0.0830	0.0105	1714	34	-4.6	1639	32
1421	F.5-1	235	210	0.895	0.230	3.348	0.077	0.1004	0.0014	0.0871	0.0103	1685	34	-3.2	1632	25

Mixed ages

1421	C2.2-2	941	38	0.040	-0.028	2.379	0.037	0.1509	0.0007	0.1187	0.0096	2262	30	4.0	2356	8
1421	F.1-6	230	107	0.464	0.024	2.309	0.052	0.1503	0.0012	0.1166	0.0099	2320	44	1.3	2350	14
1421	C.4-1	437	17	0.040	-0.012	2.295	0.041	0.1503	0.0009	0.1183	0.0099	2331	35	0.7	2349	10
1421	G.2-1	781	88	0.113	0.019	2.310	0.035	0.1477	0.0007	0.1069	0.0100	2319	29	0.0	2319	8
1421	D.5-5	134	65	0.488	0.000	2.330	0.058	0.1456	0.0014	0.1148	0.0100	2302	48	-0.3	2295	17
1421	G.3-2	295	77	0.259	0.122	2.560	0.048	0.1387	0.0011	0.1006	0.0096	2126	34	3.9	2211	13
1421	F.1-5	265	69	0.260	0.415	2.591	0.060	0.1371	0.0015	0.1052	0.0096	2104	41	3.9	2191	19
1421	G.2-2	450	191	0.424	0.000	2.694	0.045	0.1313	0.0022	0.0984	0.0096	2035	29	3.8	2116	30
1421	G.1-6	434	19	0.045	0.083	2.727	0.046	0.1313	0.0013	0.0743	0.0095	2014	29	4.8	2115	18
1421	G.3-1	229	71	0.310	0.026	2.718	0.056	0.1299	0.0011	0.0983	0.0096	2020	36	3.7	2096	15
1421	F.1-7	172	115	0.668	0.182	2.986	0.073	0.1143	0.0015	0.0921	0.0100	1862	40	0.3	1868	24
1421	D.5-1	256	91	0.357	-0.030	3.257	0.068	0.1109	0.0011	0.0886	0.0095	1726	31	4.8	1813	17

Discordance > 5%

1421	C.1-2	421	6	0.014	0.000	2.053	0.055	0.1534	0.0015	0.1126	0.0107	2558	57	-7.3	2384	17
1421	G.4-1	161	71	0.439	-0.091	3.453	0.081	0.1068	0.0014	0.0869	0.0094	1640	34	6.1	1745	23
1421	G.5-1	314	99	0.317	0.522	2.591	0.079	0.1416	0.0022	0.0975	0.0094	2104	55	6.4	2247	27
1421	F.2-4	186	308	1.655	-0.051	3.444	0.082	0.1090	0.0014	0.0862	0.0092	1643	34	7.8	1783	23

1421	F.4-2	142	145	1.021	0.000	3.488	0.091	0.1082	0.0014	0.0857	0.0092	1625	38	8.2	1770	24
1421	G.1-8	201	75	0.373	0.335	3.335	0.070	0.1148	0.0015	0.0922	0.0090	1691	31	9.9	1876	24

Supplementary Table 2-5: GSWA 209909b ankerite–quartz vein in Paulsens gabbro (GSWA 209905): xenotime

Mount no.	Grain spot	²³⁸ U (ppm)	²³² Th (ppm)	²³² Th ²³⁸ U	f206 (%)	²³⁸ U/ ²⁰⁶ Pb* ± 1 σ	²⁰⁷ Pb*/ ²⁰⁶ Pb* ± 1 σ	²⁰⁸ Pb*/ ²³² Th ± 1 σ	²³⁸ U/ ²⁰⁶ Pb* date (Ma) ± 1 σ	Disc. %	²⁰⁷ Pb*/ ²⁰⁶ Pb* date (Ma) ±1 σ					
Carbonate vein emplacement (1655 ± 37 Ma)																
1421	L.1-1	258	335	1.298	0.136	3.338	0.078	0.1034	0.0014	0.0931	0.0100	1689	34	-0.2	1686	25
1421	K.1-1	387	624	1.613	0.204	3.313	0.067	0.1027	0.0012	0.0900	0.0102	1700	30	-1.6	1673	21
1421	J.1-1	274	505	1.841	0.082	3.336	0.122	0.1009	0.0012	0.0856	0.0103	1690	54	-3.0	1641	23
1421	K.2-1	550	1354	2.465	0.133	3.381	0.061	0.1007	0.0009	0.0862	0.0102	1670	27	-2.0	1637	17
Old outlier																
1421	B.1-1	328	266	0.811	0.033	2.190	0.042	0.1562	0.0010	0.1237	0.0100	2425	39	-0.4	2415	11
Discordance >5%																
1421	I.1-1	190	258	1.356	0.398	3.637	0.090	0.1089	0.0019	0.0692	0.0088	1566	34	12.1	1781	32
1421	L.2-1	206	316	1.536	0.267	3.552	0.092	0.1048	0.0017	0.0837	0.0093	1599	37	6.5	1710	29

Supplementary Table 2-6: GSWA 209902 carbonaceous phyllite: monazite

<i>Mount no.</i>	<i>Grain spot</i>	²³⁸ U (ppm)	²³² Th (ppm)	²³² Th ²³⁸ U	<i>f</i> 206 (%)	²³⁸ U/ ²⁰⁶ Pb* ± 1σ	²⁰⁷ Pb*/ ²⁰⁶ Pb* ± 1σ	²⁰⁸ Pb*/ ²³² Th ± 1σ	²³⁸ U/ ²⁰⁶ Pb* date (Ma) ± 1σ	<i>Disc.</i> %	²⁰⁷ Pb*/ ²⁰⁶ Pb* date (Ma) ±1σ					
Hydrothermal growth (2401 ± 14 Ma)																
1423	A.1-3	312	6326	20.266	0.303	2.227	0.051	0.1580	0.0029	0.1253	0.0037	2391	45	1.8	2435	31
1423	B.1-3	185	3689	19.916	0.093	2.189	0.043	0.1562	0.0010	0.1275	0.0023	2425	39	-0.4	2415	11
1423	A.1-2	284	9519	33.469	0.503	2.184	0.050	0.1561	0.0015	0.1292	0.0037	2430	46	-0.7	2414	16
1423	A.1-1	319	6758	21.190	0.262	2.276	0.061	0.1559	0.0013	0.1223	0.0035	2348	53	2.7	2412	14
1423	B.1-1	186	4584	24.687	0.231	2.328	0.043	0.1554	0.0011	0.1221	0.0022	2304	35	4.3	2406	12
1423	A.1-5	198	8211	41.555	0.575	2.204	0.048	0.1543	0.0019	0.1218	0.0035	2411	44	-0.7	2394	21
1423	B.1-2	126	2015	15.943	0.333	2.178	0.040	0.1530	0.0014	0.1274	0.0023	2436	37	-2.4	2379	16
1423	B.1-6	284	4367	15.400	0.117	2.313	0.035	0.1529	0.0009	0.1202	0.0022	2316	29	2.6	2379	11
Young outlier																
1423	A.1-4	309	8179	26.441	0.440	2.414	0.052	0.1470	0.0016	0.1260	0.0037	2234	40	3.3	2312	19
Discordance >5%																
1423	B.1-5	135	5647	41.727	0.219	2.054	0.041	0.1570	0.0013	0.13716	0.00257	2557	42	-5.5	2423	14

Supplementary Table 2-7: GSWA 209909a altered part of Paulsens gabbro: monazite

<i>Mount no.</i>	<i>Grain spot</i>	²³⁸ U (ppm)	²³² Th (ppm)	²³² Th ²³⁸ U	<i>f</i> ₂₀₆ (%)	²³⁸ U/ ²⁰⁶ Pb* ± 1σ	²⁰⁷ Pb*/ ²⁰⁶ Pb* ± 1σ	²⁰⁸ Pb*/ ²³² Th ± 1σ	²³⁸ U/ ²⁰⁶ Pb* date (Ma) ± 1σ	<i>Disc.</i> %	²⁰⁷ Pb*/ ²⁰⁶ Pb* date (Ma) ±1σ					
Hydrothermal growth (2398 ± 37 Ma)																
1428	C.3-1	33	2865	87.213	0.018	2.072	0.056	0.1595	0.0028	0.1422	0.0042	2539	56	-3.6	2451	30
1428	C.3-2	46	837	18.159	0.326	2.285	0.059	0.1563	0.0032	0.1345	0.0039	2340	51	3.1	2416	34
1428	C.3-3	54	8224	151.026	0.536	2.074	0.055	0.1556	0.0035	0.1313	0.0038	2536	55	-5.3	2409	38
1428	C.2-1	135	7631	56.653	0.926	2.163	0.036	0.1548	0.0022	0.1354	0.0024	2449	34	-2.1	2399	24
1428	C.3-4	141	2825	20.029	1.354	2.444	0.085	0.1529	0.0036	0.1068	0.0034	2211	65	7.0	2379	40
1428	E.1-1	42	14840	355.409	1.011	2.075	0.044	0.1506	0.0035	0.1405	0.0025	2536	45	-7.8	2353	40
1428	I.1-1	55	2572	46.866	1.892	2.170	0.043	0.1473	0.0038	0.1339	0.0024	2443	40	-5.6	2315	45
High common lead																
1428	C.1-1	34	14748	428.426	6.751	2.136	0.087	0.1755	0.0115	0.1255	0.0023	2476	83	5.2	2611	109

Supplementary Table 2-8: GSWA 209912 carbonaceous phyllite: monazite

Mount no.	Grain spot	²³⁸ U (ppm)	²³² Th (ppm)	²³² Th ²³⁸ U	f206 (%)	²³⁸ U/ ²⁰⁶ Pb* ± 1σ	²⁰⁷ Pb*/ ²⁰⁶ Pb* ± 1σ	²⁰⁸ Pb*/ ²³² Th ± 1σ	²³⁸ U/ ²⁰⁶ Pb* date (Ma) ± 1σ	Disc. %	²⁰⁷ Pb*/ ²⁰⁶ Pb* date (Ma) ±1σ					
Hydrothermal growth (1730 ± 28 Ma)																
1423	D.2-8	91	5158	56.550	0.813	2.973	0.074	0.1105	0.0028	0.0845	0.0015	1869	40	-3.4	1807	45
1423	D.2-9	55	3436	62.452	0.914	3.258	0.064	0.1089	0.0040	0.0888	0.0016	1726	30	3.1	1780	67
1423	D.2-18	95	5180	54.760	0.715	3.292	0.070	0.1083	0.0023	0.0822	0.0014	1710	32	3.4	1771	40
1423	D.2-11	95	7209	76.236	0.776	3.164	0.071	0.1076	0.0024	0.0915	0.0016	1771	35	-0.7	1759	40
1423	D.2-14	90	6683	74.521	0.631	3.245	0.073	0.1058	0.0020	0.0923	0.0017	1732	34	-0.1	1729	35
1423	D.2-2	58	4641	79.475	1.374	3.179	0.095	0.1058	0.0037	0.0960	0.0017	1763	46	-2.0	1728	63
1423	D.2-16	52	5435	104.306	1.223	3.413	0.067	0.1048	0.0036	0.0876	0.0015	1656	29	3.2	1711	63
1423	D.2-13	92	3753	41.001	0.896	3.193	0.054	0.1048	0.0022	0.0963	0.0018	1757	26	-2.7	1710	39
1423	D.2-15	72	6424	89.221	1.617	3.316	0.061	0.1032	0.0037	0.0934	0.0018	1699	27	-1.0	1682	66
1423	D.2-4	72	6536	90.289	1.556	3.363	0.065	0.1017	0.0037	0.0904	0.0016	1678	28	-1.4	1655	68
1423	D.2-5	70	5233	74.652	1.602	3.247	0.064	0.1010	0.0040	0.0902	0.0016	1731	30	-5.4	1642	73
1423	D.2-17	62	5158	83.571	1.335	3.436	0.065	0.0992	0.0034	0.0868	0.0016	1647	27	-2.3	1609	64
Discordance >5%																
1423	D.1-5	81	5703	70.269	0.855	3.316	0.062	0.1144	0.0051	0.0830	0.0016	1699	28	9.1	1870	81
1423	D.2-6	53	4884	91.841	1.263	3.565	0.078	0.1048	0.0045	0.0821	0.0015	1594	31	6.8	1710	79
1423	E.1-1	86	7073	82.411	1.349	3.029	0.052	0.1029	0.0027	0.0951	0.0018	1839	28	-9.7	1677	49
1423	D.2-12	106	9809	92.164	1.418	3.124	0.052	0.1021	0.0026	0.0848	0.0015	1790	26	-7.7	1662	48
1423	D.1-2	70	13563	193.008	0.928	2.462	0.049	0.1085	0.0030	0.0849	0.0016	2197	37	-23.8	1775	51
1423	D.1-4	76	6706	87.890	1.834	2.388	0.064	0.1068	0.0036	0.0900	0.0016	2255	51	-29.2	1746	62
1423	D.2-19	74	6424	87.366	1.584	2.936	0.081	0.1039	0.0036	0.0913	0.0016	1890	45	-11.5	1695	64
1423	D.2-1	71	4659	65.900	1.603	2.959	0.075	0.1038	0.0034	0.0951	0.0018	1877	41	-10.9	1693	60
1423	D.2-7	83	7386	88.725	1.105	2.874	0.072	0.1013	0.0028	0.0841	0.0015	1925	42	-16.8	1649	51
1423	D.1-1	117	8491	72.653	1.623	3.135	0.140	0.0966	0.0040	0.0829	0.0015	1785	69	-14.5	1559	78

Supplementary Table 2-9: GSWA 219513 and 219517 carbonaceous phyllite: monazite

Mount no.	Grain spot	²³⁸ U (ppm)	²³² Th (ppm)	²³² Th ²³⁸ U	f206 (%)	²³⁸ U/ ²⁰⁶ Pb* ± 1σ	²⁰⁷ Pb*/ ²⁰⁶ Pb* ± 1σ	²⁰⁸ Pb*/ ²³² Th ± 1σ	²³⁸ U/ ²⁰⁶ Pb* date (Ma) ± 1σ	Disc. %	²⁰⁷ Pb*/ ²⁰⁶ Pb* date (Ma) ±1σ					
Hydrothermal alteration (2403 ± 38 Ma)																
1502	F.1-1	103	1286	12.537	0.414	2.201	0.079	0.1583	0.0073	0.1307	0.0056	2415	72	0.9	2437	78
1502	D.1-3	81	5282	65.540	0.264	2.162	0.067	0.1582	0.0070	0.1331	0.0057	2451	63	-0.6	2437	75
1502	F.1-2	122	3851	31.509	0.477	2.160	0.056	0.1581	0.0060	0.1334	0.0057	2453	53	-0.7	2435	64
1502	D.2-1	88	126	1.433	0.258	2.121	0.065	0.1555	0.0056	0.1471	0.0080	2490	63	-3.4	2408	61
1502	D.1-2	134	1568	11.729	0.229	2.149	0.054	0.1551	0.0042	0.1322	0.0057	2463	51	-2.5	2403	47
1502	D.1-4	120	1194	9.974	0.715	2.205	0.055	0.1497	0.0045	0.1291	0.0057	2411	50	-2.9	2343	51
1502	D.1-5	87	1719	19.643	0.388	2.138	0.035	0.1555	0.0036	0.1321	0.0060	2474	33	-2.8	2407	40
1502	D.1-6	103	1477	14.336	0.219	2.201	0.037	0.1576	0.0080	0.1250	0.0055	2414	34	0.6	2430	86
1502	D.1-7	32	654	20.756	0.928	2.188	0.171	0.1528	0.0067	0.1284	0.0071	2426	156	-2.0	2378	75
Discordance > 5% or high common lead																
1502	G.1-1	29	2436	83.610	1.958	2.439	0.103	0.1518	0.0247	0.1138	0.0049	2215	79	6.4	2367	277
1502	A.1-1	33	1241	37.344	2.141	2.235	0.084	0.1587	0.0206	0.1260	0.0054	2384	75	2.4	2442	220
1502	G.1-2	58	972	16.816	2.702	2.176	0.068	0.1482	0.0126	0.1348	0.0058	2438	63	-4.8	2325	146
1502	A.2-1	13	745	55.889	6.606	3.261	0.275	0.1006	0.0676	0.0939	0.0042	1724	126	-5.4	1636	1248
1502	D.2-2	122	592	4.869	0.013	2.026	0.051	0.1588	0.0047	0.1406	0.0062	2586	54	-5.8	2443	50
1502	G.2-1	102	647	6.357	0.022	2.024	0.056	0.1563	0.0077	0.1332	0.0059	2588	58	-7.1	2416	84
1502	D.1-1	143	3152	22.117	0.443	2.138	0.068	0.1495	0.0044	0.1310	0.0057	2473	65	-5.7	2340	51

Supplementary Table 2-10: GSWA 215912 and 219513 carbonaceous phyllite: monazite

<i>Mount no.</i>	<i>Grain spot</i>	²³⁸ U (ppm)	²³² Th (ppm)	²³² Th ²³⁸ U	<i>f</i> 206 (%)	²³⁸ U/ ²⁰⁶ Pb* ± 1 σ	²⁰⁷ Pb*/ ²⁰⁶ Pb* ± 1 σ	²⁰⁸ Pb*/ ²³² Th ± 1 σ	²³⁸ U/ ²⁰⁶ Pb* <i>date (Ma)</i> ± 1 σ	<i>Disc.</i> %	²⁰⁷ Pb*/ ²⁰⁶ Pb* <i>date (Ma)</i> ±1 σ					
Hydrothermal alteration (1721 ± 32 Ma)																
1502	B.1-8	172	4760	27.625	0.382	3.285	0.050	0.1080	0.0021	0.0895	0.0040	1713	23	3.0	1766	36
1502	B.1-7	250	2089	8.349	0.693	3.182	0.059	0.1062	0.0020	0.0950	0.0043	1761	29	-1.5	1735	34
1502	E.1-1	256	377	1.476	0.049	3.076	0.075	0.1057	0.0038	0.0954	0.0046	1814	38	-5.0	1727	66
1502	B.1-5	226	4319	19.141	0.931	3.281	0.057	0.1045	0.0025	0.0933	0.0050	1715	26	-0.5	1706	44
1502	E.1-3	187	655	3.506	0.386	3.138	0.121	0.1044	0.0031	0.1113	0.0083	1783	60	-4.7	1703	55
1502	C.1-2	1209	2930	2.424	0.169	3.334	0.127	0.1043	0.0020	0.0878	0.0040	1691	56	0.6	1702	35
1502	E.1-4	280	8946	31.938	0.668	3.264	0.088	0.1021	0.0030	0.0896	0.0046	1723	41	-3.6	1663	54
Discordance > 5% or high common lead																
1502	B.1-3	168	22578	134.605	4.952	2.919	0.078	0.1153	0.0119	0.0889	0.0042	1899	44	-0.8	1885	186
1502	E.1-2	368	3681	9.994	0.024	3.000	0.077	0.1069	0.0028	0.0948	0.0041	1855	41	-6.2	1747	48
1502	C.1-3	346	2068	5.974	0.507	3.630	0.179	0.1055	0.0035	0.0872	0.0041	1568	68	9.0	1723	60
1502	B.1-1	311	2049	6.600	0.626	3.110	0.075	0.1021	0.0032	0.0960	0.0042	1797	38	-8.1	1662	58
1502	C.1-1	323	11800	36.550	0.470	3.080	0.122	0.1011	0.0040	0.1015	0.0061	1813	63	-10.3	1644	74
1502	B.1-6	285	5926	20.811	0.560	3.160	0.045	0.1010	0.0018	0.0813	0.0052	1773	22	-8.0	1642	34
1502	B.1-4	244	8919	36.573	2.096	3.021	0.076	0.0995	0.0053	0.0958	0.0044	1843	40	-14.1	1616	100
1502	B.1-2	172	827	4.812	1.698	3.187	0.106	0.0974	0.0057	0.0914	0.0041	1759	51	-11.7	1575	110

CHAPTER 3. NEIGHBOURING OROGENIC GOLD DEPOSITS MAY BE THE PRODUCTS OF UNRELATED MINERALIZING EVENTS

The following chapter has been published in ORE GEOLOGY REVIEWS. The original format has been modified for the purposes of this thesis, but all content remains the same. The original, formatted and published version can be found in Appendix 1B.

Imogen O. H. Fielding¹, Simon P. Johnson², Jian-Wei Zi¹, Stephen Sheppard^{1,3} and Birger Rasmussen⁴, 2018, Neighbouring orogenic gold deposits may be the products of unrelated mineralizing events: Ore Geology Reviews, v. 95, p. 593-603. Doi : <https://doi.org/10.1016/j.oregeorev.2018.03.011>

¹ Department of Applied Geology, Curtin University, Kent Street, Bentley, Western Australia 6102, Australia.

² Geological Survey of Western Australia, 100 Plain Street, East Perth, Western Australia 6004, Australia.

³ Prime Geological Mapping, PO Box 3014, Carlisle South, Western Australia, 6101, Australia

⁴ School of Earth Sciences, The University of Western Australia, Perth, Western Australia 6009, Australia

3.1. ABSTRACT

Models for exploration targeting are often developed by assessing known gold deposits in a region, and targeting similar geological features such as geochemical anomalies, favourable host rocks or structural settings with the assumption that they represented the footprint of the mineralizing event. Belvedere and Paulsens are gold deposits with similar characteristics located in the Wyloo Inlier in the north Capricorn Orogen, Western Australia. Gold at both deposits is hosted in quartz–carbonate–sulfide veins within mafic intrusive rock. Prior to this study they were thought to have formed during the same hydrothermal mineralizing event. At Belvedere, in situ baddeleyite geochronology yields a weighted mean $^{207}\text{Pb}^*/^{206}\text{Pb}^*$ crystallization age of 2082 ± 30 Ma for the Belvedere dolerite which hosts the ore body. Xenotime intergrown with ore-stage alteration minerals, and encased in arsenopyrite, yielded a $^{207}\text{Pb}^*/^{206}\text{Pb}^*$ date of 1681 ± 9 Ma, interpreted to represent the timing of hydrothermal activity related to gold mineralization at the Belvedere deposit. Despite the similarities between the two deposits, our results indicate that they underwent different geological histories with primary gold mineralization at Paulsens occurring at c. 2400 Ma, pre-dating both the Belvedere dolerite and mineralization within the dolerite. Furthermore, field relationships show that the suite of dolerite dykes to which the Belvedere dolerite belongs, crosscut gold mineralization at Paulsens. The in situ U–Pb geochronology techniques employed here, combined with field relationships, have led to a better understanding on age constraints of gold deposition in the Wyloo Inlier and challenges the assumption that orogenic deposits in a given region probably formed during a single mineralizing event.

3.2. INTRODUCTION

Gold deposits within a given geological terrane that exhibit similar characteristics are commonly thought to have formed due to the same geological processes during the same hydrothermal event (Cheng, 2008; Groves et al., 1998). This is particularly apparent in orogenic gold systems as they form during collisional or accretionary orogenies resulting in numerous gold deposits of varying size that form linear trends along major faults associated with crustal boundaries (Bierlein et al., 2006; Goldfarb et al., 2001; Groves et al., 2005). Since faults and major structures can act as fluid

pathways (Hronsky et al., 2012; Korsch and Doublier, 2016), it is possible that remobilization or new mineralizing events could be superimposed along the same system. Therefore, without knowing the absolute ages of host rocks and gold mineralization at individual deposits in a region, it is not obvious as to whether they are all a result of a single mineralizing event or were formed during multiple, superimposed events. In this contribution, we examine the timing of gold mineralization at two similar, closely spaced deposits in the Wyloo Inlier in Western Australia to investigate whether they are the result of a single or multiple mineralizing events.

The Belvedere and Paulsens gold deposits are located in the Wyloo Inlier situated on the southern margin of the Pilbara Craton in Western Australia (Figure 3-1; Thorne and Trendall, 2001). The Paulsens deposit is significantly larger than Belvedere with a total endowment of 1.1 Moz of gold (Blockley, 1971; Fielding et al., 2017). The Belvedere deposit had 454 oz of gold extracted during the 1930s (Blockley, 1971) and has a remaining resource of 31,000 oz of contained gold (Northern Star Resources Limited, 2015). The deposits are 6.5 km apart and historically were interpreted as vein-hosted gold deposits associated with the 1820–1770 Ma Capricorn Orogeny (Thorne and Trendall, 2001). Originally it was thought the Capricorn Orogeny represented the collision between the Pilbara and Yilgarn cratons (Tyler and Thorne, 1990) but is now known to have been an episode of intracratonic reworking (Johnson et al., 2017; Sheppard et al., 2010). Both deposits share the main characteristics of orogenic gold deposits: 1) mineralization comprises quartz–carbonate–sulfide veins; 2) the host rocks are metamorphosed to epidote-actinolite greenschist facies (White et al., 2014); 3) ore-stage alteration assemblages consist of muscovite, carbonate and quartz; 4) the deposits contain native gold (Fielding et al., 2017; Norum, 2005; Owen, 2000), and 5) the deposits are spatially associated with a crustal-scale fault. An additional feature common to the deposits is that mafic intrusive rocks host the auriferous quartz–carbonate–sulfide veins. Despite these similarities, the suite of dolerite dykes which hosts the Belvedere deposit post-date, and cross cut gold mineralization at Paulsens, suggesting that gold mineralization at the two deposits was not synchronous.

Published data and descriptions of the Belvedere deposit are limited to brief mentions in open-file company reports held by the Department of Mines, Industry, Regulation and Safety and in Geological Survey of Western Australia reports (e.g., Blockley,

1971; Forman, 1938; Marston, 1979; Thorne and Trendall, 2001). Here we present new data, including more detailed field relationships and in situ U–Pb SHRIMP geochronology for the Belvedere gold deposit, to determine the age of the host rocks to gold mineralization and the timing of hydrothermal activity related to gold formation. These data are then compared to published information from the Paulsens gold deposit (e.g., Fielding et al., 2017) to demonstrate that gold deposits in close proximity, with similar appearances, may form at separate times and in different tectonic settings.

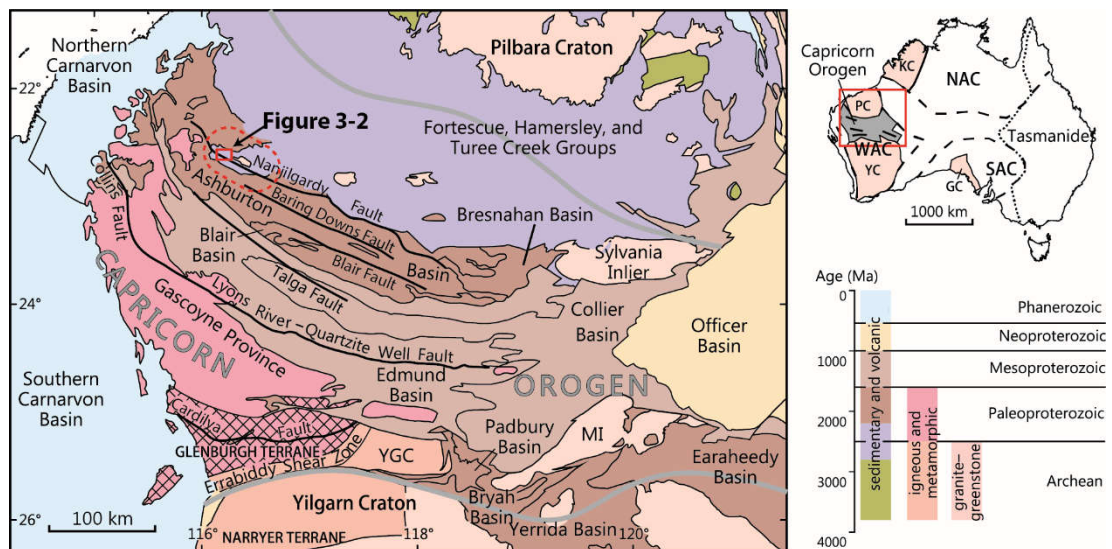


Figure 3-1: Location of the Capricorn Orogen in Western Australia, showing location of the Wyloo Inlier (dashed red ellipse) and inset location for Figure 3-2. Abbreviations: GC = Gawler Craton, KC = Kimberley Craton, MI = Marymia Inlier, NAC = North Australian Craton, PC = Pilbara Craton, SAC = South Australian Craton, WAC = West Australian Craton, YC = Yilgarn Craton, YGC = Yarlalweelor Gneiss Complex (after Johnson et al., 2013).

3.3. GEOLOGICAL SETTING

The Wyloo Inlier is situated in the northern part of the Paleoproterozoic Capricorn Orogen on the southern margin of the Pilbara Craton (Figure 3-1). The Capricorn Orogen has a complex tectonothermal evolution which includes at least seven tectonic events over approximately 1.6 billion years (Cawood and Tyler, 2004; Johnson et al., 2011; Johnson et al., 2013; Korhonen et al., 2017; Martin and Morris, 2010; Sheppard et al., 2005; Sheppard et al., 2007). The first two tectonic events (the Ophthalmia Orogeny and the Glenburgh Orogeny) mark the amalgamation of the West Australian Craton. During the 2215–2145 Ma Ophthalmia Orogeny (Johnson et al., 2011; Rasmussen et al., 2005) the Glenburgh Terrane collided with the Pilbara Craton. Subsequently, during the 2005–1950 Ma Glenburgh Orogeny, the combined Pilbara

Craton – Glenburgh Terrane collided with the Yilgarn Craton (Johnson et al., 2011; Occhipinti et al., 2004; Sheppard et al., 2004). Once assembled, the West Australian Craton experienced over a billion years of intracratonic reworking and reactivation during the 1820–1770 Ma Capricorn Orogeny (Cawood and Tyler, 2004; Sheppard et al., 2010), the 1680–1620 Ma Mangaroon Orogeny (Sheppard et al., 2005), the 1320–1170 Ma Mutherbukin Tectonic Event (Korhonen et al., 2017), the 1030–955 Ma Edmundian Orogeny (Martin and Thorne, 2004; Sheppard et al., 2007), and the c. 570 Ma Mulka Tectonic Event (Johnson et al., 2013).

Within the Wyloo Inlier, Archean basement rocks of the Pilbara Craton are overlain by Archean to Paleoproterozoic metasedimentary and metavolcanic rocks of the Fortescue Group, Hamersley Group, Turee Creek Group, Shingle Creek Group and the Paleoproterozoic Ashburton Formation of the Wyloo Group (Seymour et al., 1988; Thorne and Trendall, 2001). The rocks throughout the Wyloo Inlier are overprinted by regional-scale epidote-actinolite greenschist facies metamorphism (White et al., 2014), and intruded by at least five suites of mafic dykes and sills. Of these dyke suites, only the oldest and youngest have been dated at, respectively, 2701 ± 11 Ma (Fielding et al., 2017) and 753 ± 11 Ma (Wingate et al., 2017a).

Deep crustal seismic reflection imaging across the Capricorn Orogen identified five crustal-scale faults which show a spatial relationship with gold occurrences (Johnson et al., 2013). In the northern Capricorn Orogen, a second order structure of the Nanjilgardy Fault, known as the Hardey Fault, is spatially associated with the Belvedere deposit (Figure 3-2) and is linked to c. 2400 and 1680 Ma gold mineralizing events at Paulsens (Fielding et al., 2017).

3.4. LOCAL GEOLOGY

The Belvedere gold deposit is located in the core of the Wyloo Inlier within the Mount Roe Basalt (Figure 3-2; Thorne and Trendall, 2001). The local stratigraphy at Belvedere includes vesicular basalt, polymictic conglomerate, sandstone and siltstone (Figure 3-3).

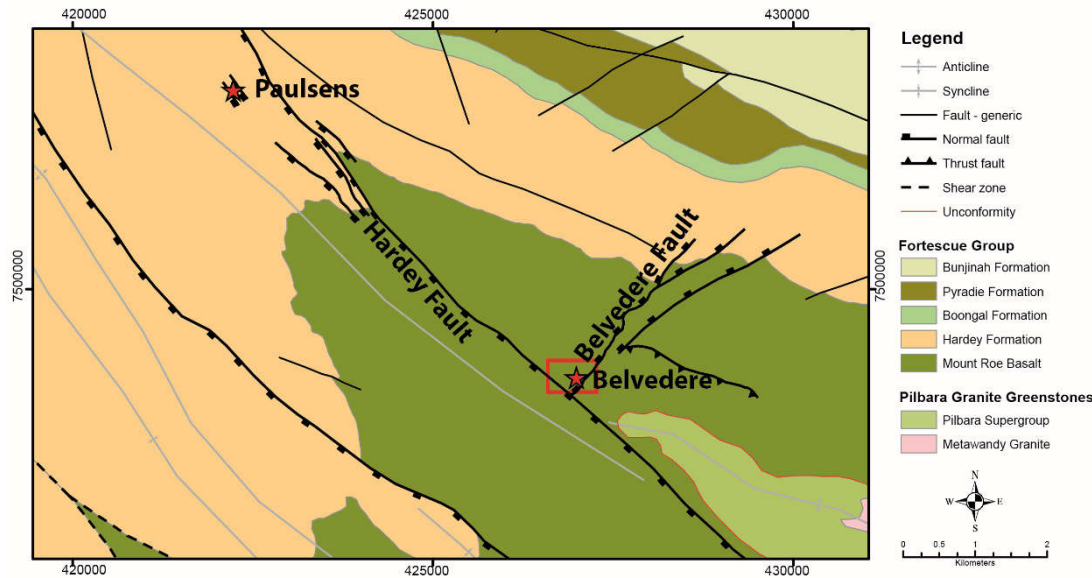


Figure 3-2: Geology map of the northern part of the Wyloo Inlier (courtesy of Northern Star Resources Ltd. Pty) showing the location of the Belvedere and Paulsens Deposits. Coordinates are in meters (MGA94 zone 50). Red box shows the location of Figure 3-3.

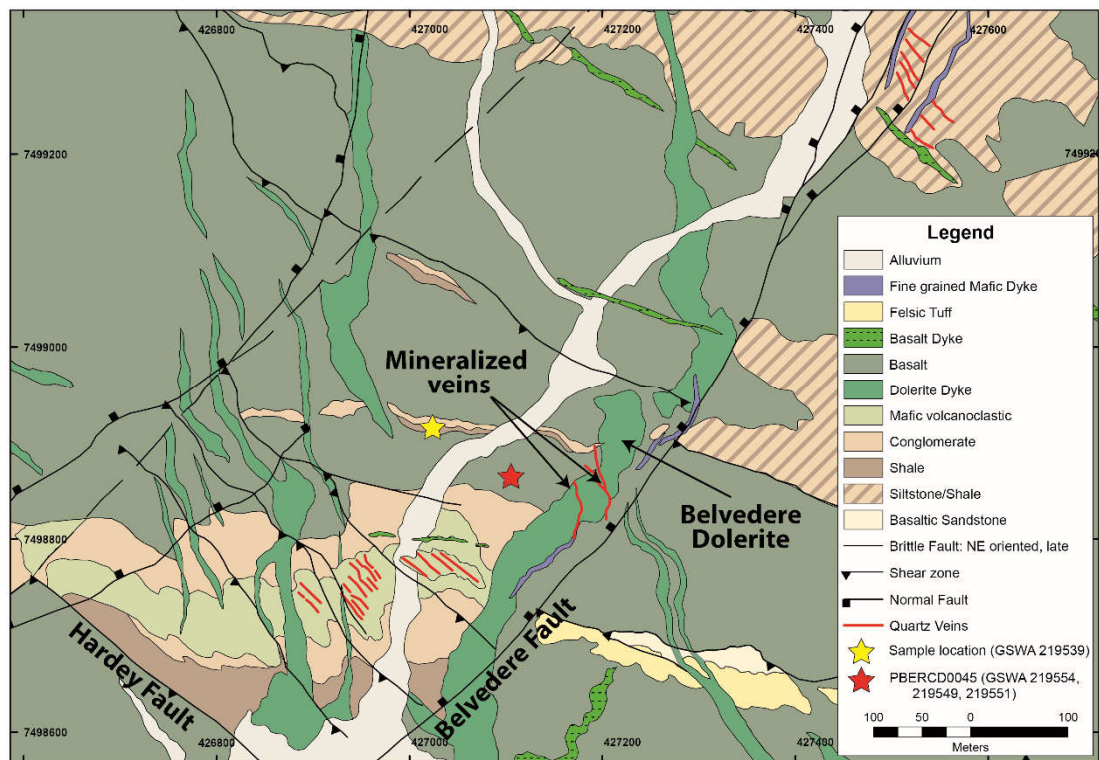


Figure 3-3: Local geology map of the Belvedere deposit showing location of the samples, Belvedere dolerite, mineralized quartz-carbonate-arsenopyrite veins and Belvedere and Hardey Faults. Coordinates are in meters (MGA94 zone 50).

At least four low-grade deformation events have affected the rocks of the Wyloo Inlier, during which two widespread cleavages formed, followed by fault reactivation along pre-existing crustal-scale faults (Krapež, 1999; Thorne and Seymour, 1991). The first event (D1) caused regional-scale, epidote-actinolite greenschist facies metamorphism

(White et al. 2014) accompanied by tight to upright folds, a penetrative, spaced, axial planar cleavage (S1) with an average orientation of 320/85SW (Fielding et al., 2017), and is thought to be related to the 2215–2145 Ma Ophthalmia Orogeny (Tyler and Thorne, 1990). The second event (D2), is characterised by lower greenschist facies metamorphism with the growth of chlorite-sericite-muscovite in pelitic and semi-pelitic rocks and chlorite-amphibole in mafic and mafic volcanoclastic rocks (Tyler, 1991; Smith et al., 1982). The D2 event is near-coaxial to D1 and is linked to the 1820–1770 Ma Capricorn Orogeny (Thorne and Seymour, 1991). It caused tightening of the F1 folds, attenuation of northern limbs to form shear zones up to 50 m wide, and development of a spaced cleavage (S2) with an average orientation of 305/85SW (Fielding et al., 2017). S1 and S2 can be difficult to differentiate in the field due to their sub-parallel nature. D3 and D4 are characterised by WNW-trending dextral followed by sinistral strike-slip reactivation (Krapez, 1999) of the Nanjilgardy Fault and its subsidiary structures, including the Hardey Fault, during the final stages of the Capricorn Orogeny (Krapež, 1999; Thorne and Seymour, 1991) and early stages of the 1680–1620 Ma Mangaroon Orogeny (Fielding et al., 2017).

Proximal to the Belvedere ore body there are three suites of mafic intrusive rocks. An early folded gabbroic dyke with an igneous crystallization age of 2734 ± 14 Ma (Wingate et al., 2017) intrudes the Mount Roe Basalt immediately north of the Belvedere deposit and is crosscut by northwest-trending S1 and S2 fabrics. Two later suites of dolerite dykes strike north and northwest and crosscut the gabbro. The relationship between the two younger suites of dolerite dykes is not clear, and currently no geochronological data are available. The dolerites are generally undeformed, although the north-striking dolerite dykes are locally kinked with a spaced cleavage preserved in the deformed zones.

3.5. DEPOSIT DESCRIPTION

The Belvedere orebody is hosted by a 30 m-thick, north-striking, $\sim 40^\circ$ -west dipping, fine- to medium-grained dolerite dyke informally known as the Belvedere dolerite. The Belvedere dolerite is largely undeformed, although it is foliated at the contact with the mineralized quartz–carbonate–arsenopyrite veins. Overall, it has a northerly strike but close to the orebody it intrudes along the northeast-striking Belvedere fault for

approximately 500 m (Figure 3-3). Sinistral strike-slip reactivation of the Belvedere fault resulted in the formation of two Riedel shear zones and associated auriferous quartz–carbonate–arsenopyrite veins, surrounded by muscovite–ankerite–quartz \pm rutile \pm albite alteration (Norum, 2005). The mineralized quartz–carbonate–arsenopyrite veins are 2–12 m wide with native gold forming irregular inclusions up to 150 μm by 20 μm (Figure 3-4a) within euhedral arsenopyrite crystals <2 mm in diameter. Metallurgical test work indicates most of the gold occurs as free gold that is not bound within the arsenopyrite crystal lattice (Owen, 2000). Small amounts of gold mineralization are also present in quartz–carbonate–arsenopyrite veins occurring sporadically within the Belvedere fault itself.

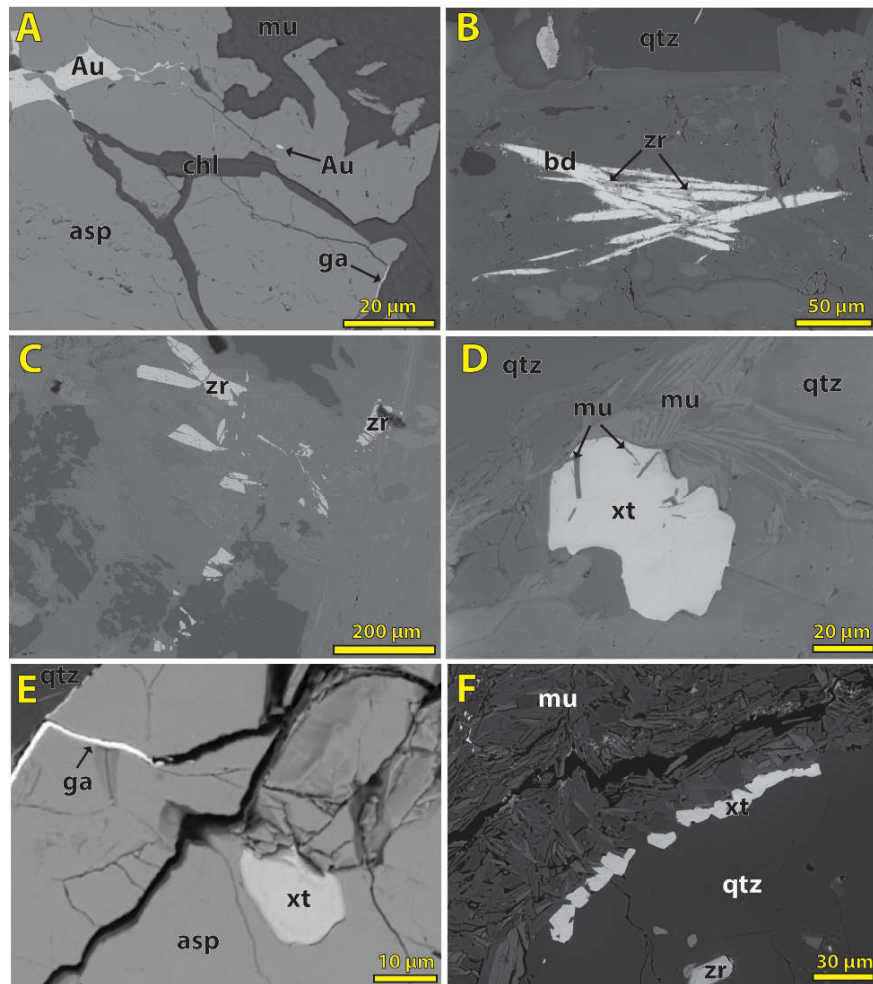


Figure 3-4: Backscattered electron microscope (BSEM) images of accessory minerals from the Belvedere deposit. A) Native gold inclusions in arsenopyrite crystals (GSWA 219551). B) Euhedral baddeleyite crystal from the Belvedere dolerite surrounded by thin zircon fringes (GSWA 219544). C) Former crystals of baddeleyite from the Belvedere dolerite which have been replaced by zircon with abundant very fine-grained inclusions (GSWA 219544). D) Anhedral xenotime crystal containing laths of ore-stage muscovite from quartz–carbonate–arsenopyrite veins (GSWA 219549). E) Anhedral xenotime crystal contained within auriferous arsenopyrite from quartz–carbonate–arsenopyrite veins (GSWA 219551). F) Elongate clusters of xenotime at the margins of a quartz clast from crenulated schist that is locally cross cut by the Belvedere dolerite (GSWA 219539). Abbreviations: asp = arsenopyrite, Au = gold, bd = baddeleyite, chl = chlorite, ga = galena, mu = muscovite, qtz = quartz, xt = xenotime, and zr = zircon.

There are currently no reliable age constraints on mineralization at Belvedere. Lead isotope ratios of galena suggest that mineralization occurred during the late Proterozoic (Richards et al., 1981), although these conclusions are ambiguous because the data plot away from the model III growth curve of Cumming and Richards (1975). Thorne and Trendall (2001) attributed gold mineralization at Belvedere to emplacement of post-Fortescue Group veins, linking their formation to the 1820–1770 Ma Capricorn Orogeny; however, this has not been verified by geochronology.

3.6. GEOCHRONOLOGY METHODS

Four samples, (Figure 3-3) including three from diamond drill core PBERCD0045 (MGA 94 zone 50 427093E 7498864N) and one from a surface outcrop (MGA 94 zone 50 427026E 7498915N), were analysed to determine the igneous crystallization age of the Belvedere dolerite, and the age of hydrothermal activity and associated gold mineralization. Polished thin sections were examined by optical and scanning electron microscope (SEM) to identify minerals suitable for in situ SHRIMP geochronology, such as monazite, xenotime and baddeleyite. Once identified, the minerals were drilled out of the polished thin section using a 2–3 mm hollow core drill bit and cast into a 25 mm epoxy SHRIMP mount. The in situ dating method preserves the textural context of minerals being dated, allowing the significance of the date obtained to be better understood. Reference materials xenotime MG1 (Fletcher et al., 2004), Xeno1 and Xeno2 (Stern and Rayner, 2003) and baddeleyite Phalaborwa (Heaman and LeCheminant, 1993) were placed on a separate SHRIMP mount which was cleaned and gold coated with the sample mounts for each analytical session.

Xenotime and baddeleyite were analysed for U, Th and Pb isotopes using the SHRIMP II instrument at the John de Laeter Centre at Curtin University in Perth, Western Australia. In situ small spot analysis of xenotime followed established procedures outline by Fletcher et al. (2004). Data were collected over several analytical sessions using varying parameters which are summarised in Table 3-1. Analytical procedures are described in detail in the supplementary data in section 3.12.1.

Session date	Mount ID	Sample ID	Target mineral	Kohler aperture (μm)	spot (approx. μm)	O2-primary (nA)	M/ Δ M (1%)	# scans
15/05/2017	IF1702	219544	Baddeleyite	50	10	0.4–0.6	4925.6	7
29/10/2016	IF1604	219539	Xenotime	30	10	0.3	5231.3	8
2/05/2017	IF1703	219539 (A-D)	Xenotime	30	10	0.2–0.3	4794.3	7
28/10/2016	IF1606	219549 (A-H)	Xenotime	30	10	0.3	5231.3	8
28–29/10/2016	IF1606	219551 (I-K)	Xenotime	30	10	0.3	5231.3	8
12/07/2017	IF1607	219551(A,E1-I,H,G)	Xenotime	30	10	0.6	5161.8	8
12/07/2017	IF1607	219551(B,I,E2-1)	Xenotime	30	10	0.2	5161.8	8

Table 3-1: SHRIMP operating parameters for all analytical sessions.

3.7. SAMPLE DETAILS AND RESULTS

All age calculations are derived from 204-corrected $^{207}\text{Pb}^*/^{206}\text{Pb}^*$ ratios (Pb* denotes radiogenic lead). Up to 2% common lead and 10% discordance for individual analyses are tolerated unless mentioned below. Data in tables and plots for individual analyses are quoted with 1σ uncertainties; weighted mean $^{207}\text{Pb}^*/^{206}\text{Pb}^*$ dates are quoted with 95% confidence intervals.

3.7.1 BADDELEYITE

3.7.1.1 GSWA 219544: BELVEDERE DOLERITE

A medium- to coarse-grained portion of the Belvedere dolerite was sampled from diamond drill hole PBERCD0045, between 54.25 and 54.60 m, to determine the emplacement age of the dolerite that hosts the mineralized quartz–carbonate–arsenopyrite veins. Euhedral baddeleyite crystals up to 150 μm long (Figure 3-4b) are common throughout the sample. Many of the baddeleyite crystals have thin fringes of very fine-grained zircon (Figure 3-4b), although in some cases the baddeleyite crystal has been entirely replaced by crystalline zircon with abundant very-fine grained inclusions (Figure 3-4c). Attempts were made to date the zircon fringes and zircon pseudomorphs but all analyses are >10% discordant.

Fifteen analyses were made on 10 baddeleyite crystals with U and Th concentrations ranging from, 73 to 251 ppm and 3 to 46 ppm, respectively. Care was taken to ensure the analysis spot did not overlap the zircon fringes. Two analyses with >2% common lead and two younger statistical outliers, possibly due to Pb-loss, were excluded from the age determination. Seven of the analyses are >10% discordant likely due to the crystal orientation effect of baddeleyite which may bias the $^{206}\text{Pb}^*/^{238}\text{U}$ ratios

(Wingate and Compston, 2000). However, the $^{207}\text{Pb}^*/^{206}\text{Pb}^*$ ratios show good consistency and are considered reliable in the age determination. Eleven analyses yield a weighted mean $^{207}\text{Pb}^*/^{206}\text{Pb}^*$ date of 2082 ± 30 Ma (MSWD = 0.96; Supplementary Table 3-1; Figure 3-5a), interpreted as the crystallization age of the Belvedere dolerite.

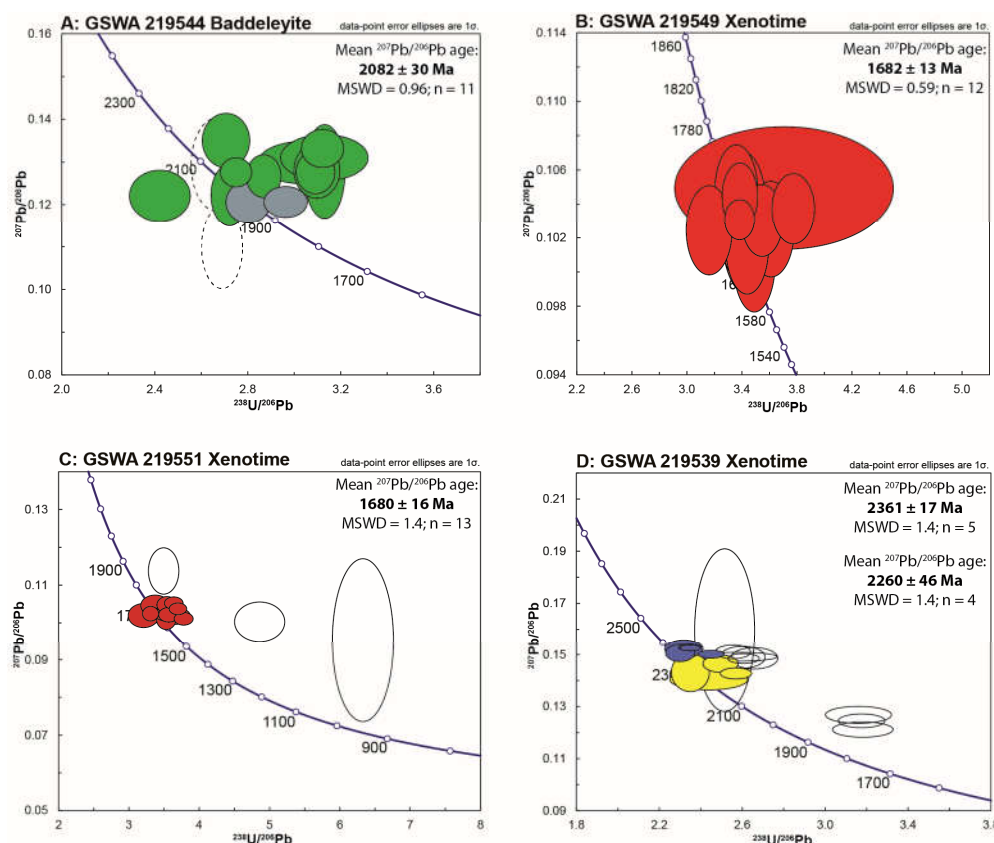


Figure 3-5: Tera-Wasserburg concordia diagrams of U-Pb data for baddeleyite and xenotime. A) Baddeleyite from the Belvedere dolerite (GSWA 219544). B) Xenotime containing laths of ore-stage muscovite within auriferous quartz-carbonate-sulfide vein (GSWA 219549), data with high common lead is not plotted, refer to Supplementary Table 3-2 for analysis details. C) Xenotime intergrown with ore-stage muscovite and auriferous arsenopyrite within auriferous quartz-carbonate-sulfide vein (GSWA 219551). D) Xenotime within a crenulated muscovite schist that is locally cross cut by the Belvedere dolerite (GSWA 219539). Key: Dark-coloured ellipses (green = c. 2080 Ma, red = c. 1680 Ma, blue = c. 2360 Ma, yellow = c. 2260 Ma) show data used in the age calculations; other ellipses are for inferior data (solid grey = young outliers, dashed ellipses = high common Pb, open black ellipses = discordant data).

3.7.2 XENOTIME

3.7.2.1 GSWA 219549: AURIFEROUS QUARTZ-CARBONATE-ARSENOPYRITE VEIN

A sample of the mineralized quartz-carbonate-arsenopyrite vein with assay results of 1.15 ppm Au, was sampled from diamond drill hole PBERCD0045 between 77.39 and 77.68 m. The sample is composed predominantly of quartz with lesser amount of ore-stage alteration including very fine-grained muscovite-carbonate-rutile and euhedral arsenopyrite crystals <1 mm long. Xenotime is mostly anhedral and commonly

contains laths of muscovite (Figure 3-4d) indicating that xenotime growth occurred during ore-stage hydrothermal activity.

Thirteen analyses were conducted on 8 xenotime crystals with U and Th concentrations ranging from 462 to 2611 ppm and 49 to 64 ppm, respectively. One analysis yielded >1% common Pb, and was excluded from the age determination. The remaining 12 analyses give a weighted mean $^{207}\text{Pb}^*/^{206}\text{Pb}^*$ date of 1682 ± 13 Ma (MSWD = 0.59; Supplementary Table 3-2, Figure 3-5b) which is interpreted to represent the timing of hydrothermal activity related to ore-stage alteration and associated gold mineralization.

3.7.2.2 GSWA 219551: AURIFEROUS QUARTZ–CARBONATE–ARSENOPYRITE VEIN

A second mineralized sample with a Au grade of 4.81 ppm was taken from diamond drill hole PBERCD0045 between 79.2 and 79.68 m. The sample is a quartz–carbonate–arsenopyrite vein containing coarse-grained, euhedral arsenopyrite and associated muscovite–ankerite–rutile alteration. Xenotime crystals are anhedral, <60 μm in size and commonly contain inclusions of, or is intergrown with, ore-stage alteration products such as muscovite. Inclusions of gold (Figure 3-4a), and small inclusions of anhedral xenotime (<30 μm ; Figure 3-4e) occurs within arsenopyrite suggesting crystallization of gold, xenotime and arsenopyrite was simultaneous.

Sixteen analyses were conducted on 12 xenotime crystals with U and Th concentrations ranging from 141 to 2105 ppm and 50 to 1446 ppm, respectively. Three analyses were excluded from the age determination due to >10% discordance. The remaining 13 analyses yielded a weighted mean $^{207}\text{Pb}^*/^{206}\text{Pb}^*$ date of 1680 ± 16 Ma (MSWD = 1.4; Supplementary Table 3-3; Figure 3-5c). Since xenotime is contained with auriferous arsenopyrite and intergrown with ore-stage alteration minerals, this date is interpreted to represent the timing of hydrothermal activity associated with gold mineralization.

As the age determinations for samples GSWA 219549 and 219551 are indistinguishable within analytical uncertainty, the data have been pooled to provide a more precise weighted mean $^{207}\text{Pb}^*/^{206}\text{Pb}^*$ date of 1681 ± 9 Ma (MSWD = 0.96) interpreted to represent the timing of hydrothermal activity related to ore-stage alteration and gold mineralization.

3.7.2.3 GSWA 219539: CRENULATED MUSCOVITE SCHIST

A very fine-grained, laminated and crenulated muscovite schist that is locally cross cut by the north-trending dolerite dykes was collected from a 2 m-wide outcrop located ~200 m west of the Belvedere deposit (Figure 3-3). The sample contains muscovite, quartz, and trace amounts of rutile, monazite and xenotime. Aggregates of very fine-grained monazite occur throughout the rock but are too small to be analysed by ion microprobe. Xenotime crystals are typically small (<30 µm) and developed as narrow, elongate clusters of crystals up to 10 x 80 µm in, or around the margins of, quartz clasts (Figure 3-4f) or as very small (<10 µm) crystals aligned in the S1 cleavage. Attempts were made to date the xenotime within the cleavage; however, the analyses were discordant because the SHRIMP analysis spot overlapped onto the surrounding minerals.

Eighteen analyses were made on 17 xenotime crystals with U and Th concentrations ranging from 362 to 3398 ppm and 47 to 2591 ppm, respectively. Five analyses were excluded from the age determination due to >10% discordance. Of the remaining 13 analyses, two discrete age components are evident with higher U and Th values in grains with the older age mode. The older mode with nine analyses yields a weighted mean $^{207}\text{Pb}^*/^{206}\text{Pb}^*$ date of 2350 ± 15 Ma (MSWD = 2.5). However, a more statistically robust date is calculated by excluding data >7% discordant providing a weighted mean $^{207}\text{Pb}^*/^{206}\text{Pb}^*$ date of 2361 ± 17 Ma (MSWD = 1.4; Supplementary Table 3-4; Figure 3-5d). The younger mode with four analyses yields a weighted mean $^{207}\text{Pb}^*/^{206}\text{Pb}^*$ date of 2260 ± 46 Ma (MSWD = 1.4; Supplementary Table 3-4, Figure 3-5d). These dates are interpreted to represent xenotime growth during hydrothermal activity at c. 2360 and 2260 Ma.

3.8. DISCUSSION

3.8.1 HOST ROCKS TO AURIFEROUS QUARTZ–CARBONATE–ARSENOPYRITE VEINS

Magmatic baddeleyite within the Belvedere dolerite yielded a crystallization age of 2082 ± 30 Ma, providing a maximum age for the emplacement of the auriferous quartz–carbonate–arsenopyrite veins. This age does not correspond with the timing of other mafic intrusions in either the Capricorn Orogen or the Pilbara region.

3.8.2 TIMING OF HYDROTHERMAL ACTIVITY AND GOLD MINERALIZATION

Three episodes of hydrothermal xenotime growth are recorded at the Belvedere gold deposit: c. 2360, 2260 and 1680 Ma. Xenotime dated at 2361 ± 17 Ma within a crenulated muscovite schist (GSWA 219539) is synchronous with widespread hydrothermal activity throughout the Pilbara region (Pickard, 2002; Rasmussen et al., 2005) and gold mineralization at the Paulsens mine which is related to a cryptic orogenic event (Fielding et al., 2017). However, this event is much older than gold mineralization at the Belvedere deposit, which must be younger than the c. 2080 Ma dolerite host (GSWA 219544). Xenotime from the same sample, dated at 2260 ± 46 Ma, is within uncertainty of monazite growth at 2216 ± 13 Ma from Mount Tom Price, which formed during the early stages of the 2215–2145 Ma Ophthalmia Orogeny (Rasmussen et al., 2005).

Xenotime fully encased in auriferous arsenopyrite and intergrown with ore-stage alteration minerals directly dates the timing of hydrothermal activity and emplacement of the auriferous quartz–carbonate–arsenopyrite veins, thus constraining the timing of gold mineralization to 1681 ± 9 Ma (GSWA 219549 and GSWA 219551). This age is coeval with intracratonic reworking during the earliest stages of the 1680–1620 Ma Mangaroon Orogeny, when medium- to high-grade metamorphism, magmatism and deformation affected rocks of the Gascoyne Province to the south (Sheppard et al., 2005). During this time, major faults throughout the Pilbara region, such as the Nanjilgardy Fault, were reactivated in response to the Mangaroon Orogeny (Fielding et al., 2017; Rasmussen et al., 2007a; Rasmussen et al., 2007b). Reactivation of the Hardey Fault at c. 1680 Ma caused either introduction of new gold or local remobilization of gold at the Paulsens mine (Fielding et al., 2017).

3.8.3 COMPARISON WITH THE PAULSENS GOLD DEPOSIT

The Belvedere and Paulsens gold deposits are situated 6.5 km apart and are associated with the Hardey Fault (Figure 3-2), which is a second order splay of the crustal-scale Nanjilgardy Fault. Gold mineralization at both deposits is contained within auriferous quartz–carbonate–sulfide veins that are hosted in mafic dykes with hydrothermal alteration characterized by muscovite–ankerite–quartz (–rutile) assemblages (Fielding et al., 2017; Thorne and Trendall, 2001). Prior to this study the timing of gold mineralization at the Belvedere deposit was poorly constrained, although ambiguous

results from lead-isotope dating of galena suggested that mineralization was late Proterozoic in age (Richards et al., 1981). Thorne and Trendall (2001) attributed gold mineralization at Belvedere and Paulsens to post-Fortescue Group veins, linking their formation to the 1820–1770 Ma Capricorn Orogeny. This age for mineralization is neither supported by field relationships nor geochronological data presented here and by Fielding et al. (2017). Our data show that the ore deposits were not only formed at different times, but have several key differences.

The Paulsens and Belvedere gold deposits are hosted in mafic intrusive rocks. Rheological (and possible chemical) differences between gabbro and surrounding siliciclastic rocks at Paulsens, and dolerite and surrounding siliciclastic rocks at Belvedere, make them suitable host rocks for gold mineralization. During reactivation of the Hardy Fault, brittle fracturing of the more competent mafic intrusive rocks allowed for emplacement of mineralized quartz-sulfide veins, whereas the surrounding siliciclastic rocks took up the strain as a foliation. Despite both deposits being hosted in mafic intrusive rocks, the mafic rocks themselves differ in type and age. At Paulsens, auriferous quartz–carbonate–sulfide veins are hosted within the pervasively altered Paulsens gabbro, a medium- to coarse-grained, mafic dyke that cuts stratigraphy at a low angle, was deformed during regional-scale F1 folding, and has been overprinted by both S1 and S2 fabrics. Emplacement of the Paulsens gabbro has been precisely dated (U–Pb SHRIMP dating of baddeleyite) at 2701 ± 11 Ma (Fielding et al., 2017). In contrast, auriferous quartz–carbonate–arsenopyrite veins at Belvedere are hosted within the fine- to medium-grained, north-striking Belvedere dolerite that intrudes stratigraphy at a high angle, and which preserves a cleavage in areas where the dolerite is kinked and locally in contact with the mineralized veins. The Belvedere dolerite dyke is much younger, with an igneous crystallization age of 2082 ± 30 Ma (GSWA 219544). Additionally, the deposits are characterized by different sulfide minerals, with Paulsens dominated by pyrite with later pyrrhotite and chalcopyrite (Fielding et al., 2017; Hancock and Thorne, 2016) whereas Belvedere contains arsenopyrite and secondary galena (Figure 3-4e).

Field relationships also demonstrate that the north-trending dolerite dykes, including the Belvedere dolerite, cross-cut and offset auriferous quartz–carbonate–sulfide veins at the Paulsens deposit (Figure 3-6; Northern Star Resources Limited, July, 2015). This is supported by U–Pb SHRIMP geochronology on hydrothermal xenotime that

indicates that primary gold mineralization at Paulsens occurred at c. 2400 Ma (Fielding et al., 2017), and thus significantly pre-dates the intrusion of the c. 2080 Ma Belvedere dolerite and subsequent mineralization.

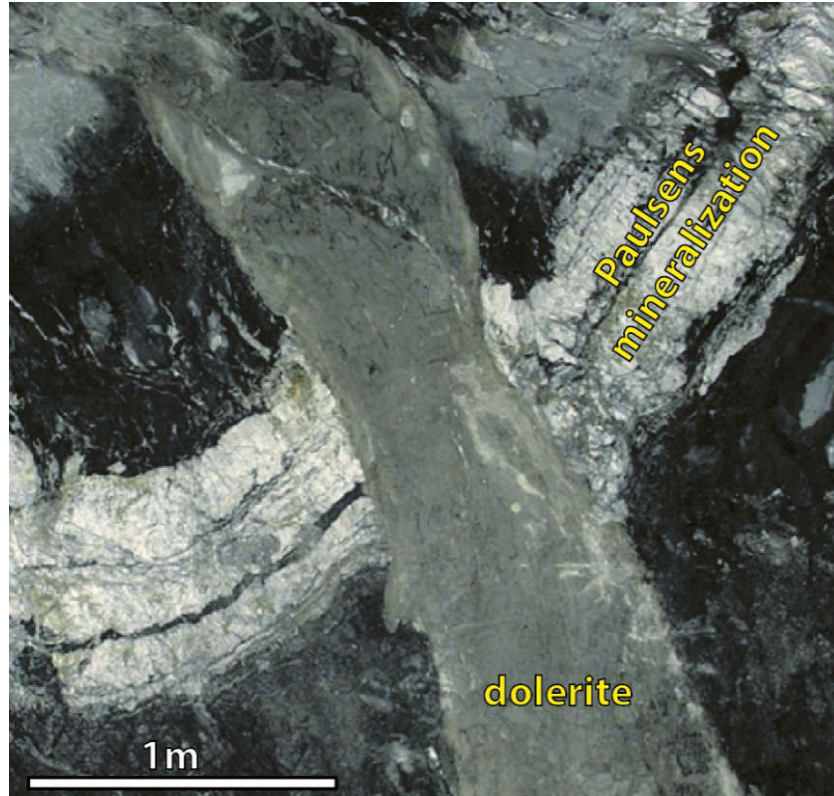


Figure 3-6: Massive fine-grained dolerite dyke (~1 m wide) in the drive wall at the Paulsens gold deposit. The dolerite is part of the same north-trending suite of dykes as the Belvedere dolerite, dated here at c. 2080 Ma. These dykes cross cut and offset auriferous, laminated quartz veins from the Lower mineralized zone at the Paulsens deposit. Level 1095E, face 36 viewed to the southeast.

3.8.4 RELATIONSHIP OF MINERALIZATION TO REGIONAL OROGENIC EVENTS

When integrated with the tectonothermal framework of the northern Capricorn Orogen (Fielding et al., 2017; Johnson et al., 2013), gold mineralization at Paulsens (c. 2400 Ma) and at Belvedere (c. 1680 Ma) formed during different orogenic events. Fielding et al. (2017) attributed c. 2400 Ma orogenic gold mineralization at Paulsens to a cryptic orogenic event, for which there is evidence of uplift and erosion along the southern Pilbara margin, as well as widespread hydrothermal alteration across the entire Pilbara Craton (Pickard, 2002; Rasmussen et al., 2005). This event is synchronous with the timing of hydrothermal xenotime growth (dated at c. 2360 Ma; GSWA 219539) within a crenulated muscovite schist at Belvedere suggesting this event is a compressional orogeny, however at this stage there is not enough information to understand its full effects.

Gold mineralization at Belvedere, here dated at c. 1680 Ma, is coeval with a second gold mineralizing event at Paulsens (Fielding et al., 2017) that is related to the reactivation of the Nanjilgardy Fault and its second-order structures (including the Hardey Fault) during the earliest stages of the intracratonic 1680–1620 Ma Mangaroon Orogeny (Sheppard et al., 2005). The Mangaroon Orogeny was defined in the Gascoyne Province to the south where its effects are most prominent (Sheppard et al., 2005). In the Gascoyne Province this event is characterized by intraplate extension, high-temperature — low-pressure metamorphism with the synchronous emplacement of voluminous granitic stocks, plutons and batholiths of the 1680–1620 Ma Durlacher Supersuite (Johnson et al., 2017; Sheppard et al., 2005). However, in the northern Capricorn Orogen and Pilbara region the effects of this orogeny are more enigmatic where it lacks evidence for granite magmatism and is of significantly lower metamorphic grade (lowermost greenschist facies). Although the effects of this event are not yet fully known or understood, the event appears to be characterized by the ?strike slip reactivation of major faults and their ancillary structures (Sheppard et al., 2006), which are accompanied by the flow of mineralizing hydrothermal fluids. These structural pathways have played a critical role in the distribution of gold mineralization throughout the region (Fielding et al., 2017; Rasmussen et al., 2007a; Rasmussen et al., 2007b).

3.8.5 IMPLICATIONS FOR EXPLORATION TARGETING

The presence of closely spaced multiple mineralizing events separated by significant differences in time has important implications for regional-scale exploration targeting. For example, the suite of c. 2080 Ma dolerite dykes is only prospective for c. 1680 Ma gold mineralization since it post-dates the c. 2400 Ma primary gold mineralizing event at Paulsens. In contrast, mafic rocks of the Fortescue and Hamersley Groups were deposited between c. 2775 and 2450 Ma (Arndt et al., 1991; Trendall et al., 2004) which makes them prospective for both c. 1680 and 2400 Ma gold mineralization. Considering that both Paulsens and Belvedere are located in structurally similar areas, and both are associated with mafic dykes, it is the presence of multiple mineralizing events at Paulsens that may account for the difference in gold endowment. Along with a favourable crustal architecture, multiple mineralizing events appear to be required to enrich gold mineralization, thus producing larger, and more economically viable deposits (Meffre et al., 2016). With this understanding, exploration strategies can focus

not only on areas with a favourable crustal architecture, but where the rocks are old enough to be overprinted by multiple hydrothermal events. Without knowing the timing of gold mineralization it is possible to erroneously target potential host rocks that have only undergone a minor mineralizing event or that actually post-date all of the mineralizing events in a region or are not in favourable mineralization sites.

3.9. CONCLUSIONS

Spatially associated gold occurrences in a geological terrane are commonly thought to have formed during the same mineralizing event (Cheng, 2008; Groves et al., 1998), but this is not the case for the gold deposits from the northern Capricorn Orogen. Here we demonstrate that the Belvedere and Paulsens deposits, which are separated by only 6.5 km, and spatially associated with the same fault (and thus crustal architecture), have different geological histories despite their seemingly similar appearance. Our results show that mineralized quartz–carbonate–arsenopyrite veins at Belvedere formed at c. 1680 Ma and are hosted within the c. 2080 Ma Belvedere dolerite, whereas the Paulsens deposit is hosted in a c. 2700 Ma mafic sill that was mineralized at c. 2400 Ma. Our results show that despite appearances, the Belvedere and Paulsens gold deposits are not the product of one unique mineralizing event, but formed at different times related to reactivation of major faults.

3.10. ACKNOWLEDGEMENT

This project was funded through an ARC linkage grant (LP130100922), the Exploration Incentive Scheme and an industry scholarship by Northern Star Resources as a part of a PhD by I.O.H. Fielding. S.P. Johnson publishes with the permission of the director of the Geological Survey of Western Australia. The SHRIMP II at the John de Laeter Centre at Curtin University was used for all geochronology. We appreciated Sandra Occhipinti and Andrew Cross for constructive comments which helped to improve the manuscript.

3.11. REFERENCES

- Arndt, N. T., Nelson, D. R., Compston, W., Trendall, A. F., and Thorne, A. M., 1991, The age of the Fortescue Group, Hamersley Basin, Western Australia, from ion microprobe zircon U-Pb results: *Australian Journal of Earth Sciences*, v. 38, no. 3, p. 261-281.
- Bierlein, F. P., Groves, D. I., Goldfarb, R. J., and Dubé, B., 2006, Lithospheric controls on the formation of provinces hosting giant orogenic gold deposits: *Mineralium Deposita*, v. 40, no. 8, p. 874-886.
- Blenkinsop, T., 2015, Scaling laws for the distribution of gold, geothermal, and gas resources: *Pure and Applied Geophysics*, v. 172, no. 7, p. 2045-2056.
- Blockley, J. G., 1971, The lead, zinc and silver deposits of Western Australia, in *Australia, Geological Survey of Western Australia., ed., Volume Mineral Resources Bulletin 9: Perth*, 237 p.
- Cawood, P. A., and Tyler, I. M., 2004, Assembling and reactivating the Proterozoic Capricorn Orogen: lithotectonic elements, orogenies, and significance: *Precambrian Research*, v. 128, no. 3-4, p. 201-218.
- Cheng, Q., 2008, Non-linear theory and power-law models for information integration and mineral resources quantitative assessments: *Mathematical Geosciences*, v. 40, no. 5, p. 503-532.
- Cumming, G. L., and Richards, J. R., 1975, Ore lead isotope ratios in a continuously changing earth: *Earth and Planetary Science Letters*, v. 28, no. 2, p. 155-171.
- Fielding, I. O. H., Johnson, S. P., Zi, J.-W., Rasmussen, B., Muhling, J. R., Dunkley, D. J., Sheppard, S., Wingate, M. T. D., and Rogers, J. R., 2017, Using In Situ SHRIMP U-Pb monazite and xenotime geochronology to determine the age of orogenic gold mineralization: an example from the Paulsens Mine, Southern Pilbara Craton: *Economic Geology*, v. 112, no. 5, p. 1205-1230.
- Fletcher, I. R., McNaughton, N. J., Aleinikoff, J. A., Rasmussen, B., and Kamo, S. L., 2004, Improved calibration procedures and new standards for U-Pb and Th-Pb dating of Phanerozoic xenotime by ion microprobe: *Chemical Geology*, v. 209, no. 3-4, p. 295-314.
- Forman, F. G., 1938, The Melrose and Belvedere gold mines and vicinity, Mt Stewart Station, Ashburton Goldfields, Department of Mines Annual Report 1937, 159 p.
- Goldfarb, R. J., Groves, D. I., and Gardoll, S., 2001, Orogenic gold and geologic time: a global synthesis: *Ore Geology Reviews*, v. 18, no. 1-2, p. 1-75.
- Groves, D. I., Condie, K. C., Goldfarb, R. J., Hronsky, J. M. A., and Vielreicher, R. M., 2005, 100th anniversary special paper: secular changes in global tectonic processes and their influence on the temporal distribution of gold-bearing mineral deposits: *Economic Geology*, v. 100, no. 2, p. 203-224.

- Groves, D. I., Goldfarb, R. J., Gebre-Mariam, M., Hagemann, S. G., and Robert, F., 1998, Orogenic gold deposits: A proposed classification in the context of their crustal distribution and relationship to other gold deposit types: *Ore Geology Reviews*, v. 13, no. 1–5, p. 7-27.
- Hancock, E. A., and Thorne, A. M., 2016, Mineralogy of gold from the Paulsens and Mount Olympus deposits, northern Capricorn Orogen: Geological Survey of Western Australia, Record 2016/14, 16 p.
- Heaman, L. M., and LeCheminant, A. N., 1993, Geochemistry of accessory minerals paragenesis and U-Pb systematics of baddeleyite (ZrO₂): *Chemical Geology*, v. 110, no. 1, p. 95-126.
- Hronsky, J. M., Groves, D. I., Loucks, R. R., and Begg, G. C., 2012, A unified model for gold mineralisation in accretionary orogens and implications for regional-scale exploration targeting methods: *Mineralium Deposita*, v. 47, no. 4, p. 339-358.
- Johnson, S. P., Korhonen, F. J., Kirkland, C. L., Cliff, J. B., Belousova, E. A., and Sheppard, S., 2017, An isotopic perspective on growth and differentiation of Proterozoic orogenic crust: From subduction magmatism to cratonization: *Lithos*, v. 268-271, p. 76-86.
- Johnson, S. P., Sheppard, S., Rasmussen, B., Wingate, M. T. D., Kirkland, C. L., Muhling, J. R., Fletcher, I. R., and Belousova, E. A., 2011, Two collisions, two sutures: Punctuated pre-1950 Ma assembly of the West Australian Craton during the Ophthalmian and Glenburgh Orogenies: *Precambrian Research*, v. 189, no. 3-4, p. 239-262.
- Johnson, S. P., Thorne, A. M., Tyler, I. M., Korsch, R. J., Kennett, B. L. N., Cutten, H. N., Goodwin, J., Blay, O., Blewett, R. S., Joly, A., Dentith, M. C., Aitken, A. R. A., Holzschuh, J., Salmon, M., Reading, A., Heinson, G., Boren, G., Ross, J., Costelloe, R. D., and Fomin, T., 2013, Crustal architecture of the Capricorn Orogen, Western Australia and associated metallogeny: *Australian Journal of Earth Sciences*, v. 60, no. 6-7, p. 681-705.
- Korhonen, F. J., Johnson, S. P., Wingate, M. T. D., Kirkland, C. L., Fletcher, I. R., Dunkley, D. J., Roberts, M. P., Sheppard, S., Muhling, J. R., and Rasmussen, B., 2017, Radiogenic heating and craton-margin plate stresses as drivers for intraplate orogeny: *Journal of Metamorphic Geology*, v. 35, no. 6, p. 631-661.
- Korsch, R. J., and Doublier, M. P., 2016, Major crustal boundaries of Australia, and their significance in mineral systems targeting: *Ore Geology Reviews*, v. 76, p. 211-228.
- Krapež, B., 1999, Stratigraphic record of an Atlantic-type global tectonic cycle in the Palaeoproterozoic Ashburton Province of Western Australia: *Australian Journal of Earth Sciences*, v. 46, no. 1, p. 71-87.
- Ludwig, K. R., 2003, Isoplot/Ex version 3.00, A geochronological toolkit for Microsoft Excel: Berkeley Geochronology Centre Special Publication No. 4, 73 p.

- Ludwig, K. R., 2009, Squid 2.50, a user's manual: Berkeley Geochronology Centre, Berkeley, California, USA, 95 p.
- Marston, R. J., 1979, Copper mineralization in Western Australia, in Australia, Geological Survey of Western Australia, Mineral Resources Bulletin 13, 227 p.
- Martin, D. M., and Morris, P. A., 2010, Tectonic setting and regional implications of ca2.2 Ga mafic magmatism in the southern Hamersley Province, Western Australia: Australian Journal of Earth Sciences, v. 57, no. 7, p. 911-931.
- Martin, D. M., and Thorne, A., 2004, Tectonic setting and basin evolution of the Bangemall Supergroup in the northwestern Capricorn Orogen: Precambrian Research, v. 128, no. 3, p. 385-409.
- Meffre, S., Large, R. R., Steadman, J. A., Gregory, D. D., Stepanov, A. S., Kamenetsky, V. S., Ehrig, K., and Scott, R. J., 2016, Multi-stage enrichment processes for large gold-bearing ore deposits: Ore Geology Reviews, v. 76, p. 268-279.
- Müller, S. G., Krapež, B., Barley, M. E., and Fletcher, I. R., 2005, Giant iron-ore deposits of the Hamersley province related to the breakup of Paleoproterozoic Australia: New insights from in situ SHRIMP dating of baddeleyite from mafic intrusions: Geology, v. 33, no. 7, p. 577-580.
- Northern Star Resources Limited, 2015, Northern Star Resources Limited 2015 annual report, (<http://www.nsr ltd.com/wp-content/uploads/2015/08/NST-Annual-Report-2015-26-8-2015-new-cover1.pdf>).
- Northern Star Resources Limited, July, 2015, Northern Star Paulsens operations fact sheet, (<http://www.nsr ltd.com/wp-content/uploads/2015/08/NSR-Paulsens-Operations-Fact-Sheet-July-2015-FINAL.pdf>).
- Norum, E., 2005, 14 November 2003 to 13 November 2004, Paulsens Project, E08/665, E08/906, E08/1125, E47/977, E47/1134, E47/1135, M08/99, M08/196 and M08/222, Combined Reporting Group C211/1997: Nustar Mining Corporation Limited; Geological Survey of Western Australia Open-file report a070119.
- Occhipinti, S. A., Sheppard, S., Passchier, C., Tyler, I. M., and Nelson, D. R., 2004, Palaeoproterozoic crustal accretion and collision in the southern Capricorn Orogen: the Glenburgh Orogeny: Precambrian Research, v. 128, no. 3–4, p. 237-255.
- Owen, S., 2000, Ashburton Project, Exploration licence 47/902 Belvedere and Tombstone Prospects: Taipan Resources N.L; Geological Survey of Western Australia Open-file report, a61500.
- Pickard, A. L., 2002, SHRIMP U–Pb zircon ages of tuffaceous mudrocks in the Brockman Iron Formation of the Hamersley Range, Western Australia: Australian Journal of Earth Sciences, v. 49, no. 3, p. 491-507.

- Rasmussen, B., Fletcher, I. R., and Muhling, J. R., 2007a, In situ U–Pb dating and element mapping of three generations of monazite: Unravelling cryptic tectonothermal events in low-grade terranes: *Geochimica et Cosmochimica Acta*, v. 71, no. 3, p. 670-690.
- Rasmussen, B., Fletcher, I. R., Muhling, J. R., Thorne, W. S., and Broadbent, G. C., 2007b, Prolonged history of episodic fluid flow in giant hematite ore bodies: Evidence from in situ U–Pb geochronology of hydrothermal xenotime: *Earth and Planetary Science Letters*, v. 258, no. 1–2, p. 249-259.
- Rasmussen, B., Fletcher, I. R., and Sheppard, S., 2005, Isotopic dating of the migration of a low-grade metamorphic front during orogenesis: *Geology*, v. 33, no. 10, p. 773-776.
- Richards, J. R., Fletcher, I. R., and Blockley, J. G., 1981, Pilbara galenas: Precise isotopic assay of the oldest Australian leads model ages and growth-curve implications: *Mineralium deposita*, v. 16, no. 1, p. 7-30.
- Robert, F., Brommecker, R., Bourne, B. T., Dobak, P. J., McEwan, C. J., Rowe, R. R., and Zhou, X., 2007, Models and exploration methods for major gold deposit types, in Milkereit, B., ed., *Exploration 07: Fifth Decennial International Conference on Mineral Exploration*: Toronto, Canada, Decennial Mineral Exploration Conferences, p. 691-711.
- Seymour, D. B., Thorne, A. M., and Blight, D. F., 1988, Wyloo, W.A., (2nd edition): Western Australia Geological Survey, 1:250 000 Geological Series Explanatory Notes, 36 p.
- Sheppard, S., Bodorkos, S., Johnson, S. P., Wingate, M. T. D., and Kirkland, C. L., 2010, The Paleoproterozoic Capricorn Orogeny: intracontinental reworking not continent–continent collision, Volume 108: Geological Survey of Western Australia, Report 108, 33 p.
- Sheppard, S., Farrell, T. R., Bodorkos, S., Hollingsworth, D., Tyler, I. M., and Pirajno, F., 2006, Late Paleoproterozoic (1680–1620 Ma) sedimentation, magmatism and tectonism in the Capricorn Orogen: Geological Survey of Western Australia extended abstracts, 2 p.
- Sheppard, S., Occhipinti, S. A., and Nelson, D. R., 2005, Intracontinental reworking in the Capricorn Orogen, Western Australia: the 1680–1620 Ma Mangaroon Orogeny: *Australian Journal of Earth Sciences*, v. 52, no. 3, p. 443-460.
- Sheppard, S., Occhipinti, S. A., and Tyler, I. M., 2004, A 2005–1970 Ma Andean-type batholith in the southern Gascoyne Complex, Western Australia: *Precambrian Research*, v. 128, no. 3–4, p. 257-277.
- Sheppard, S., Rasmussen, B., Muhling, J. R., Farrell, T. R., and Fletcher, I. R., 2007, Grenvillian-aged orogenesis in the Palaeoproterozoic Gascoyne Complex, Western Australia: 1030–950Ma reworking of the Proterozoic Capricorn Orogen: *Journal of Metamorphic Geology*, v. 25, no. 4, p. 477-494.

- Smith, R. E., Perdrix, J. L., and Parks, T. C., 1982, Burial Metamorphism in the Hamersley Basin, Western Australia: *Journal of Petrology*, v. 23, no. 1, p. 75-102.
- Stacey, J. S., and Kramers, J. D., 1975, Approximation of terrestrial lead isotope evolution by a two-stage model: *Earth and Planetary Science Letters*, v. 26, p. 207–221.
- Stern, R. A., and Rayner, N., 2003, Ages of several xenotime megacrysts by ID-TIMS: potential reference materials for ion microprobe U-Pb geochronology: Radiogenic Age and Isotopic Studies: Report 16: Geological Survey of Canada: Current Research 2003-F1, 7 p.
- Stern, R. A., Bodorkos, S., Kamo, S. L., Hickman, A. H., and Corfu, F., 2009, Measurement of SIMS Instrumental Mass Fractionation of Pb Isotopes During Zircon Dating: *Geostandards and Geoanalytical Research*, v. 33, p. 145–168.
- Thorne, A. M., Johnson, S. P., Tyler, I. M., Cutten, H. N., and Blay, O., 2011, Geology of the northern Capricorn Orogen, in Johnson, S. P., Thorne, A. M., and Tyler, I. M., eds., *Capricorn Orogen seismic and magnetotelluric (MT) workshop 2011*, Geological Survey of Western Australia, p. 7-18.
- Thorne, A. M., and Seymour, D. B., 1991, Geology of the Ashburton Basin Western Australia, Geological Survey of Western Australia, Bulletin 139, 162 p.
- Thorne, A. M., and Trendall, A. F., 2001, Geology of the Fortescue Group, Pilbara Craton, Western Australia, Geological Survey of Western Australia, Bulletin 144, 266 p.
- Trendall, A. F., Compston, W., Nelson, D. R., De Laeter, J. R., and Bennett, V. C., 2004, SHRIMP zircon ages constraining the depositional chronology of the Hamersley Group, Western Australia: *Australian Journal of Earth Sciences*, v. 51, no. 5, p. 621-644.
- Tyler, I. M., and Thorne, A. M., 1990, The northern margin of the Capricorn Orogen, Western Australia—an example of an Early Proterozoic collision zone: *Journal of Structural Geology*, v. 12, no. 5–6, p. 685-701.
- Tyler, I. M., 1991, The Geology of the Sylvania Inlier and the Southeast Hamersley Basin, Geological Survey of Western Australia, Bulletin 138, 124 p.
- White, A. J. R., Smith, R. E., Nadoll, P., and Legras, M., 2014, Regional-scale metasomatism in the Fortescue Group Volcanics, Hamersley Basin, Western Australia: implications for hydrothermal ore systems: *Journal of Petrology*, v. 55, no. 5, p. 977-1009.
- Wingate, M. T. D., and Compston, W., 2000, Crystal orientation effects during ion microprobe U–Pb analysis of baddeleyite: *Chemical Geology*, v. 168, p. 75–97.

Wingate, M. T. D., Lu, Y., Blay, O., and Johnson, S. P., 2017a, 206949: dolerite dyke, Tin Hut Bore: Geochronology Record 1432: Geological Survey of Western Australia, 4 p.

Wingate, M. T. D., Lu, Y., Blay, O., and Johnson, S. P., 2017b, 206953: dolerite sill, Tin Hut Bore: Geochronology Record 1433: Geological Survey of Western Australia, 4 p.

3.12. SUPPLEMENTARY DATA

3.12.1 ANALYTICAL METHODS

A primary beam of O²⁻ ions was focused through a 50 µm Kohler aperture for baddeleyite and 30 µm Kohler aperture for xenotime, producing an oval 10 µm wide spot on the sample surface with a current of 0.2–0.6 nA. The secondary ion system was focused through a 100 µm collector slit onto an electron multiplier to produce mass peaks with flat tops and a mass resolution (1% peak height) of 4795–5230.

Baddeleyite data were collected in sets of 7 scans, with baddeleyite reference material analysed every 3 sample analyses. Xenotime data were collected in sets of 7 or 8 scans, with xenotime reference materials analysed every 4–6 sample analyses. Count times per scan for Pb isotopes 204, background position 204.045, 206, 207, and 208 were 10 s, 10 s, 10 s, 30 s and 10 s, respectively.

Baddeleyite was analysed using the conventional zircon 9-peak run table, calibrated against baddeleyite reference material Phalaborwa (Heaman and LeCheminant, 1993). Instrumental mass fractionation (IMF) in ²⁰⁷Pb/²⁰⁶Pb ratios was monitored by repeated analysis of the 3465 Ma OGC zircon standard (OG1 of Stern et al. (2009)). No IMF correction was required since the measured values of OGC were in agreement with the reference value within 2σ uncertainties.

Xenotime was analysed with a 9-peak run table following analytical protocols in Fletcher et al. (2004). Pb/U calibrations and matrix corrections for U and Th contents were based on concurrent measurements of the primary standard MG-1 (Fletcher et al., 2004) and secondary standards z6413 (XENO1) and z6410 (XENO2) (Stern and Rayner, 2003)). Pb/Th was determined indirectly, using a fixed Th/U calibration (Fletcher et al., 2004). Matrix corrections for REE assumed the samples have REE abundances similar to Xenol.

Raw data from analyses on xenotime were processed using the SQUID 2 add-in (v. 2.50.12.03.08) for Excel 2003 (Ludwig, 2009), and plotted using the ISOPLOT add-in (v. 3.76.12.02.24) (Ludwig, 2003). Common-Pb corrections were based on measured $^{204}\text{Pb}/^{206}\text{Pb}$ ratios and contemporaneous Pb composition according to the terrestrial Pb evolution model of Stacey and Kramers (1975). Matrix effect corrections were made for all xenotime data using procedures described by Fletcher et al (2004). All ages are quoted with 95% confidence levels, whereas individual analyses are presented with 1σ errors.

3.12.2 REFERENCES

- Fletcher, I. R., McNaughton, N. J., Aleinikoff, J. A., Rasmussen, B., and Kamo, S. L., 2004, Improved calibration procedures and new standards for U–Pb and Th–Pb dating of Phanerozoic xenotime by ion microprobe: *Chemical Geology*, v. 209, p. 295–314.
- Heaman, L. M., and LeCheminant, A. N., 1993, Geochemistry of Accessory Minerals Paragenesis and U–Pb systematics of baddeleyite (ZrO_2): *Chemical Geology*, v. 110, p. 95–126.
- Ludwig, K. R., 2003, Isoplot/Ex version 3.00, A geochronological toolkit for Microsoft Excel: Berkeley Geochronology Centre Special Publication No. 4, 73 p.
- Ludwig, K. R., 2009, Squid 2.50, a user's manual: Berkeley Geochronology Centre, Berkeley, California, USA, 95 p.
- Stacey, J. S., and Kramers, J. D., 1975, Approximation of terrestrial lead isotope evolution by a two-stage model: *Earth and Planetary Science Letters*, v. 26, p. 207–221.
- Stern, R. A., Bodorkos, S., Kamo, S. L., Hickman, A. H., and Corfu, F., 2009, Measurement of SIMS Instrumental Mass Fractionation of Pb Isotopes During Zircon Dating: *Geostandards and Geoanalytical Research*, v. 33, p. 145–168.
- Stern, R. A., and Rayner, N., 2003, Ages of several xenotime megacrysts by ID-TIMS: potential reference materials for ion microprobe U–Pb geochronology: Radiogenic Age and Isotopic Studies: Report 16, Geological Survey of Canada: Current Research 2003-F1, p. 7.

3.12.3 DATA TABLES

Supplementary Table 3-1: GSWA 219544 Belvedere Dolerite Dyke

<i>Mount no.</i>	<i>Grain spot</i>	<i>U (ppm)</i>	<i>Th (ppm)</i>	<i>Th/U</i>	<i>f²⁰⁶ (%)</i>	<i>²⁰⁷Pb*/²⁰⁶Pb*</i>	<i>± 1s</i>	<i>²⁰⁶Pb*/²³⁸U</i>	<i>± 1s</i>	<i>²⁰⁷Pb*/²³⁵U</i>	<i>± 1s</i>	<i>Dis (%)</i>	<i>²⁰⁷Pb*/²⁰⁶Pb* age (Ma)</i>	<i>± 1s (Ma)</i>
Crystallization (2082 ± 30 Ma)														
1702	G.2-1	118	5	0.04	1.04	0.1351	0.0044	0.369	0.009	6.88	0.27	6	2165	56
1702	B.2-1	158	4	0.02	-0.16	0.1332	0.0031	0.320	0.006	5.88	0.17	16	2141	41
1702	G.1-3	107	6	0.06	-0.22	0.1311	0.0037	0.320	0.013	5.78	0.28	15	2113	50
1702	G.1-1	124	5	0.04	0.10	0.1299	0.0035	0.329	0.014	5.89	0.29	13	2097	47
1702	G.1-2	129	3	0.02	0.45	0.1280	0.0044	0.323	0.007	5.70	0.22	13	2071	60
1702	B.1-1	209	16	0.08	1.27	0.1278	0.0073	0.319	0.006	5.63	0.34	14	2068	101
1702	A.1-1	251	8	0.03	0.10	0.1277	0.0025	0.364	0.006	6.40	0.15	3	2066	34
1702	B.2-2	132	3	0.02	0.52	0.1277	0.0035	0.323	0.006	5.69	0.18	13	2066	48
1702	D.1-1	231	46	0.20	0.75	0.1267	0.0034	0.349	0.006	6.09	0.19	6	2053	48
1702	J.1-1	118	4	0.03	1.52	0.1223	0.0049	0.367	0.007	6.19	0.27	-1	1989	71
1702	E.1-1	152	6	0.04	0.96	0.1221	0.0041	0.413	0.015	6.95	0.34	-12	1988	60
Younger statistical outliers														
1702	B.2-3	215	7	0.03	0.41	0.1207	0.0026	0.337	0.007	5.62	0.16	5	1966	39
1702	E.1-2	158	8	0.05	1.09	0.1206	0.0034	0.357	0.008	5.94	0.21	0	1965	51
High Common lead														
1702	I.1-1	73	8	0.11	2.63	0.1295	0.0073	0.375	0.010	6.69	0.42	2	2091	99
1702	H.1-1	101	5	0.05	2.44	0.1100	0.0065	0.372	0.008	5.64	0.35	-13	1799	107

Pb* indicates radiogenic

Pb.f206 is the proportion of common Pb in ²⁰⁶Pb, determined using the measured ²⁰⁴Pb/²⁰⁶Pb and a common Pb composition from the Stacey and Kramers (1975) model at the approximate age of the sample.Disc. Is apparent discordance, as $100((t^{207}\text{Pb}^*/^{206}\text{Pb}^*) - t^{238}\text{U}/^{206}\text{Pb}^*)/t^{207}\text{Pb}^*/^{206}\text{Pb}^*$.

Same footnote applies to Supplementary Tables 3-1 and 3-4

Supplementary Table 3-2: GSWA 219549 Belvedere Mineralization

<i>Mount no.</i>	<i>Grain spot</i>	<i>U (ppm)</i>	<i>Th (ppm)</i>	<i>Th/U</i>	<i>f²⁰⁶ (%)</i>	<i>²⁰⁷Pb*/²⁰⁶Pb*</i>	<i>± 1σ</i>	<i>²⁰⁶Pb*/²³⁸U</i>	<i>± 1σ</i>	<i>²⁰⁷Pb*/²³⁵U</i>	<i>± 1σ</i>	<i>²⁰⁸Pb*/²³²Th</i>	<i>± 1σ</i>	<i>Dis (%)</i>	<i>²⁰⁷Pb*/²⁰⁶Pb* age (Ma)</i>	<i>± 1σ (Ma)</i>
Hydrothermal mineralization (1682 ± 13 Ma)																
1606	B.1-1	482	49	0.10	0.00	0.1049	0.0020	0.270	0.038	3.90	0.56	1.512	0.009	10	1713	36
1606	B.1-2	471	58	0.12	-0.14	0.1048	0.0016	0.298	0.009	4.30	0.15	1.593	0.010	2	1710	29
1606	D.2-1	931	59	0.06	-0.11	0.1045	0.0012	0.295	0.007	4.26	0.12	1.640	0.010	2	1705	20
1606	C.1-2	788	63	0.08	-0.09	0.1037	0.0012	0.265	0.007	3.79	0.11	1.456	0.009	10	1692	22
1606	G.1-1	2611	59	0.02	0.05	0.1031	0.0007	0.296	0.006	4.21	0.09	3.305	0.010	1	1681	12
1606	C.1-1	700	62	0.09	-0.05	0.1030	0.0013	0.282	0.008	4.00	0.12	1.154	0.010	5	1680	23
1606	H.1-1	595	64	0.11	0.58	0.1029	0.0025	0.293	0.010	4.15	0.18	0.581	0.010	1	1678	46
1606	B.1-3	508	59	0.12	0.15	0.1025	0.0017	0.277	0.009	3.91	0.14	1.333	0.009	6	1671	31
1606	C.2-1	1771	58	0.03	0.55	0.1025	0.0016	0.317	0.011	4.47	0.17	2.123	0.011	-6	1669	29
1606	B.1-4	462	56	0.12	0.22	0.1024	0.0018	0.294	0.009	4.15	0.15	1.494	0.010	0	1669	33
1606	E.1-1	539	63	0.12	0.20	0.1016	0.0017	0.291	0.009	4.07	0.14	0.677	0.010	0	1653	32
1606	B.1-5	561	59	0.10	0.39	0.1006	0.0018	0.287	0.008	3.98	0.14	0.949	0.010	1	1636	33
High Common lead																
1606	D.1-1	2611	53	0.02	8.05	0.1478	0.0339	0.261	0.019	5.33	1.36	4.076	0.006	35	2320	393

Supplementary Table 3-3: GSWA 219551 Belvedere Mineralization

<i>Mount no.</i>	<i>Grain spot</i>	<i>U (ppm)</i>	<i>Th (ppm)</i>	<i>Th/U</i>	<i>f²⁰⁶ (%)</i>	<i>²⁰⁷Pb*/²⁰⁶Pb*</i>	<i>± 1s</i>	<i>²⁰⁶Pb*/²³⁸U</i>	<i>± 1s</i>	<i>²⁰⁷Pb*/²³⁵U</i>	<i>± 1s</i>	<i>²⁰⁸Pb*/²³²Th</i>	<i>± 1s</i>	<i>Dis (%)</i>	<i>²⁰⁷Pb*/²⁰⁶Pb* age (Ma)</i>	<i>± 1s (Ma)</i>
Hydrothermal mineralization (1680 ± 16 Ma)																
1606	J.1-1	1261	55	0.04	0.08	0.1053	0.0010	0.275	0.007	3.99	0.10	0.506	0.009	9	1720	17
1606	I.1-2	715	53	0.07	0.09	0.1049	0.0013	0.283	0.007	4.09	0.12	0.883	0.009	6	1712	23
1607	A.1-1	1201	506	0.42	0.87	0.1047	0.0017	0.296	0.012	4.28	0.18	0.097	0.010	2	1709	29
1606	J.2-2	2105	57	0.03	0.15	0.1038	0.0009	0.271	0.006	3.87	0.09	1.323	0.009	9	1694	16
1606	I.1-3	580	59	0.10	0.11	0.1034	0.0015	0.282	0.008	4.02	0.13	1.124	0.010	5	1685	26
1607	B.2-1	1827	1446	0.79	0.22	0.1026	0.0017	0.306	0.015	4.33	0.22	0.101	0.010	-3	1671	30
1606	K.1-1	1925	54	0.03	0.52	0.1025	0.0011	0.302	0.007	4.27	0.11	2.935	0.010	-2	1670	21
1606	J.3-1	1029	57	0.06	0.09	0.1024	0.0011	0.283	0.009	3.99	0.14	0.480	0.010	4	1668	19
1606	I.1-1	780	61	0.08	0.04	0.1023	0.0011	0.280	0.007	3.95	0.11	1.114	0.010	4	1666	21
1607	E.2-1	848	196	0.23	0.29	0.1020	0.0019	0.312	0.014	4.39	0.22	0.095	0.011	-5	1661	35
1607	I.1-1	1184	335	0.28	0.06	0.1020	0.0014	0.276	0.012	3.87	0.18	0.083	0.009	6	1660	25
1606	J.2-1	1400	50	0.04	0.11	0.1012	0.0010	0.265	0.006	3.69	0.10	0.463	0.009	8	1646	18
1606	I.1-4	858	61	0.07	0.00	0.1011	0.0017	0.283	0.007	3.95	0.12	1.115	0.010	2	1644	31
Discordance >10%																
1607	G.1-1	676	634	0.94	1.79	0.1138	0.0038	0.286	0.012	4.49	0.24	0.088	0.009	13	1861	60
1607	H.1-1	141	386	2.74	-0.38	0.1003	0.0033	0.206	0.010	2.85	0.17	0.065	0.007	26	1630	60
1607	E.1-1	355	534	1.50	15.08	0.0954	0.0135	0.158	0.007	2.08	0.33	0.055	0.006	38	1535	266

Supplementary Table 3-4: GSWA 219539 Crenulated muscovite schist

<i>Mount no.</i>	<i>Grain spot</i>	<i>U (ppm)</i>	<i>Th (ppm)</i>	<i>Th/U</i>	<i>f²⁰⁶ (%)</i>	<i>²⁰⁷Pb*/²⁰⁶Pb*</i>	<i>± 1σ</i>	<i>²⁰⁶Pb*/²³⁸U</i>	<i>± 1σ</i>	<i>²⁰⁷Pb*/²³⁵U</i>	<i>± 1σ</i>	<i>²⁰⁸Pb*/²³²Th</i>	<i>± 1σ</i>	<i>Dis (%)</i>	<i>²⁰⁷Pb*/²⁰⁶Pb* age (Ma)</i>	<i>± 1σ (Ma)</i>
Main Group (2361 ± 17 Ma)																
1703	F.1.1	2468	773	0.31	0.01	0.1522	0.0009	0.426	0.007	8.94	0.15	0.103	0.010	3	2370	10
1703	C.2-1	2854	2591	0.91	0.01	0.1519	0.0008	0.426	0.006	8.92	0.14	0.119	0.010	3	2368	9
1604	A.1-1	3398	63	0.02	0.95	0.1516	0.0021	0.431	0.011	9.01	0.27	4.238	0.010	2	2364	24
1703	A.2-1	1182	1429	1.21	0.36	0.1500	0.0021	0.435	0.009	8.99	0.22	0.119	0.010	1	2346	24
1703	C.1-1	2017	1449	0.72	-0.01	0.1494	0.0010	0.408	0.007	8.41	0.16	0.079	0.009	6	2339	11
Younger group (2260 ± 46 Ma)																
1604	A.1-2	1549	60	0.04	0.47	0.1458	0.0020	0.401	0.009	8.06	0.22	4.422	0.009	5	2297	23
1604	A.2-1	1051	58	0.06	0.35	0.1425	0.0046	0.425	0.011	8.36	0.36	2.061	0.010	-1	2258	55
1703	I.1.1	1171	1783	1.52	0.03	0.1421	0.0014	0.389	0.008	7.62	0.17	0.081	0.009	6	2253	17
1604	A.3-1	1291	47	0.04	0.42	0.1397	0.0024	0.410	0.021	7.90	0.43	2.577	0.010	0	2224	30
Discordance >7%																
1703	D.1.1	370	517	1.40	2.26	0.1588	0.0197	0.398	0.015	8.71	1.18	0.119	0.009	12	2443	210
1703	B.1-1	1025	814	0.79	0.33	0.1503	0.0017	0.391	0.009	8.11	0.20	0.090	0.009	9	2350	19
1604	B.1-1	1983	62	0.03	0.06	0.1485	0.0008	0.387	0.019	7.93	0.39	3.611	0.009	9	2329	10
1604	D.1-1	2597	58	0.02	0.14	0.1483	0.0026	0.384	0.011	7.86	0.26	3.324	0.009	10	2326	30
1703	E.1.1	405	402	0.99	0.66	0.1479	0.0026	0.376	0.011	7.67	0.26	0.126	0.009	11	2322	30
1703	H.1.1	1080	662	0.61	0.17	0.1478	0.0012	0.384	0.007	7.82	0.16	0.073	0.009	10	2321	14
1604	C.1-1	362	55	0.15	0.15	0.1261	0.0020	0.316	0.011	5.50	0.21	1.524	0.009	13	2044	28
1703	A.3-1	636	1503	2.36	0.24	0.1239	0.0017	0.315	0.007	5.38	0.15	0.091	0.009	12	2012	24
1703	A.1-1	391	1213	3.10	0.00	0.1205	0.0019	0.314	0.009	5.22	0.18	0.090	0.009	10	1963	28

CHAPTER 4. LINKING GOLD MINERALIZATION TO REGIONAL-SCALE DRIVERS OF MINERAL SYSTEMS USING IN SITU U–PB GEOCHRONOLOGY AND PYRITE LA-ICP-MS ELEMENT MAPPING

The following chapter has been accepted for publication in GEOSCIENCE FRONTIERS. The original format has been modified for the purposes of this thesis, but all content remains the same. The original, formatted and published version can be found in Appendix 1C.

Imogen O. H. Fielding¹, Simon P. Johnson², Sebastien Meffre³, Jian-Wei Zi^{4,5}, Stephen Sheppard^{1,6}, Ross R. Large³ and Birger Rasmussen⁷., Linking gold mineralization to regional-scale drivers of mineral systems using in situ U–Pb geochronology and pyrite LA-ICP-MS element mapping: *Geoscience Frontiers*, v. 10, p. 89–105, doi: <https://doi.org/10.1016/j.gsf.2018.06.005>

¹ Department of Applied Geology, Curtin University, Kent Street, Bentley, WA 6102, Australia.

² Geological Survey of Western Australia, 100 Plain Street, East Perth, WA 6004, Australia.

³ CODES ARC Centre of Excellence in Ore Deposits, University of Tasmania, Private Bag 126, Hobart, TAS 7001, Australia

⁴ State Key Lab of Geological Processes and Mineral Resources, China University of Geosciences, Wuhan, 430074, China

⁵ John de Laeter Centre, Curtin University, Kent Street, Bentley, WA 6102, Australia

⁶ Prime Geological Mapping, PO Box 3014, Carlisle South, WA, 6101, Australia

⁷ School of Earth Sciences, The University of Western Australia, Perth, WA, 6009, Australia

4.1. ABSTRACT

Proterozoic orogens commonly host a range of hydrothermal ores that form in diverse tectonic settings at different times. However, the link between mineralization and the regional-scale tectonothermal evolution of orogens is usually not well understood, especially in areas subject to multiple hydrothermal events. Regional-scale drivers for mineral systems vary between the different classes of hydrothermal ore, but all involve an energy source and a fluid pathway to focus mineralizing fluids into the upper crust. The Mount Olympus gold deposit in the Proterozoic Capricorn Orogen of Western Australia was regarded as an orogenic gold deposit that formed at ca. 1738 Ma during the assembly of Proterozoic Australia. However, the trace element chemistry of the pyrite crystals closely resemble those of the Carlin deposits of Nevada, with rims that display solid solution gold accompanied by elevated As, Cu, Sb, Hg, and Tl, surrounding gold-poor cores. New SHRIMP U–Pb dating of xenotime intergrown with auriferous pyrite and ore-stage alteration minerals provided a weighted mean $^{207}\text{Pb}^*/^{206}\text{Pb}^*$ date of 1769 ± 5 Ma, interpreted as the age of gold mineralization. This was followed by two discrete episodes of hydrothermal alteration at 1727 ± 7 Ma and 1673 ± 8 Ma. The three ages are linked to multiple reactivation of the crustal-scale Nanjilgardy Fault during repeated episodes of intracratonic reworking. The regional-scale drivers for Carlin-like gold mineralization at Mount Olympus are related to a change in tectonic regime during the final stages of the intracratonic 1820–1770 Ma Capricorn Orogeny. Our results suggest that substantial sized Carlin-like gold deposits can form in an intracratonic setting during regional-scale crustal reworking.

4.2. INTRODUCTION

The mineral systems concept describes how an ore deposit is the expression of a number of processes operating at a range of spatial and temporal scales (Wyborn et al., 1994; McCuaig and Hronsky, 2014; Huston et al., 2016). At the largest scale, mineralization is driven by a regional energy source with the transport of hydrothermal fluids or magmas along crustal-scale pathways (McCuaig and Hronsky, 2014; Huston et al., 2016). Whereas the smallest scale relates to local variations within an individual prospect or deposit, such as alteration mineralogy, element association, and the type of host rocks to mineralization (Robert et al., 2007). The absolute age of mineralization

and its timing relative to regional-scale tectonothermal events, is often poorly known but is critical for understanding the causes of ore formation (Hronsky et al., 2012). Without this information, the key factors in ore generation may not be correctly identified, particularly in areas that have been subject to multiple hydrothermal or crustal reworking events (e.g. Rasmussen et al., 2006).

The drivers for orogenic and epithermal gold mineralization are relatively obvious. Orogenic deposits are associated with active margins undergoing compressional tectonic activity during accretionary or collisional orogenic events (Groves et al., 1998; Goldfarb et al., 2001), and epithermal deposits are intimately associated with coeval magmatism (e.g. Simmons et al., 2005). However, the drivers for Carlin-type deposits (Cline et al., 2005) are more enigmatic, as such deposits do not always have a clear link between regional-scale tectonomagmatic activity or crustal architecture (e.g. Hu et al., 2002; Cline et al., 2005; Muntean et al., 2011).

The Mount Olympus gold deposit is located in the northern Capricorn Orogen within the West Australian Craton (Figure 4-1). The area has been subjected to limited research with few peer reviewed publications (e.g. Şener et al., 2005; Wells et al., 2016), and the most comprehensive ore body descriptions are sourced from conference abstracts and open-file company reports (e.g. Morant and Doepel, 1997; Young et al., 2003). Mount Olympus has many of the characteristics of a Carlin-type deposit including strata-bound ore, invisible gold concentrated in arsenian pyrite, and ore-stage alteration assemblages characterized by quartz, illite and sericite with the removal of carbonate minerals (Young et al., 2003). Despite these similarities, Şener et al. (2005) linked xenotime growth (and gold deposition) at ca. 1738 Ma to orogenic events related to the assembly of Proterozoic Australia. However, there are no orogenic events known in Western Australia at ca. 1738 Ma, which falls between the 1820–1770 Ma Capricorn Orogeny and the 1680–1620 Ma Mangaroon Orogeny, both of which represent periods of intracratonic reworking that resulted in deformation, metamorphism and granite intrusion inboard of the plate margin (Sheppard et al., 2005, 2010).

This study has two aims: 1) To review the classification of gold mineralization at Mount Olympus by assessing both the macroscopic characteristics and the distribution of trace element in pyrite crystals, and making comparisons to documented Carlin-type

and orogenic gold deposits (e.g. Large, et al., 2009); and 2) to present new in situ U–Pb xenotime geochronological data obtained using the Sensitive High Resolution Ion Microprobe (SHRIMP) to determine the timing of hydrothermal events, including gold mineralization. These data are then integrated with the record of the well-established crustal architecture and tectonothermal events in the West Australian Craton (Johnson et al., 2013) to investigate the large-scale mineral system processes associated with the Mount Olympus deposit.

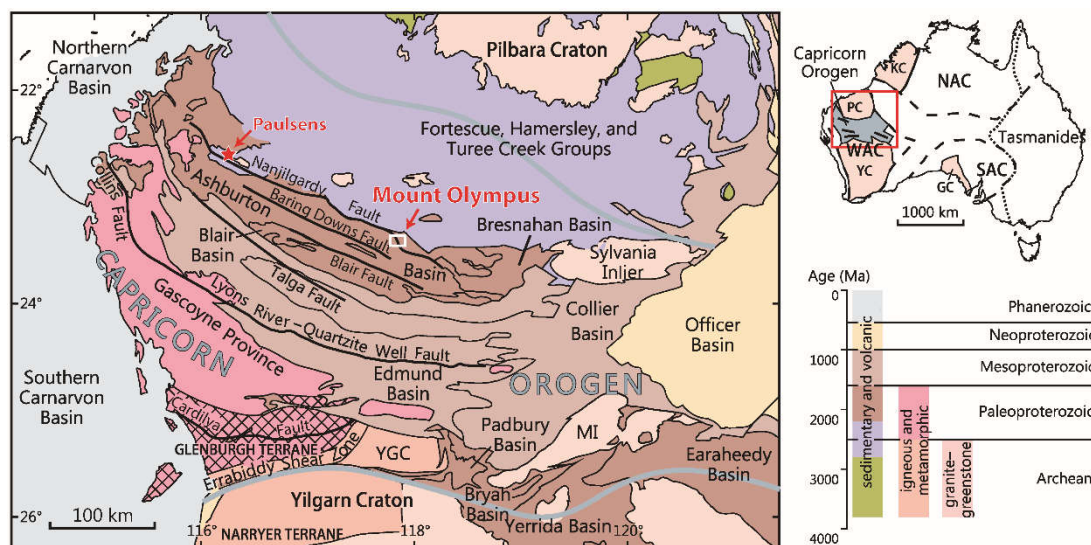


Figure 4-1. Regional geology of the northern Capricorn Orogen showing the location of Mount Olympus and Paulsens gold mines. White box indicates the inset map shown in Figure 4-2a. Abbreviations: GC = Gawler Craton, KC = Kimberley Craton, MI = Marymia Inlier, NAC = North Australian Craton, PC = Pilbara Craton, SAC = South Australian Craton, WAC = West Australian Craton, YC = Yilgarn Craton, YGC = Yarlalweelor Gneiss Complex (after Johnson et al., 2013).

4.3. GEOLOGICAL BACKGROUND

The Capricorn Orogen is a zone of variably deformed rocks between the Pilbara and Yilgarn cratons of Western Australia (Figure 4-1; Tyler and Thorne, 1990). The orogen records the two-stage assembly of the West Australian Craton by ca. 1950 Ma (Johnson et al., 2011), as well as at least five younger episodes of intracratonic reworking spanning over a billion years (Sheppard et al., 2005, 2007; Johnson et al., 2017; Korhonen et al., 2017). In the northern part of the Capricorn Orogen, Paleoproterozoic siliciclastic, carbonate and volcanic rocks of the Wyloo and Shingle Creek Groups were deformed during the 1820–1770 Ma Capricorn Orogeny (Thorne and Seymour, 1991). Mineralization throughout the region has a spatial association with crustal-scale faults (Johnson et al., 2013). The Nanjilgardy Fault (Figure 4-1), in

particular, has experienced multiple reactivations that led to deposition and remobilization of various styles of gold mineralization throughout the northern Capricorn Orogen (Johnson et al., 2013; Fielding et al., 2017).

4.4. DEPOSIT DESCRIPTION

The Mount Olympus gold deposit has a total remaining resource of 15 million tonnes (Mt) at 2.2 g/t containing ~1 Moz of gold (Northern Star Resources Limited, 2015). Mineralization occurs where the Zoe Fault, a second order splay of the Nanjilgardy Fault, juxtaposes conglomerate and coarse-grained sandstone of the Mount McGrath Formation against dolomitic mudstone of the Woolly Dolomite (Figure 4-2; Morant and Doepel, 1997; Krapež et al., 2015). The Zoe Fault is a dextral transpressional fault which has a strong control on the location of gold mineralization and is likely to have been the primary conduit for mineralizing fluids (Young et al., 2003).

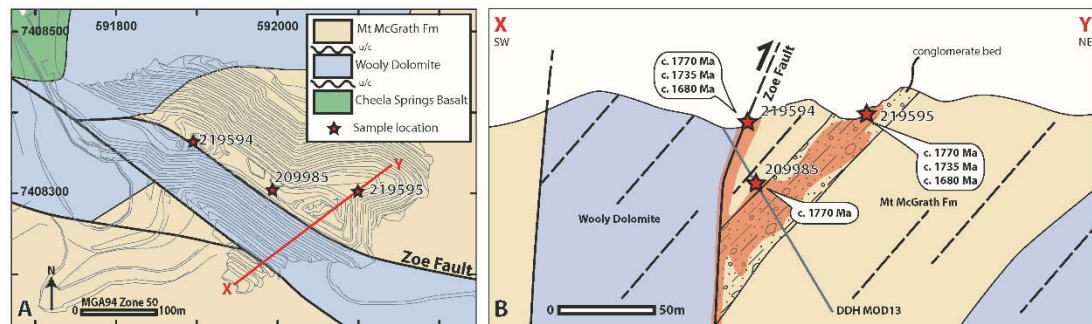


Figure 4-2. A) Prospect scale geological map of the Mount Olympus pit showing geochronology sample locations. B) Schematic cross section of the Mount Olympus ore body with geochronology sample locations.

Two distinct types of mineralized lodes are evident in the Mount Olympus pit: 1) strata-bound ore where arsenian pyrite crystals up to 1 cm in diameter are disseminated within carbonaceous and ferruginous conglomerate and sandstone of the Mount McGrath Formation, and 2) fault-hosted mineralization associated with pyrite and graphite, or in rare instances associated with strongly deformed quartz veins and stringers along the Zoe Fault (Figure 4-2b; Morant and Doepel, 1997; Young et al., 2003). In both lodes, gold forms microscopic inclusions in pyrite or as a solid solution within visibly zoned arsenian pyrite (Young et al., 2003). Ore-stage alteration assemblages are reported to have formed at up to 350°C at 1–2 kbar (Young et al., 2003) and include quartz, muscovite, kaolin-group phases (kaolinite and dickite) and pyrophyllite, with the removal of chlorite and carbonate minerals (Wells et al., 2016).

4.5. METHODS

4.5.1. LA-ICP-MS

Pyrite from within mineralized zones of the Mount Olympus deposit were collected from diamond drill cores MOD13 and NMOD002 (Table 4-1) for analysis by LA-ICP-MS. Polished 25 mm diameter rock mounts were prepared and pyrites were etched using a dilute nitric acid solution to reveal any internal growth zones in order to select areas suitable for trace element mapping by LA-ICP-MS. Trace element mapping of pyrite crystals were performed at the ARC Centre of Excellence in Ore Deposits LA-ICP-MS facility at the University of Tasmania using the New Wave 213-nm solid-state laser microprobe coupled to an Agilent 4500 quadrupole ICP-MS. The procedure outlined in Large et al. (2009) was followed and described briefly below.

Hole ID	MGA94 zone 50		Depth (m)	Description	Whole rock Au assay from diamond core
	East	North			
NMOD002	592408	7407945	377.7	Semi-massive pyrite in silicified black shale	4.86 ppm (377-378 m)
NMOD002	592408	7407945	376.2	Semi-massive pyrite in silicified black shale	3.58 ppm (376-377 m)
MOD13	591962	7408248	130.6	Sericite altered sandstone with coarse euhedral pyrite and arsenopyrite	1.92 ppm (130-131 m)
MTO90	592159	7408094	262.3	Sericite altered siltstone with coarse euhedral pyrite	0.92 ppm (262-263 m)

Table 4-1: LA-ICP-MS sample location, descriptions and gold grades.

Trace element distribution maps were generated by ablating parallel lines in a grid pattern. Beam sizes of 15, 22, 35 and 47 μm were used with a laser beam repetition rate of 10 Hz with energy maintained at 4.5 J/cm². Rastering speed for each line was equal to the beam size per second (i.e., 15–47 $\mu\text{m/s}$). Analysis consisted of 28 elements including Na, Mg, Al, Si, K, Ca, Ti, V, Mn, Fe, Co, Ni, Cu, Zn, As, Se, Mo, Ag, Sb, Te, W, Pt, Au, Hg, Tl, Pb, Bi and U. Acquisition time was set to 0.03 s for gold, 0.008 s for chalcophile elements, and 0.002 s for other elements resulting in a total quadrupole sweep time of 0.2 s (including deadtime).

Data were collected in counts per second (cps) and later converted to parts per million (ppm). The conversion was undertaken using the in-house standard STDGL2b-2, analyzed both before and after each sample with a 74 μm spot size, laser beam repetition rate of 10 Hz and energy of 4 J/cm². The standard comprises a homogenous mix of powdered sulfide and trace elements of known concentrations, fused into a lithium borate glass disk (Danyushevsky et al., 2011). Instrumental mass bias was initially determined using standard laser ablation data reduction techniques then

applied to each quadrupole sweep (i.e., each pixel in the image) assuming stoichiometric Fe (456,000 ppm) in pyrite for each line of the image. The data are expected to be accurate for the pyrite in each image, but will tend to underestimate the concentrations for other mineral phases due to the different behaviour of other minerals during ablation relative to pyrite (matrix effects). The ratios between elements will not be affected by these problems. Hg was not quantified due to the lack of standards and the volatility of the element. The Hg counts per second images can be used on a qualitative basis to identify high and low Hg zones.

4.5.2. GEOCHRONOLOGY

Three mineralized samples were examined by optical and scanning electron microscope to identify xenotime suitable for geochronology. Small disks of thin section containing xenotime crystals for SHRIMP analysis were drilled out of the polished thin-sections before being cast into 25 mm epoxy SHRIMP mounts. Xenotime standards MG1, Xeno1 and Xeno2 were placed on a separate SHRIMP mount that was gold coated along with the sample mounts. SHRIMP U–Pb dating of xenotime followed established procedures for small-spot, in situ analysis as outlined by Fletcher et al. (2000, 2004).

A primary beam of O²⁻ ions was focused through a 30 µm Kohler aperture to produce an oval 10–15 µm wide spot on the sample surface with a current of 0.2–0.8 nA. The secondary ion system was focused through a 100 µm collector slit onto an electron multiplier to produce mass peaks with flat tops and a mass resolution of >5200 in all sessions. Background counts from scattered ions were reduced using a flight retardation lens, which is known to cause slight session-dependent instrumental mass fractionation (IMF) of Pb isotopes. IMF corrections were applied to all analyses.

Data were collected in sets of 8 scans; with xenotime reference materials analyzed every 4–6 sample analyses. Count times per scan for background position 204.045, and Pb isotopes 204, 206, 207, and 208 were 10 s, 10 s, 10 s, 30 s and 10 s, respectively. Xenotime was analyzed with a 9-peak run table following analytical protocols detailed by Fletcher et al. (2004). Pb/U calibrations and matrix corrections for U and Th contents were based on concurrent measurements of the standards MG-1 (Fletcher et al., 2004) and z6413 (“Xeno1”; Stern and Rayner, 2003). Pb/Th was determined

indirectly, using a fixed Th/U calibration (Fletcher et al., 2004). Matrix corrections for REE assumed the samples have REE abundances similar to Xenol.

Raw data from analyses were processed using the SQUID 2 add-in (v. 2.50.12.03.08) for Excel 2003 (Ludwig, 2009), and plotted using the ISOPLOT add-in (v. 3.76.12.02.24; Ludwig, 2003). Common-Pb corrections were based on measured $^{204}\text{Pb}/^{206}\text{Pb}$ ratios and contemporaneous Pb composition according to the terrestrial Pb evolution model of Stacey and Kramers (1975). Matrix effect corrections were made for all xenotime data using procedures described by Fletcher et al (2004). Pooled ages are quoted with 95% confidence levels, whereas individual analyses are presented with 1σ errors.

4.6. RESULTS

4.6.1. LA-ICP-MS

The content and distribution of trace elements within massive pyrite from gold-rich samples differs between those in carbonaceous-rich material from the Zoe Fault (NMOD002), and those within sericite-altered sandstone (MOD13) from strata-bound mineralization.

4.6.1.1. ZOE FAULT

Polished 25 mm diameter rock mounts were prepared of massive pyrite-bearing black shale from the Zoe Fault in drill core NMOD002 at 377.7 m and 376.2 m to investigate the textures and internal trace element zoning within the pyrite. These samples are from a zone of high-grade mineralization containing whole rock gold assay results of 3.58 ppm (376–377 m) and 4.86 ppm (377–378 m). Two areas of pyrite from the thin sections at 377.7 m and two at 376.2 m, were mapped in detail by LA-ICP-MS.

Four types of pyrite have been defined in samples from NMOD002 (Figure 4-3 a–e) with a paragenetic sequence from pyrite 1 (py1) to pyrite 4 (py4) summarized in Table 4-2. Py1 comprises micro-crystal aggregates (Figure 4-3a and d) which often form in carbon-rich horizons (Figure 4-3b). Py2 is composed of coarse-grained, subhedral pyrite that is commonly intergrown with tetrahedrite (Figure 4-3a, b and d), or along carbonaceous layers (Figure 4-3b). Py3 forms within the silicified shale matrix as euhedral crystals with internal zoning that shows a change from the cubic to

pyritohedral crystal form from the internal zone to the rim (Figure 4-3b and c). Py4 is a coarse, inclusion-free pyrite up to 300 μm across (Figure 4-3d).

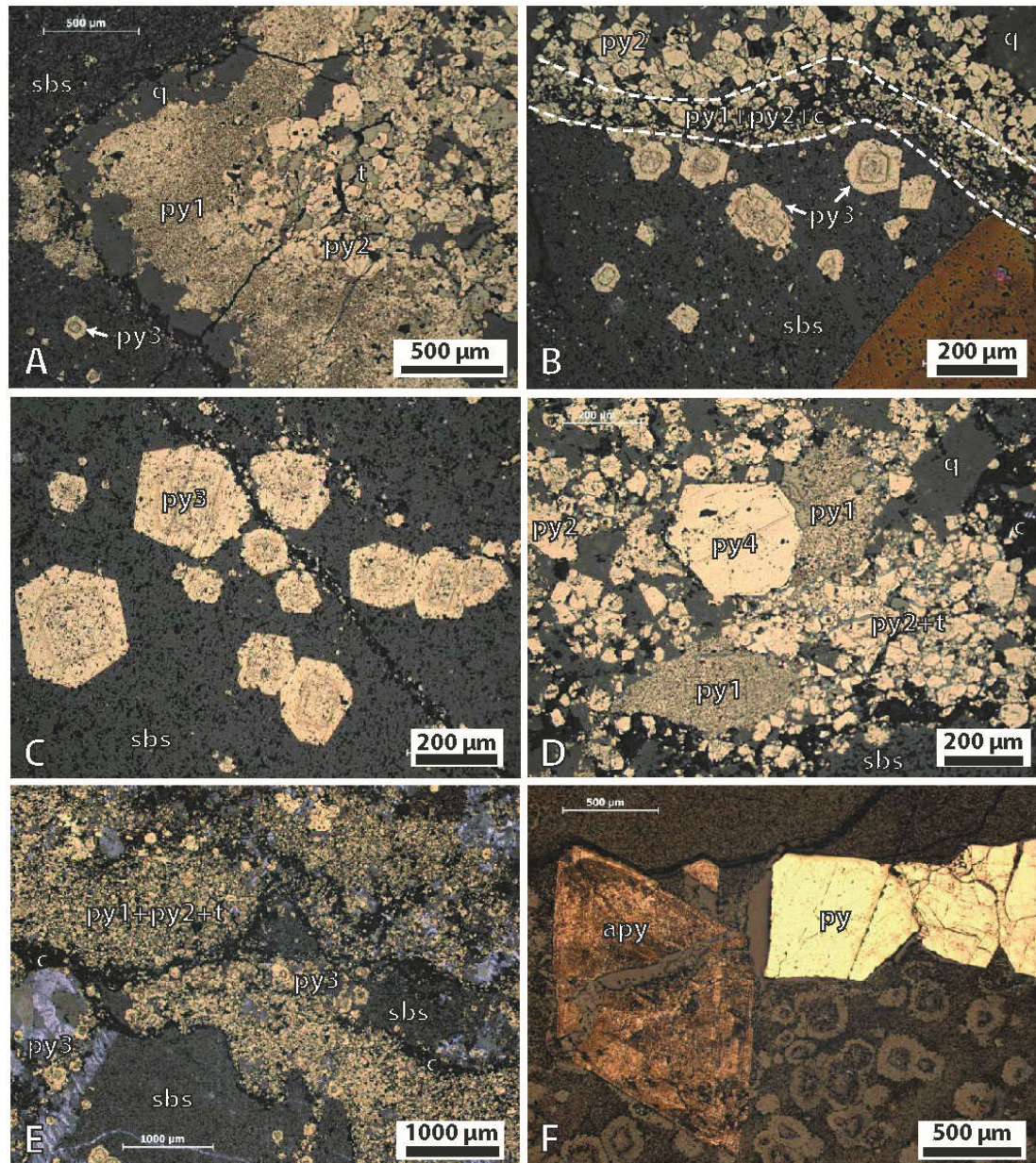


Figure 4-3. Textures of pyrite types at the Mount Olympus deposit. A) NMOD002 377.7 m depth showing py1 surrounding py2 and tetrahedrite. B) NMOD002 377.7 m depth showing a narrow band of py1, py2 and carbonaceous material separating py2 from py3. C) NMOD002 376.2 m depth growth zoning in py3. D) NMOD002 376.2 m depth py1, py2 and large euhedral py4. E) Summary image showing the py1, py2 and tetrahedrite separated from py3 by a carbonaceous rich band. F) MOD13 130.6 m depth, showing large pyrite and arsenopyrite crystals from the strata-bound mineralization. Abbreviations py = pyrite, t = tetrahedrite, sbs – silicified black shale, q = quartz, c = carbonaceous material, apy = arsenopyrite.

Drill hole	Paragenesis	Lode	Description	Trace element association
NMOD002	Py 1	Zoe Fault	Micro-crystals aggregates; formed in carbon band commonly with py 2 and tetrahedrite	Au 7.78 ppm, As, Tl+ Pb
NMOD002	Py 2	Zoe Fault	coarse grained subhedral pyrite; commonly intergrown with tetrahedrite; occurs with py 1 in carbon rich bands	low levels of Au (1.85 ppm) and As
NMOD002	Py 3	Zoe Fault	Euhedral pyrite with internal zonation; internal band is cubic, rim is pyritohedral	Core: Au 4.85 ppm; Hg-Pb-Bi Internal band: Au 67.28 ppm; Au-As-Cu-Hg-Tl-Sb Rim: Au 3.56 ppm; Co-Ni
NMOD002	Py 4	Zoe Fault	coarse (>300micron) clear pyrite	No Au; depleted in trace elements
NMOD002	tetrahedrite	Zoe Fault	coarse grained and intergrown with py 2	Cu-Zn-Ag-Sb-Hg
MOD13		Strata-bound	Coarse euhedral pyrite and arsenopyrite; thick (100-300 μ m) diffusive rim zone	Au 55.06 ppm; As enriched

Table 4-2: Summary of paragenetic sequence from py1 to py4.

Trace element images of each type of pyrite show that py1 has a mean Au grade of 8 ppm and is also enriched in As, Tl \pm Pb (Figure 4-4 and 4-5). Py2 is low in both Au and As contents (Figure 4-6), with a mean Au content of 2 ppm and is often intergrown with tetrahedrite which is enriched in Cu, Zn, Ag, Sb, Hg (Figure 4-4 and 4-5). Py3 is zoned with an internal growth band enriched in Au (Figure 4-6 and 4-7) and has the highest gold values (up to 429 ppm) of all samples analyzed. The core zone contains minor Hg, Pb and Bi with a mean Au content of 5 ppm, the internal zone has elevated Au, As, Cu, Hg, Tl and Sb and a mean Au content of 67 ppm, and the rim zone is Co and Ni rich and has a gold content of 4 ppm (Figure 4-7). The interface zone between areas with abundant py1, py2 and tetrahedrite against areas of silicified black shale containing py3 is commonly defined by a band of carbonaceous material (Figure 4-3b and e) is enriched in Au, Mo, V, U and Al (Figure 4-6). Py4 has low trace elements concentrations and does not contain any gold (Figure 4-5).

4.6.1.2. STRATA-BOUND MINERALIZATION

Polished mounts were prepared from a sericite-altered sandstone with a whole rock gold assay of 1.92 ppm (130–131 m) collected from diamond drill core MOD13 at 130.6 m (Figure 4-3f). The sample contains abundant, coarse, euhedral pyrite and arsenopyrite crystals. The pyrite has a thick (100–300 μ m) diffusive rim zone with a mean Au value of 55 ppm. This surrounds a core with lower values of both As and Au (mean 12 ppm Au). These pyrites have no other trace element associations (Figure 4-8).

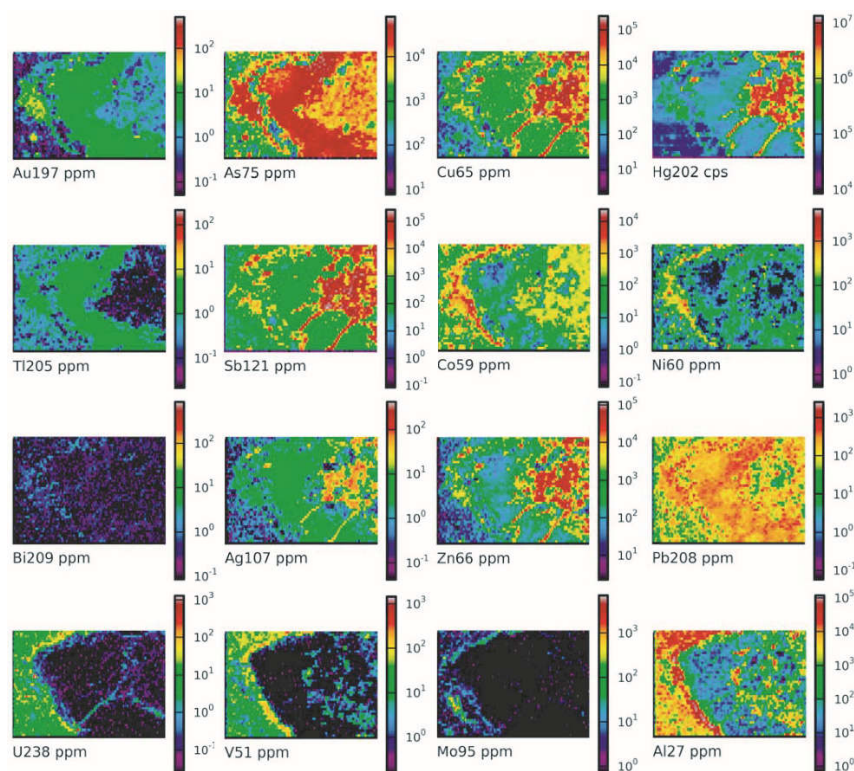


Figure 4-4. LA-ICP-MS images of trace elements in pyrite from NMOD002 377.7 m depth showing py2 and tetrahedrite surrounded by a py1 (see Figure 4-3a). Py1 which is associated with elevated Au, As, Tl and Pb, py2 is slightly enriched in Au and As and tetrahedrite is enriched in Cu, Hg, Sb, Ag and Zn.

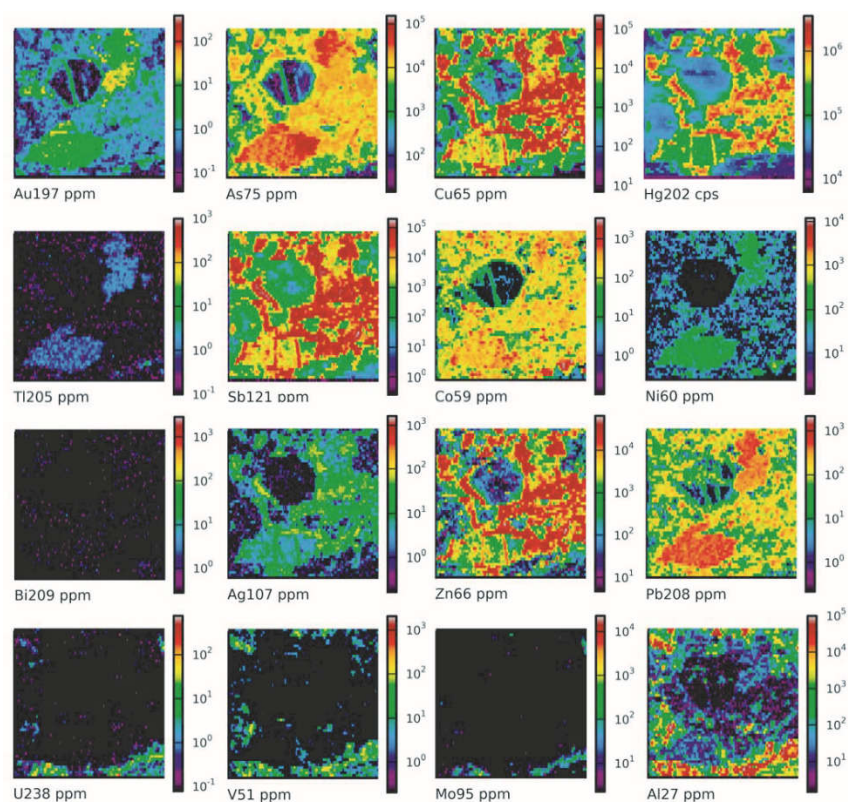


Figure 4-5. LA-ICP-MS images of trace elements in pyrite from NMOD002 376.2 m depth showing py4 with no trace element associations; py1 is enriched in Au, As, Tl, Pb, and py2 and tellurium are intergrown and enriched in Au, As, Cu, Hg, Sb, Ag and Zn (see Figure 4-3d).

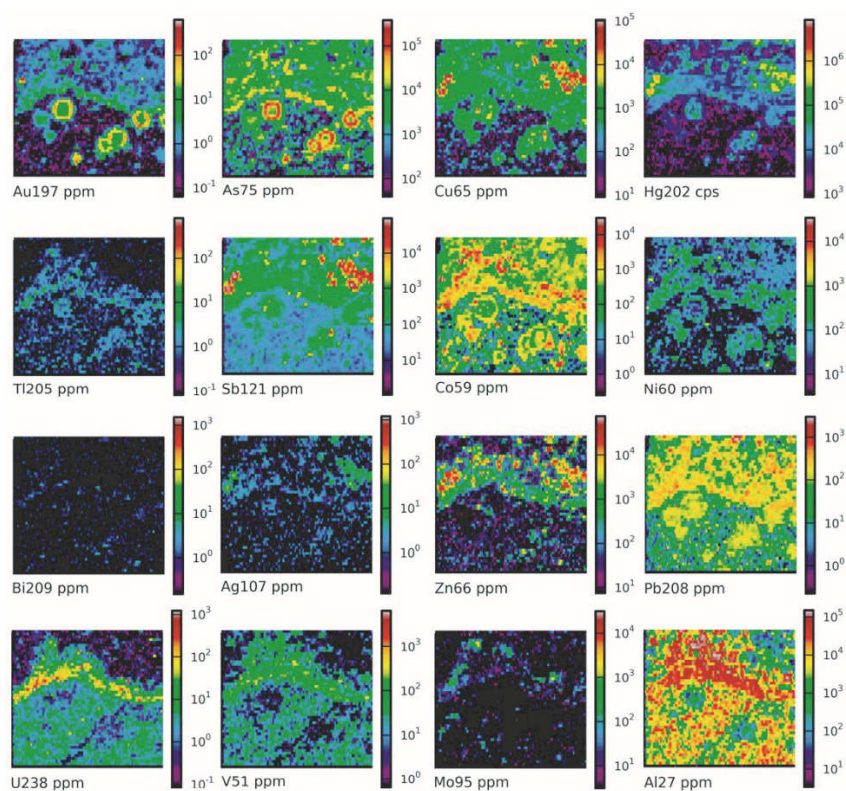


Figure 4-6. LA-ICP-MS image of trace element from pyrite in NMOD002 377.7 m depth showing a narrow band of py1, py2 and carbonaceous material separating py2 from py3 (see Figure 4-3b). The carbonaceous band is enriched in Au, U, V, Mo and Al.

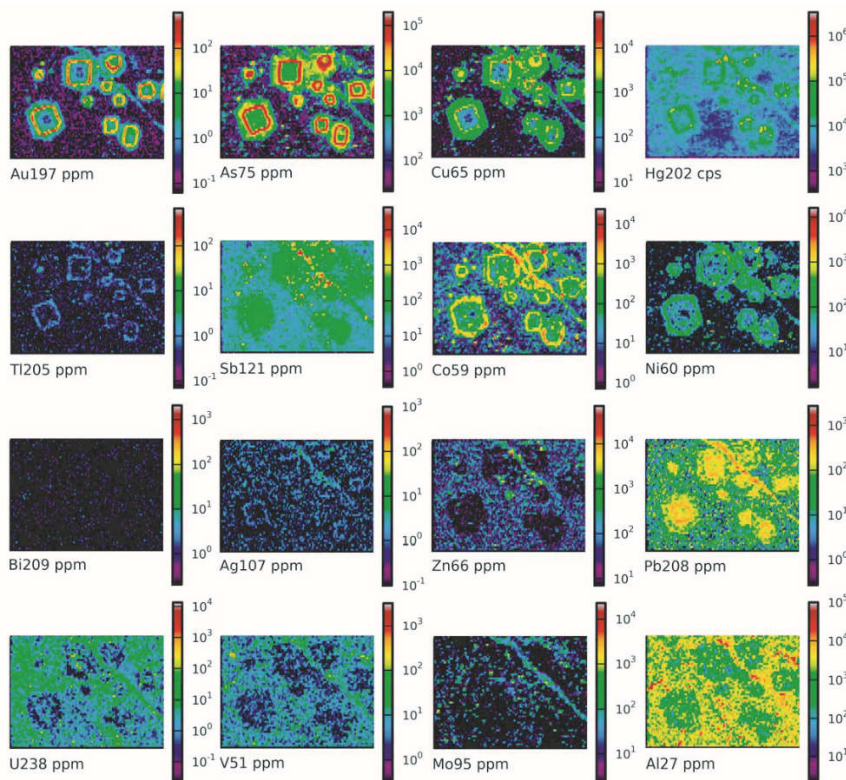


Figure 4-7. LA-ICP-MS image of trace elements from pyrite in NMOD002 376.2 m depth showing zoning in py3 with a core enriched in As, Hg, Sb and Pb, an internal band enriched in Au, As, Cu, Hg, Ti, Sb and Pb, and a rim zone associated with elevated Co and Ni.

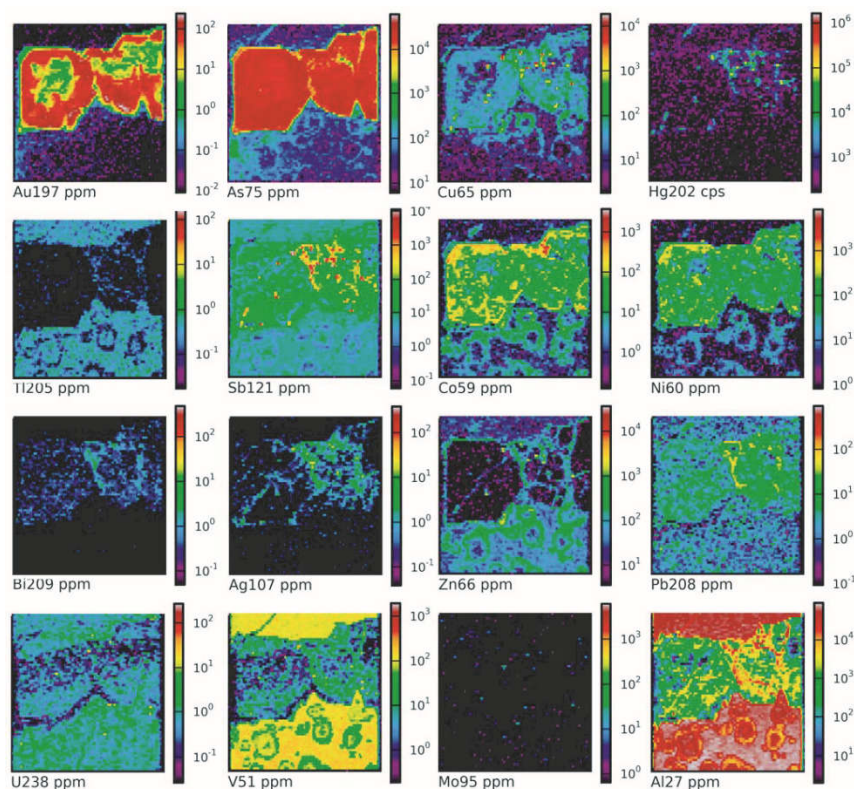


Figure 4-8. LA-ICP-MS images of trace elements from pyrite in MOD13 130.6 m depth showing elevated As with a diffusive rim zone enriched in Au.

4.6.2. GEOCHRONOLOGY

4.6.2.1. GSWA 219594: ZOE FAULT MINERALIZATION

A mineralized sample from the Zoe Fault (MGA 94 Zone 50 591903E, 7408364N) comprising brecciated pyrite (py1–4), carbonaceous material and quartz veins, contained small xenotime crystals (<20 μm diameter) in the brecciated parts of the sample. The xenotime commonly forms overgrowths on zircon crystals (Figure 4-9a) and contains inclusions of quartz, muscovite and rutile.

Twenty six analyses were conducted on 20 xenotime crystals with U contents ranging from 1053 to 4638 ppm and Th contents between 392 and 8441 ppm. Three analyses >10% discordant and two analyses with imprecise data due to poor spot placement were excluded from the age determination. The remaining 21 analyses yielded three distinct age modes (Figure 4-10a, Supplementary Table 4-1) with weighted mean $^{207}\text{Pb}^*/^{206}\text{Pb}^*$ dates of 1768 ± 8 Ma (MSWD = 1.12, n = 9), 1727 ± 8 Ma (MSWD = 1.08, n = 10) and 1671 ± 18 Ma (MSWD = 0.15, n = 2). No textural differences between the xenotime grains within each of these age modes could be identified.

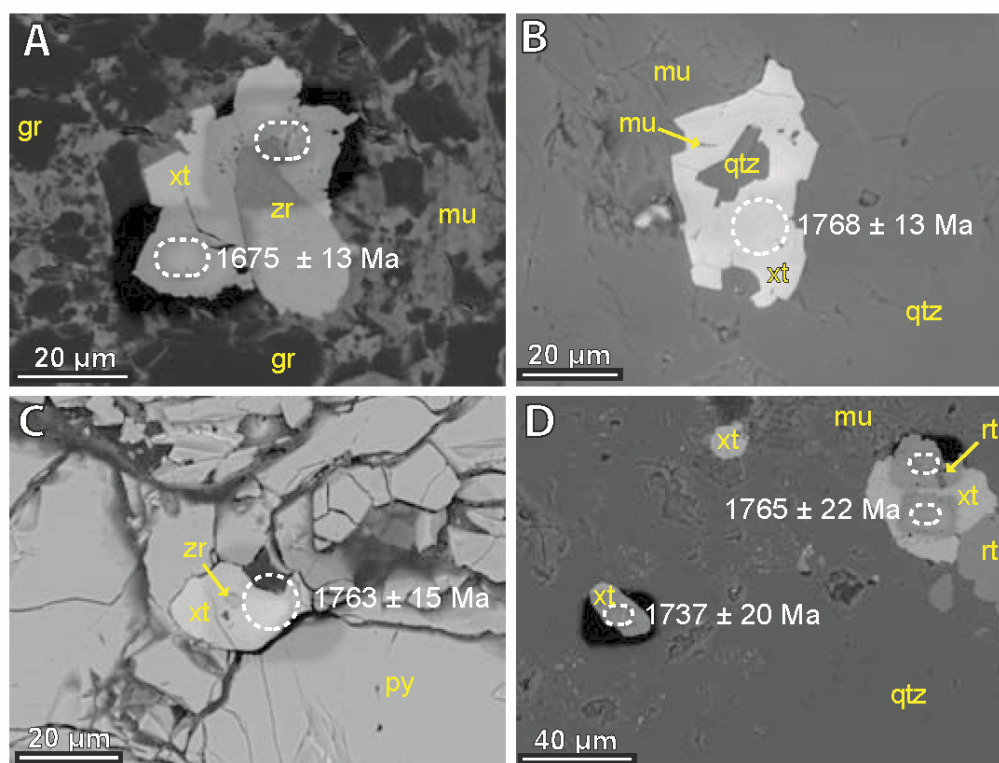


Figure 4-9. Scanning electron microscope-backscattered electron (SEM-BSE) images of dated xenotime crystals. White ellipses show analysis pits. Analysis pits with no ages represent discordant data. A) Xenotime overgrowth on zircon (GSWA 219594). B) Xenotime intergrown with muscovite and quartz from strata-bound mineralization (GSWA 909985). C) Xenotime encased in auriferous pyrite (GSWA 209985). D) Xenotime with inclusions of rutile (GSWA 219595). Mineral abbreviations: gr-graphite, mu-muscovite, py-pyrite, qtz-quartz, rt-rutile, xt-xenotime and zr-zircon.

4.6.2.2. GSWA 209985: STRATA-BOUND MINERALIZATION

A sample of strata-bound mineralization (drill hole MOD13: depth 91.23–91.25 m: MGA 94 Zone 50 591962E, 7408248N) was taken from a pervasively altered siltstone with coarse pyrite and 2.67 ppm of Au, similar to the sample analyzed by LA-ICP-MS for trace element analyses. Small xenotime (<25 µm diameter) crystals intergrown with ore-related alteration minerals, quartz and muscovite (Figure 4-9b), and some grains are fully contained within pyrite crystals (Figure 4-9c).

Twenty analyses conducted on 20 xenotime crystals with U and Th contents ranging from, 1118 to 4190 ppm and 57274 to 21590 ppm, respectively. Three of the analyses were excluded from the age determination due to >10% discordance. The remaining 17 analyses yielded a weighted mean $^{207}\text{Pb}^*/^{206}\text{Pb}^*$ date of 1770 ± 7 Ma (MSWD = 1.4; Figure 4-10b, Supplementary Table 4-2). This sample, contains 2.67 ppm Au, is the only one in which xenotime is encased in auriferous pyrite and provides a unimodal age. Together these data suggest that the date obtained represents the timing of hydrothermal alteration associated with pyrite crystallization and gold mineralization.

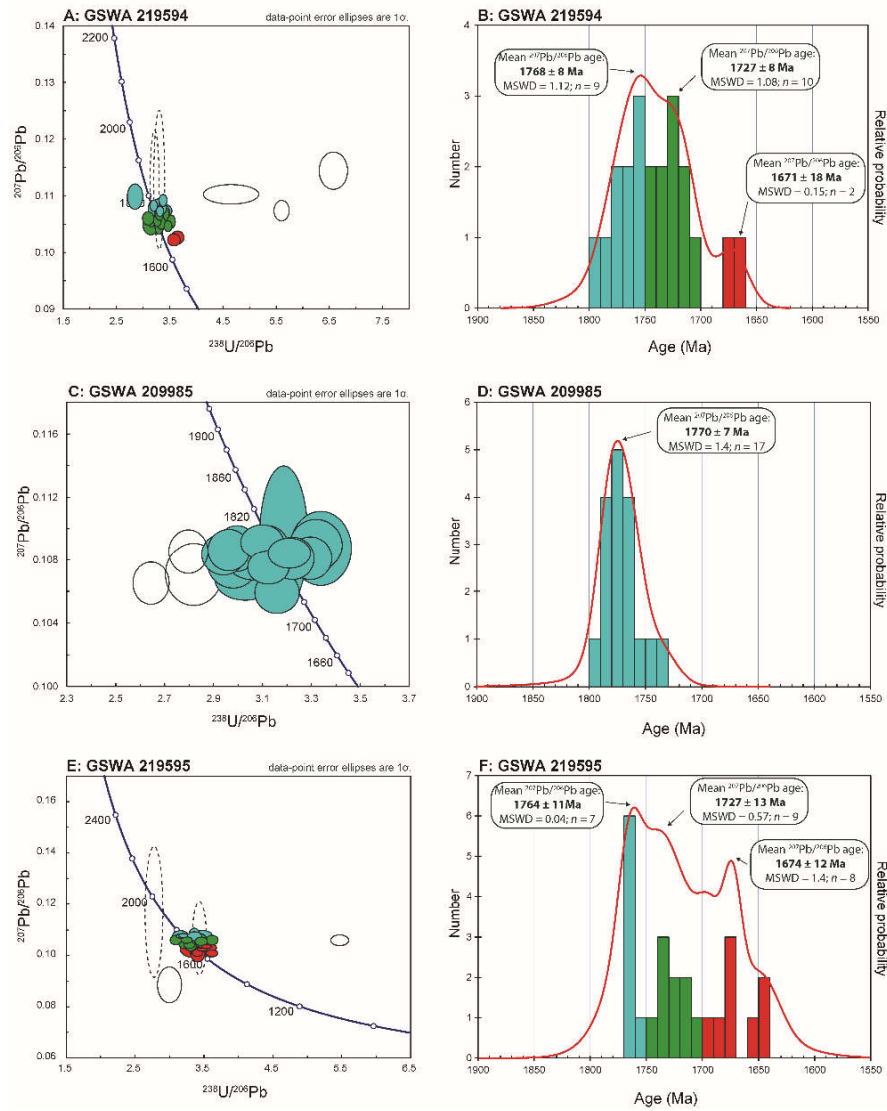


Figure 4-10. Tera-Wasserburg Concordia diagrams of U–Pb data for xenotime and probability density diagrams and histograms of xenotime ages for mineralized samples A and B: GSWA 219594 C and D: GSWA 209985 and E and F: GSWA 219595. Key for Concordia diagrams: colored ellipses (blue = ca. 1770 Ma, green = ca. 1730 Ma, red = ca. 1680 Ma) show data used in age calculations; other ellipses are for inferior data (unshaded black ellipses = >10% discordant data, dashed ellipses = poor spot placement). Probability density diagrams, red curve includes only data <10% discordant, colours used correspond to the Concordia diagrams.

4.6.2.3. GSWA 219595 STRATA-BOUND MINERALIZATION

A second sample of strata-bound mineralization (MGA 94 Zone 50 592095E, 7408303N) was collected from quartz–muscovite altered conglomerate in the Mount Olympus pit with pyrite crystals up to 2 cm. Xenotime crystals from this sample are up to 80 μm in diameter and commonly contain inclusions of quartz, zircon, rutile or muscovite (Figure 4-9d).

Twenty eight analyses on 20 xenotime crystals with U contents between 514 and 4338 ppm and Th contents from 1124 to 7288 ppm. Two analyses with >10% discordance and two analyses with imprecise data due to poor spot placement were excluded from

the age determination. The remaining 24 analyses yielded three distinct age modes (Figure 4-10c, Supplementary Table 4-3) with weighted mean $^{207}\text{Pb}^*/^{206}\text{Pb}^*$ dates of 1764 ± 11 Ma (MSWD = 0.04, $n = 7$), 1727 ± 13 Ma (MSWD = 0.57, $n = 9$) and 1674 ± 12 Ma (MSWD = 1.4, $n = 8$). No textural differences between the xenotime grains within each of these age modes could be identified.

4.6.2.4. POOLED AGE DATA

The distinct age modes obtained from all three samples are consistent (Figure 4-11) thus allowing the pooling of all data to better define the age peaks. Pooled data yield weighted mean $^{207}\text{Pb}^*/^{206}\text{Pb}^*$ dates of 1769 ± 5 Ma (MSWD = 1.02, $n = 33$), 1727 ± 7 Ma (MSWD = 0.79, $n = 19$) and 1673 ± 8 Ma (MSWD = 1.15, $n = 10$). The ca. 1730 and 1675 Ma ages are interpreted to represent discrete hydrothermal events causing new growth or dissolution and re-precipitation of xenotime, whereas the ca. 1770 Ma age, which is common to all studied samples, represents the timing of pyrite crystallization and gold mineralization. These new geochronological data indicate a more complex geological history of the Mount Olympus deposit than previously recognized by Şener et al. (2005).

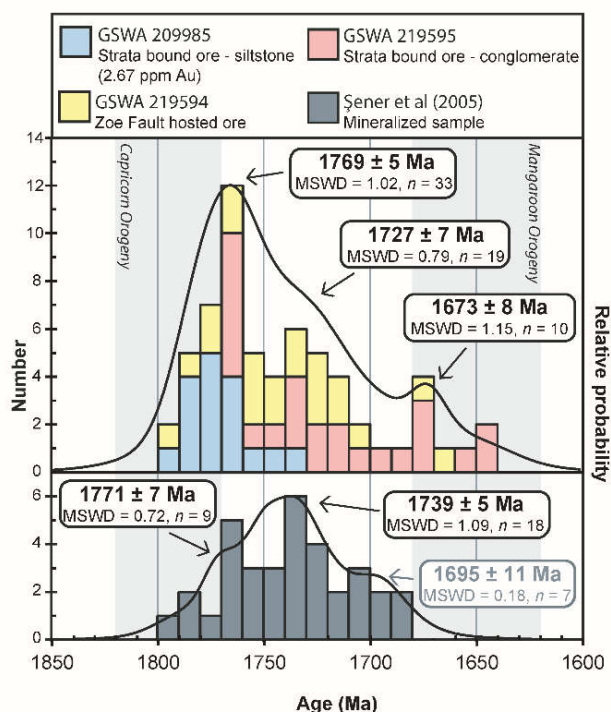


Figure 4-11. Probability plots and histograms with 10 Ma bin width for hydrothermal xenotime. Upper panel contains data from the strata-bound ore zone (GSWA 209985 and 219595) and from the Zoe Fault (GSWA 209594). The lower panel contains data from Şener et al. (2005); grey text indicates inferior data (poor spot placement or younger outliers). Weighted mean $^{207}\text{Pb}^*/^{206}\text{Pb}^*$ dates are reported with 95% confidence levels including data <10% discordant that contain $\leq 1\%$ common Pb.

4.7. DISCUSSION

4.7.1. DEPOSIT CLASSIFICATION

The classification of the Mount Olympus deposit has been reported as having features similar to both Carlin-type and orogenic gold deposits (Young et al., 2003; Şener et al., 2005); however, these styles of mineralization are significantly different (Table 4-3). Orogenic gold deposits are generally related to accretionary or collisional events where gold deposits occur as linear trends associated with trans-crustal structures that mark suture zones between continental blocks (Groves et al., 1998; Goldfarb et al., 2001; Hronsky et al., 2012). Deposits are hosted by Archean greenstones or Paleoproterozoic and Phanerozoic turbidite deposits that are metamorphosed to greenschist facies (Goldfarb and Groves, 2015). Commonly the deposits have ore-stage alteration assemblages of carbonate-iron sulfide \pm white mica \pm chlorite that formed at 200–650°C and 0.5–5 kbar (Goldfarb et al., 2001; Groves et al., 2003), with mineralization associated with quartz \pm carbonate-sulfide veins (Groves et al., 1998). Trace element compositions of pyrite in orogenic gold deposits show elevated Ni, As, Au, W, V and Cr (Belousov et al., 2016). In contrast, the Carlin-type deposits of Nevada tend to be associated with mildly extensional tectonics (Cline et al., 2005; Muntean et al., 2011). Mineralized lodes form in carbonate rocks enriched in carbonaceous material (Berger and Bagby, 1991; Cline et al., 2005) with ore-stage alteration consisting of decalcification, jasperoid and clay alteration (montmorillonite, kaolinite, illite and smectite), silicification and sulfidation forming at 180–240°C and 0.5–1 kbar (Teal and Jackson, 2002; Cline et al., 2005). Mineralization has a strong structural control which defines ore body geometries, commonly resulting in strata-bound and fault zone mineralization (Arehart, 1996). Trace element compositions of pyrite show elevated As, Au, Sb, Tl, Cu, Hg \pm Ag \pm Pb with invisible gold typically enriched in the rim zones (Large et al., 2009).

The Mount Olympus deposit shares many of the characteristics common to the Carlin deposits of Nevada, although several differences are also evident (Table 4-3). At Mount Olympus gold mineralization is both fault-hosted and strata-bound (Morant and Doepel, 1997; Young et al., 2003). The strata-bound lodes however, occur in coarser grained rocks than those at Carlin; but similar to the Carlin deposits they have a high organic carbon content, with ore-stage alteration characterized by the removal of

carbonate minerals and the addition of sericite and quartz (Wells et al., 2016). Young et al. (2003) indicated that the mineralization formed at temperatures and pressures up to 350°C and 1–2 kbar, significantly higher than the Carlin deposits that formed under conditions between 180–240°C and 0.5–1 kbar (Cline et al., 2005). However, the methods used to determine the temperature and pressure conditions at which the Mount Olympus mineralization formed are not discussed in detail, and it is difficult to assess the significance. However, since the alteration assemblages at both deposits are similar, it is possible they formed under similar conditions.

	Orogenic	Carlin-type	Mount Olympus
Temperature and pressure	200–650°C 0.5–5 kb	180–240°C 0.5–1 kb	<350°C 1–2 kb
Major host rocks	greenstones and turbidites	shelf carbonate with high carbon content	deltaic deposits and shelf carbonated with high carbon content
Alteration	sericite, quartz, carbonate	illitic sericite, quartz, jasperoid and removal of carbonate	illitic sericite, quartz, removal of carbonate
Gold form	abundant free gold; minor solid solution in pyrite	solid solution in pyrite	solid solution in pyrite; rare free gold in cracks and fractures
Trace element associations	Au, Ag, As, Te, Sb, W, S	Au, As, Sb, Cu, Tl, Hg	Au, As, Cu, Sb, Hg, Tl
Quartz veining	abundant	absent	rare; within the Zoe Fault
gold sitting	dominantly quartz veins	areas of increased porosity and permeability (faults, hinge zones of anticlines, lithological contacts, etc.)	areas of increased porosity and permeability (e.g. Zoe Fault, porous conglomerate and sandstone)
tectonic setting	compressional	mildly extensional	strike slip transpressional, compressional?
Age of mineralization	>3.0 Ga, ca. 2.8–2.55 Ga, ca. 2.1–1.8 Ga	42–36 Ma	ca. 1.7 Ga

Table 4-3: Comparison between Orogenic, Carlin-type and Mount Olympus ores.

Trace element distribution maps of pyrite from Mount Olympus show geochemical similarities to the Carlin deposits of Nevada (e.g. Large et al., 2009). The relationships between Au–As, Au–Ni and Au–V for pyrites with enriched Au–As rim zones within strata-bound mineralization (MOD13), and the internal growth zones within py3 from the Zoe Fault mineralization (NMOD002) show similar compositions to the Carlin deposits. Gold forms a positive relationship with As with all data plotting below the gold saturation line defined by Reich et al., (2005) indicating that invisible gold is locked in the pyrite crystal lattice (Figure 4-12a). Au–As enriched rims (MOD13), and internal bands in py3 (NMOD002) have the same composition as the hydrothermal ores of the Carlin deposits (Figure 4-12a) as defined by Large et al., (2009). The rims however, are much thicker and of lower grade (up to 429 ppm Au) compared to those in the Carlin deposits (up to 2000 ppm Au). A similar association between Au–Ni and Au–V exists with a negative relationship between Ni and V to Au for mineralized

pyrite (py3 internal zone and MOD13 rims) which is comparable to the hydrothermal Carlin ores (Figure 4-12b and c). Additionally, trace element distributions within py3 are identical to those at Carlin with elevated Au, As, Cu, Sb, Hg and Tl (Large et al., 2009).

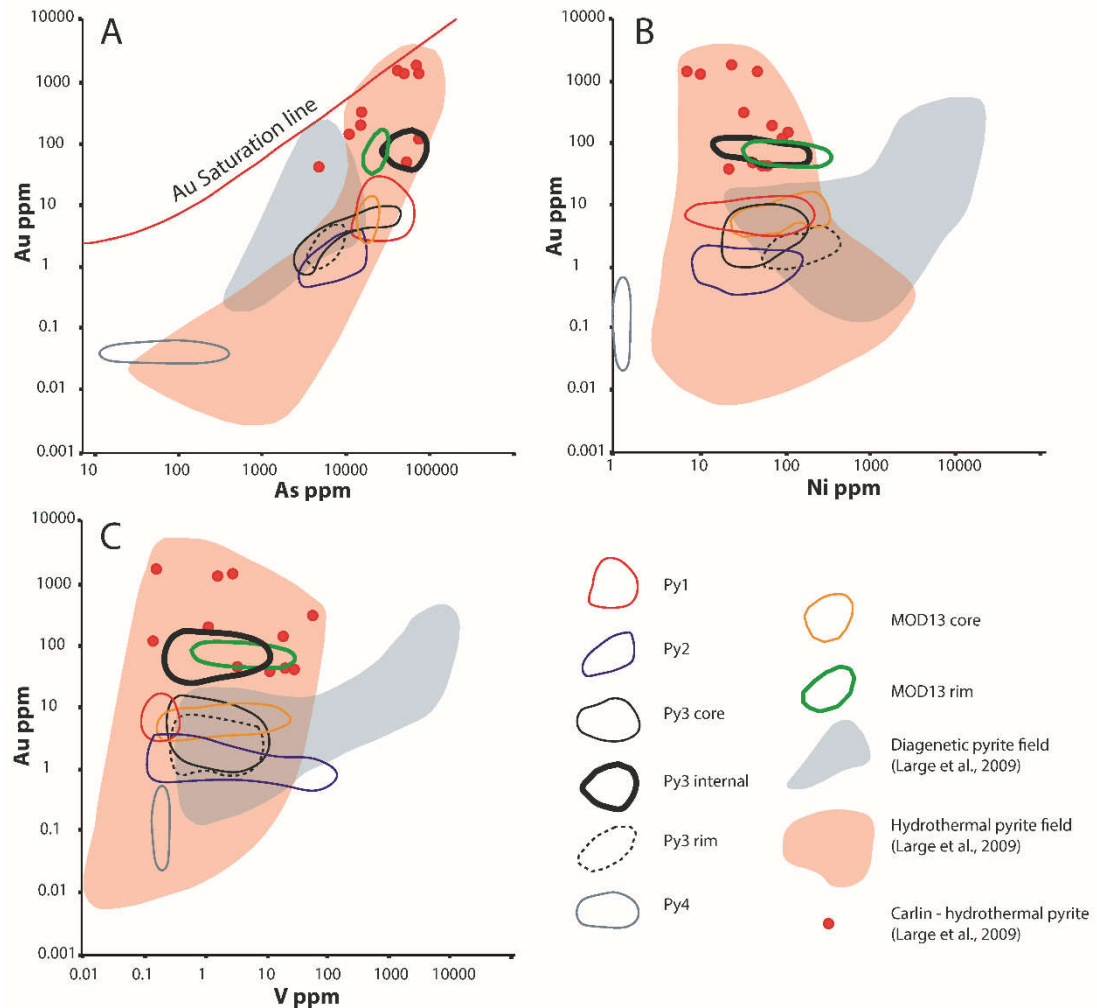


Figure 4-12. Binary plots showing comparisons of trace element concentrations in pyrite between Carlin (Large et al., 2009) and Mount Olympus mineralization. A) Au-As; B) Au-Ni and C) Au-V.

Our results indicate that all of the characteristic features of the Mount Olympus deposit are significantly different from orogenic gold deposits, including those in the northern Capricorn Orogen, where mineralization is associated with the emplacement of laminated auriferous quartz–carbonate–pyrite veins, abundant native gold, and introduction of carbonate minerals during ore-stage hydrothermal alteration (Table 4-3; Groves et al., 1998; Fielding et al., 2017). Here we reclassify the Mount Olympus deposit as a Carlin-like deposit since it has many (but not all) characteristics in common with the Carlin-type deposits of Nevada (Table 4-3).

4.7.2. TIMING OF GOLD MINERALIZATION

Trace element mapping of pyrite from the Zoe fault (NMOD002 py1–4) and strata-bound (MOD13) mineralization indicates that gold forms in a solid solution within Au–As-rich arsenian pyrite. Results suggest that py1 and py2 have compositions (Au–As, Au–Ni and Au–V ratios) similar to diagenetic pyrite (Figure 4-12; Large et al., 2009). This is consistent with their form as crystal aggregates which occur as discontinuous layers and lenses within carbonaceous-rich layers with elevated U, V, Mo and Al content (Figure 4-3). Although these pyrites are enriched in gold (mean Au py1 = 8 ppm and py2 = 2 ppm) the majority of the gold forms as diffusive Au–As-enriched rims within strata-bound mineralization (MOD13, mean Au of 55 ppm), or in Au–As-enriched internal growth zones in py3 (NMOD002; mean Au of 67 ppm) within the Zoe fault mineralization. LA-ICP-MS images of pyrite with diffusive Au–As rims (MOD13) have comparable Au–As, Au–Ni and Au–V relationships to those of the Carlin-type ores, and to Au–As enriched internal zone of py3 which have the same geochemical element associations to Carlin-type ores (Figure 4-12). Dating of hydrothermal xenotime intergrown with ore-stage alteration minerals and arsenian pyrite (Figure 4-9c) within strata-bound ore from diamond drill core MOD13 yields a date of 1769 ± 5 Ma, representing the timing of hydrothermal gold mineralization.

4.7.3. SETTING OF MINERALIZATION

The Mount Olympus deposit is located on the Zoe Fault, a second order splay of the Nanjilgardy Fault, which is a crustal-scale structure (Johnson et al., 2013). The timing of gold mineralization at ca. 1770 Ma lies at the younger end of the age range for the intracratonic 1820–1770 Ma Capricorn Orogeny (Sheppard et al., 2010), a time that represents a distinct change in tectonic regime, from predominantly northeast compression to north–northwest stresses producing dextral strike-slip reactivation of the Nanjilgardy Fault (Krapež, 1999; Young et al., 2003). Furthermore, xenotime growth dated at ca. 1730 Ma (from this study and by Şener et al. (2005)) and at ca. 1675 Ma is also contemporaneous with hydrothermal monazite and xenotime growth at the Paulsens gold mine located 150 km to the northwest (Fielding et al., 2017) and during the early stages of the 1680–1620 Ma Mangaroon Orogeny (Sheppard et al., 2005). These events are also thought to reflect the timing of punctuated reactivation on the Nanjilgardy Fault and associated hydrothermal fluid flow. These data indicate that gold mineralization at Mount Olympus occurred in an intracratonic setting, during

low- to medium- grade metamorphism and was facilitated by the focusing of hydrothermal fluids along a major crustal structure.

4.7.4. REGIONAL-SCALE DRIVERS TO MINERAL SYSTEMS

Despite the notion that orogenic, epithermal and Carlin-type gold deposits may represent a continuum of deposit types (Huston et al., 2016), with their individual characteristics defined principally by processes operating at the smallest-scales of the mineral system (Nesbitt, 1988; Dill, 2010; Robert et al., 2007; Brauhart et al., 2017), the data presented here demonstrate that there are distinct large-scale drivers for the three deposit types. Whereas orogenic gold deposits are driven by high-energy, plate margin processes associated with accretionary or collisional tectonics (Groves et al., 1998; Goldfarb et al., 2001), and epithermal deposits are driven by regional-scale magmatic processes (e.g. Simmons et al., 2005), Carlin-type deposits may form in a variety of settings (Hu et al., 2002; Cline et al., 2005; Muntean et al., 2011), provided there is an appropriate energy source (orogeny or magmatism) and favourable architecture (crustal-scale faults). The juxtaposition of tectonic blocks during collisional and accretionary orogenesis commonly results in the generation of orogenic belts that contain numerous crustal-scale structures and suture zones (Cook and Erdmer, 2005; Johnson et al., 2013). Since these belts are particularly susceptible to reactivation, they may not only contain orogenic gold deposits associated with the original collisional/accretion phase (Fielding et al., 2017), but also overprinting Carlin-like gold events. Without precise geochronology, it is not possible to unravel the difference in timing and setting of these deposits, particularly in areas where the deposits have been overprinted by subsequent hydrothermal or mineralizing events.

4.8. CONCLUSIONS

Although previous researchers noted similarities between the Mount Olympus deposit and the Carlin-type deposits of Nevada (Young et al., 2003), Mount Olympus was classified as an orogenic gold deposit, largely due to the interpretation that xenotime growth at ca. 1738 Ma was related to the assembly of Proterozoic Australia (Şener et al., 2005). At a regional scale, the deposit also does not share the characteristics of an orogenic deposit, as it formed during the waning stages of the intracratonic 1820–1770 Ma Capricorn Orogeny far from any active continental margin and after the cessation

of all felsic magmatism associated with this event (Sheppard et al., 2010). The data presented here uphold the division in hydrothermal gold types (orogenic, epithermal and Carlin) indicating that, at a mineral system level, the regional-scale drivers for each are different. Although many gold deposits worldwide are associated with collisional or accretionary orogenesis (Goldfarb et al., 2001), substantial gold deposits such as Carlin-like gold deposits can form in an intracratonic setting during regional-scale crustal reworking.

4.9. ACKNOWLEDGMENTS

This project was funded through an ARC linkage grant (LP130100922) and industry scholarship by Northern Star Resources as a part of a PhD by I. O. H. Fielding. S. P. Johnson publishes with the permission of the director of the Geological Survey of Western Australia. Xenotime analyses were carried out on the Sensitive High Resolution Ion Micro Probe mass spectrometer (SHRIMP II) at the John de Laeter Centre, Curtin University, with the financial support of the Australian Research Council and Auscope NCRIS. Pyrite trace element maps and images were analyzed by researchers at CODES, University of Tasmania and were funded through AMIRA P1041 sponsored by AngloGold Ashanti Limited, G-Resources Group, Issara Mining Limited, Newcrest Mining Limited, Newmont USA Limited, Northern Star Resources Ltd, Sipa Resources Limited. We thank an anonymous reviewer for the helpful comments.

4.10. REFERENCES

- Arehart, G. B., 1996, Characteristics and origin of sediment-hosted disseminated gold deposits: a review: *Ore Geology Reviews*, v. 11, no. 6, p. 383-403.
- Berger, B. R., and Bagby, W. C., 1991, The geology and origin of Carlin-type gold deposits, *Gold metallogeny and exploration*: Boston, MA, Springer US, p. 210-248.
- Brauhart, C. W., Grunsky, E. C., and Hagemann, S. G., 2017, Magmato-hydrothermal space: A new metric for geochemical characterisation of metallic ore deposits: *Ore Geology Reviews*, v. 86, p. 867–895.

- Cline, J. S., Hofstra, A. H., Muntean, J. L., Tosdal, R. M., and Hickey, K. A., 2005, Carlin-type gold deposits in Nevada: Critical geologic characteristics and viable models: *Economic Geology 100th Anniversary Volume*, p. 451–484.
- Cook, F., and Erdmer, P., 2005, An 1800 km cross section of the lithosphere through the northwestern North American plate: lessons from 4.0 billion years of Earth's history: *Canadian Journal of Earth Sciences*, v. 42, no. 6, p. 1295–1311.
- Danyushevsky, L., Robinson, P., Gilbert, S., Norman, M., Large, R., McGoldrick, P., and Shelley, M., 2011, Routine quantitative multi-element analysis of sulphide minerals by laser ablation ICP-MS: Standard development and consideration of matrix effects: *Geochemistry: Exploration, Environment, Analysis*, v. 11, no. 1, p. 51–60.
- Dill, H. G., 2010, The “chessboard” classification scheme of mineral deposits: Mineralogy and geology from aluminum to zirconium: *Earth-Science Reviews*, v. 100, no. 1, p. 1–420.
- Fielding, I. O. H., Johnson, S. P., Zi, J.-W., Rasmussen, B., Muhling, J. R., Dunkley, D. J., Sheppard, S., Wingate, M. T. D., and Rogers, J. R., 2017, Using In Situ SHRIMP U-Pb monazite and xenotime geochronology to determine the age of orogenic gold mineralization: an example from the Paulsens Mine, Southern Pilbara Craton: *Economic Geology*, v. 112, no. 5, p. 1205–1230.
- Fletcher, I. R., McNaughton, N. J., Aleinikoff, J. A., Rasmussen, B., and Kamo, S. L., 2004, Improved calibration procedures and new standards for U–Pb and Th–Pb dating of Phanerozoic xenotime by ion microprobe: *Chemical Geology*, v. 209, no. 3–4, p. 295–314.
- Fletcher, I. R., Rasmussen, B., and McNaughton, N. J., 2000, SHRIMP U–Pb geochronology of authigenic xenotime and its potential for dating sedimentary basins: *Australian Journal of Earth Sciences*, v. 47, no. 5, p. 845–859.
- Goldfarb, R. J., and Groves, D. I., 2015, Orogenic gold: Common or evolving fluid and metal sources through time: *Lithos*, v. 233, p. 2–26.
- Goldfarb, R. J., Groves, D. I., and Gardoll, S., 2001, Orogenic gold and geologic time: a global synthesis: *Ore Geology Reviews*, v. 18, no. 1–2, p. 1–75.
- Groves, D. I., Goldfarb, R. J., Gebre-Mariam, M., Hagemann, S. G., and Robert, F., 1998, Orogenic gold deposits: A proposed classification in the context of their crustal distribution and relationship to other gold deposit types: *Ore Geology Reviews*, v. 13, no. 1–5, p. 7–27.
- Groves, D. I., Goldfarb, R. J., Robert, F., and Hart, C. J. R., 2003, Gold deposits in metamorphic belts: Overview of current understanding, outstanding problems, future research, and exploration significance: *Economic Geology*, v. 98, no. 1, p. 1–29.
- Hronsky, J. M., Groves, D. I., Loucks, R. R., and Begg, G. C., 2012, A unified model for gold mineralisation in accretionary orogens and implications for regional-

- scale exploration targeting methods: *Mineralium Deposita*, v. 47, no. 4, p. 339–358.
- Hu, R.-Z., Su, W.-C., Bi, X.-W., Tu, G.-Z., and Hofstra, A. H., 2002, Geology and geochemistry of Carlin-type gold deposits in China: *Mineralium Deposita*, v. 37, p. 378–392.
- Huston, D. L., Mernagh, T. P., Hagemann, S. G., Doublier, M. P., Fiorentini, M., Champion, D. C., Lynton Jaques, A., Czarnota, K., Cayley, R., Skirrow, R., and Bastrakov, E., 2016, Tectono-metallogenic systems — The place of mineral systems within tectonic evolution, with an emphasis on Australian examples: *Ore Geology Reviews*, v. 76, p. 168–210.
- Johnson, S. P., Korhonen, F. J., Kirkland, C. L., Cliff, J. B., Belousova, E. A., and Sheppard, S., 2017, An isotopic perspective on growth and differentiation of Proterozoic orogenic crust: From subduction magmatism to cratonization: *Lithos*, v. 268–271, p. 76–86.
- Johnson, S. P., Sheppard, S., Rasmussen, B., Wingate, M. T. D., Kirkland, C. L., Muhling, J. R., Fletcher, I. R., and Belousova, E. A., 2011, Two collisions, two sutures: Punctuated pre-1950 Ma assembly of the West Australian Craton during the Ophthalmian and Glenburgh Orogenies: *Precambrian Research*, v. 189, no. 3–4, p. 239–262.
- Johnson, S. P., Thorne, A. M., Tyler, I. M., Korsch, R. J., Kennett, B. L. N., Cutten, H. N., Goodwin, J., Blay, O., Blewett, R. S., Joly, A., Dentith, M. C., Aitken, A. R. A., Holzschuh, J., Salmon, M., Reading, A., Heinson, G., Boren, G., Ross, J., Costelloe, R. D., and Fomin, T., 2013, Crustal architecture of the Capricorn Orogen, Western Australia and associated metallogeny: *Australian Journal of Earth Sciences*, v. 60, no. 6–7, p. 681–705.
- Korhonen, F. J., Johnson, S. P., Wingate, M. T. D., Kirkland, C. L., Fletcher, I. R., Dunkley, D. J., Roberts, M. P., Sheppard, S., Muhling, J. R., and Rasmussen, B., 2017, Radiogenic heating and craton-margin plate stresses as drivers for intrplate orogeny: *Journal of Metamorphic Geology*, v. 35, p. 631–661.
- Krapež, B., 1999, Stratigraphic record of an Atlantic-type global tectonic cycle in the Palaeoproterozoic Ashburton Province of Western Australia: *Australian Journal of Earth Sciences*, v. 46, no. 1, p. 71–87.
- Krapež, B., Müller, S. G., and Bekker, A., 2015, Stratigraphy of the Late Palaeoproterozoic (~2.03 Ga) Woolly Dolomite, Ashburton Province, Western Australia: A carbonate platform developed in a failed rift basin: *Precambrian Research*, v. 271, p. 1–19.
- Large, R. R., Danyushevsky, L., Hollit, C., Maslennikov, V., Meffre, S., Gilbert, S., Bull, S., Scott, R., Emsbo, P., Thomas, H., Singh, B., and Foster, J., 2009, Gold and trace element zonation in pyrite using a laser imaging technique: implications for the timing of gold in orogenic and Carlin-Style sediment-hosted deposits: *Economic Geology*, v. 104, no. 5, p. 635–668.

- Ludwig, K. R., 2003, Isoplot/Ex version 3.00, A geochronological toolkit for Microsoft Excel: Berkeley Geochronology Centre Special Publication No. 4, 73 p.
- Ludwig, K. R., 2009, Squid 2.50, a user's manual: Berkeley Geochronology Centre, Berkeley, California, USA, 95 p.
- McCuaig, T. C., and Hronsky, J. M. A., 2014, The mineral systems concept: The key to exploration targeting in Kelly, K. D., and Golden, H. C., ed., Building Exploration Capability for the 21st Century, Society of Economic Geologists: Special Publication 18, p. 153–175.
- Morant, P., and Doepel, G., 1997, The Mount Olympus Gold Deposit: New Generation Gold Mines '97, Perth, Western Australia, Australian Mineral Foundation, p. 6.1–6.9.
- Muntean, J. L., Cline, J. S., Simon, A. C., and Longo, A. A., 2011, Magmatic-hydrothermal origin of Nevada's Carlin-type gold deposits: *Nature Geoscience*, v. 4, no. 2, p. 122–127.
- Nesbitt, B. E., 1988, Gold deposit continuum: A genetic model for lode Au mineralization in the continental crust: *Geology*, v. 16, no. 11, p. 1044–1048.
- Northern Star Resources Limited, 2015, Northern Star Resources Limited 2015 annual report, (<http://www.nsrltd.com/wp-content/uploads/2015/08/NST-Annual-Report-2015-26-8-2015-new-cover1.pdf>).
- Rasmussen, B., Sheppard, S., and Fletcher, I. R., 2006, Testing ore deposit models using in situ U-Pb geochronology of hydrothermal monazite: Paleoproterozoic gold mineralization in northern Australia: *Geology*, v. 34, no. 2, p. 77–80.
- Reich, M., Kesler, S. E., Utsunomiya, S., Palenik, C. S., Chrysosoulis, S. L., and Ewing, R. C., 2005, Solubility of gold in arsenian pyrite: *Geochimica et Cosmochimica Acta*, v. 69, no. 11, p. 2781–2796.
- Robert, F., Brommecker, R., Bourne, B. T., Dobak, P. J., McEwan, C. J., Rowe, R. R., and AZhou, X., 2007, Models and Exploration Methods for Major Gold Deposit Types in Milkereit, B., ed., Exploration 07, Fifth Decennial International Conference on Mineral Exploration, Toronto, Canada, Decennial Mineral Exploration Conferences, p. 691–711.
- Şener, A. K., Young, C., Groves, D. I., Krapež, B., and Fletcher, I. R., 2005, Major orogenic gold episode associated with Cordilleran-style tectonics related to the assembly of Paleoproterozoic Australia?: *Geology*, v. 33, p. 225–228.
- Sheppard, S., Rasmussen, B., Muhling, J. R., Farrell, T. R., and Fletcher, I. R., 2007, Grenvillian-aged orogenesis in the Palaeoproterozoic Gascoyne Complex, Western Australia: 1030–950 Ma reworking of the Proterozoic Capricorn Orogen: *Journal of Metamorphic Geology*, v. 25, p. 477–494.

-
- Sheppard, S., Occhipinti, S. A., and Nelson, D. R., 2005, Intracontinental reworking in the Capricorn Orogen, Western Australia: the 1680–1620 Ma Mangaroon Orogeny: *Australian Journal of Earth Sciences*, v. 52, p. 443–460.
- Sheppard, S., Bodorkos, S., Johnson, S. P., Wingate, M. T. D., and Kirkland, C. L., 2010, The Paleoproterozoic Capricorn Orogeny: intracontinental reworking not continent–continent collision, Geological Survey of Western Australia, Report 108, 33 p.
- Simmons, S. F., White, N. C., and John, D. A., 2005, Geological characteristics of epithermal precious and base metal deposits, in Hedenquist, J. W., Thompson, J. F. H., Goldfarb, R. J., and Richards, J. P., ed., *Economic Geology 100th Anniversary Volume*, Society of Economic Geologists p. 485–522.
- Stacey, J. S., and Kramers, J. D., 1975, Approximation of terrestrial lead isotope evolution by a two-stage model: *Earth and Planetary Science Letters*, v. 26, p. 207–221.
- Stern, R. A., and Rayner, N., 2003, Ages of several xenotime megacrysts by ID-TIMS: potential reference materials for ion microprobe U-Pb geochronology: *Radiogenic Age and Isotopic Studies: Report 16: Geological Survey of Canada: Current Research 2003-F1*, 7 p.
- Teal, L., and Jackson, M., 2002, Geologic overview of the Carlin trend gold deposits: Gold deposits of the Carlin trend. Nevada Bureau of Mines and Geology, Bulletin, v. 111, p. 9-19.
- Thorne, A. M., and Seymour, D. B., 1991, Geology of the Ashburton Basin Western Australia, Geological Survey of Western Australia, Bulletin 139, 162 p.
- Tyler, I. M., and Thorne, A. M., 1990, The northern margin of the Capricorn Orogen, Western Australia—an example of an Early Proterozoic collision zone: *Journal of Structural Geology*, v. 12, p. 685–701.
- Wells, M., Laukamp, C., and Hancock, E. A., 2016, Reflectance spectroscopic characterisation of mineral alteration footprints associated with sediment-hosted gold mineralisation at Mt Olympus (Ashburton Basin, Western Australia): *Australian Journal of Earth Sciences*, v. 63, p. 987–1002.
- Wyborn, L. A. I., Heinrich, C. A., and Jaques, A. L., 1994, Australian Proterozoic mineral systems: essential ingredients and mappable criteria, in Hallenstein, P. C., ed., *Australian mining looks north — the challenges and choices*. Australian Institute of Mining and metallurgy; 1994 AUSIMM Annual Conference, Darwin, Northern Territory, p. 109–115.
- Young, C. J., Groves, D. I., and Morant, P., 2003, Sediment-hosted disseminated gold mineralisation in the Palaeoproterozoic Ashburton Province, Western Australia: a new epizonal orogenic gold province related to Capricorn Orogeny?, in Eliopoulos et al., ed., *Mineral exploration and sustainable development, proceedings of the 7th Biennial SGA Meeting*, Athens, Greece, Millpress, p. 835–838
-

4.11. SUPPLEMENTARY DATA

4.11.1. DATA TABLES

Supplementary Table 4-1: SHRIMP U–Pb xenotime results, GSWA 219594 Zoe Fault mineralization

<i>Mount no.</i>	<i>Grain spot</i>	<i>U (ppm)</i>	<i>Th (ppm)</i>	<i>Th/U</i>	<i>f206 (%)</i>	<i>²⁰⁷Pb*/²⁰⁶Pb*</i>	<i>± 1σ</i>	<i>²⁰⁶Pb*/²³⁸U</i>	<i>± 1σ</i>	<i>²⁰⁷Pb*/²³⁵U</i>	<i>± 1σ</i>	<i>²⁰⁸Pb*/²³²Th</i>	<i>± 1σ</i>	<i>Disc. (%)</i>	<i>²⁰⁷Pb*/²⁰⁶Pb* age (Ma)</i>	<i>± 1σ (Ma)</i>
Group 1 (1768 ± 8 Ma)																
1704	F.3-1	1747	2545	1.5	0.04	0.1100	0.0014	0.351	0.012	5.32	0.19	0.078	0.011	-8	1799	24
1704	H.1-3	1388	1318	0.9	0.01	0.1093	0.0007	0.296	0.004	4.46	0.07	0.090	0.009	6	1788	12
1704	I.1-1	1492	1275	0.9	0.05	0.1085	0.0007	0.305	0.007	4.56	0.10	0.091	0.010	3	1774	12
1705	I.1-2	1627	2152	1.3	0.16	0.1084	0.0006	0.313	0.004	4.67	0.07	0.090	0.010	1	1772	11
1704	E.1-1	1465	4320	2.9	0.04	0.1081	0.0007	0.297	0.004	4.43	0.07	0.091	0.009	5	1767	12
1704	J.2-1	1879	2508	1.3	0.07	0.1077	0.0010	0.316	0.004	4.69	0.08	0.084	0.010	0	1761	17
1704	J.1-1	1540	2490	1.6	0.12	0.1075	0.0007	0.292	0.006	4.33	0.10	0.084	0.009	6	1757	12
1704	A.1-1	2746	2849	1.0	0.01	0.1074	0.0006	0.301	0.004	4.47	0.06	0.091	0.010	3	1756	10
1704	G.1-1	2477	722	0.3	0.03	0.1071	0.0008	0.293	0.005	4.32	0.08	0.085	0.009	5	1750	14
Group 2 (1727 ± 8 Ma)																
1704	F.2-1	1915	392	0.2	0.03	0.1069	0.0007	0.302	0.004	4.45	0.07	0.058	0.010	3	1747	11
1704	H.1-1	1117	1671	1.5	0.07	0.1068	0.0008	0.294	0.005	4.32	0.08	0.089	0.010	5	1746	14
1704	K.1-1	1627	3650	2.2	0.04	0.1062	0.0008	0.323	0.007	4.73	0.11	0.096	0.010	-4	1735	14
1705	I.1-1	1053	2549	2.4	0.05	0.1061	0.0009	0.317	0.005	4.64	0.09	0.095	0.010	-2	1734	16
1705	H.3-1	2169	472	0.2	0.02	0.1058	0.0007	0.306	0.004	4.46	0.07	0.079	0.010	0	1728	12
1704	C.1-1	1550	1631	1.1	0.13	0.1056	0.0008	0.283	0.004	4.12	0.07	0.076	0.009	7	1724	13
1704	H.1-2	1144	1240	1.1	0.04	0.1054	0.0008	0.300	0.005	4.35	0.07	0.086	0.010	2	1721	13
1704	D.1-1	1808	4735	2.6	0.00	0.1049	0.0011	0.318	0.010	4.60	0.15	0.102	0.010	-4	1713	19

1704	E.2-1	2008	4459	2.2	0.07	0.1048	0.0006	0.288	0.004	4.17	0.06	0.080	0.010	5	1711	11
1705	H.1-1	1304	1171	0.9	0.14	0.1047	0.0009	0.303	0.005	4.37	0.08	0.086	0.010	0	1709	15
Group 3 (1671 ± 18 Ma)																
1704	L.1-2	1082	8441	7.8	0.01	0.1028	0.0007	0.274	0.006	3.88	0.09	0.080	0.009	7	1675	13
1704	B.1-1	1443	3309	2.3	0.05	0.1024	0.0007	0.279	0.006	3.94	0.09	0.080	0.010	5	1668	13
Discordance >10%																
1704	L.1-1	1789	1050	0.6	0.46	0.1104	0.0014	0.215	0.016	3.27	0.24	0.075	0.007	30	1806	23
1704	G.1-2	2635	2397	0.9	0.22	0.1075	0.0011	0.178	0.003	2.65	0.05	0.069	0.006	40	1758	19
1704	E.1-2	4638	3519	0.8	0.40	0.1146	0.0020	0.152	0.004	2.40	0.08	0.054	0.005	51	1873	32
Poor spot placement																
1705	H.2-1	1374	917	0.7	0.28	0.1127	0.0056	0.311	0.005	4.83	0.27	0.074	0.009	5	1844	89
1704	F.1-1	2189	1968	0.9	0.70	0.1129	0.0076	0.303	0.006	4.71	0.35	0.087	0.009	8	1847	122

Pb* indicates radiogenic

Pb.f206 is the proportion of common Pb in ^{206}Pb , determined using the measured $^{204}\text{Pb}/^{206}\text{Pb}$ and a common Pb composition from the Stacey and Kramers (1975) model at the approximate age of the sample.

Disc. Is apparent discordance, as $100(t[^{207}\text{Pb}^*/^{206}\text{Pb}^*] - t[^{238}\text{U}/^{206}\text{Pb}^*]) / t[^{207}\text{Pb}^*/^{206}\text{Pb}^*]$.

Same footnote applies to Supplementary Tables 4-1 to 4-3

Supplementary Table 4-2: SHRIMP U-Pb xenotime results, GSWA 209985 strata bound mineralization - siltstone (2.67 ppm Au)

<i>Mount no.</i>	<i>Grain spot</i>	<i>U (ppm)</i>	<i>Th (ppm)</i>	<i>Th/U</i>	<i>f206 (%)</i>	<i>²⁰⁷Pb*/²⁰⁶Pb*</i>	<i>± 1σ</i>	<i>²⁰⁶Pb*/²³⁸U</i>	<i>± 1σ</i>	<i>²⁰⁷Pb*/²³⁵U</i>	<i>± 1σ</i>	<i>²⁰⁸Pb*/²³²Th</i>	<i>± 1σ</i>	<i>Disc. (%)</i>	<i>²⁰⁷Pb*/²⁰⁶Pb* age (Ma)</i>	<i>± 1σ (Ma)</i>
Group 1 (1770 ± 7 Ma)																
1602	10-1	4353	25774	5.9	0.10	0.1088	0.0013	0.300	0.007	4.50	0.13	0.087	0.009	5	1779	22
1602	3-1	2597	14060	5.4	0.28	0.1090	0.0009	0.302	0.006	4.53	0.11	0.100	0.010	5	1783	16
1602	9-1	2853	16426	5.8	0.00	0.1082	0.0008	0.304	0.005	4.53	0.09	0.086	0.010	3	1769	13
1602	17-1	2861	16796	5.9	0.55	0.1095	0.0026	0.314	0.006	4.74	0.16	0.091	0.010	2	1791	44
1602	13-1	3695	22984	6.2	0.03	0.1081	0.0007	0.310	0.006	4.63	0.09	0.090	0.010	1	1768	13
1602	15-1	2723	16850	6.2	0.04	0.1085	0.0005	0.312	0.006	4.66	0.09	0.090	0.010	1	1774	9
1602	1-1	2093	12552	6.0	0.10	0.1091	0.0006	0.321	0.006	4.83	0.09	0.093	0.010	-1	1784	11
1602	7-1	1716	9656	5.6	0.02	0.1092	0.0006	0.323	0.006	4.86	0.10	0.094	0.010	-1	1786	10
1602	8-1	2350	12964	5.5	0.03	0.1090	0.0006	0.325	0.008	4.88	0.12	0.094	0.010	-2	1783	10
1602	11-1	2121	12127	5.7	0.07	0.1076	0.0006	0.320	0.006	4.75	0.09	0.093	0.010	-2	1759	10
1602	16-1	1564	8925	5.7	0.10	0.1060	0.0007	0.317	0.006	4.63	0.10	0.091	0.010	-2	1731	13
1602	14-1	2676	15053	5.6	0.09	0.1078	0.0006	0.326	0.008	4.85	0.12	0.094	0.010	-3	1763	10
1602	12-1	1630	9494	5.8	0.21	0.1088	0.0008	0.334	0.006	5.01	0.10	0.098	0.010	-4	1779	14
1602	2-1	2098	14074	6.7	0.12	0.1068	0.0007	0.330	0.009	4.87	0.14	0.095	0.011	-5	1746	13
1602	6-1	1656	7402	4.5	0.05	0.1087	0.0008	0.338	0.006	5.06	0.10	0.098	0.011	-6	1777	13
1602	5-1	4190	21590	5.2	0.06	0.1078	0.0009	0.336	0.008	4.99	0.12	0.099	0.011	-6	1763	15
1602	4-1	1118	5724	5.1	0.02	0.1084	0.0008	0.340	0.007	5.09	0.11	0.097	0.011	-7	1773	13
Discordance >10%																
1603	A.1-1	1603	4323	2.7	0.15	0.1086	0.0008	0.358	0.007	5.36	0.11	0.098	0.011	-11	1776	14
1603	E.2-1	2685	4395	1.6	0.06	0.1071	0.0012	0.355	0.010	5.25	0.16	0.102	0.011	-12	1751	20
1603	E.1-1	1889	2868	1.5	0.08	0.1066	0.0008	0.379	0.007	5.56	0.11	0.108	0.012	-19	1741	13

Supplementary Table 4-3: SHRIMP U–Pb xenotime results, GSWA 219595 strata bound mineralization - conglomerate

<i>Mount no.</i>	<i>Grain spot</i>	<i>U (ppm)</i>	<i>Th (ppm)</i>	<i>Th/U</i>	<i>f206 (%)</i>	<i>²⁰⁷Pb*/²⁰⁶Pb*</i>	<i>± 1σ</i>	<i>²⁰⁶Pb*/²³⁸U</i>	<i>± 1σ</i>	<i>²⁰⁷Pb*/²³⁵U</i>	<i>± 1σ</i>	<i>²⁰⁸Pb*/²³²Th</i>	<i>± 1σ</i>	<i>Disc, (%)</i>	<i>²⁰⁷Pb*/²⁰⁶Pb* age (Ma)</i>	<i>± 1σ (Ma)</i>
Group 1 (1764 ± 11 Ma)																
1705	G.1-1	4211	2103	0.5	0.00	0.1080	0.0006	0.312	0.004	4.65	0.07	0.091	0.010	1	1767	9
1705	D.2-4	882	1424	1.6	0.46	0.1080	0.0019	0.298	0.005	4.43	0.11	0.088	0.010	5	1765	31
1705	B.1-1	761	1038	1.4	0.00	0.1079	0.0013	0.316	0.008	4.71	0.13	0.093	0.010	0	1765	22
1705	C.3-1	4150	5350	1.3	0.00	0.1078	0.0006	0.316	0.004	4.69	0.07	0.091	0.010	0	1763	10
1705	A.3-1	514	1124	2.2	0.00	0.1078	0.0015	0.287	0.007	4.27	0.13	0.086	0.009	8	1763	25
1705	J.2-1	1284	1339	1.0	0.06	0.1078	0.0011	0.297	0.006	4.42	0.10	0.089	0.010	5	1762	19
1705	A.2-1	549	1441	2.6	0.31	0.1072	0.0019	0.295	0.008	4.36	0.14	0.088	0.010	5	1752	33
Group 2 (1727 ± 13 Ma)																
1705	C.1-1	877	1760	2.0	0.04	0.1069	0.0013	0.293	0.007	4.31	0.11	0.086	0.009	5	1748	22
1705	C.2-1	2257	2631	1.2	0.06	0.1063	0.0008	0.307	0.005	4.51	0.08	0.090	0.010	0	1737	14
1705	B.2-1	756	1145	1.5	0.37	0.1063	0.0011	0.324	0.006	4.74	0.10	0.092	0.010	-4	1737	20
1705	J.1-1	1030	1323	1.3	0.02	0.1063	0.0012	0.276	0.004	4.05	0.08	0.080	0.009	9	1737	21
1705	A.4-1	643	869	1.4	0.08	0.1058	0.0011	0.289	0.005	4.22	0.08	0.098	0.009	5	1729	18
1705	E.1-1	1112	1751	1.6	0.35	0.1055	0.0016	0.311	0.005	4.52	0.11	0.093	0.010	-1	1723	28
1705	D.2-1	754	1524	2.0	1.09	0.1053	0.0020	0.302	0.006	4.39	0.12	0.089	0.010	1	1719	36
1705	A.5-1	574	1300	2.3	0.23	0.1052	0.0011	0.289	0.005	4.19	0.09	0.083	0.010	5	1718	19
1705	C.5-1	1835	2092	1.1	0.14	0.1044	0.0009	0.304	0.005	4.38	0.08	0.086	0.010	-1	1703	15
Group 3 (1674 ± 12 Ma)																
1705	G.2-1	3961	7552	1.9	0.01	0.1038	0.0005	0.283	0.004	4.05	0.06	0.084	0.009	5	1693	10
1705	F.1-1	622	962	1.5	0.00	0.1033	0.0011	0.280	0.006	3.99	0.10	0.080	0.009	5	1685	20
1705	G.2-2	3485	6417	1.8	-0.01	0.1028	0.0005	0.288	0.004	4.09	0.06	0.084	0.010	3	1675	8
1705	A.1-1	654	1456	2.2	0.52	0.1027	0.0022	0.295	0.013	4.18	0.21	0.089	0.010	0	1674	39
1705	G.2-3	4338	7288	1.7	0.01	0.1026	0.0004	0.288	0.004	4.07	0.06	0.083	0.010	3	1672	8
1705	D.1-1	786	956	1.2	1.10	0.1014	0.0023	0.293	0.006	4.10	0.13	0.084	0.010	0	1651	42

1705	D.2-3	1104	2677	2.4	0.19	0.1014	0.0009	0.294	0.004	4.10	0.07	0.089	0.010	-1	1649	16
1705	D.2-2	724	1614	2.2	0.13	0.1011	0.0009	0.276	0.004	3.85	0.07	0.080	0.010	4	1645	16
Discordance >10%																
1705	A.1-3	805	863	1.1	1.97	0.0888	0.0044	0.333	0.013	4.08	0.26	0.084	0.013	-32	1400	95
1705	B.1-2	890	1106	1.2	0.54	0.1062	0.0013	0.183	0.003	2.68	0.05	0.075	0.006	38	1736	23
Poor spot placement																
1705	C.4-1	2645	3523	1.3	0.32	0.1172	0.0157	0.360	0.011	5.82	0.85	0.092	0.010	-4	1914	240
1705	A.1-2	816	1806	2.2	0.63	0.1070	0.0088	0.291	0.006	4.30	0.39	0.086	0.009	6	1748	151

CHAPTER 5. U–PB DATING OF FAULT REACTIVATION AND GOLD MINERALIZATION IN THE NORTHERN CAPRICORN OROGEN, WESTERN AUSTRALIA

The following chapter has been under review in AUSTRALIAN JOURNAL OF EARTH SCIENCES as of the 12th April, 2018

Imogen O. H. Fielding¹, Simon P. Johnson², Jian-Wei Zi^{3,4}, and Birger Rasmussen^{3,5}, U–Pb dating of fault reactivation and gold mineralization in the northern Capricorn Orogen, Western Australia; Australian Journal of Earth Sciences, under review.

¹ Department of Applied Geology, Curtin University, Kent Street, Bentley, WA 6102, Australia.

² Geological Survey of Western Australia, 100 Plain Street, East Perth, WA 6004, Australia.

³ State Key Lab of Geological Processes and Mineral Resources, China University of Geosciences, Wuhan, 430074, China

⁴ John de Laeter Centre, Curtin University, Kent Street, Bentley, WA 6102, Australia

⁵ School of Earth Sciences, The University of Western Australia, Perth, WA, 6009, Australia

5.1. ABSTRACT

Hydrothermal gold mineralization in the northern Capricorn Orogen of Western Australia has been linked to movement of crustal-scale faults and their associated structures. However, due to limited surface exposures and complex geological histories this link is largely interpretive. In this study we date fault movement by in situ U–Pb SHRIMP geochronology of xenotime intergrown with calcite from a syn-tectonic vein within the Amazon Shear Zone, to demonstrate that hydrothermal activity accompanied fault movement at 1674 ± 54 Ma. This age is within uncertainty of 1672 ± 18 Ma gold mineralization at the Star of the West gold deposit which is located in the Ashburton Basin and associated with a second order structure to the crustal-scale Baring Downs Fault. Together these data indicate that both fault movement and gold mineralization are synchronous and related to the early stages of the 1680–1620 Ma intracratonic Mangaroon Orogeny.

5.2. INTRODUCTION

The Ashburton Basin is located in the northern part of the Capricorn Orogen of Western Australia (Figure 5-1) and is host to numerous gold occurrences associated with major, crustal-scale faults (Johnson et al., 2013). However, only recently has the precise timing of gold mineralization in the northern part of the orogen, and its relationship to the regional-scale tectonothermal evolution, been addressed (e.g. Fielding et al., 2017, 2018, 2019). Both the Baring Downs and Nanjilgardy faults (Figure 5-1), which host most of the mineralization, show evidence for long lived reactivation histories (Johnson et al., 2013; Krapez, 1999; Thorne & Seymour, 1991), although, determining the exact timing and sense of movement for each individual fault reactivation is challenging and not always possible. Prior to this study fault reactivations had been largely interpretive, assuming that the timing of hydrothermal and mineralizing fluids records episodes of fault movement during known, discrete orogenic events (e.g. Fielding et al., 2017, 2018, 2019; Rasmussen, Fletcher, & Muhling, 2007; Rasmussen, Fletcher, Muhling, Thorne, & Broadbent, 2007). In this study, we use in situ U–Pb phosphate geochronology of hydrothermal monazite and xenotime to date the emplacement of a syn-tectonic quartz-calcite vein into the active Amazon Shear Zone, a splay of the Nanjilgardy Fault (Figures 5-1 and 5-2). We also

provide an age for gold mineralization at the Star of the West deposit, which is associated with the emplacement of quartz veins during reactivation of the Baring Downs Fault. Our results demonstrate that gold mineralization was related to the reactivation of crustal-scale faults across the northern Capricorn Orogen during intracratonic reworking.

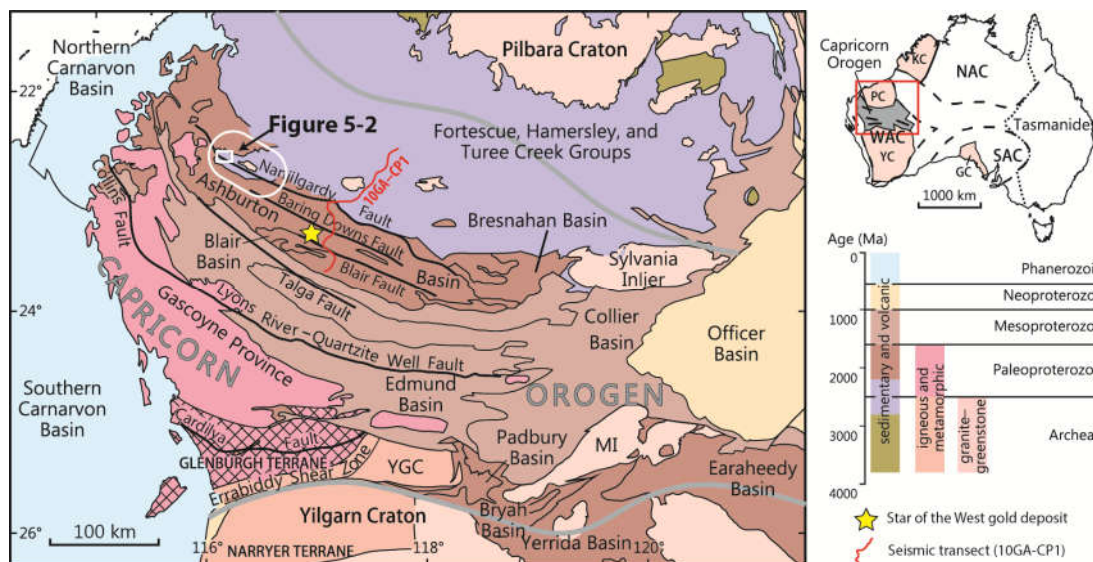


Figure 5-1: Location of the Capricorn Orogen in Western Australia. The white ellipse shows the location of the Wyloo Inlier; white box is the inset location for Figure 5-2; yellow star represents the Star of the West gold deposit location; red line is the 10GA-CP1 seismic line. Abbreviations: GC = Gawler Craton, KC = Kimberley Craton, MI = Marymia Inlier, NAC = North Australian Craton, PC = Pilbara Craton, SAC = South Australian Craton, WAC = West Australian Craton, YC = Yilgarn Craton, YGC = Yarlalweelor Gneiss Complex (after Johnson et al., 2013).

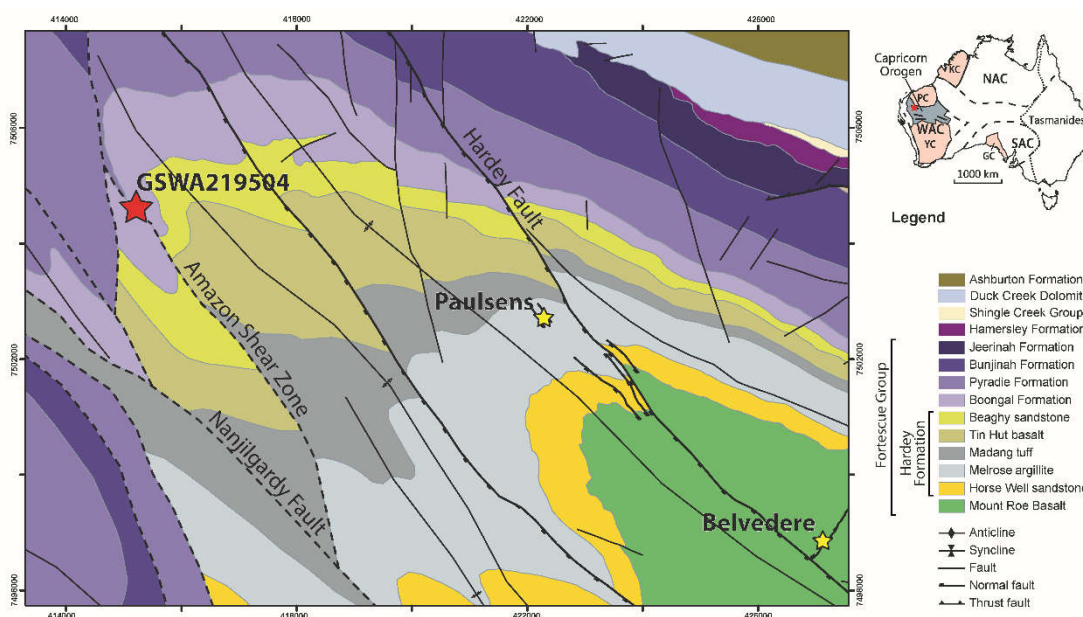


Figure 5-2: Local geology map of the Amazon Shear Zone with sample location for GSWA 219504 and the location of the Belvedere and Paulsens Gold deposits which are associated with the Hardey Fault, a second order structure to the Nanjilgardy Fault.

5.3. GEOLOGICAL SETTING

The Proterozoic Capricorn Orogen is located between the Pilbara and Yilgarn cratons of Western Australia (Figure 5-1). It is a 1000 km long by 500 km wide zone of metamorphism, magmatism and deformation which has been impacted by at least seven orogenic events. The Glenburgh Terrane collided with the Pilbara Craton during the 2215–2145 Ma Ophthalmia Orogeny (Johnson et al., 2011; Rasmussen, Fletcher, & Sheppard, 2005). A second collision between the combined Glenburgh – Pilbara Craton and the Yilgarn Craton occurred during the 2005–1950 Ma Glenburgh Orogeny which marks the assembly of the West Australian Craton (Johnson et al., 2011; Occhipinti, Sheppard, Passchier, Tyler, & Nelson, 2004; Sheppard, Occhipinti, & Tyler, 2004). This is followed by over a billion years of intracratonic reworking, reactivation, metamorphism, magmatism and basin formation (Cawood & Tyler, 2004; Johnson et al., 2013; Korhonen et al., 2017; Martin & Morris, 2010; Sheppard, Occhipinti, & Nelson, 2005; Sheppard, Rasmussen, Muhling, Farrell, & Fletcher, 2007), during the 1820–1770 Ma Capricorn Orogeny (Cawood & Tyler, 2004; Sheppard, Bodorkos, Johnson, Wingate, & Kirkland, 2010), the 1680–1620 Ma Mangaroon Orogeny (Sheppard et al., 2005), the 1321–1171 Ma Mutherbukin Tectonic Event (Korhonen et al., 2017), the 1030–955 Ma Edmondian Orogeny (Martin & Thorne, 2004; Sheppard et al., 2007), and the c. 570 Ma Mulka Tectonic Event (Johnson et al., 2013).

5.4. REGIONAL GEOLOGY

The northern Capricorn Orogen consists of Archean and Proterozoic sedimentary and volcanic rocks that overlie Pilbara granite–greenstone basement rocks, including, in ascending order, the Fortescue, Hamersley, Turee Creek, Shingle Creek, Wyloo and Capricorn groups (Thorne & Seymour, 1991; Thorne & Trendall, 2001). Rocks up to and including the c. 2200 Ma Shingle Creek Group have been multiply deformed during the Ophthalmia, Capricorn and Mangaroon orogenies (Martin & Morris, 2010; Powell & Horwitz, 1994). Younger rocks of the c. 1800 Ma Ashburton Formation were only deformed during the Capricorn and Mangaroon orogenies (Thorne & Seymour, 1991). While the Ophthalmia and Capricorn orogenies are associated with folding and cleavage development, dating of hydrothermal monazite and xenotime indicates that

in the northern part of the Capricorn Orogen, the Mangaroon Orogeny is represented by reactivation of major faults (Fielding et al., 2017, 2018, 2019).

Insight to the subsurface geology of the Capricorn Orogen and its cratonic margins is provided by deep-crustal seismic reflection data (Johnson et al., 2013), which in the northern Capricorn Orogen, identified two crustal-scale faults associated with gold mineralization. The Baring Downs Fault represents a fossil suture zone that separates the Pilbara Craton from the Bandee Seismic Province, and the Nanjilgardy Fault which transects the crust but is not a suture zone (Figure 5-3; Johnson et al., 2013). The crustal-scale faults have poor surface exposure but appear to have undergone multiple overprinting reactivations which causes difficulties in determining the movement sense during the discrete events. These faults, and their associated ancillary structures, are interpreted to have acted as fluid pathways during these reactivation events (e.g. Fielding et al., 2017, 2018, 2019; Johnson et al., 2013); however, quantifying this is difficult due to the limited surface exposures.

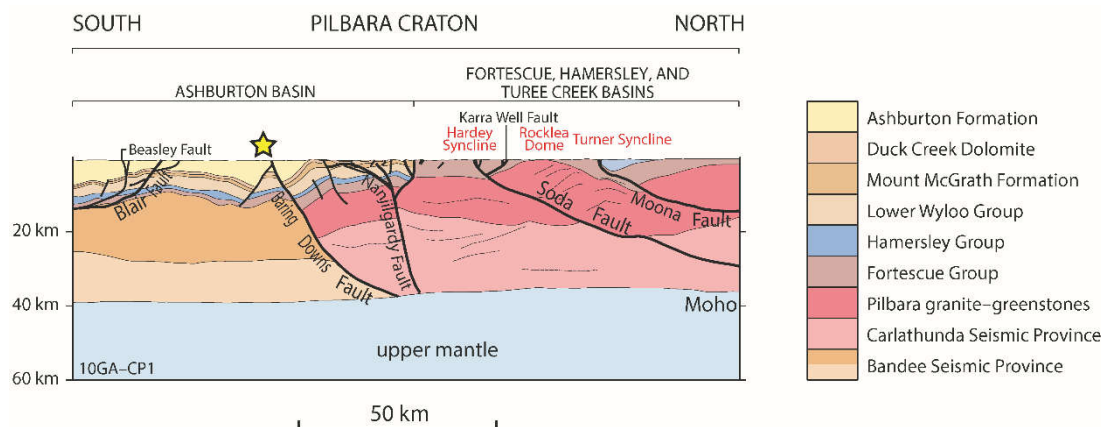


Figure 5-3: Seismic line 10GA-CP1 showing major faults in the northern Capricorn Orogen (after Johnson et al., 2013). The yellow star represents the location of the Star of the West gold deposit.

5.5. AMAZON SHEAR ZONE

The Amazon Shear Zone is a splay of the Nanjilgardy Fault situated within the Wyloo Inlier (Figure 5-1). It is defined by a ~50 m wide zone of intense foliation oriented at ~308/90° and, on the map-scale offsets stratigraphic boundaries with an apparent sinistral offset (Figure 5-2). Evidence for syn-tectonic hydrothermal activity is present along the Amazon Shear Zone with pre-, syn- and post-deformation (quartz)-calcite veins occurring within the shear zone (Figure 5-4). Pre-deformational quartz veins

form boudins along a well-developed foliation that marks the Amazon Shear Zone (Figure 5-4a), whereas calcite veins that were emplaced during movement are aligned in the foliation and the veins are deformed with the development of a spaced cleavage parallel to the foliation (Figure 5-4b). Calcite crystals have curved twin planes suggesting that they grew during deformation.

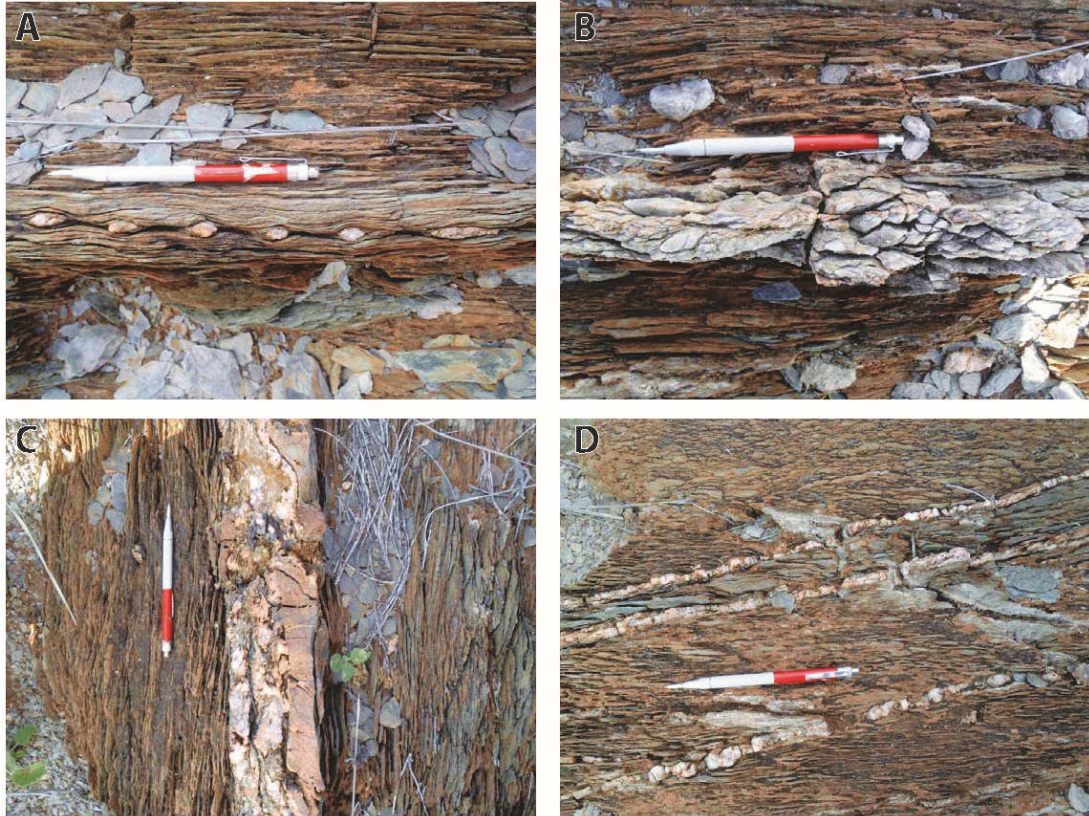


Figure 5-4: Quartz veins in the Amazon Shear Zone. A) Pre-deformation quartz vein formed as boudins along the foliation. B) Syn-deformation calcite vein aligned in the foliation with weakly developed foliation in the vein. C) Post-deformation quartz-calcite vein slightly oblique to the foliation. D) Post-deformation quartz veins that are weakly boudinaged.

Finally, at least two sets of post-fault movement quartz-calcite veins are present, including quartz-calcite veins that are near parallel to the foliation (Figure 5-4c) and quartz veins which cross cut the foliation at a high angle (Figure 5-4d). These veins post-date the main fault movement along the Amazon Shear Zone; however, they show evidence of weak post-emplacement deformation. Quartz crystals in the veins near-parallel to the foliation exhibit undulose extinction and sub-grain development, whereas the veins cross-cutting the foliation at a high angle are weakly boudinaged (Figure 5-4d). This suggests that hydrothermal fluids were circulated during fault movement. A sample of a syn-deformation vein from this location was selected for

xenotime geochronology to determine the timing of fluid movement and, by inference, the timing of fault movement.

5.6. STAR OF THE WEST GOLD DEPOSIT

5.6.1 LOCAL GEOLOGY

The Star of the West gold prospect is situated in the Ashburton Basin (Figure 5-1) and is hosted within sedimentary rock of the Ashburton Formation of the Wyloo Group (Thorne & Seymour, 1991). The Ashburton Formation was deposited in a deep-marine basin and is dominated by immature turbiditic sandstones derived from granitic rocks south of the Ashburton Basin (Thorne & Seymour, 1991). Sandstones are interbedded with minor proportions of conglomerate, mudstone, banded iron-formation, chert, and mafic and felsic volcanic rocks. No obvious, laterally consistent marker horizons exist and, coupled with structural complexities, this has made thickness estimations difficult; however, the formation is estimated to be 5–12 km thick (Sircombe, 2003; Thorne & Seymour, 1991).

The Star of the West gold deposit is hosted in a sequence of interbedded mudstone, siltstone and medium- to coarse-grained sandstone (Figure 5-5; Rolfe, 2012). Bedding is oriented at $\sim 295/60^\circ\text{N}$ and overprinted by at least two deformation events accompanied by low grade metamorphism (Thorne & Seymour, 1991). The first event, D1, is characterised by early recumbent folding (Thorne & Seymour, 1991) and the development of a crenulation cleavage at the Star of the West deposit. The effects of the D2 event are the most obvious in the area with the production of a widespread penetrative slaty cleavage (Thorne, Johnson, Tyler, Cutten, & Blay, 2011) that is axial planar to non-cylindrical folds with a wavelength of between 100 m and 6 km and axial planes dipping steeply to the southwest or northeast (Thorne & Seymour, 1991). Siliciclastic sedimentary rocks of the Ashburton Formation have been overprinted by greenschist facies metamorphism characterised by growth of quartz–chlorite–muscovite (Tyler & Thorne, 1990).

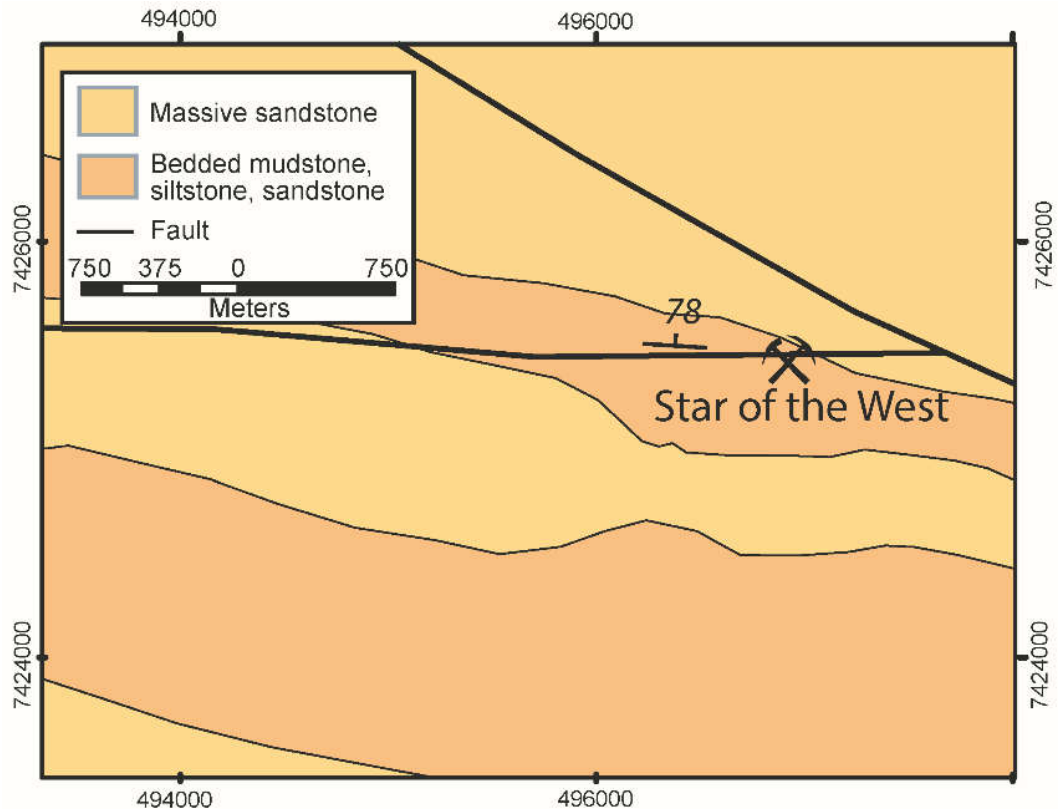


Figure 5-5: Star of the West local geology map, the mine symbol shows the location of the historical workings and sample site for GSWA 219560 (after Rolfe, 2012).

5.6.2 DEPOSIT DESCRIPTION

The Star of the West gold deposit is associated with a narrow fault oriented at $\sim 278/78^\circ\text{N}$ that is subparallel to, and interpreted as a splay of, the Baring Downs Fault. Gold mineralization occurs where siltstones and fine-grained sandstones are cross-cut by 5–20 cm wide quartz veins (Thorne & Seymour, 1991). The siliciclastic rocks adjacent to the quartz veins and fault have been pervasively altered by hydrothermal fluids producing an alteration assemblage of muscovite and large (>2 cm), euhedral pyrite crystals (Figure 5-6a and 5-6b). Thorne and Seymour (1991) indicate that the majority of gold mineralization (5–6 g/t) occurs within this alteration halo rather than in the quartz veins or fault itself. Scanning electron microscopy (SEM) and reflected light microscopy of polished thin sections indicates that gold occurs as both small, native inclusions within pyrite crystals (Figure 5-6c) and as microscopic inclusions in the altered matrix of the siliciclastic sedimentary rocks. No gold has been identified in the quartz veins. Samples of the quartz veins and alteration haloes were collected for dating of hydrothermal phosphates in order to constrain the age of hydrothermal alteration and gold mineralization at this prospect.

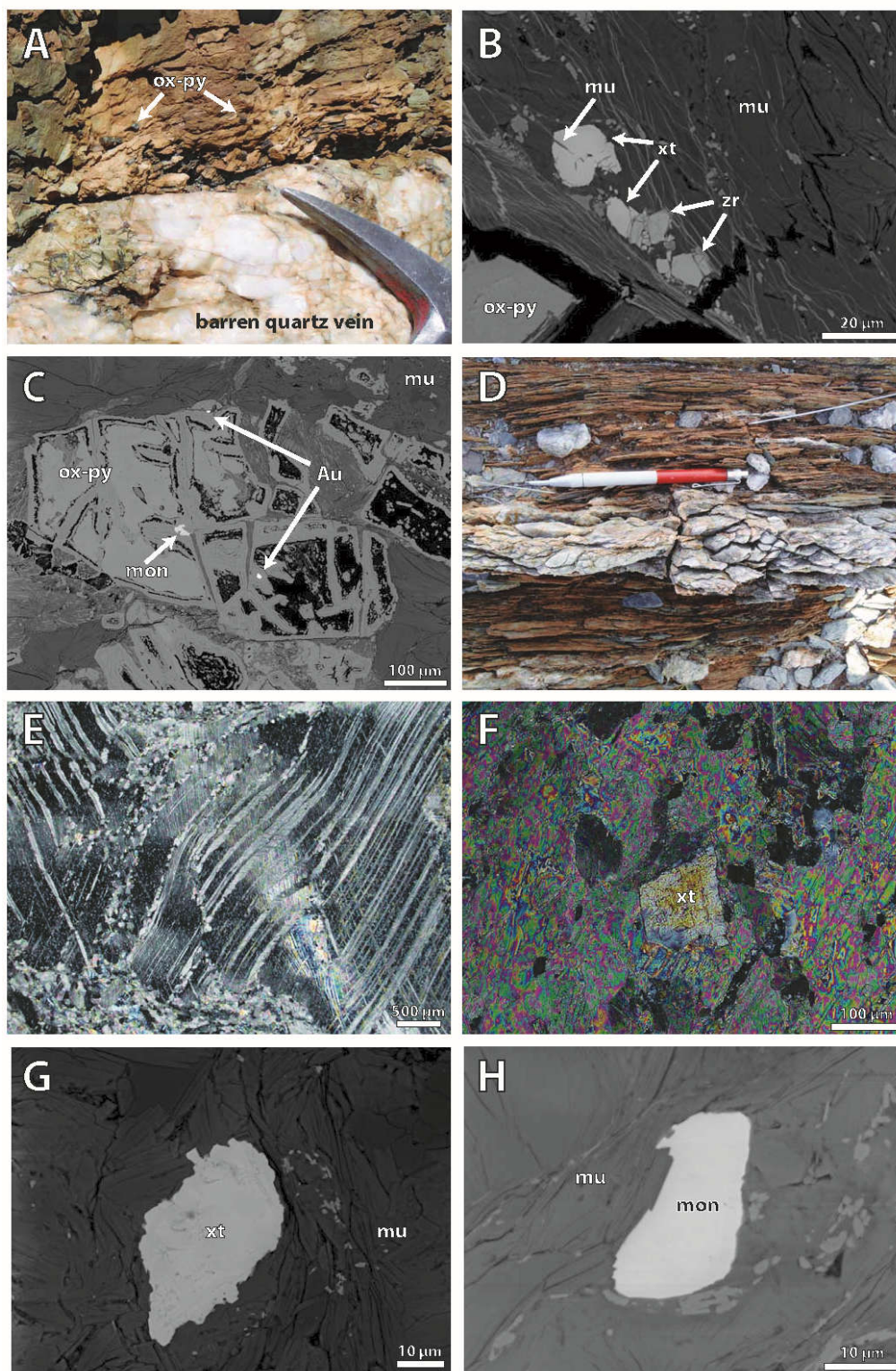


Figure 5-6: A) Alteration zone surrounding barren quartz vein at Star of the West gold deposit. Host rock comprises siltstone and sandstone with hydrothermal muscovite and oxidised, pyrite crystals. B) Back-scattered electron (BSE) image of xenotime containing laths of muscovite from the Star of the West ore zone. C) BSE image of oxidised pyrite from the Star of the West ore zone showing inclusions of monazite and gold surrounded by ore-stage muscovite alteration. D) Syn-deformational calcite vein formed along the Amazon Shear Zone that is sampled for geochronology (GSWA 219504). E) Cross-polarized light (XPL) image of curved twin planes in calcite from GSWA 219504. F) XPL image of euhedral xenotime interlocking with calcite crystals from sample GSWA 219504. G) BSE image of detrital xenotime sampled for geochronology from GSWA 219560. H) BSE image of detrital monazite sampled for geochronology (GSWA 219560). Abbreviations: Au = gold, mon = monazite, mu = muscovite, ox py = oxidised pyrite, zr = zircon.

5.7. GEOCHRONOLOGY METHODS

Polished thin sections were imaged using transmitted light and SEM to identify phosphate minerals, xenotime and monazite, for radiometric dating by the sensitive high-resolution ion microprobe (SHRIMP) instrument located in the John de Laeter Centre at Curtin University, Perth, Western Australia. Once identified the crystals were drilled out of the polished thin section with a 2 or 3 mm hollow core rotary drill before being cast in a 25 mm epoxy SHRIMP mount. Standards were placed on a separate SHRIMP mount which was cleaned and gold coated with the sample mount and analysed during the same analytical session. The monazite standards FRENCH, Z2234, and Z2908 (see Fletcher, McNaughton, Davis, and Rasmussen (2010) for details) were analysed for Pb/U and Pb/Th calibration (FRENCH), IMF corrections (Z2908), and matrix corrections required for variable U, Th, Y and Nd contents (Z2234 and Z2908). For xenotime Pb/U calibrations and matrix corrections for U and Th contents were based on concurrent measurements of the standards MG-1 (Fletcher, McNaughton, Aleinikoff, Rasmussen, & Kamo, 2004) and Z6413 (“Xeno1”; Stern & Rayner, 2003). Pb/Th was determined indirectly, using a fixed Th/U calibration (Fletcher et al., 2004). Matrix corrections for REE assumed the samples have REE abundances similar to Xeno1.

Data were collected over several analytical sessions following established methods outlined by Fletcher et al. (2004) and Fletcher et al. (2010) for xenotime and monazite, respectively, with varying operating parameters as summarised in Table 5-1. Raw data were processed using the SQUID 2 add-in (v. 2.50.12.03.08) for Excel 2003 (Ludwig, 2009), and plotted using the ISOPLOT add-in (v. 3.76.12.02.24; Ludwig, 2003). Common-Pb corrections were based on measured $^{204}\text{Pb}/^{206}\text{Pb}$ ratios and contemporaneous Pb compositions according to the terrestrial Pb evolution model of Stacey and Kramers (1975).

Session date	Mount ID	Sample ID	Target mineral	Kohler aperture (μm)	spot (approx. μm)	O2- primary (nA)	M/ΔM (1%)	# scans
6/05/2017	BR1613	219504	Xenotime	30	15	0.5–0.6	5100	8
12/07/2017	IF1708	219560	Xenotime	30	10	0.2	5160	8
17/05/2017	IF1708	219560	Monazite	30	15	0.3	5020	7

Table 5-1: SHRIMP operating parameters for all analytical sessions.

All age estimated are derived from 204-corrected $^{207}\text{Pb}^*/^{206}\text{Pb}^*$ ratios (Pb* denotes radiogenic lead) with results for individual analyses quoted with 1-sigma (1σ)

uncertainties; weighted mean $^{207}\text{Pb}^*/^{206}\text{Pb}^*$ dates are quoted with 95% confidence intervals. Up to 1% common lead and 10% discordance for individual analyses are tolerated.

5.8. SAMPLE DETAILS AND RESULTS

Two samples were collected for U–Pb analysis of xenotime and monazite. This includes a syn-deformational calcite vein emplaced within the Amazon Shear Zone, a splay of the Nanjilgardy Fault, and mineralized sericite-altered siltstone from the Star of the West gold deposit (Figures 5-1 and 5-5). The new samples were collected to gain a better understanding of the timing of fault reactivation and how it is related to gold mineralization.

5.8.1 GSWA 219504: CALCITE VEIN

Sample GSWA 219504 was taken from a barren calcite vein located at grid references MGA 94 zone 50 415210E 7504603N (Figure 5-2). It occurs in a 50 m-wide section of the Amazon Shear Zone that cut mafic rocks of the Boongal Formation of the Archean Fortescue Group (Figure 5-2). The calcite vein is approximately 10 cm wide, parallel to foliation (Figure 5-6d) and shows signs of deformation including containing calcite crystals with curved twin plans (Figure 5-6e) suggesting it was emplaced during fault movement. Euhedral xenotime crystals up to 200 μm interlocked with calcite crystals (Figure 5-6f) and are interpreted to have crystallised during vein emplacement.

Twelve analyses were made on two xenotime crystals. Four analyses >10% discordant were not considered geologically significant and were excluded from the age analysis. The remaining 8 analyses have U and Th contents of respectively, 57–237 ppm and 5–66 ppm, and yielded a weighted mean $^{207}\text{Pb}^*/^{206}\text{Pb}^*$ date of 1674 ± 54 Ma (MSWD = 1.7; Figure 5-7a and Supplementary Table 5-1). This age is interpreted to represent the timing of xenotime crystallization and the emplacement of the calcite vein.

5.8.2 GSWA 219560: GOLD-MINERALIZED SILTSTONE

Sample GSWA 219560 was taken from the Star of the West gold deposit located at MGA 94 zone 50 496986E 7425371N (Figure 5-1). The sample contains weathered and sericite-altered mudstones with oxidised pyrite cubes that are <1 cm in size that

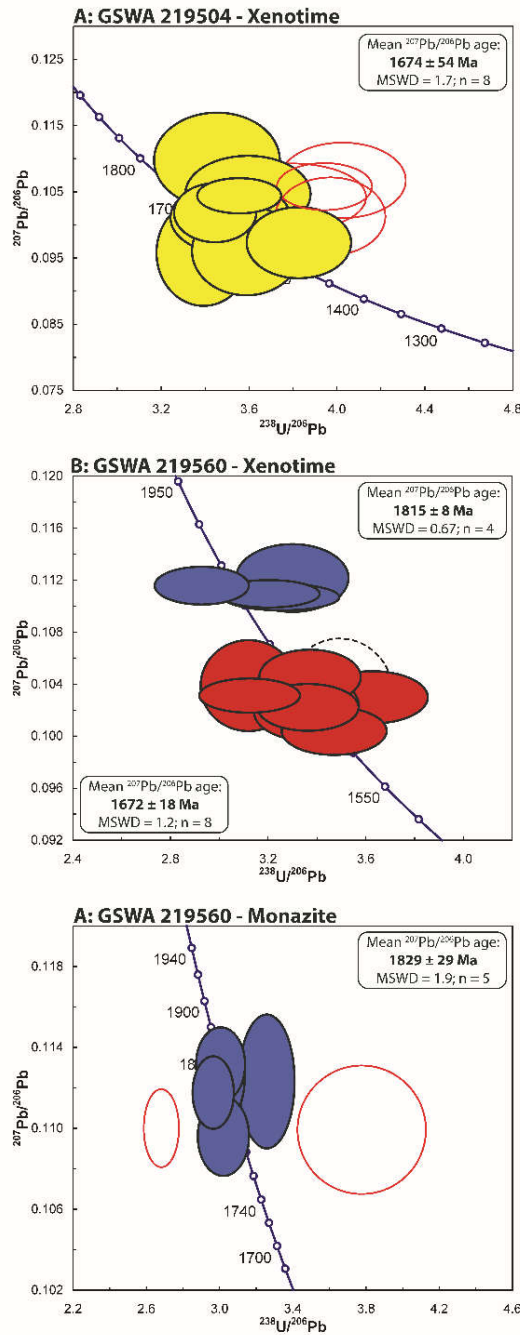


Figure 5-7: Tera-Wasserburg concordia diagrams of U–Pb data for xenotime and monazite. A) Xenotime from a syn-deformational calcite vein in the Amazon Shear Zone (GSWA 219504). B) Xenotime containing laths of ore-stage muscovite within altered siltstone at the Star of the West gold deposit (GSWA 219560). C) Monazite in altered siltstone at the Star of the West gold deposit (GSWA 219560), data high in common lead are not plotted, refer to Supplementary Table 5-3 for analysis details. Key: coloured ellipses show data used in the age calculations (yellow = hydrothermal activity at c. 1670 Ma, red = c. 1670 Ma hydrothermal gold mineralization, blue = c. 1830 Ma detrital grains). All other ellipses are for inferior data (unshaded red = >10% discordant, black dashed = >1% common Pb).

lie in the alteration halo of a quartz vein (Figure 5-6a). The sample contains both xenotime and monazite. A clear textural relationship between monazite crystals and gold mineralization is evident as small inclusions of both monazite and gold occur within the oxidised pyrite crystals (Figure 5-6c). Both xenotime and monazite occur disseminated throughout the matrix of the sample with xenotime crystals commonly intergrown with ore-stage alteration minerals that commonly contain laths of muscovite (Figure 5-6b).

Thirteen analyses were made on 7 xenotime crystals. One analysis with >1% common Pb was excluded from the age determination. Of the remaining 12 analyses two distinct age modes are evident. An older mode with 4 analyses and 8813–18982 ppm U and 16509–41245 ppm Th, yielded a weighted mean $^{207}\text{Pb}^*/^{206}\text{Pb}^*$ date of 1815 ± 8 Ma (MSWD = 0.67; Figure 5-7b and Supplementary Table 5-2). This age is obtained from a single xenotime crystal that is interpreted to be detrital in origin since it does not contain metamorphic mineral inclusions (Figure 5-6g) and has high U and Th content. It therefore is interpreted to represent a maximum age

for sediment deposition. The younger age mode is defined by 8 analyses and has from 1958 to 3831 ppm U and 2831 to 7486 ppm Th and yields a weighted mean $^{207}\text{Pb}^*/^{206}\text{Pb}^*$ date of 1672 ± 18 Ma (MSWD = 1.2; Figure 5-7b and Supplementary Table 5-2). Since this xenotime is intergrown with ore stage alteration minerals and contains laths of ore-stage muscovite (Figure 5-6b), it is interpreted to represent the timing of hydrothermal activity related to gold mineralization.

Sixty-two monazite crystals were identified in sample GSWA 219560 and occur as inclusions in auriferous oxidised pyrite and disseminated throughout the matrix. All efforts were made to date the monazite contained within the pyrite crystals; however, the results yielded high common Pb and/or discordant data (Supplementary Table 5-3). Thirteen analyses were conducted on 13 matrix monazite crystals. Six analyses with >1% common Pb and two >10% discordant were not considered geologically significant and were excluded from the age determination. The remaining five analyses have U and Th contents of 558–2786 ppm and 16450–55421 ppm, respectively, yielding a weighted mean $^{207}\text{Pb}^*/^{206}\text{Pb}^*$ date of 1829 ± 29 Ma (MSWD = 1.9; Figure 5-7c and Supplementary Table 5-3). As the monazites are all from within the matrix of the sample, contain no inclusions of ore-stage alteration minerals (Figure 5-6h) and are within uncertainty of zircon ages obtained from elsewhere in the Ashburton Formation (Evans et al., 2003; Sircombe, 2003), they are interpreted to be detrital, and thus interpreted to record a maximum age for sediment deposition.

5.9. DISCUSSION

The Star of the West gold deposit is situated within rocks of the Paleoproterozoic Ashburton Formation. Here we provide a detrital xenotime age of 1815 ± 8 Ma and a detrital monazite age of 1829 ± 29 Ma, providing a maximum depositional age for the host rocks. These ages are within analytical uncertainty of one another and are consistent with 1829–1786 Ma zircon age constraints for the deposition of the Ashburton Formation (Evans et al., 2003; Sircombe, 2003). The lack of inclusions within the monazite and xenotime crystals (Figure 5-6g and h) suggests they have a detrital origin (Rasmussen, Fletcher, & Muhling, 2007), additionally some of the monazite crystals are rounded (Figure 5-6h). Sandstones from the Ashburton Formation are believed to have an igneous source due to their composition of quartz,

feldspar and lithic fragments of sedimentary, felsic volcanic and granitic rocks (Thorne & Seymour, 1991). The high U and Th contents of the detrital xenotime (Supplementary Table 5-2) is characteristic of igneous xenotime supporting the Thorne and Seymour (1991) interpretation of igneous sourced detritus, whereas hydrothermal xenotime associated with orogenic gold deposits tends to have lower U and Th contents (McNaughton & Rasmussen, 2018).

Following deposition of the host rocks, narrow quartz veins were emplaced into these siliciclastic sedimentary rocks. Xenotime intergrown with ore-stage muscovite from gold-bearing hydrothermal aureoles around these veins yielded a date of 1672 ± 18 Ma (GSWA 219560), interpreted as timing quartz vein emplacement and associated hydrothermal activity and gold mineralization. This age is synchronous with the timing of gold mineralization associated with the Nanjilgardy Fault at both the Paulsens and Belvedere gold deposits (Fielding et al., 2017, 2018) which are interpreted to have formed during reactivation of the Nanjilgardy Fault during the early stages of the intracratonic 1680–1620 Ma Mangaroon Orogeny.

At a regional-scale, the Nanjilgardy and Baring Downs faults in the northern Capricorn Orogen show evidence of significant strike-slip movement (Figure 5-2), however, the structural history is difficult to interpret due to limited surface exposures and overprinting movement events (Johnson et al., 2013; Krapez, 1999). Dating of different hydrothermal fluid flow events in the northern Capricorn Orogen points to a complex reactivation history of these faults (e.g. Fielding et al., 2017, 2018, 2019; Rasmussen, Fletcher, & Muhling, 2007; Rasmussen, Fletcher, Muhling, et al., 2007; Sheppard et al., 2006). The Amazon Shear Zone, a splay of the Nanjilgardy Fault, shows evidence for pre-, syn- and post-fault movement hydrothermal activity (Figure 5-4). New in situ geochronology of xenotime intergrown with calcite from a syn-tectonic calcite vein, indicates that hydrothermal fluids accompanied movement on the Amazon Shear Zone at 1674 ± 54 Ma (GSWA 219504). This date is coincident with the onset of the 1680–1620 Ma Mangaroon Orogeny in the Gascoyne Province to the south (Sheppard et al., 2005) and suggests that this event in the northern part of the orogen is defined mainly by shear zone and fault reactivation. This is further supported by an Ar/Ar date of c. 1653 Ma obtained on a low-grade shear zone in the Sylvania Inlier farther to the west (Sheppard et al., 2006). These data are coincident with the timing of widespread gold mineralization at the Star of the West (this study), Paulsens

(Fielding et al., 2017) and Belvedere (Fielding et al., 2018), and with the growth of hydrothermal xenotime at the Mount Olympus gold deposit (Fielding et al., 2019). The data imply an intrinsic link between shear zone or fault reactivation, hydrothermal activity and gold mineralization and indicate that the major crustal faults and their splays provide a critical pathway for the hydrothermal fluids.

5.10. CONCLUSIONS

Gold deposits in the northern Capricorn Orogen show a spatial relationship to crustal-scale faults and their ancillary structures (Johnson et al., 2013). The assumption is that gold mineralization formed when hydrothermal fluids moved along these faults during periods of episodic reactivation associated with known orogenic events (Fielding et al., 2017, 2018; Johnson et al., 2013). In this study, we have dated a syn-tectonic calcite vein associated with the Amazon Shear Zone, demonstrating that hydrothermal fluid flow accompanied fault movement at c. 1670 Ma. This age is coeval with the timing of gold mineralization at the Star of the West Deposit, as well as widespread hydrothermal activity and gold mineralization throughout the northern Capricorn Orogen and southern Pilbara Craton. Our results indicate that during the early stages of the intracratonic Mangaroon Orogeny fault reactivation accompanied the movement of both hydrothermal and mineralizing fluids along crustal-scale faults and their associated structures.

5.11. ACKNOWLEDGMENTS

This project was funded through an ARC linkage grant (LP130100922), the Exploration Incentive Scheme and an industry scholarship by Northern Star Resources as a part of a PhD by I.O.H. Fielding. S.P. Johnson publishes with the permission of the director of the Geological Survey of Western Australia. Xenotime and monazite analyses were carried out on the Sensitive High Resolution Ion Micro Probe mass spectrometer (SHRIMP II) at the John de Laeter Centre, Curtin University, with the financial support of the Australian Research Council and Auscope NCRIS.

5.12. REFERENCES

- Cawood, P. A., & Tyler, I. M. (2004). Assembling and reactivating the Proterozoic Capricorn Orogen: lithotectonic elements, orogenies, and significance. *Precambrian Research*, 128(3-4), 201-218. doi:DOI 10.1016/j.precamres.2003.09.001
- Evans, D. A. D., Sircombe, K. N., Wingate, M. T. D., Doyle, M., McCarthy, M., Pidgeon, R. T., & Van Niekerk, H. S. (2003). Revised geochronology of magmatism in the western Capricorn Orogen at 1805-1785 Ma: diachroneity of the Pilbara-Yilgarn collision. *Australian Journal of Earth Sciences*, 50(6), 853-864. doi:DOI 10.1111/j.1400-0952.2003.01031.x
- Fielding, I. O. H., Johnson, S. P., Zi, J.-W., Rasmussen, B., Muhling, J. R., Dunkley, D. J., Rogers, J. R. (2017). Using In Situ SHRIMP U-Pb Monazite and Xenotime Geochronology to Determine the Age of Orogenic Gold Mineralization: An Example from the Paulsens Mine, Southern Pilbara Craton. *Economic Geology*, 112(5), 1205-1230. doi:10.5382/econgeo.2017.4507
- Fielding, I. O. H., Johnson, S. P., Zi, J. W., Sheppard, S., & Rasmussen, B. (2018). Neighbouring orogenic gold deposits may be the products of unrelated mineralizing events. *Ore Geology Reviews*, 95, 593-603. doi:https://doi.org/10.1016/j.oregeorev.2018.03.011
- Fielding, I. O. H., Johnson, S. P., Meffre, S., Zi, J. W., Sheppard, S., Large, R. R., & Rasmussen, B. (2019), Linking gold mineralization to regional-scale drivers of mineral systems using in situ U-Pb geochronology and pyrite LA-ICP-MS element mapping. *Geoscience Frontiers*, 10, 89-105. doi: <https://doi.org/10.1016/j.gsf.2018.06.005>
- Fletcher, I. R., McNaughton, N. J., Aleinikoff, J. A., Rasmussen, B., & Kamo, S. L. (2004). Improved calibration procedures and new standards for U-Pb and Th-Pb dating of Phanerozoic xenotime by ion microprobe. *Chemical Geology*, 209(3-4), 295-314. doi:http://dx.doi.org/10.1016/j.chemgeo.2004.06.015
- Fletcher, I. R., McNaughton, N. J., Davis, W. J., & Rasmussen, B. (2010). Matrix effects and calibration limitations in ion probe U-Pb and Th-Pb dating of monazite. *Chemical Geology*, 270(1-4), 31-44. doi:http://dx.doi.org/10.1016/j.chemgeo.2009.11.003
- Johnson, S. P., Sheppard, S., Rasmussen, B., Wingate, M. T. D., Kirkland, C. L., Muhling, J. R., Belousova, E. A. (2011). Two collisions, two sutures: Punctuated pre-1950Ma assembly of the West Australian Craton during the Ophthalmian and Glenburgh Orogenies. *Precambrian Research*, 189(3-4), 239-262. doi:10.1016/j.precamres.2011.07.011
- Johnson, S. P., Thorne, A. M., Tyler, I. M., Korsch, R. J., Kennett, B. L. N., Cutten, H. N., Fomin, T. (2013). Crustal architecture of the Capricorn Orogen, Western Australia and associated metallogeny. *Australian Journal of Earth Sciences*, 60(6-7), 681-705. doi:10.1080/08120099.2013.826735

- Korhonen, F. J., Johnson, S. P., Wingate, M. T. D., Fletcher, I. R., Dunkley, D. J., Roberts, M. P., Rasmussen, B. (2017). Radiogenic heating and craton-margin plate stresses as drivers for intraplate orogeny. *Journal of metamorphic geology*, 35 (6), 631-661. doi:10.1111/jmg.12249
- Krapez, B. (1999). Stratigraphic record of an Atlantic-type global tectonic cycle in the Palaeoproterozoic Ashburton Province of Western Australia. *Australian Journal of Earth Sciences*, 46(1), 71-87. doi:10.1046/j.1440-0952.1999.00688.x
- Ludwig, K. R. (2003). Isoplot/Ex version 3.00, A geochronological toolkit for Microsoft Excel. Berkeley Geochronology Centre Special Publication No. 4.
- Ludwig, K. R. (2009). Squid 2.50, a user's manual. Berkeley Geochronology Centre, Berkeley, California, USA.
- Martin, D. M., & Morris, P. A. (2010). Tectonic setting and regional implications of ca2.2 Ga mafic magmatism in the southern Hamersley Province, Western Australia. *Australian Journal of Earth Sciences*, 57(7), 911-931. doi:10.1080/08120099.2010.510172
- Martin, D. M., & Thorne, A. (2004). Tectonic setting and basin evolution of the Bangemall Supergroup in the northwestern Capricorn Orogen. *Precambrian Research*, 128(3), 385-409.
- McNaughton, N.J., Rasmussen, B. (2018). Geochemical characterisation of xenotime formation environments using U-Th. *Chemical Geology*, 484, 109-119. doi: <https://doi.org/10.1016/j.chemgeo.2017.08.016>
- Occhipinti, S. A., Sheppard, S., Passchier, C., Tyler, I. M., & Nelson, D. R. (2004). Palaeoproterozoic crustal accretion and collision in the southern Capricorn Orogen: the Glenburgh Orogeny. *Precambrian Research*, 128(3-4), 237-255. doi:<http://dx.doi.org/10.1016/j.precamres.2003.09.002>
- Powell, C. M., & Horwitz, R. C. (1994). Late Archaean and Early Proterozoic tectonics and basin formation of the Hamersley Ranges Vol. 4. Geological Society of Australia (WA Division) Excursion Guidebook (pp. 57).
- Rasmussen, B., Fletcher, I. R., & Muhling, J. R. (2007). In situ U–Pb dating and element mapping of three generations of monazite: Unravelling cryptic tectonothermal events in low-grade terranes. *Geochimica et Cosmochimica Acta*, 71(3), 670-690. doi:<http://dx.doi.org/10.1016/j.gca.2006.10.020>
- Rasmussen, B., Fletcher, I. R., Muhling, J. R., Thorne, W. S., & Broadbent, G. C. (2007). Prolonged history of episodic fluid flow in giant hematite ore bodies: Evidence from in situ U–Pb geochronology of hydrothermal xenotime. *Earth and Planetary Science Letters*, 258(1–2), 249-259. doi:<http://dx.doi.org/10.1016/j.epsl.2007.03.033>
- Rasmussen, B., Fletcher, I. R., & Sheppard, S. (2005). Isotopic dating of the migration of a low-grade metamorphic front during orogenesis. *Geology*, 33(10), 773-776. doi:10.1130/G21666.1

- Rolfe, M. (2012). Star of the West E 08/2232, Annual report for the period 20 October 2011- 19 October 2012. Retrieved from Geological Survey of Western Australia Open-file Report.
- Sheppard, S., Bodorkos, S., Johnson, S. P., Wingate, M. T. D., & Kirkland, C. L. (2010). The Paleoproterozoic Capricorn Orogeny: intracontinental reworking not continent–continent collision (Vol. 108, pp. 33). Geological Survey of Western Australia, Report 108.
- Sheppard, S., Farrell, T. R., Bodorkos, S., D. H., Tyler, I. M., & Pirajino, F. (Eds.). (2006). Late Paleoproterozoic (1680-1620 Ma) sedimentation, magmatism, and tectonism in the Capricorn Orogen.
- Sheppard, S., Occhipinti, S. A., & Nelson, D. R. (2005). Intracontinental reworking in the Capricorn Orogen, Western Australia: the 1680–1620 Ma Mangaroon Orogeny*. *Australian Journal of Earth Sciences*, 52(3), 443-460. doi:10.1080/08120090500134589
- Sheppard, S., Occhipinti, S. A., & Tyler, I. M. (2004). A 2005–1970 Ma Andean-type batholith in the southern Gascoyne Complex, Western Australia. *Precambrian Research*, 128(3–4), 257-277. doi:http://dx.doi.org/10.1016/j.precamres.2003.09.003
- Sheppard, S., Rasmussen, B., Muhling, J. R., Farrell, T. R., & Fletcher, I. R. (2007). Grenvillian-aged orogenesis in the Palaeoproterozoic Gascoyne Complex, Western Australia: 1030–950Ma reworking of the Proterozoic Capricorn Orogen. *Journal of Metamorphic Geology*, 25(4), 477-494. doi:10.1111/j.1525-1314.2007.00708.x
- Sircombe, K. N. (2003). Age of the Mt Boggola volcanic succession and further geochronological constraint on the Ashburton Basin, Western Australia. *Australian Journal of Earth Sciences*, 50(6), 967-974. doi:10.1111/j.1400-0952.2003.01037.x
- Stacey, J. S., & Kramers, J. D. (1975). Approximation of terrestrial lead isotope evolution by a two-stage model. *Earth and Planetary Science Letters*, 26(2), 207-221. doi:http://dx.doi.org/10.1016/0012-821X(75)90088-6
- Stern, R. A., & Rayner, N. (2003). Ages of several xenotime megacrysts by ID-TIMS: potential reference materials for ion microprobe U-Pb geochronology: Radiogenic Age and Isotopic Studies: Report 16.
- Thorne, A. M., Johnson, S. P., Tyler, I. M., Cutten, H. N., & Blay, O. (2011). Geology of the northern Capricorn Orogen S. P. Johnson, A. M. Thorne, & I. M. Tyler (Eds.), *Capricorn Orogen seismic and magnetotelluric (MT) workshop 2011* (pp. 7-18).
- Thorne, A. M., & Seymour, D. B. (1991). Geology of the Ashburton Basin Western Australia. Geological Survey of Western Australia, Bulletin 139.

- Thorne, A. M., & Trendall, A. F. (2001). Geology of the Fortescue Group, Pilbara Craton, Western Australia. Geological Survey of Western Australia, Bulletin 144.
- Tyler, I. M., & Thorne, A. M. (1990). The northern margin of the Capricorn Orogen, Western Australia—an example of an Early Proterozoic collision zone. *Journal of Structural Geology*, 12(5–6), 685–701. doi:[http://dx.doi.org/10.1016/0191-8141\(90\)90082-A](http://dx.doi.org/10.1016/0191-8141(90)90082-A)

5.13. SUPPLEMENTARY DATA

5.13.1 DATA TABLES

Supplementary Table 5–1: GSWA 219504 xenotime in calcite

<i>Mount no.</i>	<i>Grain spot</i>	<i>U (ppm)</i>	<i>Th (ppm)</i>	<i>Th/U</i>	<i>f₂₀₆ (%)</i>	<i>²⁰⁷Pb*/²⁰⁶Pb*</i>	<i>± 1σ</i>	<i>²⁰⁶Pb*/²³⁸U</i>	<i>± 1σ</i>	<i>²⁰⁷Pb*/²³⁵U</i>	<i>± 1σ</i>	<i>²⁰⁸Pb*/²³²Th</i>	<i>± 1σ</i>	<i>Dis (%)</i>	<i>²⁰⁷Pb*/²⁰⁶Pb* age (Ma)</i>	<i>± 1σ (Ma)</i>
hydrothermal xenotime (1674 ± 54 Ma)																
BR1613	G.1-1	57	5	0.09	-0.54	0.1097	0.0044	0.290	0.016	4.39	0.31	0.114	0.009	9	1795	73
BR1613	G.1-5	62	12	0.20	-0.25	0.1046	0.0035	0.278	0.015	4.02	0.26	0.096	0.009	7	1708	61
BR1613	G.1-3	237	66	0.28	0.00	0.1044	0.0015	0.282	0.010	4.05	0.16	0.086	0.009	6	1703	26
BR1613	F.1-1	220	28	0.13	0.21	0.1018	0.0027	0.291	0.010	4.08	0.19	0.077	0.010	1	1657	49
BR1613	F.1-5	61	11	0.17	0.24	0.1010	0.0033	0.285	0.015	3.97	0.25	0.086	0.010	2	1643	61
BR1613	F.1-4	139	49	0.35	0.13	0.0973	0.0033	0.261	0.011	3.51	0.19	0.078	0.010	5	1573	63
BR1613	F.1-3	102	55	0.54	0.49	0.0960	0.0041	0.279	0.013	3.70	0.24	0.075	0.010	-2	1549	81
BR1613	G.1-4	113	53	0.47	0.42	0.0958	0.0049	0.295	0.012	3.90	0.27	0.085	0.011	-8	1543	97
Discordance >10%																
BR1613	F.1-6	58	28	0.49	0.00	0.1041	0.0030	0.264	0.015	3.78	0.25	0.078	0.009	11	1699	54
BR1613	F.1-2	149	30	0.20	0.25	0.1012	0.0036	0.252	0.011	3.52	0.20	0.068	0.009	12	1647	66
BR1613	G.1-6	223	66	0.30	0.11	0.1057	0.0021	0.254	0.009	3.70	0.16	0.079	0.008	16	1727	36
BR1613	G.1-2	109	17	0.15	-0.40	0.1067	0.0035	0.249	0.012	3.66	0.22	0.081	0.008	18	1744	59

Pb* indicates radiogenic Pb.

f_{206} is the proportion of common Pb in ^{206}Pb , determined using the measured $^{204}\text{Pb}/^{206}\text{Pb}$ and a common Pb composition from the Stacey and Kramers (1975) model at the approximate age of the sample.

Disc. Is apparent discordance, as $100(t[^{207}\text{Pb}^*/^{206}\text{Pb}^*] - t[^{238}\text{U}/^{206}\text{Pb}^*])/t[^{207}\text{Pb}^*/^{206}\text{Pb}^*]$.

Same footnote applies to Supplementary Tables 5-1 to 5-3.

Supplementary Table 5-2: GSWA 219560 xenotime within altered siltstone

<i>Mount no.</i>	<i>Grain spot</i>	<i>U (ppm)</i>	<i>Th (ppm)</i>	<i>Th/U</i>	<i>f₂₀₆ (%)</i>	<i>²⁰⁷Pb*/²⁰⁶Pb*</i>	<i>± 1s</i>	<i>²⁰⁶Pb*/²³⁸U</i>	<i>± 1s</i>	<i>²⁰⁷Pb*/²³⁵U</i>	<i>± 1s</i>	<i>²⁰⁸Pb*/²³²Th</i>	<i>± 1s</i>	<i>Dis (%)</i>	<i>²⁰⁷Pb*/²⁰⁶Pb* age (Ma)</i>	<i>± 1s (Ma)</i>
Group 1 (1815 ± 8 Ma)																
IF1708	D.1-3	8997	41245	4.58	0.66	0.1121	0.0014	0.303	0.014	4.69	0.23	0.026	0.009	7	1834	22
IF1708	D.1-1	8813	16509	1.87	0.26	0.1116	0.0007	0.342	0.015	5.26	0.23	0.055	0.010	-4	1825	12
IF1708	D.1-4	14412	22031	1.53	0.19	0.1109	0.0004	0.313	0.013	4.78	0.21	0.055	0.010	3	1815	7
IF1708	D.1-2	18982	30696	1.62	0.13	0.1107	0.0004	0.307	0.015	4.69	0.23	0.066	0.010	5	1810	6
Group 2 (1672 ± 18 Ma)																
IF1708	A.1-2	3128	7486	2.39	0.52	0.1045	0.0012	0.297	0.012	4.28	0.18	0.089	0.010	2	1706	21
IF1708	L.1-1	3366	4825	1.43	0.79	0.1039	0.0021	0.321	0.013	4.59	0.22	0.093	0.011	-6	1694	37
IF1708	A.1-1	3831	2831	0.74	0.03	0.1031	0.0007	0.320	0.014	4.55	0.20	0.097	0.011	-7	1681	12
IF1708	F.1-2	1958	3050	1.56	0.08	0.1030	0.0012	0.276	0.012	3.92	0.17	0.083	0.009	6	1678	21
IF1708	E.1-1	2499	5111	2.05	0.73	0.1023	0.0015	0.297	0.012	4.19	0.19	0.090	0.010	-1	1665	26
IF1708	G.1-1	2771	4735	1.71	0.24	0.1022	0.0010	0.297	0.012	4.19	0.18	0.088	0.010	-1	1664	19
IF1708	F.1-1	2234	3137	1.40	0.39	0.1019	0.0013	0.299	0.012	4.19	0.18	0.090	0.010	-2	1658	23
IF1708	F.1-3	2613	4244	1.62	0.16	0.1004	0.0011	0.288	0.012	3.99	0.17	0.087	0.010	0	1631	19
High common Pb																
IF1708	J.1-1	3970	7543	1.90	1.51	0.1031	0.0026	0.286	0.012	4.07	0.20	0.094	0.010	3	1681	46

Supplementary Table 5-3: GSWA 219560 monazite within altered siltstone

<i>Mount no.</i>	<i>Grain spot</i>	<i>U (ppm)</i>	<i>Th (ppm)</i>	<i>Th/U</i>	<i>f²⁰⁶ (%)</i>	<i>²⁰⁷Pb*/²⁰⁶Pb*</i>	<i>± 1s</i>	<i>²⁰⁶Pb*/²³⁸U</i>	<i>± 1s</i>	<i>²⁰⁷Pb*/²³⁵U</i>	<i>± 1s</i>	<i>²⁰⁸Pb*/²³²Th</i>	<i>± 1s</i>	<i>Dis (%)</i>	<i>²⁰⁷Pb*/²⁰⁶Pb* age (Ma)</i>	<i>± 1s (Ma)</i>
Diagenetic monazite (1829 ± 29 Ma)																
IF1706	G.6-1	2035	55421	27.24	0.01	0.1131	0.0009	0.333	0.010	5.20	0.16	0.111	0.002	0	1850	14
IF1706	B.3-1	796	35238	44.27	0.06	0.1125	0.0013	0.332	0.009	5.15	0.15	0.104	0.002	0	1841	20
IF1706	E.6-1	558	31073	55.67	0.55	0.1123	0.0020	0.307	0.009	4.76	0.17	0.098	0.002	6	1837	33
IF1706	F.5-1	2786	16450	5.91	0.11	0.1118	0.0008	0.338	0.009	5.20	0.14	0.104	0.002	-3	1828	14
IF1706	G.8-1	1736	37210	21.43	0.14	0.1096	0.0010	0.331	0.010	5.01	0.16	0.104	0.002	-3	1793	16
Discordance >10%																
IF1706	E.8-1	713	18870	26.48	0.54	0.1099	0.0019	0.265	0.016	4.01	0.26	0.096	0.002	16	1798	32
IF1706	F.4-1	1234	28531	23.11	0.12	0.1100	0.0010	0.374	0.009	5.67	0.15	0.112	0.002	-14	1799	16
High common Pb																
IF1706	E.7-1	22	7092	323.03	-1.67	0.1279	0.0156	0.376	0.020	6.64	0.88	0.102	0.002	1	2070	215
IF1706	G.3-1	867	26587	30.68	1.46	0.1139	0.0086	0.343	0.009	5.39	0.43	0.094	0.003	-2	1863	136
IF1706	A.3-1	8	4350	520.38	12.62	0.1390	0.0536	0.340	0.031	6.52	2.55	0.105	0.002	15	2215	668
IF1706	A.4-1	39	27912	707.39	14.38	0.1489	0.0294	0.333	0.016	6.84	1.39	0.104	0.002	20	2333	338
IF1706	G.4-1	30	12898	429.59	24.38	0.0462	0.0486	0.289	0.021	1.84	1.92	0.103	0.002	-15502	10	2528
IF1706	A.1-1	29	15125	518.11	26.74	0.0819	0.0489	0.350	0.029	3.96	2.37	0.107	0.002	-56	1244	1169

CHAPTER 6. GOLD METALLOGENY OF A PROTEROZOIC OROGEN: THE RELATIONSHIP BETWEEN CRUSTAL ARCHITECTURE, FAULT REACTIVATION AND HYDROTHERMAL FLUID FLOW

The following chapter has been under review in ORE GEOLOGY REVIEWS as of the 17th April, 2018.

Imogen O. H. Fielding¹, Simon P. Johnson², Birger Rasmussen^{3,4}, Stephen Sheppard^{1,5}, and Jian-Wei Zi^{4,6}, Gold metallogeny of a Proterozoic orogen; the relationship between crustal architecture, fault reactivation and hydrothermal fluid flow: Ore Geology Reviews, under review.

¹Department of Applied Geology, Curtin University, Kent Street, Bentley, WA 6102, Australia.

²Geological Survey of Western Australia, 100 Plain Street, East Perth, WA 6004, Australia.

³School of Earth Sciences, The University of Western Australia, Perth, WA, 6009, Australia.

⁴State Key Lab of Geological Processes and Mineral Resources, China University of Geosciences, Wuhan, 430074, China.

⁵Prime Geological Mapping, PO Box 3014, Carlisle South, WA, 6101, Australia.

⁶John de Laeter Centre, Curtin University, Kent Street, Bentley, WA 6102, Australia.

6.1. ABSTRACT

The timing and distribution of gold mineralization in Proterozoic orogens is influenced by crustal architecture which is often established long before gold mineralization occurs. Gold occurrences in such settings are commonly associated with crustal-scale faults formed at cratonic margins. Once established, these faults provide a conduit for hydrothermal and mineralizing fluids which during repeated fault reactivations can result in multiple overprinting gold events. Recently published geochronological data for the northern part of the Proterozoic Capricorn Orogen in Western Australia shows it has experienced at least three episodes of gold mineralization occurring at c. 2400, 1770 and 1680 Ma. The timing of gold mineralization is linked to reactivation of the crustal-scale Nanjilgardy and Baring Downs Faults, and their auxiliary structures, during discrete orogenic events. Many of the gold deposits are associated with intracratonic reworking during the 1820–1770 Ma Capricorn Orogeny and 1680–1620 Ma Mangaroon Orogeny. Intracratonic settings are not considered prospective for gold mineralization due to a lack of input of juvenile material. However, it appears that repeated hydrothermal fluid flow events during multiple fault reactivations has upgraded gold mineralization and increased gold endowment throughout the northern Capricorn Orogen. Additionally, more simple histories produce smaller gold deposits whereas those with multiple pulses of mineralizing fluids or structural complexities are more likely to host larger gold deposits with the potential of >1 Moz of Au.

6.2. INTRODUCTION

Gold is a significant economic driver of many developed and developing countries but despite continued high levels of funding for gold exploration worldwide, the rate of discovery has drastically fallen over the past decade (Doggett and Zhang, 2007; Groves and Santosh, 2015; Hronsky and Groves, 2008; Jennings and Schodde, 2016; McCuaig and Hronsky, 2014; McKeith et al., 2010; Zhang et al., 2015). The odds for exploration success can be vastly improved by understanding the large-scale controlling factors that affect the distribution and occurrences of gold within a region (Hronsky et al., 2012; McCuaig et al., 2010). Determining how gold mineralization relates to the regional-scale crustal architecture and tectonothermal evolution is fundamental for effective exploration targeting (e.g. Rasmussen et al., 2006). This is

particularly important in Proterozoic orogens and Archean cratons as they both commonly show complex geological histories derived from multiple overprinting tectonic events (Johnson et al., 2017a; Raimondo et al., 2010). Such areas commonly lack a detailed chronology for the timing of hydrothermal activity and gold mineralization because dating these events can be challenging as many common chronometers are reset during post-mineralization events (Chesley, 1999; Vielreicher et al., 2003).

Crustal architecture plays a critical role in the distribution of gold deposits, with numerous studies demonstrating a close spatial relationship between giant orebodies and trans-crustal structures (Goldfarb et al., 2001; Hronsky et al., 2012; Huston et al., 2016). It is possible that a favourable crustal architecture must be established prior to mineralization events in order to provide a suitable pathway for mineralized fluids to travel from the mantle to the upper crust (Hronsky, 2011; Huston et al., 2016). Once established, reactivation of pre-existing crustal-scale faults may occur during subsequent deformation events (Joly et al., 2015) resulting in multiple overprinting mineralizing events (Fielding et al., 2017; Meffre et al., 2016). These are common characteristics for both Precambrian and Phanerozoic gold provinces worldwide. For example, Paleoproterozoic gold mineralization in the West Africa Craton has a close relationship to crustal-scale faults with evidence of multiple mineralizing events (Fougerouse et al., 2017; Le Mignot et al., 2017). Pre-existing crustal architecture plays an important role in the distribution of Phanerozoic gold mineralization in the Jiaodong Gold Province in the North China Craton (Groves and Santosh, 2015) where gold mineralization post-dates the deposition of the host rocks by ~2 billion years (Goldfarb and Santosh, 2014; Groves and Santosh, 2016). There, gold has a spatial association with three major Paleoproterozoic suture zones with a protracted reactivation history prior to, and including, the main mineralization event (Groves and Santosh, 2015).

The Capricorn Orogen of Western Australia (Figure 6-1) has a long and well-documented geological history (Cawood and Tyler, 2004; Johnson et al., 2011a, 2017a; Sheppard et al., 2005, 2010). Similar to the gold deposits in the West African Craton and the North China Craton, gold mineralization in the Capricorn Orogen shows a close spatial relationship with pre-existing crustal-scale faults that show evidence for multiple reactivation and mineralizing events (Fielding et al., 2017, 2018;

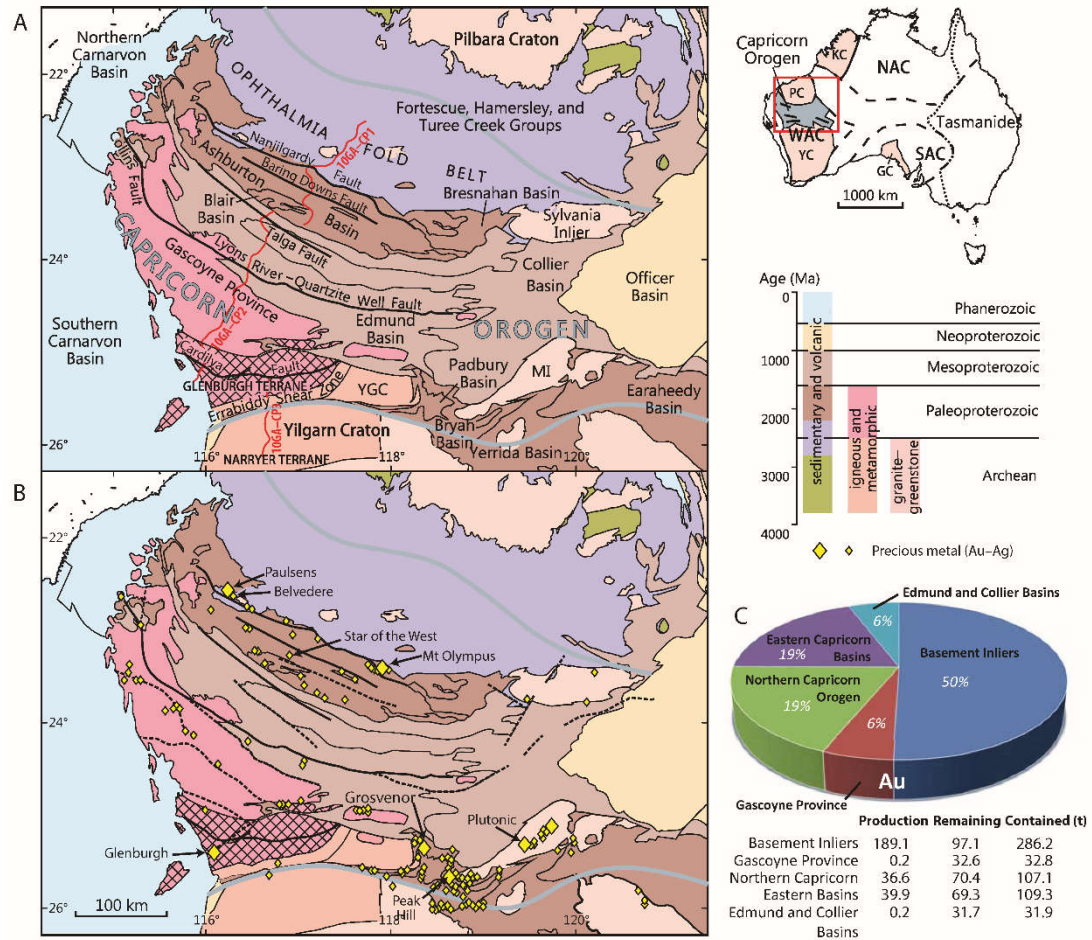


Figure 6-1: A: Simplified geological map of the Capricorn Orogen in Western Australia, showing location of the seismic transect (red line) and the orogen boundaries (thick grey line). Abbreviations: GC = Gawler Craton, KC = Kimberley Craton, MI = Marymia Inlier, NAC = North Australian Craton, PC = Pilbara Craton, SAC = South Australian Craton, WAC = West Australian Craton, YC = Yilgarn Craton, YGC = Yarlswheel Gneiss Complex. B: distribution of gold occurrences within the orogen with >1 Moz deposits shown as large symbols and dashed lines representing suture zones. C: pie chart and table showing the relative and estimated total mineral endowment (contained gold) for different parts of the orogen (after Johnson et al., 2017b).

Johnson et al., 2013; Pirajno, 2004). This makes it an ideal area to assess the relationship between the timing of gold mineralization, crustal architecture and the fault reactivation history. Many of the larger deposits within the Capricorn Orogen are focused around the periphery of the orogen (Johnson et al., 2017b) with 19% of the total gold endowment (107.1 t of Au, produced and remaining) situated in the northern part of the orogen (Figure 6-1; Johnson et al., 2017b). This includes the >1 Moz Paulsens and Mount Olympus deposits which are both associated with the Nanjilgardy Fault (Fielding et al., 2017; Young et al., 2003). The majority of gold in the southern part of the orogen is associated with either the Cardilya Fault, which marks the suture between the Yilgarn Craton and the Gascoyne Province (e.g. the Glenburgh deposit; Roche et al., 2017), or along the Yilgarn Craton margin (e.g., Plutonic, Grosvenor, and

Peak Hill deposits; Johnson et al., 2013, 2017b; Figure 6-1). This study focuses on the northern part of the orogen where there has recently been extensive new high-precision geochronology data that constrains the timing of gold mineralization, which can be integrated into the well-known tectonic history. Here we present a review of previously published data for the Capricorn Orogen in regards to crustal architecture and the timing of gold mineralization.

6.3. GEOLOGICAL SETTING

The Capricorn Orogen is a major zone of deformation, metamorphism and magmatism situated between the Pilbara and Yilgarn cratons of Western Australia (Figure 6-1). It marks the Paleoproterozoic amalgamation of the West Australian Craton during the Ophthalmia and Glenburgh orogenies (Johnson et al., 2011a; Occhipinti et al., 2004; Sheppard et al., 2004). During the 2215–2145 Ma Ophthalmia Orogeny (Johnson et al., 2011a; Rasmussen et al., 2005) the Pilbara Craton collided with the Glenburgh Terrane which subsequently collided with Yilgarn Craton during the 2005–1950 Ma Glenburgh Orogeny (Johnson et al., 2011a). Once amalgamated, the orogen experienced over a billion years of episodic intracratonic reworking and reactivation, including basin formation, metamorphism and magmatism (Figure 6-2; Cawood and Tyler, 2004; Johnson et al., 2013; Korhonen et al., 2017; Martin and Morris, 2010; Sheppard et al., 2005, 2007). This includes the 1820–1770 Ma Capricorn Orogeny (Cawood and Tyler, 2004; Sheppard et al., 2010), which was originally interpreted as representing oblique convergence between the Pilbara and Yilgarn cratons (Evans et al., 2003; Krapez, 1999; Tyler and Thorne, 1990), the 1680–1620 Ma Mangaroon Orogeny (Sheppard et al., 2005), the 1321–1171 Ma Mutherbukin Tectonic Event (Korhonen et al., 2017), the 1030–955 Ma Edmundian Orogeny (Martin and Thorne, 2004; Sheppard et al., 2007), the 931–749 Ma Kuparr Tectonic Event (Cutten and Johnson, 2018; Occhipinti and Reddy., 2009; Piechocka et al., 2018) and the c. 570 Ma Mulka Tectonic Event (Johnson et al., 2013).

6.3.1 GASCOYNE PROVINCE

The Gascoyne Province forms the core of the Capricorn Orogen (Figure 6-1) and consists of medium- to high-grade metamorphic rocks and low to medium metamorphic grade granitic rocks. The Glenburgh Terrane forms the basement to the

province and is interpreted as an exotic microcontinent which collided with the Pilbara Craton during the Ophthalmia Orogeny (Johnson et al., 2011a). The Glenburgh Terrane comprises 2555–2430 Ma heterogeneous granitic gneisses and psammitic and pelitic rocks dated at 2240–2125 Ma and 2005–1975 Ma (Johnson et al., 2011a; Sheppard et al., 2004). The Dalgaringa Supersuite forms an Andean-type batholith along the southern margin of the terrane with intermediate to granitic rocks (Sheppard et al., 2004).

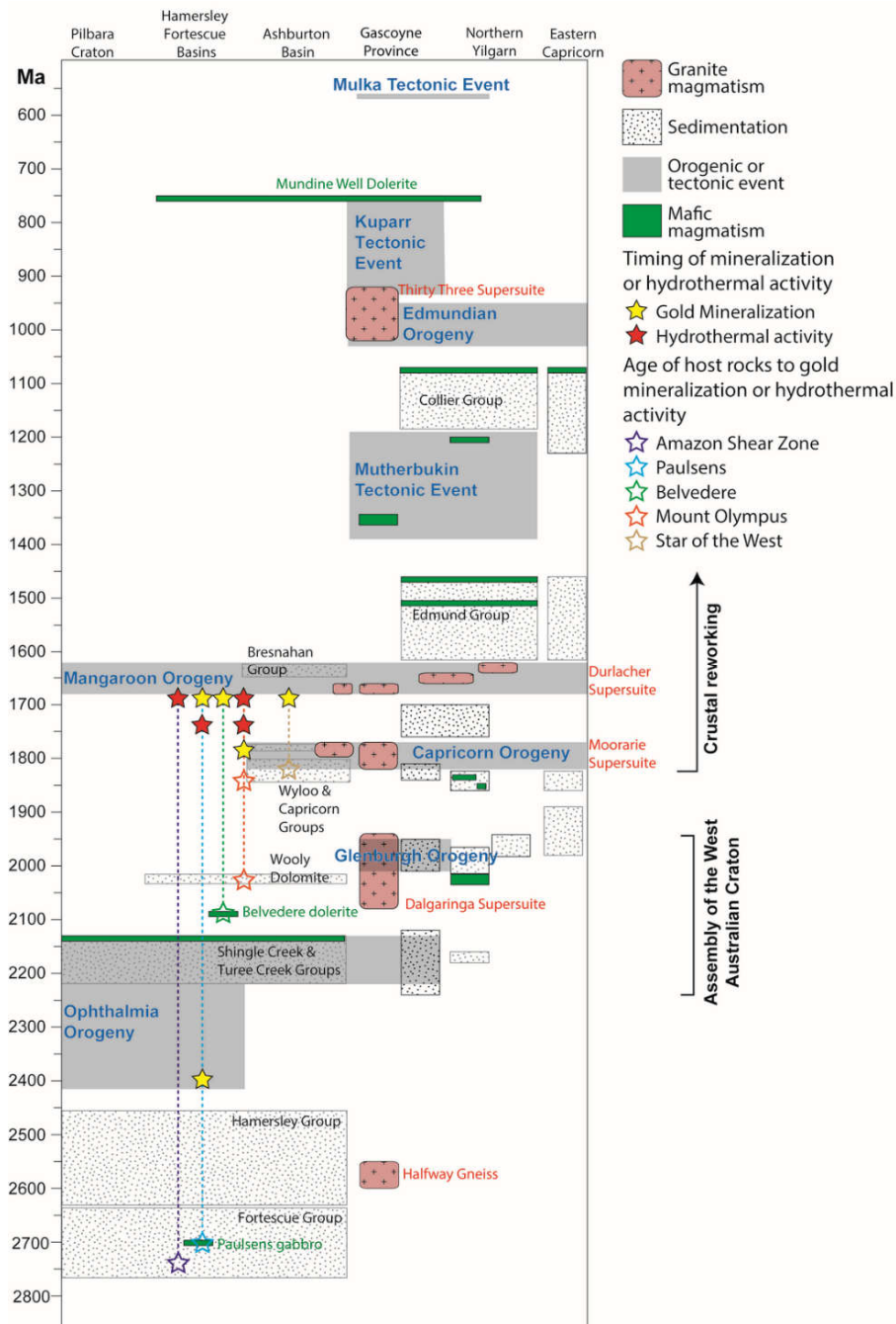


Figure 6-2: Time-space plot of the Capricorn Orogen showing the timing of hydrothermal activity and gold mineralization and how it relates to the host rocks.

The Gascoyne Province records all eight tectonic events with syn-tectonic felsic magmatism accompanying three of the intracratonic reworking events (Figure 6-2). This includes granitic rocks emplaced at 1820–1775 Ma during the Capricorn Orogeny, 1680–1620 Ma during the Mangaroon Orogeny and 995–955 Ma during the Edmundian Orogeny (Sheppard et al., 2005, 2007, 2010).

6.3.2 NORTHERN CAPRICORN OROGEN

The northern part of the orogen comprises Archean basement rocks of the Pilbara Craton overlain by Archean to Paleoproterozoic sedimentary and volcanic rocks of the Fortescue, Hamersley, Turee Creek, Shingle Creek, Wyloo, and Capricorn Groups (Figure 6-2 and 6-3; Johnson et al., 2011b, 2013). The Fortescue Group was deposited during rifting of the southern Pilbara margin between c. 2775 and 2629 Ma (Blake and Barley, 1992; Martin and Morris, 2010; Thorne and Trendall, 2001) prior to the Ophthalmia Orogeny. The southern Pilbara evolved from a rift to a passive continental margin between c. 2629 and 2445 Ma, which was accompanied by the deposition of sedimentary and volcanic rocks of the Hamersley Group (Blake and Barley, 1992; Martin and Morris, 2010; Trendall et al., 2004). Finally, between c. 2445 and 2031 Ma a series of foreland basins formed in response to the Ophthalmia Orogeny during which the Turee Creek and Single Creek Groups were deposited (Blake and Barley, 1992; Martin et al., 2000). Paleoproterozoic intracratonic reactivation during the Capricorn Orogeny resulted in the formation of the 2008–1800 Ma Ashburton, and 1800–1738 Ma Blair Basins in a possible foreland basin setting (Hall et al., 2001; Thorne and Seymour, 1991).

6.3.3 EASTERN CAPRICORN BASINS

The Paleoproterozoic Yerrida, Bryah, Padbury and Earahedy Basins (Figure 6-1) formed along the northern margin of the Yilgarn Craton between c. 2200 and 1800 Ma (Occhipinti et al., 2017; Olierook et al., 2018; Pirajno et al., 2004; Sheppard et al., 2016). Siliciclastic, carbonate and volcanoclastic sedimentary rocks were deposited in basins thought to have formed in settings associated with rifting, accretion and passive-margin tectonism (Occhipinti et al., 2017; Olierook et al., 2018; Pirajno et al., 2004; Sheppard et al., 2016). The basins are overprinted by deformation and metamorphism during the 1820–1770 Ma Capricorn Orogeny (Johnson et al., 2017b).



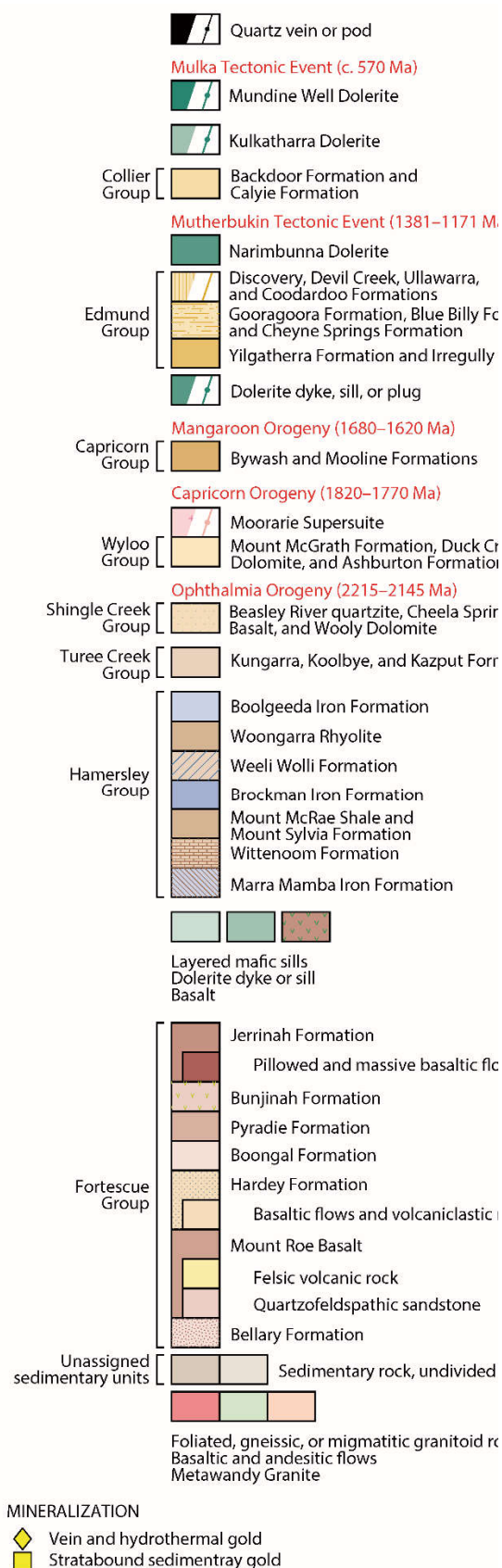


Figure 6-3: Geological map of the northern Capricorn Orogen showing the location of the seismic line (10GA-CP1) and gold deposits.

6.3.4 EDMUND AND COLLIER BASINS

The 1673–1449 Ma Edmund Basin and 1170–1067 Ma Collier Basin (Figure 6-1) comprise siliciclastic and carbonate metasedimentary rocks that were deposited in fluvial- to deep-marine environments in an intracratonic setting (Martin and Thorne, 2004). The basins were intruded by mafic sills at 1517–1505 Ma (Blay et al., 2015; Wingate et al., 2012, 2013) 1465–1449 Ma (Wingate, 2002), and 1084–1067 Ma (Wingate, 2002) prior being overprinted by widespread deformation during subsequent intracratonic reworking. The Edmund Basin was deformed and metamorphosed during the Mutherbukin Tectonic Event and the Edmundian Orogeny, whereas rocks in the Collier Basin were only affected by the Edmundian Orogeny (Cutten et al., 2016).

6.4. CRUSTAL ARCHITECTURE

The crustal architecture of the Capricorn Orogen and cratonic

boundaries were imaged in a deep-crustal seismic reflection survey (Figure 6-1; Johnson et al., 2013). Four distinctly different tectonic blocks were identified including, the Pilbara Craton, Glenburgh Terrane and Yilgarn Craton which are exposed at the surface, and the Bandee Seismic Province which has no surface expression. These tectonic blocks are separated by three suture zones, the Cardilya, Lyons River and Baring Downs Faults (Figure 6-4). Other major faults which extend to the mantle include the Nanjilgardy and Talga Faults (Johnson et al., 2011b, 2013).

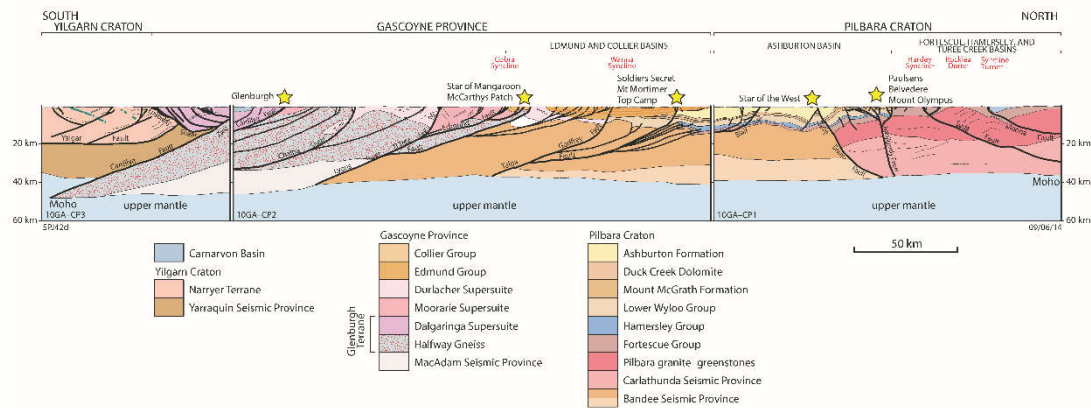


Figure 6-4: Seismic transect showing major faults, stratigraphic interpretations, and gold deposits as yellow stars (Johnson et al., 2013).

6.5. GOLD MINERALIZATION IN THE NORTHERN CAPRICORN OROGEN

Gold deposits in the northern Capricorn Orogen are intimately associated with the major crustal-scale structures identified in the seismic reflection survey (Johnson et al., 2013). In particular, the Nanjilgardy and Baring Downs Faults appear to be the most important (Figure 6-1 and 6-4; Fielding et al., 2017, 2018, 2019, under review; Johnson et al., 2013). The largest gold deposits are associated with the Nanjilgardy Fault, and include orogenic gold mineralization at the Paulsens deposit, and Carlin-like gold mineralization at the Mount Olympus deposit, both with endowments of >1 Moz (Figure 6-1 and 6-3; Fielding et al., 2017; Northern Star Resources Limited, January, 2016). Numerous smaller orogenic gold deposits occur throughout the Ashburton Basin and Wyloo Inlier (Figure 6-1 and 6-3; Thorne and Seymour, 1991; Thorne and Trendall, 2001) and include the Belvedere and Star of the West gold deposits (Fielding et al., 2018, under review). In the Ashburton Basin, these deposits have formed parallel to the youngest regional fabric and are interpreted to have

occurred during hydrothermal activity associated with the Mangaroon Orogeny (Fielding et al., under review).

6.5.1 PAULSENS

The Paulsens gold deposit is an orogenic gold deposit with an endowment of over 1 Moz Au (Northern Star Resources Limited, January, 2016, July, 2015). It is situated in the Wyloo Inlier adjacent to the Hardey Fault, which is a second order structure to the Nanjilgardy Fault (Figure 6-5; Fielding et al., 2017).

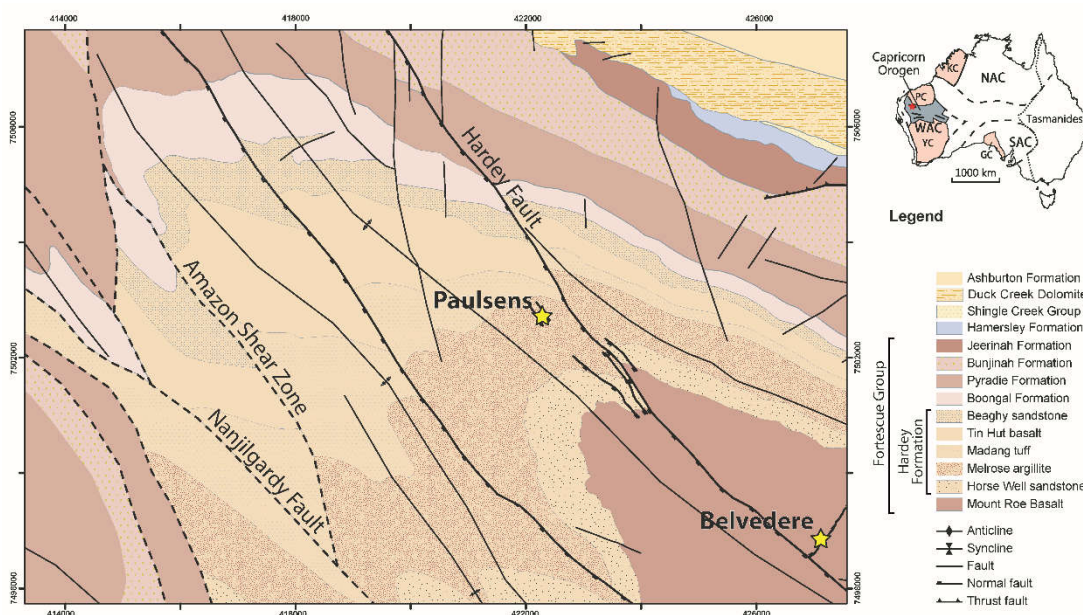


Figure 6-5: Geological map of the northern part of the Wyloo Inlier showing the location of the Paulsens and Belvedere gold deposits (yellow stars), the Hardey and Nanjilgardy faults. Coordinates are in meters (MGA94 zone 50).

A mineralized quartz-carbonate-sulfide vein is hosted within the c. 2700 Ma Paulsens Gabbro (Fielding et al., 2017) which is a 40 m-thick, folded and faulted gabbroic dyke which was emplaced into sedimentary and volcanic rocks at the base of the Fortescue Group (Owen, 2000; Thorne and Trendall, 2001). Gold mineralization occurs as two distinctive lodes at the margins of the auriferous quartz-carbonate-sulfide vein known as Paulsens Upper Zone and Paulsens Lower Zone (Figure 6-6; Fielding and Stokes, 2014). At the upper contact of the auriferous vein, the Upper Zone is made up of brecciated massive pyrite, with gold that occurs either as small rounded inclusions within the pyrite, or along fractures and grain boundaries of pyrite crystals (Fielding et al., 2017; Fielding and Stokes, 2014). Whereas the Lower Zone is characterized by laminated quartz-carbonate-sulfide veins, abundant carbonaceous stylolites and

inclusions of altered siltstone are common and are associated with abundant free gold (Fielding and Stokes, 2014) formed on the lower contact of the mineralized vein. Ore-stage alteration assemblages of muscovite–quartz–ankerite \pm chlorite \pm leucoxene surround the auriferous veins (Fielding et al., 2017).

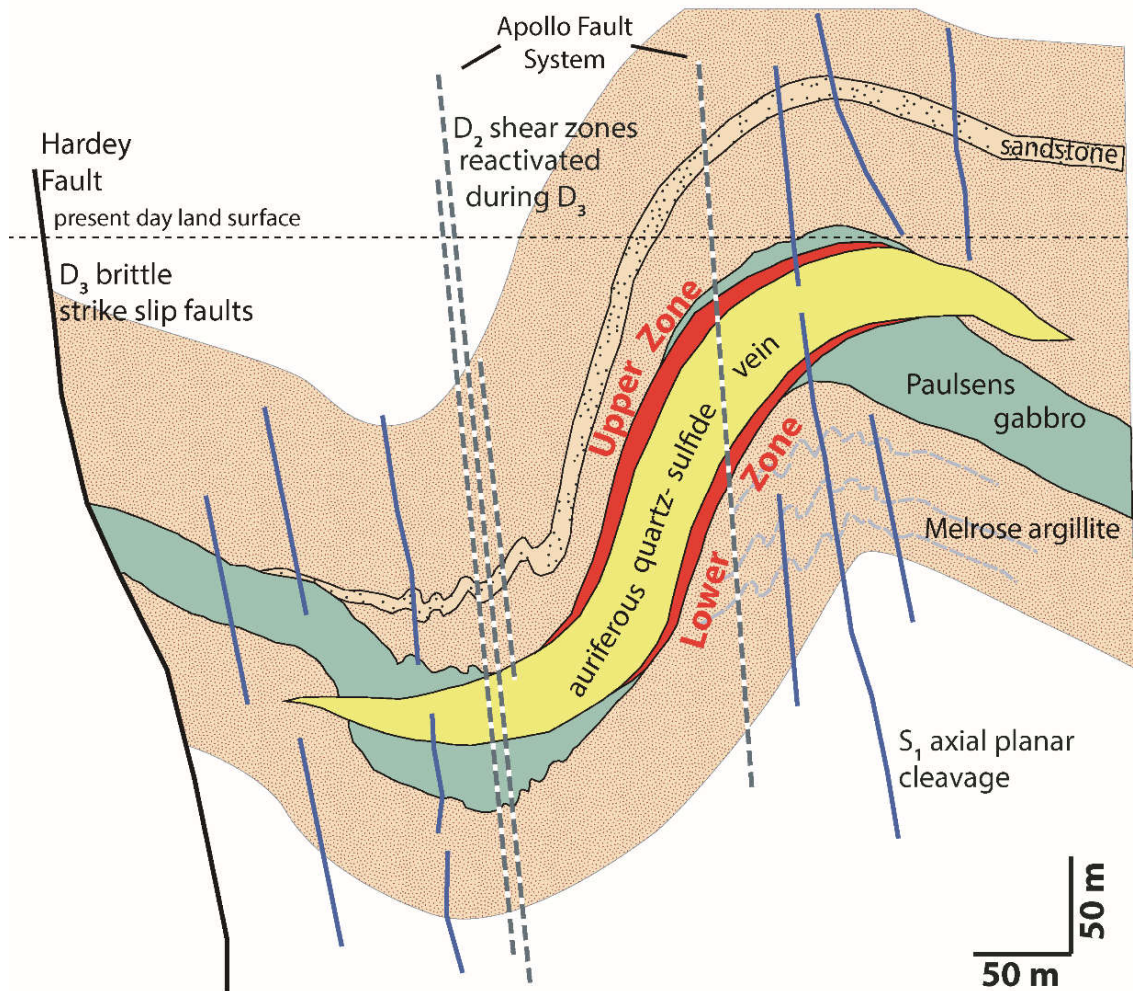


Figure 6-6: Schematic cross sections of the Paulsens ore deposit. View to the south with no vertical exaggeration.

In situ analysis of monazite and xenotime defined two discrete gold mineralization events at c. 2400 and 1680 Ma (Fielding et al., 2017). Monazite intergrown with ore-stage alteration minerals and euhedral xenotime crystals interlocking with auriferous pyrite from the Upper Zone mineralization provides an age for primary gold mineralization at c. 2400 Ma. Fielding et al. (2017) linked mineralization to a Pilbara-wide cryptic orogenic event that is accompanied by widespread hydrothermal activity and which is recorded by the growth of hydrothermal monazite throughout the western Pilbara (Rasmussen et al., 2005), hydrothermal xenotime growth at the nearby Belvedere prospect (Fielding et al., 2018), the resetting of high-U zircons in the

Hamersley Group (Pickard, 2002), as well as extensive uplift and erosion of the southern Pilbara region (Takehara et al., 2010). The second mineralization event at Paulsens, which is recorded by the brecciation of former c. 2400 Ma-aged pyrite accompanied by new xenotime growth and deposition of gold along fractures and grain boundaries, occurred at c. 1680 Ma (Fielding et al., 2017). This event was coeval with the onset of the intracratonic 1680–1620 Ma Mangaroon Orogeny (Sheppard et al., 2005) in the Gascoyne Province farther south. An additional hydrothermal event not linked to gold mineralization is recorded at c. 1730 Ma when porphyroblasts of hydrothermal monazite (intergrown with florencite) grew along the cleavage planes of highly strained phyllites (Fielding et al., 2017) and is synchronous with xenotime growth at the Mount Olympus deposit (Fielding et al., 2019).

6.5.2 MOUNT OLYMPUS

The Mount Olympus gold deposit is a Carlin-like gold deposit (Fielding et al., 2019) with a remaining resource of ~1 Moz (Northern Star Resources Limited, 2015). The mine is situated along a dextral transpressional fault, locally known as the Zoe Fault, which is a second order structure to the Nanjilgardy Fault (Figure 6-1; Young et al., 2003). The Zoe Fault acted as a pathway for hydrothermal and mineralizing fluids and has a strong control on the distribution of gold mineralization throughout the area (Fielding et al., 2019; Young et al., 2003). Most of the gold occurs in strata-bound lodes where coarse-grained, interbedded sandstone and conglomerate units of the Mount McGrath Formation are separated from dolomitic mudstones of the Woolly Dolomite by the Zoe Fault (Figure 6-7; Krapez, 1999; Morant and Doepel, 1997). Lesser amounts of gold mineralization form sporadically along the Zoe Fault within narrow, discontinuous quartz veins (Morant and Doepel, 1997). Alteration associated with the ore zones includes the addition of quartz, illite and sericite and the removal of carbonate minerals (Young et al., 2003; Wells et al., 2016). Within both strata-bound and fault hosted lodes, gold forms a solid solution within visibly zoned arsenian pyrite crystals (Young et al., 2003). LA-ICP-MS trace element mapping of pyrite crystals shows similar geochemical characteristics to the Carlin gold deposits in Nevada, with comparable relationships between Au–As, Au–Ni and Au–V for zones of pyrite enriched in Au–As, accompanied by elevated Au, As, Cu, Sb, Hg and Tl (Fielding et al., 2019).

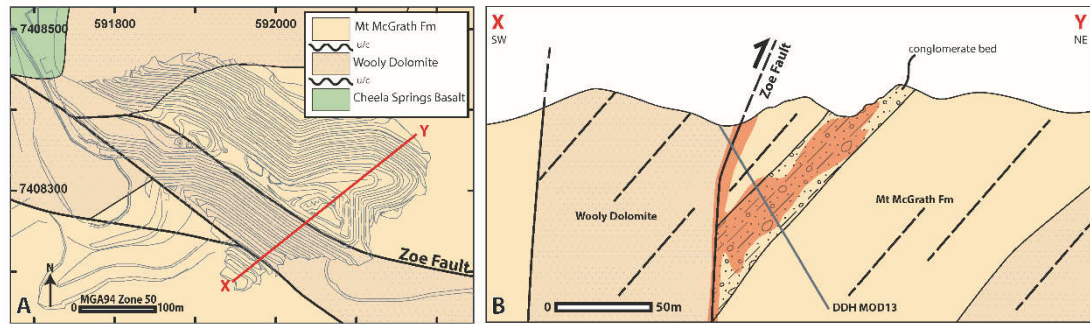


Figure 6-7: A: Prospect scale geological map of the Mount Olympus deposit. B: Schematic cross section showing strata-bound and fault hosted gold mineralization in orange. Coordinates are in meters (MGA94 zone 50; After Fielding et al., 2019).

In situ geochronology of xenotime crystals intergrown with auriferous arsenian pyrite and ore-stage alteration minerals (muscovite, quartz and rutile) provides an age for gold mineralization of c. 1770 Ma which is followed by two discrete hydrothermal events at c. 1730 and 1680 Ma (Fielding et al., 2019). Mineralization occurred during the final stages of the 1820–1770 Ma intracratonic Capricorn Orogeny during a change from dominantly compression to dextral strike-slip reactivation of the Nanjilgardy Fault and its associated structures (Krapez, 1999; Young et al., 2003). The younger two events represent periods of hydrothermal activity and possible fault reactivation. At c. 1730 Ma hydrothermal fluid movement is recorded along the Nanjilgardy Fault at both the Mount Olympus and Paulsens gold deposits (Fielding et al., 2017, 2019), but does not appear to be related to gold formation (cf. Sener et al., 2005). Finally, the c. 1680 Ma event represents widespread hydrothermal activity and gold mineralization throughout the northern Capricorn Orogen and the southern Pilbara region associated with the early stages of the intracratonic 1680–1620 Ma Mangaroon Orogeny (Fielding et al., 2017, 2018; Rasmussen et al., 2007a, 2007b).

6.5.3 BELVEDERE

Belvedere is an orogenic, vein-hosted gold deposit with a total endowment of 31,500 oz of Au (Blockley, 1971; Northern Star Resources Limited, 2015). It is located in the Wyloo Inlier approximately 6.5 km to the southeast of the Paulsens deposit adjacent to the Hardey Fault (Figure 6-1 and 6-5). Mineralized quartz–carbonate–arsenopyrite veins occur in a dolerite dyke informally known as the Belvedere dolerite (Fielding et al., 2018) which intrudes vesicular basalt, polymictic conglomerate, sandstone and siltstone of the Mount Roe Basalt (Figure 6-8; Fielding et al., 2018; Thorne and Trendall, 2001). The veins are interpreted to have formed due to sinistral movement

along the northeast striking Belvedere Fault which resulted in reidel shears and the production of dilatation quartz sulfide veins oriented at 190/52W (Figure 6–8). Mineralized veins are 2–12 m wide with gold forming as inclusions up to 150 μm within euhedral arsenopyrite crystals (Fielding et al., 2018). Ore-stage alteration assemblages of muscovite–quartz–carbonate \pm rutile \pm albite pervasively alter the rocks surrounding the mineralized veins (Norum, 2005).

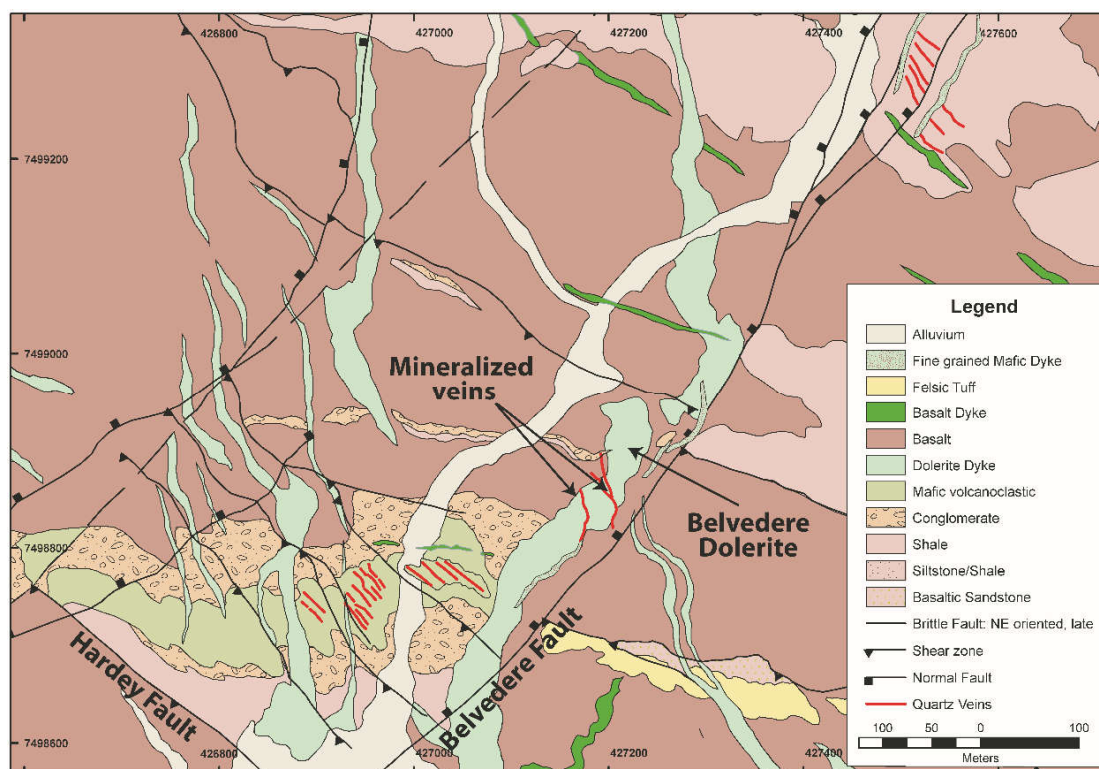


Figure 6-8: Local geology map of the Belvedere deposit showing the location of the Hardey and Belvedere faults and the Belvedere dolerite. Coordinates are in meters (MGA94 zone 50).

Dating of hydrothermal xenotime intergrown with ore-stage alteration minerals and fully encased with arsenopyrite crystals provided an age for gold mineralization at the Belvedere deposit of c. 1680 Ma (Fielding et al., 2018) related to onset of the Mangaroon Orogeny (Sheppard et al., 2005), during reactivation of the Hardey Fault (Fielding et al., 2018).

6.5.4 STAR OF THE WEST

Star of the West is an orogenic gold deposit which was mined in 1984, although no production figures are available. Thorne and Seymour (1991) reported gold grades of between 5 and 6 ppm within altered siliciclastic rocks surrounding barren quartz veins. The mine is located in the centre of the Ashburton Basin (Figure 6-1) and is hosted in

fine-grained sandstone and siltstone of the Ashburton Formation (Figure 6-9). Mineralization is associated with a second order structure to the Baring Downs Fault oriented at 278/78N (Fielding et al., under review). Gold occurs as small inclusions in euhedral, oxidised pyrite crystals up to 2 cm in diameter in muscovite altered siltstone and fine-grained sandstone that surround 5–20 cm wide quartz veins, rather than in the quartz veins or fault itself (Fielding et al., under review; Thorne and Seymour, 1991).

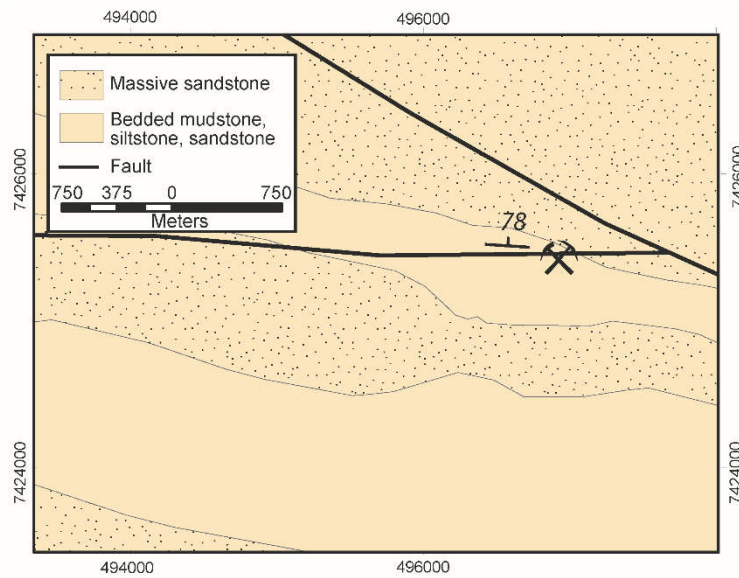


Figure 6-9: Local geology map of the Star of the West gold deposit. Coordinates are in meters (MGA94 zone 50).

Xenotime crystals containing laths of ore-stage muscovite from the Star of the West ore zone provide an age for hydrothermal activity related to gold mineralization of c. 1670 Ma (Fielding et al., under review). The age for mineralization reflects the timing of fault reactivation of structures associated with the Baring Downs Fault and is synchronous with widespread hydrothermal activity and associated gold mineralization during the early stages of the Mangaroon Orogeny (Fielding et al., 2017, 2018, 2019; Rasmussen et al., 2007a, 2007b).

6.6. DISCUSSION

6.6.1 PRIMING THE CRUST FOR GOLD MINERALIZATION

Ore deposits in many gold provinces throughout the world tend to cluster around crustal-scale faults and suture zones that commonly mark the boundaries between different tectonic blocks (Goldfarb et al., 2001; Groves and Santosh, 2015; Korsch and

Doublier, 2016; Markwitz et al., 2016). During the lead-up to the collisional or accretionary events that amalgamate these terranes, the margins of these tectonic blocks may have been the sites for emplacement of juvenile, mantle-derived material, either during initial rifting and breakup or in subsequent magmatic arcs, thus priming the crust and improving the potential for mineralization (Bierlein et al., 2009; Goldfarb et al., 2001). Considering that trans-crustal faults, such as former suture zones, provide critical pathways for the transport of fluid or magma from the mantle and lower crust to form ore deposits in the upper crust (Hronsky et al., 2012; McCuaig and Hronsky, 2014; McCuaig et al., 2010), it is probable that such a favourable crustal architecture needs to be established before gold mineralization can take place (Huston et al., 2016; Korsch and Doublier, 2016; McCuaig and Hronsky, 2014). Evidence for this is seen throughout the world in both Precambrian and Phanerozoic gold deposits. For example, Paleoproterozoic gold mineralization in the West Africa Craton (Fougerouse et al., 2017; Le Mignot et al., 2017) and Phanerozoic gold mineralization in the Jiaodong Gold Province in the North China Craton (Goldfarb and Santosh, 2014; Groves and Santosh, 2016) are both spatially associated with crustal-scale faults, the formation of which significantly pre-date primary gold mineralization.

Seismic imaging of the Capricorn Orogen and the associated cratonic margins, has significantly improved the understanding of the lithospheric architecture, demonstrating the link between major crustal-scale faults and occurrences of gold mineralization (Figure 6-4; Alghamdi et al., 2018; Johnson et al., 2013). In particular the gold deposits cluster around major faults near the Archean Pilbara and Yilgarn craton margins (Figure 6-1; Johnson et al., 2013, 2017b). Based on past production and remaining resource figures calculated in 2016 (Johnson et al., 2017b), the northern Yilgarn and southern Pilbara craton margins host the majority (88% at 502.6 tonnes) of the known gold endowment of the orogen compared to the central part, which includes the Gascoyne Province and younger basins, that hosts only 64.7 tonnes. Furthermore, the northern part of the orogen hosts a variety of styles of gold deposits (e.g. orogenic and Carlin-like mineralization) which have varying endowments, with gold interpreted to have formed during separate mineralization events related to reactivation of the Nanjilgardy and Baring Downs Faults during discrete tectonic events (Fielding et al., 2017, 2018, 2019, under review; Johnson et al., 2017b).

The Nanjilgardy Fault is associated with the majority of the gold deposits in the northern Capricorn Orogen, including the largest deposits of over 1 Moz at Paulsens and Mount Olympus (Figure 6-1). Although the fault does not represent a suture zone, it does transect the entire crust and defines the northern margin of the Ashburton Basin separating the 1840–1800 Ma Wyloo Group from the >2200 Ma Shingle Creek, Hamersley and Fortescue Groups (Johnson et al., 2013). The age at which the fault formed is unknown, although the fault offsets the Wyloo Group (Figure 6-4) suggesting movement either during or following the 1820–1770 Ma Capricorn Orogeny. Additionally, c. 2400 Ma gold mineralization at the Paulsens deposit is situated on a second order structure to the Nanjilgardy Fault, suggesting the fault formed before or at c. 2400 Ma (Fielding et al., 2017).

The Baring Downs Fault is a major suture zone separating two opposing tectonic blocks, the Pilbara Craton and the Bandee Seismic Province (Figure 6-4; Johnson et al., 2013). The time of collision is not known; however, as the 2775–2629 Ma Fortescue Group rocks are interpreted to have been deposited across the suture zone, the collisional event must be older than c. 2775 Ma (Figure 6-4; Johnson et al., 2013). This indicates that the Baring Downs Fault was established prior to all known gold events in the northern Capricorn Orogen, including the earliest event in which orogenic gold mineralization was deposited at the Paulsens Gold mine at c. 2400 Ma (Fielding et al., 2017). Once established, both the Nanjilgardy and Baring Downs faults had undergone long reactivation histories and have provided a critical plumbing system to channel hydrothermal and mineralized fluids into the upper crust.

6.6.2 IMPLICATIONS FOR MINERAL SYSTEMS

Wyborn et al. (1994) described a mineral system as “all geological factors that control the generation and preservation of mineral deposits”. By knowing how mineralization forms at a range of scales, we can better understand the distribution of gold through both space and time (Hronsky and Groves, 2008; Huston et al., 2016; McCuaig et al., 2010). McCuaig and Hronsky (2014) broke down the mineral systems concept into four critical elements: 1) favourable lithospheric architecture, including steeply dipping, crustal-scale faults which are multiply reactivated and commonly separate different tectonic blocks; 2) transient favourable geodynamics during which mineralization occurs on short timeframes due to anomalous compression, initial

stages of extension or switches in far-field stresses; 3) fertility including lithospheric enrichment in metals and; 4) preservation of primary deposition zones. These criteria can be applied to the northern Capricorn Orogen to gain an understanding of controlling factors influencing the formation and location of gold mineralization.

In the northern Capricorn Orogen, a clear relationship exists between gold occurrences and their proximity to steeply-dipping, crustal-scale faults that juxtapose different stratigraphic packages or tectonic blocks (Figure 6-4). At least three episodes of hydrothermal gold mineralization occurred at c. 2400, 1770 and 1680 Ma (Figure 6-10). The timing of gold mineralization is associated with discrete orogenic episodes where hydrothermal and auriferous fluids moved along the crustal-scale Nanjilgardy and Baring Downs Faults and their second and third order structures during episodes of punctuated fault reactivation (Fielding et al., 2017, 2018, 2019, under review).

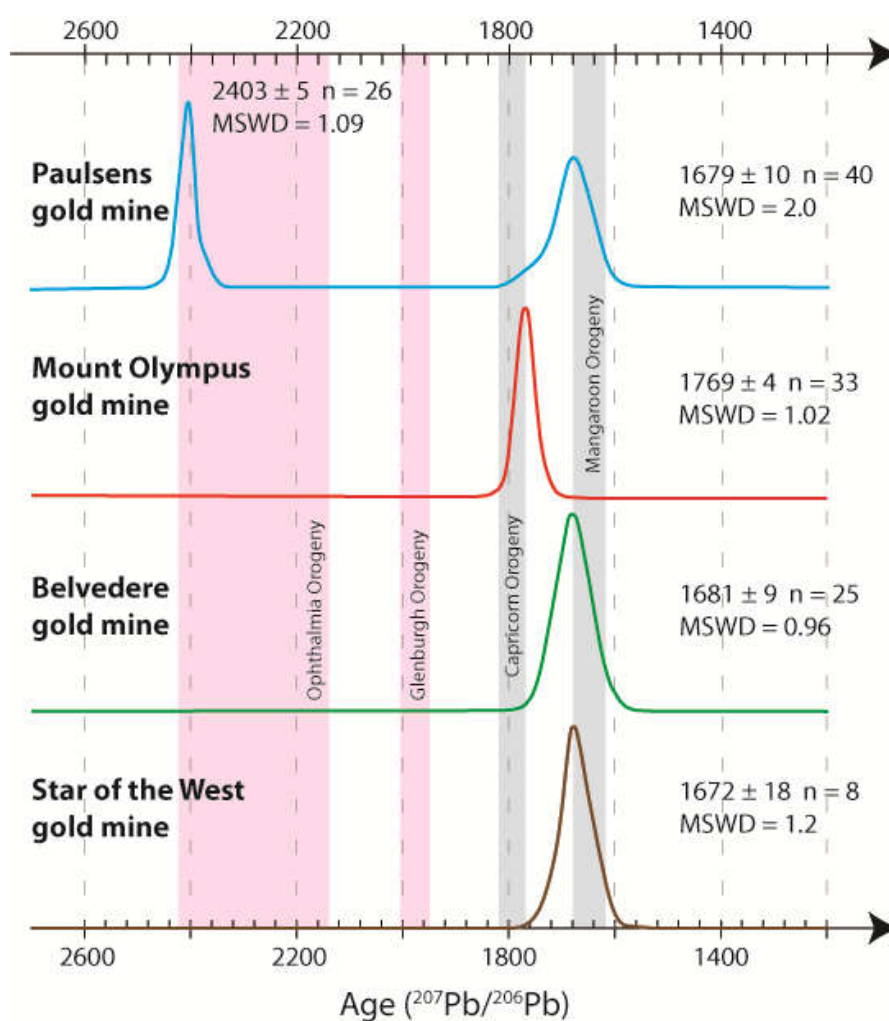


Figure 6-10: Summary histograms showing age peaks of gold mineralization at the Paulsens, Mount Olympus, Belvedere and Star of the West gold mines defined by xenotime. Known orogenic events are defined by blue shading = cryptic orogenic event at c. 2400, pink = collisional orogenies, grey = intracratonic orogenies.

These periods of fault reactivation can be linked directly to the tectonothermal evolution of the Capricorn Orogen (Figure 6-2 and 6-10). At c. 2400 Ma orogenic gold mineralization at Paulsens is linked to the timing of a cryptic orogenic event (Fielding et al., 2017). Although events of this age were not previously recognized, circumstantial evidence including the resetting of high U zircons in the Hamersley Basin (Pickard, 2002), extensive hydrothermal xenotime and monazite growth throughout the Pilbara (Rasmussen et al., 2005), and widespread uplift and erosion along the southern Pilbara margin (Takehara et al., 2010) have been documented. It is possible that these events all mark the beginning of the Ophthalmia Orogeny. This was followed by deposition of Carlin-like gold mineralization at the Mount Olympus deposit at c. 1770 Ma (Fielding et al., 2019), the timing of which can be linked to the final stages of the intracratonic 1820–1770 Ma Capricorn Orogeny (Sheppard et al., 2010) during which a change from dominantly compressional to dextral strike-slip reactivation of the Nanjilgardy Fault took place (Krapez, 1999; Young et al., 2003). The youngest known mineralization event occurred at c. 1680 Ma during the early stages of the 1680–1620 Ma Mangaroon Orogeny (Sheppard et al., 2005). This event throughout the northern Capricorn Orogen and Pilbara region is characterized by widespread hydrothermal activity and gold mineralization associated with fault reactivation (Fielding et al., 2017, 2018, 2019, under review; Rasmussen et al., 2007a, 2007b).

Most of the gold deposits in the northern Capricorn Orogen formed during intracratonic reworking. Intracratonic settings are not usually considered prospective for gold due to limited input of fertile material (Bierlein et al., 2009; Goldfarb et al., 2001). Although the Capricorn and Mangaroon Orogenies are associated with felsic magmatism (Johnson et al., 2013, 2017), these intrusive rocks were emplaced farther to the south in the Gascoyne Province and the western most parts of the Ashburton Basin (Figures 6-1 and 6-3) and have no influence on the distribution of gold in the northern part of the Capricorn Orogen. However, it is possible that in intracratonic settings, gold deposits are subsequently upgraded during multiple fault reactivation, provided that there has been an adequate priming of the crust and the construction of a favourable crustal architecture (Fielding et al., 2018). While many of the gold occurrences in the northern Capricorn Orogen have limited gold endowments, the larger deposits appear to have been subject to more complex geological histories. For

example, the Star of the West and Belvedere gold deposits are both relatively small and only show evidence for a single pulse of mineralization at c. 1680 Ma (Fielding et al., 2018, under review), whereas the >1 Moz Paulsens and Mount Olympus deposits both show evidence for multiple hydrothermal events (Figure 6-2; Fielding et al., 2017, 2019).

It is becoming increasingly evident that multiple hydrothermal events are a common feature of many large gold deposits throughout the world. For example, the Kiistala Shear Zone in northern Finland is host the Suurikuusikko (Europe's largest gold deposit) and Iso-Kuotko gold deposits with mineralization occurring at c. 1916 and 1770–1760 Ma (Molnár et al., 2018). Additionally, Africa's largest gold deposit, the Obuasi gold deposit, in Ghana also has two stages of gold mineralization with gold bearing arsenopyrite forming during D₂ deformation followed by native gold filling fractures in quartz veins during D₃ (Fougerouse et al., 2017). Episodic gold formation is also evident in many of the larger gold deposits throughout Australia such as the Golden Mile gold deposit where two mineralizing events are event (Bateman and Hagemann, 2004) at c. 2640 and 2600 Ma (Vielreicher et al., 2010). Meffre et al (2016) suggests that iterative upgrading of gold through multi-stage enrichment processes may be required for the formation of a large deposit. Such results are consistent with those presented here and these have implication for exploration targeting.

6.6.3 EXPLORATION TARGETING

In order for effective exploration targeting we must establish the primary controls on gold mineralization at a regional-scale as well as assessing deposit-scale features. By knowing the age of gold mineralization in the northern Capricorn Orogen we can demonstrate a more complex geological and mineralization history than earlier recognised. Prior to results presented over the past 2 years, gold mineralization was linked solely to the 1820–1770 Ma Capricorn Orogeny (Pirajno, 2004; Tyler, 1991). However, new geochronological information indicates that the timing of gold mineralization is more complicated.

At a regional scale, it is critical to understand the link between the timing of gold mineralization, its location with respect to craton margins and the crustal architecture in order to develop robust exploration models. Favourable crustal architecture includes the presence of crustal-scale faults and their second order structures, which extend to

the mantle, are steeply dipping, separate opposing lithospheric blocks, and have undergone a long-lived reactivation history (McCuaig and Hronsky, 2014). In the northern Capricorn Orogen the Nanjilgardy and Baring Downs faults satisfy all these criteria. Additionally, areas which document multiple pulses of mineralizing fluids or structural complexities are more likely to host gold deposits with a greater endowment (e.g. Fielding et al., 2018; Meffre et al., 2016), especially within an intracratonic setting.

6.7. CONCLUSIONS

Most gold deposits in the northern Capricorn Orogen occur at the margin of the Pilbara Craton and are related to multiple reactivation of the pre-existing, crustal-scale Nanjilgardy and Baring Downs faults (Figure 6-1). In this region, the crustal architecture had been established prior to all mineralization events. Once established, these faults acted as deep plumbing systems for the channelling of hydrothermal and mineralizing fluids. Deep crustal seismic imaging and geochronological data show that in the northern Capricorn Orogen both the Nanjilgardy and Baring Downs faults have long reactivation histories, suggesting that within an intracratonic setting episodic fault activity may be required to upgrade ore deposits from small gold occurrences into an economically viable deposit.

6.8. ACKNOWLEDGMENTS

This project was funded through an ARC linkage grant (LP130100922), the Exploration Incentive Scheme and an industry scholarship by Northern Star Resources as a part of a PhD by I.O.H. Fielding. S.P. Johnson publishes with the permission of the director of the Geological Survey of Western Australia.

6.9. REFERENCES

- Alghamdi, A.H., Aitken, A.R.A., Dentith, M.C., 2018. The composition and structure of the deep crust of the Capricorn Orogen. *Australian Journal of Earth Sciences* 65, 9-24.
- Bateman, R., and Hagemann, S., 2004, Gold mineralisation throughout about 45 Ma of Archaean orogenesis: protracted flux of gold in the Golden Mile, Yilgarn

- craton, Western Australia: *International Journal of Geology, Mineralogy and Geochemistry of Mineral Deposits*, v. 39, no. 5, p. 536-559.
- Bierlein, F.P., Groves, D.I., Cawood, P.A., 2009. Metallogeny of accretionary orogens — The connection between lithospheric processes and metal endowment. *Ore Geology Reviews* 36, 282-292.
- Blake, T.S., Barley, M.E., 1992. Tectonic evolution of the Late Archaean to Early Proterozoic Mount Bruce Megasequence Set, western Australia. *Tectonics* 11, 1415-1425.
- Blay, O.A., Johnson, S.P., Thorne, A.M., Cutten, H.N.C., 2015. Waldburg Dolerite (P_ -_wa-od): Geological Survey of Western Australia, WA Geology Online, Explanatory Notes extract, viewed 20 April 2016, www.dmp.wa.gov.au/ens.
- Blockley, J.G., 1971. The lead, zinc and silver deposits of Western Australia, Geological Survey of Western Australia, Mineral Resources Bulletin 9, 237 p.
- Cawood, P.A., Tyler, I.M., 2004. Assembling and reactivating the Proterozoic Capricorn Orogen: lithotectonic elements, orogenies, and significance. *Precambrian Research* 128, 201-218.
- Chesley, J.T., 1999. Integrative geochronology of ore deposits: New insights into the duration and timing of hydrothermal circulation, *in*: Lambert, D.D., Brown, P.E. (Eds.), *Reviews in economic geology*, pp. 115-142.
- Cutten, H. N. C., and Johnson, S. P., 2018, Kuparr Tectonic Event (KU): Geological Survey of Western Australia, WA Geology Online, Explanatory Notes extract, viewed 12 December 2018, <www.dmp.wa.gov.au/ens>
- Cutten, H.N., Johnson, S.P., Thorne, A.M., Windgate, M.T.D., Kirkland, C.L., Belousova, E.A., Blay, O.A., Zwingmann, H., 2016. Deposition, provenance, inversion history and mineralization of the Proterozoic Edmund and Collier Basins, Capricorn Orogen, Geological Survey of Western Australia, Report 127, 74 p.
- Doggett, M., Zhang, J., 2007. Production trends and economic characteristics of canadian gold mines. *Exploration and Mining Geology* 16, 1-10.
- Evans, D.A.D., Sircombe, K.N., Wingate, M.T.D., Doyle, M., McCarthy, M., Pidgeon, R.T., Van Niekerk, H.S., 2003. Revised geochronology of magmatism in the western Capricorn Orogen at 1805-1785 Ma: diachroneity of the Pilbara-Yilgarn collision. *Australian Journal of Earth Sciences* 50, 853-864.
- Fielding, I., Stokes, L., 2014. Gabbro Offset Drilling, Ashburton Basin, Pilbara - Western Australia, M08/196, Exploration Incentive Scheme Final Report. Northern Star Resources, Geological Survey of Western Australia Open-file Report, 13 p.
- Fielding, I.O.H., Johnson, S.P., Meffre, S., Zi, J.W., Sheppard, S., Large, R.R., Rasmussen, B., 2019. Linking gold mineralization to regional-scale drivers of

mineral systems using in situ U–Pb geochronology and pyrite LA-ICP-MS element mapping. *Geoscience Frontiers* 10, 89–105.

Fielding, I.O.H., Johnson, S.P., Zi, J.W., Rasmussen, B., under review. U-Pb dating of fault reactivation and gold mineralization in the northern Capricorn Orogen, Western Australia, *Australian Journal of Earth Sciences*.

Fielding, I.O.H., Johnson, S.P., Zi, J.-W., Rasmussen, B., Muhling, J.R., Dunkley, D.J., Sheppard, S., Wingate, M.T.D., Rogers, J.R., 2017. Using In Situ SHRIMP U-Pb Monazite and Xenotime Geochronology to Determine the Age of Orogenic Gold Mineralization: An Example from the Paulsens Mine, Southern Pilbara Craton. *Economic Geology* 112, 1205-1230.

Fielding, I.O.H., Johnson, S.P., Zi, J.W., Sheppard, S., Rasmussen, B., 2018. Neighbouring orogenic gold deposits may be the products of unrelated mineralizing events. *Ore Geology Reviews* 95, 593-603.

Fougerouse, D., Micklethwaite, S., Ulrich, S., Miller, J., Godel, B., Adams, D.T., McCuaig, T.C., 2017. Evidence for Two Stages of Mineralization in West Africa's Largest Gold Deposit: Obuasi, Ghana. *Economic Geology* 112, 3-22.

Goldfarb, R.J., Groves, D.I., Gardoll, S., 2001. Orogenic gold and geologic time: a global synthesis. *Ore Geology Reviews* 18, 1-75.

Goldfarb, R.J., Santosh, M., 2014. The dilemma of the Jiaodong gold deposits: Are they unique? *Geoscience Frontiers* 5, 139-153.

Groves, D.I., Santosh, M., 2015. Province-scale commonalities of some world-class gold deposits: Implications for mineral exploration. *Geoscience Frontiers* 6, 389-399.

Groves, D.I., Santosh, M., 2016. The giant Jiaodong gold province: The key to a unified model for orogenic gold deposits? *Geoscience Frontiers* 7, 409-417.

Hall, C.E., Powell, C.M., Bryant, J., 2001. Basin setting and age of the Late Palaeoproterozoic Capricorn Formation, Western Australia. *Australian Journal of Earth Sciences* 48, 731-744.

Hronsky, J.M., Groves, D.I., Loucks, R.R., Begg, G.C., 2012. A unified model for gold mineralisation in accretionary orogens and implications for regional-scale exploration targeting methods. *Mineralium Deposita* 47, 339-358.

Hronsky, J.M.A., 2011. Self-Organized Critical Systems and Ore Formation: The Key to Spatial Targeting? *SEG Newsletter* 84, 14-16.

Hronsky, J.M.A., Groves, D.I., 2008. Science of targeting: definition, strategies, targeting and performance measurement. *Australian Journal of Earth Sciences* 55, 3-12.

Huston, D.L., Mernagh, T.P., Hagemann, S.G., Doublier, M.P., Fiorentini, M., Champion, D.C., Lynton Jaques, A., Czarnota, K., Cayley, R., Skirrow, R., Bastrakov, E., 2016. Tectono-metallogenic systems — The place of mineral

- systems within tectonic evolution, with an emphasis on Australian examples. *Ore Geology Reviews* 76, 168-210.
- Jennings, K., Schodde, R., 2016. From mineral discovery to project delivery. *SEG Newsletter* 105, 20-25.
- Johnson, S.P., Korhonen, F.J., Kirkland, C.L., Cliff, J.B., Belousova, E.A., Sheppard, S., 2017a. An isotopic perspective on growth and differentiation of Proterozoic orogenic crust: From subduction magmatism to cratonization. *lithos* 268-271, 76-86.
- Johnson, S.P., Cutten, H.N., Korhonen, F.J., L., W.N., 2017b. Geology and metallogeny of the Capricorn Orogen, in: Phillips, G.N. (Ed.), *Australian Ore Deposits. The Australian Institute of Mining and Metallurgy: Melbourne*, pp. 289-392.
- Johnson, S.P., Sheppard, S., Rasmussen, B., Wingate, M.T.D., Kirkland, C.L., Muhling, J.R., Fletcher, I.R., Belousova, E.A., 2011a. Two collisions, two sutures: Punctuated pre-1950Ma assembly of the West Australian Craton during the Ophthalmian and Glenburgh Orogenies. *Precambrian Research* 189, 239-262.
- Johnson, S.P., Thorne, A.M., Tyler, I.M., 2011b. Capricorn Orogen seismic and magnetotelluric (MT) workshop 2011: Extended abstracts, Geological Survey of Western Australia, Record 2011/25, 132 p.
- Johnson, S.P., Thorne, A.M., Tyler, I.M., Korsch, R.J., Kennett, B.L.N., Cutten, H.N., Goodwin, J., Blay, O., Blewett, R.S., Joly, A., Dentith, M.C., Aitken, A.R.A., Holzschuh, J., Salmon, M., Reading, A., Heinson, G., Boren, G., Ross, J., Costelloe, R.D., Fomin, T., 2013. Crustal architecture of the Capricorn Orogen, Western Australia and associated metallogeny. *Australian Journal of Earth Sciences* 60, 681-705.
- Joly, A., Porwal, A., McCuaig, T.C., Chudasama, B., Dentith, M.C., Aitken, A.R.A., 2015. Mineral systems approach applied to GIS-based 2D-prospectivity modelling of geological regions: Insights from Western Australia. *Ore Geology Reviews* 71, 673-702.
- Korhonen, F.J., Johnson, S.P., Wingate, M.T.D., Fletcher, I.R., Dunkley, D.J., Roberts, M.P., Sheppard, S., Muhling, J.R., Rasmussen, B., 2017. Radiogenic heating and craton-margin plate stresses as drivers for intraplate orogeny. *Journal of metamorphic geology* 35, 631-661.
- Korsch, R.J., Doublier, M.P., 2016. Major crustal boundaries of Australia, and their significance in mineral systems targeting. *Ore Geology Reviews* 76, 211-228.
- Krapez, B., 1999. Stratigraphic record of an Atlantic-type global tectonic cycle in the Palaeoproterozoic Ashburton Province of Western Australia. *Australian Journal of Earth Sciences* 46, 71-87.
- Le Mignot, E., Reisberg, L., André-Mayer, A.S., Bourassa, Y., Fontaine, A., Miller, J., 2017. Re-Os geochronological evidence for multiple Paleoproterozoic gold

- events at the scale of the West African craton. *Economic Geology* 112, 145-168.
- Markwitz, V., Hein, K.A.A., Miller, J., 2016. Compilation of West African mineral deposits: Spatial distribution and mineral endowment. *Precambrian Research* 274, 61-81.
- Martin, D.M., Morris, P.A., 2010. Tectonic setting and regional implications of ca. 2.2 Ga mafic magmatism in the southern Hamersley Province, Western Australia. *Australian Journal of Earth Sciences* 57, 911-931.
- Martin, D.M., Powell, C.M., George, A.D., 2000. Stratigraphic architecture and evolution of the early Paleoproterozoic McGrath Trough, Western Australia. *Precambrian Research* 99, 33-64.
- Martin, D.M., Thorne, A., 2004. Tectonic setting and basin evolution of the Bangemall Supergroup in the northwestern Capricorn Orogen. *Precambrian Research* 128, 385-409.
- McCuaig, T.C., Beresford, S., Hronsky, J., 2010. Translating the mineral systems approach into an effective exploration targeting system. *Ore Geology Reviews* 38, 128-138.
- McCuaig, T.C., Hronsky, J.M.A., 2014. The mineral systems concept: The key to exploration targeting in: Kelly, K.D., Golden, H.C. (Eds.), *Building Exploration Capability for the 21st Century*, Society of Economic Geologists, pp. 153-175.
- McKeith, T.D., Schodde, R.C., Baltus, E.J., 2010. Gold Discovery Trends. *SEG Newsletter* 81, 1, 18-24.
- Meffre, S., Large, R.R., Steadman, J.A., Gregory, D.D., Stepanov, A.S., Kamenetsky, V.S., Ehrig, K., Scott, R.J., 2016. Multi-stage enrichment processes for large gold-bearing ore deposits. *Ore Geology Reviews* 76, 268-279.
- Molnár, F., Middleton, A., Stein, H., O'Brien, H., Lahaye, Y., Huhma, H., Pakkanen, L., and Johanson, B., 2018, Repeated syn- and post-orogenic gold mineralization events between 1.92 and 1.76 Ga along the Kiistala Shear Zone in the Central Lapland Greenstone Belt, northern Finland: *Ore Geology Reviews*, v. 101, p. 936-959.
- Morant, P., Doepel, G., 1997. The Mount Olympus Gold Deposit, New Generation Gold Mines '97. Australian Mineral Foundation, Perth, Western Australia, pp. 6.1 - 6.9.
- Northern Star Resources Limited, 2015. Northern Star Resources Limited 2015 annual report, (<http://www.nsrld.com/wp-content/uploads/2015/08/NST-Annual-Report-2015-26-8-2015-new-cover1.pdf>).
- Northern Star Resources Limited, January, 2016. Resources and Reserves, (<http://www.nsrld.com/our-assets/resources-and-reserves/>).

- Northern Star Resources Limited, July, 2015. Northern Star Paulsens operations fact sheet, (<http://www.nsrld.com/wp-content/uploads/2015/08/NSR-Paulsens-Operations-Fact-Sheet-July-2015-FINAL.pdf>).
- Norum, E., 2005. 14 November 2003 to 13 November 2004, Paulsens Project, E08/665, E08/906, E08/1125, E47/977, E47/1134, E47/1135, M08/99, M08/196 and M08/222, Combined Reporting Group C211/1997. Nustar Mining Corporation Limited; Geological Survey of Western Australia Open-file report a070119.
- Occhipinti, S., Hocking, R., Lindsay, M., Aitken, A., Copp, I., Jones, J., Sheppard, S., Pirajno, F., Metelka, V., 2017. Paleoproterozoic basin development on the northern Yilgarn Craton, Western Australia. *Precambrian Research* 300, 121-140.
- Occhipinti, S., and Reddy, S., 2009, Neoproterozoic reworking of the Palaeoproterozoic Capricorn Orogen of Western Australia and implications for the amalgamation of Rodinia. Geological Society of London, Special Publication, v. 327, p. 445–456
- Occhipinti, S.A., Sheppard, S., Passchier, C., Tyler, I.M., Nelson, D.R., 2004. Palaeoproterozoic crustal accretion and collision in the southern Capricorn Orogen: the Glenburgh Orogeny. *Precambrian Research* 128, 237-255.
- Olierook, H.K.H., Sheppard, S., Johnson, S.P., Occhipinti, S.A., Reddy, S.M., Clark, C., Fletcher, I.R., Rasmussen, B., Zi, J.-W., Pirajno, F., LaFlamme, C., Do, T., Ware, B., Blandthorn, E., Lindsay, M., Lu, Y.-J., Crossley, R.J., Erickson, T.M., 2018. Extensional episodes in the Paleoproterozoic Capricorn Orogen, Western Australia, revealed by petrogenesis and geochronology of mafic–ultramafic rocks. *Precambrian Research* 306, 22-40.
- Owen, S., 2000. Ashburton Project, Paulsens E08/665, E08/906, M08/99 and M08/196, Annual report to the Department of Minerals and Energy for the Period 15 November 1999 to 14 November 2000. Taipan Resources N.L; Geological Survey of Western Australia Open-file report, 39 p.
- Pickard, A.L., 2002. SHRIMP U–Pb zircon ages of tuffaceous mudrocks in the Brockman Iron Formation of the Hamersley Range, Western Australia. *Australian Journal of Earth Sciences* 49, 491-507.
- Piechocka, A. M., Sheppard, S., Fitzsimons, I. C. W., Johnson, S. P., Rasmussen, B., and Jordan, F., 2018, Neoproterozoic $^{40}\text{Ar}/^{39}\text{Ar}$ mica ages mark the termination of a billion years of intraplate reworking in the Capricorn Orogen, Western Australia: *Precambrian Research*, v. 310, p. 391–406.
- Pirajno, F., 2004. Metallogeny in the Capricorn Orogen, Western Australia, the result of multiple ore-forming processes. *Precambrian Research* 128, 411-439.
- Pirajno, F., Jones, J.A., Hocking, R.M., Halilovic, J., 2004. Geology and tectonic evolution of Palaeoproterozoic basins of the eastern Capricorn Orogen, Western Australia. *Precambrian Research* 128, 315-342.

- Raimondo, T., Collins, A.S., Hand, M., Walker-Hallam, A., Smithies, R.H., Evins, P.M., Howard, H.M., 2010. The anatomy of a deep intracontinental orogen. *Tectonics* 29, 31 p.
- Rasmussen, B., Fletcher, I.R., Muhling, J.R., 2007a. In situ U–Pb dating and element mapping of three generations of monazite: Unravelling cryptic tectonothermal events in low-grade terranes. *Geochimica et Cosmochimica Acta* 71, 670-690.
- Rasmussen, B., Fletcher, I.R., Muhling, J.R., Thorne, W.S., Broadbent, G.C., 2007b. Prolonged history of episodic fluid flow in giant hematite ore bodies: Evidence from in situ U–Pb geochronology of hydrothermal xenotime. *Earth and Planetary Science Letters* 258, 249-259.
- Rasmussen, B., Fletcher, I.R., Sheppard, S., 2005. Isotopic dating of the migration of a low-grade metamorphic front during orogenesis. *Geology* 33, 773-776.
- Rasmussen, B., Sheppard, S., Fletcher, I.R., 2006. Testing ore deposit models using in situ U–Pb geochronology of hydrothermal monazite: Paleoproterozoic gold mineralization in northern Australia. *Geology* 34, 77-80.
- Roche, L.K., Korhonen, F.J., Johnson, S.P., Wingate, M.T.D., Hancock, E.A., Dunkley, D., Zi, J.W., Rasmussen, B., Muhling, J.R., Occhipinti, S.A., Dunbar, M., Goldsworthy, J., 2017. The evolution of a Precambrian arc-related granulite facies gold deposit: Evidence from the Glenburgh deposit, Western Australia. *Precambrian Research* 290, 63-85.
- Şener, A.K., Young, C., Groves, D.I., Krapez, B., Fletcher, I.R., 2005. Major orogenic gold episode associated with Cordilleran-style tectonics related to the assembly of Paleoproterozoic Australia? *Geology* 33, 225-228.
- Sheppard, S., Bodorkos, S., Johnson, S.P., Wingate, M.T.D., Kirkland, C.L., 2010. The Paleoproterozoic Capricorn Orogeny: intracontinental reworking not continent–continent collision, Geological Survey of Western Australia, Report 108, 33 p.
- Sheppard, S., Fletcher, I.R., Rasmussen, B., Zi, J.-W., Muhling, J.R., Occhipinti, S.A., Wingate, M.T.D., Johnson, S.P., 2016. A new Paleoproterozoic tectonic history of the eastern Capricorn Orogen, Western Australia, revealed by U–Pb zircon dating of micro-tuffs. *Precambrian Research* 286, 1-19.
- Sheppard, S., Occhipinti, S.A., Nelson, D.R., 2005. Intracontinental reworking in the Capricorn Orogen, Western Australia: the 1680–1620 Ma Mangaroon Orogeny*. *Australian Journal of Earth Sciences* 52, 443-460.
- Sheppard, S., Occhipinti, S.A., Tyler, I.M., 2004. A 2005–1970 Ma Andean-type batholith in the southern Gascoyne Complex, Western Australia. *Precambrian Research* 128, 257-277.
- Sheppard, S., Rasmussen, B., Muhling, J.R., Farrell, T.R., Fletcher, I.R., 2007. Grenvillian-aged orogenesis in the Palaeoproterozoic Gascoyne Complex, Western Australia: 1030–950Ma reworking of the Proterozoic Capricorn Orogen. *Journal of Metamorphic Geology* 25, 477-494.

- Takehara, M., Komure, M., Kiyokawa, S., Horie, K., Yokoyama, K., 2010. Detrital zircon SHRIMP U-Pb age of the 2.3 Ga diamictites of the Meteorite Bore Member in the south Pilbara, Western Australia, in: Tyler, I.M., Knox-Robinson, C.M. (Eds.), Fifth International Archean Symposium. Geological Survey of Western Australia, Perth, Western Australia, 2 p.
- Thorne, A.M., Seymour, D.B., 1991. Geology of the Ashburton Basin Western Australia, Geological Survey of Western Australia, Bulletin 139, 162 p.
- Thorne, A.M., Trendall, A.F., 2001. Geology of the Fortescue Group, Pilbara Craton, Western Australia, Geological Survey of Western Australia, Bulletin 144, 266 p.
- Trendall, A.F., Compston, W., Nelson, D.R., De Laeter, J.R., Bennett, V.C., 2004. SHRIMP zircon ages constraining the depositional chronology of the Hamersley Group, Western Australia. *Australian Journal of Earth Sciences* 51, 621-644.
- Tyler, I.M., 1991. The Geology of the Sylvania Inlier and the Southeast Hamersley Basin, Geological Survey of Western Australia, Bulletin 138, 124 p.
- Tyler, I.M., Thorne, A.M., 1990. The northern margin of the Capricorn Orogen, Western Australia—an example of an Early Proterozoic collision zone. *Journal of Structural Geology* 12, 685-701.
- Vielreicher, N., Groves, D., Fletcher, I., McNaughton, N., Rasmussen, B., 2003. Hydrothermal monazite and xenotime geochronology: a new direction for precise dating of orogenic gold mineralization. *Society of Economic Geologists Newsletter* 53, 10-16.
- Vielreicher, N. M., Groves, D. I., Snee, L. W., Fletcher, I. R., and McNaughton, N. J., 2010, Broad synchronicity of three gold mineralization styles in the Kalgoorlie gold field SHRIMP, U-Pb, and (super 40) Ar/ (super 39) Ar geochronological evidence: *Economic Geology and the Bulletin of the Society of Economic Geologists*, v. 105, no. 1, p. 187-227.
- Wells, M., Laukamp, C., Hancock, E.A., 2016. Reflectance spectroscopic characterisation of mineral alteration footprints associated with sediment-hosted gold mineralisation at Mt Olympus (Ashburton Basin, Western Australia). *Australian Journal of Earth Sciences* 63, 987-1002.
- Wingate, MTD 2002. Age and palaeomagnetism of dolerite sills of the Bangemall Supergroup on the Edmund 1:250 000 sheet, Western Australia: Geological Survey of Western Australia, Record 2002/4, 48 p.
- Wingate, MTD, Kirkland, CL, Cutten, HN and Thorne, AM 2012. 143445: dolerite sill, Waldburg Homestead; Geochronology Record 1077: Geological Survey of Western Australia, 4 p.
- Wingate, MTD, Kirkland, CL, Blay, OA and Johnson, SP 2013. 207259: dolerite sill, Maranoo Well; Geochronology Record 1123: Geological Survey of Western Australia, 4 p.

- Wyborn, L.A.I., Heinrich, C.A., Jaques, A.L., 1994. Australian Proterozoic mineral systems: essential ingredients and mappable criteria, in: Hallenstein, P.C. (Ed.), Australian mining looks north — the challenges and choices. Australian Institute of Mining and metallurgy; 1994 AUSIMM Annual Conference, Darwin, Northern Territory, pp. 109-115.
- Young, C.J., Groves, D.I., Morant, P., 2003. Sediment-hosted disseminated gold mineralisation in the Palaeoproterozoic Ashburton Province, Western Australia: a new epizonal orogenic gold province related to Capricorn Orogeny?, in: Eliopoulos et al., eds., Mineral exploration and sustainable development: proceedings of the 7th Biennial SGA Meeting. Millpress, Athens, Greece, pp. 835-838.
- Zhang, R., Pian, H., Santosh, M., Zhang, S., 2015. The history and economics of gold mining in China. *Ore Geology Reviews* 65, 718-727.

CHAPTER 7. THESIS CONCLUSIONS

This is the first comprehensive geochronological study to address the low-temperature tectonothermal history of the northern Capricorn Orogen in relation to gold mineralization. The multi-disciplinary approach employed here has made it possible to develop a mineralization framework by integrating in situ geochronological information with targeted field mapping to establish the regional-scale controls and distribution of gold mineralization through both space and time. In situ SHRIMP geochronology of the phosphate minerals, xenotime and monazite, used here has proven to be a robust method for dating hydrothermal gold mineralization and low-temperature hydrothermal events.

Prior to this study gold mineralization in the northern part of the Capricorn Orogen was considered relatively simple, with orogenic gold mineralization thought to be associated with the timing of the Capricorn Orogeny (Cawood and Tyler, 2004; Pirajno, 2004). At the time the Capricorn Orogeny was thought to represent the amalgamation of the West Australian Craton through the single-stage oblique convergence of the Pilbara and Yilgarn Cratons occurring between c. 2200 and 1600 Ma (Evans et al., 2003; Tyler and Thorne, 1990). However, more recent research has demonstrated that the Capricorn Orogen has a complex and long lived tectonic evolution involving two collisional events (Johnson et al., 2011) followed by over a billion years of intracratonic reworking and reactivation (Johnson et al., 2017; Korhonen et al., 2017; Sheppard et al., 2005, 2007). Likewise, results and conclusions presented in chapters 2–5 of this thesis demonstrate a much more complex mineralization and low-grade hydrothermal history than previously recognised. At least five discrete episodes of hydrothermal activity are document, at c. 2400, 2260, 1770, 1740 and 1680 Ma, which includes gold mineralizing events at c. 2400, 1770 and 1680 Ma. These age data are placed into a broader geological context in the summary provided in Chapter 6 and a brief summary is provided here.

Orogenic gold mineralization dated at c. 2400 Ma is not associated with a recognised orogenic event. However, evidence for widespread hydrothermal activity and uplift and erosion along the southern Pilbara margin indicates that this event possibly marks the early stages of the Ophthalmia Orogeny during which the Pilbara Craton collided

with the Glenburgh Terrane. Carlin-type gold mineralization at the Mount Olympus deposit formed at c.1770 Ma as both strata-bound and fault-hosted lodes. The timing of mineralization is associated with the final stages of the intracratonic 1820–1770 Ma Capricorn Orogeny which is defined by a change in tectonic regime from dominantly compressional to transpressional stresses. Finally, during the early stages of the intracratonic 1680–1620 Ma Mangaroon Orogeny widespread gold mineralization and hydrothermal activity is recorded. Gold mineralization occurs at c. 1680 Ma at the Belvedere and Star of the West deposits, and as a second mineralization event at the Paulsens deposit. Additionally, xenotime from Mount Olympus and the Amazon Shear Zone have been dated at c. 1680 Ma, although, these ages date hydrothermal fluid flow that cannot be linked directly to gold mineralization.

Since gold mineralization throughout the orogen has a spatial relationship with the crustal-scale Nanjilgardy and Baring Downs Faults, it is perceived that hydrothermal and mineralizing fluids migrated along these faults during episodes of fault reactivation associated with defined orogenic events. However, this link is largely interpretive and determining the reactivation histories of these faults is not always possible due to limited outcrop and complex geological histories. In this study fault movement is dated by xenotime intergrown with calcite from a syn-tectonic vein within the Amazon Shear Zone. Results demonstrate that fault movement occurred at c. 1675 Ma, coeval with gold mineralization associated with the Baring Downs and Nanjilgardy Faults. These results indicate that during discrete orogenic events fault reactivation was accompanied by hydrothermal fluid flow and gold mineralization.

Results presented in this study have implications for mineral exploration targeting. Without knowing the age of gold mineralization and its host rocks, it is possible that rocks of an inappropriate age are targeted. For example, c. 2400 Ma orogenic gold mineralization at Paulsens is significantly older than rocks deposited in the 2008–1800 Ma Ashburton Basin which hosts numerous gold deposits including the Star of the West, Big Sarah and Lewis Prospects (Figure 1-7), and the c. 2080 Ma Belvedere dolerite which is the host rock to the Belvedere gold deposit. However, these rocks are prospective for both c. 1770 and 1680 Ma gold mineralization formed during episodes of intracratonic reworking.

Intracratonic orogens are generally not considered to be prospective for gold mineralization due to a lack of input of juvenile material. However, results described in this thesis demonstrate that gold deposits with endowments >1 Moz are possible to form in such settings, provided they are situated along a crustal-scale fault, or auxiliary structure. These structures provide a pathway for fluids to migrate from the mantle or lower crust to the upper crust, and since they are commonly subjected to multiple overprinting hydrothermal fluid flow events, this may result in the upgrading of ore.

The application of in situ phosphate geochronology used in this study has been fundamental for unravelling the low-grade hydrothermal evolution of the northern Capricorn Orogen. It provides a history that would otherwise have remained hidden since many of the common chronometers are either scarce or susceptible to isotopic resetting in orogens which have been subjected to multiple overprinting hydrothermal events. Results from this PhD have led to a mineralization framework for the northern Capricorn Orogen demonstrating a link between fault reactivation, hydrothermal and mineralizing fluid flow and orogenic events with mineralization occurring at c. 2400, 1770 and 1680 Ma.

7.1. FUTURE RESEARCH

Several questions were raised during the course of this PhD which were not addressed as they were beyond the scope of the project aims.

- The c. 2400 Ma tectonic event associated with the timing of orogenic gold mineralization at Paulsens and hydrothermal activity near the Belvedere gold deposit requires further investigation. This event affects the southern margin of the Pilbara and the northern Capricorn Orogen and possibly marks the early stages of the Ophthalmia Orogeny.
- Assess the timing of gold occurrences in the southern Pilbara region (e.g. Twin Peaks in the Rocklea Dome) to determine if c. 2400 Ma gold mineralization is a wide spread event or only associated with the Nanjilgardy Fault.
- Date other types of mineral deposits throughout the Capricorn Orogen (e.g. Cu mineralization at Bali Hi, Sb and Au at Mount Clement, Ag at Kooline). This information could be incorporated with published data including, base metal and gold mineralization in the southern Capricorn and iron ore mineralization

farther the north of the study area in the northern Capricorn Orogen to review the metallogenic frameworks of the entire orogen in regards to all commodities.

7.2. REFERENCES

- Cawood, P. A., and Tyler, I. M., 2004, Assembling and reactivating the Proterozoic Capricorn Orogen: lithotectonic elements, orogenies, and significance: *Precambrian Research*, v. 128, no. 3-4, p. 201-218.
- Evans, D. A. D., Sircombe, K. N., Wingate, M. T. D., Doyle, M., McCarthy, M., Pidgeon, R. T., and Van Niekerk, H. S., 2003, Revised geochronology of magmatism in the western Capricorn Orogen at 1805-1785 Ma: diachroneity of the Pilbara-Yilgarn collision: *Australian Journal of Earth Sciences*, v. 50, no. 6, p. 853-864.
- Johnson, S. P., Korhonen, F. J., Kirkland, C. L., Cliff, J. B., Belousova, E. A., and Sheppard, S., 2017, An isotopic perspective on growth and differentiation of Proterozoic orogenic crust: From subduction magmatism to cratonization: *Lithos*, v. 268-271, p. 76-86.
- Johnson, S. P., Sheppard, S., Rasmussen, B., Wingate, M. T. D., Kirkland, C. L., Muhling, J. R., Fletcher, I. R., and Belousova, E. A., 2011, Two collisions, two sutures: Punctuated pre-1950Ma assembly of the West Australian Craton during the Ophthalmian and Glenburgh Orogenies: *Precambrian Research*, v. 189, no. 3-4, p. 239-262.
- Korhonen, F. J., Johnson, S. P., Wingate, M. T. D., Kirkland, C. L., Fletcher, I. R., Dunkley, D. J., Roberts, M. P., Sheppard, S., Muhling, J. R., and Rasmussen, B., 2017, Radiogenic heating and craton-margin plate stresses as drivers for intraplate orogeny: *Journal of Metamorphic Geology*, v. 35, no. 6, p. 631-661.
- Pirajno, F., 2004, Metallogeny in the Capricorn Orogen, Western Australia, the result of multiple ore-forming processes: *Precambrian Research*, v. 128, no. 3-4, p. 411-439.
- Sheppard, S., Occhipinti, S. A., and Nelson, D. R., 2005, Intracontinental reworking in the Capricorn Orogen, Western Australia: the 1680–1620 Ma Mangaroon Orogeny*: *Australian Journal of Earth Sciences*, v. 52, no. 3, p. 443-460.
- Sheppard, S., Rasmussen, B., Muhling, J. R., Farrell, T. R., and Fletcher, I. R., 2007, Grenvillian-aged orogenesis in the Palaeoproterozoic Gascoyne Complex, Western Australia: 1030–950Ma reworking of the Proterozoic Capricorn Orogen: *Journal of Metamorphic Geology*, v. 25, no. 4, p. 477-494.
- Tyler, I. M., and Thorne, A. M., 1990, The northern margin of the Capricorn Orogen, Western Australia—an example of an Early Proterozoic collision zone: *Journal of Structural Geology*, v. 12, no. 5–6, p. 685-701.

CHAPTER 8. BIBLIOGRAPHY

- Alghamdi, A. H., Aitken, A. R. A., and Dentith, M. C., 2018, The composition and structure of the deep crust of the Capricorn Orogen: *Australian Journal of Earth Sciences*, v. 65, no. 1, p. 9-24.
- Arehart, G. B., 1996, Characteristics and origin of sediment-hosted disseminated gold deposits: a review: *Ore Geology Reviews*, v. 11, no. 6, p. 383-403.
- Arndt, N. T., Nelson, D. R., Compston, W., Trendall, A. F., and Thorne, A. M., 1991, The age of the Fortescue Group, Hamersley Basin, Western Australia, from ion microprobe zircon U-Pb results: *Australian Journal of Earth Sciences*, v. 38, no. 3, p. 261-281.
- Bateman, R., and Hagemann, S., 2004, Gold mineralisation throughout about 45 Ma of Archaean orogenesis: protracted flux of gold in the Golden Mile, Yilgarn craton, Western Australia: *International Journal of Geology, Mineralogy and Geochemistry of Mineral Deposits*, v. 39, no. 5, p. 536-559.
- Belousov, I., Large, R. R., Meffre, S., Danyushevsky, L. V., Steadman, J., and Beardsmore, T., 2016, Pyrite compositions from VHMS and orogenic Au deposits in the Yilgarn Craton, Western Australia: Implications for gold and copper exploration: *Ore Geology Reviews*, v. 79, p. 474-499.
- Berger, B. R., and Bagby, W. C., 1991, The geology and origin of Carlin-type gold deposits, *Gold metallogeny and exploration*: Boston, MA, Springer US, p. 210-248.
- Bierlein, F. P., Groves, D. I., and Cawood, P. A., 2009, Metallogeny of accretionary orogens — The connection between lithospheric processes and metal endowment: *Ore Geology Reviews*, v. 36, no. 4, p. 282-292.
- Bierlein, F. P., Groves, D. I., Goldfarb, R. J., and Dubé, B., 2006, Lithospheric controls on the formation of provinces hosting giant orogenic gold deposits: *Mineralium Deposita*, v. 40, no. 8, p. 874-886.
- Blake, T. S., 1993, Archaean and early proterozoic geology of the Pilbara region, Western Australia Late Archaean crustal extension, sedimentary basin formation, flood basalt volcanism and continental rifting: the Nullagine and Mount Jope Supersequences, Western Australia: *Precambrian Research*, v. 60, no. 1, p. 185-241.
- Blake, T. S., and Barley, M. E., 1992, Tectonic evolution of the Late Archaean to Early Proterozoic Mount Bruce Megasequence Set, western Australia: *Tectonics*, v. 11, no. 6, p. 1415-1425.
- Blay, O. A., Johnson, S. P., Thorne, A. M., Cutten, H. N. C., 2015, Waldburg Dolerite (P_wa-od): Geological Survey of Western Australia, WA Geology Online, Explanatory Notes extract, viewed 20 April 2016, www.dmp.wa.gov.au/ens.

- Blenkinsop, T., 2015, Scaling laws for the distribution of gold, geothermal, and gas resources: *Pure and Applied Geophysics*, v. 172, no. 7, p. 2045-2056.
- Blight, D. F., 1985, Economic potential of the lower Fortescue Group and adjacent units in the southern Hamersley Basin; A study of depositional environments: Geological Survey of Western Australia, Report 13, 32p.
- Blockley, J. G., 1971, The lead, zinc and silver deposits of Western Australia, Geological Survey of Western Australia, Mineral Resources Bulletin 9, 237p.
- Brauhart, C. W., Grunsky, E. C., and Hagemann, S. G., 2017, Magmato-hydrothermal space: A new metric for geochemical characterisation of metallic ore deposits: *Ore Geology Reviews*, v. 86, p. 867-895.
- Carpenter, R. L., Duke, N. A., Sandeman, H. A., and Stern, R., 2005, Relative and absolute timing of gold mineralization along the meliadine trend, nunavut, canada: Evidence for Paleoproterozoic gold hosted in an Archean greenstone belt: *Economic Geology*, v. 100, no. 3, p. 567-576.
- Cawood, P. A., and Tyler, I. M., 2004, Assembling and reactivating the Proterozoic Capricorn Orogen: lithotectonic elements, orogenies, and significance: *Precambrian Research*, v. 128, no. 3-4, p. 201-218.
- Cheng, Q., 2008, Non-linear theory and power-law models for information integration and mineral resources quantitative assessments: *Mathematical Geosciences*, v. 40, no. 5, p. 503-532.
- Cherniak, D. J., Watson, E. B., Grove, M., and Harrison, T. M., 2004, Pb diffusion in monazite: a combined RBS/SIMS study: *Geochimica et Cosmochimica Acta*, v. 68, no. 4, p. 829-840.
- Cherniak, D. J., 2010, diffusion in accessory minerals: zircon, titanite, apatite, monazite and xenotime: *Reviews in Mineralogy and Geochemistry*, v. 72, no. 1, p. 827-869.
- Chesley, J. T., 1999, Integrative geochronology of ore deposits: new insights into the duration and timing of hydrothermal circulation, *in* Lambert, D. D., and Brown, P. E., eds., *Reviews in economic geology*, Volume 12, p. 115-142.
- Cline, J. S., Hofstra, A. H., Muntean, J. L., Tosdal, R. M., and Hickey, K. A., 2005, Carlin-type gold deposits in Nevada: Critical geologic characteristics and viable models: *Economic Geology 100th Anniversary Volume*, p. 451-484.
- Cook, F., and Erdmer, P., 2005, An 1800 km cross section of the lithosphere through the northwestern North American plate: lessons from 4.0 billion years of Earth's history: *Canadian Journal of Earth Sciences*, v. 42, no. 6, p. 1295-1311.
- Cumming, G. L., and Richards, J. R., 1975, Ore lead isotope ratios in a continuously changing earth: *Earth and Planetary Science Letters*, v. 28, no. 2, p. 155-171.

-
- Cutten, H. N. C., and Johnson, S. P., 2018, Kuparr Tectonic Event (KU): Geological Survey of Western Australia, WA Geology Online, Explanatory Notes extract, viewed 12 December 2018, <www.dmp.wa.gov.au/ens>
- Cutten, H. N., Johnson, S. P., Thorne, A. M., Windgate, M. T. D., Kirkland, C. L., Belousova, E. A., Blay, O. A., and Zwingmann, H., 2016, Deposition, provenance, inversion history and mineralization of the Proterozoic Edmund and Collier Basins, Capricorn Orogen, Geological Survey of Western Australia, Report 127, 74p.
- Danyushevsky, L., Robinson, P., Gilbert, S., Norman, M., Large, R., McGoldrick, P., and Shelley, M., 2011, Routine quantitative multi-element analysis of sulphide minerals by laser ablation ICP-MS: Standard development and consideration of matrix effects: *Geochemistry: Exploration, Environment, Analysis*, v. 11, no. 1, p. 51-60.
- De Laeter, J. R., and Kennedy, A. K., 1998, A double focusing mass spectrometer for geochronology: *International Journal of Mass Spectrometry*, v. 178, no. 1, p. 43-50.
- Dill, H. G., 2010, The “chessboard” classification scheme of mineral deposits: Mineralogy and geology from aluminum to zirconium: *Earth-Science Reviews*, v. 100, no. 1, p. 1-420.
- Doggett, M., and Zhang, J., 2007, Production trends and economic characteristics of canadian gold mines: *Exploration and Mining Geology*, v. 16, no. 1-2, p. 1-10.
- Evans, D. A. D., Sircombe, K. N., Wingate, M. T. D., Doyle, M., McCarthy, M., Pidgeon, R. T., and Van Niekerk, H. S., 2003, Revised geochronology of magmatism in the western Capricorn Orogen at 1805-1785 Ma: diachroneity of the Pilbara-Yilgarn collision: *Australian Journal of Earth Sciences*, v. 50, no. 6, p. 853-864.
- Fielding, I. O. H., Johnson, S. P., Zi, J.-W., Rasmussen, B., Muhling, J. R., Dunkley, D. J., Sheppard, S., Wingate, M. T. D., and Rogers, J. R., 2017, Using in situ SHRIMP U-Pb monazite and xenotime geochronology to determine the age of orogenic gold mineralization: an example from the Paulsens mine, southern Pilbara Craton: *Economic Geology*, v. 112, no. 5, p. 1205-1230.
- Fielding, I. O. H., Johnson, S. P., Zi, J. W., Sheppard, S., and Rasmussen, B., 2018, Neighbouring orogenic gold deposits may be the products of unrelated mineralizing events: *Ore Geology Reviews*, v. 95, p. 593-603.
- Fielding, I. O. H., Johnson, S. P., Meffre, S., Zi, J. W., Sheppard, S., Large, R. R., Rasmussen, B., 2019, Linking gold mineralization to regional-scale drivers of mineral systems using in situ U-Pb geochronology and pyrite LA-ICP-MS element mapping: *Geoscience Frontiers*, v. 10, p. 89-105.
- Fielding, I. O. H., Johnson, S. P., Zi, J. W., Rasmussen, B., under review, U-Pb dating of fault reactivation and gold mineralization in the northern Capricorn Orogen, Western Australia; *Australia Journal of Earth Sciences*.
-

- Fielding, I., and Stokes, L., 2014, Gabbro Offset drilling, Ashburton Basin, Pilbara - Western Australia, M08/196, exploration incentive scheme final report: Northern Star Resources.
- Finger, F., Broska, I., Roberts, M. P., and Schermaier, A., 1998, Replacement of primary monazite by apatite-allanite-epidote coronas in an amphibolite facies granite gneiss from the Eastern Alps: *The American mineralogist*, v. 83, no. 3-4, p. 248-258.
- Fletcher, I. R., McNaughton, N. J., Aleinikoff, J. A., Rasmussen, B., and Kamo, S. L., 2004, Improved calibration procedures and new standards for U-Pb and Th-Pb dating of Phanerozoic xenotime by ion microprobe: *Chemical Geology*, v. 209, no. 3-4, p. 295-314.
- Fletcher, I. R., McNaughton, N. J., Davis, W. J., and Rasmussen, B., 2010, Matrix effects and calibration limitations in ion probe U-Pb and Th-Pb dating of monazite: *Chemical Geology*, v. 270, no. 1-4, p. 31-44.
- Fletcher, I. R., Rasmussen, B., and McNaughton, N. J., 2000, SHRIMP U-Pb geochronology of authigenic xenotime and its potential for dating sedimentary basins: *Australian Journal of Earth Sciences*, v. 47, no. 5, p. 845-859.
- Forman, F. G., 1938, The Melrose and Belvedere gold mines and vicinity, Mt Stewart Station, Ashburton Goldfields, Geological Survey of Western Australia, Annual Report 1937, 159p.
- Fougerouse, D., Micklethwaite, S., Ulrich, S., Miller, J., Godel, B., Adams, D. T., and McCuaig, T. C., 2017, Evidence for two stages of mineralization in West Africa's largest gold deposit: Obuasi, Ghana: *Economic Geology*, v. 112, no. 1, p. 3-22.
- Geological Survey of Western Australia, 2018, Compilation of WAROX data, 2018: Geological Survey of Western Australia, digital data package.
- Goldfarb, R. J., and Groves, D. I., 2015, Orogenic gold: Common or evolving fluid and metal sources through time: *Lithos*, v. 233, p. 2-26.
- Goldfarb, R. J., Groves, D. I., and Gardoll, S., 2001, Orogenic gold and geologic time: a global synthesis: *Ore Geology Reviews*, v. 18, no. 1-2, p. 1-75.
- Goldfarb, R. J., and Santosh, M., 2014, The dilemma of the Jiaodong gold deposits: Are they unique?: *Geoscience Frontiers*, v. 5, no. 2, p. 139-153.
- Groves, D. I., Condie, K. C., Goldfarb, R. J., Hronsky, J. M. A., and Vielreicher, R. M., 2005, 100th Anniversary Special Paper: Secular changes in global tectonic processes and their influence on the temporal distribution of gold-bearing mineral deposits: *Economic Geology*, v. 100, no. 2, p. 203-224.
- Groves, D. I., Goldfarb, R. J., Gebre-Mariam, M., Hagemann, S. G., and Robert, F., 1998, Orogenic gold deposits: A proposed classification in the context of their crustal distribution and relationship to other gold deposit types: *Ore Geology Reviews*, v. 13, no. 1-5, p. 7-27.

-
- Groves, D. I., Goldfarb, R. J., Robert, F., and Hart, C. J. R., 2003, Gold deposits in metamorphic belts: overview of current understanding, outstanding problems, future research, and exploration significance: *Economic Geology*, v. 98, no. 1, p. 1-29.
- Groves, D. I., and Santosh, M., 2015, Province-scale commonalities of some world-class gold deposits: Implications for mineral exploration: *Geoscience Frontiers*, v. 6, no. 3, p. 389-399.
- Groves, D. I., and Santosh, M., 2016, The giant Jiaodong gold province: The key to a unified model for orogenic gold deposits?: *Geoscience Frontiers*, v. 7, no. 3, p. 409-417.
- Hall, C. E., Powell, C. M., and Bryant, J., 2001, Basin setting and age of the Late Palaeoproterozoic Capricorn Formation, Western Australia: *Australian Journal of Earth Sciences*, v. 48, no. 5, p. 731-744.
- Hancock, E. A., and Thorne, A. M., 2016, Mineralogy of gold from the Paulsens and Mount Olympus deposits, northern Capricorn Orogen: *Geological Survey of Western Australia, Record 2016/14*, p. 16.
- Harrison, T. M., Catlos, E. J., and Montel, J. M., 2002, U-Th-Pb Dating of Phosphate Minerals: *Reviews in Mineralogy and Geochemistry*, v. 48, no. 1, p. 524-558.
- Heaman, L. M., and LeCheminant, A. N., 1993, geochemistry of accessory minerals paragenesis and U-Pb systematics of baddeleyite (ZrO₂): *Chemical Geology*, v. 110, no. 1, p. 95-126.
- Hronsky, J. M., Groves, D. I., Loucks, R. R., and Begg, G. C., 2012, A unified model for gold mineralisation in accretionary orogens and implications for regional-scale exploration targeting methods: *Mineralium Deposita*, v. 47, no. 4, p. 339-358.
- Hronsky, J. M. A., 2011, Self-organized critical systems and ore formation: the key to spatial targeting?: *SEG Newsletter*, v. 84, p. 14-16.
- Hronsky, J. M. A., and Groves, D. I., 2008, Science of targeting: definition, strategies, targeting and performance measurement: *Australian Journal of Earth Sciences*, v. 55, no. 1, p. 3-12.
- Hu, R.-Z., Su, W.-C., Bi, X.-W., Tu, G.-Z., and Hofstra, A. H., 2002, Geology and geochemistry of Carlin-type gold deposits in China: *Mineralium Deposita*, v. 37, no. 3, p. 378-392.
- Huston, D. L., Mernagh, T. P., Hagemann, S. G., Doublier, M. P., Fiorentini, M., Champion, D. C., Lynton Jaques, A., Czarnota, K., Cayley, R., Skirrow, R., and Bastrakov, E., 2016, Tectono-metallogenic systems — The place of mineral systems within tectonic evolution, with an emphasis on Australian examples: *Ore Geology Reviews*, v. 76, p. 168-210.
- Huston, D. L., Pehrsson, S., Eglington, B. M., and Zaw, K., 2010, The geology and metallogeny of volcanic-hosted massive sulfide deposits: *Variations through*
-

- geologic time and with tectonic setting; *Economic Geology*, v. 105, p. 571-591.
- Ireland, T., Clement, S., Compston, W., Foster, J., Holden, P., Jenkins, B., Lanc, P., Schram, N., and Williams, I., 2008, Development of SHRIMP: *Australian Journal of Earth Sciences*, v. 55, no. 6, p. 937-954.
- Ireland, T., and Williams, I. S., 2003, Considerations in zircon geochronology by SIMS: *Reviews in Mineralogy and Geochemistry*, v. 53, p. 215-241.
- Ireland, T.R., Wooden, J.L., Persing, H., Ito, B., 1999, Geological applications and analytical development of the SHRIMP-RG. *Eos Trans., American Geophysics Union* 80, F1117.
- Jennings, K., and Schodde, R., 2016, From mineral discovery to project delivery: *SEG Newsletter*, v. 105, p. 20-25.
- Johnson, S. P., Cutten, H. N., Korhonen, F. J., and Wyche, L. N., 2017, Geology and metallogeny of the Capricorn Orogen, *in* Phillips, G. N., ed., *Australian Ore Deposits*, The Australian Institute of Mining and Metallurgy: Melbourne, p. 289-392.
- Johnson, S. P., Korhonen, F. J., Kirkland, C. L., Cliff, J. B., Belousova, E. A., and Sheppard, S., 2017, An isotopic perspective on growth and differentiation of Proterozoic orogenic crust: From subduction magmatism to cratonization: *Lithos*, v. 268-271, p. 76-86.
- Johnson, S. P., Sheppard, S., Rasmussen, B., Wingate, M. T. D., Kirkland, C. L., Muhling, J. R., Fletcher, I. R., and Belousova, E. A., 2011, Two collisions, two sutures: Punctuated pre-1950Ma assembly of the West Australian Craton during the Ophthalmian and Glenburgh Orogenies: *Precambrian Research*, v. 189, no. 3-4, p. 239-262.
- Johnson, S. P., Sheppard, S., Rasmussen, B., Wingate, M. T. D., Kirkland, C. L., Muhling, J. R., Fletcher, I. R., and Belousova, E. A., 2010, The Glenburgh Orogeny as a record of Paleoproterozoic continent-continent collision, *Geological Survey of Western Australia, Record* 2010/5, 60 p.
- Johnson, S. P., Thorne, A. M., and Tyler, I. M., 2011, Capricorn Orogen seismic and magnetotelluric (MT) workshop 2011: Extended abstracts: *Geological Survey of Western Australia, Record* 2011/25, p. 132.
- Johnson, S. P., Thorne, A. M., Tyler, I. M., Korsch, R. J., Kennett, B. L. N., Cutten, H. N., Goodwin, J., Blay, O., Blewett, R. S., Joly, A., Dentith, M. C., Aitken, A. R. A., Holzschuh, J., Salmon, M., Reading, A., Heinson, G., Boren, G., Ross, J., Costelloe, R. D., and Fomin, T., 2013, Crustal architecture of the Capricorn Orogen, Western Australia and associated metallogeny: *Australian Journal of Earth Sciences*, v. 60, no. 6-7, p. 681-705.
- Joly, A., Porwal, A., McCuaig, T. C., Chudasama, B., Dentith, M. C., and Aitken, A. R. A., 2015, Mineral systems approach applied to GIS-based 2D-prospectivity

- modelling of geological regions: Insights from Western Australia: *Ore Geology Reviews*, v. 71, p. 673-702.
- Kerrich, R., and Cassidy, K. F., 1994, Temporal relationships of lode gold mineralization to accretion, magmatism, metamorphism and deformation — Archean to present: A review: *Ore Geology Reviews*, v. 9, no. 4, p. 263-310.
- Kinny, P. D., Nutman, A. P., and Occhipinti, S. A., 2004, Reconnaissance dating of events recorded in the southern part of the Capricorn Orogen: *Precambrian Research*, v. 128, no. 3, p. 279-294.
- Korhonen, F. J., and Johnson, S. P., 2015, The role of radiogenic heat in prolonged intraplate reworking: The Capricorn Orogen explained?: *Earth and Planetary Science Letters*, v. 428, p. 22-32.
- Korhonen, F. J., Johnson, S. P., Wingate, M. T. D., Kirkland, C. L., Fletcher, I. R., Dunkley, D. J., Roberts, M. P., Sheppard, S., Muhling, J. R., and Rasmussen, B., 2017, Radiogenic heating and craton-margin plate stresses as drivers for intraplate orogeny: *Journal of Metamorphic Geology*, v. 35, no. 6, p. 631-661.
- Korhonen, F. J., Johnson, S. P., Rasmussen, B., Sheppard, S., Muhling, J. R., Dunkley, D. J., Wingate, M. T. D., Fletcher, I. R., and Roberts, M. P., 2017, Circum-Yilgarn orogenesis: P–T–t constraints and implications from the Capricorn Orogen, Western Australia: *Journal of Metamorphic Geology*, accepted.
- Korsch, R. J., and Doublier, M. P., 2016, Major crustal boundaries of Australia, and their significance in mineral systems targeting: *Ore Geology Reviews*, v. 76, p. 211-228.
- Krapez, B., 1999, Stratigraphic record of an Atlantic-type global tectonic cycle in the Palaeoproterozoic Ashburton Province of Western Australia: *Australian Journal of Earth Sciences*, v. 46, no. 1, p. 71-87.
- Krapez, B., and McNaughton, N. J., 1999, SHRIMP zircon U–Pb age and tectonic significance of the Palaeoproterozoic Boolaloo Granodiorite in the Ashburton Province, Western Australia: *Australian Journal of Earth Sciences*, v. 46, no. 2, p. 283-287.
- Krapež, B., Müller, S. G., and Bekker, A., 2015, Stratigraphy of the Late Palaeoproterozoic (~2.03 Ga) Woolly Dolomite, Ashburton Province, Western Australia: A carbonate platform developed in a failed rift basin: *Precambrian Research*, v. 271, p. 1-19.
- Large, R. R., Danyushevsky, L., Hollit, C., Maslennikov, V., Meffre, S., Gilbert, S., Bull, S., Scott, R., Emsbo, P., Thomas, H., Singh, B., and Foster, J., 2009, Gold and trace element zonation in pyrite using a laser imaging technique: implications for the timing of gold in orogenic and Carlin-style sediment-hosted deposits: *Economic Geology*, v. 104, no. 5, p. 635-668.
- Le Mignot, E., Reisberg, L., André-Mayer, A. S., Bourassa, Y., Fontaine, A., and Miller, J., 2017, Re-Os geochronological evidence for multiple

- Paleoproterozoic gold events at the scale of the West African craton: *Economic Geology*, v. 112, no. 1, p. 145-168.
- Ludwig, K. R., 2003, Isoplot/Ex version 3.00, A geochronological toolkit for Microsoft Excel, Berkeley Geochronology Centre Special Publication No. 4, 73 p.
- Ludwig, K. R., 2009, Squid 2.50, a user's manual, Berkeley Geochronology Centre, Berkeley, California, USA, 95 p.
- Markwitz, V., Hein, K. A. A., and Miller, J., 2016, Compilation of West African mineral deposits: Spatial distribution and mineral endowment: *Precambrian Research*, v. 274, p. 61-81.
- Marston, R. J., 1979, Copper mineralization in Western Australia, Geological Survey of Western Australia, Mineral Resources Bulletin 13 Perth, 227 p.
- Martin, D. M., and Morris, P. A., 2010, Tectonic setting and regional implications of ca2.2 Ga mafic magmatism in the southern Hamersley Province, Western Australia: *Australian Journal of Earth Sciences*, v. 57, no. 7, p. 911-931.
- Martin, D. M., Powell, C. M., and George, A. D., 2000, Stratigraphic architecture and evolution of the early Paleoproterozoic McGrath Trough, Western Australia: *Precambrian Research*, v. 99, no. 1-2, p. 33-64.
- Martin, D. M., Sheppard, S., and Thorne, A. M., 2005, Geology of the Maroonah, Ullawarra, Capricorn, Mangaroon, Edmund and Elliott Creek 1:100 000 sheets, Geological Survey of Western Australia, 1:100 000 Geological Series Explanatory Notes, 81 p.
- Martin, D. M., Sircombe, K. N., Thorne, A. M., Cawood, P. A., and Nemchin, A. A., 2008, Provenance history of the Bangemall Supergroup and implications for the Mesoproterozoic paleogeography of the West Australian Craton: *Precambrian Research*, v. 166, no. 1, p. 93-110.
- Martin, D. M., and Thorne, A., 2004, Tectonic setting and basin evolution of the Bangemall Supergroup in the northwestern Capricorn Orogen: *Precambrian Research*, v. 128, no. 3, p. 385-409.
- McCuaig, T. C., Beresford, S., and Hronsky, J., 2010, Translating the mineral systems approach into an effective exploration targeting system: *Ore Geology Reviews*, v. 38, no. 3, p. 128-138.
- McCuaig, T. C., and Hronsky, J. M. A., 2014, The mineral systems concept: The key to exploration targeting *in* Kelly, K. D., and Golden, H. C., eds., *Building Exploration Capability for the 21st Century*, Volume Special Publication 18: Society of Economic Geologists, p. 153-175.
- McKeith, T. D., Schodde, R. C., and Baltus, E. J., 2010, Gold Discovery Trends: *SEG Newsletter*, v. 81, p. 1, 18-24.

- McNaughton, N. J., and Rasmussen, B., 2018, Geochemical characterisation of xenotime formation environments using U-Th: *Chemical Geology*.
- Meffre, S., Large, R. R., Steadman, J. A., Gregory, D. D., Stepanov, A. S., Kamenetsky, V. S., Ehrig, K., and Scott, R. J., 2016, Multi-stage enrichment processes for large gold-bearing ore deposits: *Ore Geology Reviews*, v. 76, p. 268-279.
- Molnár, F., Middleton, A., Stein, H., O'Brien, H., Lahaye, Y., Huhma, H., Pakkanen, L., and Johanson, B., 2018, Repeated syn- and post-orogenic gold mineralization events between 1.92 and 1.76 Ga along the Kiistala Shear Zone in the Central Lapland Greenstone Belt, northern Finland: *Ore Geology Reviews*, v. 101, p. 936-959.
- Morant, P., and Doepel, G., 1997, The Mount Olympus Gold Deposit, New Generation Gold Mines '97: Perth, Western Australia, Australian Mineral Foundation, p. 6.1 - 6.9.
- Müller, S. G., 2005, The tectonic evolution and volcanism of the Lower Wyloo Group, Ashburton Province, with timing implications for giant iron-ore deposits of the Hamersley Province, Western Australia, Unpublished Ph.D thesis, Perth, Western Australia, University of Western Australia, School of Earth and Geographical Sciences, 192 p.
- Müller, S. G., Krapez, B., Barley, M. E., and Fletcher, I. R., 2005, Giant iron-ore deposits of the Hamersley province related to the breakup of Paleoproterozoic Australia: New insights from in situ SHRIMP dating of baddeleyite from mafic intrusions: *Geology*, v. 33, no. 7, p. 577-580.
- Muntean, J. L., Cline, J. S., Simon, A. C., and Longo, A. A., 2011, Magmatic-hydrothermal origin of Nevada's Carlin-type gold deposits: *Nature Geoscience*, v. 4, no. 2, p. 122-127.
- Nesbitt, B. E., 1988, Gold deposit continuum: A genetic model for lode Au mineralization in the continental crust: *Geology*, v. 16, no. 11, p. 1044-1048.
- Northern Star Resources Limited, 2013, Ashburton Resource Soars 66% to 1.7MOz, <http://www.nsrld.com/wp-content/uploads/2013/02/AshburtonResourceIncreases66to1point7Moz.pdf>.
- Northern Star Resources Limited, 2015, Northern Star Resources Limited 2015 annual report, (<http://www.nsrld.com/wp-content/uploads/2015/08/NST-Annual-Report-2015-26-8-2015-new-cover1.pdf>).
- Northern Star Resources Limited, January, 2016, Resources and Reserves, (<http://www.nsrld.com/our-assets/resources-and-reserves/>).
- Northern Star Resources Limited, July, 2015, Northern Star Paulsens operations fact sheet, (<http://www.nsrld.com/wp-content/uploads/2015/08/NSR-Paulsens-Operations-Fact-Sheet-July-2015-FINAL.pdf>).

- Norum, E., 2005, 14 November 2003 to 13 November 2004, Paulsens Project, E08/665, E08/906, E08/1125, E47/977, E47/1134, E47/1135, M08/99, M08/196 and M08/222, Combined Reporting Group C211/1997: Nustar Mining Corporation Limited; Geological Survey of Western Australia Open-file report a070119.
- Occhipinti, S., Hocking, R., Lindsay, M., Aitken, A., Copp, I., Jones, J., Sheppard, S., Pirajno, F., and Metelka, V., 2017, Paleoproterozoic basin development on the northern Yilgarn Craton, Western Australia: *Precambrian Research*, v. 300, p. 121-140.
- Occhipinti, S., and Reddy, S., 2009, Neoproterozoic reworking of the Palaeoproterozoic Capricorn Orogen of Western Australia and implications for the amalgamation of Rodinia. Geological Society of London, Special Publication, v. 327, p. 445–456
- Occhipinti, S. A., Sheppard, S., Nelson, D. R., Myers, J. S., and Tyler, I. M., 1998, Syntectonic granite in the southern margin of the Palaeoproterozoic Capricorn Orogen, Western Australia: *Australian Journal of Earth Sciences*, v. 45, no. 4, p. 509-512.
- Occhipinti, S. A., Sheppard, S., Passchier, C., Tyler, I. M., and Nelson, D. R., 2004, Palaeoproterozoic crustal accretion and collision in the southern Capricorn Orogen: the Glenburgh Orogeny: *Precambrian Research*, v. 128, no. 3–4, p. 237-255.
- Olierook, H. K. H., Sheppard, S., Johnson, S. P., Occhipinti, S. A., Reddy, S. M., Clark, C., Fletcher, I. R., Rasmussen, B., Zi, J.-W., Pirajno, F., LaFlamme, C., Do, T., Ware, B., Blandthorn, E., Lindsay, M., Lu, Y.-J., Crossley, R. J., and Erickson, T. M., 2018, Extensional episodes in the Paleoproterozoic Capricorn Orogen, Western Australia, revealed by petrogenesis and geochronology of mafic–ultramafic rocks: *Precambrian Research*, v. 306, p. 22-40.
- Owen, S., 2000, Ashburton Project, Exploration licence 47/902 Belvedere and Tombstone Prospects: Taipan Resources N.L; Geological Survey of Western Australia Open-file report, a61500.
- Owen, S., 2000, Ashburton Project, Paulsens E08/665, E08/906, M08/99 and M08/196, Annual report to the Department of Minerals and Energy for the Period 15 November 1999 to 14 November 2000: Taipan Resources N.L; Geological Survey of Western Australia Open-file report.
- Pickard, A. L., 2002, SHRIMP U–Pb zircon ages of tuffaceous mudrocks in the Brockman Iron Formation of the Hamersley Range, Western Australia: *Australian Journal of Earth Sciences*, v. 49, no. 3, p. 491-507.
- Piechocka, A. M., Sheppard, S., Fitzsimons, I. C. W., Johnson, S. P., Rasmussen, B., and Jordan, F., 2018, Neoproterozoic $^{40}\text{Ar}/^{39}\text{Ar}$ mica ages mark the termination of a billion years of intraplate reworking in the Capricorn Orogen, Western Australia: *Precambrian Research*, v. 310, p. 391–406.

- Pirajno, F., 2004, Metallogeny in the Capricorn Orogen, Western Australia, the result of multiple ore-forming processes: *Precambrian Research*, v. 128, no. 3–4, p. 411-439.
- Pirajno, F., Jones, J. A., Hocking, R. M., and Halilovic, J., 2004, Geology and tectonic evolution of Palaeoproterozoic basins of the eastern Capricorn Orogen, Western Australia: *Precambrian Research*, v. 128, no. 3–4, p. 315-342.
- Powell, C. M., and Horwitz, R. C., 1994, Late Archaean and Early Proterozoic tectonics and basin formation of the Hamersley Ranges, Geological Society of Australia (WA Division) Excursion Guidebook, Volume 4, p. 57.
- Raimondo, T., Collins, A. S., Hand, M., Walker-Hallam, A., Smithies, R. H., Evins, P. M., and Howard, H. M., 2010, The anatomy of a deep intracontinental orogen: *Tectonics*, v. 29, no. 4. 31 p.
- Rasmussen, B., Fletcher, I. R., and McNaughton, N. J., 2001, Dating low-grade metamorphic events by SHRIMP U-Pb analysis of monazite in shales: *Geology*, v. 29, no. 10, p. 963-966.
- Rasmussen, B., Fletcher, I. R., and Muhling, J. R., 2007, In situ U-Pb dating and element mapping of three generations of monazite: Unravelling cryptic tectonothermal events in low-grade terranes: *Geochimica et Cosmochimica Acta*, v. 71, no. 3, p. 670-690.
- Rasmussen, B., Fletcher, I.R., Muhling, J.R., 2008. Pb/Pb geochronology, petrography and chemistry of Zr-rich accessory minerals (zirconolite, tranquillityite and baddeleyite) in mare basalt 10047. *Geochimica et Cosmochimica Acta*, v. 72, p. 5799–5818.
- Rasmussen, B., Fletcher, I. R., Muhling, J. R., Thorne, W. S., and Broadbent, G. C., 2007, Prolonged history of episodic fluid flow in giant hematite ore bodies: Evidence from in situ U-Pb geochronology of hydrothermal xenotime: *Earth and Planetary Science Letters*, v. 258, no. 1–2, p. 249-259.
- Rasmussen, B., Fletcher, I. R., and Sheppard, S., 2005, Isotopic dating of the migration of a low-grade metamorphic front during orogenesis: *Geology*, v. 33, no. 10, p. 773-776.
- Rasmussen, B., and Muhling, J. R., 2007, Monazite begets monazite: evidence for dissolution of detrital monazite and reprecipitation of syntectonic monazite during low-grade regional metamorphism: *Contributions to Mineralogy and Petrology*, v. 154, no. 6, p. 675-689.
- Rasmussen, B., and Muhling, J. R., 2009, Reactions destroying detrital monazite in greenschist-facies sandstones from the Witwatersrand basin, South Africa: *Chemical Geology*, v. 264, no. 1–4, p. 311-327.
- Rasmussen, B., Sheppard, S., and Fletcher, I. R., 2006, Testing ore deposit models using in situ U-Pb geochronology of hydrothermal monazite: Paleoproterozoic gold mineralization in northern Australia: *Geology*, v. 34, no. 2, p. 77-80.

- Reich, M., Kesler, S. E., Utsunomiya, S., Palenik, C. S., Chrysosoulis, S. L., and Ewing, R. C., 2005, Solubility of gold in arsenian pyrite: *Geochimica et Cosmochimica Acta*, v. 69, no. 11, p. 2781-2796.
- Richards, J. R., Fletcher, I. R., and Blockley, J. G., 1981, Pilbara galenas: Precise isotopic assay of the oldest Australian leads model ages and growth-curve implications: *Mineralium Deposita*, v. 16, no. 1, p. 7-30.
- Robert, F., Brommecker, R., Bourne, B. T., Dobak, P. J., McEwan, C. J., Rowe, R. R., and Zhou, X., 2007, Models and Exploration Methods for Major Gold Deposit Types. *in* Milkereit, B., ed., *Exploration 07: Fifth Decennial International Conference on Mineral Exploration*: Toronto, Canada, Decennial Mineral Exploration Conferences, p. 691-711.
- Roche, L. K., Korhonen, F. J., Johnson, S. P., Wingate, M. T. D., Hancock, E. A., Dunkley, D., Zi, J. W., Rasmussen, B., Muhling, J. R., Occhipinti, S. A., Dunbar, M., and Goldsworthy, J., 2017, The evolution of a Precambrian arc-related granulite facies gold deposit: Evidence from the Glenburgh deposit, Western Australia: *Precambrian Research*, v. 290, p. 63-85.
- Rolfe, M., 2012, Star of the West E 08/2232, Annual report for the period 20 October 2011- 19 October 2012: Northern Star Resources.
- Şener, A. K., Young, C., Groves, D. I., Krapez, B., and Fletcher, I. R., 2005, Major orogenic gold episode associated with Cordilleran-style tectonics related to the assembly of Paleoproterozoic Australia?: *Geology*, v. 33, no. 3, p. 225-228.
- Seymour, D. B., Thorne, A. M., and Blight, D. F., 1988, Wyloo, W.A., (2nd edition): Western Australia Geological Survey, 1:250 000 Geological Series Explanatory Notes, 36 p.
- Sheppard, S., Bodorkos, S., Johnson, S. P., Wingate, M. T. D., and Kirkland, C. L., 2010, The Paleoproterozoic Capricorn Orogeny: intracontinental reworking not continent–continent collision, Volume 108: Geological Survey of Western Australia, Report 108, p. 33.
- Sheppard, S., Farrell, T. R., Bodorkos, S., D, H., Tyler, I. M., and Pirajino, F., 2006, Late Paleoproterozoic (1680-1620 Ma) sedimentation, magmatism, and tectonism in the Capricorn Orogen, in GSWA 2006 extended abstracts: Promoting the prospectivity of Western Australia; Geological Survey of Western Australia; Record 2006/3, p. 11-12.
- Sheppard, S., Fletcher, I. R., Rasmussen, B., Zi, J.-W., Muhling, J. R., Occhipinti, S. A., Wingate, M. T. D., and Johnson, S. P., 2016, A new Paleoproterozoic tectonic history of the eastern Capricorn Orogen, Western Australia, revealed by U–Pb zircon dating of micro-tuffs: *Precambrian Research*, v. 286, p. 1-19.
- Sheppard, S., Occhipinti, S. A., and Nelson, D. R., 2005, Intracontinental reworking in the Capricorn Orogen, Western Australia: the 1680–1620 Ma Mangaroon Orogeny: *Australian Journal of Earth Sciences*, v. 52, no. 3, p. 443-460.

- Sheppard, S., Occhipinti, S. A., and Tyler, I. M., 2003, The relationship between tectonism and composition of granitoid magmas, Yarlalweelor Gneiss Complex, Western Australia: *Lithos*, v. 66, no. 1, p. 133-154.
- Sheppard, S., Occhipinti, S. A., and Tyler, I. M., 2004, A 2005–1970 Ma Andean-type batholith in the southern Gascoyne Complex, Western Australia: *Precambrian Research*, v. 128, no. 3–4, p. 257-277.
- Sheppard, S., Rasmussen, B., Muhling, J. R., Farrell, T. R., and Fletcher, I. R., 2007, Grenvillian-aged orogenesis in the Palaeoproterozoic Gascoyne Complex, Western Australia: 1030–950Ma reworking of the Proterozoic Capricorn Orogen: *Journal of Metamorphic Geology*, v. 25, no. 4, p. 477-494.
- Sillitoe, R. H., 1997, Characteristics and controls of the largest porphyry copper-gold and epithermal gold deposits in the circum-Pacific region: *Australian Journal of Earth Sciences*, v. 44, no. 3, p. 373-388.
- Simmons, S. F., White, N. C., and John, D. A., 2005, Geological characteristics of epithermal precious and base metal deposits, *in* Hedenquist, J. W., Thompson, J. F. H., Goldfarb, R. J., and Richards, J. P., eds., *Economic Geology 100th anniversary volume: Society of Exonomic Geologists* p. 485-522.
- Simonson, B. M., O'brien, M., Buchwaldt, R., Bowring, S. A., Hassler, S. W., and Beukes, N. J., 2014, New geochronological data from the Boolgeeda BIF and Woongarra Rhyolite, Hamersley Group (Western Australia), 2014 GSA Annual Meeting: Vancouver, British Columbia.
- Sircombe, K. N., 2003, Age of the Mt Boggola volcanic succession and further geochronological constraint on the Ashburton Basin, Western Australia: *Australian Journal of Earth Sciences*, v. 50, no. 6, p. 967-974.
- Smith, R. E., Perdrix, J. L., and Parks, T. C., 1982, Burial Metamorphism in the Hamersley Basin, Western Australia: *Journal of Petrology*, v. 23, no. 1, p. 75-102.
- Stacey, J. S., and Kramers, J. D., 1975, Approximation of terrestrial lead isotope evolution by a two-stage model: *Earth and Planetary Science Letters*, v. 26, no. 2, p. 207-221.
- Stern, R. A., 1997, The GSC Sensitive High Resolution Ion Microprobe (SHRIMP): analytical techniques of zircon U-Th-Pb age determinations and performance evaluation, *in* *Radiogenic age and isotope studies: Report 10; Geological Survey of Canada, Current Research 1997-F*, p. 1-31.
- Stern, R. A., 2001, New isotopic and trace-element standard for the ion microprobe: preliminary thermal ionization mass spectrometry (TIMS) U–Pb and electron microprobe data; *Radiogenic Age and Isotopic Studies: Report 14: Geological Survey of Canada, Current Research 2001-F1*.
- Stern, R. A., and Berman, R. G., 2001, Monazite U–Pb and Th–Pb geochronology by ion microprobe, with an application to in situ dating of an Archean metasedimentary rock: *Chemical Geology*, v. 172, no. 1, p. 113-130.

- Stern, R. A., Bodorkos, S., Kamo, S. L., Hickman, A. H., and Corfu, F., 2009, Measurement of SIMS Instrumental Mass Fractionation of Pb Isotopes During Zircon Dating: *Geostandards and Geoanalytical Research*, v. 33, no. 2, p. 145-168.
- Stern, R. A., and Rayner, N., 2003, Ages of several xenotime megacrysts by ID-TIMS: potential reference materials for ion microprobe U-Pb geochronology: *Radiogenic Age and Isotopic Studies: Report 16: Geological Survey of Canada: Current Research 2003-F1*.
- Takehara, M., Komure, M., Kiyokawa, S., Horie, K., and Yokoyama, K., 2010, Detrital zircon SHRIMP U-Pb age of the 2.3 Ga diamictites of the Meteorite Bore Member in the south Pilbara, Western Australia, *in* Tyler, I. M., and Knox-Robinson, C. M., eds., *Fifth International Archean Symposium, Volume Record 2010/18: Perth, Western Australia, Geological Survey of Western Australia*, p. 2.
- Teal, L., and Jackson, M., 2002, Geologic overview of the Carlin trend gold deposits: Gold deposits of the Carlin trend. Nevada Bureau of Mines and Geology, *Bulletin*, v. 111, p. 9-19.
- Thorne, A. M., Johnson, S. P., Tyler, I. M., Cutten, H. N., and Blay, O., 2011, Geology of the northern Capricorn Orogen, *in* Johnson, S. P., Thorne, A. M., and Tyler, I. M., eds., *Capricorn Orogen seismic and magnetotelluric (MT) workshop 2011, Geological Survey of Western Australia*, p. 7-18.
- Thorne, A. M., and Seymour, D. B., 1991, Geology of the Ashburton Basin Western Australia, Geological Survey of Western Australia, *Bulletin* 139, 162 p.
- Thorne, A. M., and Trendall, A. F., 2001, Geology of the Fortescue Group, Pilbara Craton, Western Australia, Geological Survey of Western Australia, *Bulletin* 144, 266 p.
- Townsend, K. J., Miller, C. F., D'Andrea, J. L., Ayers, J. C., Harrison, T. M., and Coath, C. D., 2000, Low temperature replacement of monazite in the Ireteba granite, Southern Nevada: geochronological implications: *Chemical Geology*, v. 172, no. 1, p. 95-112.
- Trendall, A. F., Compston, W., Nelson, D. R., De Laeter, J. R., and Bennett, V. C., 2004, SHRIMP zircon ages constraining the depositional chronology of the Hamersley Group, Western Australia: *Australian Journal of Earth Sciences*, v. 51, no. 5, p. 621-644.
- Tyler, I. M., 1991, The Geology of the Sylvania Inlier and the Southeast Hamersley Basin, Geological Survey of Western Australia, *Bulletin* 138, 124 p.
- Tyler, I. M., and Thorne, A. M., 1990, The northern margin of the Capricorn Orogen, Western Australia—an example of an Early Proterozoic collision zone: *Journal of Structural Geology*, v. 12, no. 5–6, p. 685-701.
- Vielreicher, N., Groves, D., Fletcher, I., McNaughton, N., and Rasmussen, B., 2003, Hydrothermal monazite and xenotime geochronology: a new direction for

- precise dating of orogenic gold mineralization: Society of Economic Geologists Newsletter, v. 53, no. 1, p. 10-16.
- Vielreicher, N. M., Groves, D. I., Snee, L. W., Fletcher, I. R., and McNaughton, N. J., 2010, Broad synchronicity of three gold mineralization styles in the Kalgoorlie gold field SHRIMP, U-Pb, and (super 40) Ar/ (super 39) Ar geochronological evidence: Economic Geology and the Bulletin of the Society of Economic Geologists, v. 105, no. 1, p. 187-227.
- Vielreicher, N., Groves, D., McNaughton, N., and Fletcher, I., 2015, The timing of gold mineralization across the eastern Yilgarn craton using U-Pb geochronology of hydrothermal phosphate minerals: Mineralium Deposita, v. 50, no. 4, p. 391-428.
- Wells, M., Laukamp, C., and Hancock, E. A., 2016, Reflectance spectroscopic characterisation of mineral alteration footprints associated with sediment-hosted gold mineralisation at Mt Olympus (Ashburton Basin, Western Australia): Australian Journal of Earth Sciences, v. 63, no. 8, p. 987-1002.
- White, A., Burgess, R., Charnley, N., Selby, D., Whitehouse, M., Robb, L., and Waters, D., 2014, Constraints on the timing of late-Eburnean metamorphism, gold mineralisation and regional exhumation at Damang mine, Ghana: Precambrian research., v. 243, p. 18-38.
- White, A. J. R., Smith, R. E., Nadoll, P., and Legras, M., 2014, Regional-scale metasomatism in the Fortescue Group volcanics, Hamersley Basin, Western Australia: implications for hydrothermal ore systems: Journal of Petrology, v. 55, no. 5, p. 977-1009.
- Williams, I. S., 1998, U-Th-Pb geochronology by ion microprobe. *in* Application of Microanalytical Techniques to Understanding Mineralizing Processes. Eds., McKibben, M. A., Shanks W., C and Ridley, W. I., Reviews of Economic Geology, v. 7, p. 1-35.
- Williams, I.S., Buick, I.S., Cartwright, I., 1996, An extended episode of early Mesoproterozoic metamorphic fluid flow in the Reynolds Range, central Australia. Journal of Metamorphic Geology, v. 14, p. 29-47.
- Wingate, M. T. D., and Compston, W., 2000, Crystal orientation effects during ion microprobe U-Pb analysis of baddeleyite: Chemical Geology, v. 168, p. 75-97.
- Wingate, M. T. D., 2002, Age and palaeomagnetism of dolerite sills of the Bangemall Supergroup on the Edmund 1:250 000 sheet, Western Australia: Geological Survey of Western Australia, Record 2002/4, 48p.
- Wingate, M. T. D., Kirkland, C. L., Cutten, H. N., and Thorne, A. M., 2012, 143445: dolerite sill, Waldburg Homestead; Geochronology Record 1077: Geological Survey of Western Australia, 4p.

- Wingate, M. T. D., Kirkland, C. L., Blay, O. A., and Johnson, S. P., 2013, 207259: dolerite sill, Maranoo Well; Geochronology Record 1123: Geological Survey of Western Australia, 4p.
- Wingate, M. T. D., and Lu, Y., 2016, Introduction to geochronology information released in 2014: Geological Survey of Western Australia p. 5.
- Wingate, M. T. D., Lu, Y., Blay, O., and Johnson, S. P., 2017, 206949: dolerite dyke, Tin Hut Bore: Geochronology Record 1432: Geological Survey of Western Australia, p. 4.
- Wingate, M. T. D., Lu, Y., Blay, O., and Johnson, S. P., 2017, 206953: dolerite sill, Tin Hut Bore: Geochronology Record 1433: Geological Survey of Western Australia, p. 4.
- Wyborn, L. A. I., Heinrich, C. A., and Jaques, A. L., 1994, Australian Proterozoic mineral systems: essential ingredients and mappable criteria, *in* Hallenstein, P. C., ed., Australian mining looks north — the challenges and choices. Australian Institute of Mining and metallurgy; 1994 AUSIMM Annual Conference: Darwin, Northern Territory, p. 109-115.
- Young, C. J., Groves, D. I., and Morant, P., 2003, Sediment-hosted disseminated gold mineralisation in the Palaeoproterozoic Ashburton Province, Western Australia: a new epizonal orogenic gold province related to Capricorn Orogeny?, *in* Eliopoulos et al., eds., Mineral exploration and sustainable development: proceedings of the 7th Biennial SGA Meeting: Athens, Greece, Millpress, p. 835-838.
- Zhang, J., Linnen, R., Lin, S., Davis, D., and Martin, R., 2014, Paleoproterozoic hydrothermal reactivation in a neoarchean orogenic lode-gold deposit of the southern Abitibi subprovince: U-Pb monazite geochronological evidence from the Young-Davidson mine, Ontario: *Precambrian Research*, v. 249, p. 263-272.
- Zhang, R., Pian, H., Santosh, M., Zhang, S., 2015, The history and economics of gold mining in China. *Ore Geology Reviews*, v 65, p.718-727.
- Zi, J.-W., Rasmussen, B., Muhling, J. R., Fletcher, I. R., Thorne, A. M., Johnson, S. P., Cutten, H. N., Dunkley, D. J., and Korhonen, F. J., 2015, In situ U–Pb geochronology of xenotime and monazite from the Abra polymetallic deposit in the Capricorn Orogen, Australia: Dating hydrothermal mineralization and fluid flow in a long-lived crustal structure: *Precambrian Research*, v. 260, p. 91-112.

Every reasonable effort has been made to acknowledge the owners of copyright material. I would be pleased to hear from any copyright owners who has been omitted or incorrectly acknowledged.

APPENDIX 1: FIRST AUTHOR JOURNAL PUBLICATIONS

APPENDIX 1A: PAULSENS

STATEMENT OF CONTRIBUTION OF OTHERS

Title of Paper: Using in situ SHRIMP U–Pb monazite and xenotime geochronology to determine the age of orogenic gold mineralization: an example from the Paulsens mine, southern Pilbara Craton

Publication status: Published

AUTHOR CONTRIBUTIONS

By signing the Statement of Authorship, each author certified that their stated contribution to the publication is accurate and that permission is granted for the publication to be included in the candidate's thesis.

Name of Principal Author: Imogen O. H. Fielding

Contribution to the paper: Led all aspects of the research including, all field work, diamond core logging and sample selection. Conducted most of the petrography including locating and imaging phosphate minerals for analysis and identifying any internal zonation. Preparation of SHRIMP mounts and data acquisition for approximately ½ the samples. Interpretation of all results, writing and drafting images for the manuscript.

Overall Percentage: 70%

Signature:

Date: 23/04/2018

Name of Co-Author: Simon P. Johnson

Contribution to the Paper: Assisted with field work, data interpretation, editing and revision of the manuscript.

Overall Percentage: 10%

Signature:

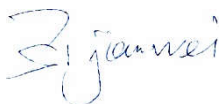
Date: 24/04/2018

Name of Co-Author: Jianwei Zi

Contribution to the Paper: Phosphate geochronology assisted with data collection, data processing and interpretation and manuscript editing.

Overall Percentage: 6%

Signature:



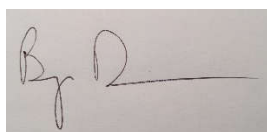
Date: 28/04/2018

Name of Co-Author: Birger Rasmussen

Contribution to the Paper: Assisted with manuscript editing.

Overall Percentage: 3%

Signature:



Date: 23/04/2018

Name of Co-Author: Janet R. Muhling

Contribution to the Paper: SEM imaging of phosphate minerals in approximately ½ the samples, assisted with editing of manuscript.

Overall Percentage: 3%

Signature:



Date: 04/04/2018

Name of Co-Author: Daniel J. Dunkley

Contribution to the Paper: Data acquisition and data reduction for approximately ½ the samples.

Overall Percentage: 3%

Signature:



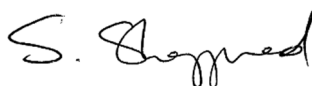
Date: 03/04/2018

Name of Co-Author: Stephen Sheppard

Contribution to the Paper: Assisted with editing the manuscript.

Overall Percentage: 2%

Signature:



Date: 21/04/2018

Name of Co-Author: Michael T. D. Wingate

Contribution to the Paper: Zircon geochronology data acquisition and data reduction.

Overall Percentage: 2%

Signature:



Date: 24/04/2018

Name of Co-Author: Jamie R. Rogers

Contribution to the Paper: Information about the local geology.

Overall Percentage: 1%

Signature:



Date: 03/04/2018

COPYRIGHT

Fielding, I. O. H., Johnson, S. P., Zi, J.-W., Rasmussen, B., Muhling, J. R., Dunkley, D. J., Sheppard, S., Wingate, M. T. D., and Rogers, J. R., 2017, Using In Situ SHRIMP U-Pb Monazite and Xenotime Geochronology to Determine the Age of Orogenic Gold Mineralization: An Example from the Paulsens Mine, Southern Pilbara Craton: *Economic Geology*, v. 112, no. 5, p. 1205-1230, doi: <https://doi.org/10.5382/econgeo.2017.4507> is published as an open access article under a Creative Commons Attribution Licence (CC BY) and can be reproduced with no copyright infringements as a part of this thesis. See http://www.segweb.org/SEG/Publications/Open_Access/SEG/_Publications/Open_Access.aspx for further details.



Using In Situ SHRIMP U-Pb Monazite and Xenotime Geochronology to Determine the Age of Orogenic Gold Mineralization: An Example from the Paulsens Mine, Southern Pilbara Craton

I. O. H. Fielding,^{1,†} S. P. Johnson,² J. -W. Zi,¹ B. Rasmussen,¹ J. R. Muhling,^{1,3} D. J. Dunkley,¹ S. Sheppard,¹ M. T. D. Wingate,^{2,3} and J. R. Rogers⁴

¹ Department of Applied Geology, Curtin University, Kent Street, Bentley, Western Australia 6102, Australia

² Geological Survey of Western Australia, 100 Plain Street, East Perth, Western Australia 6004, Australia

³ School of Earth and Environment, University of Western Australia, 35 Stirling Highway, Crawley, Western Australia 6009, Australia

⁴ Northern Star Resources Ltd, Level 1, 388 Hay Street, Subiaco, Western Australia 6008, Australia

Abstract

Paulsens is a mesothermal orogenic gold deposit located in the Wyloo Inlier on the southern margin of the Pilbara craton of Western Australia. Gold occurs in quartz-sulfide veins hosted within a folded and faulted gabbro dike, from which baddeleyite yields a U-Pb crystallization age of 2701 ± 11 Ma. Monazite and xenotime in the veins and from hydrothermally altered country rocks yield three distinct U-Pb dates of ca. 2400, 1730, and 1680 Ma. Textural relationships between euhedral xenotime and pyrite with rounded native gold inclusions from within the quartz-sulfide veins show that the primary gold mineralization was synchronous with xenotime crystallization at 2403 ± 5 Ma, and coeval with pervasive alteration of the host rocks, which yield monazite ages of 2398 ± 37 and 2403 ± 38 Ma. Regional-scale hydrothermal events at ca. 1730 and 1680 Ma are linked to the growth of monazite within phyllic rocks at 1730 ± 28 and 1721 ± 32 Ma, carbonate veining at 1655 ± 37 Ma, and gold remobilization or introduction of new gold at 1680 ± 9 Ma. The ca. 2400 Ma age for mineralization and hydrothermal alteration does not correspond with any known deformation event in the region, indicating a significantly different and more complicated low-temperature tectonothermal evolution for the southern Pilbara region than previously recognized. The in situ secondary ion mass spectrometry dating of monazite and xenotime employed here will lead to better targeting of orogenic gold deposits in the northern Capricorn Orogen, and these techniques can be utilized for orogenic gold exploration worldwide.

Introduction

Exploration targeting of gold deposits can be significantly improved by understanding metallogenic events in both space and time (Hronsky et al., 2012). By knowing the ages of hydrothermal mineralization, host rocks, and regional tectonothermal events, the search space can be minimized, and the financial risk to explorers greatly reduced (Rasmussen et al., 2006; Hronsky and Groves, 2008). However, many chronometers either are scarce in orogenic gold deposits or are susceptible to isotopic resetting during subsequent metamorphism and deformation (Kerrick and Cassidy, 1994; Chesley, 1999), so that the ages of many gold deposits worldwide are poorly constrained (Chesley, 1999). Nevertheless, many orogenic gold deposits contain trace amounts of the rare earth element (REE)-bearing phosphate minerals monazite ((Ce,La,Nd,Th)PO₄) or xenotime (YPO₄) intergrown with ore minerals (Vielreicher et al., 2003; Carpenter et al., 2005; Zhang et al., 2014). These phosphate minerals are robust chronometers that are resistant to diffusive Pb loss at temperatures up to 750°C (Harrison et al., 2002; Cherniak, 2010). Instead, monazite and xenotime undergo dissolution and reprecipitation reactions at temperatures <400°C (Townsend et al., 2000; Rasmussen and Muhling, 2007), leading to crystals that have multiple, but discrete, age domains from which precise dates can be obtained.

The Paulsens gold deposit is located in the northern part of the Capricorn Orogen, on the southern margin of the Pilbara

craton in Western Australia, and is hosted in low-grade metasedimentary and metavolcanic rocks of the ca. 2775 to 2629 Ma Fortescue Group in the Wyloo Inlier (Thorne and Trendall, 2001; Thorne et al., 2011; Fig. 1). Paulsens has an endowment of 1,114,000 ounces of gold, comprising 854,000 ounces mined between 2005 and 2016 (Northern Star Resources Limited, 2015a, 2016), and a remaining resource of 943,000 t at 8.58 g/t of gold for a total of 260,000 ounces contained gold as of June 30, 2016 (Northern Star Resources Limited, 2016). Historically, Paulsens was known as the Melrose mine, which was active in the 1930s with reports of 916 ounces of gold recovered from 2,955 t of ore (Forman, 1938; Blight, 1985; Northern Star Resources Limited, 2015b). The geological evolution of the area around Paulsens is not well known, and information is restricted to exploration company reports and short summaries in reports of the Geological Survey of Western Australia. Gold mineralization is contained within auriferous quartz-sulfide veins hosted in a folded and faulted gabbro dike (Fielding and Stokes, 2014; Northern Star Resources Limited, 2015b).

In this study, a combination of field mapping, petrography, and multimetal U-Th-Pb sensitive high-resolution ion microprobe (SHRIMP) geochronology has been used to address the absolute timing of mineralization at Paulsens and its relationship to known tectonothermal events in the region. Samples were taken from the Paulsens East and Gabbro Offset prospects that are located adjacent to the main Paulsens deposit (Fig. 2). These prospects share many similarities with Paulsens, but have not been subject to the same degree of

[†] Corresponding author: e-mail, imogen.fielding@postgrad.curtin.edu.au

1206

FIELDING ET AL.

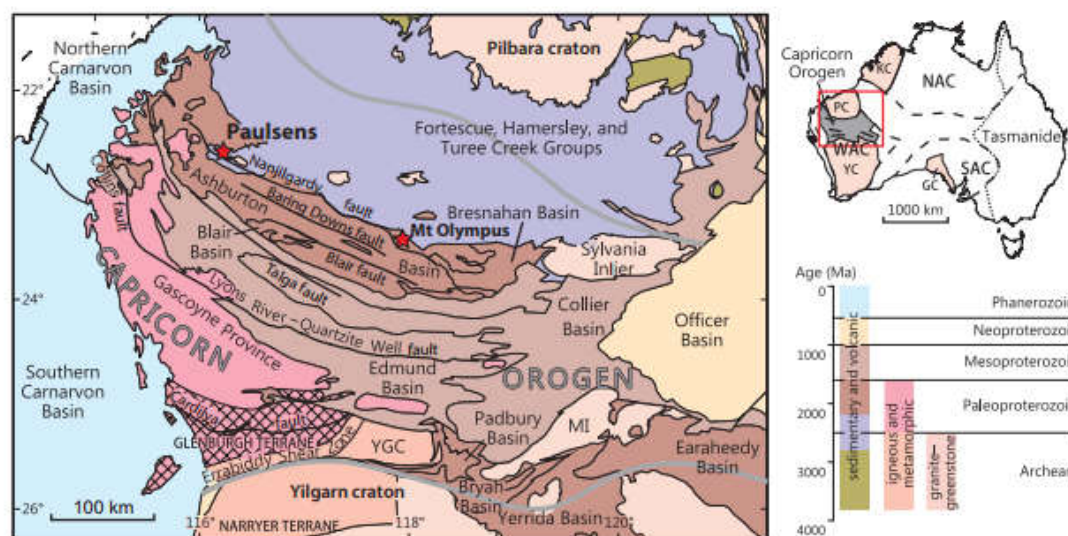


Fig. 1. Regional geologic setting of the northern Capricorn Orogen, showing the location of the Paulsens gold mine. Abbreviations: GC = Gawler craton, KC = Kimberley craton, MI = Marymia Inlier, NAC = North Australian craton, PC = Pilbara craton, SAC = South Australian craton, WAC = West Australian craton, YC = Yilgarn craton, YGC = Yarlswheel Gneiss Complex (after Johnson et al., 2013).

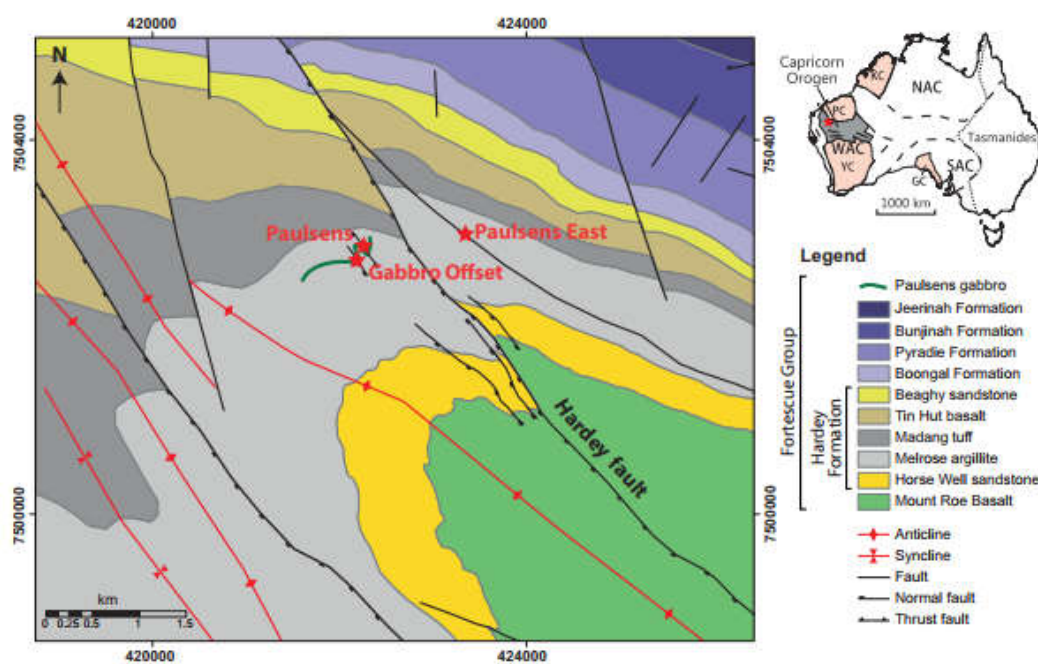


Fig. 2. Local geologic map of the northwest corner of the Wyloo Inlier, showing the location of the Paulsens, Gabbro Offset, and Paulsens East deposits. Coordinates are in meters (MGA94 zone 50).

deformation, thereby making it easier to establish relationships between deformation and ore formation. Results from this study provide U-Pb ages for (1) the emplacement of the gabbroic host rocks and maximum depositional ages for the Hardey Formation and (2) the timing of punctuated hydrothermal alteration and gold mineralization.

Geologic Setting

The Proterozoic Capricorn Orogen in Western Australia is a major zone of deformation, metamorphism, and magmatism located between the Yilgarn and Pilbara cratons (Tyler and Thorne, 1990; Cawood and Tyler, 2004; Sheppard et al., 2010; Thorne et al., 2011). It is the product of at least seven tectonic events, with intracratonic reworking and basin formation spanning more than 1.6 billion years (Martin and Morris, 2010; Sheppard et al., 2010; Johnson et al., 2011, 2013). Tectonothermal events include the 2215 to 2145 Ma Ophthalmia Orogeny, which is thought to reflect collision of the Pilbara craton with the Glenburgh terrane (Ochipinti et al., 2004; Johnson et al., 2011), and the 2005 to 1950 Ma Glenburgh Orogeny, which records collision of the Yilgarn craton with the combined Pilbara craton-Glenburgh terrane and marks the assembly of the West Australian craton (Johnson et al., 2011). This was followed by intracontinental reworking during the 1820 to 1770 Ma Capricorn Orogeny (Cawood and Tyler, 2004; Sheppard et al., 2010), the 1680 to 1620 Ma Mangaroon Orogeny (Sheppard et al., 2005), the 1320 to 1170 Ma Mutherbuckin Tectonic Event (Korhonen et al., 2017), the 1030 to 955 Ma Edmundian Orogeny (Martin and Thorne, 2004; Sheppard et al., 2007), and the ca. 570 Ma Mulka Tectonic Event (Johnson et al., 2013). The northern part of the Capricorn Orogen includes Archean rocks of the Pilbara craton, which are overlain by Archean to Paleoproterozoic rocks of, in ascending order, the Fortescue Group, Hamersley Group, Turee Creek Group, Shingle Creek Group (formerly the lower Wyloo Group), Wyloo Group (formerly the upper Wyloo Group), and Capricorn Group (Fig. 3A; Thorne and Trendall, 2001).

The Fortescue Group was deposited during protracted rifting of the Pilbara craton between ca. 2775 and 2629 Ma. In the South Pilbara sub-basin, deposition was controlled by E- to SE-trending extensional faults (Blake, 1993; Thorne and Trendall, 2001; Trendall et al., 2004; Thorne et al., 2011). Here the group is composed of a 6.5-km-thick succession of metasedimentary and metavolcanic rocks deposited unconformably on granite-greenstone rocks of the Pilbara craton and comprises, in ascending order, the Bellary Formation, Mt. Roe Basalt, Hardey Formation, Boongal Formation, Pyradie Formation, Bunjinah Formation, and Jeerinah Formation (Thorne and Trendall, 2001; Thorne et al., 2011; Fig. 3B). Thorne and Trendall (2001) divided the stratigraphy into five major tectonostratigraphic sequences with different depositional settings. Sequences 1 and 2 were deposited in fault-bounded subbasins in a coastal to shallow-marine environment, and comprise, respectively, sedimentary rocks, basaltic lavas, and volcanoclastic rocks of the Bellary Formation and Mt. Roe Basalt, and mixed sedimentary and volcanic rocks of the Hardey Formation. Merging of the subbasins, subsidence, and regional tilting resulted in deposition of sequences 3 and 4, which consist of subaqueous basaltic to

komatiitic lavas of the Boongal Formation and the Bunjinah and Pyradie formations, respectively, which were deposited in a deep shelf setting. Further subsidence resulted in a major marine transgression and the deposition of sequence 5, consisting of interbedded deep-marine sedimentary and volcanoclastic rocks, and basaltic lavas of the Jeerinah Formation.

A deep-crustal seismic reflection survey across the Capricorn Orogen imaged the crustal architecture of the orogen and the cratonic margins, identifying at least five major mantle-tapping structures (Johnson et al., 2013). In the northern Capricorn Orogen, the Nanjilgardy, Baring Downs, and Blair faults are of particular interest because they are spatially associated with gold and base metal occurrences, including the Paulsens and Mount Olympus deposits (Johnson et al., 2013; Fig. 1). Deformation, metamorphism, and hydrothermal activity in the Wyloo Inlier have been interpreted to be related to either the 2215 to 2145 Ma Ophthalmia Orogeny (Rasmussen et al., 2005; Martin and Morris, 2010) or the 1820 to 1770 Ma Capricorn Orogeny (Thorne and Trendall, 2001) or both, although no geochronological data are available from around Paulsens to verify these suggestions.

Local Geology

The Paulsens gold mine is situated at the northwestern end of the Wyloo Inlier, within metasedimentary and metavolcanic rocks of the Hardey Formation, near the base of the Fortescue Group (Owen, 2000; Thorne and Trendall, 2001). The mine geologists at Paulsens divided the Hardey Formation into five informal members—from oldest to youngest, the Horwell sandstone, Melrose argillite, Madang tuff, Tin Hut basalt, and Beaghy sandstone (Fig. 2; Owen, 2000). These strata are cut at a low angle by a ~50-m-thick, folded and faulted, medium- to coarse-grained mafic dike, known as the Paulsens gabbro, which, over short distances, follows the contact between fine-grained sandstone and laminated carbonaceous shale of the Melrose argillite (Fielding and Stokes, 2014). Regional-scale epidote-actinolite greenschist facies metamorphism has affected the rocks throughout the Wyloo Inlier (White et al., 2014a).

Structural observations across the Wyloo Inlier, as well as from underground drives and diamond drill core, show that the rocks were subjected to at least three low-grade deformation events (Owen, 2000). The first two events were responsible for the production of two dominant regional-scale cleavages. The S_1 cleavage is axially planar to regional-scale, tight to upright folds that define the long axis of the Wyloo Inlier. The S_1 fabric is a penetrative, spaced cleavage with an average orientation of 140/85SW, and is tentatively correlated with the $D_{3\text{oph}}$ event of the Ophthalmia Orogeny (Tyler and Thorne, 1990; Tyler, 1991). The D_2 event is also marked by a spaced cleavage (S_2) that is subparallel to the regional S_1 fabric, with an average orientation of 125/85SW. D_2 caused the tightening of F_1 folds and attenuation of the northern limbs to form narrow, intense shear zones up to 50 m wide. The D_2 event may be equivalent to the $D_{2\text{sch}}$ event of the Capricorn Orogeny, during which preexisting structures were either reactivated or tightened (Thorne and Seymour, 1991). Due to the near-coaxial nature of the two cleavages, distinguishing between S_1 and S_2 in the field can be difficult. The third event (D_3) is characterized by strike-slip faulting, possibly through

1208

FIELDING ET AL.

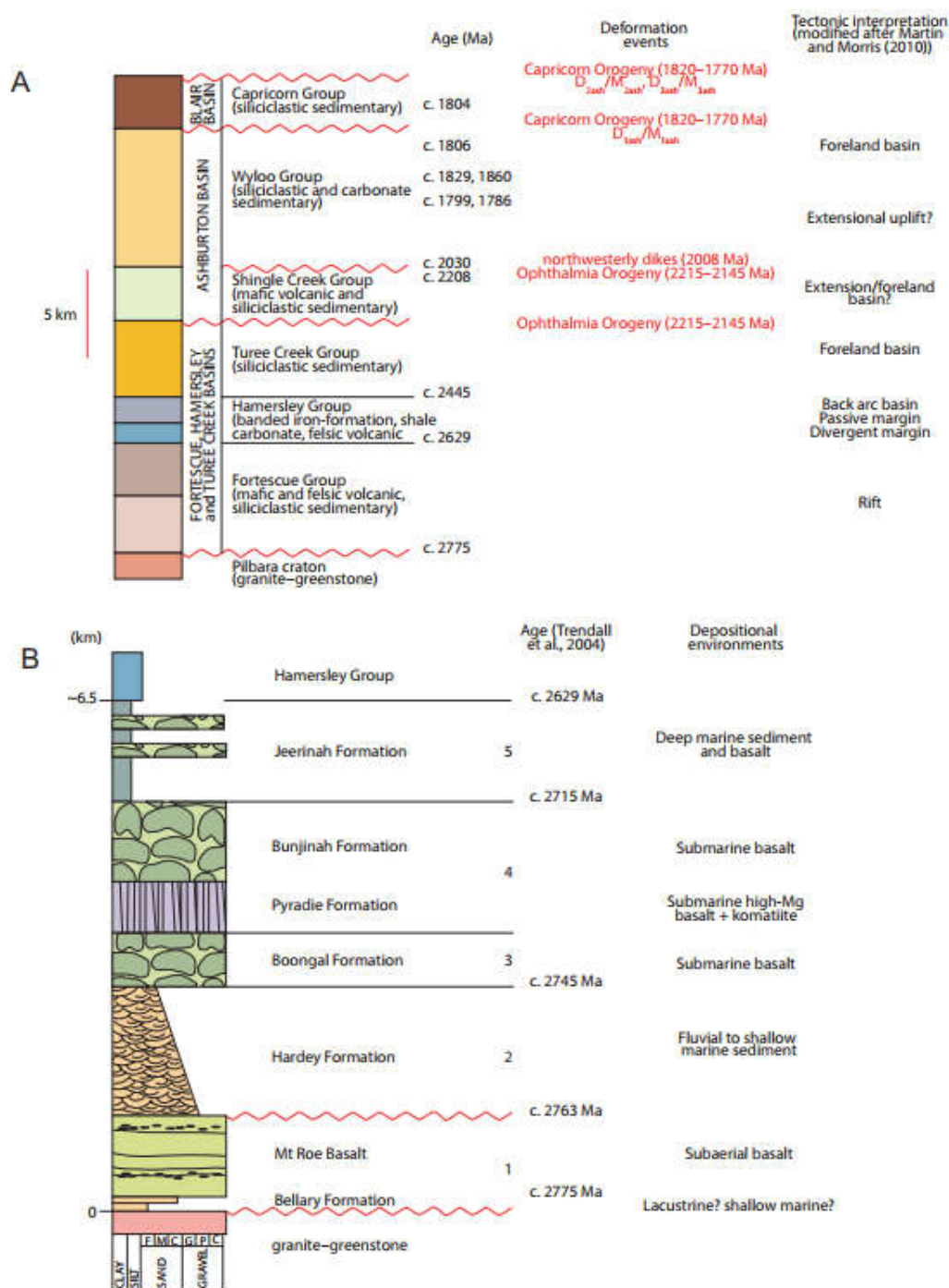


Fig. 3. A. Lithostratigraphic column and chronology of events for units in the northern Capricorn Orogen. B. Lithostratigraphic column, ages, and depositional environments for the Fortescue Group (adapted from Thorne et al., 2011). Grain size abbreviations: sand—C = coarse, F = fine, M = medium; gravel—C = cobble, G = granule, P = pebble.

the reactivation of preexisting faults, such as the Hardey fault to the northeast of the Paulsens mine (Fig. 2). The Hardey fault is a splay of the crustal-scale Nanjilgardy fault, which may have been a conduit for both hydrothermal and mineralized fluids during reactivation over multiple deformation events (Johnson et al., 2013).

Mineralization and Alteration

The Paulsens orebody is hosted by a 40-m-thick auriferous quartz-sulfide vein within the Paulsens gabbro, where the gabbro crosscuts fine-grained carbonaceous sandstone and siltstone of the Melrose argillite. Rheological contrasts between the gabbro and surrounding sedimentary rocks resulted in brittle fracturing of the gabbro during regional-scale F_1 folding, allowing for deposition of the auriferous quartz-sulfide vein (Fielding and Stokes, 2014; Fig. 4). Mineralization is located at the margins of the vein and is referred to as Paulsens Upper zone and Paulsens Lower zone mineralization (Northern Star Resources Limited, 2015b). Upper zone mineralization is defined by brecciated massive pyrite (Fig. 5A; Owen, 2000). Gold is rarely observed in hand specimen in the Upper zone, but petrographic studies show that early gold forms rounded inclusions within pyrite crystals and displays simple monocrystalline twinned microstructures with silver contents of 8.0 to 8.5 wt %. A second phase of gold formed along fractures and at grain boundaries where the pyrite is brecciated. This style of gold is typically associated with chalcopyrite and

pyrrhotite, and has a lower silver content, ranging from 6.6 to 7.2 wt %, with simple monocrystalline microstructure and some twin planes (Hancock and Thorne, 2016). Lower zone mineralization is hosted within the finely laminated basal part of the quartz-sulfide vein, which contains abundant carbonaceous stylolites and highly altered wall-rock inclusions of argillite that are pervasively altered to muscovite-ankerite \pm chlorite (Fig. 5B). The stylolites and wall-rock inclusions are associated with abundant free gold (Fielding and Stokes, 2014), with silver contents between 6.8 and 7.6 wt % and simple polycrystalline microstructure with polysynthetic and incoherent twins similar to the second style of gold in the Upper zone mineralization (Hancock and Thorne, 2016).

Proximal to the Paulsens mineralization, regional-scale greenschist facies metamorphic assemblages are overprinted by a hydrothermal alteration assemblage that is associated with gold mineralization. Primary mineral assemblages within the Paulsens gabbro are almost entirely replaced, with plagioclase altered to muscovite, and pyroxene replaced mainly by ankerite but with patches of muscovite-quartz-ankerite. Iron oxide minerals, possibly originally ilmenite and titanomagnetite, have been totally altered to leucoxene. Sedimentary rocks of the Melrose argillite member are now composed almost entirely of muscovite with minor quartz-ankerite \pm chlorite. Alteration distal to the orebody is difficult to differentiate from the regional metamorphic background; however, a change from ankerite to calcite along with an increase in

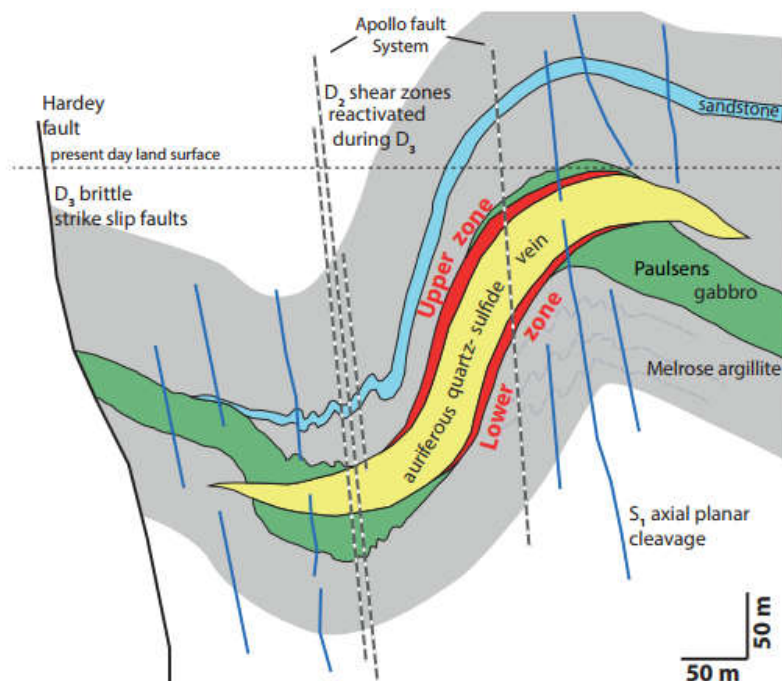


Fig. 4. Schematic vertical cross section of the Paulsens deposit (adapted from Fielding and Stokes, 2014). Viewed southeast with no vertical exaggeration.

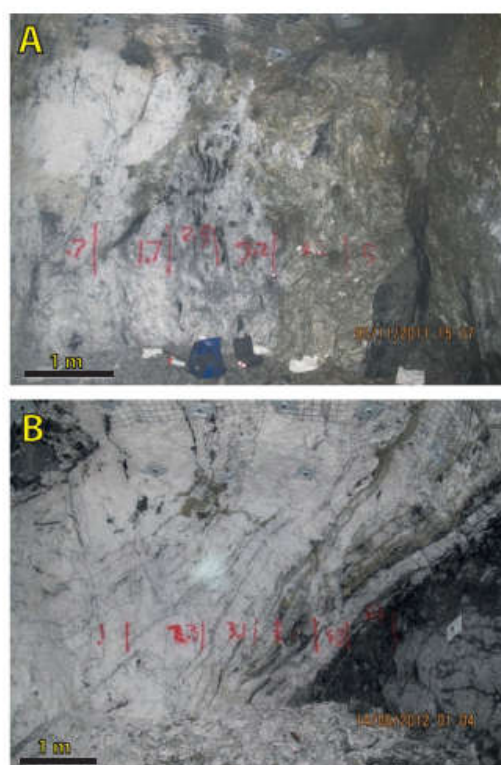


Fig. 5. A. Photograph of Paulsens Upper zone mineralization, showing massive pyrite at the margin of the auriferous quartz-sulfide vein. B. Paulsens Lower zone mineralization, showing laminated quartz-sulfide veins with abundant wall-rock inclusions and stylolites parallel to the vein margin.

chlorite and decrease in muscovite content occurs progressively away from the orebody.

Gabbro Offset and Paulsens East are two smaller prospects adjacent to the main Paulsens orebody (Fig. 2). They share many characteristics of Paulsens, but have not been subject to the same degree of deformation, which allows more straightforward determination of timing relationships between ore formation and the regional geologic history. Gabbro Offset is located 350 m southwest of the main Paulsens orebody and consists of a series of parallel quartz-carbonate-sulfide veins within the Paulsens gabbro. Mineralized veins are typically narrow, usually between 0.1 and 10 m wide, with visible gold along their margins or within massive pyrite similar to Paulsens Upper zone mineralization. Petrographic examination of pyrite from samples (GSWA 209907) from Gabbro Offset reveals two styles of native gold inclusions within the pyrite. Pyrite crystals show subtle zoning with an inclusion-rich core surrounded by a thin rim (<1 mm) of solid pyrite. Rounded blebs of native gold and chalcocopyrite within the cores are interpreted to be primary inclusions (Fig. 6A). These inclusions are up to 200 μm in diameter and form the majority

of visible gold in the samples. The pyrite is locally brecciated, and chalcocopyrite, pyrrhotite, and gold occur along fractures and pyrite grain boundaries (Fig. 6B). Although there is some evidence for gold remobilization (from the rounded gold inclusions in the cores of pyrites) at a local scale (Fig. 6C), it is possible that this secondary gold represents the introduction of new gold from an additional hydrothermal event.

Pulsens East mineralization is located approximately 1 km east of the main Paulsens orebody (Fig. 2) and, historically, gold was extracted from a series of shallow workings. Mineralization is hosted within parallel, steeply NE dipping, 1- to 5-m-wide veins comprising quartz, carbonate, and oxidized sulfides that are hosted within the Melrose argillite on the northern side of the Hardey fault. Sedimentary rocks in contact with the mineralized veins at Pulsens East have been deformed and pervasively altered to an assemblage containing muscovite-quartz \pm ankerite \pm chlorite \pm monazite (Fig. 6D), similar to that of the main Paulsens orebody.

Style of Gold Mineralization

The Pulsens deposit exhibits many of the characteristics of a typical orogenic gold deposit. Orogenic gold deposits form in the upper to middle crust in compressional tectonic settings related to accretionary or collisional orogenesis and tend to have a close spatial relationship to transcrustal structures which mark the boundaries between continental blocks (Groves et al., 1998; Goldfarb et al., 2001; Hronsky et al., 2012). Host rocks are varied, with Archean deposits commonly formed in volcanic-dominated sequences and Paleoproterozoic and Phanerozoic deposits formed in siliciclastic sequences (Goldfarb and Groves, 2015). Most deposits are hosted by rocks that have been metamorphosed to greenschist facies and commonly have alteration assemblages of carbonate-iron sulfide \pm white mica \pm chlorite (Goldfarb et al., 2001). Gold mineralization is characteristically high grade (5–30 g/t Au) and associated with quartz \pm carbonate veins with ≤ 3 to 5% sulfides (Groves et al., 1998). Unlike other styles of mineralization (e.g., epithermal and intrusion related), orogenic gold deposits cannot be related to individual intrusions and do not display zoned alteration halos (Sillitoe, 1997; Goldfarb and Groves, 2015). Pulsens has many of these traits: a spatial relationship to the mantle-tapping Nanjilgardy fault, siliciclastic sedimentary host rocks that have been metamorphosed to greenschist facies, the high-grade nature of gold mineralization (average 8.59 g/t Au), gold hosted in quartz-carbonate-sulfide veins surrounded by muscovite-ankerite \pm chlorite alteration, and an absence of coeval igneous intrusions.

Samples and Analytical Methods

Samples from Gabbro Offset were collected from three drill cores supplied by Northern Star Resources (PDU2153, PLDD015W1, and PDU2217); samples from Pulsens East were collected from outcrops where relationships between mineralization and deformation could be ascertained. A list of dated samples is provided in Table 1.

Monazite, xenotime, zircon, and baddeleyite were analyzed for U, Th, and Pb isotopes using the SHRIMP II instrument at the John de Laeter Centre at Curtin University in Perth, Western Australia. Appendix 1 describes the methodology in detail.

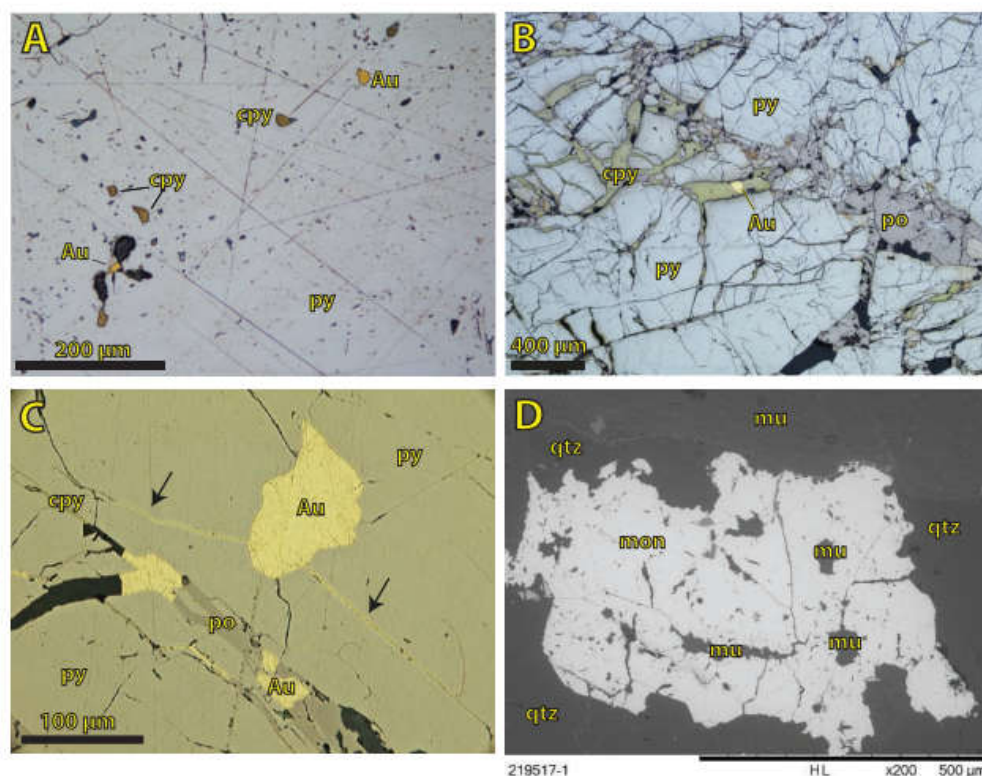


Fig. 6. A. Reflected light photomicrograph showing rounded blebs of native gold and chalcopyrite contained within pyrite (GSWA 209907). B. Reflected light photomicrograph showing brecciated pyrite with native gold, chalcopyrite, and pyrrhotite along the fractures (GSWA 209907). C. Reflected light photomicrograph showing local remobilization of gold along a fracture in pyrite; the arrows highlight local remobilization of gold from the primary rounded blebs of gold (GSWA 209907). D. Scanning electron microscope-backscattered electron (SEM-BSE) image showing a large monazite crystal with inclusions of muscovite from the alteration halo surrounding an auriferous quartz-sulfide vein at the Paulsens East deposit (GSWA 219517). Mineral abbreviations: cpy = chalcopyrite, mon = monazite, mu = muscovite, po = pyrrhotite, py = pyrite, qtz = quartz.

Detrital zircons were separated from sedimentary host rocks using standard magnetic and density techniques. Zircons, together with zircon reference materials (BR266 and OGC), were cast in 25-mm epoxy mounts and polished to expose the interiors of the crystals. Each mount was gold coated and characterized using transmitted light, reflected light, and cathodoluminescence (CL) images (Fig. 7).

U-Th-Pb analysis of monazite, xenotime, and baddeleyite was conducted in situ in order to preserve textural context. Grains for analysis were identified using a scanning electron microscope (SEM) in polished thin sections, and 2- or 3-mm-diameter plugs were extracted from the polished thin sections with a hollow-core rotary drill and mounted in 25-mm-diameter epoxy discs. The mounts were cleaned and gold coated before each analytical session. Reference materials were set into separate mounts and gold coated simultaneously with sample mounts. Standard and sample mounts were loaded together into the SHRIMP for concurrent analysis during each analytical session.

Geochronology Results and Interpretation

For all samples, age estimates are derived from 204-corrected $^{207}\text{Pb}/^{206}\text{Pb}^*$ ratios. Results for individual analyses are quoted with 1σ uncertainties; weighted mean $^{207}\text{Pb}/^{206}\text{Pb}^*$ dates are quoted with 95% confidence intervals.

Detrital zircon

Detrital zircons from two Hardey Formation sandstone samples (Table 1) were dated to provide a maximum depositional age for the supracrustal rocks into which the Paulsens gabbro was emplaced.

GSWA 209903—quartz sandstone, Hardey Formation: Medium-grained, strongly cleaved, quartz sandstone of the Melrose argillite member of the Hardey Formation was collected from 109.3- to 109.7-m depth in drill core PDU2153 in the hanging wall of the Gabbro Offset deposit.

Zircons are generally colorless, up to 150 μm in length, and euhedral, although rounded terminations and pitting are

Table 1. List of Sample Locations and Descriptions

GSWA Sample no.	Deposit	Target mineral	MGA94 zone 50		Drill core number	Depth (m)	Sample description	Formation
			Easting	Northing				
209902	Gabbro Offset	Monazite	421626	7503994	PDU2153	164.2–164.3	Carbonaceous phyllite	Hardey Formation
209903	Gabbro Offset	Zircon	421626	7503994	PDU2153	109.3–109.7	Quartz sandstone	Hardey Formation
209905	Gabbro Offset	Baddeleyite	421626	7503994	PDU2153	346.0–346.2	Dolerite sill	Paulsens gabbro
209907	Gabbro Offset	Xenotime	421626	7503994	PDU2153	394.4–395.5	Massive Au-bearing sulfide vein	—
209909a	Gabbro Offset	Monazite	421626	7503994	PDU2153	345.1–345.3	Altered part of dolerite sill (209905)	Paulsens gabbro
209909b	Gabbro Offset	Xenotime	421626	7503994	PDU2153	345.1–345.3	Ankerite-quartz vein in dolerite sill (209905)	—
209911	Gabbro Offset	Zircon	421995	7503917	PLDD015W1	473.6–473.9	Quartz sandstone	Hardey Formation
209912	Gabbro Offset	Monazite	421617	7503972	PDU2217	103.8–104.0	Carbonaceous phyllite	Hardey Formation
219512	Paulsens East	Monazite	423092	7503087	Outcrop	Surface	Slightly weathered micaceous phyllite	Hardey Formation
219513	Paulsens East	Monazite	423092	7503087	Outcrop	Surface	Slightly weathered micaceous phyllite	Hardey Formation
219517	Paulsens East	Monazite	423068	7503073	Outcrop	Surface	Slightly weathered micaceous phyllite	Hardey Formation

indicative of detrital transport (Fig. 7A). Sixty-five analyses were made of 64 zircons, of which two analyses >5% discordant were excluded from the age analysis. The zircons range in age from ca. 3456 to 2923 Ma ($n = 63$). The youngest detrital zircon age component consists of 15 analyses that yield a weighted mean $^{207}\text{Pb}^*/^{206}\text{Pb}^*$ date of 2941 ± 5 Ma (MSWD =

1.4; Table 2, Fig. 8A, C), providing a maximum age for deposition of the quartz sandstone.

GSWA 209911—quartz sandstone, Hardey Formation: Medium- and fine-grained quartz sandstone, with very fine grained matrix, from the Melrose argillite member was collected from the hanging wall to the Gabbro Offset deposit from drill core PLDD015W1 between 473.6- and 473.9-m depth.

Zircons are euhedral, up to 150 μm long, and mainly colorless, and have rounded terminations and pitting characteristic of detrital transport (Fig. 7B). Sixty-two analyses were made on 62 grains, of which 20 analyses >5% discordant were excluded from the age analysis. The zircons range in age from ca. 3450 to 2700 Ma. The youngest detrital zircon age component, consisting of nine analyses, yields a weighted mean $^{207}\text{Pb}^*/^{206}\text{Pb}^*$ date of 2750 ± 10 Ma (MSWD = 1.5; Table 3, Fig. 8B, D), providing a maximum age for deposition of the sandstone.

Baddeleyite

GSWA 209905—altered dolerite, Paulsens gabbro: A fine-grained, dark-colored portion of the Paulsens gabbro that is host to the Gabbro Offset deposit was collected from 346.0- to 346.2-m depth in drill core PDU2153 (Table 1). At this locality, the gabbro is highly altered and primary plagioclase and pyroxene are replaced by muscovite and ankerite \pm muscovite \pm chlorite, respectively, and iron oxide minerals have been altered to leucoxene. However, euhedral baddeleyite crystals up to 100 μm long are preserved throughout the sample. The outer surfaces of baddeleyite grains are commonly altered to very fine grained aggregates of zircon (Fig. 9A).

Seventeen analyses were made of 11 baddeleyite grains. Two analyses with elevated common Pb and two analyses >5% discordant were excluded from the age analysis. A single analysis yielded a concordant $^{207}\text{Pb}^*/^{206}\text{Pb}^*$ date significantly younger than the main cluster, and is interpreted to reflect ancient Pb loss during alteration. The remaining 12 analyses yield a weighted mean $^{207}\text{Pb}^*/^{206}\text{Pb}^*$ date of 2701 ± 11 Ma (MSWD = 1.4; Table 4, Fig. 10A), interpreted as the time of

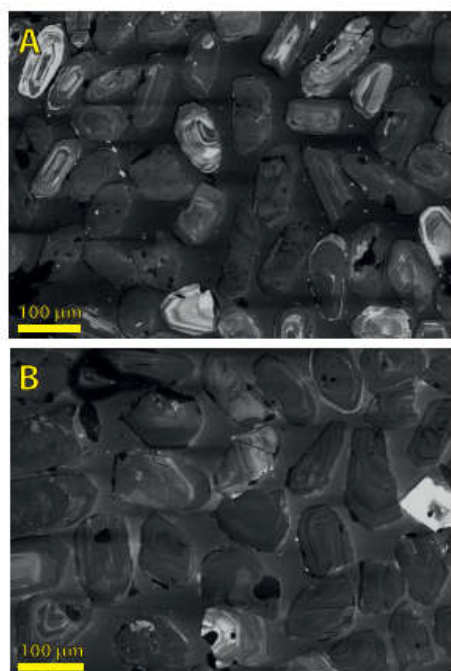


Fig. 7. Cathodoluminescence (CL) images of representative detrital zircon grains in Hardey Formation sandstone samples. A. Sample GSWA 209903. B. Sample GSWA 209911.

IN SITU SHRIMP GEOCHRONOLOGY, PAULSENS MINE, SOUTHERN PILBARA CRATON

1213

Table 2. SHRIMP Analytical Results for Detrital Zircon from Sample GSWA 209603: Quartz Sandstone of the Hardey Formation

Mont no.	Grain spot	U (ppm)	Th U	Th U	206 ppm	207 ppm	208 ppm	209 ppm	210 ppm	232 ppm	234 ppm	235 ppm	236 ppm	238 ppm	239 ppm	240 ppm	241 ppm	242 ppm	243 ppm	244 ppm	245 ppm	246 ppm	247 ppm	248 ppm	249 ppm	250 ppm	251 ppm	252 ppm	253 ppm	254 ppm	255 ppm	256 ppm	257 ppm	258 ppm	259 ppm	260 ppm	261 ppm	262 ppm	263 ppm	264 ppm	265 ppm	266 ppm	267 ppm	268 ppm	269 ppm	270 ppm	271 ppm	272 ppm	273 ppm	274 ppm	275 ppm	276 ppm	277 ppm	278 ppm	279 ppm	280 ppm	281 ppm	282 ppm	283 ppm	284 ppm	285 ppm	286 ppm	287 ppm	288 ppm	289 ppm	290 ppm	291 ppm	292 ppm	293 ppm	294 ppm	295 ppm	296 ppm	297 ppm	298 ppm	299 ppm	300 ppm	301 ppm	302 ppm	303 ppm	304 ppm	305 ppm	306 ppm	307 ppm	308 ppm	309 ppm	310 ppm	311 ppm	312 ppm	313 ppm	314 ppm	315 ppm	316 ppm	317 ppm	318 ppm	319 ppm	320 ppm	321 ppm	322 ppm	323 ppm	324 ppm	325 ppm	326 ppm	327 ppm	328 ppm	329 ppm	330 ppm	331 ppm	332 ppm	333 ppm	334 ppm	335 ppm	336 ppm	337 ppm	338 ppm	339 ppm	340 ppm	341 ppm	342 ppm	343 ppm	344 ppm	345 ppm	346 ppm	347 ppm	348 ppm	349 ppm	350 ppm	351 ppm	352 ppm	353 ppm	354 ppm	355 ppm	356 ppm	357 ppm	358 ppm	359 ppm	360 ppm	361 ppm	362 ppm	363 ppm	364 ppm	365 ppm	366 ppm	367 ppm	368 ppm	369 ppm	370 ppm	371 ppm	372 ppm	373 ppm	374 ppm	375 ppm	376 ppm	377 ppm	378 ppm	379 ppm	380 ppm	381 ppm	382 ppm	383 ppm	384 ppm	385 ppm	386 ppm	387 ppm	388 ppm	389 ppm	390 ppm	391 ppm	392 ppm	393 ppm	394 ppm	395 ppm	396 ppm	397 ppm	398 ppm	399 ppm	400 ppm	401 ppm	402 ppm	403 ppm	404 ppm	405 ppm	406 ppm	407 ppm	408 ppm	409 ppm	410 ppm	411 ppm	412 ppm	413 ppm	414 ppm	415 ppm	416 ppm	417 ppm	418 ppm	419 ppm	420 ppm	421 ppm	422 ppm	423 ppm	424 ppm	425 ppm	426 ppm	427 ppm	428 ppm	429 ppm	430 ppm	431 ppm	432 ppm	433 ppm	434 ppm	435 ppm	436 ppm	437 ppm	438 ppm	439 ppm	440 ppm	441 ppm	442 ppm	443 ppm	444 ppm	445 ppm	446 ppm	447 ppm	448 ppm	449 ppm	450 ppm	451 ppm	452 ppm	453 ppm	454 ppm	455 ppm	456 ppm	457 ppm	458 ppm	459 ppm	460 ppm	461 ppm	462 ppm	463 ppm	464 ppm	465 ppm	466 ppm	467 ppm	468 ppm	469 ppm	470 ppm	471 ppm	472 ppm	473 ppm	474 ppm	475 ppm	476 ppm	477 ppm	478 ppm	479 ppm	480 ppm	481 ppm	482 ppm	483 ppm	484 ppm	485 ppm	486 ppm	487 ppm	488 ppm	489 ppm	490 ppm	491 ppm	492 ppm	493 ppm	494 ppm	495 ppm	496 ppm	497 ppm	498 ppm	499 ppm	500 ppm	501 ppm	502 ppm	503 ppm	504 ppm	505 ppm	506 ppm	507 ppm	508 ppm	509 ppm	510 ppm	511 ppm	512 ppm	513 ppm	514 ppm	515 ppm	516 ppm	517 ppm	518 ppm	519 ppm	520 ppm	521 ppm	522 ppm	523 ppm	524 ppm	525 ppm	526 ppm	527 ppm	528 ppm	529 ppm	530 ppm	531 ppm	532 ppm	533 ppm	534 ppm	535 ppm	536 ppm	537 ppm	538 ppm	539 ppm	540 ppm	541 ppm	542 ppm	543 ppm	544 ppm	545 ppm	546 ppm	547 ppm	548 ppm	549 ppm	550 ppm	551 ppm	552 ppm	553 ppm	554 ppm	555 ppm	556 ppm	557 ppm	558 ppm	559 ppm	560 ppm	561 ppm	562 ppm	563 ppm	564 ppm	565 ppm	566 ppm	567 ppm	568 ppm	569 ppm	570 ppm	571 ppm	572 ppm	573 ppm	574 ppm	575 ppm	576 ppm	577 ppm	578 ppm	579 ppm	580 ppm	581 ppm	582 ppm	583 ppm	584 ppm	585 ppm	586 ppm	587 ppm	588 ppm	589 ppm	590 ppm	591 ppm	592 ppm	593 ppm	594 ppm	595 ppm	596 ppm	597 ppm	598 ppm	599 ppm	600 ppm	601 ppm	602 ppm	603 ppm	604 ppm	605 ppm	606 ppm	607 ppm	608 ppm	609 ppm	610 ppm	611 ppm	612 ppm	613 ppm	614 ppm	615 ppm	616 ppm	617 ppm	618 ppm	619 ppm	620 ppm	621 ppm	622 ppm	623 ppm	624 ppm	625 ppm	626 ppm	627 ppm	628 ppm	629 ppm	630 ppm	631 ppm	632 ppm	633 ppm	634 ppm	635 ppm	636 ppm	637 ppm	638 ppm	639 ppm	640 ppm	641 ppm	642 ppm	643 ppm	644 ppm	645 ppm	646 ppm	647 ppm	648 ppm	649 ppm	650 ppm	651 ppm	652 ppm	653 ppm	654 ppm	655 ppm	656 ppm	657 ppm	658 ppm	659 ppm	660 ppm	661 ppm	662 ppm	663 ppm	664 ppm	665 ppm	666 ppm	667 ppm	668 ppm	669 ppm	670 ppm	671 ppm	672 ppm	673 ppm	674 ppm	675 ppm	676 ppm	677 ppm	678 ppm	679 ppm	680 ppm	681 ppm	682 ppm	683 ppm	684 ppm	685 ppm	686 ppm	687 ppm	688 ppm	689 ppm	690 ppm	691 ppm	692 ppm	693 ppm	694 ppm	695 ppm	696 ppm	697 ppm	698 ppm	699 ppm	700 ppm	701 ppm	702 ppm	703 ppm	704 ppm	705 ppm	706 ppm	707 ppm	708 ppm	709 ppm	710 ppm	711 ppm	712 ppm	713 ppm	714 ppm	715 ppm	716 ppm	717 ppm	718 ppm	719 ppm	720 ppm	721 ppm	722 ppm	723 ppm	724 ppm	725 ppm	726 ppm	727 ppm	728 ppm	729 ppm	730 ppm	731 ppm	732 ppm	733 ppm	734 ppm	735 ppm	736 ppm	737 ppm	738 ppm	739 ppm	740 ppm	741 ppm	742 ppm	743 ppm	744 ppm	745 ppm	746 ppm	747 ppm	748 ppm	749 ppm	750 ppm	751 ppm	752 ppm	753 ppm	754 ppm	755 ppm	756 ppm	757 ppm	758 ppm	759 ppm	760 ppm	761 ppm	762 ppm	763 ppm	764 ppm	765 ppm	766 ppm	767 ppm	768 ppm	769 ppm	770 ppm	771 ppm	772 ppm	773 ppm	774 ppm	775 ppm	776 ppm	777 ppm	778 ppm	779 ppm	780 ppm	781 ppm	782 ppm	783 ppm	784 ppm	785 ppm	786 ppm	787 ppm	788 ppm	789 ppm	790 ppm	791 ppm	792 ppm	793 ppm	794 ppm	795 ppm	796 ppm	797 ppm	798 ppm	799 ppm	800 ppm	801 ppm	802 ppm	803 ppm	804 ppm	805 ppm	806 ppm	807 ppm	808 ppm	809 ppm	810 ppm	811 ppm	812 ppm	813 ppm	814 ppm	815 ppm	816 ppm	817 ppm	818 ppm	819 ppm	820 ppm	821 ppm	822 ppm	823 ppm	824 ppm	825 ppm	826 ppm	827 ppm	828 ppm	829 ppm	830 ppm	831 ppm	832 ppm	833 ppm	834 ppm	835 ppm	836 ppm	837 ppm	838 ppm	839 ppm	840 ppm	841 ppm	842 ppm	843 ppm	844 ppm	845 ppm	846 ppm	847 ppm	848 ppm	849 ppm	850 ppm	851 ppm	852 ppm	853 ppm	854 ppm	855 ppm	856 ppm	857 ppm	858 ppm	859 ppm	860 ppm	861 ppm	862 ppm	863 ppm	864 ppm	865 ppm	866 ppm	867 ppm	868 ppm	869 ppm	870 ppm	871 ppm	872 ppm	873 ppm	874 ppm	875 ppm	876 ppm	877 ppm	878 ppm	879 ppm	880 ppm	881 ppm	882 ppm	883 ppm	884 ppm	885 ppm	886 ppm	887 ppm	888 ppm	889 ppm	890 ppm	891 ppm	892 ppm	893 ppm	894 ppm	895 ppm	896 ppm	897 ppm	898 ppm	899 ppm	900 ppm	901 ppm	902 ppm	903 ppm	904 ppm	905 ppm	906 ppm	907 ppm	908 ppm	909 ppm	910 ppm	911 ppm	912 ppm	913 ppm	914 ppm	915 ppm	916 ppm	917 ppm	918 ppm	919 ppm	920 ppm	921 ppm	922 ppm	923 ppm	924 ppm	925 ppm	926 ppm	927 ppm	928 ppm	929 ppm	930 ppm	931 ppm	932 ppm	933 ppm	934 ppm	935 ppm	936 ppm	937 ppm	938 ppm	939 ppm	940 ppm	941 ppm	942 ppm	943 ppm	944 ppm	945 ppm	946 ppm	947 ppm	948 ppm	949 ppm	950 ppm	951 ppm	952 ppm	953 ppm	954 ppm	955 ppm	956 ppm	957 ppm	958 ppm	959 ppm	960 ppm	961 ppm	962 ppm	963 ppm	964 ppm	965 ppm	966 ppm	967 ppm	968 ppm	969 ppm	970 ppm	971 ppm	972 ppm	973 ppm	974 ppm	975 ppm	976 ppm	977 ppm	978 ppm	979 ppm	980 ppm	981 ppm	982 ppm	983 ppm	984 ppm	985 ppm	986 ppm	987 ppm	988 ppm	989 ppm	990 ppm	991 ppm	992 ppm	993 ppm	994 ppm	995 ppm	996 ppm	997 ppm	998 ppm	999 ppm	1000 ppm
-------------	---------------	------------	---------	---------	------------	------------	------------	------------	------------	------------	------------	------------	------------	------------	------------	------------	------------	------------	------------	------------	------------	------------	------------	------------	------------	------------	------------	------------	------------	------------	------------	------------	------------	------------	------------	------------	------------	------------	------------	------------	------------	------------	------------	------------	------------	------------	------------	------------	------------	------------	------------	------------	------------	------------	------------	------------	------------	------------	------------	------------	------------	------------	------------	------------	------------	------------	------------	------------	------------	------------	------------	------------	------------	------------	------------	------------	------------	------------	------------	------------	------------	------------	------------	------------	------------	------------	------------	------------	------------	------------	------------	------------	------------	------------	------------	------------	------------	------------	------------	------------	------------	------------	------------	------------	------------	------------	------------	------------	------------	------------	------------	------------	------------	------------	------------	------------	------------	------------	------------	------------	------------	------------	------------	------------	------------	------------	------------	------------	------------	------------	------------	------------	------------	------------	------------	------------	------------	------------	------------	------------	------------	------------	------------	------------	------------	------------	------------	------------	------------	------------	------------	------------	------------	------------	------------	------------	------------	------------	------------	------------	------------	------------	------------	------------	------------	------------	------------	------------	------------	------------	------------	------------	------------	------------	------------	------------	------------	------------	------------	------------	------------	------------	------------	------------	------------	------------	------------	------------	------------	------------	------------	------------	------------	------------	------------	------------	------------	------------	------------	------------	------------	------------	------------	------------	------------	------------	------------	------------	------------	------------	------------	------------	------------	------------	------------	------------	------------	------------	------------	------------	------------	------------	------------	------------	------------	------------	------------	------------	------------	------------	------------	------------	------------	------------	------------	------------	------------	------------	------------	------------	------------	------------	------------	------------	------------	------------	------------	------------	------------	------------	------------	------------	------------	------------	------------	------------	------------	------------	------------	------------	------------	------------	------------	------------	------------	------------	------------	------------	------------	------------	------------	------------	------------	------------	------------	------------	------------	------------	------------	------------	------------	------------	------------	------------	------------	------------	------------	------------	------------	------------	------------	------------	------------	------------	------------	------------	------------	------------	------------	------------	------------	------------	------------	------------	------------	------------	------------	------------	------------	------------	------------	------------	------------	------------	------------	------------	------------	------------	------------	------------	------------	------------	------------	------------	------------	------------	------------	------------	------------	------------	------------	------------	------------	------------	------------	------------	------------	------------	------------	------------	------------	------------	------------	------------	------------	------------	------------	------------	------------	------------	------------	------------	------------	------------	------------	------------	------------	------------	------------	------------	------------	------------	------------	------------	------------	------------	------------	------------	------------	------------	------------	------------	------------	------------	------------	------------	------------	------------	------------	------------	------------	------------	------------	------------	------------	------------	------------	------------	------------	------------	------------	------------	------------	------------	------------	------------	------------	------------	------------	------------	------------	------------	------------	------------	------------	------------	------------	------------	------------	------------	------------	------------	------------	------------	------------	------------	------------	------------	------------	------------	------------	------------	------------	------------	------------	------------	------------	------------	------------	------------	------------	------------	------------	------------	------------	------------	------------	------------	------------	------------	------------	------------	------------	------------	------------	------------	------------	------------	------------	------------	------------	------------	------------	------------	------------	------------	------------	------------	------------	------------	------------	------------	------------	------------	------------	------------	------------	------------	------------	------------	------------	------------	------------	------------	------------	------------	------------	------------	------------	------------	------------	------------	------------	------------	------------	------------	------------	------------	------------	------------	------------	------------	------------	------------	------------	------------	------------	------------	------------	------------	------------	------------	------------	------------	------------	------------	------------	------------	------------	------------	------------	------------	------------	------------	------------	------------	------------	------------	------------	------------	------------	------------	------------	------------	------------	------------	------------	------------	------------	------------	------------	------------	------------	------------	------------	------------	------------	------------	------------	------------	------------	------------	------------	------------	------------	------------	------------	------------	------------	------------	------------	------------	------------	------------	------------	------------	------------	------------	------------	------------	------------	------------	------------	------------	------------	------------	------------	------------	------------	------------	------------	------------	------------	------------	------------	------------	------------	------------	------------	------------	------------	------------	------------	------------	------------	------------	------------	------------	------------	------------	------------	------------	------------	------------	------------	------------	------------	------------	------------	------------	------------	------------	------------	------------	------------	------------	------------	------------	------------	------------	------------	------------	------------	------------	------------	------------	------------	------------	------------	------------	------------	------------	------------	------------	------------	------------	------------	------------	------------	------------	------------	------------	------------	------------	------------	------------	------------	------------	------------	------------	------------	------------	------------	------------	------------	------------	------------	------------	------------	------------	------------	------------	------------	------------	------------	------------	------------	------------	------------	------------	------------	------------	------------	------------	------------	------------	------------	------------	------------	------------	------------	------------	------------	------------	------------	------------	------------	------------	------------	------------	------------	------------	------------	------------	------------	------------	------------	------------	------------	------------	------------	------------	------------	------------	------------	------------	------------	------------	------------	------------	------------	------------	------------	------------	------------	------------	------------	------------	------------	------------	------------	------------	------------	------------	------------	------------	------------	------------	------------	------------	------------	------------	------------	------------	------------	------------	------------	------------	------------	------------	------------	------------	------------	------------	------------	------------	------------	------------	------------	------------	------------	------------	------------	------------	------------	------------	------------	------------	------------	------------	------------	------------	------------	------------	------------	------------	------------	------------	------------	------------	------------	------------	------------	------------	------------	------------	------------	------------	------------	------------	------------	------------	------------	------------	------------	-------------

1214

FIELDING ET AL.

Table 2. (Cont.)

Mount no.	Grain spot	U (ppm)	Th (ppm)	Th/U	f206 (%)	206Pb/208Pb ± 1σ	206Pb/208Pb ± 1σ	206Pb/208Pb ± 1σ	206Pb/208Pb ± 1σ	206Pb/208Pb ± 1σ	206Pb/208Pb ± 1σ	206Pb/208Pb ± 1σ	Disc. (%)	206Pb/208Pb ± 1σ	date (Ma)	± 1σ
Youngest detrital zircon age component (2941 ± 5 Ma)																
C14-15	903-60.1	108	51	0.492	0.060	1.781	0.029	0.2174	0.0010	1.782	0.029	0.2169	0.0010	2871	2958	8
C14-15	903-17.1	111	59	0.553	0.070	1.755	0.029	0.2164	0.0011	1.756	0.030	0.2158	0.0011	2906	2950	8
C14-15	903-29.1	110	65	0.606	0.109	1.699	0.028	0.2166	0.0010	1.701	0.028	0.2156	0.0010	2980	2948	8
C14-15	903-55.1	236	151	0.658	0.068	1.723	0.025	0.2161	0.0007	1.724	0.025	0.2155	0.0007	2949	2947	5
C14-15	903-28.1	132	74	0.574	0.027	1.706	0.027	0.2157	0.0009	1.706	0.027	0.2154	0.0010	2974	2947	7
C14-15	903-34.1	137	65	0.494	0.131	1.717	0.028	0.2165	0.0009	1.719	0.028	0.2153	0.0010	2955	2946	7
C14-15	903-47.1	91	48	0.545	0.063	1.746	0.029	0.2158	0.0010	1.747	0.029	0.2153	0.0010	2917	2946	8
C14-15	903-50.1	63	28	0.458	0.112	1.775	0.032	0.2158	0.0012	1.777	0.032	0.2148	0.0013	2879	2942	10
C14-15	903-9.1	130	72	0.570	0.030	1.741	0.028	0.2149	0.0010	1.741	0.028	0.2146	0.0010	2925	2941	8
C14-15	903-1.1	161	86	0.550	0.125	1.754	0.029	0.2151	0.0010	1.756	0.029	0.2140	0.0010	2906	2936	8
C14-15	903-58.1	187	94	0.517	0.006	1.736	0.026	0.2140	0.0007	1.736	0.026	0.2140	0.0008	2933	2936	6
C14-15	903-26.1	92	53	0.591	0.172	1.745	0.030	0.2152	0.0014	1.748	0.030	0.2137	0.0015	2916	2933	11
C14-15	903-56.1	221	29	0.136	0.046	1.727	0.025	0.2139	0.0007	1.728	0.025	0.2135	0.0007	2944	2932	5
C14-15	903-12.1	147	78	0.547	0.072	1.736	0.027	0.2138	0.0011	1.737	0.027	0.2132	0.0011	2931	2930	9
C14-15	903-42.1	103	61	0.608	0.214	1.697	0.029	0.2142	0.0010	1.701	0.029	0.2123	0.0011	2981	2923	9
Discordance >5%																
C14-15	903-52.1	91	47	0.529	0.060	1.672	0.028	0.2539	0.0011	1.673	0.028	0.2534	0.0012	3021	3206	7
C14-15	903-19.1	185	19	0.108	0.023	1.713	0.027	0.2561	0.0010	1.714	0.027	0.2559	0.0010	2963	3221	6

Notes: Pb* indicates radiogenic Pb; f₂₀₆ is the proportion of common Pb in 206Pb, determined using the measured 206Pb/208Pb and a common Pb composition from the Stacey and Kramers (1975) model at the approximate age of the sample; Disc. is apparent discordance, as 100[(206Pb/208Pb)*date] - [206Pb/208Pb]*date]; same definitions apply to Tables 3 to 11

igneous crystallization of the Paulsens gabbro, the host rock to gold mineralization.

Xenotime

GSWA 209907—*auriferous quartz-sulfide vein*: In the lower part of drill core PDU2153 between 394.4 and 395.5 m, a series of 1-cm to 1- to 2-m-wide massive sulfide and quartz-sulfide veins are abundant. These veins are part of the Gabbro Offset deposit and share similarities to Paulsens Upper zone mineralization. A massive sulfide vein was sampled for geochronology (Table 1), the lower 10 cm of which contained xenotime. The sample is associated with gold grades of 21 ppm, with gold formed as rounded inclusions within pyrite crystals (Fig. 6A) and along grain boundaries and fractures in areas where the pyrite is brecciated (Fig. 6B). The sample comprises an interlocking assemblage of quartz and pyrite, and contains xenotime in a number of textural settings: as euhedral grains enclosed entirely within pyrite (Fig. 9C), as subhedral grains within the quartz-pyrite matrix commonly intergrown along the margins of brecciated pyrite (Fig. 9D), and as euhedral to subhedral grains within the quartz matrix. Commonly, the matrix xenotime grains are chemically zoned, showing core and rim growth structures (Fig. 9D).

Eighty analyses were made on 37 grains, with multiple analyses performed within or across single grains. Irrespective of age or site of analysis, uranium and thorium contents range from 104 to 928 ppm and 2 to 695 ppm, respectively. Six analyses >5% discordant and 12 analyses that represent mixed ages, or parts of grains that have undergone Pb loss, are not considered geologically significant and are excluded from the age analysis. Twenty-six analyses of euhedral xenotime grains entirely enclosed within pyrite grains or as core zones of matrix xenotime present along brecciated pyrite grain boundaries (Fig. 9D) yield a weighted mean ²⁰⁷Pb/²⁰⁶Pb* date of 2403 ± 5 Ma (MSWD = 1.1; Table 5, Fig. 10B). Thirty-six analyses of xenotime rims and discrete grains within the quartz matrix yield a weighted mean ²⁰⁷Pb/²⁰⁶Pb* date of 1680 ± 9 Ma (MSWD = 1.4). We interpret these two dates to represent times of xenotime growth and subsequent dissolution-reprecipitation during two discrete periods of hydrothermal activity. The first event at ca. 2403 Ma is interpreted to date the formation of the quartz-sulfide vein, because grains of this age are contained entirely within the pyrite crystals. The second date at ca. 1680 Ma is interpreted to represent a subsequent period of hydrothermal activity, responsible for the brecciation and fracturing of pyrite grains and the dissolution-reprecipitation of preexisting ca. 2403 Ma xenotime.

GSWA 209909b—*ankerite-quartz vein*: Minor, 5- to 10-cm-wide carbonate veins within the fine-grained portion of the Paulsens gabbro (GSWA 209905) at the Gabbro Offset deposit were sampled from drill core PDU2153 between 345.1 and 345.3 m (Table 1). Assays from depths between 345 and 346 m returned up to 48 ppm Au. Xenotime occurs in the carbonate vein as irregular grains up to 50 μm across, interstitial to and included within other minerals.

Seven analyses were made on seven xenotime grains. Uranium and thorium contents vary from 200 to 550 ppm and 250 to 1,350 ppm, respectively. Two analyses >5% discordant were not used in the age analysis. One grain is significantly older than the others, with a date of 2415 ± 11 Ma (1σ). There

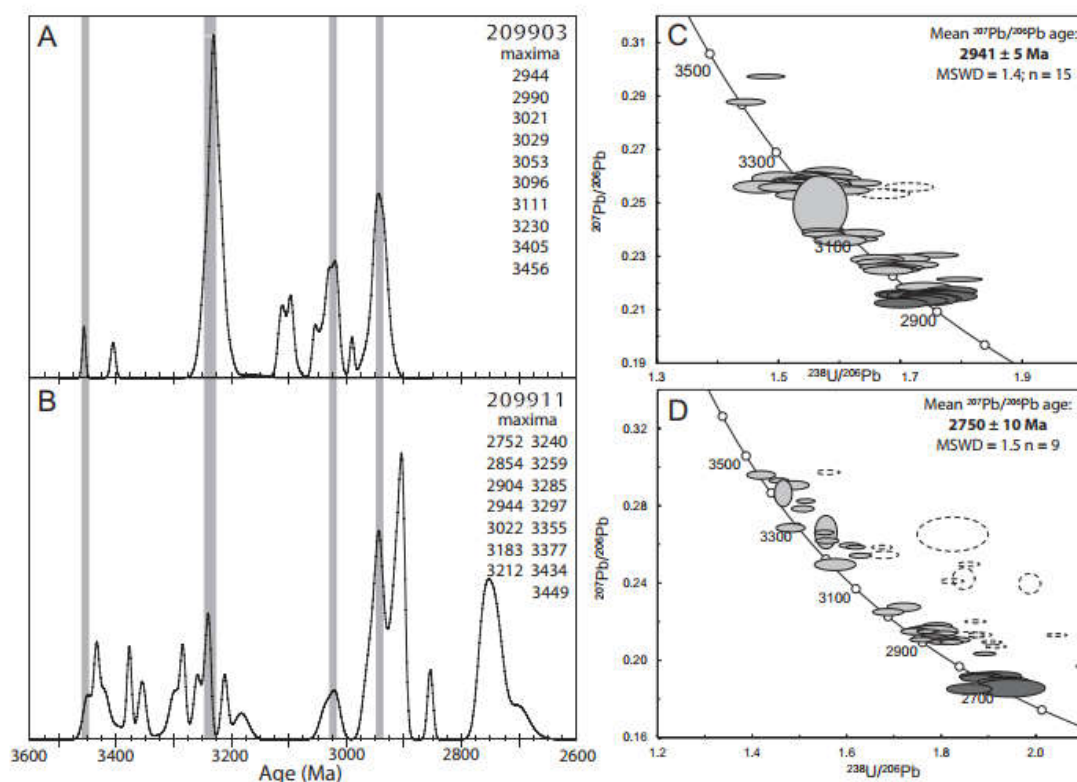


Fig. 8. Probability density diagrams of zircon ages for (A) sample GSWA 209903 (63 analyses of 63 zircons) and (B) sample GSWA 209911 (42 analyses of 42 zircons). Black curves include only data <5% discordant. C, D. Tera-Wasserburg concordia diagrams of U-Pb data for detrital zircons from samples GSWA 209903 and GSWA 209911. Dark gray ellipses indicate analyses comprising the youngest detrital age component; light gray ellipses are the remaining data <5% discordant; and dashed ellipses indicate data >5% discordant.

are no textural or chemical differences between this grain and the others analyzed. The remaining four analyses of four grains yield a weighted mean $^{207}\text{Pb}/^{206}\text{Pb}$ date of 1655 ± 37 Ma (MSWD = 1.3; Table 6, Fig. 10C). The older xenotime date corresponds with the age of monazite in the altered host gabbro (GSWA 209909a) and is interpreted to be inherited from the hydrothermally altered host rocks. The younger age of xenotime growth at ca. 1655 Ma, obtained from multiple grains, is attributed to a second, discrete hydrothermal event, probably dating emplacement of the ankerite-quartz veins, and is within uncertainty of xenotime rims in the auriferous quartz-sulfide vein (GSWA 209907).

Monazite

GSWA 209902—carbonaceous phyllite, Hardey Formation: Very fine grained, black, carbonaceous, quartz-muscovite-chlorite phyllite of the Melrose argillite member was sampled from drill core PDU2153 between 164.2 and 164.3 m in the hanging wall to the Gabbro Offset deposit (Table 1). The phyllite has a very strong foliation that has disrupted

and deformed 3- to 20-mm-thick quartz \pm pyrite veins. The sample contains randomly distributed, 1-mm-long, elongate porphyroblasts consisting of intergrown monazite and apatite, in equal amounts, with lesser chlorite and quartz. It is possible that the apatite has replaced monazite, a common reaction during greenschist to amphibolite facies metamorphism and hydrothermal alteration (Finger et al., 1998; Rasmussen and Muhling, 2009; White et al., 2014b). However, it is not clear whether the monazites are primary metamorphic or hydrothermal porphyroblasts or whether they replaced former regional-scale peak-metamorphic porphyroblasts such as andalusite (?) that grew at the same time as the foliation.

Monazite within two porphyroblasts was analyzed, with five spots on each. Uranium and thorium contents are 200 to 300 ppm and 2,000 to 10,000 ppm, respectively. Of the 10 analyses, one analysis is >5% discordant, and one is significantly younger than other analyses from the same grain and probably reflects partial Pb loss. These two analyses are not considered to be geologically significant and were not included in the age analysis. The remaining eight analyses define a

1216

FIELDING ET AL.

Table 3. SHRIMP Analytical Results for Detrital Zircon from Sample GSWA 206911: Quartz Sandstone of the Hurley Formation

Mount no.	Grain spot	U (ppm)	Th (ppm)	Th/U	ϵ_{206} (%)	$^{206}\text{Pb}/^{206}\text{Pb}^*$	$\pm 1\sigma$	$^{207}\text{Pb}/^{206}\text{Pb}$	$\pm 1\sigma$	$^{207}\text{Pb}/^{206}\text{Pb}^*$	$\pm 1\sigma$	$^{208}\text{Pb}/^{206}\text{Pb}^*$	date (Ma)	$\pm 1\sigma$	Disc. (%)	$^{206}\text{Pb}/^{206}\text{Pb}^*$	date (Ma)	$\pm 1\sigma$
Older detrital zircons																		
G14-13	911-42.1	86	45	0.5338	0.038	1.418	0.0015	0.2964	0.0015	1.419	0.020	0.2960	0.0015	3.439	37	0.3	3.450	8
G14-13	911-40.1	244	135	0.570	0.004	1.456	0.0009	0.2931	0.0009	1.456	0.014	0.2931	0.0009	3.370	25	1.9	3.434	5
G14-13	911-31.1	79	47	0.618	0.029	1.487	0.0015	0.2910	0.0015	1.488	0.021	0.2908	0.0015	3.314	38	3.1	3.422	8
G14-13	911-38.1	375	338	0.933	0.017	1.466	0.0046	0.2868	0.0046	1.466	0.012	0.2866	0.0046	3.353	22	1.4	3.369	25
G14-13	911-11.1	494	293	0.614	0.006	1.513	0.0013	0.2826	0.0007	1.513	0.013	0.2826	0.0007	3.271	21	3.2	3.377	4
G14-13	911-21.1	390	184	0.633	0.000	1.507	0.0011	0.2785	0.0011	1.507	0.016	0.2785	0.0011	3.281	27	2.2	3.355	6
G14-13	911-13.1	103	171	1.706	-0.043	1.482	0.0014	0.2883	0.0014	1.482	0.020	0.2887	0.0014	3.325	36	-0.8	3.298	8
G14-13	911-5.1	256	32	0.128	-0.019	1.556	0.0056	0.2663	0.0056	1.556	0.015	0.2664	0.0056	3.199	25	2.6	3.285	33
G14-13	911-43.1	319	218	0.705	0.008	1.552	0.0007	0.2663	0.0007	1.552	0.014	0.2662	0.0007	3.206	22	2.4	3.284	4
G14-13	911-25.1	181	104	0.592	0.028	1.558	0.0010	0.2623	0.0010	1.558	0.016	0.2620	0.0010	3.196	27	1.9	3.259	6
G14-13	911-27.1	226	252	1.102	0.030	1.606	0.0008	0.2598	0.0008	1.607	0.015	0.2596	0.0008	3.119	24	3.8	3.244	5
G14-13	911-19.1	567	386	0.703	0.003	1.619	0.0013	0.2587	0.0007	1.619	0.013	0.2586	0.0007	3.101	20	4.2	3.238	4
G14-13	911-14.1	318	161	0.522	0.017	1.628	0.0009	0.2544	0.0009	1.628	0.015	0.2543	0.0009	3.087	23	3.9	3.212	5
G14-13	911-11.1	67	54	0.825	-0.149	1.577	0.0019	0.2483	0.0019	1.575	0.029	0.2486	0.0020	3.169	47	0.4	3.182	13
G14-13	911-8.1	143	129	0.932	-0.071	1.722	0.0014	0.2270	0.0014	1.720	0.023	0.2277	0.0014	2.954	32	2.7	3.036	10
G14-13	911-62.1	109	81	0.766	0.075	1.686	0.0011	0.2259	0.0011	1.687	0.021	0.2252	0.0012	2.901	31	0.6	3.018	8
G14-13	911-39.1	138	131	0.977	0.053	1.790	0.0010	0.2184	0.0010	1.791	0.020	0.2180	0.0010	2.860	27	3.6	2.966	8
G14-13	911-53.1	157	97	0.642	0.040	1.765	0.0010	0.2167	0.0010	1.766	0.020	0.2163	0.0010	2.893	26	2.1	2.954	8
G14-13	911-7.1	130	61	0.490	0.066	1.757	0.0013	0.2161	0.0013	1.758	0.024	0.2155	0.0013	2.903	32	1.5	2.947	10
G14-13	911-41.1	49	50	1.044	0.000	1.787	0.0017	0.2155	0.0017	1.787	0.031	0.2155	0.0017	2.865	41	2.8	2.947	12
G14-13	911-2.1	201	170	0.873	0.086	1.743	0.0010	0.2159	0.0010	1.745	0.020	0.2151	0.0011	2.920	28	0.8	2.944	8
G14-13	911-28.1	290	141	0.522	0.056	1.771	0.0016	0.2155	0.0007	1.772	0.016	0.2150	0.0007	2.884	21	2.0	2.944	5
G14-13	911-23.1	376	80	0.218	0.024	1.805	0.0008	0.2143	0.0008	1.805	0.017	0.2141	0.0008	2.841	22	3.2	2.937	6
G14-13	911-56.1	387	305	0.787	0.009	1.781	0.0008	0.2127	0.0008	1.782	0.016	0.2126	0.0008	2.872	21	1.8	2.926	6
G14-13	911-60.1	207	171	0.850	-0.014	1.789	0.0008	0.2115	0.0008	1.789	0.018	0.2116	0.0008	2.863	23	1.9	2.918	6
G14-13	911-24.1	241	258	1.106	0.056	1.758	0.0017	0.2113	0.0008	1.759	0.017	0.2108	0.0008	2.902	23	0.4	2.912	6
G14-13	911-17.1	242	170	0.724	0.009	1.833	0.0009	0.2107	0.0009	1.833	0.018	0.2107	0.0009	2.897	23	3.6	2.911	7
G14-13	911-56.1	200	191	0.986	0.038	1.808	0.0008	0.2108	0.0008	1.809	0.018	0.2105	0.0009	2.857	23	2.5	2.909	7
G14-13	911-32.1	442	306	0.715	0.010	1.795	0.0014	0.2097	0.0006	1.795	0.014	0.2096	0.0006	2.854	19	1.7	2.903	4
G14-13	911-53.1	354	352	1.026	0.022	1.795	0.0015	0.2068	0.0006	1.796	0.015	0.2066	0.0007	2.854	20	1.7	2.902	5
G14-13	911-15.1	378	239	0.655	0.039	1.820	0.0016	0.2069	0.0007	1.821	0.016	0.2065	0.0007	2.822	20	2.8	2.902	6
G14-13	911-29.1	368	322	0.903	0.035	1.891	0.0016	0.2038	0.0006	1.891	0.016	0.2035	0.0006	2.736	19	4.1	2.854	5
G14-13	911-37.1	136	50	0.383	-0.013	1.906	0.0010	0.1926	0.0010	1.906	0.022	0.1927	0.0010	2.719	26	1.7	2.765	9
Youngest detrital zircon age component (2750 \pm 10 Ma)																		
G14-13	911-4.1	108	42	0.397	0.000	1.926	0.0014	0.1922	0.0014	1.926	0.029	0.1922	0.0014	2.696	33	2.3	2.761	12
G14-13	911-10.1	114	65	0.587	-0.084	1.879	0.0013	0.1910	0.0013	1.878	0.026	0.1917	0.0013	2.752	31	0.2	2.757	11
G14-13	911-12.1	112	77	0.707	-0.074	1.892	0.0025	0.1909	0.0012	1.890	0.025	0.1915	0.0013	2.737	30	0.7	2.755	11
G14-13	911-45.1	99	75	0.787	-0.071	1.880	0.0027	0.1903	0.0012	1.878	0.025	0.1909	0.0012	2.752	30	-0.1	2.750	11
G14-13	911-55.1	85	42	0.512	0.059	1.936	0.0012	0.1903	0.0012	1.937	0.027	0.1898	0.0013	2.683	31	2.1	2.741	11
G14-13	911-61.1	92	57	0.633	0.054	1.944	0.0012	0.1900	0.0012	1.945	0.026	0.1895	0.0012	2.674	30	2.3	2.738	11
G14-13	911-51.1	83	57	0.702	0.061	1.916	0.0027	0.1885	0.0013	1.918	0.027	0.1889	0.0013	2.705	32	1.0	2.733	11
G14-13	911-46.1	25	13	0.540	0.577	1.934	0.0024	0.1909	0.0024	1.945	0.048	0.1858	0.0030	2.674	55	1.2	2.705	27
G14-13	911-9.1	68	39	0.597	0.231	1.854	0.0016	0.1873	0.0016	1.859	0.031	0.1852	0.0018	2.775	39	-2.8	2.700	16

Table 3. (Cont.)

Mount no.	Grain spot	U (ppm)	Th (ppm)	Th/U	$\delta^{206}\text{Pb}$ (%)	$\delta\text{U}/\text{U}_{\text{Pb}}$ ± 1 σ	$\delta\text{Th}/\text{Th}_{\text{Pb}}$ ± 1 σ	$\delta\text{U}/\text{U}_{\text{Pb}}^*$ ± 1 σ	$\delta\text{Th}/\text{Th}_{\text{Pb}}^*$ ± 1 σ	$\delta\text{U}/\text{U}_{\text{Pb}}^*$ ± 1 σ	Disc. (%)	$\delta\text{U}/\text{U}_{\text{Pb}}^*$ ± 1 σ	$\delta\text{Th}/\text{Th}_{\text{Pb}}^*$ ± 1 σ					
Discordance >5%																		
G14-13	911-22.1	522	415	0.822	0.020	1.560	0.017	0.2975	0.0008	1.560	0.017	0.2974	0.0008	3193	27	7.6	3456	4
G14-13	911-16.1	665	471	0.731	0.014	1.824	0.050	0.2654	0.0058	1.824	0.050	0.2653	0.0058	2818	63	14.1	3278	34
G14-13	911-47.1	376	191	0.524	0.004	1.675	0.014	0.2586	0.0007	1.675	0.014	0.2585	0.0007	3018	20	6.8	3228	4
G14-13	911-49.1	117	4	0.036	0.120	1.677	0.020	0.2557	0.0012	1.679	0.020	0.2546	0.0012	3012	29	6.3	3214	8
G14-13	911-57.1	300	320	0.847	0.012	1.857	0.016	0.2469	0.0007	1.857	0.016	0.2467	0.0007	2777	19	12.8	3183	5
G14-13	911-58.1	391	255	0.674	0.012	1.847	0.015	0.2424	0.0037	1.848	0.015	0.2423	0.0037	2789	19	11.1	3135	24
G14-13	911-3.1	421	144	0.354	0.005	1.822	0.017	0.2410	0.0008	1.822	0.017	0.2410	0.0008	2820	21	9.8	3127	5
G14-13	911-52.1	576	501	0.899	0.037	1.987	0.015	0.2400	0.0034	1.987	0.015	0.2397	0.0034	2627	16	13.7	3118	23
G14-13	911-18.1	317	124	0.405	0.013	2.202	0.020	0.2272	0.0005	2.202	0.020	0.2271	0.0005	2413	18	20.4	3032	6
G14-13	911-44.1	545	180	0.342	0.037	1.872	0.014	0.2304	0.0005	1.872	0.014	0.2301	0.0006	2759	17	7.5	2982	2
G14-13	911-59.1	255	42	0.172	0.031	1.880	0.017	0.2300	0.0008	1.880	0.017	0.2132	0.0008	2749	21	6.2	2930	6
G14-13	911-26.1	133	67	0.521	0.044	1.856	0.021	0.2135	0.0010	1.857	0.021	0.2131	0.0010	2777	26	5.2	2929	8
G14-13	911-30.1	688	291	0.437	0.026	2.043	0.015	0.2133	0.0005	2.043	0.015	0.2131	0.0005	2568	16	12.3	2929	4
G14-13	911-48.1	497	418	0.808	0.034	1.905	0.015	0.2097	0.0005	1.905	0.015	0.2094	0.0005	2720	17	6.2	2901	4
G14-13	911-54.1	462	301	0.674	0.007	1.914	0.015	0.2092	0.0006	1.914	0.015	0.2072	0.0006	2710	18	6.0	2883	4
G14-13	911-20.1	691	89	0.133	0.026	2.402	0.019	0.2038	0.0007	2.403	0.019	0.2035	0.0007	2243	15	21.4	2855	6
G14-13	911-54.1	650	781	1.242	0.007	2.105	0.016	0.1969	0.0005	2.105	0.016	0.1969	0.0005	2506	15	10.5	2800	4
G14-13	911-6.1	901	565	0.649	0.022	2.405	0.018	0.1922	0.0006	2.406	0.018	0.1920	0.0006	2241	14	18.8	2760	5
G14-13	911-55.1	598	129	0.223	0.033	2.698	0.020	0.1852	0.0005	2.699	0.020	0.1849	0.0005	2032	13	24.7	2698	5
G14-13	911-50.1	803	859	1.105	0.048	2.554	0.019	0.1802	0.0055	2.555	0.019	0.1798	0.0055	2129	13	19.7	2651	50

Refer to Table 2 notes for definitions.

weighted mean $^{207}\text{Pb}^*/^{206}\text{Pb}^*$ date of 2401 ± 14 Ma (MSWD = 1.5; Table 7, Fig. 10D), interpreted as the age of monazite growth during hydrothermal alteration of the carbonaceous phyllite. This date is indistinguishable from that obtained on xenotime interpreted to date the timing of emplacement of the auriferous quartz-sulfide vein (GSA 209907).

GSWA 209909a—*altered dolerite, Paulsens gabbro*: A fine-grained, highly altered portion of the Paulsens gabbro (that is host to the Gabbro Offset deposit) containing a thin ankerite-quartz vein (GSWA 209909b) was collected from drill core PDU2153 between 345.1 and 345.3 m (Table 1). This sample is located 1 m above gabbro sample GSWA 209905, which yielded a baddeleyite crystallization age of ca. 2701 Ma. Locally, the sampled dolerite is pervasively altered by muscovite-ankerite-leucoxene \pm chlorite, crosscut by ankerite-quartz veins, and contains up to 48 ppm Au. Monazite in the sample occurs as irregular grains up to 100 μ m across, intergrown with and containing inclusions of leucoxene after iron oxide minerals.

Eight analyses were made of five monazite grains. Uranium and thorium contents are 30 to 140 ppm and 15,000 to 55,000 ppm, respectively. Among the eight analyses, one indicates high common Pb and is excluded. The remaining seven analyses yield consistent $^{207}\text{Pb}^*/^{206}\text{Pb}^*$ dates, but $^{238}\text{U}/^{206}\text{Pb}^*$ dates that vary broadly with Th content, which is probably a residual effect from the Th-correlated interference correction on ^{204}Pb or from the matrix correction. Therefore, a less rigorous (10%) discordance cutoff was applied to these analyses. The seven analyses yield a weighted mean $^{207}\text{Pb}^*/^{206}\text{Pb}^*$ date of 2398 ± 37 Ma (MSWD = 1.4; Table 8, Fig. 10E), interpreted as the age of monazite growth during hydrothermal alteration of the dolerite. This age is indistinguishable from that obtained from hydrothermal monazite in sample GSWA 209902 and the age of xenotime cores in the auriferous quartz-sulfide vein (GSWA 209907).

GSWA 2009/12—carbonaceous phyllite, Hardey Formation: A fine-grained, strongly foliated, black carbonaceous muscovite phyllite of the Melrose argillite member was sampled from drill core PDU2217 between 103.8 and 104.0 m in the footwall to the Gabbro Offset deposit (Table 1). The sample is located in a D₂/D₃ high-strain zone and contains lenses and stringers of quartz veins and coarse-grained pyrite. The sample also contains elongate porphyroblasts up to 3 mm long comprising intergrowths of monazite and fluorine in sub-equal amounts with lesser quartz and chlorite. In this sample, it appears that the monazite is partially replaced by fluorine, which is common during greenschist facies metamorphism (Rasmussen and Muhling, 2009). However, it is unclear if the growth of monazite is related to low-grade metamorphism and deformation associated with fault reactivation or if it has locally replaced former regional-scale peak metamorphic porphyroblasts (such as andalusite [?]) during hydrothermal alteration.

Twenty-two analyses were made on three monazite grains within the porphyroblasts. Uranium and thorium contents vary from 50 to 120 ppm and 3,400 to 14,000 ppm, respectively. The largest grain yielded 12 analyses <5% discordant; the remaining data vary in their $^{238}\text{U}/^{206}\text{Pb}^*$ ages, partly due to the low precision of low-U analyses. The 12 concordant analyses define a weighted mean $^{207}\text{Pb}^*/^{206}\text{Pb}^*$ date of 1730

1218

FIELDING ET AL.

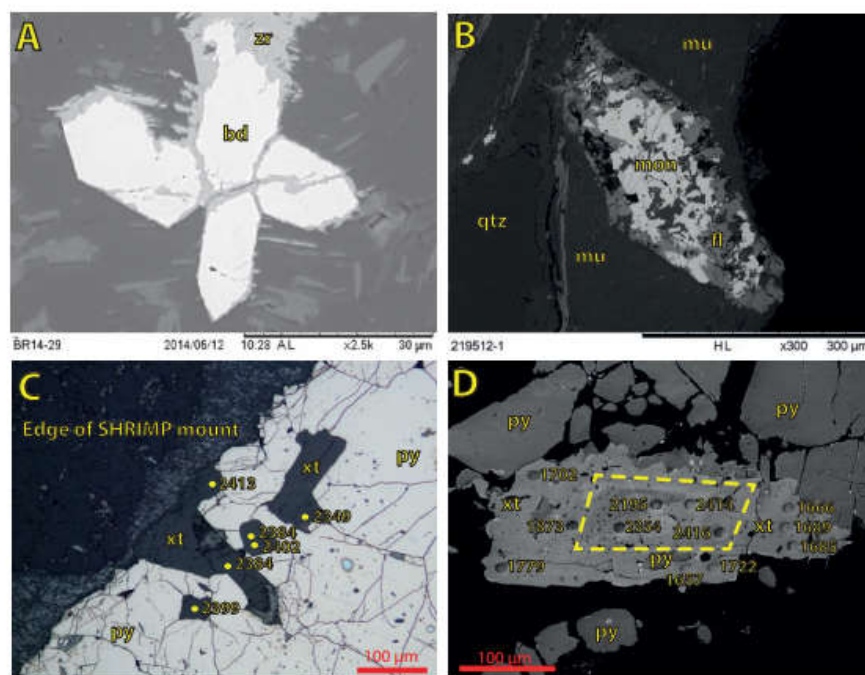


Fig. 9. A. SEM-BSE image of euhedral baddeleyite crystals with altered rim of very fine grained zircon (GSWA 209905). B. SEM-BSE image of florencite-monzite porphyroblast (GSWA 219512). C. Reflected light image of euhedral xenotime grains enclosed entirely within pyrite grains with analytical sites marked by dots showing ca. 2400 Ma dates (GSWA 209907). D. SEM-BSE image of xenotime intergrown with pyrite (oval pits on the grain are SHRIMP analysis sites) revealing a ca. 2400 Ma core surrounded by a ca. 1680 Ma rim. Mineral abbreviations: bd = baddeleyite, fl = florencite, mon = monazite, mu = muscovite, py = pyrite, xt = xenotime, zr = zircon.

Table 4. SHRIMP Analytical Results for Baddeleyite from Sample GSWA 209905: Paulsens Gabbro

Mount no.	Grain spot	U (ppm)	Th (ppm)	Th/U	f206 (%)	$^{238}\text{U}/^{206}\text{Pb}^*$	$\pm 1\sigma$	$^{207}\text{Pb}^*/^{206}\text{Pb}^*$	$\pm 1\sigma$	$^{238}\text{U}/^{206}\text{Pb}^*$ date (Ma)	$\pm 1\sigma$	Disc. (%)	$^{207}\text{Pb}^*/^{206}\text{Pb}^*$ date (Ma)	$\pm 1\sigma$
Crystallization (2701 \pm 11 Ma)														
1429	I.1-1	510	107	0.217	0.027	1.9080	0.0781	0.1796	0.0029	2717	91	-3.1	2649	26
1429	H.1-2	241	29	0.126	0.257	2.0650	0.0961	0.1814	0.0028	2546	98	5.4	2666	26
1429	A.2-2	263	52	0.203	0.171	1.8272	0.0718	0.1834	0.0022	2814	90	-6.0	2684	20
1429	B.2-1	456	33	0.074	0.318	1.9508	0.0750	0.1835	0.0016	2668	84	0.8	2685	15
1429	C.1-2	181	15	0.088	-0.256	1.9727	0.0818	0.1839	0.0034	2644	90	2.0	2689	31
1429	H.1-1	477	50	0.108	0.080	1.9889	0.0933	0.1852	0.0018	2626	101	3.3	2700	16
1429	D.1-1	492	15	0.031	0.244	1.9436	0.0746	0.1853	0.0015	2676	84	1.1	2701	14
1429	J.1-1	278	32	0.120	-0.045	1.8749	0.0740	0.1855	0.0019	2756	88	-2.4	2703	17
1429	G.1-1	314	31	0.101	0.063	2.0217	0.0796	0.1858	0.0023	2591	84	5.1	2705	20
1429	F.1-1	534	67	0.129	0.000	1.9219	0.0744	0.1869	0.0017	2701	85	0.7	2715	15
1429	C.1-1	475	25	0.054	0.142	2.0402	0.0840	0.1892	0.0021	2571	87	7.3	2736	18
1429	D.1-2	590	30	0.053	-0.067	1.9445	0.0743	0.1899	0.0030	2675	84	3.0	2741	26
Young outlier														
1429	E.1-1	281	111	0.407	0.125	2.1479	0.0840	0.1686	0.0018	2464	80	3.8	2544	17
Discordance >5% or high common lead														
1429	I.1-2	366	144	0.406	0.412	2.4155	0.1279	0.1596	0.0020	2233	100	10.5	2451	21
1429	F.1-3	337	13	0.041	0.637	1.9625	0.0768	0.1779	0.0027	2655	85	-1.0	2633	25
1429	F.1-2	215	16	0.076	1.540	1.9693	0.0796	0.1818	0.0058	2647	88	1.0	2670	53
1429	B.1-1	1,206	33	0.029	0.021	1.6160	0.0656	0.1866	0.0013	3105	100	-18.3	2713	12

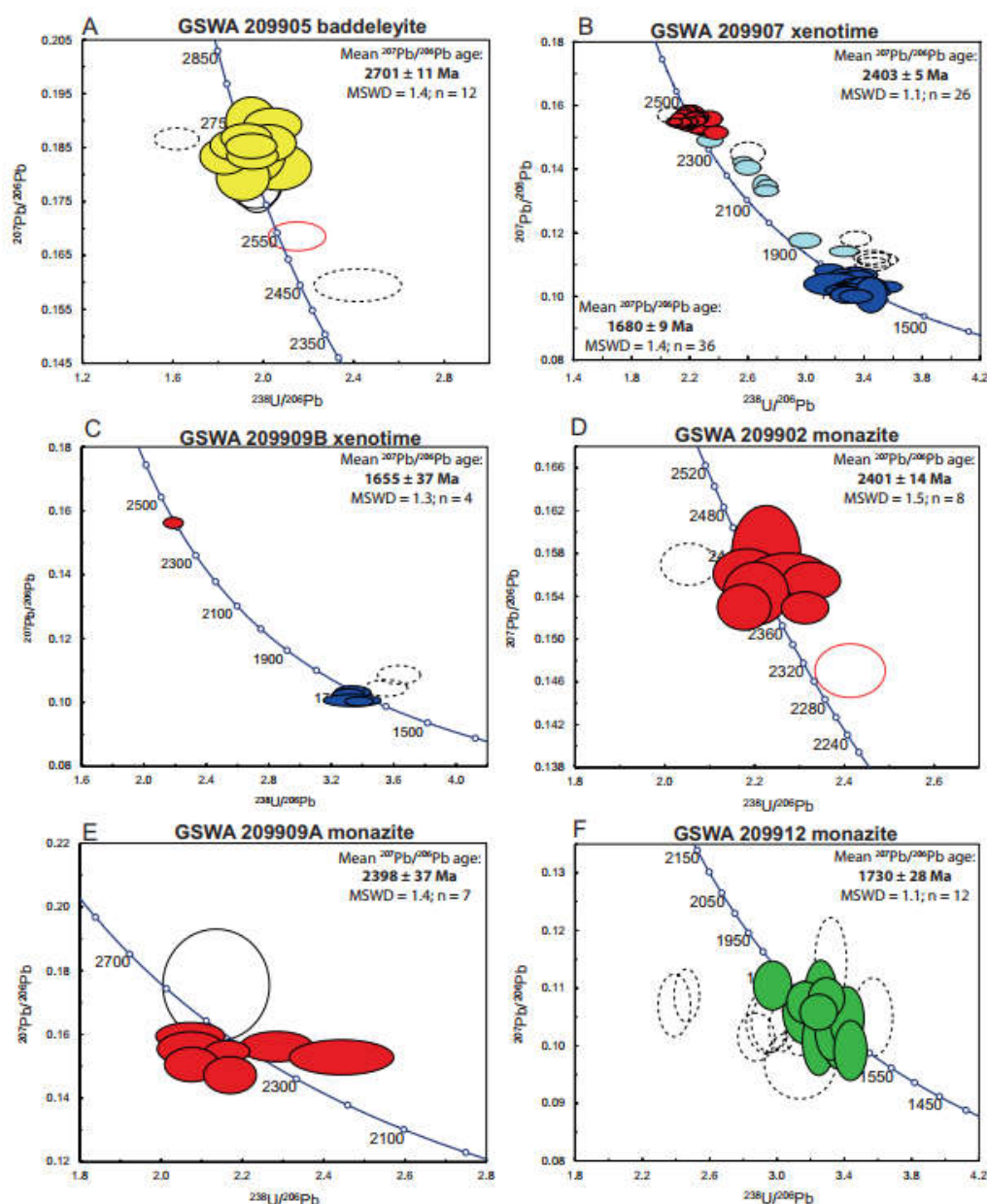


Fig. 10. Tera-Wasserburg concordia diagrams of U-Pb data for baddeleyite, xenotime, and monazite. A. Baddeleyite in gabbroic host rock to gold mineralization at the Gabbro Offset deposit (GSWA 209905). B. Xenotime in auriferous quartz-sulfide veins at the Gabbro Offset deposit (GSWA 209907). C. Xenotime in ankerite-quartz vein within the strongly altered Paulsens gabbro at the Gabbro Offset deposit (GSWA 209909b). D. Monazite porphyroblasts in carbonaceous phyllites at Gabbro Offset deposit (GSWA 209902). E. Monazite in pervasively altered portion of the Paulsens gabbro at the Gabbro Offset deposit (GSWA 209909a). F. Monazite porphyroblasts in carbonaceous phyllites at the Gabbro Offset deposit (GSWA 209912). G. Monazite in micaceous phyllites surrounding gold mineralization at the Paulsens East deposit (GSWA 219513/219517). H. Monazite porphyroblasts in micaceous phyllites at the Paulsens East deposit (GSWA 219512/219513). Key: Dark-colored ellipses (yellow, ca. 2700 Ma dates; red, ca. 2400 Ma dates; green, ca. 1730 Ma dates; dark blue, ca. 1680 Ma dates) show data used in the age calculations; other ellipses are for inferior data (pale blue, mixed ages; dashed ellipses, discordance >5%; unshaded red ellipses, outliers; unshaded black ellipses, high common Pb).

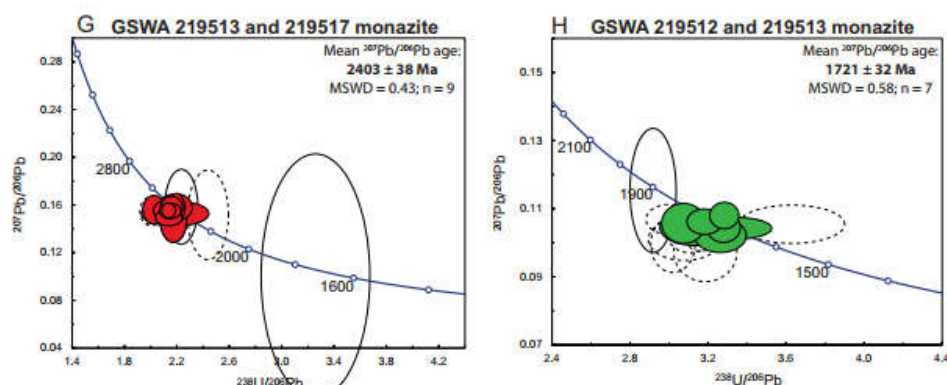


Fig. 10. (Cont.)

± 28 Ma (MSWD = 1.1; Table 9, Fig. 10F). This date is interpreted as the age of monazite growth during hydrothermal alteration of the carbonaceous phyllite, possibly during fault reactivation.

GSWA 219512, 219513, and 219517—micaceous phyllites, Hardey Formation: Fine-grained and slightly weathered phyllites were collected from shallow adits at Paulsens East (Table 1) in a 0.5- to 1.0-m-wide hydrothermal alteration halo surrounding 1- to 2-m-wide mineralized quartz-sulfide veins. Samples 219513 and 219517 contain large monazite grains up to 3 mm long, intergrown with minerals that define the main hydrothermal alteration assemblage (muscovite, quartz, and pyrite; Fig. 6D). The quartz-sulfide veins yielded rock-chip assays up to 6.65 ppm Au (Owen, 2000).

Sixteen analyses were made on seven monazite grains. Uranium and thorium contents of the samples varied from 30 to 135 ppm and 590 to 5,280 ppm, respectively. Four analyses >5% discordant and three with elevated common Pb were excluded from the age analysis. The remaining nine analyses provide concordant data that define a weighted mean $^{207}\text{Pb}/^{206}\text{Pb}$ date of 2403 ± 38 Ma (MSWD = 0.43; Table 10, Fig. 10G). This date is interpreted to represent the timing of hydrothermal alteration associated with the emplacement of the auriferous quartz-sulfide veins at Paulsens East and is within uncertainty of ages of hydrothermal monazite from altered samples at the Gabbro Offset deposit (GSWA 209902 and 209909a) as well as ages of xenotime cores from the auriferous quartz-sulfide vein at Gabbro Offset (GSWA 209907).

Samples GSWA 219512 and 219513 also contain abundant 1- to 3-mm-long, elongate porphyroblasts of interlocking monazite-florensite (Fig. 9B), together with minor chlorite and quartz, similar to the monazite-florensite porphyroblasts in sample GSWA 209912. Fifteen analyses were made on three monazite porphyroblasts. Uranium and thorium contents vary from 170 to 1,210 ppm and 380 to 8,945 ppm, respectively. Seven analyses >5% discordant and one analysis with elevated common Pb were excluded from the age analysis. The remaining seven concordant analyses define a weighted mean $^{207}\text{Pb}/^{206}\text{Pb}$ date of 1721 ± 32 Ma (MSWD

= 0.58; Table 11, Fig. 10H). Because sample GSWA 219513 also contains abundant, coarse-grained ca. 2403 Ma monazite intergrown with the main hydrothermal alteration assemblage (i.e., not detrital), the date of ca. 1721 Ma for the monazite porphyroblasts must represent the age of a secondary hydrothermal event that affected the phyllites. This age is within uncertainty of that of monazite porphyroblasts (GSWA 209912) in a D_2/D_3 shear zone at the Gabbro Offset deposit.

Discussion

SHRIMP U-Th-Pb geochronology has been used to define the age of the host rocks to gold mineralization at the Gabbro Offset deposit, as well as the timing of regional-scale hydrothermal activity associated with the emplacement of the auriferous quartz-sulfide veins and subsequent regional-scale hydrothermal events (Fig. 11, Table 12).

Age of the host rocks

Sedimentary rocks of the Hardey Formation were deposited between ca. 2763 and 2745 Ma (Trendall et al., 2004). The detrital zircon data presented here from two quartz sandstone samples from near the middle of the Hardey Formation (Melrose argillite) have relatively similar detrital age modes (Fig. 8), although sample GSWA 209911 contains a significant proportion of detritus older than ca. 3400 Ma and younger than ca. 2900 Ma compared with sample GSWA 209903. Despite these differences, the similarity in age modes at ca. 3450, 3240 to 3230, 3020, and 2944 Ma indicate that they both shared a common source region. The age of 2750 ± 10 Ma for the youngest detrital zircon age component in sandstone sample GSWA 209911 (Fig. 8) therefore provides a maximum depositional age for the Hardey Formation in the South Pilbara sub-basin. A minimum age constraint is provided by the baddeleyite crystallization age of 2701 ± 11 Ma for the Paulsens gabbro (Fig. 10A; GSWA 209905), which intrudes these sedimentary rocks. The crystallization age of the Paulsens gabbro suggests it may have been a feeder to mafic volcanic horizons in the 2715 to 2629 Ma Jeerinah Formation (Trendall et al., 2004).

IN SITU SHRIMP GEOCHRONOLOGY, PAULSEN'S MINE, SOUTHERN PILBARA CRATON

1221

Table 5. SHRIMP Analytical Results for Xenotime from Sample CSWA 200607: Auriferous Quartz-Sulfide Vein

Mount no.	Grain spot	U (ppm)	Th (ppm)	Th/U	(206/238)U (%)	$\frac{206}{208}\text{Pb}^*$	$\pm 1\sigma$	$\frac{207}{208}\text{Pb}^*$	$\pm 1\sigma$	$\frac{207}{206}\text{Pb}^*$	$\pm 1\sigma$	Disc. %	$\frac{207}{206}\text{Pb}^*$ date (Ma)	$\pm 1\sigma$
Euhedral xenotime and matrix xenotime cores (2403 \pm 5 Ma)														
1421	D-7-1	278	36	1.28	0.293	2.197	0.041	0.1569	0.0020	0.1481	0.0100	0.2	2422	22
1421	C-5-1	884	10	0.011	-0.011	2.171	0.033	0.1508	0.0018	0.1206	0.0101	-0.9	2421	19
1421	D-2-2	473	12	0.025	0.083	2.156	0.039	0.1586	0.0014	0.1068	0.0102	-1.6	2419	16
1421	D-5-3	338	25	0.074	0.086	2.242	0.042	0.1565	0.0010	0.1000	0.0098	1.7	2419	11
1421	D-3-1	212	71	0.338	0.044	2.259	0.047	0.1565	0.0012	0.1206	0.0098	2.3	2418	13
1421	D-1-1	131	35	0.264	0.000	2.188	0.039	0.1563	0.0025	0.1226	0.0100	-0.4	2418	27
1421	D-4-2	404	27	0.067	-0.013	2.235	0.041	0.1563	0.0069	0.1282	0.0069	1.4	2416	10
1421	C-6-1	125	17	0.133	0.106	2.221	0.058	0.1562	0.0025	0.1262	0.0069	0.8	2415	27
1421	C-2-2	876	7	0.008	-0.024	2.121	0.032	0.1560	0.0010	0.1726	0.0103	-3.2	2413	11
1421	F1-1	163	11	0.068	0.111	2.334	0.060	0.1559	0.0016	0.0969	0.0065	4.7	2411	17
1421	F1-4	309	2	0.005	0.036	2.252	0.046	0.1557	0.0011	0.0462	0.0068	1.7	2409	12
1421	C2-1-1	325	3	0.009	0.030	2.171	0.042	0.1557	0.0010	0.0902	0.0101	-1.4	2409	11
1421	D-3-2	139	37	0.268	0.000	2.178	0.054	0.1553	0.0014	0.1300	0.0101	-1.3	2405	15
1421	D-4-1	410	15	0.037	0.038	2.252	0.041	0.1552	0.0009	0.1072	0.0069	1.5	2404	10
1421	D-6-1	443	24	0.054	0.025	2.203	0.036	0.1550	0.0008	0.1301	0.0100	-0.5	2402	9
1421	D-8-1	126	27	0.213	0.098	2.191	0.054	0.1550	0.0015	0.1214	0.0101	-0.9	2402	16
1421	C1-1	319	52	0.164	0.040	2.181	0.053	0.1550	0.0018	0.1280	0.0101	-1.3	2402	20
1421	D-5-4	398	51	0.128	0.025	2.224	0.041	0.1550	0.0009	0.1241	0.0100	0.3	2402	10
1421	C2-1-2	274	85	0.310	0.034	2.219	0.044	0.1549	0.0011	0.1326	0.0100	0.1	2401	12
1421	F7-2	928	18	0.020	0.006	2.009	0.032	0.1549	0.0007	0.1204	0.0105	-4.6	2401	8
1421	D-5-2	423	21	0.051	0.045	2.095	0.037	0.1549	0.0009	0.1246	0.0105	-4.8	2401	10
1421	D-2-1	749	68	0.091	0.007	2.159	0.035	0.1549	0.0008	0.1282	0.0102	-2.2	2400	8
1421	C-3-1	195	75	0.384	0.000	2.130	0.044	0.1547	0.0012	0.1358	0.0103	-3.5	2369	13
1421	D-1-2	129	4	0.033	0.167	2.253	0.063	0.1539	0.0017	0.0883	0.0069	1.0	2360	19
1421	C2-2-1	520	20	0.038	0.043	2.309	0.072	0.1523	0.0009	0.1136	0.0068	2.2	2372	10
1421	F8-1	173	31	0.180	-0.029	2.379	0.055	0.1516	0.0013	0.1157	0.0065	4.3	2364	15
Matrix xenotime discrete grains and rims (1680 \pm 9 Ma)														
1421	F1-5	246	103	0.420	0.208	3.165	0.069	0.1085	0.0013	0.0550	0.0100	0.2	1774	22
1421	C1-5	150	147	0.982	-0.102	3.375	0.080	0.1070	0.0014	0.0872	0.0066	4.4	1749	24
1421	C1-4	265	371	1.403	0.266	3.335	0.065	0.1068	0.0019	0.0883	0.0067	3.1	1745	32
1421	F11-2	239	352	1.471	0.950	3.257	0.070	0.1059	0.0020	0.0919	0.0100	0.2	1730	35
1421	F1-9	253	149	0.588	0.106	3.306	0.071	0.1056	0.0012	0.0570	0.0069	1.2	1724	21
1421	F1-2	104	57	0.543	0.084	3.309	0.097	0.1052	0.0018	0.0872	0.0069	0.9	1717	31
1421	F2-2	179	169	0.944	-0.055	3.364	0.082	0.1050	0.0023	0.0850	0.0068	2.2	1715	40
1421	D-5-6	352	189	0.538	0.000	3.439	0.063	0.1047	0.0009	0.0865	0.0066	3.8	1710	15
1421	F9-1	151	134	0.883	0.214	3.254	0.082	0.1044	0.0016	0.0889	0.0101	-1.4	1703	28
1421	C1-10	341	140	0.412	0.072	3.190	0.135	0.1042	0.0023	0.0805	0.0103	-3.4	1669	40
1421	C1-9	352	159	0.452	0.072	3.438	0.061	0.1039	0.0010	0.0867	0.0067	2.9	1665	17
1421	E1-2	290	248	0.857	-0.071	3.329	0.063	0.1037	0.0015	0.0878	0.0100	-0.1	1691	26
1421	E1-5	337	192	0.570	0.000	3.354	0.061	0.1036	0.0008	0.0871	0.0100	0.4	1689	15
1421	F2-3	248	435	1.753	0.150	3.453	0.074	0.1035	0.0013	0.0836	0.0067	2.9	1688	23
1421	F12-1	364	173	0.476	-0.046	3.285	0.062	0.1035	0.0009	0.0866	0.0102	-1.5	1687	16
1421	F1-12	232	264	1.141	0.000	3.549	0.077	0.1033	0.0012	0.0867	0.0065	5.0	1684	21

1222

FIELDING ET AL.

Table 5. (Cont.)

Mount no.	Grain spot	U (ppm)	Th (ppm)	Th/U	$^{206}\text{Pb}/^{238}\text{U}$ (%)	$\frac{206\text{Pb}}{207\text{Pb}} \pm 1\sigma$	$\frac{207\text{Pb}}{206\text{Pb}} \pm 1\sigma$	$\frac{207\text{Pb}}{232\text{Th}}$	$\frac{207\text{Pb}}{206\text{Pb}} \pm 1\sigma$	date (Ma) $\pm 1\sigma$	Disc. %	date (Ma) $\pm 1\sigma$
Matrix xenotime discrete grains and rims (1680 \pm 9 Ma) (Cont.)												
1421	F11-1	272	492	1.808	-0.063	0.068	0.1032	0.0889	0.0101	1697	-0.8	1683
1421	F11-1	196	140	0.715	0.055	0.086	0.1032	0.0846	0.0098	1650	1.9	1682
1421	G11-7	347	297	0.857	0.023	0.062	0.1031	0.0860	0.0098	1651	1.8	1681
1421	F11-10	258	209	0.808	0.111	0.073	0.1031	0.0871	0.0101	1690	-0.5	1680
1421	G11-1	294	160	0.546	0.000	0.064	0.1028	0.0865	0.0069	1659	1.1	1677
1421	F2-5	135	209	1.553	0.068	0.092	0.1028	0.0849	0.0069	1657	1.1	1676
1421	F5-2	306	165	0.539	0.000	0.067	0.1027	0.0884	0.0101	1692	-1.1	1673
1421	G11-3	209	86	0.414	0.035	0.106	0.1025	0.0891	0.0102	1696	-1.6	1670
1421	F7-1	274	130	0.474	0.070	0.071	0.1025	0.0861	0.0100	1673	-0.3	1669
1421	E11-3	318	239	0.751	0.043	0.059	0.1024	0.0887	0.0104	1742	-4.5	1668
1421	F11-3	116	97	0.842	0.227	0.098	0.1021	0.0791	0.0100	1655	0.5	1663
1421	G11-2	284	163	0.574	0.245	0.062	0.1020	0.0868	0.0102	1688	-1.7	1661
1421	F10-1	281	113	0.402	0.029	0.067	0.1018	0.0888	0.0104	1717	-3.6	1657
1421	F2-1	316	695	2.200	0.090	0.070	0.1016	0.0841	0.0069	1630	1.4	1653
1421	F4-1	297	202	0.679	0.087	0.069	0.1012	0.0823	0.0100	1643	0.2	1646
1421	E11-1	303	188	0.621	0.070	0.062	0.1012	0.0852	0.0102	1685	-2.4	1645
1421	F5-1	227	84	0.372	0.116	0.073	0.1009	0.0829	0.0103	1685	-3.3	1641
1421	F3-1	274	130	0.475	0.807	0.072	0.1008	0.0817	0.0100	1641	-0.1	1639
1421	E11-4	167	165	0.987	0.503	0.073	0.1008	0.0830	0.0105	1714	-4.6	1639
1421	F5-1	235	210	0.895	0.230	0.077	0.1004	0.0871	0.0103	1685	-3.2	1632
Mixed ages												
1421	C2-2	941	38	0.040	-0.028	0.037	0.1509	0.1187	0.0096	2262	4.0	2356
1421	F1-6	230	107	0.464	0.024	0.052	0.1503	0.1166	0.0099	2320	1.3	2350
1421	G1-1	437	17	0.040	-0.012	0.041	0.1503	0.1183	0.0069	2331	0.7	2349
1421	G2-1	781	88	0.113	0.019	0.035	0.1477	0.1069	0.0100	2319	0.0	2319
1421	D3-5	134	65	0.488	0.000	0.058	0.1456	0.1148	0.0100	2302	-0.3	2295
1421	G3-2	295	77	0.259	0.122	0.048	0.1387	0.1006	0.0096	2126	3.9	2211
1421	F11-5	265	69	0.260	0.415	0.060	0.1371	0.1052	0.0096	2104	3.9	2191
1421	G2-2	450	191	0.424	0.000	0.045	0.1313	0.0984	0.0096	2035	3.8	2116
1421	G11-6	434	19	0.045	0.083	0.046	0.1313	0.0743	0.0095	2014	4.8	2115
1421	G3-1	229	71	0.310	0.026	0.056	0.1299	0.0983	0.0096	2020	3.7	2096
1421	F11-7	172	115	0.668	0.182	0.086	0.1143	0.0921	0.0100	1862	0.3	1868
1421	D5-1	256	91	0.357	-0.030	0.065	0.1109	0.0886	0.0095	1726	4.8	1813
Discordance >5%												
1421	C11-2	421	6	0.014	0.000	0.035	0.1534	0.1126	0.0107	2558	-7.3	2384
1421	G1-1	161	71	0.439	-0.091	0.081	0.1068	0.0869	0.0094	1640	6.1	1745
1421	G5-1	314	99	0.317	0.522	0.079	0.1416	0.0975	0.0094	2104	6.4	2247
1421	F2-4	186	308	1.655	-0.051	0.082	0.1090	0.0862	0.0092	1643	7.8	1783
1421	F4-2	142	145	1.021	0.000	0.091	0.1082	0.0857	0.0092	1625	8.2	1770
1421	G11-8	201	75	0.373	0.335	0.070	0.1148	0.0922	0.0090	1691	9.9	1876

Refer to Table 2 notes for definitions

Table 6. SHRIMP Analytical Results for Xenotime from Sample CSWA 206606b: Ankerite-Quartz Vein in Paulsens Gabbro (CSWA 206605)

Mount no.	Grain spot	U (ppm)	Th (ppm)	Th/U	$\frac{^{206}\text{Pb}}{^{208}\text{Pb}}$ (%)	$\frac{^{206}\text{Pb}}{^{208}\text{Pb}}$ ± 1σ	$\frac{^{207}\text{Pb}}{^{208}\text{Pb}}$ ± 1σ	$\frac{^{207}\text{Pb}}{^{206}\text{Pb}}$ ± 1σ	$\frac{^{207}\text{Pb}}{^{206}\text{Pb}}$ date (Ma) ± 1σ	Disc. %	$\frac{^{207}\text{Pb}}{^{206}\text{Pb}}$ date (Ma) ± 1σ
Carbonate vein emplacement (1655 ± 37 Ma)											
1421	L1-1	258	535	1.298	0.136	0.078	0.1034	0.0014	0.0931	0.0100	1689
1421	K1-1	387	624	1.613	0.204	0.067	0.1027	0.0012	0.0900	0.0102	1700
1421	J1-1	274	505	1.841	0.082	0.122	0.1009	0.0012	0.0856	0.0103	1690
1421	K2-1	550	1,354	2.465	0.133	0.061	0.1007	0.0009	0.0962	0.0102	1670
Old outlier											
1421	B1-1	328	266	0.811	0.033	0.042	0.1562	0.0010	0.1237	0.0100	2425
Discordance >5%											
1421	L1-1	190	258	1.356	0.398	0.637	0.1089	0.0019	0.0692	0.0088	1566
1421	L2-1	206	316	1.536	0.267	0.552	0.1048	0.0017	0.0837	0.0063	1599

Refer to Table 2 notes for definitions

Table 7. SHRIMP Analytical Results for Monazite from Sample CSWA 206902: Carbonaceous Phyllite

Mount no.	Grain spot	U (ppm)	Th (ppm)	Th/U	$\frac{^{206}\text{Pb}}{^{208}\text{Pb}}$ (%)	$\frac{^{206}\text{Pb}}{^{208}\text{Pb}}$ ± 1σ	$\frac{^{207}\text{Pb}}{^{208}\text{Pb}}$ ± 1σ	$\frac{^{207}\text{Pb}}{^{206}\text{Pb}}$ ± 1σ	$\frac{^{207}\text{Pb}}{^{206}\text{Pb}}$ date (Ma) ± 1σ	Disc. %	$\frac{^{207}\text{Pb}}{^{206}\text{Pb}}$ date (Ma) ± 1σ
Hydrothermal growth (2401 ± 14 Ma)											
1423	A1-3	312	6,326	20.266	0.303	0.051	0.1580	0.0029	0.1253	0.0037	2391
1423	B1-3	185	3,689	19.916	0.093	0.043	0.1562	0.0010	0.1275	0.0023	2425
1423	A1-2	284	9,519	33.469	0.503	0.050	0.1561	0.0015	0.1262	0.0037	2430
1423	A1-1	319	6,758	21.190	0.262	0.061	0.1539	0.0013	0.1223	0.0035	2348
1423	B1-1	186	4,584	24.657	0.231	0.043	0.1554	0.0011	0.1221	0.0022	2304
1423	A1-5	198	8,211	41.535	0.575	0.048	0.1543	0.0019	0.1218	0.0035	2411
1423	B1-2	126	2,015	15.943	0.333	0.040	0.1530	0.0014	0.1274	0.0023	2436
1423	B1-6	284	4,367	15.400	0.117	0.035	0.1529	0.0009	0.1202	0.0022	2316
Young outlier											
1423	A1-4	309	8,179	26.441	0.440	0.052	0.1470	0.0016	0.1260	0.0037	2234
Discordance >5%											
1423	B1-5	135	5,647	41.727	0.219	0.041	0.1570	0.0013	0.13716	0.00257	2557

Refer to Table 2 notes for definitions

1224

FIELDING ET AL.

Table 8. SHRIMP Analytical Results for Monazite from Sample CSWA 200606a: Altered Part of Paulsens Gabbro

Mount no.	Grain spot	U (ppm)	Th (ppm)	Th/U	f206 (%)	206/208Pb*	±1σ	206Pb*/208Pb*	±1σ	206Pb*/208Pb*	±1σ	206Pb*/208Pb*	±1σ	Disc. %	206Pb*/208Pb*	date (Ma)	±1σ
Hydrothermal growth (2308 ± 37 Ma)																	
1428	C.3-1	33	2865	87.213	0.018	2.072	0.036	0.1305	0.0028	0.1422	0.0042	2539	56	-3.6	2451	30	
1428	C.3-2	46	837	18.139	0.326	2.285	0.039	0.1363	0.0032	0.1345	0.0039	2340	51	3.1	2416	34	
1428	C.3-3	54	8224	151.026	0.536	2.074	0.035	0.1356	0.0035	0.1313	0.0038	2536	55	-5.3	2409	38	
1428	C.2-1	135	7631	56.653	0.926	2.163	0.036	0.1348	0.0022	0.1354	0.0024	2449	34	-2.1	2369	24	
1428	C.3-4	141	2825	20.029	1.354	2.444	0.085	0.1529	0.0036	0.1068	0.0034	2211	65	7.0	2379	40	
1428	E.1-1	42	14840	355.409	1.011	2.075	0.044	0.1366	0.0035	0.1405	0.0025	2536	45	-7.8	2353	40	
1428	L.1-1	55	2572	46.866	1.892	2.170	0.043	0.1473	0.0038	0.1339	0.0024	2443	40	-5.6	2315	45	
High common lead																	
1428	C.1-1	34	14,748	428.426	6.751	2.136	0.087	0.1755	0.0115	0.1255	0.0023	2476	83	5.2	2611	109	

Refer to Table 2 notes for definitions

Table 9. SHRIMP Analytical Results for Monazite Porphyroblasts from Sample CSWA 200912: Carbonaceous Phyllite

Mount no.	Grain spot	U (ppm)	Th (ppm)	Th/U	f206 (%)	206/208Pb*	±1σ	206Pb*/208Pb*	±1σ	206Pb*/208Pb*	±1σ	206Pb*/208Pb*	±1σ	Disc. %	206Pb*/208Pb*	date (Ma)	±1σ
Hydrothermal growth (1730 ± 28 Ma)																	
1423	D.2-8	91	5,158	56.550	0.813	2.973	0.074	0.1105	0.0028	0.0945	0.0015	1969	40	-3.4	1807	45	
1423	D.2-9	55	3,436	62.452	0.914	3.258	0.064	0.1089	0.0040	0.0888	0.0016	1726	30	3.1	1780	67	
1423	D.2-18	95	5,180	54.760	0.715	3.292	0.070	0.1083	0.0023	0.0822	0.0014	1710	32	3.4	1771	40	
1423	D.2-11	95	7,209	76.236	0.776	3.164	0.071	0.1076	0.0024	0.0915	0.0016	1771	35	-0.7	1759	40	
1423	D.2-14	90	6,653	74.521	0.631	3.245	0.073	0.1058	0.0020	0.0923	0.0017	1732	34	-0.1	1729	35	
1423	D.2-2	58	4,611	79.475	1.374	3.179	0.095	0.1058	0.0037	0.0960	0.0017	1763	46	-2.0	1728	63	
1423	D.2-16	52	5,435	104.306	1.223	3.413	0.067	0.1048	0.0036	0.0876	0.0015	1656	29	3.2	1711	63	
1423	D.2-13	92	3,753	41.001	0.896	3.193	0.054	0.1048	0.0022	0.0963	0.0018	1757	26	-2.7	1710	39	
1423	D.2-15	72	6,424	89.231	1.617	3.316	0.061	0.1032	0.0037	0.0934	0.0018	1699	27	-1.0	1682	66	
1423	D.2-4	72	6,536	90.289	1.556	3.363	0.065	0.1017	0.0037	0.0904	0.0016	1678	28	-1.4	1655	68	
1423	D.2-5	70	5,233	74.652	1.602	3.247	0.064	0.1010	0.0040	0.0902	0.0016	1731	30	-5.4	1642	73	
1423	D.2-17	62	5,158	83.571	1.335	3.436	0.065	0.0992	0.0034	0.0988	0.0016	1647	27	-2.3	1609	64	
Discordance >5%																	
1423	D.1-5	81	5,703	70.289	0.855	3.316	0.062	0.1144	0.0051	0.0830	0.0016	1699	28	9.1	1870	81	
1423	D.2-6	53	4,884	91.841	1.263	3.565	0.078	0.1048	0.0045	0.0821	0.0015	1594	31	6.8	1710	79	
1423	E.1-1	86	7,073	82.411	1.349	3.029	0.032	0.1029	0.0027	0.0851	0.0018	1839	28	-9.7	1677	49	
1423	D.2-12	106	9,809	92.164	1.418	3.124	0.032	0.1021	0.0026	0.0848	0.0015	1790	26	-7.7	1662	48	
1423	D.1-2	70	13,963	193.008	0.928	2.462	0.049	0.1085	0.0030	0.0849	0.0016	2197	37	-23.8	1775	51	
1423	D.1-4	76	6,706	87.890	1.534	2.385	0.064	0.1068	0.0036	0.0900	0.0016	1890	51	-29.2	1746	62	
1423	D.2-19	74	6,424	87.366	1.584	2.936	0.081	0.1039	0.0036	0.0913	0.0016	1890	45	-11.5	1695	64	
1423	D.2-1	71	4,659	65.900	1.603	2.959	0.075	0.1038	0.0034	0.0951	0.0018	1877	41	-10.9	1693	60	
1423	D.2-7	83	7,886	88.725	1.105	2.874	0.072	0.1013	0.0028	0.0841	0.0015	1925	42	-16.8	1649	51	
1423	D.1-1	117	8,491	72.653	1.623	3.135	0.140	0.0966	0.0040	0.0829	0.0015	1755	69	-14.5	1559	78	

Refer to Table 2 notes for definitions

IN SITU SHRIMP GEOCHRONOLOGY, PAULSENS MINE, SOUTHERN PILBARA CRATON

1225

Table 10. SHRIMP Analytical Results for Matrix Monazite from Samples CSWA 219513 and 219517; Carbonaceous Phyllite

Mount no.	Grain spot	U (ppm)	Th (ppm)	Th/U	$\frac{^{206}\text{Pb}}{^{238}\text{Pb}}$ (%)	$\frac{^{206}\text{Pb}}{^{238}\text{Pb}}$ ± 1σ	$\frac{^{207}\text{Pb}}{^{235}\text{Pb}}$ ± 1σ	$\frac{^{207}\text{Pb}}{^{235}\text{Pb}}$ ± 1σ	$\frac{^{207}\text{Pb}}{^{235}\text{Pb}}$ ± 1σ	Disc. %	$\frac{^{207}\text{Pb}}{^{235}\text{Pb}}$ date (Ma)	$\frac{^{207}\text{Pb}}{^{235}\text{Pb}}$ ± 1σ
Hydrothermal alteration (2403 ± 38 Ma)												
I502	F1-1	103	1.286	12.537	0.414	2.201	0.079	0.1583	0.0073	0.1307	2415	72
I502	D1-3	81	5.282	65.540	0.264	2.160	0.067	0.1582	0.0070	0.1331	2451	63
I502	F1-2	122	3.851	31.509	0.477	2.160	0.056	0.1581	0.0060	0.1334	2453	53
I502	D2-1	88	126	1.433	0.258	2.121	0.065	0.1555	0.0056	0.1471	2490	63
I502	D1-2	134	1.568	11.729	0.229	2.149	0.054	0.1551	0.0042	0.1322	2463	51
I502	D1-4	120	1.194	9.974	0.715	2.205	0.055	0.1497	0.0045	0.1291	2411	50
I502	D1-5	87	1.719	19.643	0.388	2.138	0.035	0.1555	0.0036	0.1321	2474	33
I502	D1-6	103	1.477	14.336	0.219	2.201	0.037	0.1576	0.0080	0.1250	2414	34
I502	D1-7	32	654	20.756	0.928	2.188	0.171	0.1528	0.0067	0.1284	2426	156
Discordance >5% or high common lead												
I502	G1-1	29	2.436	83.610	1.958	2.439	0.103	0.1518	0.0247	0.1138	2215	79
I502	A1-1	33	1.241	37.344	2.141	2.235	0.084	0.1587	0.0206	0.1260	2384	75
I502	G1-2	58	972	16.816	2.702	2.176	0.068	0.1482	0.0126	0.1348	2438	63
I502	A2-1	13	745	55.889	6.606	3.261	0.275	0.1066	0.0676	0.0939	2042	126
I502	D2-2	122	592	4.869	0.013	2.026	0.051	0.1588	0.0047	0.1406	2586	54
I502	G2-1	102	647	6.357	0.022	2.024	0.056	0.1563	0.0077	0.1332	2588	58
I502	D1-1	143	3.152	22.117	0.443	2.138	0.068	0.1405	0.0044	0.1310	2473	65

Refer to Table 2 notes for definitions

Table 11. SHRIMP Analytical Results for Monazite Porphyroblasts from Samples CSWA 215912 and 219513; Carbonaceous Phyllite

Mount no.	Grain spot	U (ppm)	Th (ppm)	Th/U	$\frac{^{206}\text{Pb}}{^{238}\text{Pb}}$ (%)	$\frac{^{206}\text{Pb}}{^{238}\text{Pb}}$ ± 1σ	$\frac{^{207}\text{Pb}}{^{235}\text{Pb}}$ ± 1σ	$\frac{^{207}\text{Pb}}{^{235}\text{Pb}}$ ± 1σ	$\frac{^{207}\text{Pb}}{^{235}\text{Pb}}$ ± 1σ	Disc. %	$\frac{^{207}\text{Pb}}{^{235}\text{Pb}}$ date (Ma)	$\frac{^{207}\text{Pb}}{^{235}\text{Pb}}$ ± 1σ
Hydrothermal alteration (1721 ± 32 Ma)												
I502	B1-5	172	4.760	27.625	0.382	3.285	0.050	0.1080	0.0021	0.0895	1713	23
I502	B1-7	250	2.089	8.349	0.603	3.182	0.059	0.1062	0.0020	0.0950	1761	29
I502	E1-1	256	377	1.476	0.049	3.076	0.075	0.1057	0.0038	0.0954	1814	38
I502	B1-5	226	4.319	19.141	0.931	3.281	0.057	0.1045	0.0025	0.0933	1715	26
I502	E1-3	187	655	3.506	0.386	3.138	0.121	0.1044	0.0031	0.1113	1783	60
I502	C1-2	1,209	2,930	2.424	0.169	3.334	0.127	0.1043	0.0020	0.0878	1691	56
I502	E1-4	280	8,946	31.938	0.668	3.264	0.088	0.1021	0.0030	0.0896	1723	41
Discordance >5% or high common lead												
I502	B1-5	168	22,578	134.605	4.952	2.919	0.078	0.1153	0.0119	0.0889	1899	44
I502	E1-2	368	3,681	9.994	0.024	3.000	0.077	0.1069	0.0028	0.0948	1855	41
I502	C1-3	346	2,068	5.974	0.507	3.630	0.179	0.1055	0.0035	0.0872	1568	68
I502	B1-1	311	2,049	6.600	0.626	3.110	0.075	0.1021	0.0032	0.0960	1797	38
I502	C1-1	323	11,900	36,550	0.470	3.080	0.122	0.1011	0.0040	0.1015	1813	63
I502	B1-6	285	5,926	20.811	0.560	3.160	0.045	0.1010	0.0018	0.0813	1773	22
I502	B1-4	244	8,919	36,573	2.006	3.021	0.076	0.0995	0.0053	0.0958	1843	40
I502	B1-2	172	827	4.812	1.698	3.187	0.106	0.0974	0.0057	0.0914	1759	51

Refer to Table 2 notes for definitions

1226

FIELDING ET AL.

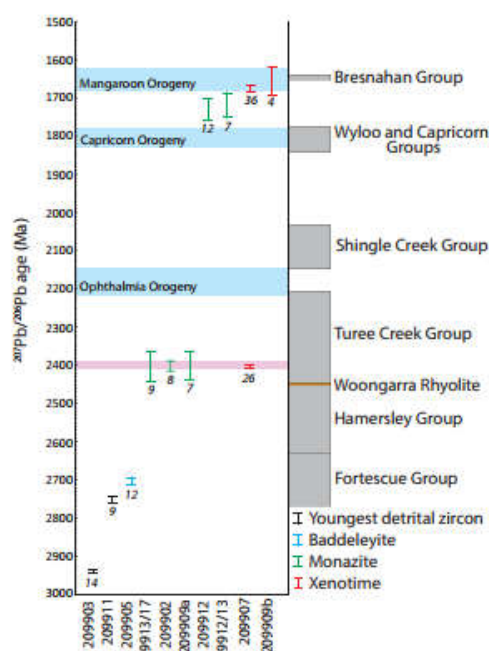


Fig. 11. Summary diagram for all samples dated in this study. Known orogenic events are highlighted, showing that mineralization at Paulsens is not associated with either the Ophthalmia Orogeny or the Capricorn Orogeny. A proposed cryptic orogenic event at ca. 2400 Ma is highlighted in pink. Depositional age ranges for sedimentary basins are indicated by gray boxes, and felsic volcanic rocks as orange. The number of analyses in each sample is marked next to the 95% error bars.

Timing of hydrothermal activity and gold mineralization

Euhedral xenotime within and interlocking with pyrite grains is dated at 2403 ± 5 Ma (GSWA 209907, Fig. 9C), providing a direct crystallization age for the auriferous quartz-sulfide veins at the Gabbro Offset deposit, which are peripheral to the main Paulsens lode. Additionally, hydrothermal monazite within a pervasively altered part of the Paulsens gabbro (2398 ± 37 Ma; GSWA 209909a) and in the altered wall-rock margins to quartz-sulfide veins at Paulsens East (2403 ± 38 Ma; GSWA 219513 and 219517) also records a period of regional- to local-scale hydrothermal activity associated with the emplacement of auriferous quartz-sulfide veins at ca. 2400 Ma. Within the main quartz-sulfide vein at Gabbro Offset, xenotime crystals were also dated at 1680 ± 9 Ma. These grains only occur within the quartz matrix or at the margins of brecciated sulfide grains, suggesting that this date represents a second period of hydrothermal alteration during which ca. 2400 Ma xenotime grains underwent dissolution and reprecipitation.

Gold mineralization at Gabbro Offset is present in two distinct forms: (1) as rounded inclusions within euhedral pyrite grains (Fig. 6A) and (2) as free gold located along cracks and fractures of brecciated pyrite grains (Fig. 6B). Because the euhedral pyrite is intergrown with and contains euhedral grains of xenotime dated at ca. 2400 Ma, the rounded, primary gold inclusions in this pyrite are also interpreted to

Table 12. Summary of Geochronology Results

GSWA sample no.	Deposit	Target mineral	Grain textures	$^{207}\text{Pb}/^{206}\text{Pb}$ date (Ma)	$\pm 2\sigma$	Number of analyses	MSWD	Interpretation
209903	Gabbro Offset	Zircon	Detrital	2941	5	15	1.4	Youngest detrital component
209911	Gabbro Offset	Zircon	Detrital	2750	10	9	1.5	Youngest detrital component
209905	Gabbro Offset	Baddeleyite	Migmatite	2701	11	12	1.4	Gabbro crystallization
209907	Gabbro Offset	Xenotime	Euhedral/cores	2403	5	26	1.1	Growth during hydrothermal alteration associated with vein emplacement
209907	Gabbro Offset	Xenotime	Matrix/rims	1680	9	36	1.4	Dissolution and reprecipitation of xenotime during hydrothermal activity
209909b	Gabbro Offset	Xenotime	Matrix	1655	37	4	1.3	Carbonate vein emplacement
209902	Gabbro Offset	Monazite	Matrix	2401	14	8	1.5	Growth during hydrothermal alteration
209909a	Gabbro Offset	Monazite	Matrix	2398	37	7	1.4	Growth during hydrothermal alteration
209912	Gabbro Offset	Monazite	Porphyroblasts	1730	26	12	1.1	Growth during hydrothermal alteration
219512 / 219513	Paulsens East	Monazite	Porphyroblasts	1721	32	7	0.6	Growth during hydrothermal alteration
219513 / 219517	Paulsens East	Monazite	Matrix	2403	38	9	0.4	Alteration associated with vein emplacement

MSWD = mean square of weighted deviates.

have formed at this time. However, where the pyrite is locally fractured or brecciated, containing flakes of free gold (Fig. 6B), chalcopyrite, and pyrrhotite, xenotime in the matrix and along pyrite grain boundaries has undergone dissolution and reprecipitation reactions at ca. 1680 Ma. This suggests that these rocks were subjected to a secondary hydrothermal event responsible for the brittle deformation of pyrite grains, xenotime dissolution, and reprecipitation, and either the local remobilization (Fig. 6C) or introduction of new gold, or both, at ca. 1680 Ma. Additionally, xenotime from ankerite-quartz veins emplaced within the Paulsens gabbro, which are associated with up to 48 ppm Au, has been dated at 1655 ± 37 Ma (GSWA 209909b). This indicates that this second hydrothermal event was also responsible for the emplacement of gold-bearing ankerite-quartz veins. A study on the mineralogy and chemistry of gold at the main Paulsens lode indicates that the youngest phase of gold mineralization is also associated with free gold with elevated Hg and Ag which formed in pyrite fractures and along stylolites (Hancock and Thorne, 2016), indicating a commonality between the youngest gold mineralizing event at the main Paulsens lode and the secondary event at the Gabbro Offset deposit.

Relationships to regional orogenic events

Our in situ dating of monazite and xenotime at the Paulsens deposit has identified three discrete hydrothermal events at ca. 2400, 1730, and 1680 Ma. The first hydrothermal event at ca. 2400 Ma is marked by the emplacement of auriferous quartz-sulfide veins at Gabbro Offset and Paulsens East, resulting in pervasive alteration of gabbroic and phyllitic host rocks as well as the growth of monazite within carbonaceous phyllites, either as primary porphyroblasts or as pseudomorphs of former metamorphic porphyroblasts. The timing of the mineralizing hydrothermal event (ca. 2400 Ma) does not correlate with any known hydrothermal or deformational event in the northern Capricorn Orogen. However, cryptic events, including the growth of monazite in phyllitic rocks across the Pilbara region from Whim Creek in the north to Mt. Tom Price in the south (Rasmussen et al., 2005) and resetting of high-U zircon in tuffaceous mudstones of the Hamersley Group (Pickard, 2002), are recorded between ca. 2430 and 2399 Ma. The age of monazite growth decreases progressively southward (Rasmussen et al., 2005) and the data presented here are within uncertainty of monazite growth at 2399 ± 6 Ma at Mt. Tom Price, located 150 km to the east of the Paulsens deposit (Rasmussen et al., 2005).

In the Pilbara region, the cause of this cryptic event is currently unknown, but indirect evidence for a tectonic event at ca. 2400 Ma is present in the stratigraphic record of Proterozoic sedimentary rocks along the southern Pilbara margin. A study of detrital zircons from the matrix of the Meteorite Bore Member of the Kungarra Formation in the 2445 to 2208 Ma Turee Creek Group indicates that they were sourced, together with abundant rhyolite clasts, from the 2449 to 2445 Ma Woongarra Rhyolite (Blake and Barley, 1992; Takahara et al., 2010; Simonson et al., 2014). In the Hardey syncline, from where the samples were taken, the Woongarra Rhyolite is situated 1,500 m stratigraphically below the Meteorite Bore Member, implying at least 500 to 1,000 m of uplift and erosion of sedimentary rocks along the southern Pilbara margin between ca. 2445 and 2208 Ma (Takahara et al., 2010). Our

data show that this event was associated with the emplacement of quartz-sulfide veins during extensive hydrothermal activity and gold mineralization at Paulsens (Fig. 11).

The second hydrothermal event is marked by the growth of monazite within carbonaceous phyllites of the Hardey Formation at 1730 ± 27 and 1721 ± 32 Ma. It is unclear if the monazite in these samples grew during low-grade metamorphism and deformation associated with fault reactivation (GSWA 209912 is located in a D_2/D_3 shear zone at the Gabbro Offset deposit) or if it has locally altered former regional-scale peak metamorphic porphyroblasts during subsequent hydrothermal activity. However, we note that this event is within uncertainty of dextral strike-slip faulting and hydrothermal gold mineralization at the Mt. Olympus deposit, dated at 1738 ± 5 Ma (Young et al., 2003; Şener et al., 2005), about 150 km to the southeast of Paulsens.

The youngest hydrothermal event is recorded at the Gabbro Offset deposit by the dissolution and reprecipitation of xenotime rims, dated at 1680 ± 9 Ma, on older ca. 2400 Ma xenotime cores within the quartz matrix of the auriferous quartz-sulfide vein, and by xenotime grains, dated at 1655 ± 37 Ma, within discrete ankerite-quartz veins. This hydrothermal event appears to have been responsible for the local brecciation and fracturing of pyrite grains in the quartz-sulfide vein and for the local remobilization of gold (Fig. 6C). However, it is possible that this event was also responsible for the introduction of new gold precipitated as free gold in pyrite fractures and within stylolites at the main Paulsens lode (Hancock and Thorne, 2016). This event is coincident with medium- to high-grade metamorphism, deformation, and magmatism during the 1680 to 1620 Ma Mangaroon Orogeny (Sheppard et al., 2005), which affected rocks of the Gascoyne Province farther south. Rasmussen et al. (2007a) also noted hydrothermal monazite growth at ca. 1650 Ma in the Soansville Group in the Pilbara craton and attributed it to reactivation along preexisting N- to NE-trending, craton-scale structures that acted as conduits for hydrothermal fluid flow during the Mangaroon Orogeny. Rasmussen et al. (2007b) also documented the presence of ca. 1670 Ma hydrothermal xenotime at the Mt. Tom Price iron ore mine. The structural effect of this event at Paulsens is not known, but may have resulted in the reactivation of preexisting faults, such as the Nanjilgardy and Hardey faults.

Importantly, we find no evidence for hydrothermal activity related to either the 2215 to 2145 Ma Ophthalmia Orogeny or the 1820 to 1770 Ma Capricorn Orogeny. This is surprising because these events played a significant role in the tectonic evolution of the region elsewhere in the southern Pilbara craton and northern Capricorn Orogen (Young et al., 2003; Rasmussen et al., 2005, 2006; Şener et al., 2005; Thorne et al., 2011).

Conclusions

Our results reveal a significantly different and more complicated low-temperature tectonothermal evolution for the southern Pilbara region than had been thought. Previous studies (e.g., Thorne and Seymour, 1991) suggested that gold mineralization in the Wyloo Inlier is associated with post-Wyloo Group quartz veins, linking the timing of orogenic gold mineralization to the 1820 to 1770 Ma Capricorn Orogeny. Results from this study show that two gold mineralizing events occurred at

Paulsens. Primary gold mineralization at Paulsens was much older, occurring at ca. 2400 Ma, and does not correlate with a known orogenic event in the northern Capricorn Orogen. However, uplift, erosion, and hydrothermal activity throughout the Pilbara craton may reflect a previously unrecognized orogenic event at ca. 2400 Ma. The second gold event, at ca. 1680 Ma, may be linked to reactivation of the Hardey fault, which forms a splay off the lithospheric-scale Nanjilgardy fault (Fig. 1).

Recognition of a new orogenic event has important implications for exploration targeting of orogenic gold deposits in the northern Capricorn Orogen. Previously, rocks affected by the Capricorn Orogeny, up to and including the Ashburton Formation, were considered the most prospective for orogenic gold mineralization similar to that at Paulsens. However, we have demonstrated that the primary mineralization at Paulsens, which shares many of the characteristics of orogenic gold deposits, occurred at ca. 2400 Ma, about 570 million years prior to deposition of Wyloo Group sedimentary rocks. Therefore, older rocks of the Fortescue and Hamersley groups are more likely candidates to host significant gold mineralization similar to that at Paulsens. The second gold event occurring at ca. 1680 Ma is possibly related to the reactivation of major lithospheric fault structures and their splays. This event, at least locally, caused the remobilization of preexisting gold, but may also have been responsible for the introduction of new gold along these mantle-tapping structures. Nevertheless, the age constraints for mineralization at Paulsens differ from those proposed by Young et al. (2003) and Şener et al. (2005) for the timing of gold mineralization at Mount Olympus (1738 ± 5 Ma) in the Wyloo Group, suggesting the potential for several different gold mineralizing events across the northern Capricorn Orogen associated with major structures such as the Nanjilgardy fault.

For exploration of orogenic gold, it is critical to have an understanding of the distribution of mineralization through both space and time. In situ geochronology of monazite and xenotime has important implications for exploration targeting by providing absolute ages for orogenic gold mineralization and allowing mineralization to be linked to specific orogenic events. In turn, this allows explorers to minimize their exploration search area by targeting the most prospective tectono-thermal events and host stratigraphy.

Acknowledgments

This research is part of a Ph.D. project by I. Fielding, funded through an ARC Linkage grant (LP130100922), an industry scholarship by Northern Star Resources (NSR), and the WA Government Exploration Incentive Scheme. Geochronology was carried out using a SHRIMP II ion microprobe at the John de Laeter Centre at Curtin University. SPJ and MTDW publish with permission of the director of the Geological Survey of Western Australia. We thank NSR for samples and for permission to publish, and A. White, D. Huston, and an anonymous reviewer for their helpful comments.

REFERENCES

- Blake, T.S., 1993, Archean and Early Proterozoic geology of the Pilbara region, Western Australia: Late Archean crustal extension, sedimentary basin formation, flood basalt volcanism and continental rifting: The Nulagine and Mount Jope supersequences, Western Australia: *Precambrian Research*, v. 60, p. 185–241.
- Blake, T.S., and Barley, M.E., 1992, Tectonic evolution of the Late Archean to Early Proterozoic Mount Bruce megasequence set, Western Australia: *Tectonics*, v. 11, p. 1415–1425.
- Blight, D.F., 1985, Economic potential of the lower Fortescue Group and adjacent units in the southern Hamersley Basin: A study of depositional environments: Geological Survey of Western Australia, Report 13, p. 32.
- Carpenter, R.L., Duke, N.A., Sandeman, H.A., and Stern, R., 2005, Relative and absolute timing of gold mineralization along the Meliadine trend, Nunavut, Canada: Evidence for Paleoproterozoic gold hosted in an Archean greenstone belt: *Economic Geology*, v. 100, p. 567–576.
- Cawood, P.A., and Tyler, I.M., 2004, Assembling and reactivating the Proterozoic Capricorn orogen: Lithotectonic elements, orogenies, and significance: *Precambrian Research*, v. 128, p. 201–218.
- Cherniak, D.J., 2010, Diffusion in accessory minerals: Zircon, titanite, apatite, monazite and xenotime: *Reviews in Mineralogy and Geochemistry*, v. 72, p. 827–869.
- Chesley, J.T., 1999, Integrative geochronology of ore deposits: New insights into the duration and timing of hydrothermal circulation: *Reviews in Economic Geology*, v. 12, p. 115–142.
- Fielding, I., and Stokes, L., 2014, Gabbro offset drilling, Ashburton Basin, Pilbara – Western Australia, M08/196, exploration incentive scheme final report: Geological Survey of Western Australia Open-File Report, p. 13.
- Finger, F., Broska, I., Roberts, M.P., and Schermaier, A., 1998, Replacement of primary monazite by apatite-allanite-epidote coronas in an amphibolite facies granite gneiss from the eastern Alps: *American Mineralogist*, v. 83, p. 248–258.
- Fletcher, I.R., McNaughton, N.J., Aleinikoff, J.A., Rasmussen, B., and Kamo, S.L., 2004, Improved calibration procedures and new standards for U-Pb and Th-Pb dating of Phanerozoic xenotime by ion microprobe: *Chemical Geology*, v. 209, p. 295–314.
- Fletcher, I.R., McNaughton, N.J., Davis, W.J., and Rasmussen, B., 2010, Matrix effects and calibration limitations in ion probe U-Pb and Th-Pb dating of monazite: *Chemical Geology*, v. 270, p. 31–44.
- Forman, F.G., 1938, The Melrose and Belvedere gold mines and vicinity, Mt Stewart Station, Ashburton Goldfields: Geological Survey of Western Australia, Annual Report 1937, p. 62–63.
- Goldfarb, R.J., and Groves, D.I., 2015, Orogenic gold: Common or evolving fluid and metal sources through time: *Lithos*, v. 233, p. 2–26.
- Goldfarb, R.J., Groves, D.I., and Gardoll, S., 2001, Orogenic gold and geologic time: A global synthesis: *Ore Geology Reviews*, v. 18, p. 1–75.
- Groves, D.I., Goldfarb, R.J., Gebre-Mariam, M., Hagemann, S.G., and Robert, F., 1998, Orogenic gold deposits: A proposed classification in the context of their crustal distribution and relationship to other gold deposit types: *Ore Geology Reviews*, v. 13, p. 7–27.
- Hancock, E.A., and Thorne, A.M., 2016, Mineralogy of gold from the Paulsens and Mount Olympus deposits, northern Capricorn orogen: Geological Survey of Western Australia, Record 2016/14, p. 16.
- Harrison, T.M., Catlos, E.J., and Montel, J.M., 2002, U-Th-Pb dating of phosphate minerals: Reviews in Mineralogy and Geochemistry, v. 48, p. 524–558.
- Heaman, L.M., and LeCheminant, A.N., 1993, Geochemistry of accessory minerals paragenesis and U-Pb systematics of baddeleyite (ZrO₂): *Chemical Geology*, v. 110, p. 95–126.
- Hronsky, J.M.A., and Groves, D.I., 2008, Science of targeting: Definition, strategies, targeting and performance measurement: *Australian Journal of Earth Sciences*, v. 55, p. 3–12.
- Hronsky, J.M., Groves, D.I., Loucks, R.R., and Begg, G.C., 2012, A unified model for gold mineralisation in accretionary orogens and implications for regional-scale exploration targeting methods: *Mineralium Deposita*, v. 47, p. 339–358.
- Johnson, S.P., Sheppard, S., Rasmussen, B., Wingate, M.T.D., Kirkland, C.L., Muhliling, J.R., Fletcher, I.R., and Belousova, E.A., 2011, Two collisions, two sutures: Punctuated pre-1950 Ma assembly of the West Australian craton during the Ophthalman and Glenburgh orogenies: *Precambrian Research*, v. 189, p. 239–262.
- Johnson, S.P., Thorne, A.M., Tyler, I.M., Korsch, R.J., Kennett, B.L.N., Cutten, H.N., Goodwin, J., Blay, O., Blewett, R.S., Joly, A., Dentith, M.C., Aitken, A.R.A., Holzschuh, J., Salmon, M., Reading, A., Heinsohn, G., Boren, G., Ross, J., Costelloe, R.D., and Fomin, T., 2013, Crustal architecture of the Capricorn Orogen, Western Australia and associated metallogeny: *Australian Journal of Earth Sciences*, v. 60, p. 681–705.
- Kerrich, R., and Cassidy, K.F., 1994, Temporal relationships of lode gold mineralization to accretion, magmatism, metamorphism and deformation—Archean to present: A review: *Ore Geology Reviews*, v. 9, p. 263–310.

- Korhonen, F.J., Johnson, S.P., Rasmussen, B., Sheppard, S., Muhling, J.R., Dunkley, D.J., Wingate, M.T.D., Fletcher, I.R., and Roberts, M.P., 2017, Circum-Yilgarn orogenesis: P-T-t constraints and implications from the Capricorn Orogen, Western Australia: *Journal of Metamorphic Geology*, in press, doi: 10.1111/jmg.12249.
- Ludwig, K.R., 2003, Isoplot/Ex version 3.00, a geochronological toolkit for Microsoft Excel: Berkeley Geochronology Centre Special Publication, no. 4, 73 p.
- 2009, Squid 2.50, a user's manual: Berkeley, California, USA, Berkeley Geochronology Centre, 95 p.
- Martin, D.M., and Morris, P.A., 2010, Tectonic setting and regional implications of ca. 2.2 Ga mafic magmatism in the southern Hamersley Province, Western Australia: *Australian Journal of Earth Sciences*, v. 57, p. 911–931.
- Martin, D.M., and Thorne, A.M., 2004, Tectonic setting and basin evolution of the Bangemall Supergroup in the northwestern Capricorn orogen: *Precambrian Research*, v. 128, p. 385–409.
- Northern Star Resources Limited, 2015a, Northern Star Resources Limited 2015 annual report: <http://www.nsrld.com/wp-content/uploads/2015/08/NSR-Annual-Report-2015-26-8-2015-new-cover1.pdf>, 76 p.
- 2015b, Northern Star Paulsens operations fact sheet: <http://www.nsrld.com/wp-content/uploads/2015/08/NSR-Paulsens-Operations-Fact-Sheet-July-2015-FINAL.pdf>, 5 p.
- 2016, Resources and reserves: <http://www.nsrld.com/our-assets/resources-and-reserves/>.
- Occhipinti, S.A., Sheppard, S., Passchier, C., Tyler, I.M., and Nelson, D.R., 2004, Palaeoproterozoic crustal accretion and collision in the southern Capricorn orogen: The Glenburgh orogeny: *Precambrian Research*, v. 128, p. 237–255.
- Owen, S., 2000, Ashburton project, Paulsens E08/665, E08/906, M08/99 and M08/196, annual report to the Department of Minerals and Energy for the period 15 November 1999 to 14 November 2000, Taipan Resources N.L.: Geological Survey of Western Australia, Open-File Report, p. 39.
- Pickard, A.L., 2002, SHRIMP U-Pb zircon ages of tuffaceous mudrocks in the Brockman iron formation of the Hamersley Range, Western Australia: *Australian Journal of Earth Sciences*, v. 49, p. 491–507.
- Rasmussen, B., and Muhling, J.R., 2007, Monazite begets monazite: Evidence for dissolution of detrital monazite and reprecipitation of syntectonic monazite during low-grade regional metamorphism: *Contributions to Mineralogy and Petrology*, v. 154, p. 675–689.
- 2009, Reactions destroying detrital monazite in greenschist-facies sandstones from the Witwatersrand basin, South Africa: *Chemical Geology*, v. 264, p. 311–327.
- Rasmussen, B., Fletcher, I.R., and Sheppard, S., 2005, Isotopic dating of the migration of a low-grade metamorphic front during orogenesis: *Geology*, v. 33, p. 773–776.
- Rasmussen, B., Sheppard, S., and Fletcher, I.R., 2006, Testing ore deposit models using in situ U-Pb geochronology of hydrothermal monazite: Palaeoproterozoic gold mineralization in northern Australia: *Geology*, v. 34, p. 77–80.
- Rasmussen, B., Fletcher, I.R., and Muhling, J.R., 2007a, In situ U-Pb dating and element mapping of three generations of monazite: Unravelling cryptic tectonothermal events in low-grade terranes: *Geochimica et Cosmochimica Acta*, v. 71, p. 670–690.
- Rasmussen, B., Fletcher, I.R., Muhling, J.R., Thorne, W.S., and Broadbent, G.C., 2007b, Prolonged history of episodic fluid flow in giant hematite ore bodies: Evidence from in situ U-Pb geochronology of hydrothermal xenotime: *Earth and Planetary Science Letters*, v. 258, p. 249–259.
- Şener, A.K., Young, C., Groves, D.L., Krapez, B., and Fletcher, I.R., 2005, Major orogenic gold episode associated with Cordilleran-style tectonics related to the assembly of Palaeoproterozoic Australia?: *Geology*, v. 33, p. 225–228.
- Sheppard, S., Occhipinti, S.A., and Nelson, D.R., 2005, Intracontinental reworking in the Capricorn orogen, Western Australia: The 1690–1620 Ma Mangaroon orogeny: *Australian Journal of Earth Sciences*, v. 52, p. 443–460.
- Sheppard, S., Rasmussen, B., Muhling, J.R., Farrell, T.R., and Fletcher, I.R., 2007, Grenvillian-aged orogenesis in the Palaeoproterozoic Gascoyne Complex, Western Australia: 1030–950 Ma reworking of the Proterozoic Capricorn orogen: *Journal of Metamorphic Geology*, v. 25, p. 477–494.
- Sheppard, S., Bodorkos, S., Johnson, S.P., Wingate, M.T.D., and Kirkland, C.L., 2010, The Palaeoproterozoic Capricorn orogeny: Intracontinental reworking not continent-continent collision: Geological Survey of Western Australia, Report 108, p. 33.
- Sillitoe, R.H., 1997, Characteristics and controls of the largest porphyry copper-gold and epithermal gold deposits in the circum-Pacific region: *Australian Journal of Earth Sciences*, v. 44, p. 373–388.
- Simonson, B.M., O'Brien, M., Buchwaldt, R., Bowring, S.A., Hassler, S.W., and Beukes, N.J., 2014, New geochronological data from the Boolgeeda BIF and Woongarra Rhyolite, Hamersley Group (Western Australia): Geological Society of America, Annual Meeting, Vancouver, British Columbia, 2014, Proceedings, 1 p.
- Stacey, J.S., and Kramers, J.D., 1975, Approximation of terrestrial lead isotope evolution by a two-stage model: *Earth and Planetary Science Letters*, v. 26, p. 207–221.
- Stern, R.A., 2001, New isotopic and trace-element standard for the ion microprobe: Preliminary thermal ionization mass spectrometry (TIMS) U-Pb and electron microprobe data: Geological Survey of Canada, Radiogenic Age and Isotopic Studies, Report 14, Current Research 2001-F1, p. 7.
- Stern, R.A., and Rayner, N., 2003, Ages of several xenotime megacrysts by ID-TIMS: Potential reference materials for ion microprobe U-Pb geochronology: Geological Survey of Canada, Radiogenic Age and Isotopic Studies, Report 16, Current Research 2003-F1, p. 7.
- Stern, R.A., Bodorkos, S., Kamo, S.L., Hickman, A.H., and Corfu, F., 2009, Measurement of SIMS instrumental mass fractionation of Pb isotopes during zircon dating: *Geostandards and Geoanalytical Research*, v. 33, p. 145–168.
- Takahara, M., Komuro, M., Kiyokawa, S., Horie, K., and Yokoyama, K., 2010, Detrital zircon SHRIMP U-Pb age of the 2.3 Ga diamictites of the Meteorite Bore Member in the south Pilbara, Western Australia [abs.]: Geological Survey of Western Australia, Fifth International Archean Symposium, Perth, Western Australia, 2010, Abstracts, Record 2010/18, p. 223–224.
- Thorne, A.M., and Seymour, D.B., 1991, Geology of the Ashburton basin, Western Australia: Geological Survey of Western Australia, Bulletin 139, 162 p.
- Thorne, A.M., and Trendall, A.F., 2001, Geology of the Fortescue Group, Pilbara craton, Western Australia: Geological Survey of Western Australia, Bulletin 144, 266 p.
- Thorne, A.M., Johnson, S.P., Tyler, I.M., Cutten, H.N., and Blay, O., 2011, Geology of the northern Capricorn orogen, in Johnson, S.P., Thorne, A.M., and Tyler, I.M., eds., Capricorn orogen seismic and magnetotelluric (MT) workshop 2011: Perth, WA, Geological Survey of Western Australia, p. 12.
- Townsend, K.J., Miller, C.F., D'Andrea, J.L., Ayers, J.C., Harrison, T.M., and Coath, C.D., 2000, Low temperature replacement of monazite in the Ireteba granite, southern Nevada: Geochronological implications: *Chemical Geology*, v. 172, p. 95–112.
- Trendall, A.F., Compston, W., Nelson, D.R., De Laeter, J.R., and Bennett, V.C., 2004, SHRIMP zircon ages constraining the depositional chronology of the Hamersley Group, Western Australia: *Australian Journal of Earth Sciences*, v. 51, p. 621–644.
- Tyler, I.M., 1991, The geology of the Sylvania Inlier and the southeast Hamersley basin: Geological Survey of Western Australia, Bulletin 138, 124 p.
- Tyler, I.M., and Thorne, A.M., 1990, The northern margin of the Capricorn orogen, Western Australia—an example of an Early Proterozoic collision zone: *Journal of Structural Geology*, v. 12, p. 685–701.
- Vielreicher, N., Groves, D., Fletcher, I., McNaughton, N., and Rasmussen, B., 2003, Hydrothermal monazite and xenotime geochronology: A new direction for precise dating of orogenic gold mineralization: *Society of Economic Geologists Newsletter*, no. 53, p. 1, 10–16.
- White, A.J.R., Smith, R.E., Nadoll, P., and Legras, M., 2014a, Regional-scale metasomatism in the Fortescue Group volcanics, Hamersley basin, Western Australia: Implications for hydrothermal ore systems: *Journal of Petrology*, v. 55, p. 977–1009.
- White, A., Burgess, R., Charnley, N., Selby, D., Whitehouse, M., Robb, L., and Waters, D., 2014b, Constraints on the timing of late-Eburnean metamorphism, gold mineralisation and regional exhumation at Damang mine, Ghana: *Precambrian Research*, v. 243, p. 18–38.
- Wingate, M.T.D., and Lu, Y., 2016, Introduction to geochronology information released in 2014: Perth, WA, Geological Survey of Western Australia, p. 5.
- Young, C.J., Groves, D.L., and Morant, P., 2003, Sediment-hosted disseminated gold mineralisation in the Palaeoproterozoic Ashburton Province, Western Australia: A new epizonal orogenic gold province related to Capricorn orogeny?, in Eliopoulos et al., eds., Mineral exploration and sustainable development: Proceedings of the 7th Biennial SGA Meeting: Athens, Greece, Millpress, p. 835–838.
- Zhang, J., Linnen, R., Lin, S., Davis, D., and Martin, R., 2014, Palaeoproterozoic hydrothermal reactivation in a Neoproterozoic orogenic lode-gold deposit of the southern Abitibi subprovince: U-Pb monazite geochronological evidence from the Young-Davidson mine, Ontario: *Precambrian Research*, v. 249, p. 263–272.

APPENDIX 1

Analytical Methods*U-Pb zircon geochronology*

Analytical methods for U-Pb zircon geochronology are described in detail by Wingate and Lu (2016), and only a summary is provided here. During all analytical sessions, an O_2 primary beam with a spot size of 20 to 30 μm was used with beam intensity of 1.5 to 3.5 nA. The secondary ion beam was focused through a 100- μm collector slit onto an electron multiplier to produce mass peaks with flat tops and a mass resolution (1% peak height) of 5,100 to 5,460.

Data were collected in sets of six scans, with reference standards analyzed after every five sample analyses. Count times per scan for Pb isotopes 204, background positions 204.1, 206, 207, and 208, were 10, 10, 10, 30, and 10 s, respectively. U-Th-Pb ratios and absolute abundances were determined relative to the BR266 standard zircon (559 Ma, 903 ppm U; Stern, 2001), analyses of which were interspersed with those of unknown zircons. Instrumental mass fractionation (IMF) in $^{207}\text{Pb}/^{206}\text{Pb}$ ratios was monitored during each session by repeated analysis of the 3465 Ma OGC zircon standard (OG1 of Stern et al., 2009). No IMF correction was required because the measured values of OGC were in agreement with the reference value within 2σ uncertainties. Raw zircon data were processed using the SQUID 2 add-in (v. 2.50.12.03.08) for Excel 2003 (Ludwig, 2009) and plotted using the ISOPLOT add-in (v. 3.76.12.02.24; Ludwig, 2003). Measured compositions were corrected for common Pb using nonradiogenic ^{204}Pb and contemporaneous Pb composition according to the terrestrial Pb evolution model of Stacey and Kramers (1975). Mean ages are quoted with 95% confidence levels.

In situ U-Pb baddeleyite, monazite, and xenotime geochronology

For in situ baddeleyite, monazite, and xenotime analysis, a primary beam of O_2^+ ions was focused through a 50- μm Kohler aperture to produce an oval 10- μm -wide spot on the sample surface with a current of 0.2 to 0.4 nA. The secondary ion system was focused through a 100- μm collector slit onto an electron multiplier to produce mass peaks with flat tops and a mass resolution (1% peak height) of >5,200 in all sessions. Background counts from scattered ions were reduced using a

flight retardation lens, which is known to cause slight session-dependent IMF of Pb isotopes. IMF corrections were applied to all analyses using the monazite standard Z2908 as an IMF monitor (see below).

Data were collected in sets of eight scans, with monazite, xenotime, or baddeleyite reference material analyzed every four to six sample analyses. Count times per scan for Pb isotopes 204, background position 204.045, 206, 207, and 208, were 10, 10, 10, 30, and 10 s, respectively.

Baddeleyite was analyzed using the conventional zircon 9-peak run table, calibrated against baddeleyite reference material Phalaborwa (Heaman and LeCheminant, 1993). Monazite was analyzed with a 13-peak run table as defined in Fletcher et al. (2010), which includes mass stations for the estimation of La, Ce, and Nd (REEPO_2) and Y (YCeO^+). Measurements of monazite standards FRENCH, Z2234, and Z2908 (see Fletcher et al., 2010, for details) were done concurrently for Pb/U and Pb/Th calibration (FRENCH), IMF corrections (Z2908), and matrix corrections required for variable U, Th, Y, and Nd contents (Z2234 and Z2908).

Xenotime was analyzed with a 9-peak run table following analytical protocols in Fletcher et al. (2004) and Fletcher et al. (2010). Pb/U calibrations and matrix corrections for U and Th contents were based on concurrent measurements of the standards MG-1 (Fletcher et al., 2004) and Z6413 ("Xenol"; Stern and Rayner, 2003). Pb/Th was determined indirectly, using a fixed Th/U calibration (Fletcher et al., 2004). Matrix corrections for REEs assumed the samples have REE abundances similar to Xenol.

Raw data from analyses on baddeleyite, monazite, and xenotime were processed using the SQUID 2 add-in (v. 2.50.12.03.08) for Excel 2003 (Ludwig, 2009) and plotted using the ISOPLOT add-in (v. 3.76.12.02.24; Ludwig, 2003). Common Pb corrections were based on measured $^{204}\text{Pb}/^{206}\text{Pb}$ ratios and contemporaneous Pb composition, according to the terrestrial Pb evolution model of Stacey and Kramers (1975). Matrix effect corrections were made for all monazite and xenotime data using procedures described by Fletcher et al. (2010) and Fletcher et al. (2004), respectively. Pooled ages are quoted with 95% confidence levels, whereas individual analyses are presented with 1σ errors.

APPENDIX 1B: BELVEDERE

STATEMENT OF CONTRIBUTION OF OTHERS

Title of Paper: Neighbouring orogenic gold deposits may be the products of unrelated mineralizing events.

Publication status: Published

AUTHOR CONTRIBUTIONS

By signing the Statement of Authorship, each author certified that their stated contribution to the publication is accurate and that permission is granted for the publication to be included in the candidate's thesis.

Name of Principal Author: Imogen O. H. Fielding

Contribution to the paper: Led all aspects of the research including all field work, drill core logging and sample selection/collection. Completed all petrography, locating and characterization of minerals for geochronology and preparation of all SHRIMP mounts. Data acquisition and interpretation of results. Writing and drafting images for the manuscript.

Overall Percentage: 75%

Signature:

Date: 23/04/2018

Name of Co-Author: Simon P. Johnson

Contribution to the Paper: Assisted with field work, data interpretation, editing and revision of the manuscript.

Overall Percentage: 10%

Signature:

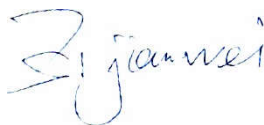
Date: 24/04/2018

Name of Co-Author: Jianwei Zi

Contribution to the Paper: Assisted with SHRIMP set up, data acquisition and processing.

Overall Percentage: 10%

Signature:



Date: 28/04/2018

Name of Co-Author: Stephen Sheppard

Contribution to the Paper: Assisted with manuscript editing.

Overall Percentage: 3%

Signature:



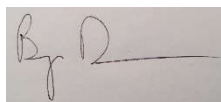
Date: 21/4/2018

Name of Co-Author: Birger Rasmussen

Contribution to the Paper: Assisted with manuscript editing.

Overall Percentage: 2%

Signature:



Date: 23/04/2018

COPYRIGHT

Fielding, I. O. H., Johnson, S. P., Zi, J. W., Sheppard, S., and Rasmussen, B., 2018, Neighbouring orogenic gold deposits may be the products of unrelated mineralizing events: Ore Geology Reviews, v. 95, p. 593-603. Doi: <https://doi.org/10.1016/j.oregeorev.2018.03.011> is published as an open access article under a Creative Commons Attribution Licence (CC BY) and can be reproduced with no copyright infringements as a part of this thesis. Further details can be found at <https://s100.copyright.com/AppDispatchServlet?publisherName=ELS&contentID=S0169136818300155&orderBeanReset=true>



Contents lists available at ScienceDirect

Ore Geology Reviews

journal homepage: www.elsevier.com/locate/oregeorev

Neighbouring orogenic gold deposits may be the products of unrelated mineralizing events

Imogen O.H. Fielding^{a,*}, Simon P. Johnson^b, Jian-Wei Zi^a, Stephen Sheppard^{a,c}, Birger Rasmussen^d

^a Department of Applied Geology, Curtin University, Kent Street, Bentley, Western Australia 6102, Australia

^b Geological Survey of Western Australia, 100 Main Street, East Perth, Western Australia 6004, Australia

^c Prime Geological Mapping, PO Box 3014, Carlisle South, Western Australia, 6101, Australia

^d School of Earth Sciences, The University of Western Australia, Perth, Western Australia 6009, Australia

ARTICLE INFO

Keywords:
Geochronology
Xenotime
Baddeleyite
SHRIMP
Gold
Capricorn Orogen

ABSTRACT

Models for exploration targeting are often developed by assessing known gold deposits in a region, and targeting similar geological features such as geochemical anomalies, favourable host rocks or structural settings with the assumption that they represented the footprint of the mineralizing event. Belvedere and Paulsens are gold deposits with similar characteristics located in the Wyloo Inlier in the north Capricorn Orogen, Western Australia. Gold at both deposits is hosted in quartz-carbonate-sulfide veins within mafic intrusive rock. Prior to this study they were thought to have formed during the same hydrothermal mineralizing event. At Belvedere, in situ baddeleyite geochronology yields a weighted mean $^{207}\text{Pb}/^{206}\text{Pb}$ crystallization age of 2082 ± 30 Ma for the Belvedere dolerite which hosts the ore body. Xenotime intergrown with ore-stage alteration minerals, and encased in arsenopyrite, yielded a $^{207}\text{Pb}/^{206}\text{Pb}$ date of 1681 ± 9 Ma, interpreted to represent the timing of hydrothermal activity related to gold mineralization at the Belvedere deposit. Despite the similarities between the two deposits, our results indicate that they underwent different geological histories with primary gold mineralization at Paulsens occurring at c. 2400 Ma, pre-dating both the Belvedere dolerite and mineralization within the dolerite. Furthermore, field relationships show that the suite of dolerite dykes to which the Belvedere dolerite belongs, crosscut gold mineralization at Paulsens. The in situ U–Pb geochronology techniques employed here, combined with field relationships, have led to a better understanding on age constraints of gold deposition in the Wyloo Inlier and challenges the assumption that orogenic deposits in a given region probably formed during a single mineralizing event.

1. Introduction

Gold deposits within a given geological terrane that exhibit similar characteristics are commonly thought to have formed due to the same geological processes during the same hydrothermal event (Cheng, 2008; Groves et al., 1998). This is particularly apparent in orogenic gold systems as they form during collisional or accretionary orogenies resulting in numerous gold deposits of varying size that form linear trends along major faults associated with crustal boundaries (Bierlein et al., 2006; Goldfarb et al., 2001; Groves et al., 2005). Since faults and major structures can act as fluid pathways (Hronsky et al., 2012; Korsch and Doublier, 2016), it is possible that remobilization or new mineralizing events could be superimposed along the same system. Therefore, without knowing the absolute ages of host rocks and gold mineralization at individual deposits in a region, it is not obvious as to whether

they are all a result of a single mineralizing event or were formed during multiple, superimposed events. In this contribution, we examine the timing of gold mineralization at two similar, closely spaced deposits in the Wyloo Inlier in Western Australia to investigate whether they are the result of a single or multiple mineralizing events.

The Belvedere and Paulsens gold deposits are located in the Wyloo Inlier situated on the southern margin of the Pilbara Craton in Western Australia (Fig. 1; Thorne and Trendall, 2001). The Paulsens deposit is significantly larger than Belvedere with a total endowment of 1.1 Moz of gold (Blockley, 1971; Fielding et al., 2017). The Belvedere deposit had 454 oz of gold extracted during the 1930s (Blockley, 1971) and has a remaining resource of 31,000 oz of contained gold (Northern Star Resources Limited, 2015a). The deposits are 6.5 km apart and historically were interpreted as vein-hosted gold deposits associated with the 1820–1770 Ma Capricorn Orogeny (Thorne and Trendall, 2001).

* Corresponding author.

E-mail address: imogen.fielding@postgrad.curtin.edu.au (I.O.H. Fielding).

<https://doi.org/10.1016/j.oregeorev.2018.03.011>

Received 9 January 2018; Received in revised form 8 March 2018; Accepted 13 March 2018
Available online 14 March 2018

0169-1368/ Crown Copyright © 2018 Published by Elsevier B.V. This is an open access article under the CC BY license (<http://creativecommons.org/licenses/by/4.0/>).

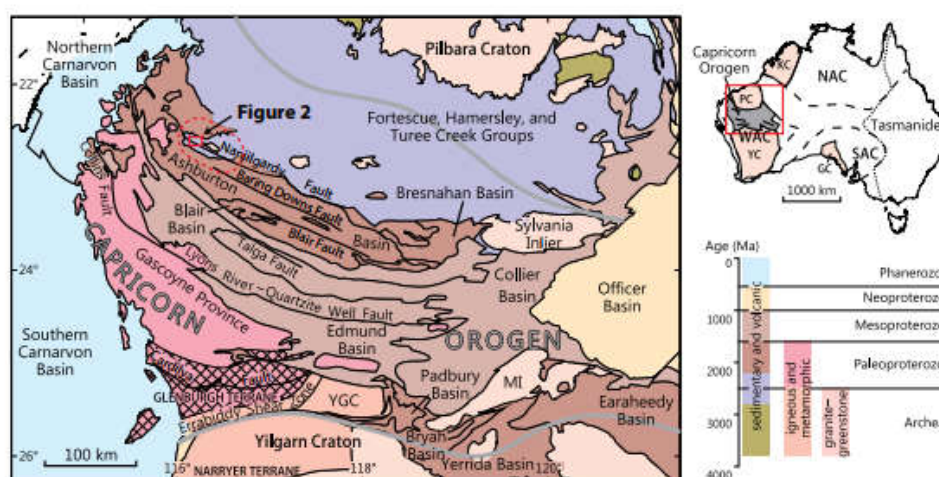


Fig. 1. Location of the Capricorn Orogen in Western Australia, showing location of the Wyloo Inlier (dashed red ellipse) and inset location for Fig. 2. Abbreviations: GC = Gawler Craton, KC = Kimberley Craton, MI = Maryina Inlier, NAC = North Australian Craton, PC = Pilbara Craton, SAC = South Australian Craton, WAC = West Australian Craton, YC = Yilgarn Craton, YGC = Yarlalwee Gneiss Complex (after Johnson et al., 2013).

Originally it was thought the Capricorn Orogen represented the collision between the Pilbara and Yilgarn cratons (Tyler and Thorne, 1990) but is now known to have been an episode of intracratonic reworking (Johnson et al., 2017; Sheppard et al., 2010). Both deposits share the main characteristics of orogenic gold deposits: 1) mineralization comprises quartz–carbonate–sulfide veins; 2) the host rocks are metamorphosed to epidote–actinolite greenschist facies (White et al., 2014); 3) ore-stage alteration assemblages consist of muscovite, carbonate and quartz; 4) the deposits contain native gold (Fielding et al., 2017; Norum, 2005; Owen, 2000), and 5) the deposits are spatially associated with a crustal-scale fault. An additional feature common to the deposits is that mafic intrusive rocks host the auriferous quartz–carbonate–sulfide veins. Despite these similarities, the suite of dolerite dykes which hosts the Belvedere deposit post-date, and cross cut gold mineralization at Paulsens, suggesting that gold mineralization at the two deposits was not synchronous.

Published data and descriptions of the Belvedere deposit are limited to brief mentions in open-file company reports held by the Department of Mines, Industry, Regulation and Safety and in Geological Survey of Western Australia reports (e.g., Blockley, 1971; Forman, 1938; Marston, 1979; Thorne and Trendall, 2001). Here we present new data, including more detailed field relationships and in situ U–Pb SHRIMP geochronology for the Belvedere gold deposit, to determine the age of the host rocks to gold mineralization and the timing of hydrothermal activity related to gold formation. These data are then compared to published information from the Paulsens gold deposit (e.g., Fielding et al., 2017) to demonstrate that gold deposits in close proximity, with similar appearances, may form at separate times and in different tectonic settings.

2. Geological setting

The Wyloo Inlier is situated in the northern part of the Paleoproterozoic Capricorn Orogen on the southern margin of the Pilbara Craton (Fig. 1). The Capricorn Orogen has a complex tectono-thermal evolution which includes at least seven tectonic events over approximately 1.6 billion years (Cawood and Tyler, 2004; Johnson et al., 2011, 2013; Korhonen et al., 2017; Martin and Morris, 2010; Sheppard et al., 2005, 2007). The first two tectonic events (the Ophthalmia Orogeny and the Glenburgh Orogeny) mark the amalgamation

of the West Australian Craton. During the 2215–2145 Ma Ophthalmia Orogeny (Johnson et al., 2011; Rasmussen et al., 2005) the Glenburgh Terrane collided with the Pilbara Craton. Subsequently, during the 2005–1950 Ma Glenburgh Orogeny, the combined Pilbara Craton – Glenburgh Terrane collided with the Yilgarn Craton (Johnson et al., 2011; Occhipinti et al., 2004; Sheppard et al., 2004). Once assembled, the West Australian Craton experienced over a billion years of intracratonic reworking and reactivation during the 1820–1770 Ma Capricorn Orogeny (Cawood and Tyler, 2004; Sheppard et al., 2010), the 1680–1620 Ma Mangaroon Orogeny (Sheppard et al., 2005), the 1320–1170 Ma Mutherbuckin Tectonic Event (Korhonen et al., 2017), the 1030–955 Ma Edmundian Orogeny (Martin and Thorne, 2004; Sheppard et al., 2007), and the c. 570 Ma Mulka Tectonic Event (Johnson et al., 2013).

Within the Wyloo Inlier, Archean basement rocks of the Pilbara Craton are overlain by Archean to Paleoproterozoic metasedimentary and metavolcanic rocks of the Fortescue Group, Hamersley Group, Turee Creek Group, Shingle Creek Group and the Paleoproterozoic Ashburton Formation of the Wyloo Group (Seymour et al., 1988; Thorne and Trendall, 2001). The rocks throughout the Wyloo Inlier are overprinted by regional-scale epidote–actinolite greenschist facies metamorphism (White et al., 2014), and intruded by at least five suites of mafic dykes and sills. Of these dyke suites, only the oldest and youngest have been dated at, respectively, 2701 ± 11 Ma (Fielding et al., 2017) and 753 ± 11 Ma (Wingate et al., 2017a).

Deep crustal seismic reflection imaging across the Capricorn Orogen identified five crustal-scale faults which show a spatial relationship with gold occurrences (Johnson et al., 2013). In the northern Capricorn Orogen, a second order structure of the Nanjilgardy Fault, known as the Hardey Fault, is spatially associated with the Belvedere deposit (Fig. 2) and is linked to c. 2400 and 1680 Ma gold mineralizing events at Paulsens (Fielding et al., 2017).

3. Local geology

The Belvedere gold deposit is located in the core of the Wyloo Inlier within the Mount Roe Basalt (Fig. 2; Thorne and Trendall, 2001). The local stratigraphy at Belvedere includes vesicular basalt, polymictic conglomerate, sandstone and siltstone (Fig. 3).

I.O.H. Fielding et al.

Ore Geology Reviews 95 (2018) 593–603

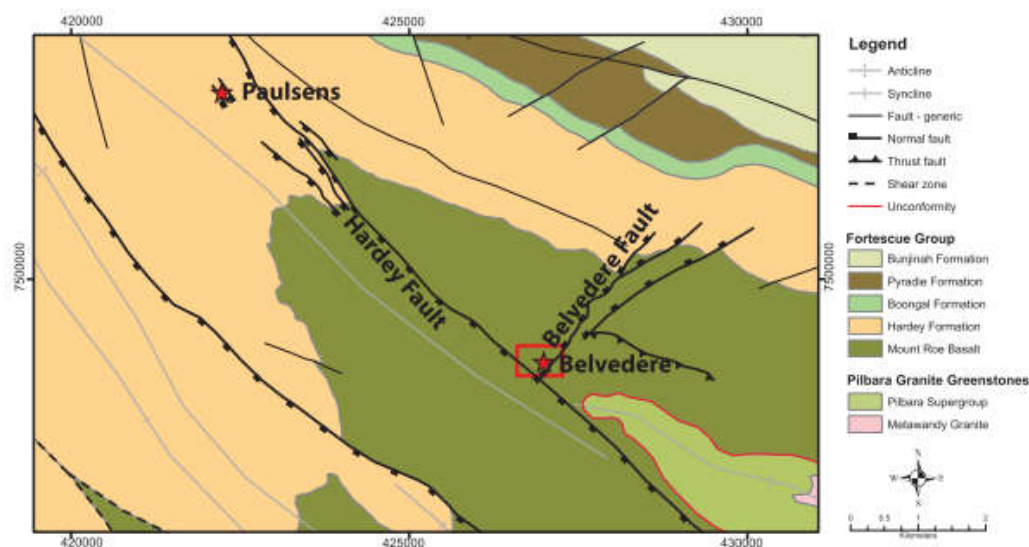


Fig. 2. Geology map of the northern part of the Wyloo Inlier (courtesy of Northern Star Resources Ltd. Pty) showing the location of the Belvedere and Paulsens Deposits. Coordinates are in meters (MGA94 zone 50). Red box shows the location of Fig. 3.

At least four low-grade deformation events have affected the rocks of the Wyloo Inlier, during which two widespread cleavages formed, followed by fault reactivation along pre-existing crustal-scale faults (Krapež, 1999; Thorne and Seymour, 1991). The first event (D_1) caused regional-scale, epidote-actinolite greenschist facies metamorphism (White et al. 2014) accompanied by tight to upright folds, a penetrative, spaced, axial planar cleavage (S_1) with an average orientation of 320/85SW (Fielding et al., 2017), and is thought to be related to the

2215–2145 Ma Ophthalmia Orogeny (Tyler and Thorne, 1990). The second event (D_2), is characterized by lower greenschist facies metamorphism with the growth of chlorite-sericite-muscovite in pelitic and semi-pelitic rocks and chlorite-amphibole in mafic and mafic volcanoclastic rocks (Tyler, 1991; Smith et al., 1982). The D_2 event is near-coaxial to D_1 and is linked to the 1820–1770 Ma Capricorn Orogeny (Thorne and Seymour, 1991). It caused tightening of the F_1 folds, attenuation of northern limbs to form shear zones up to 50 m wide, and

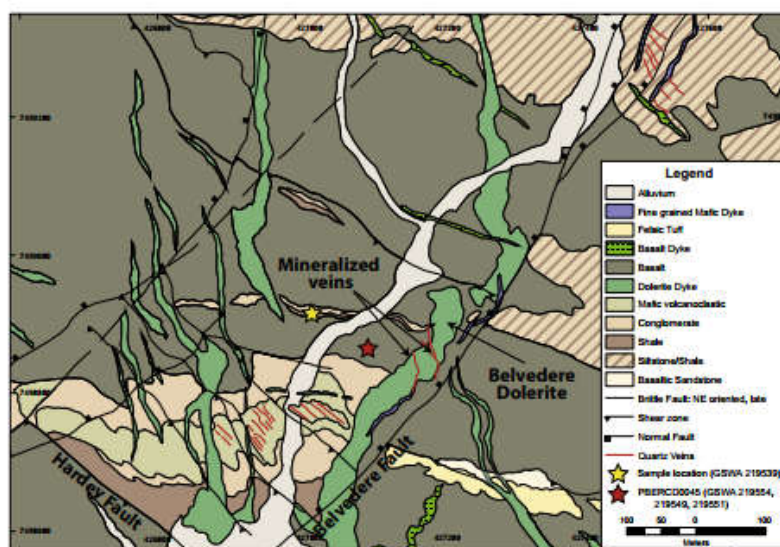


Fig. 3. Local geology map of the Belvedere deposit showing location of the samples, Belvedere dolerite, mineralized quartz-carbonate-arsenopyrite veins and Belvedere and Harley Faults. Coordinates are in meters (MGA94 zone 50).

development of a spaced cleavage (S_2) with an average orientation of 305/85SW (Fielding et al., 2017). S_1 and S_2 can be difficult to differentiate in the field due to their sub-parallel nature. D_3 and D_4 are characterized by WNW-trending dextral followed by sinistral strike-slip reactivation (Krapež, 1999) of the Nanjilgardy Fault and its subsidiary structures, including the Hardey Fault, during the final stages of the Capricorn Orogeny (Krapež, 1999; Thorne and Seymour, 1991) and early stages of the 1680–1620 Ma Mangaroon Orogeny (Fielding et al., 2017).

Proximal to the Belvedere ore body there are three suites of mafic intrusive rocks. An early folded gabbroic dyke with an igneous crystallization age of 2734 ± 14 Ma (Wingate et al., 2017a,b) intrudes the Mount Roe Basalt immediately north of the Belvedere deposit and is crosscut by northwest-trending S_1 and S_2 fabrics. Two later suites of dolerite dykes strike north and northwest and crosscut the gabbro. The relationship between the two younger suites of dolerite dykes is not clear, and currently no geochronological data are available. The dolerites are generally undeformed, although the north-striking dolerite dykes are locally kinked with a spaced cleavage preserved in the deformed zones.

4. Deposit description

The Belvedere orebody is hosted by a 30-m-thick, north-striking, ~40°-west dipping, fine- to medium-grained dolerite dyke informally known as the Belvedere dolerite. The Belvedere dolerite is largely undeformed, although it is foliated at the contact with the mineralized quartz–carbonate–arsenopyrite veins. Overall, it has a northerly strike but close to the orebody it intrudes along the northeast-striking Belvedere fault for approximately 500 m (Fig. 3). Sinistral strike-slip reactivation of the Belvedere fault resulted in the formation of two Riedel shear zones and associated auriferous quartz–carbonate–arsenopyrite veins, surrounded by muscovite–ankerite–quartz \pm rutile \pm albite alteration (Norum, 2005). The mineralized quartz–carbonate–arsenopyrite veins are 2–12 m wide with native gold forming irregular inclusions up to 150 μ m by 20 μ m (Fig. 4A) within euhedral arsenopyrite crystals < 2 mm in diameter. Metallurgical test work indicates most of the gold occurs as free gold that is not bound within the arsenopyrite crystal lattice (Owen, 2000). Small amounts of gold mineralization are also present in quartz–carbonate–arsenopyrite veins occurring sporadically within the Belvedere Fault itself.

There are currently no reliable age constraints on mineralization at Belvedere. Lead isotope ratios of galena suggest that mineralization occurred during the late Proterozoic (Richards et al., 1981), although these conclusions are ambiguous because the data plot away from the model III growth curve of Cumming and Richards (1975). Thorne and Trendall (2001) attributed gold mineralization at Belvedere to emplacement of post-Fortescue Group veins, linking their formation to the 1820–1770 Ma Capricorn Orogeny; however, this has not been verified by geochronology.

5. Geochronology methods

Four samples, (Fig. 3) including three from diamond drill core PBERCD0045 (MGA 94 zone 50 427093E 7498864N) and one from a surface outcrop (MGA 94 zone 50 427026E 7498915N), were analysed to determine the igneous crystallization age of the Belvedere dolerite, and the age of hydrothermal activity and associated gold mineralization. Polished thin sections were examined by optical and scanning electron microscope (SEM) to identify minerals suitable for in situ SHRIMP geochronology, such as monazite, xenotime and baddeleyite. Once identified, the minerals were drilled out of the polished thin section using a 2–3 mm hollow core drill bit and cast into a 25 mm epoxy SHRIMP mount. The in situ dating method preserves the textural context of minerals being dated, allowing the significance of the date obtained to be better understood. Reference materials xenotime MGI

(Fletcher et al., 2004), Xeno1 and Xeno2 (Stern and Rayner, 2003) and baddeleyite Phalaborwa (Heaman and LeCheminant, 1993) were placed on a separate SHRIMP mount which was cleaned and gold coated with the sample mounts for each analytical session.

Xenotime and baddeleyite were analysed for U, Th and Pb isotopes using the SHRIMP II instrument at the John de Laeter Centre at Curtin University in Perth, Western Australia. In situ small spot analysis of xenotime followed established procedures outlined by Fletcher et al. (2004). Data were collected over several analytical sessions using varying parameters which are summarised in Table 1. The appendix describes the analytical procedures in detail.

6. Sample details and results

All age calculations are derived from 204-corrected $^{207}\text{Pb}^*/^{206}\text{Pb}^*$ ratios (Pb^* denotes radiogenic lead). Up to 2% common lead and 10% discordance for individual analyses are tolerated unless mentioned below. Data in tables and plots for individual analyses are quoted with 1 σ uncertainties; weighted mean $^{207}\text{Pb}^*/^{206}\text{Pb}^*$ dates are quoted with 95% confidence intervals.

6.1. Baddeleyite

6.1.1. GSWA 219544: Belvedere dolerite

A medium- to coarse-grained portion of the Belvedere dolerite was sampled from diamond drill hole PBERCD0045, between 54.25 and 54.60 m, to determine the emplacement age of the dolerite that hosts the mineralized quartz–carbonate–arsenopyrite veins. Euhedral baddeleyite crystals up to 150 μ m long (Fig. 4B) are common throughout the sample. Many of the baddeleyite crystals have thin fringes of very fine-grained zircon (Fig. 4B), although in some cases the baddeleyite crystal has been entirely replaced by crystalline zircon with abundant very-fine grained inclusions (Fig. 4C). Attempts were made to date the zircon fringes and zircon pseudomorphs but all analyses are > 10% discordant.

Fifteen analyses were made on 10 baddeleyite crystals with U and Th concentrations ranging from 73 to 251 ppm and 3 to 46 ppm, respectively. Care was taken to ensure the analysis spot did not overlap the zircon fringes. Two analyses with > 2% common lead and two younger statistical outliers, possibly due to Pb-loss, were excluded from the age determination. Seven of the analyses are > 10% discordant likely due to the crystal orientation effect of baddeleyite which may bias the $^{206}\text{Pb}^*/^{238}\text{U}$ ratios (Wingate and Compston, 2000). However, the $^{207}\text{Pb}^*/^{206}\text{Pb}^*$ ratios show good consistency and are considered reliable in the age determination. Eleven analyses yield a weighted mean $^{207}\text{Pb}^*/^{206}\text{Pb}^*$ date of 2082 ± 30 Ma (MSWD = 0.96; Table 2; Fig. 5A), interpreted as the crystallization age of the Belvedere dolerite.

6.2. Xenotime

6.2.1. GSWA 219549: Auriferous quartz–carbonate–arsenopyrite vein

A sample of the mineralized quartz–carbonate–arsenopyrite vein with assay results of 1.15 ppm Au, was sampled from diamond drill hole PBERCD0045 between 77.39 and 77.68 m. The sample is composed predominantly of quartz with lesser amount of ore-stage alteration including very fine-grained muscovite–carbonate–rutile and euhedral arsenopyrite crystals < 1 mm long. Xenotime is mostly anhedral and commonly contains laths of muscovite (Fig. 4D) indicating that xenotime growth occurred during ore-stage hydrothermal activity.

Thirteen analyses were conducted on 8 xenotime crystals with U and Th concentrations ranging from 462 to 2611 ppm and 49 to 64 ppm, respectively. One analysis yielded > 1% common Pb, and was excluded from the age determination. The remaining 12 analyses give a weighted mean $^{207}\text{Pb}^*/^{206}\text{Pb}^*$ date of 1682 ± 13 Ma (MSWD = 0.59; Table 3, Fig. 5B) which is interpreted to represent the timing of hydrothermal activity related to ore-stage alteration and associated gold

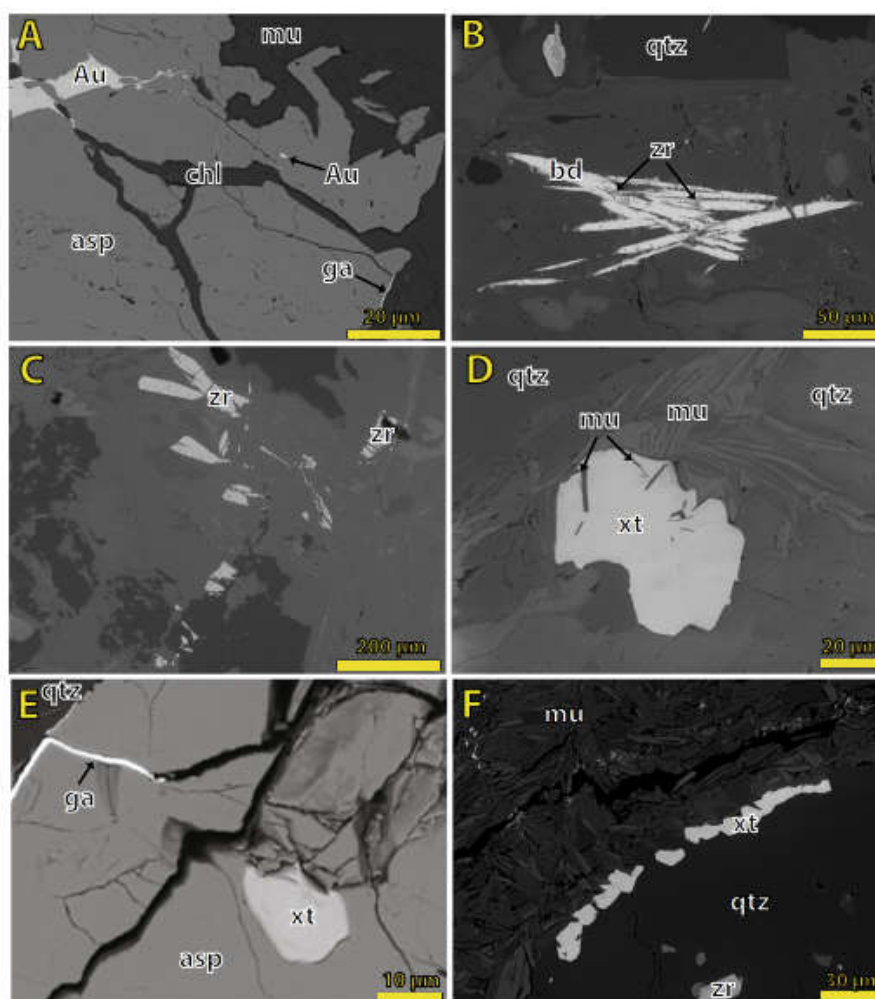


Fig. 4. Backscattered electron microscope (BSE) images of accessory minerals from the Belvedere deposit. A) Native gold inclusions in arsenopyrite crystals (GSWA 219551). B) Euhedral baddeleyite crystal from the Belvedere dolerite surrounded by thin zircon fringes (GSWA 219544). C) Former crystals of baddeleyite from the Belvedere dolerite which have been replaced by zircon with abundant very fine-grained inclusions (GSWA 219544). D) Anhedral xenotime crystal containing laths of ore-stage muscovite from quartz-carbonate-arsenopyrite veins (GSWA 219549). E) Anhedral xenotime crystal contained within auriferous arsenopyrite from quartz-carbonate-arsenopyrite veins (GSWA 219551). F) Elongate clusters of xenotime at the margins of a quartz clast from crenulated schist that is locally cross cut by the Belvedere dolerite (GSWA 219539). Abbreviations: asp = arsenopyrite, Au = gold, bd = baddeleyite, chl = chlorite, ga = galena, mu = muscovite, qtz = quartz, xt = xenotime, and zr = zircon.

Table 1
SHRIMP operating parameters for all analytical sessions.

Session date	Mount ID	Sample ID	Target mineral	Kohler aperture (μm)	spot (approx. μm)	O ₂ ⁺ primary (nA)	M/ΔM (1%)	# scans
15-05-2017	IF1702	219,544	Baddeleyite	50	10	0.4–0.6	4925.6	7
29-10-2016	IF1604	219,539	Xenotime	30	10	0.3	5231.3	8
02-05-2017	IF1703	219,539 (A–D)	Xenotime	30	10	0.2–0.3	4794.3	7
28-10-2016	IF1606	219,549 (A–H)	Xenotime	30	10	0.3	5231.3	8
28-29/10/2016	IF1606	219,551 (I–K)	Xenotime	30	10	0.3	5231.3	8
12-07-2017	IF1607	219551(A,E1–1,H,G)	Xenotime	30	10	0.6	5161.8	8
12-07-2017	IF1607	219551(B,I,E2–1)	Xenotime	30	10	0.2	5161.8	8

Table 2
SHRIMP analytical results for baddeleyite from sample GSWA 219544: Belvedere dolerite.

GSWA 219,544 Belvedere Dolerite Dyke													
Mount No.	Grain spot	U (ppm)	Th (ppm)	Th/U	f206 (%)	$^{207}\text{Pb}^*/^{235}\text{Pb}^*$	$\pm 1\sigma$	$^{206}\text{Pb}^*/^{238}\text{U}$	$\pm 1\sigma$	$^{207}\text{Pb}^*/^{235}\text{U}$	$\pm 1\sigma$	Dis (%)	$^{207}\text{Pb}^*/^{235}\text{Pb}^*$ age (Ma)
Crystallization (2082 \pm 30 Ma)													
1702	G.2-1	118	5	0.04	1.04	0.1351	0.0044	0.369	0.009	6.88	0.27	6	2165
1702	B.2-1	158	4	0.02	-0.16	0.1332	0.0031	0.320	0.006	5.88	0.17	16	2141
1702	G.1-3	107	6	0.06	-0.22	0.1311	0.0037	0.320	0.013	5.78	0.28	15	2113
1702	G.1-1	124	5	0.04	0.10	0.1299	0.0035	0.329	0.014	5.89	0.29	13	2097
1702	G.1-2	129	3	0.02	0.45	0.1280	0.0044	0.323	0.007	5.70	0.22	13	2071
1702	B.1-1	209	16	0.08	1.27	0.1278	0.0073	0.319	0.006	5.63	0.34	14	2068
1702	A.1-1	251	8	0.03	0.10	0.1277	0.0025	0.364	0.006	6.40	0.15	3	2066
1702	B.2-2	132	3	0.02	0.52	0.1277	0.0035	0.323	0.006	5.69	0.18	13	2066
1702	D.1-1	231	46	0.20	0.75	0.1267	0.0034	0.349	0.006	6.09	0.19	6	2053
1702	J.1-1	118	4	0.03	1.52	0.1223	0.0049	0.367	0.007	6.19	0.27	-1	1989
1702	E.1-1	152	6	0.04	0.96	0.1221	0.0041	0.413	0.015	6.95	0.34	-12	1988
Younger statistical outliers													
1702	B.2-3	215	7	0.03	0.41	0.1207	0.0026	0.337	0.007	5.62	0.16	5	1966
1702	E.1-2	158	8	0.05	1.09	0.1206	0.0034	0.357	0.008	5.94	0.21	0	1965
High common lead													
1702	L.1-1	73	8	0.11	2.63	0.1295	0.0073	0.375	0.010	6.69	0.42	2	2091
1702	H.1-1	101	5	0.05	2.44	0.1100	0.0065	0.372	0.008	5.64	0.35	-13	1799

Pb* indicates radiogenic Pb.

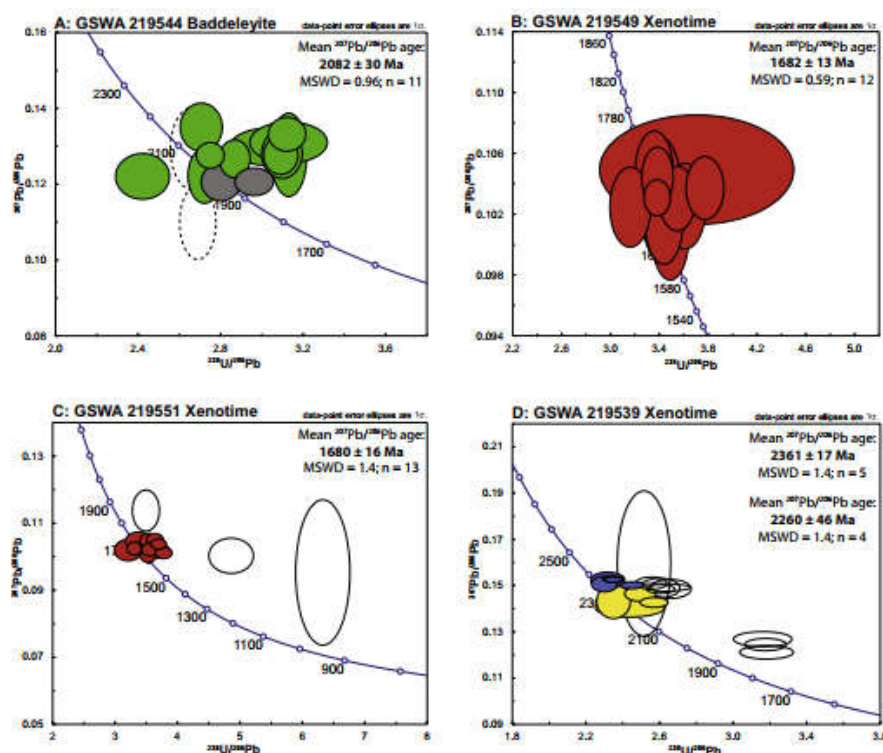


Fig. 5. Tera-Wasserburg concordia diagrams of U–Pb data for baddeleyite and xenotime. A) Baddeleyite from the Belvedere dolerite (GSWA 219544). B) Xenotime containing laths of ore-stage muscovite within auriferous quartz-carbonate-sulfide vein (GSWA219549), data with high common lead is not plotted, refer to Table 3 for analysis details. C) Xenotime intergrown with ore-stage muscovite and auriferous arsenopyrite within auriferous quartz-carbonate-sulfide vein (GSWA219551). D) Xenotime within a crenulated muscovite schist that is locally cross cut by the Belvedere dolerite (GSWA 219539). Key: Dark-coloured ellipses (green = c. 2080 Ma, red = c. 1680 Ma, blue = c. 2360 Ma, yellow = c. 2260 Ma) show data used in the age calculations; other ellipses are for inferior data (solid grey = young outliers, dashed ellipses = high common Pb, open black ellipses = discordant data).

Table 3
SHRIMP analytical results for xenotime from sample GSWA 219549: Belvedere mineralization.

GSWA 219,549 Belvedere mineralization																
Mount No.	Grain spot	U (ppm)	Th (ppm)	Th/U	f206 (%)	$^{207}\text{Pb}^*/^{206}\text{Pb}^*$	$\pm 1 \sigma$	$^{206}\text{Pb}^*/^{238}\text{U}$	$\pm 1 \sigma$	$^{207}\text{Pb}^*/^{235}\text{U}$	$\pm 1 \sigma$	$^{208}\text{Pb}^*/^{232}\text{Th}$	$\pm 1 \sigma$	Dis (%)	$^{207}\text{Pb}^*/^{206}\text{Pb}^*$ age (Ma)	$\pm 1 \sigma$ (Ma)
Hydrothermal mineralization (1682 \pm 13 Ma)																
1606	B.1-1	482	49	0.10	0.00	0.1049	0.0020	0.270	0.038	3.90	0.56	1.512	0.009	10	1713	36
1606	B.1-2	471	58	0.12	-0.14	0.1048	0.0016	0.298	0.009	4.30	0.15	1.593	0.010	2	1710	29
1606	D.2-1	931	59	0.06	-0.11	0.1045	0.0012	0.295	0.007	4.26	0.12	1.640	0.010	2	1705	20
1606	C.1-2	788	63	0.08	-0.09	0.1037	0.0012	0.265	0.007	3.79	0.11	1.456	0.009	10	1692	22
1606	G.1-1	2611	59	0.02	0.05	0.1031	0.0007	0.296	0.006	4.21	0.09	3.305	0.010	1	1681	12
1606	C.1-1	700	62	0.09	-0.05	0.1030	0.0013	0.282	0.008	4.00	0.12	1.154	0.010	5	1680	23
1606	H.1-1	595	64	0.11	0.58	0.1029	0.0025	0.293	0.010	4.15	0.18	0.581	0.010	1	1678	46
1606	B.1-3	508	59	0.12	0.15	0.1025	0.0017	0.277	0.009	3.91	0.14	1.333	0.009	6	1671	31
1606	C.2-1	1771	58	0.03	0.55	0.1025	0.0016	0.317	0.011	4.47	0.17	2.123	0.011	-6	1669	29
1606	B.1-4	462	56	0.12	0.22	0.1024	0.0018	0.294	0.009	4.15	0.15	1.494	0.010	0	1669	33
1606	E.1-1	539	63	0.12	0.20	0.1016	0.0017	0.291	0.009	4.07	0.14	0.677	0.010	0	1653	32
1606	B.1-5	561	59	0.10	0.39	0.1006	0.0018	0.287	0.008	3.98	0.14	0.949	0.010	1	1636	33
High common lead																
1606	D.1-1	2611	53	0.02	8.05	0.1478	0.0339	0.261	0.019	5.33	1.36	4.076	0.006	35	2320	393

mineralization.

6.2.2. GSWA 219551: Auriferous quartz-carbonate-arsenopyrite vein

A second mineralized sample with a Au grade of 4.81 ppm was taken from diamond drill hole PBERCD0045 between 79.2 and 79.68 m. The sample is a quartz-carbonate-arsenopyrite vein containing coarse-grained, euhedral arsenopyrite and associated muscovite-ankerite-rutile alteration. Xenotime crystals are anhedral, < 60 µm in size and commonly contain inclusions of, or is intergrown with, ore-stage alteration products such as muscovite. Inclusions of gold (Fig. 4A), and small inclusions of anhedral xenotime (< 30 µm; Fig. 4E) occurs within arsenopyrite suggesting crystallization of gold, xenotime and arsenopyrite was simultaneous.

Sixteen analyses were conducted on 12 xenotime crystals with U and Th concentrations ranging from 141 to 2105 ppm and 50 to 1446 ppm, respectively. Three analyses were excluded from the age determination due to > 10% discordance. The remaining 13 analyses yielded a weighted mean $^{207}\text{Pb}^*/^{206}\text{Pb}^*$ date of 1680 ± 16 Ma (MSWD = 1.4; Table 4; Fig. 5C). Since xenotime is contained with auriferous arsenopyrite and intergrown with ore-stage alteration minerals, this date is interpreted to represent the timing of hydrothermal

activity associated with gold mineralization.

As the age determinations for samples GSWA 219,549 and 219,551 are indistinguishable within analytical uncertainty, the data have been pooled to provide a more precise weighted mean $^{207}\text{Pb}^*/^{206}\text{Pb}^*$ date of 1681 ± 9 Ma (MSWD = 0.96) interpreted to represent the timing of hydrothermal activity related to ore-stage alteration and gold mineralization.

6.2.3. GSWA 219539: Crenulated muscovite schist

A very fine-grained, laminated and crenulated muscovite schist that is locally cross cut by the north-trending dolerite dykes was collected from a 2 m-wide outcrop located ~200 m west of the Belvedere deposit (Fig. 3). The sample contains muscovite, quartz, and trace amounts of rutile, monazite and xenotime. Aggregates of very fine-grained monazite occur throughout the rock but are too small to be analysed by ion microprobe. Xenotime crystals are typically small (< 30 µm) and developed as narrow, elongate clusters of crystals up to 10×80 µm in, or around the margins of, quartz clasts (Fig. 4F) or as very small (< 10 µm) crystals aligned in the S_1 cleavage. Attempts were made to date the xenotime within the cleavage; however, the analyses were discordant because the SHRIMP analysis spot overlapped onto the

Table 4
SHRIMP analytical results for xenotime from sample GSWA 219551: Belvedere mineralization.

GSWA 219,551 Belvedere Mineralization																
Mount No.	Grain spot	U (ppm)	Th (ppm)	Th/U	f206 (%)	$^{207}\text{Pb}^*/^{206}\text{Pb}^*$	$\pm 1 \sigma$	$^{206}\text{Pb}^*/^{238}\text{U}$	$\pm 1 \sigma$	$^{207}\text{Pb}^*/^{235}\text{U}$	$\pm 1 \sigma$	$^{208}\text{Pb}^*/^{232}\text{Th}$	$\pm 1 \sigma$	Dis (%)	$^{207}\text{Pb}^*/^{206}\text{Pb}^*$ age (Ma)	$\pm 1 \sigma$ (Ma)
Hydrothermal mineralization (1680 \pm 16 Ma)																
1606	J.1-1	1261	55	0.04	0.08	0.1053	0.0010	0.275	0.007	3.99	0.10	0.506	0.009	9	1720	17
1606	L.1-2	715	53	0.07	0.09	0.1049	0.0013	0.283	0.007	4.09	0.12	0.883	0.009	6	1712	23
1607	A.1-1	1201	506	0.42	0.87	0.1047	0.0017	0.296	0.012	4.28	0.18	0.097	0.010	2	1709	29
1606	J.2-2	2105	57	0.03	0.15	0.1038	0.0009	0.271	0.006	3.87	0.09	1.323	0.009	9	1694	16
1606	L.1-3	580	59	0.10	0.11	0.1034	0.0015	0.282	0.008	4.02	0.13	1.124	0.010	5	1685	26
1607	B.2-1	1827	1446	0.79	0.22	0.1026	0.0017	0.306	0.015	4.33	0.22	0.101	0.010	-3	1671	30
1606	K.1-1	1925	54	0.03	0.52	0.1025	0.0011	0.302	0.007	4.27	0.11	2.935	0.010	-2	1670	21
1606	J.3-1	1029	57	0.06	0.09	0.1024	0.0011	0.283	0.009	3.99	0.14	0.480	0.010	4	1668	19
1606	L.1-1	780	61	0.08	0.04	0.1023	0.0011	0.280	0.007	3.95	0.11	1.114	0.010	4	1666	21
1607	E.2-1	848	196	0.23	0.29	0.1020	0.0019	0.312	0.014	4.39	0.22	0.095	0.011	-5	1661	35
1607	L.1-1	1184	335	0.28	0.06	0.1020	0.0014	0.276	0.012	3.87	0.18	0.083	0.009	6	1660	25
1606	J.2-1	1400	50	0.04	0.11	0.1012	0.0010	0.265	0.006	3.69	0.10	0.463	0.009	8	1646	18
1606	L.1-4	858	61	0.07	0.00	0.1011	0.0017	0.283	0.007	3.95	0.12	1.115	0.010	2	1644	31
Discordance > 10%																
1607	G.1-1	676	634	0.94	1.79	0.1138	0.0038	0.286	0.012	4.49	0.24	0.088	0.009	13	1861	60
1607	H.1-1	141	386	2.74	-0.38	0.1003	0.0033	0.206	0.010	2.85	0.17	0.065	0.007	26	1630	60
1607	E.1-1	355	534	1.50	15.08	0.0954	0.0135	0.158	0.007	2.08	0.33	0.055	0.006	38	1535	266

Table 5
SHRIMP analytical results for xenotime from sample GSWA 219539: Crenulated muscovite schist.

GSWA 219,539 Crenulated muscovite schist																
Mount No.	Grain spot	U (ppm)	Th (ppm)	Th/U	f206 (%)	$^{207}\text{Pb}^*/^{206}\text{Pb}^*$	$\pm 1 \sigma$	$^{206}\text{Pb}^*/^{238}\text{U}$	$\pm 1 \sigma$	$^{207}\text{Pb}^*/^{235}\text{U}$	$\pm 1 \sigma$	$^{208}\text{Pb}^*/^{232}\text{Th}$	$\pm 1 \sigma$	Dis (%)	$^{207}\text{Pb}^*/^{206}\text{Pb}^*$ age (Ma)	$\pm 1 \sigma$ (Ma)
Main group (2361 \pm 17 Ma)																
1703	F.1.1	2468	773	0.31	0.01	0.1522	0.0009	0.426	0.007	8.94	0.15	0.103	0.010	3	2370	10
1703	C.2-1	2854	2591	0.91	0.01	0.1519	0.0008	0.426	0.006	8.92	0.14	0.119	0.010	3	2368	9
1604	A.1-1	3398	63	0.02	0.95	0.1516	0.0021	0.431	0.011	9.01	0.27	4.238	0.010	2	2364	24
1703	A.2-1	1182	1429	1.21	0.36	0.1500	0.0021	0.435	0.009	8.99	0.22	0.119	0.010	1	2346	24
1703	C.1-1	2017	1449	0.72	-0.01	0.1494	0.0010	0.408	0.007	8.41	0.16	0.079	0.009	6	2339	11
Younger group (2260 \pm 46 Ma)																
1604	A.1-2	1549	60	0.04	0.47	0.1458	0.0020	0.401	0.009	8.06	0.22	4.422	0.009	5	2297	23
1604	A.2-1	1051	58	0.06	0.35	0.1425	0.0046	0.425	0.011	8.36	0.36	2.061	0.010	-1	2258	55
1703	L.1.1	1171	1783	1.52	0.03	0.1421	0.0014	0.389	0.008	7.62	0.17	0.081	0.009	6	2253	17
1604	A.3-1	1291	47	0.04	0.42	0.1397	0.0024	0.410	0.021	7.90	0.43	2.577	0.010	0	2224	30
Discordance > 7%																
1703	D.1.1	370	517	1.40	2.26	0.1588	0.0197	0.398	0.015	8.71	1.18	0.119	0.009	12	2443	210
1703	B.1-1	1025	814	0.79	0.33	0.1503	0.0017	0.391	0.009	8.11	0.20	0.090	0.009	9	2350	19
1604	B.1-1	1983	62	0.03	0.06	0.1485	0.0008	0.387	0.019	7.93	0.39	3.611	0.009	9	2329	10
1604	D.1-1	2597	58	0.02	0.14	0.1483	0.0026	0.384	0.011	7.86	0.26	3.324	0.009	10	2326	30
1703	E.1.1	405	402	0.99	0.66	0.1479	0.0026	0.376	0.011	7.67	0.26	0.126	0.009	11	2322	30
1703	H.1.1	1080	662	0.61	0.17	0.1478	0.0012	0.384	0.007	7.82	0.16	0.073	0.009	10	2321	14
1604	C.1-1	362	55	0.15	0.15	0.1261	0.0020	0.316	0.011	5.50	0.21	1.524	0.009	13	2044	28
1703	A.3-1	636	1503	2.36	0.24	0.1239	0.0017	0.315	0.007	5.38	0.15	0.091	0.009	12	2012	24
1703	A.1-1	391	1213	3.10	0.00	0.1205	0.0019	0.314	0.009	5.22	0.18	0.090	0.009	10	1963	28

surrounding minerals.

Eighteen analyses were made on 17 xenotime crystals with U and Th concentrations ranging from 362 to 3398 ppm and 47 to 2591 ppm, respectively. Five analyses were excluded from the age determination due to > 10% discordance. Of the remaining 13 analyses, two discrete age components are evident with higher U and Th values in grains with the older age mode. The older mode with nine analyses yields a weighted mean $^{207}\text{Pb}^*/^{206}\text{Pb}^*$ date of 2350 ± 15 Ma (MSWD = 2.5). However, a more statistically robust date is calculated by excluding data > 7% discordant providing a weighted mean $^{207}\text{Pb}^*/^{206}\text{Pb}^*$ date of 2361 ± 17 Ma (MSWD = 1.4; Table 5; Fig. 5D). The younger mode with four analyses yields a weighted mean $^{207}\text{Pb}^*/^{206}\text{Pb}^*$ date of 2260 ± 46 Ma (MSWD = 1.4; Table 5, Fig. 5D). These dates are interpreted to represent xenotime growth during hydrothermal activity at c. 2360 and 2260 Ma.

7. Discussion

7.1. Host rocks to auriferous quartz–carbonate–arsenopyrite veins

Magmatic baddeleyite within the Belvedere dolerite yielded a crystallization age of 2082 ± 30 Ma, providing a maximum age for the emplacement of the auriferous quartz–carbonate–arsenopyrite veins. This age does not correspond with the timing of other mafic intrusions in either the Capricorn Orogen or the Pilbara region.

7.2. Timing of hydrothermal activity and gold mineralization

Three episodes of hydrothermal xenotime growth are recorded at the Belvedere gold deposit: c. 2360, 2260 and 1680 Ma. Xenotime dated at 2361 ± 17 Ma within a crenulated muscovite schist (GSWA 219539) is synchronous with widespread hydrothermal activity throughout the Pilbara region (Pickard, 2002; Rasmussen et al., 2005) and gold mineralization at the Paulsens mine which is related to a cryptic orogenic event (Fielding et al., 2017). However, this event is much older than gold mineralization at the Belvedere deposit, which must be younger than the c. 2080 Ma dolerite host (GSWA 219544). Xenotime from the same sample, dated at 2260 ± 46 Ma, is within uncertainty of monazite growth at 2216 ± 13 Ma from Mount Tom Price, which formed

during the early stages of the 2215–2145 Ma Ophthalmia Orogeny (Rasmussen et al., 2005).

Xenotime fully encased in auriferous arsenopyrite and intergrown with ore-stage alteration minerals directly dates the timing of hydrothermal activity and emplacement of the auriferous quartz–carbonate–arsenopyrite veins, thus constraining the timing of gold mineralization to 1681 ± 9 Ma (GSWA 219549 and GSWA 219551). This age is coeval with intracratonic reworking during the earliest stages of the 1680–1620 Ma Mangaroon Orogeny, when medium- to high-grade metamorphism, magmatism and deformation affected rocks of the Gascoyne Province to the south (Sheppard et al., 2005). During this time, major faults throughout the Pilbara region, such as the Nanjilgardy Fault, were reactivated in response to the Mangaroon Orogeny (Fielding et al., 2017; Rasmussen et al., 2007a,b). Reactivation of the Hardey Fault at c. 1680 Ma caused either introduction of new gold or local remobilization of gold at the Paulsens mine (Fielding et al., 2017).

7.3. Comparison with the Paulsens gold deposit

The Belvedere and Paulsens gold deposits are situated 6.5 km apart and are associated with the Hardey Fault (Fig. 2), which is a second order splay of the crustal-scale Nanjilgardy Fault. Gold mineralization at both deposits is contained within auriferous quartz–carbonate–sulfide veins that are hosted in mafic dykes with hydrothermal alteration characterized by muscovite–ankerite–quartz (–rutile) assemblages (Fielding et al., 2017; Thorne and Trendall, 2001). Prior to this study the timing of gold mineralization at the Belvedere deposit was poorly constrained, although ambiguous results from lead-isotope dating of galena suggested that mineralization was late Proterozoic in age (Richards et al., 1981). Thorne and Trendall (2001) attributed gold mineralization at Belvedere and Paulsens to post-Fortescue Group veins, linking their formation to the 1820–1770 Ma Capricorn Orogeny. This age for mineralization is neither supported by field relationships nor geochronological data presented here and by Fielding et al. (2017). Our data show that the ore deposits were not only formed at different times, but have several key differences.

The Paulsens and Belvedere gold deposits are hosted in mafic intrusive rocks. Rheological (and possible chemical) differences between gabbro and surrounding siliciclastic rocks at Paulsens, and dolerite and

surrounding siliciclastic rocks at Belvedere, make them suitable host rocks for gold mineralization. During reactivation of the Hardy Fault, brittle fracturing of the more competent mafic intrusive rocks allowed for emplacement of mineralized quartz-sulfide veins, whereas the surrounding siliciclastic rocks took up the strain as a foliation. Despite both deposits being hosted in mafic intrusive rocks, the mafic rocks themselves differ in type and age. At Paulsens, auriferous quartz-carbonate-sulfide veins are hosted within the pervasively altered Paulsens gabbro, a medium- to coarse-grained, mafic dyke that cuts stratigraphy at a low angle, was deformed during regional-scale F_1 folding, and has been overprinted by both S_1 and S_2 fabrics. Emplacement of the Paulsens gabbro has been precisely dated (U–Pb SHRIMP dating of baddeleyite) at 2701 ± 11 Ma (Fielding et al., 2017). In contrast, auriferous quartz-carbonate-arsenopyrite veins at Belvedere are hosted within the fine- to medium-grained, north-striking Belvedere dolerite that intrudes stratigraphy at a high angle, and which preserves a cleavage in areas where the dolerite is kinked and locally in contact with the mineralized veins. The Belvedere dolerite dyke is much younger, with an igneous crystallization age of 2082 ± 30 Ma (GSWA 219544). Additionally, the deposits are characterized by different sulfide minerals, with Paulsens dominated by pyrite with later pyrrhotite and chalcopyrite (Fielding et al., 2017; Hancock and Thorne, 2016) whereas Belvedere contains arsenopyrite and secondary galena (Fig. 4E).

Field relationships also demonstrate that the north-trending dolerite dykes, including the Belvedere dolerite, cross-cut and offset auriferous quartz-carbonate-sulfide veins at the Paulsens deposit (Fig. 6; Northern Limited Resources Limited, July 2015b). This is supported by U–Pb SHRIMP geochronology on hydrothermal xenotime that indicates that primary gold mineralization at Paulsens occurred at c. 2400 Ma (Fielding et al., 2017), and thus significantly pre-dates the intrusion of the c. 2080 Ma Belvedere dolerite and subsequent mineralization.

7.4. Relationship of mineralization to regional orogenic events

When integrated with the tectonothermal framework of the northern Capricorn Orogen (Fielding et al., 2017; Johnson et al., 2013), gold mineralization at Paulsens (c. 2400 Ma) and at Belvedere (c. 1680 Ma) formed during different orogenic events. Fielding et al.

(2017) attributed c. 2400 Ma orogenic gold mineralization at Paulsens to a cryptic orogenic event, for which there is evidence of uplift and erosion along the southern Pilbara margin, as well as widespread hydrothermal alteration across the entire Pilbara Craton (Pickard, 2002; Rasmussen et al., 2005). This event is synchronous with the timing of hydrothermal xenotime growth (dated at c. 2360 Ma; GSWA 219539) within a crenulated muscovite schist at Belvedere suggesting this event is a compressional orogeny, however at this stage there is not enough information to understand its full effects.

Gold mineralization at Belvedere, here dated at c. 1680 Ma, is coeval with a second gold mineralizing event at Paulsens (Fielding et al., 2017) that is related to the reactivation of the Nanjilgardy Fault and its second-order structures (including the Hardy Fault) during the earliest stages of the intracratonic 1680–1620 Ma Mangaroon Orogeny (Sheppard et al., 2005). The Mangaroon Orogeny was defined in the Gascoyne Province to the south where its effects are most prominent (Sheppard et al., 2005). In the Gascoyne Province this event is characterized by intraplate extension, high-temperature – low-pressure metamorphism with the synchronous emplacement of voluminous granitic stocks, plutons and batholiths of the 1680–1620 Ma Durlacher Supersuite (Johnson et al., 2017; Sheppard et al., 2005). However, in the northern Capricorn Orogen and Pilbara region the effects of this orogeny are more enigmatic where it lacks evidence for granite magmatism and is of significantly lower metamorphic grade (lowermost greenschist facies). Although the effects of this event are not yet fully known or understood, the event appears to be characterized by the strike slip reactivation of major faults and their ancillary structures (Sheppard et al., 2006), which are accompanied by the flow of mineralizing hydrothermal fluids. These structural pathways have played a critical role in the distribution of gold mineralization throughout the region (Fielding et al., 2017; Rasmussen et al., 2007a,b).

7.5. Implications for exploration targeting

The presence of closely spaced multiple mineralizing events separated by significant differences in time has important implications for regional-scale exploration targeting. For example, the suite of c. 2080 Ma dolerite dykes is only prospective for c. 1680 Ma gold mineralization since it post-dates the c. 2400 Ma primary gold mineralizing event at Paulsens. In contrast, mafic rocks of the Fortescue and Hamersley Groups were deposited between c. 2775 and 2450 Ma (Arndt et al., 1991; Trendall et al., 2004) which makes them prospective for both c. 1680 and 2400 Ma gold mineralization. Considering that both Paulsens and Belvedere are located in structurally similar areas, and both are associated with mafic dykes, it is the presence of multiple mineralizing events at Paulsens that may account for the difference in gold endowment. Along with a favourable crustal architecture, multiple mineralizing events appear to be required to enrich gold mineralization, thus producing larger, and more economically viable deposits (Meffre et al., 2016). With this understanding, exploration strategies can focus not only on areas with a favourable crustal architecture, but where the rocks are old enough to be overprinted by multiple hydrothermal events. Without knowing the timing of gold mineralization it is possible to erroneously target potential host rocks that have only undergone a minor mineralizing event or that actually post-date all of the mineralizing events in a region or are not in favourable mineralization sites.

8. Conclusions

Spatially associated gold occurrences in a geological terrane are commonly thought to have formed during the same mineralizing event (Cheng, 2008; Groves et al., 1998), but this is not the case for the gold deposits from the northern Capricorn Orogen. Here we demonstrate that the Belvedere and Paulsens deposits, which are separated by only 6.5 km, and spatially associated with the same fault (and thus crustal architecture), have different geological histories despite their seemingly

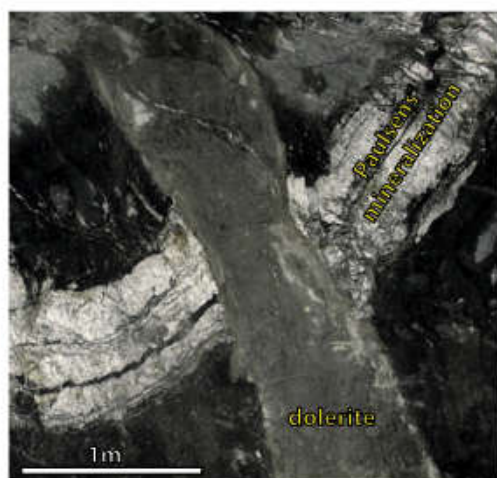


Fig. 6. Massive fine-grained dolerite dyke (~1m wide) in the drive wall at the Paulsens gold deposit. The dolerite is part of the same north-trending suite of dykes as the Belvedere dolerite, dated here at c. 2080 Ma. These dykes cross cut and offset auriferous, laminated quartz veins from the Lower mineralized zone at the Paulsens deposit. Level 1095E, face 36 viewed to the southeast.

similar appearance. Our results show that mineralized quartz–carbonate–arsenopyrite veins at Belvedere formed at c. 1680 Ma and are hosted within the c. 2080 Ma Belvedere dolerite, whereas the Paulsens deposit is hosted in a c. 2700 Ma mafic sill that was mineralized at c. 2400 Ma. Our results show that despite appearances, the Belvedere and Paulsens gold deposits are not the product of one unique mineralizing event, but formed at different times related to reactivation of major faults.

Acknowledgement

This project was funded through an ARC linkage grant (LP130100922), the Exploration Incentive Scheme and an industry scholarship by Northern Star Resources as a part of a PhD by I.O.H. Fielding. S.P. Johnson publishes with the permission of the director of the Geological Survey of Western Australia. The SHRIMP II at the John de Laeter Centre at Curtin University was used for all geochronology. We appreciated Sandra Occhipinti and Andrew Cross for constructive comments which helped to improve the manuscript.

Appendix

Analytical methods

A primary beam of O_2^- ions was focused through a 50 μ m Kohler aperture for baddeleyite and 30 μ m Kohler aperture for xenotime, producing an oval 10 μ m wide spot on the sample surface with a current of 0.2–0.6 nA. The secondary ion system was focused through a 100 μ m collector slit onto an electron multiplier to produce mass peaks with flat tops and a mass resolution (1% peak height) of 4795–5230.

Baddeleyite data were collected in sets of 7 scans, with baddeleyite reference material analysed every 3 sample analyses. Xenotime data were collected in sets of 7 or 8 scans, with xenotime reference materials analysed every 4–6 sample analyses. Count times per scan for Pb isotopes 204, background position 204.045, 206, 207, and 208 were 10 s, 10 s, 10 s, 30 s and 10 s, respectively.

Baddeleyite was analysed using the conventional zircon 9-peak run table, calibrated against baddeleyite reference material Phalaborwa (Heaman and LeCheminant, 1993). Instrumental mass fractionation (IMF) in $^{207}Pb/^{206}Pb$ ratios was monitored by repeated analysis of the 3465 Ma OGC zircon standard (OG1 of Stern et al. (2009)). No IMF correction was required since the measured values of OGC were in agreement with the reference value within 2 σ uncertainties.

Xenotime was analysed with a 9-peak run table following analytical protocols in Fletcher et al. (2004). Pb/U calibrations and matrix corrections for U and Th contents were based on concurrent measurements of the primary standard MG-1 (Fletcher et al., 2004) and secondary standards z6413 (XENO1) and z6410 (XENO2) (Stern and Rayner, 2003). Pb/Th was determined indirectly, using a fixed Th/U calibration (Fletcher et al., 2004). Matrix corrections for REE assumed the samples have REE abundances similar to Xeno1.

Raw data from analyses on xenotime were processed using the SQUID 2 add-in (v. 2.50.12.03.08) for Excel 2003 (Ludwig, 2009), and plotted using the ISOPLOT add-in (v. 3.76.12.02.24) (Ludwig, 2003). Common-Pb corrections were based on measured $^{204}Pb/^{206}Pb$ ratios and contemporaneous Pb composition according to the terrestrial Pb evolution model of Stacey and Kramers (1975). Matrix effect corrections were made for all xenotime data using procedures described by Fletcher et al. (2004). All ages are quoted with 95% confidence levels, whereas individual analyses are presented with 1 σ errors.

References

- Amdt, N.T., Nelson, D.R., Compston, W., Trendall, A.F., Thorne, A.M., 1991. The age of the Fortescue Group Hamersley Basin, Western Australia, from ion microprobe zircon U–Pb results. *Austral. J. Earth Sci.* 38 (3), 261–281.

- Bierlein, F.P., Groves, D.L., Goldfarb, R.J., Dubé, B., 2006. Lithospheric controls on the formation of provinces hosting giant orogenic gold deposits. *Mineral. Depos.* 40 (8), 874–886.
- Blockley, J. G., 1971. The lead, zinc and silver deposits of Western Australia, in Australia, G. S. o. W., ed., Volume Mineral Resources Bulletin 9: Perth, pp. 237.
- Cawood, P.A., Tyler, I.M., 2004. Assembling and reactivating the Proterozoic Capricorn Orogen: lithotectonic elements, orogenesis, and significance. *Precamb. Res.* 128 (3–4), 201–218.
- Cheng, Q., 2008. Non-linear theory and power-law models for information integration and mineral resources quantitative assessments. *Mathemat. Geosci.* 40 (5), 503–532.
- Cumming, G.L., Richards, J.R., 1975. Ore lead isotope ratios in a continuously changing earth. *Earth Planet. Sci. Lett.* 28 (2), 155–171.
- Fielding, I.O.H., Johnson, S.P., Zi, J.-W., Rasmussen, B., Mühling, J.R., Dunkley, D.J., Sheppard, S., Wingate, M.T.D., Rogers, J.R., 2017. Using in situ SHRIMP U–Pb monazite and xenotime geochronology to determine the age of orogenic gold mineralization: an example from the Paulsens mine. *South. Pilbara Crat. Econ. Geol.* 112 (5), 1205–1230.
- Fletcher, I.R., McNaughton, N.J., Aleinikoff, J.A., Rasmussen, B., Kamo, S.L., 2004. Improved calibration procedures and new standards for U–Pb and Th–Pb dating of Phanerozoic xenotime by ion microprobe. *Chem. Geol.* 209 (3–4), 295–314.
- Forman, F. G., 1938. The Melrose and Belvedere gold mines and vicinity, Mt Stewart Station, Ashburton Goldfields.
- Goldfarb, R.J., Groves, D.L., Gardoll, S., 2001. Orogenic gold and geologic time: a global synthesis. *Ore Geol. Rev.* 18 (1–2), 1–75.
- Groves, D.L., Cundie, K.C., Goldfarb, R.J., Hronsky, J.M.A., Vielreicher, R.M., 2005. 100th Anniversary special paper: secular changes in global tectonic processes and their influence on the temporal distribution of gold-bearing mineral deposits. *Econ. Geol.* 100 (2), 203–224.
- Groves, D.L., Goldfarb, R.J., Gebre-Mariam, M., Hagemann, S.G., Robert, F., 1998. Orogenic gold deposits: a proposed classification in the context of their crustal distribution and relationship to other gold deposit types. *Ore Geol. Rev.* 13 (1–5), 7–27.
- Hancock, E.A., Thorne, A.M., 2016. Mineralogy of gold from the Paulsens and Mount Olympus deposits, northern Capricorn Orogen. *Geological Survey of Western Australia, Record 2016/14*, pp. 16.
- Heaman, L.M., LeCheminant, A.N., 1993. Geochemistry of accessory minerals paragenesis and U–Pb systematics of baddeleyite (ZrO_2). *Chem. Geol.* 110 (1), 95–126.
- Hronsky, J.M., Groves, D.L., Loucks, R.R., Begg, G.C., 2012. A unified model for gold mineralisation in accretionary orogens and implications for regional-scale exploration targeting methods. *Mineral. Depos.* 47 (4), 339–358.
- Korsch, R.J., Doublier, M.P., 2016. Major crustal boundaries of Australia, and their significance in mineral systems targeting. *Ore Geol. Rev.* 76, 211–228.
- Johnson, S.P., Korhonen, F.J., Kirkland, C.L., Cliff, J.B., Belousova, E.A., Sheppard, S., 2017. An isotopic perspective on growth and differentiation of proterozoic orogenic crust: from subduction magmatism to cratonization. *LITHOS* 268–271, 76–86.
- Johnson, S.P., Sheppard, S., Rasmussen, B., Wingate, M.T.D., Kirkland, C.L., Mühling, J.R., Fletcher, I.R., Belousova, E.A., 2011. Two collisions, two sutures: Punctuated pre-1950 Ma assembly of the West Australian Craton during the Ophthalman and Glenburgh Orogenies. *Precamb. Res.* 189 (3–4), 239–262.
- Johnson, S.P., Thorne, A.M., Tyler, I.M., Korsch, R.J., Kennett, R.L.N., Cutten, H.N., Goodwin, J., Blay, O., Blewett, R.S., Joly, A., Dentith, M.C., Aitken, A.R.A., Holzschult, J., Salmon, M., Reading, A., Heinonen, G., Boren, G., Ross, J., Custellon, R.D., Fomin, T., 2013. Crustal architecture of the Capricorn Orogen Western Australia and associated metallogeny. *Austral. J. Earth Sci.* 60 (6–7), 681–705.
- Korhonen, F.J., Johnson, S.P., Wingate, M.T.D., Fletcher, I.R., Dunkley, D.J., Roberts, M.P., Sheppard, S., Mühling, J.R., Rasmussen, B., 2017. Radiogenic heating and orato-magmatic plate stresses as drivers for intraplate orogeny. *J. Metamorph. geol.*
- Krapel, B., 1999. Stratigraphic record of an Atlantic-type global tectonic cycle in the Palaeoproterozoic Ashburton Province of Western Australia. *Austral. J. Earth Sci.* 46 (1), 71–87.
- Ludwig, K.R., 2003. Isoplot/Ex version 3.00. A geochronological toolkit for Microsoft Excel: Berkeley Geochronology Centre Special Publication pp. 73.
- Ludwig, K.R., 2009. Squid 2.50, a user's manual. Berkeley Geochronology Centre, Berkeley, California, USA pp. 95.
- Manson, R. J., 1979. Copper mineralization in Western Australia, in Australia, G. S. o. W., ed., Volume Mineral Resources Bulletin 13 Perth, pp. 227.
- Martin, D.M., Morris, P.A., 2010. Tectonic setting and regional implications of ca.2.2 Ga mafic magmatism in the southern Hamersley Province, Western Australia. *Austral. J. Earth Sci.* 57 (7), 911–931.
- Martin, D.M., Thorne, A., 2004. Tectonic setting and basin evolution of the Bangemall Supergroup in the northwestern Capricorn Orogen. *Precamb. Res.* 128 (3), 385–409.
- Meffre, S., Large, R.R., Steadman, J.A., Gregory, D.D., Stepanov, A.S., Kamenetsky, V.S., Ehrig, K., Scott, R.J., 2016. Multi-stage enrichment processes for large gold-bearing ore deposits. *Ore Geol. Rev.* 76, 268–279.
- Northern Star Resources Limited, 2015. Northern Star Resources Limited 2015 annual report, (<http://www.nsrld.com/wp-content/uploads/2015/08/NST-Annual-Report-2015-26-8-2015-new-cover1.pdf>).
- Northern Star Resources Limited, July, 2015. Northern Star Paulsens operations fact sheet, (<http://www.nsrld.com/wp-content/uploads/2015/08/NSR-Paulsens-Operations-Fact-Sheet-July-2015-FINAL.pdf>).
- Norun, E., 2005, 14 November 2003 to 13 November 2004, Paulsens Project, E08/665, E08/906, E08/1125, E47/977, E47/1134, E47/1135, M08/99, M08/196 and M08/222, Combined Reporting Form C211/1997: Nustar Mining Corporation Limited; Geological Survey of Western Australia Open-file report a070119.
- Occhipinti, S.A., Sheppard, S., Passchier, C., Tyler, I.M., Nelson, D.R., 2004. Palaeoproterozoic crustal accretion and collision in the southern Capricorn Orogen: the Glenburgh Orogeny. *Precamb. Res.* 128 (3–4), 237–255.

- Owen, S., 2000. Ashburton Project, Exploration licence 47/902 Belvedere and Tombstone Prospects: Tailpan Resources N.L.; Geological Survey of Western Australia Open-file report, a61500.
- Pickard, A.L., 2002. SHRIMP U-Pb zircon ages of tuffaceous mudrocks in the Brockman iron formation of the Hamersley range Western Australia. *Austral. J. Earth Sci.* 49 (3), 491–507.
- Rasmussen, B., Fletcher, L.R., Muhliling, J.R., 2007a. In situ U-Pb dating and element mapping of three generations of monazite: Unravelling cryptic tectonothermal events in low-grade terranes. *Geochim. Cosmochim. Acta* 71 (3), 670–690.
- Rasmussen, B., Fletcher, L.R., Muhliling, J.R., Thorne, W.S., Broadbent, G.C., 2007b. Prolonged history of episodic fluid flow in giant hematite ore bodies: evidence from in situ U-Pb geochronology of hydrothermal xenotime. *Earth Planet. Sci. Lett.* 258 (1–2), 249–259.
- Rasmussen, B., Fletcher, L.R., Sheppard, S., 2005. Isotopic dating of the migration of a low-grade metamorphic front during orogenesis. *Geology* 33 (10), 773–776.
- Richards, J.R., Fletcher, L.R., Blockley, J.G., 1981. Pilbara galeas: Precise isotopic assay of the oldest Australian leads model ages and growth-curve implications. *Mineral. Depos.* 16 (1), 7.
- Seymour, D. B., Thorne, A. M., and Blight, D. F., 1988, Wyloo, W.A., (2nd ed.): Western Australia Geological Survey, 1:250 000 Geological Series Explanatory Notes, p. 36.
- Sheppard, S., Bodorkos, S., Johnson, S. P., Wingate, M. T. D., and Kirkland, C. L., 2010. The Paleoproterozoic Capricorn Orogeny: intracontinental reworking not continent–continent collision, Volume 108: Geological Survey of Western Australia, Report 108, pp. 33.
- Sheppard, S., Farrell, T. R., Bodorkos, S., Hollingsworth, D., Tyler, I. M., and Pirajoo, F., 2006. Late Paleoproterozoic (1680–1620 Ma) sedimentation, magmatism and tectonism in the Capricorn Orogen: Geological Survey of Western Australia extended abstracts, pp. 2.
- Sheppard, S., Occhipinti, S.A., Nelson, D.R., 2005. Intracontinental reworking in the Capricorn Orogen, Western Australia: the 1680–1620 Ma Mangaroon Orogeny. *Austral. J. Earth Sci.* 52 (3), 443–460.
- Sheppard, S., Occhipinti, S.A., Tyler, I.M., 2004. A 2005–1970 Ma Andean-type batholith in the southern Gascoyne Complex, Western Australia. *Precamb. Res.* 128 (3–4), 257–277.
- Sheppard, S., Rasmussen, B., Muhliling, J.R., Farrell, T.R., Fletcher, L.R., 2007. Grenvillian-aged orogenesis in the Palaeoproterozoic Gascoyne Complex, Western Australia: 1030–950Ma reworking of the Proterozoic Capricorn Orogen. *J. Metamorp. Geol.* 25 (4), 477–494.
- Smith, R.E., Percdrix, J.L., Parks, T.C., 1982. Burial Metamorphism in the Hamersley Basin Western Australia. *J. Petrol.* 23 (1), 75–102.
- Stacey, J.S., Kramers, J.D., 1975. Approximation of terrestrial lead isotope evolution by a two-stage model. *Earth Planet. Sci. Lett.* 26, 207–221.
- Stern, R. A., and Rayner, N., 2003. Ages of several xenotime megacrysts by ID-TIMS: potential reference materials for ion microprobe U-Pb geochronology: Radiogenic Age and Isotopic Studies: Report 16: Geological Survey of Canada: Current Research 2003-F1, pp. 7.
- Stern, R.A., Bodorkos, S., Kamo, S.L., Hickman, A.H., Corfu, F., 2009. Measurement of SIMS instrumental mass fractionation of Pb isotopes during zircon dating. *Geostand. Geoanal. Res.* 33, 145–168.
- Thorne, A. M., and Seymour, D. B., 1991, *Geology of the Ashburton Basin Western Australia*, Geological Survey of Western Australia, Bulletin 139, pp. 162.
- Thorne, A.M., Trendall, A.F., 2001. Geology of the Fortescue Group, Pilbara Craton, Western Australia, Geological Survey of Western Australia. Bulletin 144, 266.
- Trendall, A.F., Compston, W., Nelson, D.R., De Laeter, J.R., Bennett, V.C., 2004. SHRIMP zircon ages constraining the depositional chronology of the Hamersley Group Western Australia. *Austral. J. Earth Sci.* 51 (5), 621–644.
- Tyler, I.M., Thorne, A.M., 1990. The northern margin of the Capricorn Orogen, Western Australia—an example of an Early Proterozoic collision zone. *J. Struct. Geol.* 12 (5–6), 685–701.
- Tyler, I.M., 1991. The Geology of the Sylvania Inlier and the Southeast Hamersley Basin, Geological Survey of Western Australia. Bulletin 138, 124.
- White, A.J.R., Smith, R.E., Nadoll, P., Legras, M., 2014. Regional-scale metasomatism in the Fortescue group volcanics Hamersley Basin, Western Australia: implications for hydrothermal ore systems. *J. Petrol.* 55 (5), 977–1009.
- Wingate, M.T.D., Compston, W., 2000. Crystal orientation effects during ion microprobe U-Pb analysis of baddeleyite. *Chem. Geol.* 168, 75–97.
- Wingate, M. T. D., Lu, Y., Blay, O., and Johnson, S. P., 2017a, 206949: dolerite dyke, Tin Hut Bore: Geochronology Record 1432: Geological Survey of Western Australia, pp. 4.
- Wingate, M. T. D., Lu, Y., Blay, O., and Johnson, S. P., 2017b, 206953: dolerite sill, Tin Hut Bore: Geochronology Record 1433: Geological Survey of Western Australia, pp. 4.

APPENDIX 1C: MOUNT OLYMPUS

STATEMENT OF CONTRIBUTION OF OTHERS

Title of Paper: Linking gold mineralization to regional-scale drivers of mineral systems using in situ U–Pb geochronology and pyrite LA-ICP-MS element mapping.

Publication status: Published

AUTHOR CONTRIBUTIONS

By signing the Statement of Authorship, each author certified that their stated contribution to the publication is accurate and that permission is granted for the publication to be included in the candidate's thesis.

Name of Principal Author: Imogen O. H. Fielding

Contribution to the paper: Led all aspects of the research including, field work, sample collection and sample preparation for SHRIMP geochronology. SHRIMP Data acquisition through to interpretation of all geochronology. Interpretation of LA-ICP-MS pyrite maps. Drafting of manuscript and images.

Overall Percentage: 75%

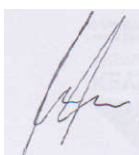
Signature: 

Date: 23/04/2018

Name of Co-Author: Simon P. Johnson

Contribution to the Paper: Assisted with sample collection, field work, data interpretation, editing and revision of the manuscript.

Overall Percentage: 5%

Signature: 

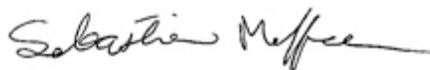
Date: 24/04/2018

Name of Co-Author: Sebastien Meffre

Contribution to the Paper: Assistance with LA-ICP-MS data reduction and processing, and editing of manuscript.

Overall Percentage: 5%

Signature:



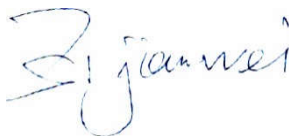
Date: 04/04/2018

Name of Co-Author: Jianwei Zi

Contribution to the Paper: Assistance with phosphate geochronology data acquisition, processing and interpretation.

Overall Percentage: 5%

Signature:



Date: 28/04/2018

Name of Co-Author: Stephen Sheppard

Contribution to the Paper: Assisted with editing the manuscript.

Overall Percentage: 5%

Signature:



Date: 21/04/2018

Name of Co-Author: Ross R. Large

Contribution to the Paper: Assistance with LA-ICP-MS data collection and processing, and editing of manuscript.

Overall Percentage: 2%

Signature:



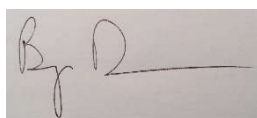
Date: 24/04/2018

Name of Co-Author: Birger Rasmussen

Contribution to the Paper: Assisted with manuscript editing.

Overall Percentage: 3%

Signature:



Date: 23/04/2018

COPYRIGHT

Imogen O. H. Fielding, Simon P. Johnson, Sebastien Meffre, Jian-Wei Zi, Stephen Sheppard, Ross R. Large and Birger Rasmussen., Linking gold mineralization to regional-scale drivers of mineral systems using in situ U–Pb geochronology and pyrite LA-ICP-MS element mapping: *Geoscience Frontiers*, v. 10, p. 89–105, doi: <https://doi.org/10.1016/j.gsf.2018.06.005> is published as an open access article under a Creative Commons Attribution-Non Commercial-No Derivs (CC BY-NC-ND) and can be reproduced with no copyright infringements as a part of this thesis. Further details can be found at <https://creativecommons.org/licenses/by-nc-nd/4.0/>



Contents lists available at ScienceDirect
China University of Geosciences (Beijing)

Geoscience Frontiers

journal homepage: www.elsevier.com/locate/gsf



Research Paper

Linking gold mineralization to regional-scale drivers of mineral systems using in situ U–Pb geochronology and pyrite LA-ICP-MS element mapping

Imogen O.H. Fielding^{a,*}, Simon P. Johnson^b, Sebastien Meffre^c, Jianwei Zi^{d,e},
Stephen Sheppard^f, Ross R. Large^c, Birger Rasmussen^g

^aDepartment of Applied Geology, Curtin University, Kent Street, Bentley, WA, 6102, Australia

^bGeological Survey of Western Australia, 100 Plain Street, East Perth, WA, 6004, Australia

^cCODES ARC Centre of Excellence in Ore Deposits, University of Tasmania, Private Bag 126, Hobart, TAS, 7001, Australia

^dState Key Lab of Geological Processes and Mineral Resources, China University of Geosciences, Wuhan 430074, China

^eJohn de Laeter Centre, Curtin University, Kent Street, Bentley, WA, 6102, Australia

^fCalidus Resources Ltd, Suite 12, 11 Ventnor Avenue, West Perth, WA, 6005, Australia

^gSchool of Earth Sciences, The University of Western Australia, Perth, WA, 6009, Australia

ARTICLE INFO

Article history:

Received 13 March 2018

Received in revised form

24 April 2018

Accepted 17 June 2018

Available online 24 July 2018

Keywords:

Geochronology

Xenotime

SHRIMP

LA-ICP-MS

Gold mineralization

Capricorn orogen

ABSTRACT

Proterozoic orogens commonly host a range of hydrothermal ores that form in diverse tectonic settings at different times. However, the link between mineralization and the regional-scale tectonothermal evolution of orogens is usually not well understood, especially in areas subject to multiple hydrothermal events. Regional-scale drivers for mineral systems vary between the different classes of hydrothermal ore, but all involve an energy source and a fluid pathway to focus mineralizing fluids into the upper crust. The Mount Olympus gold deposit in the Proterozoic Capricorn Orogen of Western Australia, was regarded as an orogenic gold deposit that formed at ca. 1738 Ma during the assembly of Proterozoic Australia. However, the trace element chemistry of the pyrite crystals closely resembles those of the Carlin deposits of Nevada, with rims that display solid solution gold accompanied by elevated As, Cu, Sb, Hg, and Tl, surrounding gold-poor cores. New SHRIMP U–Pb dating of xenotime intergrown with auriferous pyrite and ore-stage alteration minerals provided a weighted mean $^{207}\text{Pb}/^{206}\text{Pb}$ date of 1769 ± 5 Ma, interpreted as the age of gold mineralization. This was followed by two discrete episodes of hydrothermal alteration at 1727 ± 7 Ma and 1673 ± 8 Ma. The three ages are linked to multiple reactivation of the crustal-scale Nanjilgardy Fault during repeated episodes of intracratonic reworking. The regional-scale drivers for Carlin-like gold mineralization at Mount Olympus are related to a change in tectonic regime during the final stages of the intracratonic 1820–1770 Ma Capricorn Orogeny. Our results suggest that substantial sized Carlin-like gold deposits can form in an intracratonic setting during regional-scale crustal reworking.

© 2018, China University of Geosciences (Beijing) and Peking University. Production and hosting by Elsevier B.V. This is an open access article under the CC BY-NC-ND license (<http://creativecommons.org/licenses/by-nc-nd/4.0/>).

1. Introduction

The mineral systems concept describes how an ore deposit is the expression of a number of processes operating at a range of spatial and temporal scales (Wyborn et al., 1994; McCuaig and Hronsky, 2014; Huston et al., 2016). At the largest scale, mineralization is driven by a regional energy source with the transport of

hydrothermal fluids or magmas along crustal-scale pathways (McCuaig and Hronsky, 2014; Huston et al., 2016). Whereas the smallest scale relates to local variations within an individual prospect or deposit, such as alteration mineralogy, element association, and the type of host rocks to mineralization (Robert et al., 2007). The absolute age of mineralization and its timing relative to regional-scale tectonothermal events, is often poorly known but is critical for understanding the causes of ore formation (Hronsky et al., 2012). Without this information the key factors in ore generation may not be correctly identified, particularly in areas that have been subject to multiple hydrothermal or crustal reworking events (e.g. Rasmussen et al., 2006).

* Corresponding author.

E-mail address: imogen.fielding@postgrad.curtin.edu.au (I.O.H. Fielding).

Peer-review under responsibility of China University of Geosciences (Beijing).

<https://doi.org/10.1016/j.gsf.2018.06.005>

1674-9871/© 2018, China University of Geosciences (Beijing) and Peking University. Production and hosting by Elsevier B.V. This is an open access article under the CC BY-NC-ND license (<http://creativecommons.org/licenses/by-nc-nd/4.0/>).

The drivers for orogenic and epithermal gold mineralization are relatively obvious. Orogenic deposits are associated with active margins undergoing compressional tectonic activity during accretionary or collisional orogenic events (Groves et al., 1998; Goldfarb et al., 2001), and epithermal deposits are intimately associated with coeval magmatism (e.g. Simmons et al., 2005). However, the drivers for Carlin-type deposits (Cline et al., 2005) are more enigmatic because such deposits do not always have a clear link between regional-scale tectonomagmatic activity and crustal architecture (e.g. Hu et al., 2002; Cline et al., 2005; Muntean et al., 2011).

The Mount Olympus gold deposit is located in the northern Capricorn Orogen within the West Australian Craton (Fig. 1). The area has been subjected to limited research with few peer reviewed publications (e.g. Şener et al., 2005; Wells et al., 2016), and the most comprehensive ore-body descriptions are sourced from conference abstracts and open-file company reports (e.g. Morant and Doeppel, 1997; Young et al., 2003). Mount Olympus has many of the characteristics of a Carlin-type deposit including strata-bound ore, invisible gold concentrated in arsenian pyrite, and ore-stage alteration assemblages characterized by quartz, illite and sericite with the removal of carbonate minerals (Young et al., 2003). Despite these similarities, Şener et al. (2005) linked xenotime growth (and gold deposition) at ca. 1738 Ma to orogenic events related to the assembly of Proterozoic Australia. However, there are no orogenic events known in Western Australia at ca. 1738 Ma, which falls between the 1820–1770 Ma Capricorn Orogeny and the 1680–1620 Ma Mangaroon Orogeny, both of which represent periods of intracratonic reworking that resulted in deformation, metamorphism and granite intrusion inboard of the plate margin (Sheppard et al., 2005, 2010).

This study has two aims: (1) to review the classification of gold mineralization at Mount Olympus by assessing both the macroscopic characteristics and the distribution of trace element in pyrite crystals, and making comparisons to documented Carlin-type and orogenic gold deposits (e.g. Large et al., 2009); and (2) to present

new in situ U–Pb xenotime geochronological data obtained using the Sensitive High Resolution Ion Microprobe (SHRIMP) to determine the timing of hydrothermal events, including gold mineralization. These data are then integrated with the record of the well-established crustal architecture and tectonothermal events in the West Australian Craton (Johnson et al., 2013) to investigate the large-scale mineral system processes associated with the Mount Olympus deposit.

2. Geological background

The Capricorn Orogen is a zone of variably deformed rocks between the Pilbara and Yilgarn cratons of Western Australia (Fig. 1; Tyler and Thorne, 1990). The orogen records the two-stage assembly of the West Australian Craton by ca. 1950 Ma (Johnson et al., 2011), as well as at least five younger episodes of intracratonic reworking spanning over a billion years (Sheppard et al., 2005, 2007; Johnson et al., 2017; Korhonen et al., 2017). In the northern part of the Capricorn Orogen, Paleoproterozoic siliciclastic, carbonate and volcanic rocks of the Wyloo and Shingle Creek Groups were deformed during the 1820–1770 Ma Capricorn Orogeny (Thorne and Seymour, 1991). Mineralization throughout the region has a spatial association with crustal-scale faults (Johnson et al., 2013). The Nanjilgardy Fault (Fig. 1), in particular, has experienced multiple reactivations that led to deposition and remobilization of various styles of gold mineralization throughout the northern Capricorn Orogen (Johnson et al., 2013; Fielding et al., 2017).

3. Deposit description

The Mount Olympus gold deposit has a total remaining resource of 15 million tonnes (Mt) at 2.2 g/t containing ~1 Moz of gold (Northern Star Resources Limited, 2015). Mineralization occurs where the Zoe Fault, a second order splay of the Nanjilgardy Fault,

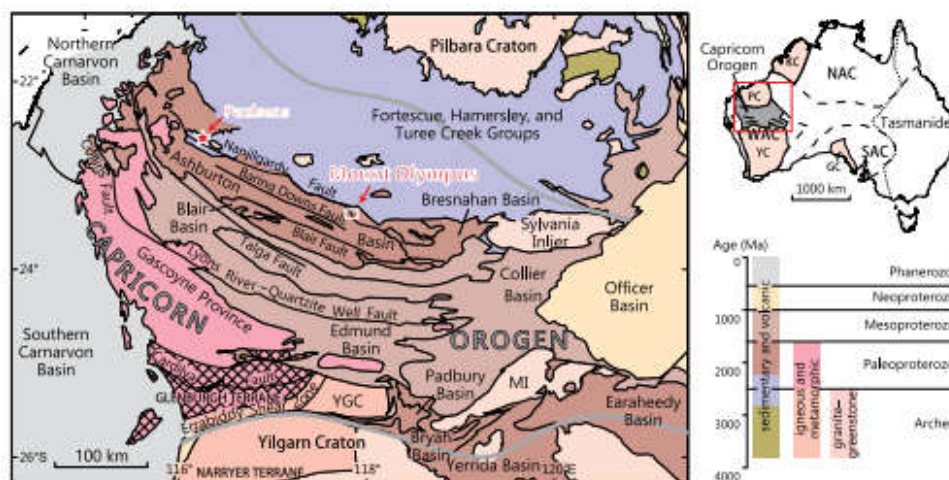


Figure 1. Regional geology of the northern Capricorn Orogen showing the location of Mount Olympus and Paulsens gold mines. White box indicates the inset map shown in Fig. 2A. Abbreviations: GC = Gawler Craton, KC = Kimberley Craton, MI = Marymia Inlier, NAC = North Australian Craton, PC = Pilbara Craton, SAC = South Australian Craton, WAC = West Australian Craton, YC = Yilgarn Craton, YGC = Yilgarn Gneiss Complex (after Johnson et al., 2013).

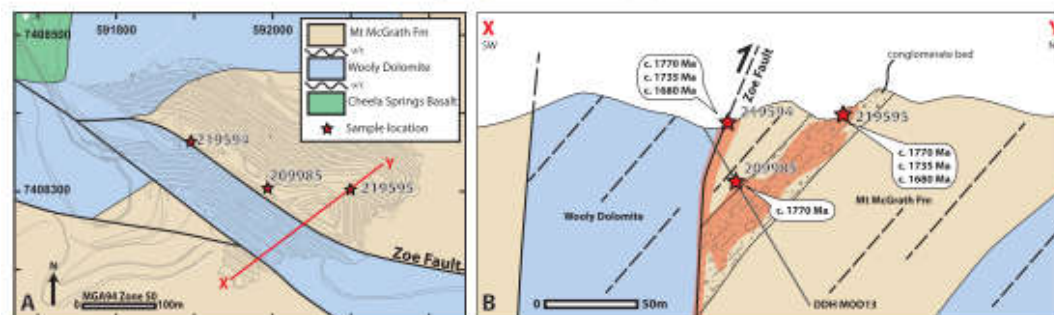


Figure 2. (A) Prospect scale geological map of the Mount Olympus pit showing geochronology sample locations. (B) Schematic cross section of the Mount Olympus ore body with geochronology sample locations.

juxtaposes conglomerate and coarse-grained sandstone of the Mount McGrath Formation against dolomitic mudstone of the Woolly Dolomite (Fig. 2; Morant and Doepele, 1997; Krapež et al., 2015). The Zoe Fault is a dextral transpressional fault which has a strong control on the location of gold mineralization and is likely to have been the primary conduit for mineralizing fluids (Young et al., 2003).

Two distinct types of mineralized lodes are evident in the Mount Olympus pit: (1) strata-bound ore where arsenian pyrite crystals up to 1 cm in diameter are disseminated within carbonaceous and ferruginous conglomerate and sandstone of the Mount McGrath Formation, and (2) fault-hosted mineralization is associated with pyrite and graphite, or in rare instances is associated with strongly deformed quartz veins and stringers along the Zoe Fault (Fig. 2B; Morant and Doepele, 1997; Young et al., 2003). In both lodes, gold forms microscopic inclusions in pyrite or as a solid solution within visibly zoned arsenian pyrite (Young et al., 2003). Ore-stage alteration assemblages are reported to have formed at up to 350 °C at 1–2 kbar (Young et al., 2003) and include quartz, muscovite, kaolin-group phases (kaolinite and dickite) and pyrophyllite, with the removal of chlorite and carbonate minerals (Wells et al., 2016).

4. Methods

4.1. LA-ICP-MS

Pyrite from within mineralized zones of the Mount Olympus deposit were collected from diamond drill cores MOD13 and NMOD002 (Table 1) for analysis by LA-ICP-MS. Polished 25 mm diameter rock mounts were prepared and pyrites were etched using a dilute nitric acid solution to reveal any internal growth zones in order to select areas suitable for trace element mapping by LA-ICP-MS. Trace element mapping of pyrite crystals were performed at the ARC Centre of Excellence in Ore Deposits LA-ICP-MS facility at

the University of Tasmania using the New Wave 213-nm solid-state laser microprobe coupled to an Agilent 4500 quadrupole ICP-MS. The procedure outlined in Large et al. (2009) was followed and described briefly below.

Trace element distribution maps were generated by ablating parallel lines in a grid pattern. Beam sizes of 15, 22, 35 and 47 µm were used with a laser beam repetition rate of 10 Hz with energy maintained at 4.5 J/cm². Rastering speed for each line was equal to the beam size per second (i.e., 15–47 µm/s). Analysis consisted of 28 elements including Na, Mg, Al, Si, K, Ca, Ti, V, Mn, Fe, Co, Ni, Cu, Zn, As, Se, Mo, Ag, Sb, Te, W, Pt, Au, Hg, Tl, Pb, Bi and U. Acquisition time was set to 0.03 s for gold, 0.008 s for chalcophile elements, and 0.002 s for other elements resulting in a total quadrupole sweep time of 0.2 s (including deadtime).

Data were collected in counts per second (cps) and later converted to parts per million (ppm). The conversion was undertaken using the in-house standard STDGL2b-2, analyzed both before and after each sample with a 74 µm spot size, laser beam repetition rate of 10 Hz and energy of 4 J/cm². The standard comprises a homogenous mix of powdered sulfide and trace elements of known concentrations, fused into a lithium borate glass disk (Danyushevsky et al., 2011). Instrumental mass bias was initially determined using standard laser ablation data reduction techniques then applied to each quadrupole sweep (i.e., each pixel in the image) assuming stoichiometric Fe (456,000 ppm) in pyrite for each line of the image. The data are expected to be accurate for the pyrite in each image, but will tend to underestimate the concentrations for other mineral phases due to the different behavior of other minerals during ablation relative to pyrite (matrix effects). The ratios between elements will not be affected by these problems. Hg was not quantified due to the lack of standards and the volatility of the element. The Hg counts per second images can be used on a qualitative basis to identify high and low Hg zones.

Table 1
LA-ICP-MS sample location, descriptions and gold grades.

Hole ID	MGA94 zone 50		Depth (m)	Description	Whole rock Au assay from diamond core
	East	North			
NMOD002	592408	7407945	377.7	Semi-massive pyrite in silicified black shale	4.86 ppm (377–378 m)
NMOD002	592408	7407945	376.2	Semi-massive pyrite in silicified black shale	3.58 ppm (376–377 m)
MOD13	591962	7408248	130.6	Sericite altered sandstone with coarse euhedral pyrite and arsenopyrite	1.92 ppm (130–131 m)
MT090	592159	7408094	262.3	Sericite altered siltstone with coarse euhedral pyrite	0.92 ppm (262–263 m)

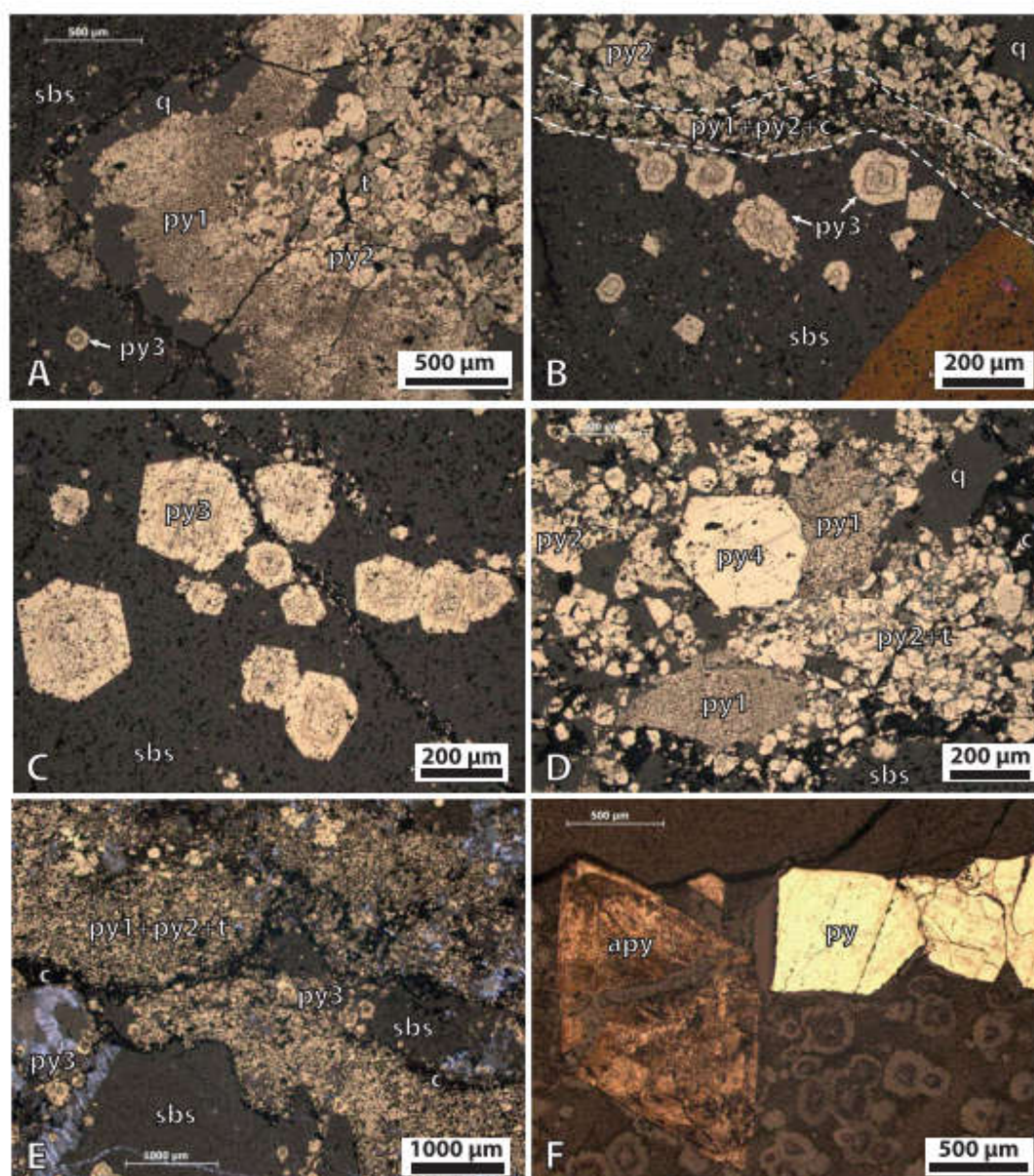


Figure 3. Textures of pyrite types at the Mount Olympus deposit. (A) NMOD002 377.7 m in depth showing py1 surrounding py2 and tetrahedrite. (B) NMOD002 377.7 m in depth showing a narrow band of py1, py2 and carbonaceous material separating py2 from py3. (C) NMOD002 376.2 m in depth growth zoning in py3. (D) NMOD002 376.2 m in depth py1, py2 and large euhedral py4. (E) Py1, py2 and tetrahedrite separated from py3 by a carbonaceous rich band and silicified black shale. (F) MOD13 130.6 m in depth, showing large pyrite and arsenopyrite crystals from the strata-bound mineralization. Abbreviations: py=pyrite, t=tetrahedrite, sbs=silicified black shale, q=quartz, c=carbonaceous material, apy=arsenopyrite.

4.2. Geochronology

Three mineralized samples were examined by optical and scanning electron microscope to identify xenotime suitable for geochronology. Small disks of thin section containing xenotime crystals for SHRIMP analysis were drilled out of the polished thin-sections before being cast into 25 mm epoxy SHRIMP mounts. Xenotime standards MG1, Xeno1 and Xeno2 were placed on a separate SHRIMP mount that was gold coated along with the sample mounts. SHRIMP U–Pb dating of xenotime followed established procedures for small-spot, in situ analysis as outlined by Fletcher et al. (2000, 2004).

A primary beam of O^{2-} ions was focused through a 30 μ m Kohler aperture to produce an oval 10–15 μ m wide spot on the sample surface with a current of 0.2–0.8 nA. The secondary ion system was focused through a 100 μ m collector slit onto an electron multiplier to produce mass peaks with flat tops and a mass resolution of >5200 in all sessions. Background counts from scattered ions were reduced using a flight retardation lens, which is known to cause slight session-dependent instrumental mass fractionation (IMF) of Pb isotopes. IMF corrections were applied to all analyses.

Data were collected in sets of 8 scans, with xenotime reference materials analyzed every 4–6 sample analyses. Count times per scan for background position 204.045, and Pb isotopes 204, 206, 207, and 208 were 10, 10, 10, 30 and 10 s, respectively. Xenotime was analyzed with a 9-peak run table following analytical protocols detailed by Fletcher et al. (2004). Pb/U calibrations and matrix corrections for U and Th contents were based on concurrent measurements of the standards MG-1 (Fletcher et al., 2004) and z6413 ("Xeno1"; Stern and Rayner, 2003). Pb/Th was determined indirectly, using a fixed Th/U calibration (Fletcher et al., 2004). Matrix corrections for REE assumed the samples have REE abundances similar to Xeno1.

Raw data from analyses were processed using the SQUID 2 add-in (v. 2.50.12.03.08) for Excel 2003 (Ludwig, 2009), and plotted using the ISOPLOT add-in (v. 3.76.12.02.24; Ludwig, 2003). Common-Pb corrections were based on measured $^{204}\text{Pb}/^{206}\text{Pb}$ ratios and contemporaneous Pb composition according to the terrestrial Pb evolution model of Stacey and Kramers (1975). Matrix effect corrections were made for all xenotime data using procedures described by Fletcher et al. (2004). Pooled ages are quoted with 95% confidence levels, whereas individual analyses are presented with 1 σ errors.

5. Results

5.1. LA-ICP-MS

The content and distribution of trace elements within massive pyrite from gold-rich samples differs between those in

carbonaceous-rich material from the Zoe Fault (NM0002), and those within sericite-altered sandstone (MOD13) from strata-bound mineralization.

5.1.1. Zoe Fault

Polished 25 mm diameter rock mounts were prepared of massive pyrite-bearing black shale from the Zoe Fault in drill core NM0002 at 377.7 m and 376.2 m to investigate the textures and internal trace element zoning within the pyrite. These samples are from a zone of high-grade mineralization containing whole-rock gold assay results of 3.58 ppm (376–377 m) and 4.86 ppm (377–378 m). Two areas of pyrite from the thin sections at 377.7 m and two at 376.2 m, were mapped in detail by LA-ICP-MS.

Four types of pyrite have been defined in samples from NM0002 (Fig. 3A–E) with a paragenetic sequence from pyrite 1 (py1) to pyrite 4 (py4) summarized in Table 2. Py1 comprises micro-crystal aggregates (Fig. 3A, D) which often form in carbon-rich horizons (Fig. 3B). Py2 is composed of coarse-grained, subhedral pyrite that is commonly intergrown with tetrahedrite (Fig. 3A, B, D), or along carbonaceous layers (Fig. 3B). Py3 forms within the silicified shale matrix as euhedral crystals with internal zoning that shows a change from the cubic to pyritohedral crystal form from the internal zone to the rim (Fig. 3B and C). Py4 is a coarse, inclusion-free pyrite up to 300 μ m across (Fig. 3D).

Trace element images of each type of pyrite show that py1 has a mean Au grade of 8 ppm and is also enriched in As, Ti \pm Pb (Figs. 4 and 5). Py2 is low in both Au and As (Fig. 6), with a mean Au content of 2 ppm and is often intergrown with tetrahedrite which is enriched in Cu, Zn, Ag, Sb, Hg (Figs. 4 and 5). Py3 is zoned with an internal growth band enriched in Au (Figs. 6 and 7) and has the highest gold values (up to 429 ppm) of all samples analyzed. The core zone contains minor Hg, Pb and Bi with a mean Au content of 5 ppm, the internal zone has elevated Au, As, Cu, Hg, Ti and Sb and a mean Au content of 67 ppm, and the rim zone is Co and Ni rich and has a gold content of 4 ppm (Fig. 7). The interface zone between areas with abundant py1, py2 and tetrahedrite against areas of silicified black shale containing py3 is commonly defined by a band of carbonaceous material (Fig. 3B, E) enriched in Au, Mo, V, U and Al (Fig. 6). Py4 has low trace elements concentrations and does not contain any gold (Fig. 5).

5.1.2. Strata-bound mineralization

Polished mounts were prepared from a sericite-altered sandstone with a whole rock gold assay of 1.92 ppm (130–131 m) collected from diamond drill core MOD13 at 130.6 m (Fig. 3F). The sample contains abundant, coarse, euhedral pyrite and arsenopyrite crystals. The pyrite has a thick (100–300 μ m) diffusive rim zone with a mean Au value of 55 ppm. This surrounds a core with lower values of both As and Au (mean 12 ppm Au). These pyrites have no other trace element associations (Fig. 8).

Table 2
Summary of paragenetic sequence from py1 to py4.

Drill hole	Paragenesis	Lode	Description	Trace element association
NM0002	Py1	Zoe Fault	Micro-crystals aggregates; formed in carbon band commonly with py2 and tetrahedrite	Au 7.78 ppm; As, Ti \pm Pb
NM0002	Py2	Zoe Fault	Coarse grained subhedral pyrite; commonly intergrown with tetrahedrite; occurs with py1 in carbon rich bands	Low levels of Au (1.85 ppm) and As
NM0002	Py3	Zoe Fault	Euhedral pyrite with internal zonation; internal band is cubic, rim is pyritohedral	Core: Au 4.85 ppm; Hg-Pb-Bi Internal band: Au 67.28 ppm; Au-As-Cu-Hg-Ti-Sb Rim: Au 3.56 ppm; Co-Ni No Au; depleted in trace elements Cu-Zn-Ag-Sb-Hg
NM0002	Py4	Zoe Fault	Coarse (>300 μ m) clear pyrite	Au 55.06 ppm; As enriched
NM0002	Tetrahedrite	Zoe Fault	Coarse grained and intergrown with py2	
MOD13		Strata-bound	Coarse euhedral pyrite and arsenopyrite; thick (100–300 μ m) diffusive rim zone	

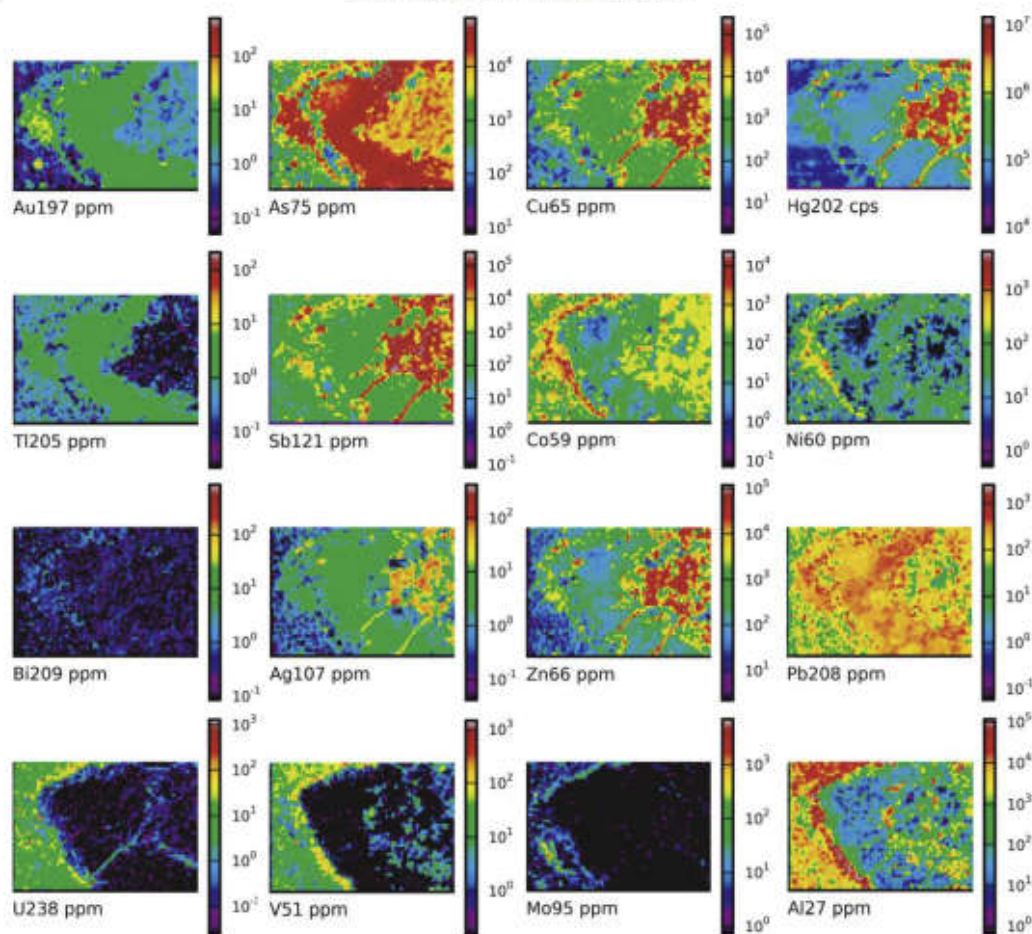


Figure 4. LA-ICP-MS images of trace elements in pyrite from NMDC002 377.7 m depth showing py2 and tetrahedrite surrounded by a py1 (refer to Fig. 3A). Py1 is associated with elevated Au, As, Tl and Pb, py2 is slightly enriched in Au and As and tetrahedrite is enriched in Cu, Hg, Sb, Ag and Zn.

6. Geochronology

6.1. GSWA 219594: Zoe Fault mineralization

A mineralized sample from the Zoe Fault (MGA 94 Zone 50 591903E, 7408364N) comprising brecciated pyrite (py1–4), carbonaceous material and quartz veins, contained small xenotime crystals (<20 μm diameter) in the brecciated parts of the sample. The xenotime commonly forms overgrowths on zircon crystals (Fig. 9A) and contains inclusions of quartz, muscovite and rutile.

Twenty-six analyses were conducted on 20 xenotime crystals with U contents ranging from 1053 ppm to 4638 ppm and Th contents between 392 ppm and 8441 ppm. Three analyses >10% discordant and two analyses with imprecise data due to poor spot placement were excluded from the age determination. The remaining 21 analyses yielded three distinct age modes (Fig. 10A, Table 3) with weighted mean $^{207}\text{Pb}^*/^{206}\text{Pb}^*$ dates of 1768 ± 8 Ma

(MSWD = 1.12, $n = 9$), 1727 ± 8 Ma (MSWD = 1.08, $n = 10$) and 1671 ± 18 Ma (MSWD = 0.15, $n = 2$). No textural differences between the xenotime grains within each of these age modes could be identified.

6.2. GSWA 209985: strata-bound mineralization

A sample of strata-bound mineralization (drill hole MOD13, depth 91.23–91.25 m, MGA 94 Zone 50 591962E, 7408248N) was taken from a pervasively altered siltstone with coarse pyrite and 2.67 ppm of Au, similar to the sample analyzed by LA-ICP-MS for trace element analyses. Small xenotime (<25 μm diameter) crystals intergrown with ore-related alteration minerals, quartz and muscovite (Fig. 9B), and some grains are fully contained within pyrite crystals (Fig. 9C).

Twenty analyses conducted on 20 xenotime crystals with U and Th contents ranging from 1118 ppm to 4190 ppm and 57,274 ppm to

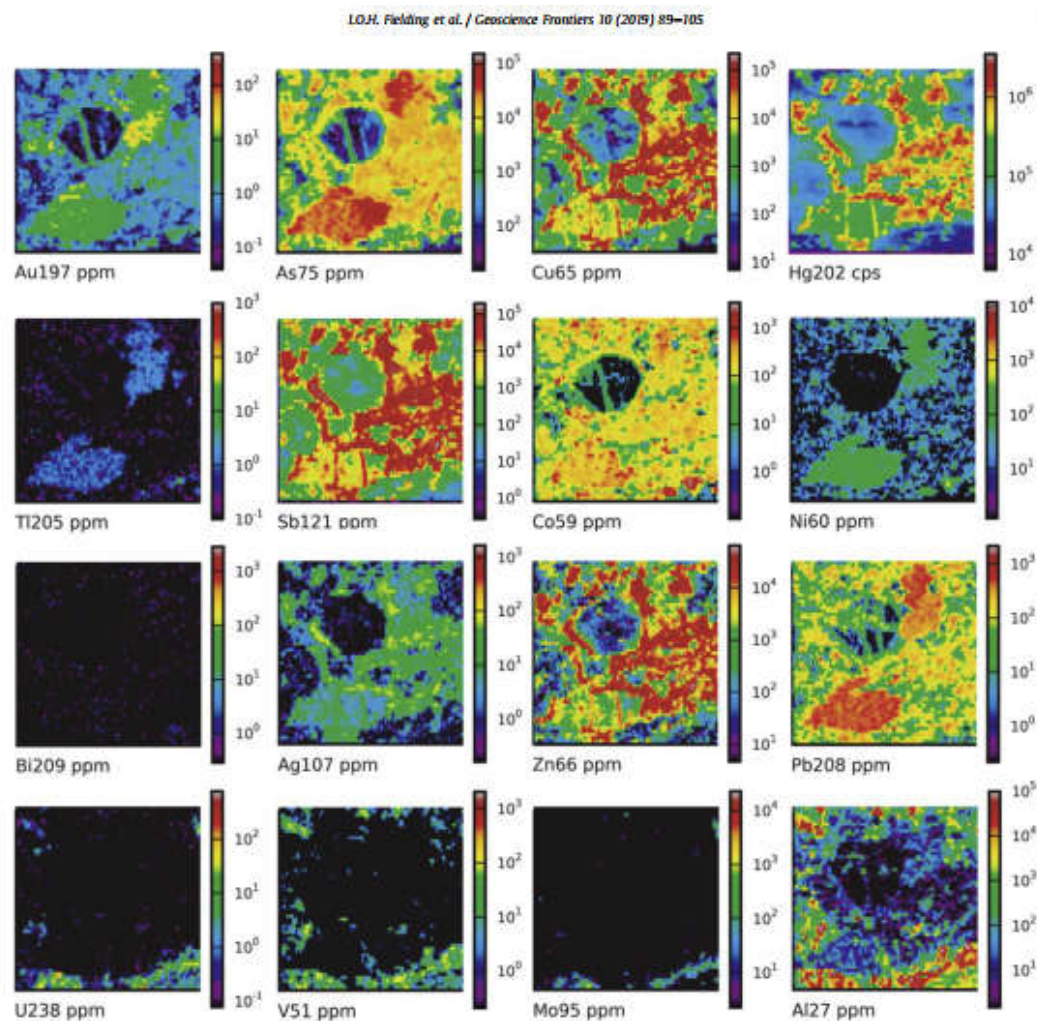


Figure 5. LA-ICP-MS images of trace elements in pyrite from NM00002 376.2 m in depth (refer to Fig. 3D) showing py4 with no trace element associations. Py1 is enriched in Au, As, Ti, Pb, and py2 and tellurium are intergrown and enriched in Au, As, Cu, Hg, Sb, Ag and Zn.

21,590 ppm, respectively. Three of the analyses were excluded from the age determination due to >10% discordance. The remaining 17 analyses yielded a weighted mean $^{207}\text{Pb}^*/^{206}\text{Pb}^*$ date of 1770 ± 7 Ma (MSWD = 1.4; Fig. 10B, Table 4). This sample, which contains 2.67 ppm Au, is the only one in which xenotime is encased in auriferous pyrite and provides a unimodal age. Together these data suggest that the date obtained represents the timing of hydrothermal alteration associated with pyrite crystallization and gold mineralization.

6.3. GSWA 219595 strata-bound mineralization

A second sample of strata-bound mineralization (MGA 94 Zone 50 592095E, 7408303N) was collected from quartz–muscovite-

altered conglomerate in the Mount Olympus pit with pyrite crystals up to 2 cm. Xenotime crystals from this sample are up to 80 μm in diameter and commonly contain inclusions of quartz, zircon, rutile or muscovite (Fig. 9D).

Twenty-eight analyses were obtained on 20 xenotime crystals with U contents between 514 and 4338 ppm and Th contents from 1124 to 7288 ppm. Two analyses with >10% discordance and two analyses with imprecise data due to poor spot placement were excluded from the age determination. The remaining 24 analyses yielded three distinct age modes (Fig. 10C, Table 5) with weighted mean $^{207}\text{Pb}^*/^{206}\text{Pb}^*$ dates of 1764 ± 11 Ma (MSWD = 0.04, $n = 7$), 1727 ± 13 Ma (MSWD = 0.57, $n = 9$) and 1674 ± 12 Ma (MSWD = 1.4, $n = 8$). No textural differences between the xenotime grains within each of these age modes could be identified.

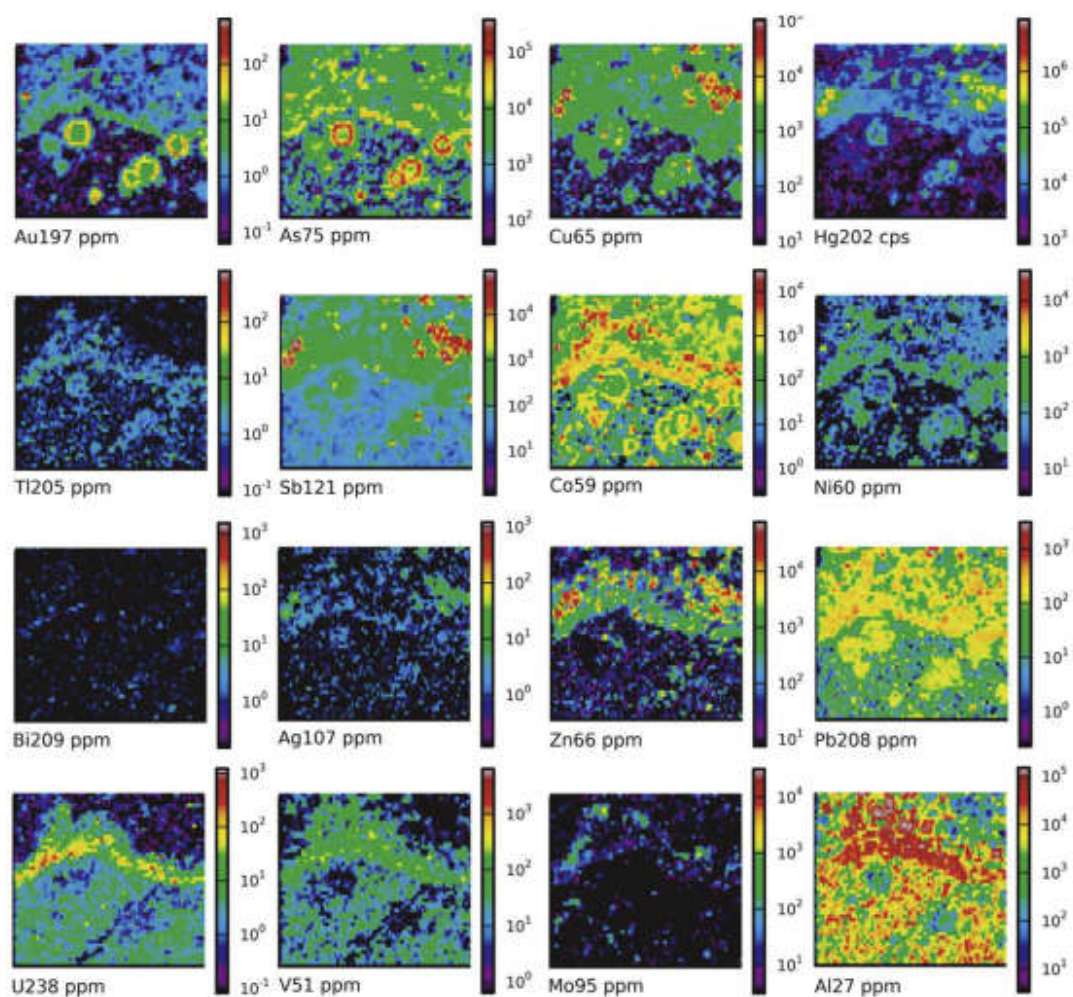


Figure 6. LA-ICP-MS image of trace element from pyrite in NM00002 377.7 m depth showing a narrow band of py1, py2 and carbonaceous material separating py2 from py3 (refer to Fig. 3B). The carbonaceous band is enriched in Au, U, V, Mo and Al.

6.4. Pooled age data

The distinct age modes obtained from all three samples are consistent (Fig. 11) thus allowing the pooling of all data to better define the age peaks. Pooled data yield weighted mean $^{207}\text{Pb}/^{206}\text{Pb}$ dates of 1769 ± 4 Ma (MSWD = 1.02, $n = 33$), 1727 ± 7 Ma (MSWD = 0.79, $n = 19$) and 1673 ± 8 Ma (MSWD = 1.15, $n = 10$). The ca. 1730 Ma and 1675 Ma ages are interpreted to represent discrete hydrothermal events causing new growth or dissolution and re-precipitation of xenotime, whereas the ca. 1770 Ma age, which is common to all studied samples, represents the timing of pyrite crystallization and gold mineralization. These new geochronological data indicate a more complex geological history of the Mount Olympus deposit than previously recognized by Şener et al. (2005).

7. Discussion

7.1. Deposit classification

The classification of the Mount Olympus deposit has been reported as having features similar to both Carlin-type and orogenic gold deposits (Young et al., 2003; Şener et al., 2005); however, these styles of mineralization are significantly different (Table 6). Orogenic gold deposits are generally related to accretionary or collisional events where gold deposits occur as linear trends associated with trans-crustal structures that mark suture zones between continental blocks (Groves et al., 1998; Goldfarb et al., 2001; Hronsky et al., 2012). Deposits are hosted by Archean greenstones or Paleoproterozoic and Phanerozoic turbidite deposits that are metamorphosed to greenschist facies (Goldfarb and Groves, 2015). Commonly the

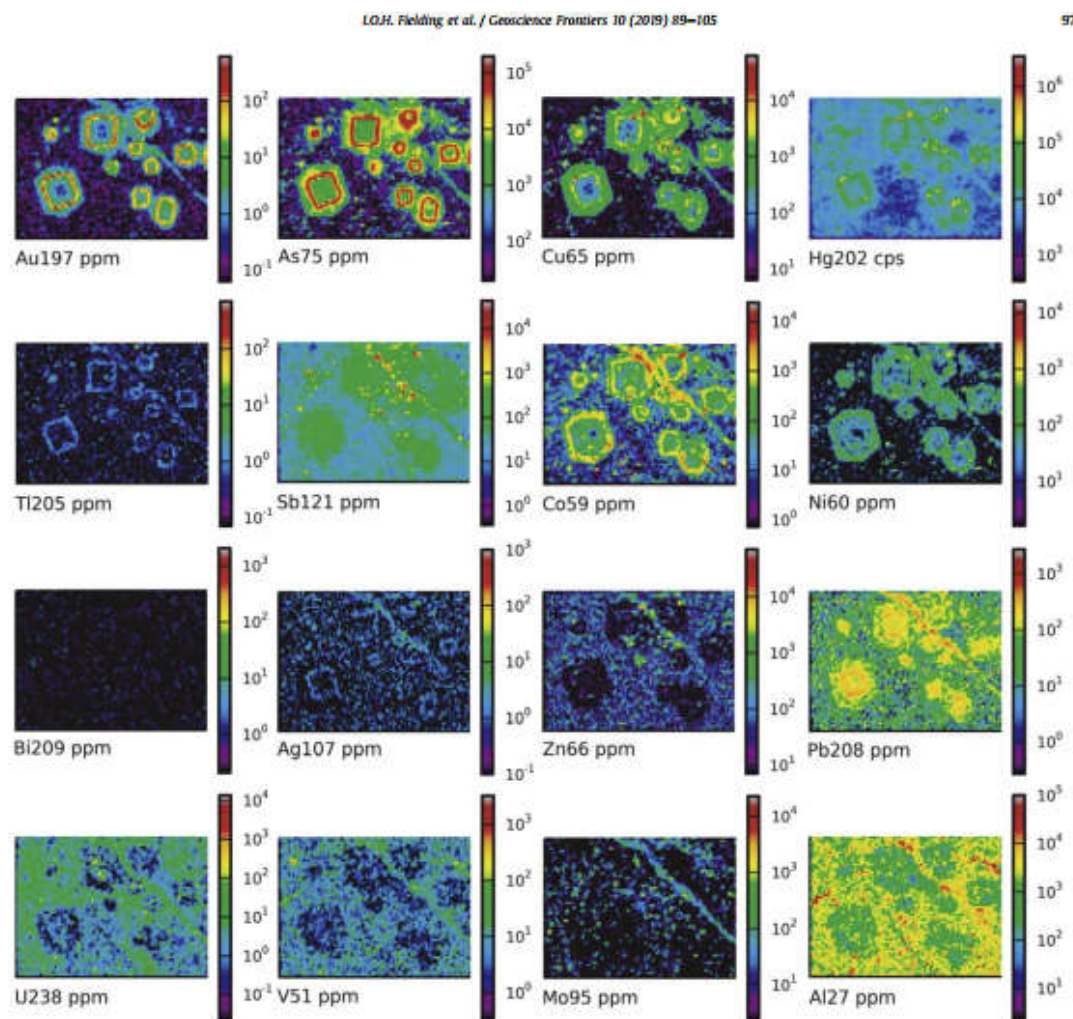


Figure 7. LA-ICP-MS image of trace elements from pyrite in NMOD002 376.2 m depth showing zoning in py3 (see Fig. 3C) with an core enriched in As, Hg, Sb and Pb, an internal band enriched in Au, As, Cu, Hg, Tl, Sb and Pb, and a rim zone associated with elevated Co and Ni.

deposits have ore-stage alteration assemblages of carbonate-iron sulfide \pm white mica \pm chlorite that formed at 200–650 °C and 0.5–5 kbar (Goldfarb et al., 2001; Groves et al., 2003) in which mineralization is associated with quartz \pm carbonate-sulfide veins (Groves et al., 1998). Trace element compositions of pyrite in orogenic gold deposits show elevated Ni, As, Au, W, V and Cr (Belousov et al., 2016). In contrast, the Carlin-type deposits of Nevada tend to be associated with mildly extensional tectonics (Cline et al., 2005; Muntean et al., 2011). Mineralized lodes form in carbonate rocks enriched in carbonaceous material (Berger and Bagby, 1991; Cline et al., 2005) with ore-stage alteration consisting of decalcification, jasperoid and clay alteration (montmorillonite, kaolinite, illite and smectite), silicification and sulfidation forming at 180–240 °C and 0.5–1 kbar (Teal and Jackson, 2002; Cline et al.,

2005). Mineralization has a strong structural control which defines ore body geometries, commonly resulting in strata-bound and fault zone mineralization (Arehart, 1996). Trace element compositions of pyrite show elevated As, Au, Sb, Tl, Cu, Hg \pm Ag \pm Pb with invisible gold typically enriched in the rim zones (Large et al., 2009).

The Mount Olympus deposit shares many of the characteristics of the Carlin deposits in Nevada, although several differences are also evident (Table 6). At Mount Olympus gold mineralization is both fault-hosted and strata-bound (Morant and Doepel, 1997; Young et al., 2003). The strata-bound lodes however, occur in coarser grained rocks than those at Carlin; but similar to the Carlin deposits they have a high organic carbon content, with ore-stage alteration characterized by the removal of carbonate minerals and the addition of sericite and quartz (Wells et al., 2016). Young et al.

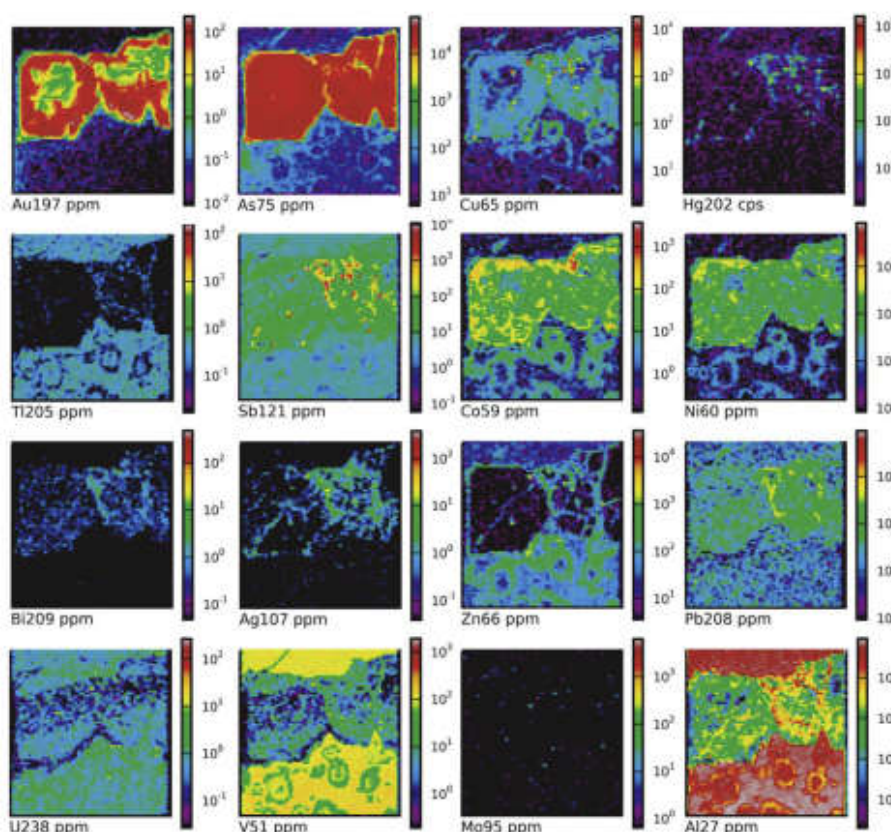


Figure 8. LA-ICP-MS images of trace elements from pyrite in MOD13 130.6 m in depth (refer to Fig. 3F) showing elevated As with a diffusive rim zone enriched in Au.

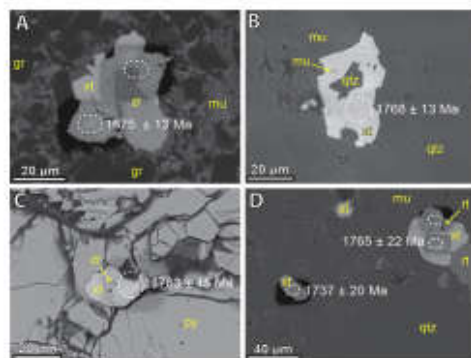


Figure 9. Scanning electron microscope-backscattered electron (SEM-BSE) images of dated xenotime crystals. White ellipses show analysis pits. Analysis pits with no ages represent discordant data. (A) Xenotime overgrowth on zircon (GSWA 219594). (B) Xenotime intergrown with muscovite and quartz from strata-bound mineralization (GSWA 909985). (C) Xenotime encased in auriferous pyrite (GSWA 209985). (D) Xenotime with inclusions of rutile (GSWA 219595). Mineral abbreviations: gr=graphite, mu=muscovite, py=pyrite, qtz=quartz, rt=rutile, xt=xenotime and zr=zircon.

(2003) indicated that the mineralization formed at temperatures and pressures up to 350 °C and 1–2 kbar, significantly higher than the Carlin deposits which formed at 180–240 °C and 0.5–1 kbar (Cline et al., 2005). However, the methods used to determine the temperature and pressure conditions at which the Mount Olympus mineralization formed are not discussed in detail, and it is difficult to assess their significance. However, since the alteration assemblages at both deposits are similar, it is possible they formed under similar conditions.

Trace element distribution maps of pyrite from Mount Olympus show geochemical similarities to the Carlin deposits of Nevada (e.g. Large et al., 2009). The relationships between Au–As, Au–Ni and Au–V for pyrites with enriched Au–As rim zones within strata-bound mineralization (MOD13), and the internal growth zones within py3 from the Zoe Fault mineralization (NMOD002) show similar compositions to the Carlin deposits. Gold forms a positive relationship with As with all data plotting below the gold saturation line defined by Reich et al. (2005) indicating that invisible gold is locked in the pyrite crystal lattice (Fig. 12A). Au–As enriched rims (MOD13), and internal bands in py3 (NMOD002) have the same composition as the hydrothermal ores of the Carlin deposits (Fig. 12A) as defined by Large et al. (2009). The rims however, are much thicker and of lower grade (up to 429 ppm Au) compared to

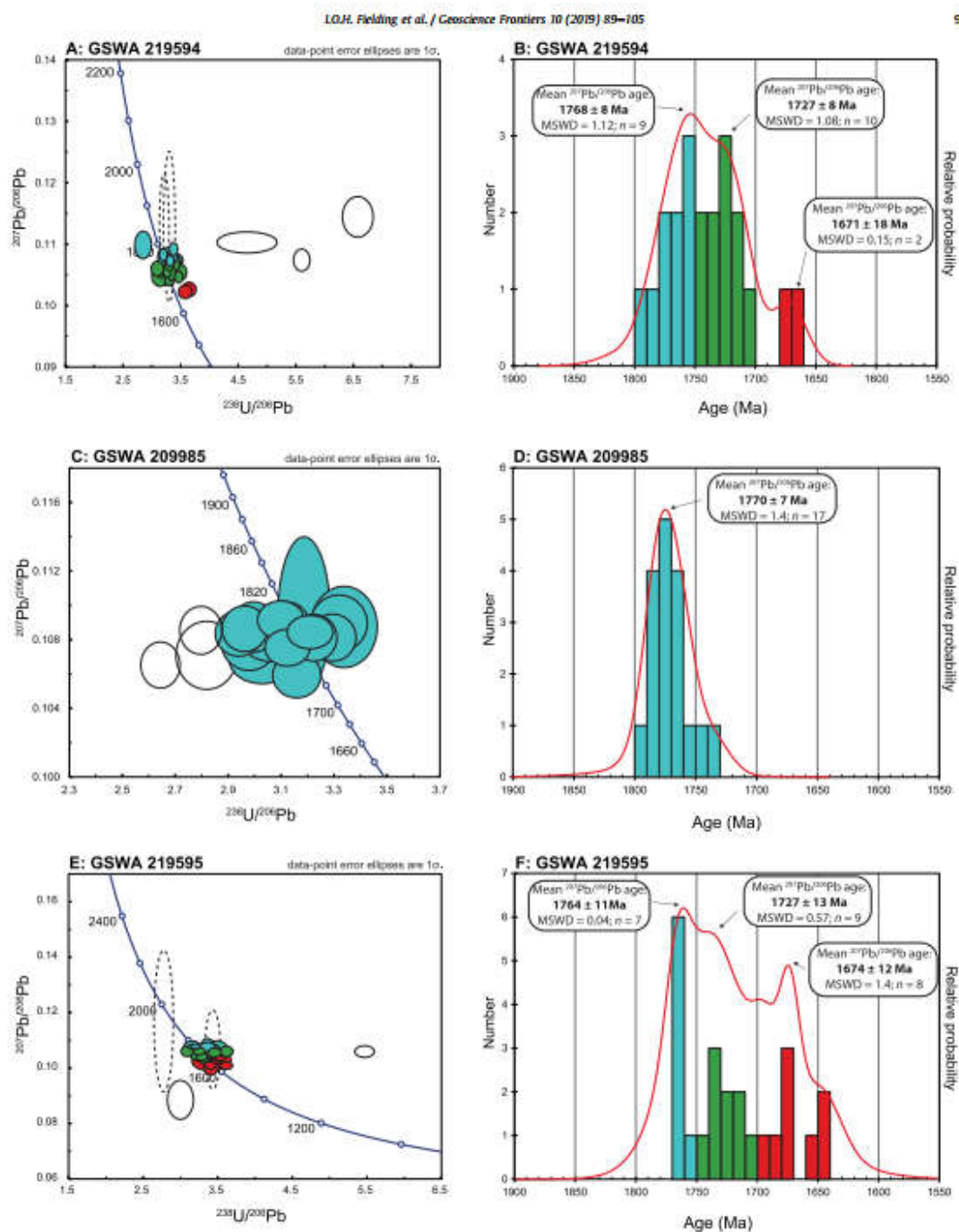


Figure 10. Tera-Wasserburg Concordia diagrams of U–Pb data for xenotime and probability density diagrams and histograms of xenotime ages for mineralized samples A and B (GSWA 219594), C and D (GSWA, 209985), E and F (GSWA 219595). Key for Concordia diagrams: colored ellipses (blue = ca. 1770 Ma, green = ca. 1730 Ma, red = ca. 1680 Ma) show data used in age calculations; other ellipses are for inferior data (unshaded black ellipses = >10% discordant data, dashed ellipses = poor spot placement). Probability density diagrams, red curve includes only data <10% discordant, colours used correspond to the Concordia diagrams.

Table 3
SHRIMP U–Pb xenotime results, CSNA, 219594 Zoe Fault mineralization.

Mount No.	Grain spot	U (ppm)	Th (ppm)	TiO ₂ (wt%)	f_{iso} (%)	$^{207}\text{Pb}/^{206}\text{Pb}^*$	$\pm 1\sigma$	$^{207}\text{Pb}/^{238}\text{U}$	$\pm 1\sigma$	$^{207}\text{Pb}/^{235}\text{U}$	$\pm 1\sigma$	Disc. (%)	$^{207}\text{Pb}/^{206}\text{Pb}^*$	$\pm 1\sigma$ (Ma)
Group 1 (1768 \pm 8 Ma)														
1704	E3-1	1747	2545	1.5	0.04	0.1100	0.0014	0.151	0.012	5.32	0.19	0.078	0.011	1759
1704	H1-3	1388	1318	0.9	0.01	0.1093	0.0007	0.296	0.004	4.46	0.07	0.090	0.009	1788
1704	L1-1	1482	1275	0.9	0.05	0.1085	0.0007	0.305	0.007	4.56	0.10	0.091	0.010	1774
1705	L1-2	1627	2152	1.3	0.16	0.1084	0.0006	0.313	0.004	4.67	0.07	0.090	0.010	1772
1704	E3-1	1465	4320	2.9	0.04	0.1081	0.0007	0.297	0.004	4.43	0.07	0.091	0.009	1767
1704	L2-1	1879	2508	1.3	0.07	0.1077	0.0010	0.316	0.004	4.69	0.08	0.084	0.010	1761
1704	L1-1	1540	2490	1.6	0.12	0.1075	0.0007	0.292	0.006	4.33	0.10	0.084	0.009	1757
1704	A1-1	2746	2849	1.0	0.01	0.1074	0.0006	0.301	0.004	4.47	0.06	0.091	0.010	1756
1704	G1-1	2477	722	0.3	0.03	0.1071	0.0008	0.293	0.005	4.32	0.08	0.085	0.009	1750
Group 2 (1727 \pm 8 Ma)														
1704	E2-1	1915	392	0.2	0.03	0.1069	0.0007	0.302	0.004	4.45	0.07	0.058	0.010	1747
1704	H1-1	1117	1671	1.5	0.07	0.1068	0.0008	0.294	0.005	4.32	0.08	0.089	0.010	1746
1704	K1-1	1627	3650	2.2	0.04	0.1062	0.0008	0.323	0.007	4.71	0.11	0.096	0.010	1735
1705	L1-1	1063	2549	2.4	0.05	0.1061	0.0009	0.317	0.005	4.64	0.09	0.095	0.010	1734
1705	H3-1	2169	472	0.2	0.02	0.1058	0.0007	0.306	0.004	4.46	0.07	0.079	0.010	1728
1704	C1-1	1550	1631	1.1	0.13	0.1056	0.0008	0.283	0.004	4.12	0.07	0.076	0.009	1724
1704	H1-2	1144	1240	1.1	0.04	0.1054	0.0008	0.300	0.005	4.35	0.07	0.086	0.010	1721
1704	D1-1	1808	4735	2.6	0.00	0.1049	0.0011	0.318	0.010	4.60	0.15	0.102	0.010	1713
1704	E2-1	2008	4459	2.2	0.07	0.1048	0.0006	0.288	0.004	4.17	0.06	0.080	0.010	1711
1705	H1-1	1304	1171	0.9	0.14	0.1047	0.0009	0.303	0.005	4.37	0.08	0.086	0.010	1709
Group 3 (1671 \pm 18 Ma)														
1704	L1-2	1082	8441	7.8	0.01	0.1028	0.0007	0.274	0.006	3.88	0.09	0.080	0.009	1675
1704	R1-1	1443	3309	2.3	0.05	0.1024	0.0007	0.279	0.006	3.94	0.09	0.080	0.010	1668
Discordance > 10%														
1704	L1-1	1789	1050	0.6	0.46	0.1104	0.0014	0.215	0.016	3.27	0.24	0.075	0.007	1806
1704	G1-2	2635	2397	0.9	0.22	0.1075	0.0011	0.178	0.003	2.65	0.05	0.069	0.006	1758
1704	E1-2	4638	3519	0.8	0.40	0.1146	0.0020	0.152	0.004	2.40	0.08	0.054	0.005	1873
Poor spot placement														
1705	H2-1	1374	917	0.7	0.28	0.1127	0.0056	0.311	0.005	4.83	0.27	0.074	0.009	1844
1704	E1-1	2189	1968	0.9	0.70	0.1129	0.0076	0.303	0.006	4.71	0.35	0.087	0.009	1847

Pb* indicates radiogenic Pb.
 f_{iso} is the proportion of common Pb in ^{207}Pb , determined using the measured $^{207}\text{Pb}/^{206}\text{Pb}$ and a common Pb composition from the Stacey and Kramers (1975) model at the approximate age of the sample.
 Disc. is apparent discordance, as $100 \times ((^{207}\text{Pb}/^{206}\text{Pb})^* - (^{207}\text{Pb}/^{206}\text{Pb})_{\text{model}}) / ((^{207}\text{Pb}/^{206}\text{Pb})^* + (^{207}\text{Pb}/^{206}\text{Pb})_{\text{model}})$.

Table 4
SHRIMP U–Pb xenotime results, GSWA 2009005 strata bound mineralization – silstone (2.67 ppm Au).

Mount No.	Grain spot	U (ppm)	Th (ppm)	Th/U	f_{ZrO_2} (%)	$^{207}\text{Pb}/^{235}\text{U}$	$^{207}\text{Pb}/^{238}\text{U}$	$^{207}\text{Pb}/^{235}\text{U}$	$^{207}\text{Pb}/^{238}\text{U}$	$^{207}\text{Pb}/^{235}\text{U}$	$^{207}\text{Pb}/^{238}\text{U}$	Disc. (%)	$^{207}\text{Pb}/^{235}\text{U}$	age (Ma)	$\pm 1\sigma$ (Ma)
Group 1 (1770 \pm 7 Ma)															
1602	10-1	4353	25774	5.9	0.10	0.1088	0.0013	0.300	0.007	4.50	0.087	5	1779	22	
1602	3-1	2597	14060	5.4	0.28	0.1090	0.0009	0.302	0.006	4.53	0.11	5	1783	16	
1602	9-1	2853	16426	5.8	0.00	0.1082	0.0008	0.304	0.005	4.53	0.09	3	1769	13	
1602	17-1	2861	16796	5.9	0.55	0.1095	0.0026	0.314	0.006	4.74	0.091	2	1791	44	
1602	13-1	3095	22584	6.2	0.03	0.1081	0.0007	0.310	0.006	4.63	0.09	0.090	1768	13	
1602	15-1	2723	16850	6.2	0.04	0.1085	0.0005	0.312	0.006	4.66	0.09	0.090	1774	9	
1602	1-1	2093	12552	6.0	0.10	0.1091	0.0006	0.321	0.006	4.83	0.10	1	1784	11	
1602	7-1	1716	9656	5.6	0.02	0.1092	0.0006	0.323	0.006	4.86	0.10	1	1786	10	
1602	8-1	2350	12964	5.5	0.03	0.1090	0.0006	0.325	0.006	4.88	0.12	0.094	1783	10	
1602	11-1	2121	12127	5.7	0.07	0.1076	0.0006	0.320	0.006	4.75	0.09	0.093	1759	10	
1602	16-1	1564	8025	5.7	0.10	0.1060	0.0007	0.317	0.006	4.63	0.10	0.091	1731	13	
1602	14-1	2676	15053	5.6	0.09	0.1078	0.0006	0.326	0.008	4.85	0.12	0.094	1763	10	
1602	12-1	1630	9494	5.8	0.21	0.1088	0.0008	0.334	0.006	5.01	0.10	0.088	1779	14	
1602	2-1	2098	14074	6.7	0.12	0.1068	0.0007	0.330	0.009	4.87	0.14	0.095	1746	13	
1602	6-1	1656	7402	4.5	0.05	0.1087	0.0008	0.338	0.006	5.06	0.10	0.098	1777	13	
1602	5-1	4190	21590	5.2	0.06	0.1078	0.0008	0.336	0.008	4.99	0.12	0.099	1763	15	
1602	4-1	1118	5724	5.1	0.02	0.1084	0.0008	0.340	0.007	5.09	0.11	0.097	1773	13	
Discordance > 10%															
1603	A1-1	1603	4323	2.7	0.15	0.1086	0.0008	0.358	0.007	5.16	0.11	0.098	1776	14	
1603	E2-1	2685	4395	1.6	0.06	0.1071	0.0012	0.355	0.010	5.25	0.16	0.102	1751	20	
1603	E1-1	1889	2868	1.5	0.08	0.1066	0.0008	0.379	0.007	5.56	0.11	0.108	1741	13	

Pb^* indicates radiogenic Pb .
 f_{ZrO_2} is the proportion of common Pb in ^{207}Pb , determined using the measured $^{207}\text{Pb}/^{235}\text{U}$ and a common Pb composition from the Stacey and Kramers (1975) model at the approximate age of the sample.
Disc. is apparent discordance, as $100 \times (1 - \frac{^{207}\text{Pb}/^{235}\text{U}}{^{207}\text{Pb}/^{235}\text{U}}) \times 100$.

those in the Carlin deposits (up to 2000 ppm Au). A similar association between Au–Ni and Au–V exists with a negative relationship between Ni and V to Au for mineralized pyrite (py3 internal zone and MOD13 rims) which is comparable to the hydrothermal Carlin ores (Fig. 12B and C). Additionally, trace element distributions within py3 are identical to those at Carlin with elevated Au, As, Cu, Sb, Hg and Tl (Large et al., 2009).

Our results indicate that all of the characteristic features of the Mount Olympus deposit are significantly different from orogenic gold deposits, including those in the northern Capricorn Orogen, where mineralization is associated with the emplacement of laminated auriferous quartz–carbonate–pyrite veins, abundant native gold, and introduction of carbonate minerals during ore-stage hydrothermal alteration (Table 6; Groves et al., 1998; Fielding et al., 2017). Here we reclassify the Mount Olympus deposit as a Carlin-like deposit since it has many (but not all) characteristics in common with the Carlin-type deposits of Nevada (Table 6).

7.2. Timing of gold mineralization

Trace element mapping of pyrite from the Zoe Fault (NMOD002 py1–4) and strata-bound (MOD13) mineralization indicates that gold forms in a solid solution within Au–As-rich arsenian pyrite. Results suggest that py1 and py2 have compositions (Au–As, Au–Ni and Au–V ratios) similar to diagenetic pyrite (Fig. 12; Large et al., 2009). This is consistent with their form as crystal aggregates which occur as discontinuous layers and lenses within carbonaceous-rich layers with elevated U, V, Mo and Al content (Fig. 6). Although these pyrites are enriched in gold (mean Au py1 = 8 ppm and py2 = 2 ppm) the majority of the gold forms as diffusive Au–As-enriched rims within strata-bound mineralization (MOD13, mean Au of 55 ppm) or in Au–As-enriched internal growth zones in py3 (NMOD002; mean Au of 67 ppm) within the Zoe Fault. LA-ICP-MS images of pyrite with diffusive Au–As rims (MOD13) have comparable Au–As, Au–Ni and Au–V relationships to those of the Carlin-type ores, and to Au–As enriched internal zone of py3 which have the same geochemical element associations to Carlin-type ores (Fig. 12). Dating of hydrothermal xenotime intergrown with ore-stage alteration minerals and arsenian pyrite (Fig. 9C) within strata-bound ore from diamond drill core MOD13 yields a date of 1769 ± 5 Ma, representing the timing of hydrothermal gold mineralization.

7.3. Setting of mineralization

The Mount Olympus deposit is located on the Zoe Fault, a second order splay of the Nanjilgardy Fault, which is a crustal-scale structure (Johnson et al., 2013). The timing of gold mineralization at ca. 1770 Ma lies at the younger end of the age range for the intracratonic 1820–1770 Ma Capricorn Orogeny (Sheppard et al., 2010), a time that represents a distinct change in tectonic regime, from predominantly northeast compression to north–northwest stresses producing dextral strike-slip reactivation of the Nanjilgardy Fault (Krapež, 1999; Young et al., 2003). Furthermore, xenotime growth dated at ca. 1730 Ma (from this study and by Šener et al., 2005) and ca. 1675 Ma is also contemporaneous with hydrothermal monazite and xenotime growth at the Paulsens gold mine located 150 km to the northwest (Fielding et al., 2017) and coincides with the early stages of the 1680–1620 Ma Mangaroon Orogeny (Sheppard et al., 2005). These events are also thought to reflect the timing of punctuated reactivation on the Nanjilgardy Fault and associated hydrothermal fluid flow. These data indicate that gold mineralization at Mount Olympus occurred in an intracratonic setting, during low- to medium-grade metamorphism and

Table 5
SHRIMP U–Pb xenotime results, GSWA 215955 staurolite bound mineralization – conglomerate.

Mount No.	Grain spot	U (ppm)	Th (ppm)	Th/U	f_{iso} (%)	$^{207}\text{Pb}/^{206}\text{Pb}^*$	$^{207}\text{Pb}/^{206}\text{Pb}^* \pm 1\sigma$	$^{207}\text{Pb}/^{206}\text{Pb}^* \pm 1\sigma$	$^{207}\text{Pb}/^{206}\text{Pb}^* \pm 1\sigma$	Disc. (%)	$^{207}\text{Pb}/^{206}\text{Pb}^* \text{ age (Ma)}$	$\pm 1\sigma$ (Ma)
Group 1 (1764 ± 11 Ma)												
1705	G1-1	4211	2103	0.5	0.00	0.1080	0.0006	0.0006	0.001	1	1767	9
1705	D2-4	882	1424	1.6	0.46	0.1080	0.0019	0.0019	0.008	5	1765	31
1705	R1-1	761	1038	1.4	0.00	0.1079	0.0013	0.0013	0.003	0	1765	22
1705	C3-1	4150	5350	1.3	0.00	0.1078	0.0006	0.0006	0.001	0	1763	10
1705	A3-1	514	1124	2.2	0.00	0.1078	0.0015	0.0015	0.006	8	1763	25
1705	L2-1	1284	1339	1.0	0.06	0.1078	0.0011	0.0011	0.008	5	1762	19
1705	A2-1	549	1441	2.6	0.31	0.1072	0.0019	0.0019	0.008	5	1752	33
Group 2 (1727 ± 13 Ma)												
1705	C1-1	877	1760	2.0	0.04	0.1069	0.0013	0.0013	0.006	5	1748	22
1705	C2-1	2257	2631	1.2	0.06	0.1063	0.0008	0.0008	0.000	14	1737	14
1705	R2-1	756	1145	1.5	0.37	0.1063	0.0011	0.0011	0.002	4	1737	20
1705	L1-1	1090	1323	1.3	0.02	0.1063	0.0012	0.0012	0.006	9	1737	21
1705	A4-1	643	869	1.4	0.08	0.1058	0.0011	0.0011	0.008	5	1729	18
1705	E1-1	1112	1751	1.6	0.35	0.1055	0.0016	0.0016	0.003	1	1723	28
1705	D2-1	754	1524	2.0	1.09	0.1053	0.0020	0.0020	0.009	1	1719	36
1705	A5-1	574	1300	2.3	0.23	0.1052	0.0011	0.0011	0.008	5	1718	19
1705	C5-1	1835	2092	1.1	0.14	0.1044	0.0009	0.0009	0.006	1	1703	15
Group 3 (1674 ± 12 Ma)												
1705	C2-1	3981	7552	1.9	0.01	0.1038	0.0005	0.0005	0.004	5	1693	10
1705	E1-1	622	962	1.5	0.00	0.1033	0.0011	0.0011	0.000	5	1685	20
1705	C2-2	3485	6417	1.8	–0.01	0.1028	0.0005	0.0005	0.004	3	1675	8
1705	A1-1	654	1456	2.2	0.52	0.1027	0.0022	0.0022	0.013	0	1674	39
1705	C2-3	4338	7288	1.7	0.01	0.1026	0.0004	0.0004	0.004	3	1672	8
1705	D1-1	786	956	1.2	1.10	0.1014	0.0023	0.0023	0.013	0	1651	42
1705	D2-3	1104	2677	2.4	0.19	0.1014	0.0009	0.0009	0.004	1	1649	16
1705	D2-2	724	1614	2.2	0.13	0.1011	0.0009	0.0009	0.007	4	1645	16
Discordance > 10%												
1705	A1-3	805	863	1.1	1.97	0.0888	0.0044	0.0044	0.013	–32	1400	95
1705	R1-2	890	1106	1.2	0.54	0.1062	0.0013	0.0013	0.005	38	1736	23
Poor spot placement												
1705	C4-1	2645	3523	1.3	0.32	0.1172	0.0157	0.0157	0.085	–4	1914	240
1705	A1-2	816	1806	2.2	0.63	0.1070	0.0088	0.0088	0.039	6	1748	151

Pb* indicates radiogenic Pb.

f_{iso} is the proportion of common Pb in ^{207}Pb , determined using the measured $^{207}\text{Pb}/^{206}\text{Pb}$ and a common Pb composition from the *Stacey and Kramers (1975)* model at the approximate age of the sample.

Disc. is apparent discordance, as $100 \times ((^{207}\text{Pb}/^{206}\text{Pb})^* - (^{207}\text{Pb}/^{206}\text{Pb})^*_{\text{model}}) / (^{207}\text{Pb}/^{206}\text{Pb})^*$.

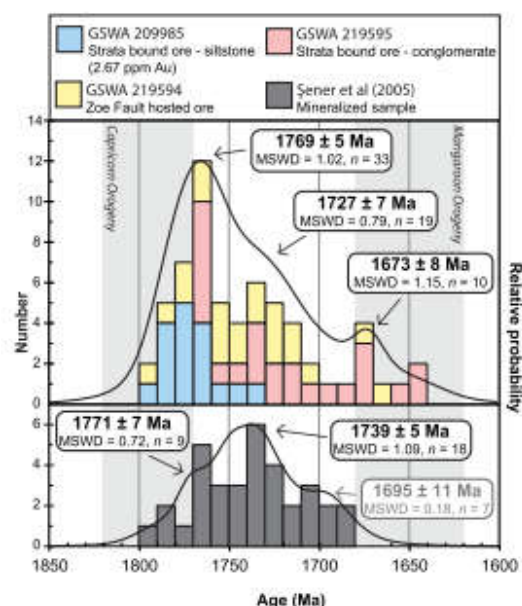


Figure 11. Probability plots and histograms with 10 Ma bin width for hydrothermal xenotime. Upper panel contains data from the strata-bound ore zone (GSWA, 209985 and 219595) and from the Zoe Fault (GSWA, 209594). The lower panel contains data from Şener et al. (2005), grey text indicates inferior data (poor spot placement or younger outliers). Weighted mean $^{207}\text{Pb}/^{206}\text{Pb}$ dates are reported with 95% confidence levels including data <10% discordant that contain $\leq 1\%$ common Pb.

was facilitated by the focusing of hydrothermal fluids along a major crustal structure.

7.4. Regional-scale drivers to mineral systems

Despite the notion that orogenic, epithermal and Carlin-type gold deposits may represent a continuum of deposit types (Huston et al., 2016), with their individual characteristics defined

principally by processes operating at the smallest-scales of the mineral system (Nesbitt, 1988; Robert et al., 2007; Dill, 2010; Brauhart et al., 2017), the data presented here demonstrate that there are distinct large-scale drivers for the three deposit types. Whereas orogenic gold deposits are driven by high-energy, plate margin processes associated with accretionary or collisional tectonics (Groves et al., 1998; Goldfarb et al., 2001), and epithermal deposits are driven by regional-scale magmatic processes (e.g. Simmons et al., 2005), Carlin-type deposits may form in a variety of settings (Hu et al., 2002; Cline et al., 2005; Muntean et al., 2011), provided there is an appropriate energy source (orogeny or magmatism) and favorable architecture (crustal-scale faults). The juxtaposition of tectonic blocks during collisional and accretionary orogenesis commonly results in the generation of orogenic belts that contain numerous crustal-scale structures and suture zones (Cook and Erdmer, 2005; Johnson et al., 2013). Since these belts are particularly susceptible to reactivation, they may not only contain orogenic gold deposits associated with the original collisional/accretion phase (Fielding et al., 2017), but also overprinting Carlin-like gold events. Without precise geochronology it is not possible to unravel the difference in timing and setting of these deposits, particularly in areas where the deposits have been overprinted by subsequent hydrothermal or mineralizing events.

8. Conclusions

Although previous researchers noted similarities between the Mount Olympus deposit and the Carlin-type deposits of Nevada (Young et al., 2003), Mount Olympus was classified as an orogenic gold deposit, largely due to the interpretation that xenotime growth at ca. 1738 Ma was related to the assembly of Proterozoic Australia (Şener et al., 2005). At a regional scale, the deposit does not share the characteristics of an orogenic deposit, as it formed during the waning stages of the intracratonic 1820–1770 Ma Capricorn Orogeny far from any active continental margin, and after the cessation of all felsic magmatism associated with this event (Sheppard et al., 2010). The data presented here uphold the division in hydrothermal gold types (orogenic, epithermal and Carlin) indicating that, at a mineral system level, the regional-scale drivers for each are different. Although many gold deposits worldwide are associated with collisional or accretionary orogenesis (Goldfarb et al., 2001), substantial gold deposits such as Carlin-like gold deposits can form in an intracratonic setting during regional-scale crustal reworking.

Table 6
Comparison between Orogenic, Carlin-type and Mount Olympus ores.

	Orogenic	Carlin-type	Mount Olympus
Temperature and pressure	200–650 °C, 0.5–5 kbar	180–240 °C, 0.5–1 kbar	<350 °C 1–2 kbar
Major host rocks	Greenstones and turbidites	Shelf carbonate with high carbon content	Deltaic deposits and shelf carbonated with high carbon content
Alteration	Sericite, quartz, carbonate	Illitic sericite, quartz, jasperoid, removal of carbonate	Illitic sericite, quartz, removal of carbonate
Gold form	Abundant free gold; minor solid solution in pyrite	Solid solution in pyrite	Solid solution in pyrite; rare free gold in cracks and fractures
Trace element associations	Au, Ag, As, Te, Sb, W, S	Au, As, Sb, Cu, Ti, Hg	Au, As, Cu, Sb, Hg, Ti
Quartz veining	Abundant	Absent	Rare; within the Zoe Fault
Gold setting	Dominantly quartz veins	Areas of increased porosity and permeability (faults, hinge zones of anticlines, lithological contacts, etc.)	Areas of increased porosity and permeability (e.g. Zoe Fault, porous conglomerate and sandstone)
Tectonic setting	Compressional	Mildly extensional	Strike slip transpressional, compressional?
Age of mineralization	>3.0 Ga, ca. 2.8–2.55 Ga, ca. 2.1–1.8 Ga	42–36 Ma	ca. 1.7 Ga

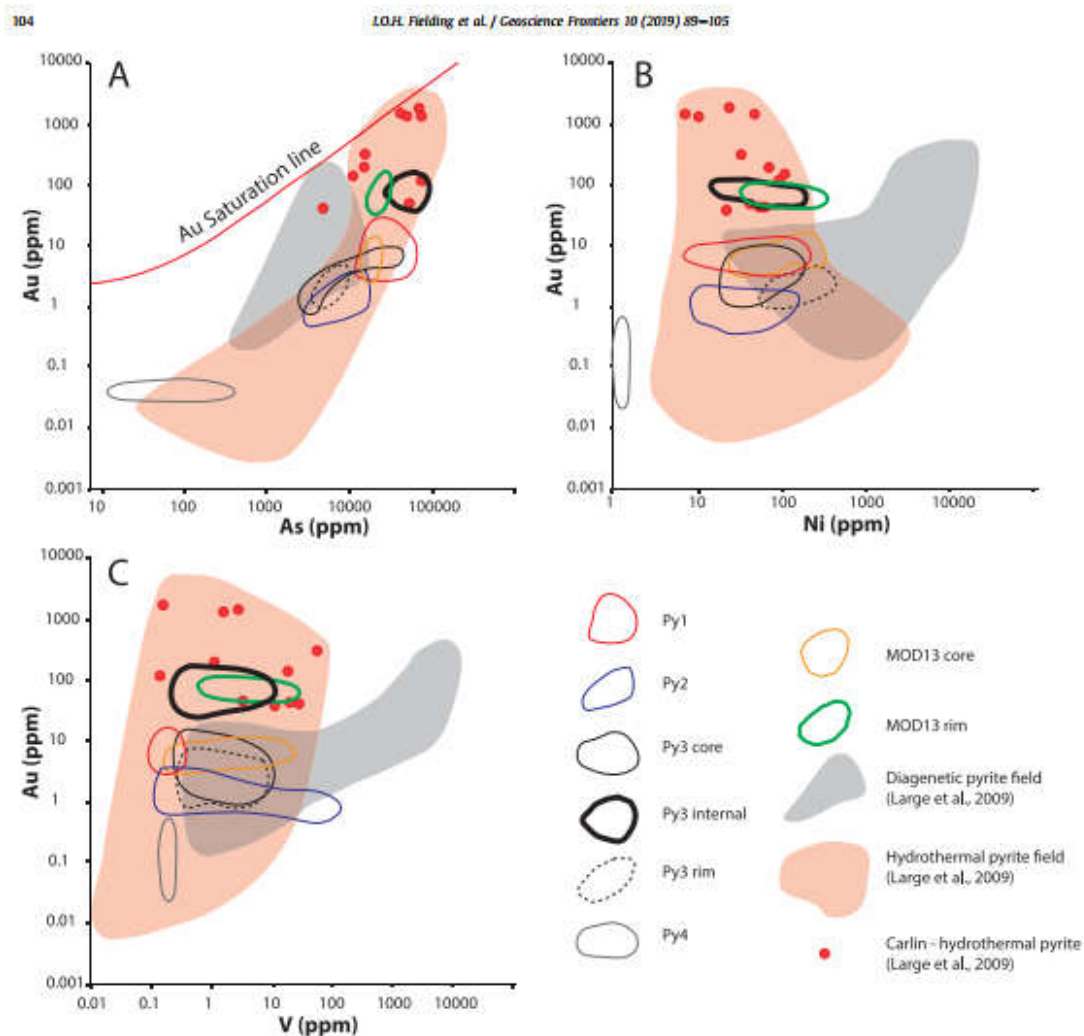


Figure 12. Binary plots showing comparisons of trace element concentrations in pyrite between Carlin (Large et al., 2009) and Mount Olympus mineralization. (A) Au–As; (B) Au–Ni and (C) Au–V.

Acknowledgments

This project was funded through an ARC linkage grant (LP130100922) and industry scholarship by Northern Star Resources as a part of a PhD by I. O. H. Fielding. S. P. Johnson publishes with the permission of the director of the Geological Survey of Western Australia. Xenotime and baddeleyite analyses were carried out on the Sensitive High Resolution Ion Micro Probe mass spectrometer (SHRIMP II) at the John de Laeter Centre, Curtin University, with the financial support of the Australian Research Council and Auscope NCRIS. Pyrite trace element maps and images were analyzed by researchers at CODES, University of Tasmania and were funded through AMIRA P1041 sponsored by AngloGold Ashanti Limited, G-Resources Group, Issara Mining Limited, Newcrest

Mining Limited, Newmont USA Limited, Northern Star Resources Ltd, Sipa Resources Limited. We thank an anonymous reviewer for the helpful comments.

References

- Arehart, G.B., 1996. Characteristics and origin of sediment-hosted disseminated gold deposits: a review. *Ore Geology Reviews* 11 (6), 383–403.
- Berger, B.R., Bagby, W.C., 1991. *The Geology and Origin of Carlin-type Gold Deposits, Gold Metallogeny and Exploration*. Springer US, Boston, MA, pp. 210–248.
- Belousov, I., Large, R.R., Meffre, S., Danyushevsky, L.V., Steadman, J., Beardsmore, T., 2016. Pyrite compositions from VHMS and orogenic Au deposits in the Yilgarn Craton, Western Australia: implications for gold and copper exploration. *Ore Geology Reviews* 79, 474–499.

- Brauhart, C.W., Grunsky, E.C., Hagemann, S.G., 2017. Magmato-hydrothermal space: a new metric for geochemical characterisation of metallic ore deposits. *Ore Geology Reviews* 86, 867–895.
- Cline, J.S., Hofstra, A.H., Muntean, J.L., Tosdal, R.M., Hickey, K.A., 2005. Carlin-type gold deposits in Nevada: critical geologic characteristics and viable models. *Economic Geology* 100th Anniversary Volume 451–484.
- Cook, F., Erdmer, P., 2005. An 1800 km cross section of the lithosphere through the northwestern North American plate: lessons from 4.0 billion years of Earth's history. *Canadian Journal of Earth Sciences* 42 (6), 1295–1311.
- Danyushevsky, L., Robinson, P., Gilbert, S., Norman, M., Large, R., McGoldrick, P., Shelley, M., 2011. Routine quantitative multi-element analysis of sulphide minerals by laser ablation ICP-MS: standard development and consideration of matrix effects. *Geochemistry Exploration Environment Analysis* 11 (1), 51–60.
- Dill, H.G., 2010. The "chestboard" classification scheme of mineral deposits: mineralogy and geology from aluminum to zirconium. *Earth Science Reviews* 100 (1), 1–420.
- Fielding, I.O.H., Johnson, S.P., Zi, J.-W., Rasmussen, B., Muhling, J.R., Dunkley, D.J., Sheppard, S., Wingate, M.T.D., Rogers, J.R., 2017. Using in situ SHRIMP U–Pb monazite and xenotime geochronology to determine the age of orogenic gold mineralization: an example from the Palaeozoic mine. *Southern Pilbara Craton Economic Geology* 112 (5), 1205–1230.
- Fletcher, I.R., McNaughton, N.J., Aleinikoff, J.A., Rasmussen, B., Kamo, S.L., 2004. Improved calibration procedures and new standards for U–Pb and Th–Pb dating of Phanerozoic xenotime by ion microprobe. *Chemical Geology* 209 (3–4), 295–314.
- Fletcher, I.R., Rasmussen, B., McNaughton, N.J., 2000. SHRIMP U–Pb geochronology of authigenic xenotime and its potential for dating sedimentary basins. *Australian Journal of Earth Sciences* 47 (5), 845–859.
- Goldfarb, R.J., Groves, D.I., 2015. Orogenic gold: common or evolving fluid and metal sources through time. *Lithos* 233, 2–26.
- Goldfarb, R.J., Groves, D.I., Gardoll, S., 2001. Orogenic gold and geologic time: a global synthesis. *Ore Geology Reviews* 18 (1–2), 1–75.
- Groves, D.I., Goldfarb, R.J., Gebre-Mariam, M., Hagemann, S.G., Robert, F., 1998. Orogenic gold deposits: a proposed classification in the context of their crustal distribution and relationship to other gold deposit types. *Ore Geology Reviews* 13 (1–5), 7–27.
- Groves, D.I., Goldfarb, R.J., Robert, F., Hart, C.J.R., 2003. Gold deposits in metamorphic belts: overview of current understanding, outstanding problems. *Future Research and Exploration Significance Economic Geology* 98 (1), 1–29.
- Hronsky, J.M., Groves, D.I., Loucks, R.R., Begg, G.C., 2012. A unified model for gold mineralisation in accretionary orogens and implications for regional-scale exploration targeting methods. *Mineralium Deposita* 47 (4), 339–358.
- Hu, R.-Z., Su, W.-C., Bi, X.-W., Tu, G.-Z., Hofstra, A.H., 2002. Geology and geochemistry of Carlin-type gold deposits in China. *Mineralium Deposita* 37, 378–392.
- Huston, D.L., Merragh, T.P., Hagemann, S.G., Doublier, M.P., Fiorentini, M., Champion, D.C., Lynton Jacques, A., Czarnota, K., Cayley, R., Skirrow, R., Basmakov, E., 2016. Tectono-metallogenic systems — the place of mineral systems within tectonic evolution, with an emphasis on Australian examples. *Ore Geology Reviews* 76, 168–210.
- Johnson, S.P., Korhonen, F.J., Kirkland, C.L., Cliff, J.R., Belousova, E.A., Sheppard, S., 2017. An isotopic perspective on growth and differentiation of Proterozoic orogenic crust: from subduction magmatism to cratonization. *Lithos* 268–271, 76–86.
- Johnson, S.P., Sheppard, S., Rasmussen, B., Wingate, M.T.D., Kirkland, C.L., Muhling, J.R., Fletcher, I.R., Belousova, E.A., 2011. Two collisions, two sutures: punctuated pre-1950 Ma assembly of the West Australian craton during the ophiolitic and Glenburgh orogenies. *Precambrian Research* 189 (3–4), 239–262.
- Johnson, S.P., Thorne, A.M., Tyler, I.M., Korsch, R.J., Kennett, B.L.N., Cutten, H.N., Goodwin, J., Blay, O., Blewett, R.S., Joly, A., Dentith, M.C., Arken, A.R.A., Holzschuh, J., Salmon, M., Reading, A., Heinsohn, G., Boren, G., Ross, J., Costelloe, R.D., Fomin, T., 2013. Crustal architecture of the Capricorn orogen, Western Australia and associated metallogeny. *Australian Journal of Earth Sciences* 60 (6–7), 681–705.
- Korhonen, F.J., Johnson, S.P., Wingate, M.T.D., Kirkland, C.L., Fletcher, I.R., Dunkley, D.J., Roberts, M.P., Sheppard, S., Muhling, J.R., Rasmussen, B., 2017. Radiogenic heating and craton-margin plate stresses as drivers for intraplate orogeny. *Journal of Metamorphic Geology* 35, 631–661.
- Krapet, B., 1999. Stratigraphic record of an Atlantic-type global tectonic cycle in the palaeoproterozoic Ashburton province of Western Australia. *Australian Journal of Earth Sciences* 46 (1), 71–82.
- Krapet, B., Müller, S.G., Bekker, A., 2015. Stratigraphy of the late palaeoproterozoic (~2.03 Ga) Woolly dolomite, Ashburton province, Western Australia: a carbonate platform developed in a failed rift basin. *Precambrian Research* 271, 1–19.
- Large, R.R., Danyushevsky, L., Hollit, C., Maslennikov, V., Meffre, S., Gilbert, S., Bull, S., Scott, R., Emsbo, P., Thomas, H., Singh, B., Foster, J., 2009. Gold and trace element zonation in pyrite using a laser imaging technique: implications for the timing of gold in orogenic and carlin-style sediment-hosted deposits. *Economic Geology* 104 (5), 635–668.
- Ludwig, K.R., 2003. Isoplot/Ex Version 3.00, a Geochronological Toolkit for Microsoft Excel, vol. 4. Berkeley Geochronology Centre Special Publication, p. 73.
- Ludwig, K.R., 2009. Squid 2.50, a User's Manual. Berkeley Geochronology Centre, Berkeley, California, USA, p. 95.
- McCaig, T.C., Hronsky, J.M.A., 2014. The mineral systems concept: the key to exploration targeting. In: Kelly, K.D., Golden, H.C. (Eds.), *Building Exploration Capability for the 21st Century*, vol. 18. Society of Economic Geologists: Special Publication, pp. 153–175.
- Morant, P., Doepel, G., 1997. The Mount Olympus Gold Deposit: New Generation Gold Mines, vol. 97. Australian Mineral Foundation, Perth, Western Australia, pp. 61–69.
- Muntean, J.L., Cline, J.S., Simon, A.C., Longo, A.A., 2011. Magmatic-hydrothermal origin of Nevada's Carlin-type gold deposits. *Nature Geoscience* 4 (2), 122–127.
- Nesbitt, B.E., 1988. Gold deposit continuum: a genetic model for lode Au mineralization in the continental crust. *Geology* 16 (11), 1044–1048.
- Northern Star Resources Limited, 2015. *Northern Star Resources Limited 2015 Annual Report*. <http://www.nsrld.com/wp-content/uploads/2015/08/NST-Annual-Report-2015-26-8-2015-new-cover-1.pdf>.
- Rasmussen, B., Sheppard, S., Fletcher, I.R., 2006. Testing ore deposit models using in situ U–Pb geochronology of hydrothermal monazite: Palaeoproterozoic gold mineralization in northern Australia. *Geology* 34 (2), 77–80.
- Reich, M., Kesler, S.E., Utsumiya, S., Palenik, C.S., Chrysosoulis, S.L., Ewing, R.C., 2005. Solubility of gold in arsenian pyrite. *Geochimica et Cosmochimica Acta* 69 (11), 2781–2796.
- Robert, F., Brommecker, R., Bourne, R.T., Dobak, P.J., McEwan, C.J., Rowe, R.R., Zhou, X., 2007. Models and Exploration Methods for Major Gold Deposit Types in Millerville, B. In: *Exploration 07, Fifth Decennial International Conference on Mineral Exploration*, Toronto, Canada. Decennial Mineral Exploration Conference, pp. 691–711.
- Sener, A.K., Young, C., Groves, D.I., Krapet, B., Fletcher, I.R., 2005. Major orogenic gold episode associated with Cordilleran-style tectonics related to the assembly of Palaeoproterozoic Australia? *Geology* 33, 225–228.
- Sheppard, S., Rasmussen, B., Muhling, J.R., Farnell, T.R., Fletcher, I.R., 2007. Grenvillian-aged orogenesis in the palaeoproterozoic Gascoyne complex, Western Australia: 1030–950 Ma reworking of the proterozoic Capricorn orogen. *Journal of Metamorphic Geology* 25, 477–494.
- Sheppard, S., Occhipinti, S.A., Nelson, D.R., 2005. Intracontinental reworking in the Capricorn orogen, Western Australia: the 1680 – 1620 Ma Mangaroon orogeny. *Australian Journal of Earth Sciences* 52, 443–460.
- Sheppard, S., Bodorkos, S., Johnson, S.P., Wingate, M.T.D., Kirkland, C.L., 2010. The Palaeoproterozoic Capricorn Orogeny: intracontinental reworking not continent–continent collision. *Geological Survey of Western Australia Report* 108, 33.
- Simmons, S.F., White, N.C., John, D.A., 2005. Geological characteristics of epithermal precious and base metal deposits. In: Hedenquist, J.W., Thompson, J.H., Goldfarb, R.J., Richards, J.P. (Eds.), *Economic Geology* 100th Anniversary Volume. Society of Economic Geologists, pp. 485–522.
- Stacey, J.S., Kramers, J.D., 1975. Approximation of terrestrial lead isotope evolution by a two-stage model. *Earth and Planetary Science Letters* 26, 207–221.
- Stern, R.A., Rayner, N., 2003. Ages of Several Xenotime Megacrysts by ID-TIMS: Potential Reference Materials for Ion Microprobe U–Pb Geochronology: Radiogenic Age and Isotopic Studies: Report 16. Geological Survey of Canada: Current Research 2003-F1, p. 7.
- Teal, L., Jackson, M., 2002. Geologic overview of the Carlin trend gold deposits: gold deposits of the Carlin trend. Nevada Bureau of Mines and Geology, Bulletin 111, 9–29.
- Thorne, A.M., Seymour, D.B., 1991. Geology of the Ashburton basin Western Australia. Geological Survey of Western Australia Bulletin 139, 162.
- Tyler, I.M., Thorne, A.M., 1990. The northern margin of the Capricorn Orogen, Western Australia—an example of an Early Proterozoic collision zone. *Journal of Structural Geology* 12, 685–701.
- Wells, M., Laukamp, C., Hancock, E.A., 2016. Reflectance spectroscopic characterisation of mineral alteration footprints associated with sediment-hosted gold mineralisation at Mt Olympus (Ashburton Basin, Western Australia). *Australian Journal of Earth Sciences* 63, 987–1002.
- Wyborn, L.A.I., Heinrich, C.A., Jacques, A.L., 1994. Australian Proterozoic mineral systems: essential ingredients and mappable criteria. In: Hallenstien, P.C. (Ed.), *Australian Mining Looks North — the Challenges and Choices*. Australian Institute of Mining and Metallurgy: 1994 AUSIMM Annual Conference, Darwin, Northern Territory, pp. 109–115.
- Young, C.J., Groves, D.I., Morant, P., 2003. Sediment-hosted disseminated gold mineralisation in the Palaeoproterozoic Ashburton Province, Western Australia: a new epizonal orogenic gold province related to Capricorn Orogeny? In: Eliopoulos, et al. (Eds.), *Mineral Exploration and Sustainable Development, Proceedings of the 7th Biennial SGA Meeting*. Millpress, Athens, Greece, pp. 835–838.

APPENDIX 1D: STAR OF THE WEST

STATEMENT OF CONTRIBUTION OF OTHERS

Title of Paper: U-Pb dating of fault reactivation and gold mineralization in the northern Capricorn Orogen, Western Australia

Publication status: Under review (12/04/2018)

AUTHOR CONTRIBUTIONS

By signing the Statement of Authorship, each author certified that their stated contribution to the publication is accurate and that permission is granted for the publication to be included in the candidate's thesis.

Name of Principal Author: Imogen O. H. Fielding

Contribution to the paper: Conducted all field work, sample selection, sample preparation for SHRIMP analysis, including SEM identification and characterization of minerals prior to geochronology, petrography and production of SHRIMP mounts. Operation and interpretation of SHRIMP results, preparation of all images and writing and revisions of the manuscript.

Overall Percentage: 89%

Signature:

Date: 23/04/2018

Name of Co-Author: Simon P. Johnson

Contribution to the Paper: Assisted with sample collection and field work for the Amazon Shear Zone, data interpretation, editing and revision of the manuscript.

Overall Percentage: 5%

Signature:

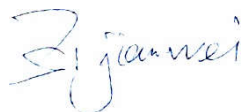
Date: 24/04/2018

Name of Co-Author: Jianwei Zi

Contribution to the Paper: Assisted with phosphate geochronology data collection, processing and manuscript editing.

Overall Percentage: 5%

Signature:



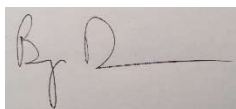
Date: 28/04/2018

Name of Co-Author: Birger Rasmussen

Contribution to the Paper: Assisted with manuscript editing.

Overall Percentage: 1%

Signature:



Date: 23/04/2018

APPENDIX 1E: GOLD METALLOGENY

STATEMENT OF CONTRIBUTION OF OTHERS

Title of Paper: Gold metallogeny of a Proterozoic orogen: the relationship between crustal architecture, fault reactivation and hydrothermal fluid flow.

Publication status: under review (17/04/2018)

AUTHOR CONTRIBUTIONS

By signing the Statement of Authorship, each author certified that their stated contribution to the publication is accurate and that permission is granted for the publication to be included in the candidate's thesis.

Name of Principal Author: Imogen O. H. Fielding

Contribution to the paper: Interpretation of results. Writing the manuscript and drafting/editing all images used in the manuscript.

Overall Percentage: 84%

Signature:



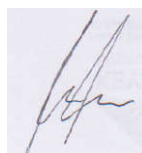
Date: 23/04/2018

Name of Co-Author: Simon P. Johnson

Contribution to the Paper: Assisted with data interpretation, editing and revision of the manuscript.

Overall Percentage: 10%

Signature:



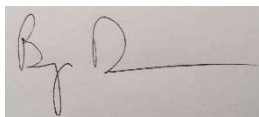
Date: 24/04/2018

Name of Co-Author: Birger Rasmussen

Contribution to the Paper: Assisted with manuscript editing.

Overall Percentage: 2%

Signature:



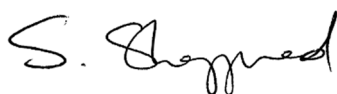
Date: 23/04/2018

Name of Co-Author: Stephen Sheppard

Contribution to the Paper: Assisted with editing the manuscript.

Overall Percentage: 2%

Signature:



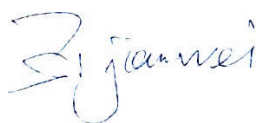
Date: 21/04/2018

Name of Co-Author: Jianwei Zi

Contribution to the Paper: Assisted with manuscript editing.

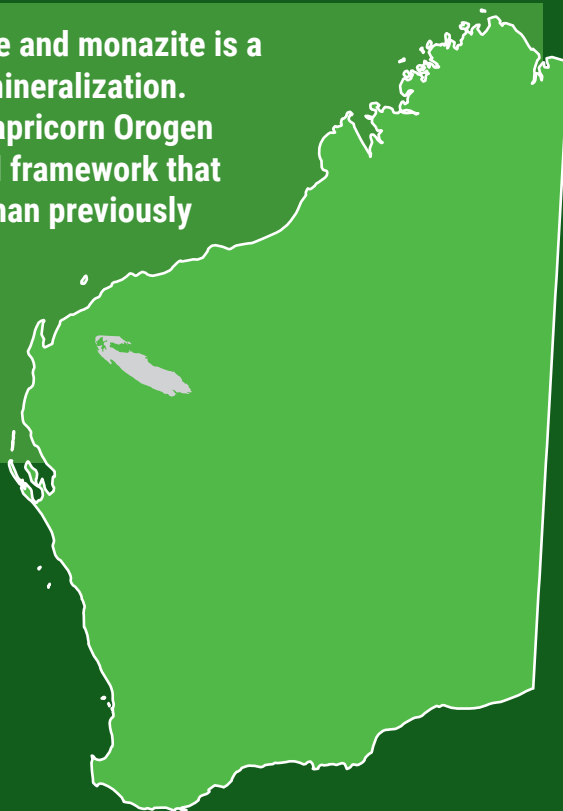
Overall Percentage: 2%

Signature:



Date: 28/04/2018

In situ SHRIMP U-Pb geochronology of xenotime and monazite is a powerful method for dating hydrothermal gold mineralization. This method has been applied to the northern Capricorn Orogen of Western Australia, providing a new geological framework that reveals a more complex mineralization history than previously recognized. The study has identified three gold mineralization events at 2.4, 1.77 and 1.68 Ga and demonstrates a direct link between fault reactivation, hydrothermal fluid flow and orogenesis.



Further details of geoscience products are available from:

Information Centre
Department of Mines, Industry Regulation and Safety
100 Plain Street
EAST PERTH WA 6004
Phone: (08) 9222 3459 Fax: (08) 9222 3444
www.dmp.wa.gov.au/GSWApublications